

SKYRMIONS AND MONOPOLES
IN CHIRAL MAGNETS
&
CORRELATED HETEROSTRUCTURES

Inaugural-Dissertation
zur
Erlangung des Doktorgrades
der Mathematisch-Naturwissenschaftlichen Fakultät
der Universität zu Köln
vorgelegt von

Christoph Schütte

aus

Dormagen



Köln 2014

Berichterstatter: Prof. Dr. Achim Rosch
(Gutachter)
Priv.-Doz. Dr. Ralf Bulla

Tag der mündlichen Prüfung: 17. April 2014

Abstract

The first part of this thesis is called “Skyrmions and Monopoles in Chiral Magnets” and concerned with topological spin textures in chiral magnets. The second part, “Correlated Heterostructures”, studies layered, strongly correlated devices within the framework of dynamical mean-field theory.

In magnets without inversion symmetry, so called chiral magnets, weak spin-orbit coupling leads to the formation of smooth twisted magnetic structures with a long period. Recently, a new magnetic phase of a lattice of topologically stable whirl-lines was discovered. In the first chapter we introduce the concept of a such a whirling texture and briefly mention its occurrence in other areas of physics. In chapters 2 we review the Ginzburg-Landau theory for chiral magnetic structures describing their equilibrium properties followed by a description of a numerical minimisation technique to explore the mean-field configuration of the free energy functional. In chapter 3 we review the Langevin description for a system at finite temperature and concentrate on especially on the description of magnetic systems. We describe how a numerical integration of the equations of motion, a stochastically differential equation, can be achieved to compute ensemble-averaged quantities. Chapter 4 we present the discovery of emergent magnetic monopoles as the driving mechanism behind topological phase transitions from the Skyrmion lattice into topologically trivial phases. We describe how a Skyrmion lattice unwinds due to the motion of magnetic monopoles in the system as seen both in experiment and numerical simulations. We investigate how the energetics of and forces between monopoles and antimonopoles influence their creation rate and dynamics. In chapter 5 we turn to the dynamical properties of single Skyrmions in ferromagnetic backgrounds. In a first approach we study analytically the fluctuations around the mean-field configuration and determine the spectrum of the bound states, the scattering solutions and their phase shifts and coupling mechanism to the collective Skyrmion coordinate. By integrating out the fluctuations we discover a strongly frequency-dependent effective mass for the collective Skyrmion coordinate. We approach the same question from a different angle in the second part of the chapter. Here we

start from numerical simulations of the stochastic Landau-Lifshitz-Gilbert equation and determine the coefficients of the effective equations of motion from a statistical analysis of the collective coordinate fluctuations. We find a strongly frequency-dependent effective mass and a new peculiar damping mechanism proportional to the acceleration of the Skyrmion that we call ‘gyro-damping’.

The second part of this thesis explores the interface effects in strongly correlated heterostructures. Multilayered heterostructures in the nano sized realm (also known as multilayered nanostructures) are the most common electronic devices. A classic multilayered nanostructure is a tunnel junction consisting of two metallic leads connected by a “weak link”, often a conventional band insulator. The connection between the two leads is thus governed by inherently quantum mechanical effects. We begin with an introduction to model Hamiltonians, in particular the Hubbard and the single impurity Anderson model. The second chapter describes the static mean-field treatment of anti-ferromagnetic order in the Hubbard model. Chapter 3 introduces the reader to the dynamical mean-field theory (DMFT) and describes extensions of the DMFT to system with antiferromagnetic order. The DMFT maps the lattice problem onto an effective impurity problem. In chapter 4 we review how the single impurity Anderson model can be solved using the numerical renormalisation group (NRG). The generalisation of DMFT to inhomogeneous, layered systems is given in chapter 5 including the effects of long-range Coulomb interactions on the Hartree level. Here we also outline our generalisation of the inhomogeneous DMFT to systems with antiferromagnetic order. In chapter 6 we derive expressions for the layer-resolved optical conductivity and the Hall conductivity. We apply the former to the Mott-Band-Mott heterostructure where we study the transport properties of the two-dimensional metallic state at the interface where we find a rich temperature dependence. In chapter 7 we turn to the question how the transmission amplitude through a Mott insulator in a linear potential depends on temperature.

Kurzzusammenfassung

Der erste Teil dieser Arbeit "Skyrmionen und Monopole in chiralen Magneten" beschäftigt sich mit topologischen Magnetisierungs-Texturen in chiralen Magneten. Der zweite Teil, "Korrelierte Heterostrukturen", untersucht Korrelations-Effekte an Grenzschichten zwischen verschiedenen Materialien in Heterostrukturen.

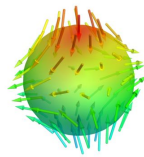
In chiralen Magneten bilden sich auf Grund schwacher Spin-Bahn- Wechselwirkung verdrillte, magnetische Konfigurationen aus, wie beispielsweise Helizes mit einer langen Periodenlänge. Kürzlich wurde eine neue magnetische Texture bestehend aus topologisch stabilen "Wirbel-Linien", sogenannten Skyrmionen, entdeckt. In dieser Arbeit untersuchen wir den topologischen Mechanismus, der zu einer Zerstörung des Skyrmionen-Gitters in Phasenübergängen führt. Wir untersuchen darüber hinaus die dynamischen Eigenschaften von getriebenen Skyrmionen eingebettet in einen ferromagnetischen Hintergrund.

Im zweiten Teil dieser Arbeit beschäftigen wir uns mit Heterostrukturen in Rahmen der dynamischen Molekularfeld Theorie. Speziell untersuchen wir Grenzschichteffekte von stark-korrelierten, geschichteten Systemen. Wir berechnen schicht-aufgelöste Transportkoeffizienten und Tunnelwahrscheinlichkeiten durch Mott-Barrieren.

Contents

I	Skyrmions and Monopoles in Chiral Magnets	1
II	Correlated Heterostructures	143

Skyrmions and Monopoles in Chiral Magnets



Introduction

Nowadays, topology has firmly established itself as a vital tool in every physicists' mathematical arsenal and all modern theories contain topological ideas of some sort or another. The applications range from the gauge theories in particle physics, where monopoles, instantons and solitons describe non-perturbative excitations, to the space time topology of general relativity. Also in condensed matter physics topology has proven itself indispensable. Noteworthy occurrences include topological insulators, the quantum Hall effect and defects in ordered media. The unique role topology plays in physics established its status as a universal and ubiquitous paradigm.

The links between the very old subject of physics and the much younger¹ mathematical discipline of topology date back to the 19th century. The earliest connection occurs in the work of Kirchhoff, 1847, who uses graph-theoretical methods to solve the equations for a general electric network [51]. But also mathematicians have found interesting applications of topological ideas to physical problems. For instance, Gauss noted that Ampere's law may be understood as the linking number between two curves and iterated his confidence that this is only one of many topological ideas to be eventually discovered in the field of physics [37]. One of the most common applications of topology in present-day condensed matter physics may be homotopy theory which is vital for the description of topological solitons.

Topological solitons are classical solutions of the Lagrangian equations of motion homotopically distinct from the vacuum solution. Often this occurs when the surface on which the boundary condition is specified has a non-trivial homotopy group. Such solutions can be interpreted as particles of the theory which owe their stability against (quantum-) fluctuations to their non-trivial topology. Historically, the first example of a topological soliton model for an elementary particle was the Skyrmion. The Skyrmion emerged from the Yukawa model, a field theory for the three types of spinless pions. Skyrme believed that the particles in a nucleus were moving in a non-linear, classical pion medium [93]. Symmetry arguments lead to a particular form of the Lagrangian which allowed topologically stable soliton solutions of the classical field equations, distinct from the vacuum. These solutions could then be understood as baryons.

As mathematical objects Skyrmons have also gained importance in solid state physics. Here a noteworthy example is a two-dimensional electron gas exhibiting the integer quantum Hall effect. The low energy theory of such a system has the structure of a quantum ferromagnet with elementary excitations given by dressed particles

¹Listing was the first to use the term 'Topologie' in 1836 [61].

whose local magnetisation wraps the Bloch sphere once when exploring the two-dimensional plane. In analogy to the mathematical structure of Skyrme’s solutions these excitations are referred to as Skyrmions. Another occurrence of Skyrmions in solid state physics was discovered in 2009 when a Skyrmion lattice was shown to exist in the chiral magnet MnSi as the stable phase in a region of the magnetic phase diagram [72]. Here similar to a vortex lattice in type-II superconductors, the magnetic phase is characterised by a hexagonal lattice of magnetic whirls arranged in a plane perpendicular to an applied magnetic field and translationally invariant along the direction of the field. The magnetisation throughout the unit cell remains finite, wraps the unit sphere once and can thus be described by an integer-valued topological index, i.e. a winding number. The discovery of the Skyrmion lattice has spurred great interest in these whirling spin textures and raised hopes that they might find application in spintronic devices and future information storage technologies.

In this part of the thesis, we study the dynamical properties of Skyrmions in chiral magnets. We begin with a general introduction to Skyrmions and a brief summary of their discovery in chiral magnets in chapter 1. In the following we outline the Ginzburg-Landau theory for magnetic systems in chapter 2 and the Langevin approach to magnetic systems at finite temperature in chapter 3. The non-trivial topology of Skyrmions has important implications for the destruction of the Skyrmion lattice. For instance, due to the conservation of topological charge phase transitions from the Skyrmion lattice into a topologically trivial phase necessarily lead to the appearance of magnetic point defects in the system since the destruction of Skyrmions changes the winding number of the system. In accordance with topological constraints these defects exhibit properties characteristic of magnetic monopoles and we thus refer to them as “emergent magnetic monopoles”. Chapter 4 describes the experimental discovery and analyses their energetics and dynamics through micro-magnetic simulations and numerical minimisation of the free energy functional.

The study of the effective dynamics of single Skyrmion excitations in the ferromagnetic background is important both from the point of view of fundamental research and possible applications in spintronic devices. In chapter 5 we analyse the fluctuation spectrum around the classical solution of the Lagrangian equations of motion in the single Skyrmion sector by explicitly calculating both the scattering wave functions and internal modes of the Skyrmion. A perturbative expansion in the fluctuations yields a fluctuation-induced inertia term. In section 5.2 we extract the effective equations of motion for a Skyrmion from the statistical analysis of its diffusive motion and study its dynamics when driven by time-dependent electric currents and magnetic field gradients.

Contents

1	Skyrmions	7
1.1	What is a Skyrmion?	7
1.2	Skyrmions in other areas of physics	9
1.3	Discovery of the Skyrmion lattice in MnSi	11
I	Methods	19
2	Ginzburg-Landau theory for Helimagnets	21
2.1	Theory of continuum phase transitions	21
2.2	Ginzburg-Landau theory for magnetic systems	23
2.2.1	Inversion-symmetric magnetic systems	24
2.2.2	Non-inversion-symmetric magnetic systems	25
2.3	Numerical minimisation of the Ginzburg-Landau functional	26
2.4	First applications	29
3	Langevin dynamics of magnetic systems	33
3.1	The Langevin equation	33
3.1.1	The Langevin approach to Brownian motion	34
3.1.2	The Itô and Stratonovich dilemma	36
3.2	Equations of motion for magnetic systems	37
3.2.1	Landau-Lifschitz-Gilbert equation	37
3.2.2	Spin-Transfer Torques	38
3.2.3	Stochastic Landau-Lifschitz-Gilbert equation	40
3.2.4	Numerical integration of the stochastic Landau-Lifschitz-Gilbert equation	42
II	Projects	47
4	Emergent magnetic monopoles	49
4.1	The Dirac monopole	50
4.2	Magnetic Monopoles in Spin Ice	51
4.3	Emergent Magnetic Monopoles in Chiral Magnets	54
4.3.1	Emergent Electrodynamics of Skyrmions	54
4.3.2	Unwinding of a Skyrmion Lattice	61

4.3.3	Dynamics and energetics of emergent magnetic monopoles . . .	71
4.4	Conclusion	80
5	Effective Mass of the Skyrmion	83
5.1	Quantum Mass of the Skyrmion	84
5.1.1	Effective mass in the ϕ^4 field theory	84
5.1.2	Model and skyrmion solution	85
5.1.3	Fluctuation spectrum and scattering phase shifts	89
5.1.4	Fluctuation-induced inertia terms	97
5.2	Effective Equations of Motion from Micromagnetic Simulations	103
5.2.1	Effective equations of motion for a single skyrmion	104
5.2.2	Dynamics of a driven Skyrmion	110
5.3	Conclusion	113
	Bibliography	115
A	Materials	125
A.1	Iron-Cobalt-Silicide - $\text{Fe}_{1-x}\text{Co}_x\text{Si}$	125
A.2	Iron-Germanium - FeGe	126
A.3	Multiferroic Cu_2OSeO_3	127
B	Experimental Techniques	131
B.1	Small Angle Neutron Scattering	131
B.2	Real-Space Imaging Techniques	133
B.2.1	Magnetic Force Microscopy	134
B.2.2	Lorentz Transmission Electron Microscopy	134
C	Conjugate Gradient Algorithm	137
C.1	Conjugate directions	137
C.2	Conjugate gradients	139
C.3	Minimisation of general functions	139
D	Appendix Quantum Mass	141
D.1	Expression for $\tilde{H}_{\alpha\beta}$	141
D.2	WKB	141

Chapter 1

Skyrmions

In the original sense of the word, a ‘Skyrmion’ is a topological soliton solution known to occur in a non-linear field theory for interacting pions originally conceived by the nuclear physicist Tony Skyrme [93]. In a more permissive interpretation of the word Skyrmions, as mathematical objects, have found versatile application in a variety of different areas in physics. In this chapter we briefly review the historic origin of the Skyrmion and define the generalised concept that is nowadays understood as a ‘Skyrmion’. We outline previous applications in different fields of physics and then forward to 2009 to give a concise account of the discovery of the Skyrmion lattice phase in the chiral magnet MnSi.

1.1 What is a Skyrmion?

In 1961 before the advent of quantum chromodynamics (QCD) the nuclear physicist T.H.R. Skyrme conjectured that the interior of a nucleus is dominated by a medium formed from three pion fields [93]. He introduced the Skyrme model, a non-linear sigma model, with the intention to describe baryons as the quantised soliton solutions of a field theory which involves only bosonic degrees of freedom. The model is understood as an intermediate between the traditional models which represent the nucleons as point particles interacting through a potential, and a complete description based on quarks and gluons [4]. The pion fields $\boldsymbol{\pi} = (\pi_1, \pi_2, \pi_3)$ are combined into a $SU(2)$ -valued field

$$U(\mathbf{x}) = \sqrt{1 - \boldsymbol{\pi}(\mathbf{x}) \cdot \boldsymbol{\pi}(\mathbf{x})} \mathbb{1} + i\boldsymbol{\pi}(\mathbf{x}) \cdot \boldsymbol{\sigma} , \quad (1.1)$$

where $\boldsymbol{\sigma}$ is the vector of Pauli matrices and we have suppressed a possible time dependence of the fields. For static fields the energy in the Skyrme model is given by

$$E = \int d^3\mathbf{r} \left(-\frac{1}{2}\text{Tr}(R_i R_i) - \frac{1}{16}\text{Tr}([R_i, R_j][R_i, R_j]) \right) , \quad (1.2)$$

where we have introduced an associated current $R_i = (\partial_i U)U^\dagger$ and $[\cdot, \cdot]$ denotes the commutator. The vacuum is represented by $U(\mathbf{x}) = \mathbb{1}$. For the energy to be finite, U must approach a constant at infinity [65]. The energy is invariant under translations

and rotations in \mathbb{R}^3 and also under the transformation $U \rightarrow AUA^\dagger$ with $A \in SU(2)$, one may thus choose $U(\mathbf{r} \rightarrow \infty) = \mathbb{1}$. Effectively, due to this boundary condition space is then topologically (but not metrically) compactified to \mathbb{S}^3 , and since the group manifold of $SU(2)$ is also \mathbb{S}^3 , U defines a map from \mathbb{S}^3 to \mathbb{S}^3 . The structure of the homotopically distinct maps U is given by the third homotopy group $\pi_3(\mathbb{S}^3)$ which happens to be isomorphic to \mathbb{Z} . The space of all maps $U : \mathbb{S}^3 \rightarrow \mathbb{S}^3$ decomposes into distinct subsets characterised by an integer-valued topological charge $B = \int d^3\mathbf{r} \mathcal{B}$ with the topological charge density \mathcal{B} given by

$$\mathcal{B} = -\frac{1}{24\pi^2} \epsilon_{ijk} \text{Tr}(R_i R_j R_k) . \quad (1.3)$$

The minimal energy solutions for each B are called Skyrmions and their energy is identified with their mass and B with the Baryon number of the nucleus. The $B = 1$ Skyrmion has the spherically symmetric hedgehog form [65]

$$U(\mathbf{x}) = \exp(if(r)\hat{\mathbf{r}} \cdot \boldsymbol{\sigma}) , \quad (1.4)$$

where $f(r)$ is a radial profile function obeying an ordinary differential equation with the boundary conditions $f(0) = \pi$ and $f(r \rightarrow \infty) = 0$.

Skyrmions in their original sense are therefore smooth, topologically stable extremal field configurations which are trivial at spatial infinity and have a finite energy. They are defined by surjective mappings into the order parameter space \mathbb{S}^3 and characterised by a non-trivial topological charge B . Since the n th homotopy group of \mathbb{S}^n is isomorphic to \mathbb{Z} for any $n \geq 1$, a more permissive definition of ‘‘Skyrmion’’ is given by

A skyrmion is a smooth field configuration defined by a topologically non-trivial, surjective mapping from a base manifold \mathcal{M} into the order parameter space $\mathcal{T} \simeq \mathbb{S}^n$, trivial on the surface of \mathcal{M} and characterised by a finite integer-valued topological charge.

Fig. 1.1 shows the construction recipe for $\mathcal{M} = \mathbb{R}^2$ and $\mathcal{T} = \mathbb{S}^2$. We start with the identity map, $\hat{\Omega}(\hat{\mathbf{x}}) = \hat{\mathbf{x}}$, with $\hat{\mathbf{x}} \in \mathbb{S}^2$ which can be visualised as a hedgehog configuration (c.f. Fig. 1.1, top left). The stereographic projection \mathcal{P} maps the sphere onto the two-dimensional plane, $\mathcal{P}(\hat{\mathbf{x}}) \in \mathbb{R}^2$ and thus a Skyrmion configuration is given by the mapping $\hat{M} : \mathbb{R}^2 \rightarrow \mathbb{S}^2$, $\hat{M} : \mathbf{r} \mapsto \hat{\Omega} \circ \mathcal{P}^{-1}(\mathbf{r})$. The corresponding topological charge W is given by $\int d^2\mathbf{r} \mathcal{W}$ where we have defined the topological charge density \mathcal{W} as

$$\mathcal{W} = \frac{1}{8\pi} \hat{M} \cdot (\partial_x \hat{M} \times \partial_y \hat{M}) . \quad (1.5)$$

W counts the number of times the mapping \hat{M} sweeps out the target manifold \mathbb{S}^2 . From the construction recipe above it is obvious that for the Skyrmion (Fig. 1.1 lower left) $W = -1$. The color code has been chosen such that arrows pointing to the north pole are plotted in red and those to the south pole as blue and the equator in green.

A chiral, non-inversion symmetric Skyrmion can be constructed if the hedgehog is additionally ‘combed’ by performing a $\pi/2$ rotation \mathcal{R} about the \hat{z} -axis in order parameter space (Fig. 1.1 top right), $\hat{N} : \mathbf{r} \mapsto \mathcal{R} \circ \hat{\Omega} \circ \mathcal{P}^{-1}(\mathbf{r})$. \mathcal{R} is a linear map on \mathcal{S}^2

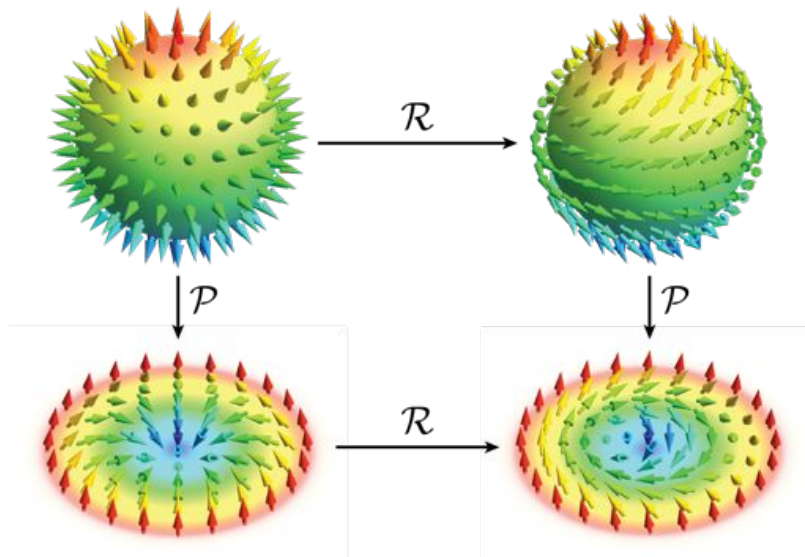


Figure 1.1: Construction recipes for the non-chiral and chiral skyrmion from the hedgehog configuration. \mathcal{R} denotes a rotation about the \hat{z} -axis acting in order parameter space and \mathcal{P} the stereographic projection.

and therefore $W = -1$ for this configuration as well. These later, chiral Skyrmions (Fig. 1.1 lower right) will be the main focus of this thesis. In contrast to a Skyrmion, a vortex does not sweep out the whole sphere. For example a vortex configuration is given by the map $V : \mathbb{R}^2 \rightarrow \mathbb{S}^2$, $V : \mathbf{r} \mapsto \hat{e}_\phi(\mathbf{r})$, where $\hat{e}_\phi = (-\sin(\phi), \cos(\phi), 0)^T$ in polar coordinates (r, ϕ) . The vortex only sweeps out the equator, is singular at $\mathbf{r} = 0$ and has a non-trivial winding for $\mathbf{r} \rightarrow \infty$.

1.2 Skyrmions in other areas of physics

Within this generalised understanding Skyrmions have found versatile application in many different fields of physics. Here we only mention a few.

In 1985 Klebanov proposed the possibility of a Skyrmion crystal [52]. A phenomenological application of this kind of a solution could be a neutron crystal, which may exist under high pressure inside neutron stars [108]. The theory might resolve puzzles concerning discrepancies about the maximum mass of stable neutron stars between observations and predictions by more traditional equation of state descriptions [47].

Liquid crystals are states of matter which show characteristics of those of a conventional liquid and those of a solid crystal. Many interesting ordering phenomena have been reported in these systems where the local order parameter is describe by a director field (a field of headless vectors) rather than a vector field [110]. Among these the blue phases which have a regular three-dimensional cubic structure of defects with lattice periods of several hundred nanometers are particularly interesting. Here so-called 2π disclinations are singular line defects where the 2π indicates that

the director rotates a full 360° as the singular line is encircled. These singular defect configurations are unstable towards a non-singular configuration that differs from its original one only in the immediate neighborhood of the formerly singular line. For the 2π disclinations these non-singular configurations are given by Skyrmion configurations of directors in $n = 2$. Recently it was shown theoretically [34], with the aid of numerical methods, that a highly chiral nematic liquid crystal can accommodate a quasi-two-dimensional Skyrmion lattice as a thermodynamically stable state, when it is confined to a thin film between two parallel surfaces.

Skyrmions were predicted to occur in quantum Hall systems close to the Landau level filling fraction $\nu = 1$ for sufficiently small Zeeman splitting $g\mu_B B$ (compared to the the cyclotron gap $\omega_c = eB/mc$) [97]. The incompressible ground state of a two-dimensional electron gas at this filling fraction is ferromagnetic. For sufficiently small $g < g_c$ the charged excitations of the system were argued to be Skyrmions where their winding number is related to the charge νe of the Skyrmion. The equivalence of physical charge and topological charge in the system is a consequence of the quantum Hall effect and is responsible for the dominating role of Skyrmions in determining many physical properties [28]. Brey and collaborators proposed that ground state close to $\nu = 1$ is a crystal of charged Skyrmions [11]. Nuclear magnetic resonance measurements in GaAs provided only indirect evidence [3, 92].

Topologically, skyrmions are equivalent to certain magnetic bubbles (cylindrical domains) in ferromagnetic thin films, which were extensively explored in the 1970s for data storage applications [64]. In ferromagnets where long-range order is frustrated due to long-range dipole-dipole interactions a wealth of different magnetic patterns can be seen, such as domain walls, vortices and periodic stripes. In Ref. [112] Lorentz transmission electron microscopy (LTEM) was used to show that a magnetic field applied perpendicular to a thin film of hexaferrite turns the periodic stripe domain state into a periodic, hexagonal lattice of chiral Skyrmion bubbles (c.f. Fig 1.1 lower right). In contrast to other materials however where the inversion symmetry of the atomic unit cell is broken, in hexaferrite the helicity of the Skyrmion is not fixed by crystal structure, but represent a \mathbb{Z}_2 degree of freedom and a random distribution of different helicities in the lattice can be observed. Here even helicity reversals within a single Skyrmion where observed. Note that the helicity is independent of the winding number which can be seen from the fact that one may smoothly deform helicities into one another.

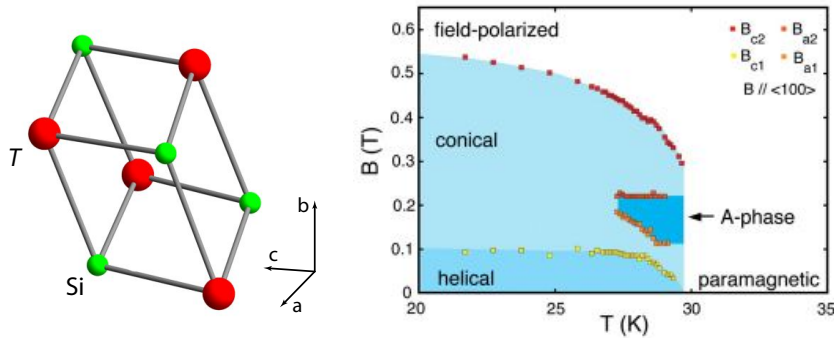
Bogdanov and collaborators studied the mean-field theory of easy-axis ferromagnets with chiral spin-orbit interactions. They argued that in certain parameter regimes a mixed state with a finite density of Skyrmions much like the vortex lattice in type II superconductors becomes the thermodynamically stable phase [10]. Although the stability analysis was carried out in the circular unit cell approximation the Skyrmion lattice was predicted to be hexagonal [10]. Here the presence of easy-axis anisotropy turned out to be a necessary ingredient for the stabilisation of the mixed phase within the mean-field treatment. Also they assumed the magnetization vector to be homogeneous along the z-axis [9].

1.3 Discovery of the Skyrmion lattice in MnSi

In 2009 Mühlbauer et al. reported the discovery of a Skyrmion lattice phase in the chiral magnet MnSi by a small angle neutron scattering study (SANS). Although in this section we concentrate on MnSi as the first chiral magnet the spontaneous formation of this phase of whirling magnetisation has been observed in, the Skyrmion lattice phase has since then been discovered in many other compounds as well. In 2010 the same group discovered a Skyrmion lattice phase in the doped semiconductor $\text{Fe}_{1-x}\text{Co}_x\text{Si}$ [73, 114]. The Skyrmion lattice phase in this material was also later confirmed by real-space images using Lorentz transmission electron microscopy (Lorentz TEM) [114]. Since then the Skyrmion lattice has been observed in a variety of different materials both as a bulk phase as well as in thin films. Appendix A gives a more elaborate description of the material properties and the magnetic phase diagram of various materials the phase has been observed in. Here we only want to mention that the electronic properties of this set of compounds is very diverse: Among these are metals, insulators, semi-conductors and also a multi-ferroic material. This show that the Skyrmion lattice is not a peculiarity of MnSi but rather a general phenomenon in this class of materials.

The unifying property for all of these materials is that they crystallise in the so-called B20 structure. The symmetry transformations are described by the space group $P2_13$ with a cubic Bravais lattice [38]. With only 12 symmetry operations this space group is among the smallest compatible with the cubic lattice crystal system. The point symmetry at the component sites is C_3 , the cyclic group of 3-fold $2\pi/3$ rotations about an appropriate [111] axis. The nonsymmorphic group $P2_13$ contains in addition 3 screw rotations which involve 2-fold rotations about one of the three [100] axis followed by an appropriate non-primitive translation $(0, \frac{1}{2}, \frac{1}{2})$. Most notably the list of symmetry transformations does not include the inversion. The lack of inversion symmetry has profound consequences for the Ginzburg-Landau free energy description of these materials and for the symmetry constraints on the magnetic configuration that the materials can show. Materials with non-inversion symmetric atomic unit-cells can support non-inversion symmetric magnetic structures. There are other mechanisms by which Skyrmion lattice phase can be stabilised. We will return to this point at the end of this chapter. Although we concentrate prodominantly on MnSi in this chapter, the magnetic phases of MnSi are generic for chiral magnets. Particularly the phase diagram Fig. 1.2b can be seen as a generic phase diagram for B20 compounds that order helimagnetically.

The primitive cell of manganese silicide (MnSi) contains four pairs of the 2 component formula units Mn and Si located at (u, u, u) , $(\frac{1}{2} + u, \frac{1}{2} - u, \bar{u})$, $(\frac{1}{2} - u, \bar{u}, \frac{1}{2} + u)$, and $(\bar{u}, \frac{1}{2} + u, \frac{1}{2} - u)$ with $u_{\text{Mn}} = 0.138$ and $u_{\text{Si}} = 0.845$. MnSi is an itinerant ferromagnet with a fluctuating magnetic moment of $0.4 \mu_{\text{B}}$ and a saturated moment of $2.2 \mu_{\text{B}}$ per manganese atom. Before the discovery of the skyrmion lattice phase, it already attracted attention due to a high pressure anomaly: Although described very well by Fermi-liquid theory at ambient pressure, MnSi shows a non-Fermi liquid phase above a critical pressure of $p_c \sim 14.6$ kbar with the temperature dependence of the resistivity given by $T^{3/2}$ [81, 79]. In addition in the pressure region 12 kbar – 20 kbar



(a) The atomic unit cell comprising four formula units of TSi with $T = Mn$. The atoms are located at (u, u, u) , $(\frac{1}{2} + u, \frac{1}{2} - u, \bar{u})$, $(\frac{1}{2} - u, \bar{u}, \frac{1}{2} + u)$, and $(\bar{u}, \frac{1}{2} + u, \frac{1}{2} - u)$ with $u_{Mn} = 0.138$ and $u_{Si} = 0.845$.

(b) Magnetic phase diagram of MnSi. For $B = 0$, helimagnetic order develops below $T_c = 29.5$ K. Above B_{c2} the material field polarises. For intermediate field values the conical phase develops with the Skyrmion lattice phase (A-phase) as a small phase pocket inset in a specific temperature and field range. Taken from Ref. [72].

Figure 1.2

a state of partial magnetic order was encountered in neutron scattering experiments [80].

At ambient pressure and zero applied magnetic field, MnSi develops magnetic order below a transition temperature $T_c = 29.5K$ that is the result of three hierarchical energy scales. The strongest scale is the ferromagnetic exchange favoring a uniform spin polarisation (spin alignment). The lack of inversion symmetry of the cubic B20 crystal structure results in chiral spin-orbit interactions, which may be described by the rotationally invariant Dzyaloshinsky Moriya (DM) interaction favoring canted spin configurations [22, 69]. The DM interaction originates from relativistic effects, i.e. spin orbit coupling $\lambda_{SO} \sim 10^{-2}$, and is the lowest order chiral spin-orbit interaction [2, 74, 83]. In addition there are very weak crystalline field interactions which break the rotational symmetry and align the ordering wave vector of the magnetic structures along the $[111]$ axes [83].

Magnetic phases of MnSi

The magnetic phase diagram of MnSi, Fig. 1.2b, shows four distinct magnetic phases: a helical phase, a conical phase, a field-polarized phase and the previously mentioned skyrmion lattice phase (for historical reasons referred to as the ‘‘A-phase’’ in the diagram). In the following we briefly describe the magnetic order in each of these.

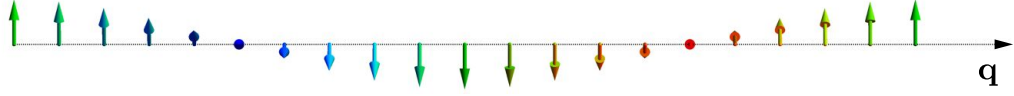


Figure 1.3: In the helical phase the magnetisation winds around the propagation vector \mathbf{q} . The magnetization vectors stand perpendicular on \mathbf{q} . Red arrows point into the paper, blue arrows out of it while green arrows lie in the plane of the paper.

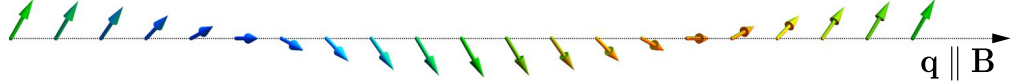


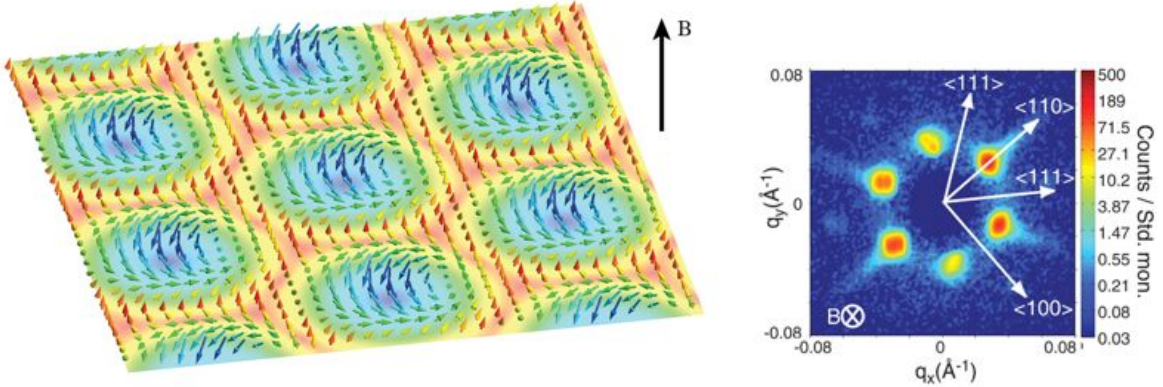
Figure 1.4: In the conical phase the spiral propagation vector \mathbf{q} aligns parallel to the applied magnetic field \mathbf{B} . The magnetization winds around the \mathbf{q} similar to the helical phase, however here the magnetic moments also tilt towards the propagation vector giving the configuration a uniform magnetisation component along \mathbf{B} . Red arrows point into the paper, blue arrows out of it while green arrows lie in the plane of the paper.

Helical phase

Cooling the system at zero or only small applied magnetic field below the critical temperature $T_c \sim 29$ K a phase transition to the helical phase is encountered. In this phase the magnetization winds around an axis parallel to the spiral propagation vector \mathbf{q} as shown in Fig. 1.3 with the local magnetic moment \mathbf{M} perpendicular to \mathbf{q} . The period of the helix, $\lambda_h = 2\pi/|\mathbf{q}|$ is controlled by the competition of the ferromagnetic exchange with the chiral spin-orbit coupling. The weakness of the spin-orbit interaction leads to a wavelength $\lambda_h \sim 190\text{\AA}$ which is large as compared with the lattice constant, $a \sim 4.56\text{\AA}$. This large separation of length scales results in an efficient decoupling of the magnetic and atomic structures. The direction of propagation $\hat{q} = \mathbf{q}/|\mathbf{q}|$ is determined by tiny crystal field anisotropies. Therefore, the alignment of the helical spin spiral along the cubic space diagonal [111] is weak and is only fourth power in the small spin-orbit coupling, λ_{SO}^4 . The decoupling from the underlying atomic structure results in an extremely coherent helical phase with a huge correlation length of 10^4\AA as reported in this neutron scattering study [59]. While the paramagnetic to helical transition is expected to be second order on a mean-field level, interactions between the helimagnetic fluctuations were theoretically predicted to give rise to important corrections. Indeed it was recently shown that a Brazovskii-type scenario is realized where an abundance of strongly interacting fluctuation distributed uniformly over a sphere in momentum space drives the transition first order [48].

Conical phase

Setting out in the helical phase one finds a phase change upon increasing the applied magnetic field above $B_{c_1} \sim 0.1$ T. The stronger magnetic field allows for a net reduction in free energy by building up a uniform magnetic moment in the direction of the applied field. While for high magnetic fields above $B_{c_2} \sim 0.6$ T the DM interaction can be completely neglected and the magnetic configuration completely



(a) In the skyrmion lattice phase the magnetic structure forms a hexagonal lattice of anti-skyrmions in the plane perpendicular to the applied magnetic field. The lattice constant is given by $2\lambda_h/\sqrt{3}$. The state possesses a translational invariance along the field magnetic field direction and should therefore be visualised as an ordered arrangement of whirling tubes. Here we show only one layer.

(b) Typical SANS intensities for the SkX phase. Red (blue) corresponds to high (low) intensity. The color scale is logarithmic to enhance small features. See main text for details.

polarizes, there is an intermediate field range where the magnetization winds both around a spiral propagation vector \mathbf{q} parallel to \mathbf{B} and in addition possesses a uniform magnetization in the direction of \mathbf{B} as the magnetisation vectors tilt towards $\hat{q} = \hat{B}$. The phase is referred to as the conical phase and is depicted in Fig. 1.4. On general grounds a crossover between the helical and the conical phase is expected where the ordering wave vector \mathbf{q} rotates continuously from the helical [111] direction towards the direction of the applied field. If applied along special high symmetry axis one may encounter a second order phase transition however. The angle between the propagation vector \mathbf{q} and the local magnetization \mathbf{M} is smooth function of the applied magnetic field \mathbf{B} and decreases to zero for $\mathbf{B} > \mathbf{B}_{c2}$.

Skyrmion lattice phase

A first order phase transition separates a tiny pocket in the magnetic phase diagram close to T_c at finite magnetic field from the surrounding conical phase. This region, termed for historical reasons “A-phase”, has a hexagonal lattice of anti-skyrmions perpendicular to the applied magnetic field as its ground state. An illustration of the skyrmion lattice is depicted in Fig. 1.5a. The configuration possesses a translational invariance along the direction of the applied magnetic field. The magnetisation configuration should therefore be imagined as an ordered arrangement of whirling tubes similar to the flux lattice in a type II superconductor. Fig. 1.5a shows only a single layer. The magnetic configuration can be approximated by a superposition of three helices with their propagation vectors lying in a plane perpendicular to the applied magnetic field and relative angles of 120° plus a uniform magnetic moment antiparallel to the applied field. The relative phases are aligned such that the magnetization in the center of the skyrmion points antiparallel to \mathbf{B} . The lattice constant is therefore

given by $2\lambda_h/\sqrt{3}$. The large lattice constant ensures an efficient decoupling of the magnetic structure from the underlying atomic lattice and allows for the orientation towards the applied field. The orientation of the hexagonal lattice within the plane however is determined by crystal field anisotropies. For a magnetic field in the [001] direction, for instance, one of the three \mathbf{q} vectors pins weakly in the [110] direction of the atomic crystal. The building blocks of the lattice are referred to as *anti*-skyrmions as their winding number per magnetic unit cell

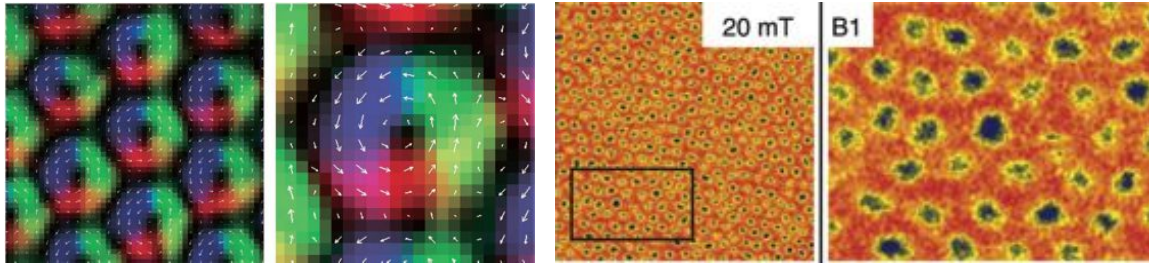
$$W = \frac{1}{4\pi} \int_{\text{UC}} \hat{M} \left(\partial_x \hat{M} \times \partial_y \hat{M} \right) \quad (1.6)$$

is quantized to -1. Here $\hat{M} = \mathbf{M}/|\mathbf{M}|$ and the integration is taken over the two-dimensional magnetic unit cell, which contains exactly one “knot”.

The experimental technique used by Mühlbauer et al. was small angle neutron scattering (SANS). Neutron scattering is an ideal tool for the study of magnetic order in bulk phases as neutrons predominantly scatter from the magnetic structure in a solid-state system due to their magnetic moment. The lack of an electric charge allows them to penetrate deep into the system under investigation. The neutrons scatter elastically due to the interaction of their spin with the nuclei and unpaired electrons of the magnetic atoms in the sample and the scattered neutrons are recorded by detectors placed behind the sample. The Fourier modes in the magnetic order are recorded as Bragg peaks in reciprocal space. A more detailed description of SANS can be found in Appendix B. The Skyrmion lattice can be approximated by three helices with their ordering wavevectors in a plane normal to the applied magnetic field and relative angles of 120° . In a typical neutron scattering experiment the incoming neutron beam is perpendicular to the applied magnetic field. In such a setup not all of the 6 reflection spots (two per helix at $+\mathbf{q}$ and $-\mathbf{q}$) can be seen simultaneously. The setup chosen by Mühlbauer et al. aligned the incoming beam parallel to the applied field. This setup is much more advantageous and allows to record all 6 spots at the same time, c.f. Fig. 1.5b.

Other experimental techniques were also able to prove the existence of the Skyrmion lattice. In recent years powerful real-space imaging techniques have been modified and applied to chiral magnetic systems which allow for a direct visualization of the spatial magnetization configuration. The advantage of such methods is that not only a single spin texture, but also the crystallization and melting process during phase conversions can be observed. Fig. 1.6a shows images of the Skyrmion lattice phase in a thin film of $\text{Fe}_{0.5}\text{Co}_{0.5}\text{Si}$ recorded by Lorentz transmission electron microscopy (LTEM). LTEM is a modification of traditional electron microscopy in which the Lorentz forces between the electrons in a beam and the sample are utilised to generate images which allow for the real-space observation of the magnetic structure of materials. The drawback of LTEM is that samples have to be electron transparent and therefore the technique can only be applied to thin films. Also LTEM images only the in-plane component of the magnetisation.

Real-space images of the surface of bulk materials can be recorded using the magnetic field microscopy (MFM). MFM images forces between the surface of a sample and the magnetic stray field of a cantilever tip coated with a ferromagnetic film. The total force acting on the cantilever is inferred from small changes in its resonance



(a) Lorentz TEM images of the Skyrmion lattice in $\text{Fe}_{0.5}\text{Co}_{0.5}\text{Si}$. Taken from Ref. [113]. (b) MFM images of Skyrmions from the surface of bulk $\text{Fe}_{0.5}\text{Co}_{0.5}\text{Si}$. Taken from Ref. [67].

Figure 1.6

frequency. It is complementary to LTEM in the sense that it is only sensitive to the out-of-plane component of the magnetisation. Fig. 1.6b shows MFM images of Skyrmions from the surface of bulk $\text{Fe}_{0.5}\text{Co}_{0.5}\text{Si}$. Red (blue) color indicates an out-of-plane component of the magnetisation that is anti-parallel (parallel) to the line of sight. For more information about real-space imaging techniques, see Appendix B.

Other physical quantities also show signatures in the Skyrmion lattice phase. For instance the magnetic AC susceptibility χ shows a sudden drop to a lower value when entering the Skyrmion phase from the conical phase by increasing the applied field. It then rises exceeding the value in the conical phase before entering the conical phase once again for higher magnetic fields [101]. A more dramatic effect can be seen in measurements of the Hall effect in MnSi. Here due to the unique topology of the Skyrmion lattice an additional top hat contribution to the Hall signal can be seen in the Skyrmion lattice phase [85]. Chapter 4 contains an elaborate discussion of the physical effect and the experimental measurements.

Ever since the original discovery of Skyrmions in chiral magnets in 2009, many exciting developments have deepened our understanding of these fascinating structures. Here we mention only a few. Neubauer et al. showed that the topological properties of the Skyrmion lattice lead to additional contribution to the Hall signal, called the topological Hall effect [75]. Everschor et al. analyzed the spin-transfer effects resulting from an electric current driven through a Skyrmion lattice, and, in particular, focussed on the current-induced rotation of the magnetic texture by an angle in such a setup [26]. Schulz and collaborators have shown that the forces acting on conduction electrons moving through a Skyrmion lattice can be accounted for by the introduction of emergent (fictitious) electromagnetic fields. This offered fundamental insights into the connection between the emergent and real electrodynamics of skyrmions in chiral magnets [88]. Iwasaki et al. showed in a numerical study that a single skyrmion can be created by an electric current in a simple constricted geometry comprising a plate-shaped specimen of suitable size and geometry [45]. In experimental realisation of Skyrmion creation however with a different mechanism was reported by Romming and collaborators in 2013. They showed that on an ultrathin magnetic film in which individual skyrmions can be written and deleted in a controlled fashion with local spin-polarized currents from a scanning tunneling microscope [86]. There have been

many more interesting and noteworthy publications which we cannot mention here and without question there will be many more.

Part I

Methods

Chapter 2

Ginzburg-Landau theory for Helimagnets

In the vicinity of a second order phase transition, the correlation length of a system diverges. This indicates that the properties near the critical point are independent of the microscopic details. Many universal system properties can therefore be described by phenomenological theories which reduce the redundancy in the system description greatly. A phenomenological theory for continuum phase transitions is given by the so called Ginzburg-Landau theory. Based on Landau's theory of second-order phase transitions [57], Ginzburg and Landau expanded the free energy of a superconductor in terms of an order parameter ψ , which is nonzero in the ordered phase and vanishes above the transition temperature T_c thus laying the foundation for what became one of the most successful and widely used theories in condensed matter physics.

In this chapter we will give an introduction to Ginzburg-Landau theory for the description of magnetic systems. In section 2.1 we will start with a very general description of the structure of this theory and then apply it to the special case of helimagnets in section 2.2.1.

2.1 Theory of continuum phase transitions

The microscopic origin of magnetism in metals involves the quantum mechanical treatment of spinful, itinerant electrons and is highly complicated and material dependent. The full theory allows to answer the question which materials will exhibit ferromagnetism. However assuming that a given system shows such behaviour, a microscopic theory is neither necessary nor desirable to describe for instance the disappearance of magnetic order due to thermal fluctuations. The degrees of freedom which describe the transition are long wave-length collective spin excitations with typical length scales much in excess of the lattice constant. Therefore an effective description can be achieved by coarse-graining the system and modelling the magnetic order by the *average* magnetization of a large number of spins. The average magnetization is then a smooth function on the the length scale of the lattice constant and one arrives at a continuum theory.

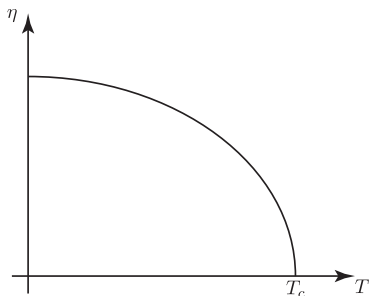


Figure 2.1: The order parameter depends on temperature and other external parameters. In second-order phase transitions the order parameter is a continuous function of the system temperature T and vanishes above a critical temperature T_c .

The state of many condensed matter systems can be described by the appearance of a certain order in the system or the absence of the same. The order parameter is a concept which seeks to quantify the “amount of order” present in the system. Examples of order parameters are, for instance: magnetization M (ferromagnets), polarization P (ferroelectrics), distortions (structural transitions) and the complex order parameter field Ψ in superconducting systems.

Typically at high temperatures the system is disordered as the state is chosen by minimization of the corresponding thermodynamic potential, i.e. Gibbs free energy. For large T the deciding factor is the entropy of the system, which it seeks to maximize hence favouring disordered system. Lowering the temperature the importance of the entropy is diminished and the system seeks to optimize its internal energy arranging its degrees of freedom in an ordered fashion.

Therefore the order parameter η of the system depends on temperature and other external parameters. For now we will assume that the state of the system can be described by a spatially homogeneous order parameter. It is non-zero in the ordered phase of the system and vanishes upon increasing the system temperature above the critical temperature T_c . For second order phase transitions this happens in a continuous fashion, Fig. 2.1. The state of the system and in particular the value of the order parameter η is determined by the condition that the (Gibbs) free energy G is minimized. The free energy is related to the system's partition function Z

$$Z = e^{-G} = \int \mathcal{D}\eta e^{-F[\eta]}, \quad (2.1)$$

where $F[\eta]$ is the free energy functional.

Due to the smallness of η close to the critical point T_c the free energy functional $F[\eta]$ can be expanded in a power series

$$F[\eta] = F_0 + \alpha\eta + \beta\eta^2 + \gamma\eta^3 + \delta\eta^4 + \dots \quad (2.2)$$

It should be noted that this expansion can only involve terms, which are compatible with the symmetries of the microscopic Hamiltonian. The coefficients are functions of the external system parameters. In the mean-field approximation one simply looks at

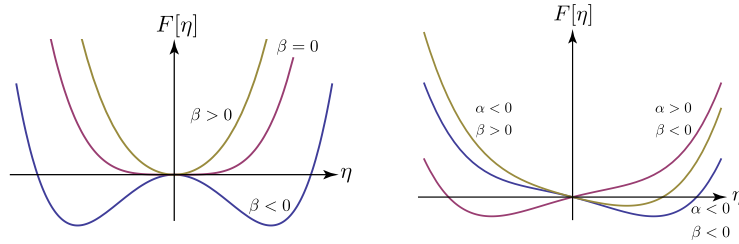


Figure 2.2: Sketched dependence of the free energy $F[\eta]$ on the parameters α and β . For $\alpha = 0$ (no external field) the order parameter vanishes above the transition temperature, i.e. $\beta(T > T_c) \geq 0$.

the stationary points of the free energy functional, neglecting any fluctuations around this point,

$$G \sim \min_{\eta} F[\eta] = F[\eta_0]. \quad (2.3)$$

For a vanishing linear term $\sim \alpha$ the free energy functional develops a minimum at $\eta = 0$ for $T > T_c$; the order parameter vanishes above the critical temperature. The quadratic term must obey the conditions

$$\begin{aligned} \beta(T) &< 0, \text{ for } T > T_c \\ \beta(T) &> 0, \text{ for } T < T_c \end{aligned} \quad (2.4)$$

If the expansion of the free energy is truncated at 4th order the thermodynamic stability of the system is ensured, i.e. a diverging order parameter η is prevented, only if the prefactor of the quartic term is positive, $\delta > 0$. The dependence of $F[\eta]$ is sketched in Fig. 2.2.

The Gaussian fluctuations around the mean field η_0 are the leading order correction to the mean field result

$$G \sim F[\eta_0] + \frac{1}{2} \ln \det \left(\frac{\delta^2 F}{\delta \eta \delta \eta} \right) \Big|_{\eta_0} \quad (2.5)$$

As we will see later these fluctuations can play a decisive role as to what phase the system will actually realize.

2.2 Ginzburg-Landau theory for magnetic systems

For a ferromagnetic system, such as iron, the order parameter is given by the magnetization \mathbf{M} . Below the critical temperature T_c , the Curie temperature, the system spontaneously orders characterized by a finite magnetization \mathbf{M} , the thermal average of the microscopic magnetic moments. The magnetization is the conjugate, thermodynamic variable to the applied magnetic field \mathbf{H} . Fixing the direction of $\mathbf{H} = H \hat{e}_z$ one finds that for temperatures $T < T_c$ the regime $H > 0$ and $H < 0$ is separated by a line of phase transitions, which ends at $T = T_c$ at the critical point C , see Fig. 2.3. The system may be brought from the one regime to the other either by choosing a discontinuous path which crosses the phase boundary (path **A**) or continuously by driving it around the critical point, $T > T_c$ (path **B**).

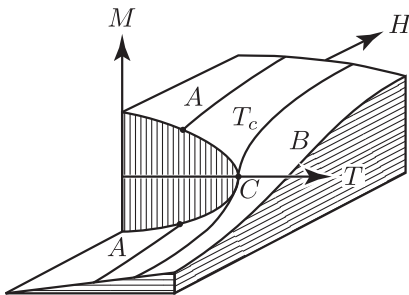


Figure 2.3: Phase diagram for a ferromagnet. Here the surface of the equation of state is shown in the space of the conjugate variables, magnetization \mathbf{M} and external magnetic field \mathbf{H} , and temperature T . For any two states in the state space a connecting, continuous path may be found that avoids the line of phase transition, $\mathbf{H} = 0$ and $0 \leq T < T_c$, by going around the critical point C .

2.2.1 Inversion-symmetric magnetic systems

In the absence of an applied magnetic field the Hamiltonian of typical ferromagnetic system is invariant under

1. spatial inversion, $\mathbf{r} \rightarrow \mathbf{r}' = -\mathbf{r}$
2. time-reversal, $t \rightarrow t' = -t$

In addition in the presence of a magnetic field \mathbf{H} it possesses the symmetry $\mathbf{M} \rightarrow -\mathbf{M}$ if $\mathbf{H} \rightarrow -\mathbf{H}$. As can be seen in Fig. 2.3 the magnetization \mathbf{M} is small in the immediate vicinity of the Curie point C and the correlation length ζ diverges. Therefore it is possible to expand the free energy functional $F[\mathbf{M}]$ in terms of \mathbf{M} and $\nabla\mathbf{M}$. The above list of transformations poses a minimal symmetry requirement that each term in the expansion has to fulfil. Assuming the validity of these claims the expansion of the free energy functional $F[\mathbf{M}]$ assumes the form

$$F[\mathbf{M}] = \int d^3\mathbf{r} [-H_j M_j + r_0 M_j^2 + U M_j^4 + J (\partial_i M_j)^2 + \dots]. \quad (2.6)$$

Appropriate phenomenological parameters r_0 , U and J must be chosen for the particular microscopic system. J parametrizes the ferromagnetic exchange: a positive J describes the tendency of neighbouring magnetic moments to align parallel to each other by penalizing spatially modulated order parameter configurations. As already mentioned in section 2.1 the stability of the system requires $U > 0$. Condition 2.4 constraints the temperature dependence of r_0 . In order to have a finite (vanishing) magnetization for $T < T_c$ ($T > T_c$) r_0 should be negative (positive) below (above) the Curie temperature T_c . Linearizing the temperature the dependence of r_0 around T_c one finds

$$r_0(T) = \alpha(T - T_c) + \dots \quad (2.7)$$

with a positive constant, $\alpha > 0$.

For $T < T_c$, \mathbf{H} the free energy functional $F[\mathbf{M}]$ is minimised by spatially homogeneous configuration $\mathbf{M}(\mathbf{r}) = \mathbf{M}_0$. The ferromagnetic exchange term proportional to J

vanishes. The functional Eq. 2.6 is rotationally invariant in this case and the direction of \mathbf{M}_0 is spontaneously chosen. The magnitude of M_0 is fixed by minimising the free energy functional

$$|\mathbf{M}_0| = \sqrt{\frac{-r_0}{2U}}. \quad (2.8)$$

As for $T > T_c$ r_0 changes sign and assumes positive values, the square root becomes imaginary and signals a vanishing of the magnetisation, $\mathbf{M}_0 = 0$. For $T < T_c$ $|\mathbf{M}_0|$ assumes finite, positive values.

2.2.2 Non-inversion-symmetric magnetic systems

In certain materials so-called chiral magnets the atomic unit cell lacks inversion symmetry. Appendix A describe 4 exemplary materials which belong to this class. The absence of this symmetry transformation relaxes the symmetry requirements imposed on the free energy functional $F[\mathbf{M}]$ and allows for additional terms to appear in the expansion: terms with an odd number of spatial derivatives transform odd under inversion symmetry. Of these previously forbidden terms that may now appear in Eq. 2.6 the Dzyaloshinskii-Moriya (DM) interaction with only a single spatial derivative is the most important contribution.

$$\int d^3\mathbf{r} \ 2D \mathbf{M} \cdot (\nabla \times \mathbf{M}) \quad (2.9)$$

Originally derived on phenomenological grounds by Dzyaloshinskii [22] to explain the appearance of weak antiferromagnetism in materials such as Fe_2O_3 and the carbonates of Mn and Co, Moryia went on to explain the origin of this term as a combination of superexchange interaction and spin-orbit interaction [69]. Thereby the coupling constant D scales linearly in the spin-orbit coupling, $D \sim \lambda_{\text{SO}}$.

Canted magnetization configurations minimize the DM interaction term. The competition with the ferromagnetic exchange interaction leads to the appearance of helical order in the system characterized by an ordering wave vector $\mathbf{q} = q \hat{\mathbf{q}}$, where the magnetization winds around an axis $\hat{\mathbf{q}}$. The pitch q of this helix is determined by the relative strength of the coupling constants D and J .

$$q = \frac{D}{J} \quad (2.10)$$

The spin-orbit coupling for the materials we are interested (Appendix A) is small, $\lambda_{\text{SO}} \sim 10^{-2}$. This leads to a small DM interaction and a very large periodicity of the magnetic structures, often making the magnetic unit cell orders of magnitude larger than the atomic unit cell. One finds for the periodicity ξ_{mag} of the magnetic structure

$$\xi_{\text{mag}} \sim q^{-1} \sim D^{-1} \sim \lambda_{\text{SO}}^{-1} \quad (2.11)$$

As spatial derivatives are inversely proportional to the typical length scale over which the magnetization rotates $\nabla \sim \xi_{\text{SO}}$, terms with higher orders of spatial derivatives are suppressed by the weakness of the spin-orbit coupling λ_{SO} .

Nevertheless the appearance of terms $O(\lambda_{\text{SO}}^3)$ has important consequences. The presence of higher order terms in the spin-orbit coupling due to crystal field anisotropies breaks the rotational symmetry of the free energy functional $F[\mathbf{M}]$ and allows the ordering wave vector \mathbf{q} to choose a preferred orientation ($\langle 111 \rangle$ in the case of MnSi, see Appendix A).

2.3 Numerical minimisation of the Ginzburg-Landau functional

The mean-field configurations of the magnetisation can be studied by numerical minimisation of an appropriately discretised Ginzburg-Landau functional. For the study of phases with a translational invariance a discretisation in momentum space is advantageous. For helimagnets a characteristic length scale is defined by the ratio between the ferromagnetic exchange J and the DM interaction D which in term defines a characteristic momentum, Eq. 2.10. A discretisation of the Functional in terms of q and higher-order moments gives even for a small number of minimisation parameters accurate results. However we will be predominantly interested in mean-field configurations which lack translational invariance. In this case better results are achieved if one discretises in real-space. The free-energy functional for a helimagnet up to order λ_{SO}^2 is given by

$$F[\mathbf{M}] = \int d^3\mathbf{r} [r_0\mathbf{M}^2 + J(\nabla\mathbf{M})^2 + 2D\mathbf{M} \cdot (\nabla \times \mathbf{M}) + U\mathbf{M}^4 - \mathbf{H} \cdot \mathbf{M}] . \quad (2.12)$$

It turns out that the number of parameters in the above functional can be reduced by an appropriate rescaling of the length, magnetisation, magnetic field and energy units. By the rescaling

$$\begin{aligned} \mathbf{r} &\rightarrow \frac{D}{J}\mathbf{r} \\ \mathbf{H} &\rightarrow \sqrt{U\left(\frac{J}{D}\right)^3}\mathbf{H} \\ \mathbf{M} &\rightarrow \sqrt{\frac{UJ}{D^2}}\mathbf{M} \end{aligned} \quad (2.13)$$

the free energy functional $F[\mathbf{M}]$, Eq. 2.12, can be brought to the form [72]

$$F[\mathbf{M}] = \gamma \int d^3\mathbf{r} [\tilde{r}_0\mathbf{M}^2 + (\nabla\mathbf{M})^2 + \mathbf{M} \cdot (\nabla \times \mathbf{M}) + \mathbf{M}^4 - \mathbf{H} \cdot \mathbf{M}] , \quad (2.14)$$

with the rescaled $\tilde{r}_0 = \frac{J}{D^2}r_0$ and the new energy unit $\gamma = \frac{JD}{U}$. From the above expression we see that the only parameters determining the physics in the Ginzburg-Landau regime are r_0 and \mathbf{H} . A discretisation in real-space of the above expression can be achieved when the continuous variable $\mathbf{r} \in \mathbb{R}^3$ is replaced with a grid $\mathbf{r}_{ijk} = ia\hat{\mathbf{e}}_x + ja\hat{\mathbf{e}}_y + ka\hat{\mathbf{e}}_z$ with $i, j, k \in \mathbb{N}$ and a the discretisation constant. The magnetisation

density \mathbf{M} will be replaced by the average magnetisation \mathbf{m}_{ijk} in a single cell with volume a^3 , \mathbf{m}_{ijk} . In order to keep the energy of the discretised system finite in the limit $a \rightarrow 0$ one has to rescale the magnetisation according to

$$\int d^3\mathbf{r} \mathbf{M}(\mathbf{r})^4 \rightarrow \sum_{ijk} a^3 \mathbf{M}_{ijk}^4 \stackrel{!}{=} \sum_{ijk} \mathbf{m}_{ijk}^4. \quad (2.15)$$

where $\mathbf{M}_{ijk} = \mathbf{M}(\mathbf{r}_{ijk})$. From the above consideration follows that $\mathbf{m}_{ijk} = a^{-3/4} \mathbf{M}_{ijk}$. With the same reasoning one finds for the magnetic field $\mathbf{h}_{ijk} = a^{9/4} \mathbf{H}(\mathbf{r}_{ijk})$ and for $\bar{r}_0 = a^{3/2} \tilde{r}_0$. Finding the mean-field configuration of a system parametrised by $(r_0, U, J, D, \mathbf{B})$ therefore involves two steps. First one rescales the system according to Eq. 2.14 and finds \tilde{r}_0 . Then a discretisation parameter a is chosen small enough so that the discretised model approximates the continuum model accurately enough and the parameters \mathbf{b} and \bar{r}_0 of the discretised system are calculated. A numerical minimisation yields a discretised magnetisation configuration which can be translated back to the original model with the above relations.

The discretisation of the model involves the discretisation of the differential operators in the expression for the free energy. After partial integration the ferromagnetic exchange term and its discrete approximation are given by

$$\int d^3\mathbf{r} (-\mathbf{M}\nabla^2\mathbf{M}) \approx a^{-1/2} \sum_{ijk} -(\mathbf{m}_{i+1jk} + \mathbf{m}_{i-1jk}) \cdot \mathbf{m}_{ijk} - (\mathbf{m}_{ij+1k} + \mathbf{m}_{ij-1k}) \cdot \mathbf{m}_{ijk} \\ - (\mathbf{m}_{ijk+1} + \mathbf{m}_{ijk-1}) \cdot \mathbf{m}_{ijk} + 6\mathbf{m}_{ijk}^2. \quad (2.16)$$

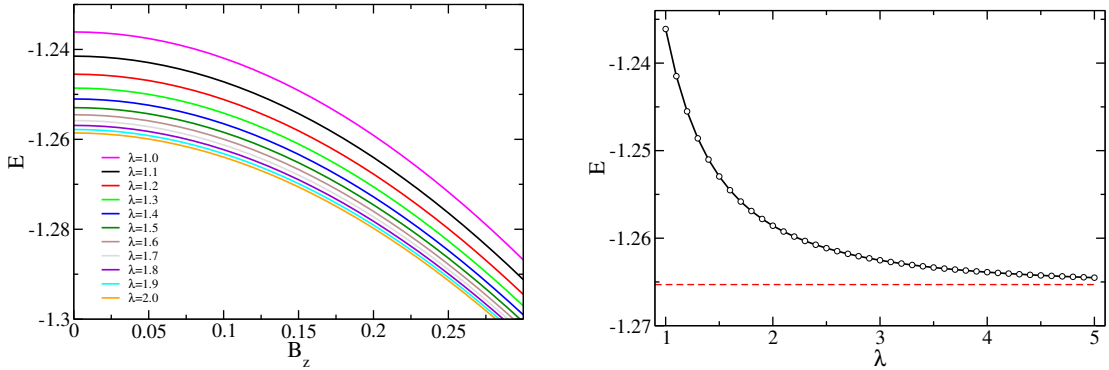
Similarly the approximation for the DM interaction term assumes the form

$$\int d^3\mathbf{r} \mathbf{M} \cdot (\nabla \times \mathbf{M}) \approx -a^{1/2} \sum_{ijk} \mathbf{m}_{ijk} \times \mathbf{m}_{i+1jk} \cdot \hat{\mathbf{e}}_x + \mathbf{m}_{ijk} \times \mathbf{m}_{ij+1k} \cdot \hat{\mathbf{e}}_y + \mathbf{m}_{ijk} \times \mathbf{m}_{ijk+1} \cdot \hat{\mathbf{e}}_z. \quad (2.17)$$

In summary the discretised model is given by

$$f[\mathbf{m}] = \gamma \sum_{ijk} \left[(\bar{r}_0 + 6/a^{1/2}) \mathbf{m}_{ijk}^2 + \mathbf{m}_{ijk}^4 - \mathbf{h}_{ijk} \cdot \mathbf{m}_{ijk} - a^{-1/2} (\mathbf{m}_{i+1jk} + \mathbf{m}_{i-1jk}) \cdot \mathbf{m}_{ijk} \right. \\ \left. - a^{-1/2} (\mathbf{m}_{ij+1k} + \mathbf{m}_{ij-1k}) \cdot \mathbf{m}_{ijk} - a^{-1/2} (\mathbf{m}_{ijk+1} + \mathbf{m}_{ijk-1}) \cdot \mathbf{m}_{ijk} \right. \\ \left. - a^{1/2} \mathbf{m}_{ijk} \times \mathbf{m}_{i+1jk} \cdot \hat{\mathbf{e}}_x - a^{1/2} \mathbf{m}_{ijk} \times \mathbf{m}_{ij+1k} \cdot \hat{\mathbf{e}}_y - a^{1/2} \mathbf{m}_{ijk} \times \mathbf{m}_{ijk+1} \cdot \hat{\mathbf{e}}_z \right] \quad (2.18)$$

For a continuum model discretised on a $N \times N \times N$ grid the above expression is a function of $3N^3$ optimisation parameters. An mean-field magnetisation configuration can be calculated on a computer using numerical minimisation algorithms. The conjugate gradient method (CG) is a standard algorithm for the minimisation of quadratic functions of the form $\|\mathbf{A} \cdot \mathbf{x} - \mathbf{b}\|^2$ with the dimensionality of x so large that a direct calculation is too time-consuming. At the minimum \mathbf{x}^* the gradient vanishes, $\nabla f(\mathbf{x}) = 2\mathbf{A}^T(\mathbf{A} \cdot \mathbf{x} - \mathbf{b}) = 0$. CG therefore calculates an approximate solution of the equation $\tilde{\mathbf{A}} \cdot \mathbf{x} = \tilde{\mathbf{b}}$ with $\tilde{\mathbf{A}} = \mathbf{A}^T \mathbf{A}$ and $\tilde{\mathbf{b}} = \mathbf{A}^T \mathbf{b}$. The conjugate



(a) Energy density E of a discretised helix as a function of the applied field B_z for various discretisations λ . For larger λ they quickly converge to the continuum solution.

(b) Energy density of a helix at $B_z = 0$ as a function of the discretisation λ . The approximate energy converges quadratically in λ against the exact solution of the continuum model (red dashed line).

Figure 2.4

gradient method has been generalised (non-linear conjugate gradient method) to non-linear optimisation problems. The generalisation may work if the non-linear function is approximately quadratic near the minimum, which is always the case if the function is twice differentiable at the minimum. Over the years a number of different optimisation strategies for non-linear functions have been developed - all based on the CG [31]. For the numerical optimisation of the free energy functional above we use the Fletcher-Reeves variant of the non-linear CG algorithm as implemented in the GSL (GNU Scientific Library). A more detailed account of the algorithm can be found in Appendix C. It should be noted though that the CG method finds *local* minima - it is not guaranteed to find the global minimum of the functional.

The lattice discretisation a can be used to control how accurately the discretised model approximates the continuum model. As an example we calculate the mean-field configuration of a system with $\bar{r}_0 = 2$ and small magnetic field \mathbf{h} . For these parameters the system is in the helical phase and we therefore initialise the system by writing a single period of a helix with the ordering vector \mathbf{q} pointing along the x -direction into a system of size $10\lambda \times 1 \times 1$ with periodic boundary conditions in the x -, y - and z -direction. Note that due to the translational invariance of the configuration in the y - and z -direction it suffices to choose 1 for N_y and N_z . For the discretised system on a lattice the pitch of the helix is given by $\tan(q) = \frac{D}{J} = a$ with a the lattice discretisation. The parameter λ is therefore related to a via $a = \tan(2\pi/10\lambda)$. Fig. 2.4a shows the energy density E after convergence of the minimisation algorithm as a function of B_z for various discretisations λ . The solutions are seen to quickly converge towards an asymptotic solution for larger λ s. Fig. 2.4a shows the energy density of the approximation for $B_z = 0$ as a function of the parameter λ . The solutions converge quadratically in λ against the energy of the exact solution for the continuum model (red dashed line).

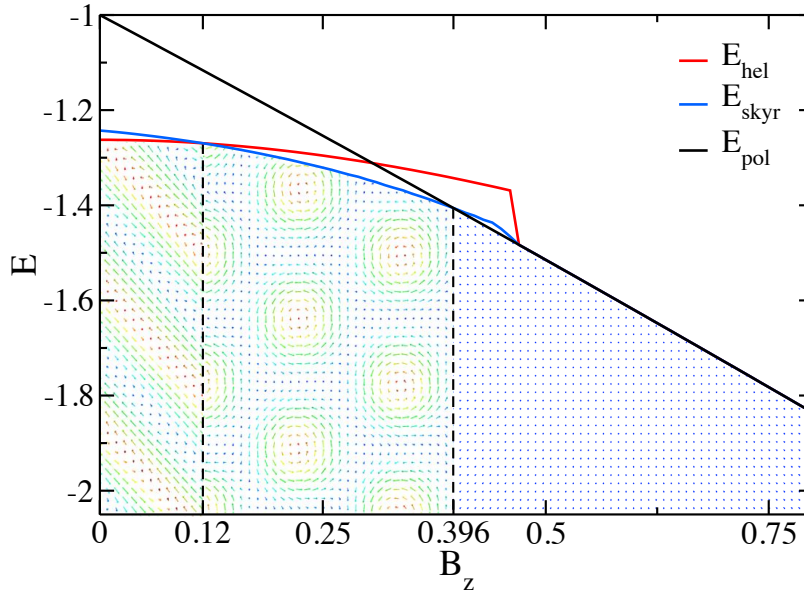


Figure 2.5: Mean-field phase diagram of a 2D helimagnet at $T = 0$.

2.4 First applications

Magnetic phase diagram of 2D helimagnet

We calculate the magnetic phase diagram (in mean-field approximation) of the two-dimensional helimagnet (in the x - y plane) for $\bar{r}_0 = 1$ and the magnetic field \mathbf{h} applied perpendicular to the system, i.e. $\mathbf{h} = h\hat{\mathbf{e}}_z$. We discretise the system on a $100 \times 100 \times 1$ -grid with periodic boundary conditions in the x - and y - direction. The local minimum the minimisation algorithm converges to is determined by the initial position in the parameter space, i.e. the initial magnetisation configuration. The only way to determine reliably the actual phase the system will exhibit is to start the algorithm in all possible choices, let it converge and then compare the final free energy densities. The phase with the lowest free energy density is the stable phase of the system. For a two-dimensional helimagnet there are three competing ordered phases: a helical phase, the Skymion lattice phase and the field-polarised phase. Fig. 2.5 shows the free energy density of the converged solutions for the three phases as a function of the applied magnetic field B_z . For fields in the range $0 \leq B_z < 0.12 \equiv B_{c1}$ the helical phase has the lowest energy. At $B_z \approx 0.12$ the free energy density of the helical and the SkX phase become degenerate and for $0.12 \leq B_z < 0.4 \equiv B_{c2}$ the SkX phase has the minimal free energy. Above $B_z > 0.4$ the system is field-polarised. These results are in qualitative agreement with Monte Carlo results for two-dimensional helimagnetic systems [19].

Defected phases

Up until now we have considered only phases with a translational symmetry. In such situations it is much more efficient to express the free energy function, Eq. 2.14,

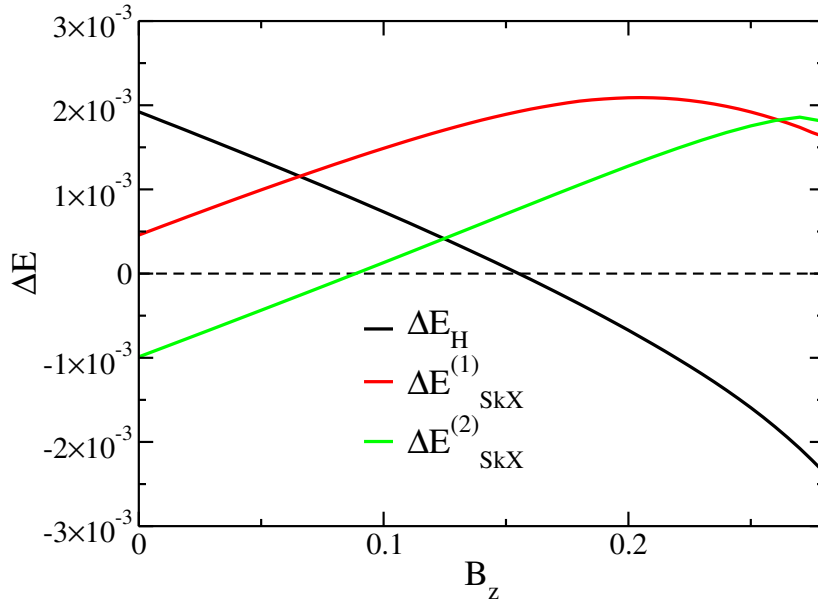


Figure 2.6: Energetic cost for the introduction of a single defect in the helical (black line) and Skyrmion lattice phase (green line: 2 skyrmions merged, red line: vacancy). The removal of a single Skyrmion from the lattice always costs a positive energy.

first in Fourier space and then discretize the momenta. The strength of the real-space discretisation however lies in the possibility to study the energetics of defected configurations. Here we compare the energetic costs of two types of defects. The addition of a single skyrmionic defect to an otherwise helical changes its total winding number from 0 to 1, c.f. Fig. 2.7 (left). The removal of a single Skyrmion from the SkX reduces the total winding number by 1, c.f. Fig. 2.7 (middle and right). There are two ways to remove a single from the Skyrmion lattice, corresponding to two different local minima that the minimisation algorithm may converge to: one can remove a single Skyrmion by overwriting it with a field polarised configuration, thus creating a vacancy in the lattice (right) or one may merge two neighbouring skyrmions (middle). In these visualisations the magnetic field vector points towards the observer, blue color signifies magnetic moments pointing towards the observer as well while red region marks areas where the moments point away. We compare the energy of these three defects as a function of the applied magnetic field B_z . The expectation is that for small applied fields the addition of a single skyrmionic defect to the helical phase is energetically costly since the helical phase is the ground state. For larger fields however the SkX becomes the ground state, c.f. Fig. 2.5, and the addition of a single Skyrmion could even lower the total system energy as it brings the system closer to its ground state configuration. For vacancies in the SkX and the merging of two Skyrmions the situation is just opposite we expect high energetic costs at high B_z fields and a reduction of the cost as the applied field is lowered. Close to the critical field B_{c_1} a situation could arise where the energetic cost for both types of defects is negative. In such a situation an additional phase is stabilised which is characterised by a finite density of defects. Fig. 2.6 shows the energy of the two types of defects as a function of the applied field. Indeed the addition of a single

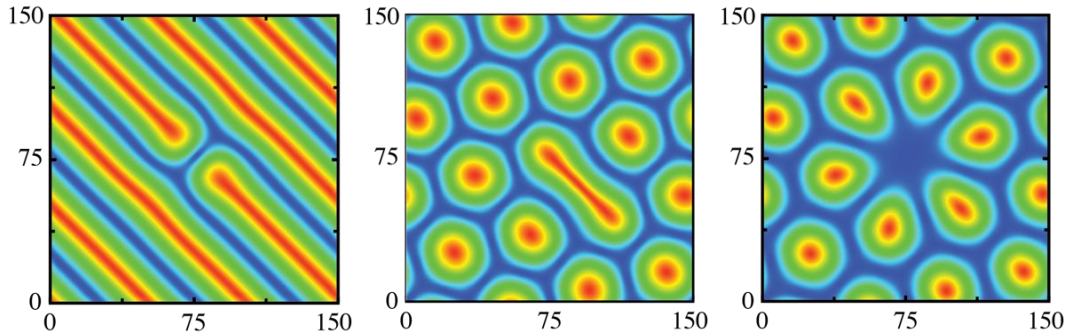


Figure 2.7: Left: Defected helical phase. Middle: defected Skyrmion lattice phase, vacancy. Right: defected Skyrmion lattice phase, 2 skyrmions merged.

Skyrmion to the helical phase costs a large positive amount of free energy ΔE_H for small applied fields. Slightly above the critical field strength the cost function ΔE_H changes sign and the addition of defects become energetically favourable. Although the curve for the removal of a Skyrmion from the SkX by creating a vacancy (red curve) shows the expected slope, a vacancy costs for all field strengths a finite amount of energy $\Delta E_{\text{SkX}}^{(1)}$. This is in contrast to the merging of two Skyrmions which costs a positive energy $\Delta E_{\text{SkX}}^{(2)}$ for large fields and becomes favourable for field strengths below $B_z \lesssim 0.9$. There is however no value of B_z for which both the merging of two skyrmions in the skyrmion lattice phase and the introduction of single skyrmion defect in the helical phase are both energetically favourable. We therefore find no indication for an additional phase with a finite defect concentration. Since we have only studied the cost of a single defect we can however not exclude this idea either.

Chapter 3

Langevin dynamics of magnetic systems

For deterministic, macroscopically known systems the effect of fluctuations can be studied using the Langevin approach. Fluctuations are introduced into the equations of motion by adding random force terms, so called “noise generators”. This approach gives a more concrete picture than the Fokker-Planck equation. In this chapter we briefly review the introduction of the Langevin approach to Brownian motion in section 3.1. We then discuss the generalisation of the approach to magnetic systems in section 3.2 followed by a description of the necessary steps to calculate an approximate time evolution numerically in section 3.2.4.

3.1 The Langevin equation

In 1827 botanist Robert Brown gave a detailed account of what later became known as “Brownian motion” while studying the plant life of the South Seas. He examined suspensions of pollen in water under a microscope when he noticed that in all cases the pollen is in rapid oscillatory motion. Initially many speculations surrounded the observed phenomenon ranging from Brown’s original assertion that the motion was peculiar to the male sexual cells of plants to the early attempt by Nägeli [17] to explain the observation by considering the the conservation of momentum. But it was left to Einstein in 1905 [23] to explain the Brownian motion on the basis of a consistent stochastic theory.

Einstein’s reasoning can be summarised as this: If a Brownian particle immersed in a fluid collides with a fluid particle, its velocity changes. However in the limit of a very viscous fluid the velocity is quickly dissipated away and the effect of the collision is merely a *displacement* of the Brownian particle. Therefore in Einstein’s view the process consisted of random jumps performed by the particle; that is, the particle performs a random walk. With the assumptions that the increments are small he derived a differential equation for the probability density distribution, a Fokker-Planck equation, of the particle’s displacements. After obtaining its solution he derived that the mean-square displacement grows linearly in time. Using the fact that at equilibrium the Maxwellian distribution should hold for the velocities it was

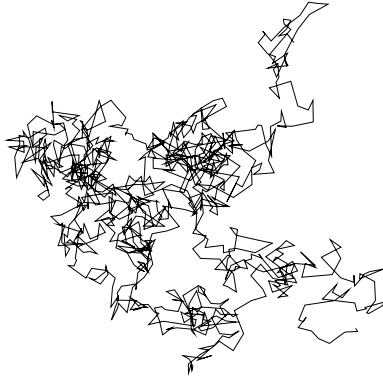


Figure 3.1: Exemplary trajectory of a Brownian particle.

possible to express the Avogadro constant in terms of the viscosity of the fluid and the system temperature. Subsequent experimental measurements by Perrin in 1908 found agreement in the extracted Avogadro constant to within 19% with the accepted value [78].

3.1.1 The Langevin approach to Brownian motion

The theory by Einstein and Smoluchowski [95] is expressed entirely in terms of the underlying probability distribution of the Brownian particles and the Fokker-Planck equation. Although in agreement with experiments the description strongly abstracts from the underlying Newtonian physics. In 1908 Langevin introduced the concept of a equation of motion for a random variable and in doing so invented the subject of *stochastic differential equations*. Langevin simply wrote down the Newtonian equation of motion of the Brownian particle under the assumptions that it experiences two forces: (a) a deterministic frictional force $\alpha\dot{x}$ which models the dynamical friction experienced by the particle as it brushes against the surrounding fluid and (b) rapidly fluctuating forces $F(t)$ which are also due to an interaction with the surrounding fluid: impacts by fluid atoms.

The equation of motion therefore assumes the form

$$m\ddot{x}(t) = -\alpha\dot{x}(t) + F(t) \quad (3.1)$$

where m is the mass of the Brownian particle and $\alpha > 0$ the strength of the dissipative mechanism which can be thought of as Stokes' law. The equations of motion are extended here with the Langevin noise term $F(t)$ by a mere addition. In this case the noise term is said to be *additive*. Three assumptions about the statistical nature of the force underly the mathematical treatment of the above equation:

1. The force $F(t)$ does not depend on the current particle position x .
2. The time scale on which the force $F(t)$ varies is extremely short as compared to the timescale of observation.

3. The statistical average of $F(t)$ taken over an ensemble of particles vanishes, i.e. $\overline{F(t)} = 0$.

From assumption 2 one can deduce that the particle collision are basically instantaneous. This can be expressed by making the autocorrelation time of the random variable $F(t)$ arbitrarily small

$$\overline{F(t)F(t')} = 2\alpha k_B T \delta(t - t') \quad (3.2)$$

where δ is the Dirac delta distribution. Eq. (3.2) is a mathematical idealisation of assumption 2 and as such certainly open to criticism. In reality the autocorrelation function starting from $2\alpha k_B T$ quickly drops to zero [17]. The *white* noise becomes *coloured*.

Eq. (3.2) relates the autocorrelations of the fluctuations to the strength of the dissipative mechanism α and as such it is a *fluctuation-dissipation theorem* [55, 68]. The physical picture is this: the random kicks of the noise term $F(t)$ have a tendency to spread out \dot{x} while the damping term tries to bring \dot{x} back to zero. The balance between these two opposing tendencies is the equilibrium distribution.

To make a connection with Einstein's theory it is easy to derive from Eq. (3.1) the formula for the mean square-displacement of the Brownian particle. Upon multiplying Eq. (3.1) with x and noting that

$$\dot{x}x = \frac{1}{2} \frac{d}{dt} x^2 \quad \text{and} \quad \ddot{x}x = \frac{1}{2} \frac{d^2}{dt^2} x^2 - \dot{x}^2 \quad (3.3)$$

we find after taking the thermal average

$$\frac{m}{2} \frac{d^2}{dt^2} \overline{x^2} - m \overline{\dot{x}^2} = -\frac{\alpha}{2} \frac{d}{dt} \overline{x^2} + \overline{F x} \quad (3.4)$$

Due to assumption 1 in the above list the force F and the particle position x are completely *uncorrelated*, therefore the last term in Eq. (3.4) will vanish, i.e. $\overline{F x} = 0$.

Statistical mechanics tells us that in the presence of the dissipative mechanism α the system will approach thermal equilibrium in the long time limit thus connecting our above considerations to the notion of temperature: the Maxwellian distribution can be assumed to hold for the velocity of the Brownian particle so that the *mean* velocity becomes

$$\frac{1}{2} m \overline{\dot{x}^2} = \frac{1}{2} k_B T \quad (3.5)$$

Defining $u \equiv d/dt \overline{x^2}$ Eq. (3.4) becomes

$$\frac{m}{2} \frac{du}{dt} + \frac{\alpha}{2} u = k_B T \quad (3.6)$$

which is solved by $u = C e^{-\alpha t/m} + 2k_B T/\alpha$ where C is a constant of integration. For large t the exponential will play no role owing to the fact that the system will forget its initial conditions and one finds a linear growth of the mean-square displacement, i.e. a diffusive motion,

$$\overline{\Delta x^2} = \left\langle (x(t) - x(0))^2 \right\rangle = 2 \frac{k_B T}{\alpha} t \quad (3.7)$$

which is just the result derived by Einstein.

3.1.2 The Itô and Stratonovich dilemma

The Langevin approach has been used by many authors to treat non-linear systems [116]. For non-linear systems additional problems arise concerning the interpretation of the Langevin equation. This is important for the treatment of magnetic system as their equations of motion are inherently non-linear.

Let us suppose we have a physical system with a non-linear equation of motion, $\dot{y} = A(y)$ and following the Langevin approach we add a noise term to model the fluctuations in the system. In the following we will suppose that the system is “fully non-linear” which means that the noise term is not merely added (*additive noise*) to the equations of motion but is multiplied by a function $B(y)$ of the dynamical variable y (*multiplicative noise*)

$$\dot{y} = A(y) + B(y)F(t) \quad (3.8)$$

In case the spectrum of the noise term $F(t)$ is truly white, the above equation (without further information) bears no meaning. The problem lies in the Langevin noise term. If the autocorrelation function of $F(t)$ is truly proportional to a Dirac delta function (white noise), $F(t)$ can be visualised as a sequence of delta peaks occurring at random times [105]. Since according to Eq. (3.9) each delta function causes a jump in the dynamical variable y , the value of y is not defined at that time and hence also the value of $B(y)$ is not defined. Eq. (3.9) does not specify whether $B(y)$ should be evaluated before or after the jump or maybe the mean of both. This is not only a question of mathematical rigour but rather these various choices lead to different Fokker-Planck equations and hence to different probability density distributions.

Physicists typically prefer the Stratonovich interpretation who opted for the mean value. After integrating Eq. (3.9) it assumes the following form in the Stratonovich interpretation

$$y(t + \Delta t) - y(t) = A(y(t)) \Delta t + B\left(\frac{y(t) + y(t + \Delta t)}{2}\right) \int_t^{t+\Delta t} F(t') dt' \quad (3.9)$$

Another way to arrive at this equation is to follow the treatment of Doob [20] who removes the non-linearity in the noise term of the equations of motion by defining the transformation

$$z = \int dt' \frac{\dot{y}}{B(y)}, \text{ and } \mathcal{A}(z) = \frac{A(y)}{B(y)} \quad (3.10)$$

and proves that this choice leads to Eq. (3.9). This shows that the naive use of our usual rules of calculus lead to the Stratonovich interpretation.

Itô opted for the value of y before the arrival of the delta peak. The corresponding integrated equation assumes the form

$$y(t + \Delta t) - y(t) = A(y(t)) \Delta t + B(y(t)) \int_t^{t+\Delta t} F(t') dt' \quad (3.11)$$

This interpretation requires new transformation laws incompatible with the usual rules. They require a new form of calculus: Itô calculus. The Itô interpretation can be made equivalent to the Stratonovich result if an additional “drift” term is added to the stochastic differential equation [36].

These difficulties have to be kept in mind, especially if numerical solutions of stochastic differential equations are to be obtained. Different numerical integration schemes converge to different stochastic interpretations. Sometimes it is difficult to tell from the integration rule when exactly $B(y)$ is being evaluated. Care must be taken that a form of the stochastic equation is chosen that is compatible with the choice of stochastic quadrature rule.

3.2 Equations of motion for magnetic systems

3.2.1 Landau-Lifschitz-Gilbert equation

Mechanics tells us that the time rate of change of angular momentum is given by the applied torque.

$$\frac{d}{dt}\mathbf{L} = \mathbf{T} \quad (3.12)$$

Considering a lattice of magnetic moments \mathbf{m} in a magnetic field \mathbf{H}_{eff} the angular momentum is given by \mathbf{m}/γ where γ is the gyromagnetic ratio and the torque acting on the magnetic moment by $-\mathbf{m} \times \mathbf{H}_{\text{eff}}$; thus

$$\frac{d}{dt}\mathbf{m} = -\gamma\mathbf{m} \times \mathbf{H}_{\text{eff}} \quad (3.13)$$

This describes the precession of the magnetic moment \mathbf{m} in the effective magnetic field. Upon scalar multiplication of Eq. (3.13) with the magnetisation \mathbf{m} the right hand side vanishes. Therefore the above equation describes the dynamics of magnetic moments with a fixed amplitude $m = |\mathbf{m}|$. The field \mathbf{H}_{eff} contains both contributions from an applied field and also from exchange and demagnetisation fields. The effective magnetic field \mathbf{H}_{eff} can be obtained from the Ginzburg-Landau free energy functional $F[\mathbf{m}]$

$$\mathbf{H}_{\text{eff}} = -\frac{\delta F[\mathbf{m}]}{\mathbf{m}} \quad (3.14)$$

For $F[\mathbf{m}] = -\mathbf{m} \cdot \mathbf{H}_0$ with \mathbf{H}_0 a constant magnetic field one finds indeed $\mathbf{H}_{\text{eff}} = \mathbf{H}_0$. In a more general situation \mathbf{H}_{eff} will also include effects such as magnetic anisotropy, interacting with other spins, etc.

There are several processes in a solid which give rise to a damping of the magnetic motion (magnons, phonons, etc.). Starting from the Dirac equation for electrons in magnetic and electric potentials it has been shown that magnetic damping can arise from spin-orbit coupling as relativistic corrections to the spin Hamiltonian [43]. Typically however, fundamental analysis of damping mechanisms is difficult and therefore damping terms are usually added on phenomenological grounds. The simplest relaxation term which can be written down is the so called Gilbert damping

$$\frac{\alpha}{m}\mathbf{m} \times \frac{d}{dt}\mathbf{m} \quad (3.15)$$

It is important to appreciate the extent to which the coupling to these subsystems is included in this expression: here $-\alpha d/dt \mathbf{m}$ is only the dissipative effective field

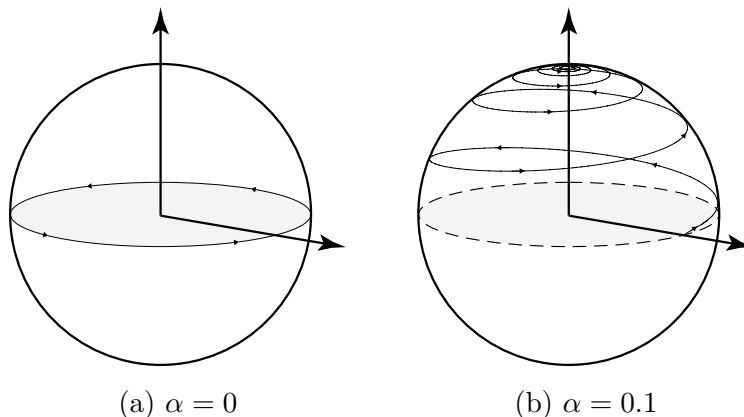


Figure 3.2: Solutions of the equations of motion

and describes only the (ensemble) average of rapidly fluctuating random forces. For an individual moment this expression should be augmented by a term $\mathbf{h}_f(t)$ whose statistical average is zero. More on that later.

The full Landau-Lifschitz-Gilbert equation takes the form

$$\frac{d}{dt}\mathbf{m} = -\gamma\mathbf{m} \times \mathbf{H}_{\text{eff}} + \gamma\frac{\alpha}{m}\mathbf{m} \times (\mathbf{m} \times \mathbf{H}_{\text{eff}}) \quad (3.16)$$

As an example we show in Fig. 3.2 the time evolution for a single spin of length $|\mathbf{m}| = 1$ with the initial condition $\mathbf{m}^{(0)} = (1, 0, 0)^T$ in an applied magnetic field $\mathbf{H}^{(\text{ext})} = (0, 0, 0.01)^T$ with Gilbert damping $\alpha = 0$ (Fig. 3.2a) and $\alpha = 0.1$ (Fig. 3.2b). For $\alpha = 0$ the energy of the system is conserved as the only dissipative mechanism is switched off. The spin precesses at a constant polar angle $\theta = \pi/2$ around the applied magnetic field $\mathbf{H}^{(\text{ext})}$ with angular velocity $\omega = H_z^{(\text{ext})}$ (we set $\gamma = 1$). For the $\alpha = 0.1$ the spin simply relaxes in a spiral towards the applied magnetic field $\mathbf{H}^{(\text{ext})}$ on a timescale of the order $1/\alpha$.

3.2.2 Spin-Transfer Torques

The field of spintronics seeks to manipulate magnetic configurations by electric effects. The short switching times for electric currents and the possibility to apply them locally using appropriately designed circuitry promises, especially in the context of applications for future information technology devices, tremendous advantageous over the control through magnetic fields. The giant magnetoresistance (GMR) effect, discovered in 1988 independently by Grünberg [8] and Fert [1], is an example of a successful knowledge transfer from the solid state community to technology companies. Here a very efficient control of electric currents is achieved by altering magnetic structures. The effect is observed in thin-film structures composed of alternating ferromagnetic and non-magnetic conductive layers leads to a significant change in the electrical resistance depending on whether the magnetization of adjacent ferromagnetic layers are in a parallel or an antiparallel alignment. The main application of GMR is magnetic field sensors, which are used to read data in hard disk drives.

In the middle of 1980s Berger [6, 33] proposed the possibility to drive domain walls by the application of electric currents. However it was not until the discovery of the spin-transfer torques in the 1990s due to Berger [7] and Slonczewski [94] that research on current-driven magnetisation dynamics made serious progress. A demonstration of how these physical ideas might be used for the creation of new information technology devices was given by Parkin and his group [76] who developed a prototypical race-track memory device in which spin-transfer torques were used to move ~ 100 bits encoded in a domain wall pattern along spatially fixed read and write heads by applying electric currents. The great disadvantage of domain walls in this respect are the large current-densities ($\sim 10^{11}$ A/m²) necessary to depin them. This leads to substantial ohmic heating and a destruction of the magnetic state. Jonietz et al. [49] showed in 2010 that a Skyrmion lattice, on the other hand, exhibits an ultra-low electrical threshold current density of $\sim 10^6$ A/m² about five order of magnitude smaller compared to domain walls. Here the application of a thermal gradient and an ultra-low electrical current lead to a rotation of the Skyrmion lattice which could be consistently explained by spin-transfer torque effects. In their numerical study Iwasaki et al. [46] demonstrated that the order of magnitude for this threshold current is robust even in the presence of easy-axis anisotropies.

The effects of spin transfer torques on the magnetisation dynamics can be accounted for on the level of description provided by the LLG when additional terms are included. In Ref. [62] Lucassen et al. give an intuitive picture of the origin of these terms: The conduction electrons traversing the smoothly varying magnetisation texture adiabatically adjust their spin orientation parallel to the local magnetisation direction. By conservation of spin, there is an opposite torque on the magnetisation texture, which leads to a net displacement of the texture in the same direction as the electric current \mathbf{j} .

Zhang and Li [115] account for the coupling between the itinerant electrons of transport and the localized electrons of magnetisation by an s-d Hamiltonian. They derive a linear response function for the conduction electrons in the presence of a time and spatially varying local moment, and the by using the same s-d model calculate the spin torque on the magnetisation dynamics. Duine et al. [21] present a microscopic treatment of current-induced torques based on a functional formulation of the Keldysh formalism. They find in agreement with Ref. [115] that the LLG in the presence of a partially spin-polarised current is given by

$$\left(\frac{d}{dt} + \mathbf{v}_s \cdot \nabla\right) \mathbf{m} = -\gamma \mathbf{m} \times \mathbf{H}_{\text{eff}} + \gamma \frac{\alpha}{m} \mathbf{m} \times \left(\frac{d}{dt} + \frac{\beta}{\alpha} \mathbf{v}_s \cdot \nabla\right) \mathbf{m}, \quad (3.17)$$

with β a dimensionless constant which describes the dissipative, non-adiabatic effects of the spin-transfer torques. It is immediately clear that for $\alpha = \beta$ the above equation is found when the time derivatives in equation Eq. 3.17 are replaced by the ‘‘comoving’’ derivative $D/Dt = d/dt + \mathbf{v}_s \cdot \nabla$. For this special the system is Galilei invariant and a solution of the above equation in terms of a solution for $\mathbf{v}_s = 0$, \mathbf{m}_0 , is achieved by $\mathbf{m}(t) = \mathbf{m}_0(\mathbf{r} - \int_0^t \mathbf{v}_s(t) dt)$. Usually, in realistic systems no Galilei invariance is found. Microscopically the β -term has contributions from all processes that violate spin conservation and therefore correspond to terms in the microscopic Hamiltonian that are not invariant under spin rotations [21].

3.2.3 Stochastic Landau-Lifschitz-Gilbert equation

The stochastic Landau-Lifschitz-Gilbert equation is the basic Langevin equation for classical spins. Originally introduced by Brown [12] to treat the dynamics of small ferromagnetic particles and explain phenomena such as superparamagnetism and the magnetic aftereffect. Subsequent work by Kubo and Hashitsume [56] who studied general classical spins showed how a Fokker-Planck equation for the stochastic motion of the spin moment can be derived. Both, although presented separately in literature, are essentially equivalent.

So far we have only discussed how systems without thermal fluctuations can be simulated. Following the Langevin approach the effective magnetic field \mathbf{H}_{eff} has to be augmented by a *fluctuating or stochastic field* $\mathbf{h}_{\text{fl}}(t)$ to describe a system at finite temperature. Similar to the case of Brownian motion this field accounts for the effects of the interaction of \mathbf{m} with other microscopic degrees of freedom (phonons, conduction-electrons, nuclear spins, etc.), which cause fluctuations of the magnetic moment's orientation. It should be noted that the *same* microscopic degrees of freedom are also responsible for the magnetic relaxation (Gilbert damping) described by the α -term. Therefore the fluctuation-dissipation theorem is able to link the statistics of these fluctuations to the strength of the dissipative mechanism.

The starting equation in the Brown-Kubo-Hashitsume model of classical (interacting) spins at finite temperature is the stochastic Gilbert equation written here in the Landau-Lifschitz form

$$\frac{d}{dt}\mathbf{m} = -\gamma \mathbf{m} \times (\mathbf{H}_{\text{eff}} + \mathbf{h}_{\text{fl}}(t)) + \gamma \frac{\alpha}{m} \mathbf{m} \times [\mathbf{m} \times (\mathbf{H}_{\text{eff}} + \mathbf{h}_{\text{fl}}(t))] \quad (3.18)$$

where γ is the gyromagnetic ratio and α is the previously introduced dimensionless damping constant for the Gilbert damping. We will refer to the above equation as the stochastic Landau-Lifschitz-Gilbert equation. The deterministic effective field \mathbf{H}_{eff} is given by Eq. (3.14). With the inclusion of the Gilbert damping term the effective field describes the effects of interactions with microscopic degrees of freedom (phonons, conduction electrons, nuclear spins, etc.) on the level of averages. It has to be augmented by a stochastic, fluctuating field $\mathbf{h}_{\text{fl}}(t)$ to properly treat the effects of fluctuations.

The typical assumptions about the field $\mathbf{h}_{\text{fl}}(t)$ are that it is a Gaussian stochastic process with the following statistical properties

$$\begin{aligned} \langle \mathbf{h}_{\text{fl},i}(\mathbf{r}, t) \rangle &= 0 \\ \langle \mathbf{h}_{\text{fl},i}(\mathbf{r}, s) \mathbf{h}_{\text{fl},j}(\mathbf{r}', t) \rangle &= 2\alpha \frac{k_B T}{\gamma m} \delta_{ij} \delta(\mathbf{r} - \mathbf{r}') \delta(s - t) \end{aligned} \quad (3.19)$$

where i and j are cartesian components and $\langle \dots \rangle$ denotes an average taken over different *realizations* of the fluctuating field $\mathbf{h}_{\text{fl}}(t)$. The Gaussian property of the process stems from the interaction of with a large number of microscopic degrees of freedom with identical statistical properties (central limit theorem). The delta-correlation in time in the second equation (3.19) expresses that for the temperature we are interested in the autocorrelation time of $\mathbf{h}_{\text{fl}}(t)$ is much shorter than the rotational-response time of the system. The Kronecker δ shows that different components of are

uncorrelated. Finally the fluctuating fields acting on different magnetic moments are independent.

Equations (3.18) and (3.19) seem to fully determine the dynamical problem under consideration. However one quickly sees that the equation of motion Eq. (3.18) is subject to the Itô and Stratonovich dilemma, c.f. section 3.1.2. The added noise term is *multiplicative* and not *additive*. Therefore the problem specification is only complete once the stochastic interpretation to be used for the stochastic differential equation, Eq. (3.18), is fixed. Interpreting the equation according to Stratonovich calculus renders the correct physical results. The Itô interpretation would require a modification of Eq. (3.18) where an additional “noise-induced” drift term is added. From a physical point of view the Stratonovich interpretation makes sense: if one sees the delta correlation of the fluctuations as mathematical idealization for physical noise with a short auto-correlation time, it is the Stratonovich interpretation one arrives at if one takes the formal zero-autocorrelation time limit of fluctuations with a finite autocorrelation time [36].

Fluctuation-dissipation theorem

As already mentioned in the introduction a fluctuation dissipation theorem links the strength of the dissipative mechanism to the variation of the fluctuations. The original derivation of this expression as according to Brown [12] is complicated and uses advanced stochastic methods. We will present here the more direct and simpler derivation presented by Garanin [35].

For the purpose of this derivation we assume that the variance of the fluctuations is parametrized by the unknown constant D

$$\langle \mathbf{h}_{\mathbf{a},i}(\mathbf{r}, s) \mathbf{h}_{\mathbf{a},j}(\mathbf{r}', t) \rangle = 2D \delta_{ij} \delta(\mathbf{r} - \mathbf{r}') \delta(s - t) \quad (3.20)$$

We first derive the Fokker-Planck equation corresponding to Eq. (3.18) and then determine the constant D by demanding that the Maxwellian equilibrium distribution is a static solution of the same.

We start by introducing the distribution function of spins n

$$n(\mathbf{M}, t) \equiv \langle \pi_t[\mathbf{h}_{\mathbf{a}}] \rangle_{\mathbf{h}_{\mathbf{a}}} \quad \text{where } \pi_t[\mathbf{h}_{\mathbf{a}}] = \delta(\mathbf{M} - \mathbf{m}(t)) \quad (3.21)$$

the time derivative of n can be calculated using

$$\frac{d}{dt} \pi = - \frac{\partial \pi}{\partial \mathbf{M}} \frac{d}{dt} \mathbf{m} \quad (3.22)$$

and the equation of motion for the magnetic moments \mathbf{m} , Eq. (3.18). One finds (for a more detailed account please see Ref. [35])

$$\frac{\partial n}{\partial t} = - \frac{\partial}{\partial \mathbf{M}} \left\{ \left[\gamma (\mathbf{M} \times \mathbf{H}_{\text{eff}}) - \gamma \frac{\alpha}{M} (\mathbf{M} \times (\mathbf{M} \times \mathbf{H}_{\text{eff}})) + \gamma^2 D \left(\mathbf{M} \times \left(\mathbf{M} \times \frac{\partial}{\partial \mathbf{M}} \right) \right) \right] n \right\}. \quad (3.23)$$

In order to ensure that the stationary properties of the system described by Eq. (3.18) have the correct equilibrium properties, the above Fokker-Planck equation has to have the Maxwellian equilibrium distribution

$$n_0(\mathbf{M}) \propto e^{-\beta\mathcal{F}[\mathbf{M}]} \quad (3.24)$$

as a stationary solution. This demand will fix the constant D . Using

$$\frac{\partial n_0}{\partial \mathbf{M}} = -\beta \frac{\partial \mathcal{F}[\mathbf{M}]}{\partial \mathbf{M}} n_0 = \beta \mathbf{H}_{\text{eff}} n_0 \quad (3.25)$$

one proves that the expression $\mathbf{M} \times \mathbf{H}_{\text{eff}} n_0$ is divergence-free

$$\begin{aligned} \frac{\partial}{\partial \mathbf{M}} (\mathbf{M} \times \mathbf{H}_{\text{eff}} n_0) &= n_0 \frac{\partial}{\partial \mathbf{M}} (\mathbf{M} \times \mathbf{H}_{\text{eff}}) + (\mathbf{M} \times \mathbf{H}_{\text{eff}}) \cdot \frac{\partial}{\partial \mathbf{M}} n_0 \\ &= 0 + \beta n_0 (\mathbf{M} \times \mathbf{H}_{\text{eff}}) \cdot \mathbf{H}_{\text{eff}} = 0 \end{aligned} \quad (3.26)$$

For $n = n_0$ the first term of the Fokker-Planck equation therefore vanishes and one finds that one has to choose

$$\beta \gamma^2 D = \gamma \frac{\alpha}{M} \quad (3.27)$$

to make n_0 a solution of Eq. (3.23) in agreement with Eq. (3.19).

3.2.4 Numerical integration of the stochastic Landau-Lifschitz-Gilbert equation

In our presentation of the numerical integration scheme we follow Ref. [36]. We consider a general system of Langevin equations

$$\frac{dy_i}{dt} = A_i(\mathbf{y}, t) + \sum_k B_{ik}(\mathbf{y}, t) L_k(t) \quad (3.28)$$

where $\mathbf{y} = (y_1, \dots, y_n)^T$ are the dynamical variables of the system and L_k are Langevin sources of noise. The $L_k(t)$ obey the following stochastic properties

$$\langle L_k(t) \rangle = 0 \quad \text{and} \quad \langle L_i(s) L_j(t) \rangle = 2D \delta_{ij} \delta(t - s) \quad (3.29)$$

When the functions $B_{ik}(\mathbf{y}, t)$ depend on \mathbf{y} , the noise is said to be “multiplicative” else it is “additive” (Itô = Stratonovich).

The next step is to find an appropriate iterative method which can be used for the temporal discretization and approximative solution of Eq. (3.28). In case the noise terms are “multiplicative” care must be taken in the choice of numerical integration scheme. First, there is a problem at the level of definition: different integration schemes converge to either Itô or Stratonovich calculus. A scheme must be chosen which actually converges to the stochastic interpretation of one’s choosing. But even apart from these problems serious difficulties arise in the construction of higher-order integration schemes. The naive adaption of schemes used for deterministic systems of equations may not converge for the stochastic problem at all and even if so usually with lower order [53].

The simplest integration scheme is given by Euler’s approximation. For a given time discretisation $t^{(0)} < t^{(1)} < \dots < t^{(N)}$ the Euler approximation fulfils the following recurrence relation

$$y_i^{(n+1)} = y_i^{(n)} + A_i(t^{(n)}, \mathbf{y}^{(n)}) (t^{(n+1)} - t^{(n)}) + \sum_k B_{ik}(\mathbf{y}^{(n)}, t^{(n)}) \left(L_k^{t^{(n+1)}} - L_k^{t^{(n)}} \right) \quad (3.30)$$

The random increments $\Delta L_k^n \equiv L_k^{t^{(n+1)}} - L_k^{t^{(n)}}$ are generated from pseudorandom numbers with the properties

$$\begin{aligned} \langle \Delta L_k^n \rangle &= 0 \\ \langle (\Delta L_k^n)^2 \rangle &= 2D\Delta t^{(n)} \end{aligned} \quad (3.31)$$

where $\Delta t^{(n)} \equiv t^{(n+1)} - t^{(n)}$. With the initial condition

$$y_i^{(0)} = y_i^{\text{init}} \quad (3.32)$$

the above equations can be implemented on a computer to calculate an approximate solution of the system of stochastic differential equations. Typically the error is defined as

$$\epsilon = \langle |\mathbf{y}^{(N)} - \mathbf{Y}(t^{(N)})| \rangle \quad (3.33)$$

here $\langle \dots \rangle$ denotes an ensemble average and $\mathbf{Y}(t^{(N)})$ the (typically unknown) exact solution of the stochastic equations of motion. It can be shown that for “well-behaved” stochastic equations the systematic error of the Euler approximation follows $\epsilon(\Delta t) \approx \sqrt{\Delta t}$ (Ref. [53], Theorem 10.2.2). It should be noted that this estimate involves only the systematic error of the approximation. On any computing architecture with a finite floating-point accuracy additional rounding errors accumulate. This causes the “sweet-spot” to lie at a finite Δt and consequently one cannot drive the error to 0 by simply making Δt smaller and smaller (not at constant floating-point accuracy). Another important point is that the Euler approximation converges in the form written above to the Itô interpretation. Therefore modifications are necessary to the equations of motion prior to application if they were constructed in the Stratonovich language. The necessary modification is the addition of a noise-induced drift term [53]

$$\begin{aligned} y_i^{(n+1)} = y_i^{(n)} + & \left(A_i(t^{(n)}, \mathbf{y}^{(n)}) + D \sum_{jk} B_{jk}(\mathbf{y}^{(n)}, t^{(n)}) \frac{\partial B_{ik}(\mathbf{y}^{(n)}, t^{(n)})}{\partial y_j} \right) (t^{(n+1)} - t^{(n)}) \\ & + \sum_k B_{ik}(\mathbf{y}^{(n)}, t^{(n)}) \left(L_k^{t^{(n+1)}} - L_k^{t^{(n)}} \right) \end{aligned} \quad (3.34)$$

The construction of higher-order integration schemes for stochastic differential equations is difficult [36], however one can do better than the Euler approximation. For the Euler method we simply froze the right hand side of the stochastic equation at $(t^{(0)}, \mathbf{y}^{(n)})$ at the beginning of each discretisation subinterval. An obvious

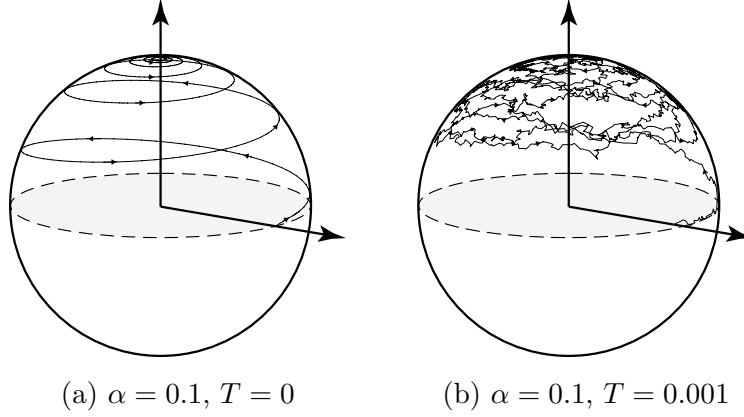


Figure 3.3: Exemplary, numerical solutions of the equation of motion, Eq. (3.18).

improvement is to include additional information from elsewhere in the subinterval. For instance, we could use the average of both endpoints

$$\begin{aligned}
y_i^{(n+1)} &= y_i^{(n)} + \frac{1}{2} (A_i(t^{(n)}, \mathbf{y}^{(n)}) + A_i(t^{(n+1)}, \mathbf{y}^{(n+1)})) (t^{(n+1)} - t^{(n)}) \\
&+ \sum_k \frac{1}{2} (B_{ik}(\mathbf{y}^{(n)}, t^{(n)}) + B_{ik}(\mathbf{y}^{(n+1)}, t^{(n+1)})) (L_k^{t^{(n+1)}} - L_k^{t^{(n)}}) \quad (3.35)
\end{aligned}$$

This is an implicit scheme as the unknown quantity $\mathbf{y}^{(n+1)}$ appears on both sides of the equation. This prevents us from an algebraic evaluation of the above equation. However we can replace the occurrences of $\mathbf{y}^{(n+1)}$ on the right hand side by Euler approximations of the same.

$$\begin{aligned}
\tilde{y}_i^{(n+1)} &= y_i^{(n)} + A_i(t^{(n)}, \mathbf{y}^{(n)}) (t^{(n+1)} - t^{(n)}) + \sum_k B_{ik}(\mathbf{y}^{(n)}, t^{(n)}) (L_k^{t^{(n+1)}} - L_k^{t^{(n)}}) \\
y_i^{(n+1)} &= y_i^{(n)} + \frac{1}{2} (A_i(t^{(n)}, \mathbf{y}^{(n)}) + A_i(t^{(n+1)}, \tilde{\mathbf{y}}^{(n+1)})) (t^{(n+1)} - t^{(n)}) \\
&+ \sum_k \frac{1}{2} (B_{ik}(\mathbf{y}^{(n)}, t^{(n)}) + B_{ik}(\tilde{\mathbf{y}}^{(n+1)}, t^{(n+1)})) (L_k^{t^{(n+1)}} - L_k^{t^{(n)}}) \quad (3.36)
\end{aligned}$$

The above integration rule is called *Heun's scheme*. The quantity $\tilde{\mathbf{y}}^{(n+1)}$ is referred to as the predictor. Heun's scheme converges in quadratic mean to the solution of the stochastic differential equation if interpreted in the sense of Stratonovich [53].

Application to the stochastic Landau-Lifschitz-Gilbert equation

For the treatment of the stochastic Landau-Lifschitz-Gilbert equation, Eq. (3.18), we will use Heun's scheme. This is done because it converges naturally without modification to the Stratonovich interpretation. Since the deterministic part of the differential equations is treated with a higher order integration rule, Heun's scheme is more stable than Euler-type approaches [36]. The Landau-Lifschitz-Gilbert equation

can be written in the language introduced in the last section by identifying

$$\begin{aligned} A_i &= -\gamma \left[\mathbf{m} \times \mathbf{H}_{\text{eff}} - \frac{\alpha}{m} \mathbf{m} \times (\mathbf{m} \times \mathbf{H}_{\text{eff}}) \right] \\ B_{ik} &= -\gamma \left[\sum_j \epsilon_{ijk} m_j + \frac{\alpha}{m} (\mathbf{m}^2 \delta_{ik} - m_i m_k) \right] \end{aligned} \quad (3.37)$$

As a test of the above scheme we integrate the equations of motion for a single spin of length $|\mathbf{m}| = 1$ with the initial condition $\mathbf{m}^{(0)} = (1, 0, 0)^T$ in an applied magnetic field $\mathbf{H}^{(\text{ext})} = (0, 0, 0.01)^T$ with Gilbert damping $\alpha = 0.1$ for temperature $T = 0$ (Fig. 3.3a) and $T = 0.001$ (Fig. 3.3b). For the $T = 0$ the spin simply relaxes in a spiral towards the applied magnetic field $\mathbf{H}^{(\text{ext})}$ on a timescale of the order $1/\alpha$. For finite T the spiral can still be seen, but the path is noisy due to the thermal fluctuations.

Part II

Projects

Chapter 4

Emergent magnetic monopoles

Experimentally one observes that the electric charge always appears as an integer multiple $q_e = ne$ of an elementary charge e . Why this is the case is unknown as charge quantisation is still an unresolved physical problem. The situation changes however if there were magnetic charges. Dirac (1931, [18]) postulated the existence of magnetic monopoles and showed that quantum mechanics is only then consistent if the product of any pair of magnetic charge q_m and electric charge q_e is an integer multiple of $2\pi\hbar$.

The idea of magnetic monopoles dates back to the earliest days of magnetism as magnets appear to have two magnetic poles of opposite strength. In the middle of the nineteenth century the electric currents were recognised as a source of magnetism and later the magnetism found in materials was explained by magnetic dipole moments associated with fundamental particles such as the electron. To this day despite intensive search throughout the observable universe the elementary magnetic monopole remains a hypothetical particle.

The absence of magnetic charges is built into Maxwell's equations. The equation $\nabla \cdot \mathbf{B} = 0$ for the magnetic field \mathbf{B} implies by the Gauss' law that the magnetic flux through any closed surface vanishes and that hence there is no source of the magnetic flux. However it is possible to include magnetic charges into Maxwell's theory bringing the equations of electrodynamics to a symmetric form

$$\begin{aligned} \nabla \times \mathbf{H} &= \dot{\mathbf{E}} + \mathbf{j}_e, & \nabla \cdot \mathbf{D} &= \rho_e, & \mathbf{D} &= \epsilon_0 \mathbf{E} \\ -\nabla \times \mathbf{E} &= \dot{\mathbf{B}} + \mathbf{j}_m, & \nabla \cdot \mathbf{B} &= \rho_m, & \mathbf{B} &= \mu_0 \mathbf{H} \end{aligned} \quad (4.1)$$

where we have introduced the magnetic charge density ρ_m and the magnetic current density \mathbf{j}_m . As a consequence of the above equation the magnetic charge obeys the continuity equation $\dot{\rho}_m + \nabla \cdot \mathbf{j}_m = 0$ and is hence conserved like the electric charges. There is however a difference in the transformation properties of magnetic and electric charges. To conserve parity invariance of the electromagnetic theory ρ_m has to transform like a pseudo-scalar and \mathbf{j}_m like an axial vector. Therefore as electric charges have a sign, magnetic charges have a handedness, c.f. Fig 4.1.

Section 4.1 outlines the original idea of Dirac. We then mention occurrences of magnetic monopoles in solid state systems in 4.2 especially emphasising on the case of spin ice. The main part of this chapter is devoted to the discussion of *emergent* magnetic monopoles in chiral magnets in section 4.3.

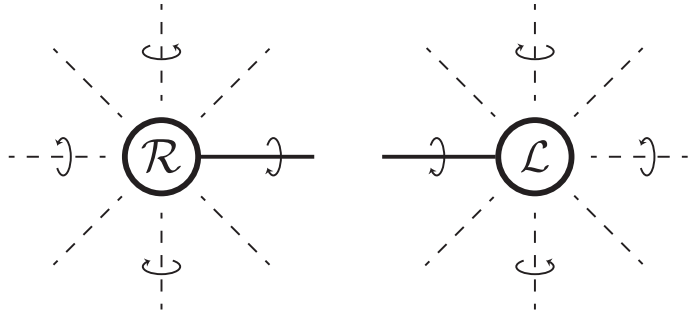


Figure 4.1: Magnetic fields of right- and left-handed monopoles.

4.1 The Dirac monopole

Dirac begins his seminal paper about “*Quantised Singularities in the Electromagnetic Field*” with a rather long introduction to the growing propinquity of mathematics and physics trying to set the mood for what follows as an essentially mathematical argument.

A magnetic point charge of strength q_m at rest at the origin creates a magnetic field

$$\mathbf{B} = \frac{q_m}{4\pi\mathbf{r}^2}\hat{\mathbf{r}}, \quad \nabla \cdot \mathbf{B} = q_m\delta(\mathbf{r}). \quad (4.2)$$

Away from the origin the vacuum equations are fulfilled, however at the origin there is a delta charge. Dirac insists that a vector potential for the above magnetic field configuration exists. Due to the singular charge distribution such a vector potential will have a singularity which poses no significant problem. The more serious mathematical obstacle is the fact that even with the origin excluded no smooth vector potential can be globally defined on $\mathbb{R}^3 \setminus \{\mathbf{o}\}$. Dirac tackles the problem by a generalisation of the wave function concept: fixing an origin $\mathbf{o} \in \mathbb{R}^3$ a wave function $\Psi(\mathbf{x})$ not only depends on the point \mathbf{x} but on a particular path $\gamma_{\mathbf{x}}$ connecting \mathbf{o} and \mathbf{x} thus becoming a functional $\Psi : \gamma_{\mathbf{x}} \rightarrow \Psi[\gamma_{\mathbf{x}}]$. A necessary condition to remove redundancy is that a single reference path $\gamma_{\mathbf{x}}$ joining \mathbf{o} and \mathbf{x} already determines the wave function of all other paths $\gamma'_{\mathbf{x}}$ ending at \mathbf{x} . This means that for any two paths Ψ and Ψ' connecting \mathbf{o} with the same point \mathbf{x} the wave functions have to be related to each other by a known phase factor

$$\Psi[\gamma'_{\mathbf{x}}] = e^{2\pi i\Phi(S)}\Psi[\gamma_{\mathbf{x}}], \quad \text{with } \Phi(S) = e/h \int_S \mathbf{B} \cdot d^2\mathbf{n} \quad (4.3)$$

where S is an oriented surface with $\partial S = \gamma'_{\mathbf{x}} - \gamma_{\mathbf{x}}$ and $\Phi(S)$ is the magnetic flux through the surface S , Fig. 4.4. He continues to point out that if the magnetic field is finite, the functional $\Psi[\gamma_{\mathbf{x}}]$ is smooth and therefore small changes in the path $\gamma_{\mathbf{x}}$ will lead to small changes in the wave function only. For the phase factor however this is only true if the wave function does not vanish

$$\arg \Psi[\gamma_{\mathbf{x}}] = \frac{1}{2i} \log (\Psi[\gamma_{\mathbf{x}}]/\Psi^*[\gamma_{\mathbf{x}}]) . \quad (4.4)$$

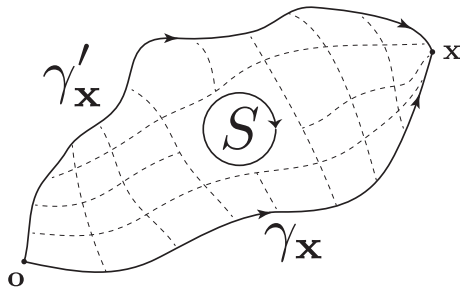


Figure 4.2

Since in 3 dimensions for a vanishing of the wave function two conditions have to be satisfied, $\text{Re } \Psi = 0$ and $\text{Im } \Psi = 0$, typically lines of vanishing Ψ are found, that Dirac refers to as *nodal lines*. Due to condition Eq. (4.4) the change of phase around a nodal line need not be small. All that can be said is that the phase picked up on a closed path around such a nodal line must be an integer multiple of 2π for the phase to be a continuous function. Since traversing a chosen path around a line backwards accumulates the negative phase, the winding of the phase around a nodal line endows it with a sense of circulation. The connection of this sense of circulation with phase factor is given by equation (4.3). If the direction of circulation around the nodal lines agrees with the internal orientation of the surface S the phase counts positive.

Dirac now suggests the possibility for nodal lines to have points of origin and termination, *nodal singularities*. In order for the phase factor $\Phi(S)$ to be well defined one has to augment the theory with another constraint. Since for a given pair of paths γ and γ' one may choose any surface S or S' as long as their boundaries agree, $\partial S = \partial S' = \gamma' - \gamma$, one has to demand $\Phi(S) = \Phi(S')$. With the possibilities of nodal lines to start and terminate this poses a problem as one can construct the situation where S intersects with the nodal line while S' does not leading to a discrepancy of $\pm 2\pi n$. Therefore Eq. (4.3) has to be adjusted

$$\Phi(S) = e/h \int_S \mathbf{B} \cdot d^2\mathbf{n} + \sum_i \pm n_i \quad (4.5)$$

where the sum extends over all nodal lines intersecting with the surface S and the correct sign is chosen by comparison of orientations as mentioned above.

Since $\int_S \mathbf{B} \cdot d^2\mathbf{n}$ computes the magnetic flux through S , Dirac concluded by considering the case of a closed surface $S = \partial U$ with U a volume that $\Phi(\partial U) = 0$ and thus the i th nodal singularity can be considered as magnetic monopole with charge $\frac{2\pi\hbar}{e}n_i$ with $n_i \in \mathbb{Z}$. This receives the Dirac's condition for the quantisation of magnetic and electric charges

$$eq_m \in 2\pi\hbar\mathbb{Z} \quad (4.6)$$

4.2 Magnetic Monopoles in Spin Ice

Although magnetic monopoles have so far not been observed as elementary particles there are condensed matter systems where collective behaviour leads to emergent

phenomena that resemble certain aspects of magnetic monopoles. To understand the relation between the magnetic monopole as an elementary particle and its occurrence in condensed matter system one has to appreciate the difference between the microscopic and macroscopic Maxwell equations. The microscopic Maxwell equations describe the electromagnetic fields due to the charge and current densities on a atomic scale. Although this has universal applicability for a complicated condensed matter system this is typically not feasible to calculate. Instead one retracts to the description of electromagnetic phenomena on larger length scales by essentially subsuming microscopic behaviour. This is achieved by the introduction of two auxiliary fields, the displacement field \mathbf{D} and the magnetising field \mathbf{H} . Phenomenological constituent equations relate the additional fields to the electric field \mathbf{E} and the magnetic field \mathbf{B} [14].

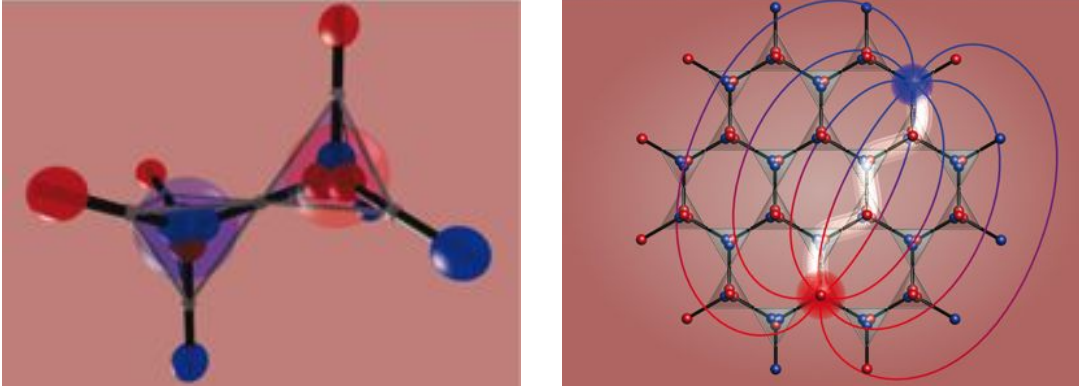
The observation of even a single magnetic monopole would contradict the Maxwell equation $\nabla \cdot \mathbf{B} = 0$. No such contradiction has been observed to this day and one must assume that the constraint posed by the above equation is in place. However for condensed matter systems and the magnetising field \mathbf{H} no such constraint applies. Indeed a number of systems exists where sources of the magnetising field have been observed. Here we only present the most prominent example of spin ice and later contrast monopoles in spin ice to those found in chiral magnets.

The first materials identified as spin ices were the pyrochlores $\text{Dy}_2\text{Ti}_2\text{O}_7$ (dysprosium titanate), $\text{Ho}_2\text{Ti}_2\text{O}_7$ (holmium titanate) and $\text{Ho}_2\text{Sn}_2\text{O}_7$ (holmium stannate). The magnetic properties of these materials can be understood if one considers a three-dimensional lattice of magnetic moments organised at the edges of corner sharing tetrahedra. Spin ice can be realised on this lattice when spins placed on the vertices are constrained to point radially into the or out of the tetrahedra and coupled ferromagnetically.

The word ice in the name stems from a similarity to an entropic effect in water ice. In 1935 Linus Pauling[77] noted that the structure of ice contains oxygen atoms with four neighbouring hydrogen atoms. The distance between oxygen and hydrogen atoms is not the same however as two hydrogen atoms are near forming the traditional H_2O molecule and two are further away being the hydrogen atoms of neighbouring water molecules. This gives rise to the *ice rules*: Two atoms have to be near, two have to be further away. He concluded that this leads to a residual entropy even upon cooling to zero temperature. Ice therefore exhibits degrees of freedom which remain disordered even at absolute zero. The number of configurations conforming to these ice rules grows exponentially with the system size, and therefore that the zero-temperature entropy of ice was expected to be extensive. Pauling's findings were later confirmed by specific heat measurements.

In the above mentioned pyrochlores the spin rules apply to the configuration of the spins at the vertices of the tetrahedra. Here geometric frustration causes the lowest energy spin configuration to obey the rule that two spins have to point in and two out of each tetrahedron. Indeed the Pauling ice entropy, $S \approx R/2 \ln(3/2)$ per spin with R the gas constant, found in these materials reflects a huge low-energy density of states in zero magnetic field [84].

Excitations above this ground state manifold are given by local violations of these ice rules. A single spin flip violates the rules on two neighbouring tetrahedra, at a



(a) The dumbbell picture is obtained by replacing each spin with a pair of opposite magnetic charges placed on the adjacent sites of the diamond lattice. Inverting the shared spin creates a pair of magnetic monopoles on adjacent sites.

(b) A pair of separated magnetic monopoles. The chain of inverted dipoles (*Dirac string* or *nodal line*) between them is highlighted in white and magnetic field lines are sketched.

Figure 4.3: Picture taken from Ref. [14].

cost of ≈ 2 K in $\text{Dy}_2\text{Ti}_2\text{O}_7$. The characteristics of these excitations were studied by Castelnovo et al. [14] by replacing the interaction energy of the magnetic dipoles by the interaction energy of magnetic dumbbells, see Fig. 4.3a. Demanding that the dipole moment of the original spin is reproduced fixes the magnetic charges to $\pm\mu/a_d$ with the diamond lattice bond length $a_d = \sqrt{3/2} a$ and μ the magnetic permeability of the material.

Inverting a spin on a vertex between two tetrahedra creates in the dumbbell picture a pair of magnetic monopoles on adjacent sites. The interaction energy is now computed by the pairwise interaction of magnetic charges as given by the Coulomb law

$$V(r_{\alpha\beta}) = \begin{cases} \frac{\mu_0 Q_\alpha Q_\beta}{4\pi} r_{\alpha\beta} & \alpha \neq \beta \\ \frac{1}{2} \nu_0 Q_\alpha^2 & \alpha = \beta \end{cases} \quad (4.7)$$

with Q_α the net magnetic charge on site α and $r_{\alpha\beta}$ the distance between two sites. Monopoles may be separated from one another without further violations of the ice rules by flipping a chain of adjacent dumbbells as shown in Fig. 4.3b. This string may be directly compared to the *Dirac string* or *nodal line* introduced earlier [70]. It takes only a finite amount of energy to separate the two monopoles to infinity so they are the true elementary excitations of the system. Therefore the monopoles are truly deconfined as the the cost of creating the Dirac string remains finite as its length grows. In a typical spin ice state at finite temperature one finds a “soup” of Dirac strings of different length.

With respect to the Dirac quantisation condition, Eq. (4.6), one should remember that the charge quantisation condition stems from the fact that the Dirac string has to be unobservable for quantum mechanics to be consistent. The string soup characteristic of spin ice at low T makes the Dirac string energetically unimportant albeit not unobservable. Therefore monopoles in spin ice have no quantised charge. Their

charge is determined by the characteristics of the concrete material under consideration and can even be tuned continuously by applying pressure [70].

4.3 Emergent Magnetic Monopoles in Chiral Magnets

In this section we introduce the concept of *emergent* magnetic monopoles in chiral magnets. In 2012 Schulz and collaborators [88] showed that a particularly illuminative way to describe the forces that act on both an electron traversing a smooth magnetic structure and the structure itself can be accounted for by the introduction of a fictitious, emergent electrodynamic potential. It is in this sense that an unwinding of a Skyrmion lattice is accompanied by the appearance of quantised emergent magnetic charges. In subsection 4.3.1 we give a short introduction to emergent electrodynamics and emphasise especially on the emergent magnetic field. We briefly discuss the experimental observation of this field as a topological contribution to the Hall effect. Then we turn in subsection 4.3.2 to the discovery of the emergent magnetic monopoles and the roles they play in phase transitions. Most of the results in this subsection have been published in Ref. [67].

4.3.1 Emergent Electrodynamics of Skyrmions

Non-collinear magnetic structures induce forces in moving conduction electrons. For smooth structures the dominant coupling mechanism is due to Berry phases picked up by the electron as its spin aligns adiabatically to the background magnetisation direction. These forces may be accounted for in an elegant way by the introduction of emergent electrodynamic potentials. As we will see the topology of the magnetic configuration also induces topological constraints in the geometry of the emergent vector potential.

The importance of Berry phases has been known for a long time. Volovik addressed the problem of linear momentum in ferromagnets using a technique which we also prove useful for the study of skyrmion lattices [107]. In ferromagnets Haldane[41] pointed out that the canonical momentum of the coherent magnetisation motion is not invariant under spin rotations and in general not conserved. The reason is that a separation of the fermionic, incoherent subsystem from the coherent motion of the local magnetisation makes the respective momenta ill defined. Both linear and angular momenta of coherent motion transfer to the incoherent degrees of freedom in the subsystem of fermionic excitations. He described the dynamics of the soft variable \mathbf{m} , the local magnetisation, by the introduction of fictitious emergent electrodynamic fields. Here we present an analogous treatment for chiral magnets.

Due to the smoothness of the magnetic structure the wavelength of the conduction electrons is small compared to the typical scale on which the magnetisation varies. As mentioned in chapter A the typical lattice constant of the skyrmion lattice in MnSi is $\approx 200 \text{ \AA}$. Therefore one can assume to a good approximation that the electron's spin aligns adiabatically with the direction of the local background magnetisation. We will later discuss the assumption of adiabaticity further and also mention the

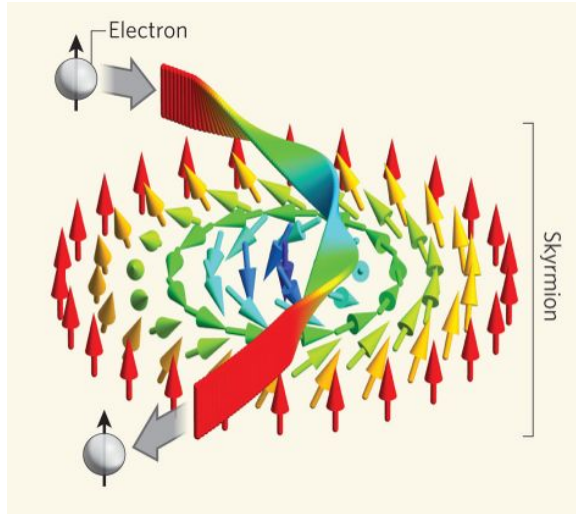


Figure 4.4: With the magnetic moment of the electron adjusting adiabatically to the direction of the local background magnetisation, the electron picks a geometrical phase called the Berry phase. Picture taken from [82]

most important mechanisms which may lead to violations of this assumption (see also [88] and [111]).

During their motion through space time the adjustment of the spin causes the electrons to pick up a geometrical, quantum-mechanical phase known as the Berry phase, see Fig. 4.4. The accumulated phase really depends on the background magnetisation changes encountered on the concrete choice of path in space time. Therefore the phase depends on the details of the magnetic configuration which can be conveniently accounted for by the introduction of a fictitious emergent electrodynamic potential. In the following derivation we borrow from both [24] and [111].

We consider a simple model Hamiltonian for free spin- $\frac{1}{2}$ electrons moving through a smoothly varying magnetic structure $\mathbf{M}(\mathbf{r}, t)$. Here the free electron Stoner model provides a first approximation to the electronic structure of an itinerant magnet

$$H = -\frac{\hbar}{2m}\nabla^2\mathbb{1} - J\sigma \cdot \hat{M}(\mathbf{r}, t) \quad (4.8)$$

where σ is the vector of Pauli matrices and \hat{M} the direction of the local magnetisation $\hat{M} = \mathbf{M}/|\mathbf{M}|$. The coupling constant J parametrizes the strength of the exchange coupling in the sense that it is chosen such that the Zeeman splitting between the two spin bands in the above equation reproduces the quantum mechanical exchange energy and therefore also contains the magnitude of the magnetisation.

The dynamics is then given by the Schrödinger equation

$$i\hbar \partial_t \psi(\mathbf{r}, t) = \left[-\frac{\hbar}{2m}\nabla^2\mathbb{1} - J\sigma \cdot \hat{M}(\mathbf{r}, t) \right] \psi(\mathbf{r}, t) \quad (4.9)$$

One can now trivialise the last term by the introduction of a local unitary transformation which rotates the local spin quantisation axis to lie parallel to \hat{M} . This however

comes at the cost of additional (partial) derivatives of the transformation matrix on the right-hand and the first term of the left-hand side. We introduce the local 2×2 unitary matrix $U(\mathbf{r}, t)$ by

$$U(\mathbf{r}, t) = \exp\left(-i\frac{\theta(\mathbf{r}, t)}{2}\sigma \cdot \hat{n}(\mathbf{r}, t)\right) \quad (4.10)$$

here $\hat{n}(\mathbf{r}, t)$ is the axis of rotation given by $\hat{n}(\mathbf{r}, t) = \hat{e}_z \times \hat{M}/|\hat{e}_z \times \hat{M}|$ orthogonal to both \hat{M} and the original axis of spin quantisation (we choose the z -axis here) and $\theta(\mathbf{r}, t)$ the angle of rotation. With the substitution $\psi(\mathbf{r}, t) = U(\mathbf{r}, t)\phi(\mathbf{r}, t)$ and after multiplication with $U^\dagger(\mathbf{r}, t)$ from the right, Eq. (4.9) becomes

$$i\hbar\partial_t\phi(\mathbf{r}, t) - q^e V^e \phi(\mathbf{r}, t) = \left[\frac{(\mathbf{p}\mathbb{1} - \mathbf{A}^e)^2}{2m} - J\sigma_z\right]\phi(\mathbf{r}, t), \quad \text{with} \quad \begin{cases} V^e = -i\hbar/q^e U^\dagger \partial_t U \\ \mathbf{A}^e = -i\hbar/q^e U^\dagger \nabla U \end{cases} \quad (4.11)$$

Note that V^e and \mathbf{A}^e are still both 2×2 matrices although they were already given names which suggest otherwise. q^e is an arbitrary constant which (currently) drops out of the equation and will be given meaning in a moment.

The two components of the Schrödinger equation describe the electrons in the majority and minority spin band respectively. For slowly varying magnetic structures the ground state of the fermionic system may be considered as two unequally populated Fermi spheres of electrons with spins (anti-)parallel to the local magnetisation. The difference in population determines the size of the local magnetic moment $n_+ - n_- = 2|\mathbf{M}|/\gamma\hbar$. Off-diagonal terms in both V^e and \mathbf{A}^e describe scattering between these bands. To estimate the strength of these processes one has to take the 3 length scales inherent to our problem into account: (i) the Fermi wavelength of the electrons ξ_F , (ii) the typical length scale on which the magnetic structure varies ξ_M and (iii) the typical mean free path ξ_{MFP} .

We consider the limit in which the Fermi wavelength is short compared to the mean free path. This limit allows the description of the states of the system in terms of the eigenstates of the system in the absence of scattering. When the mean free path is much longer than the characteristic size of the structure, the distribution function f_σ of electrons with spin parallel/anti-parallel to the background magnetisation describes the occupancy of the eigenstates of the entire system. This distribution function f_σ is independent of the spatial coordinate and we refer to this approach as global. In the opposite limit, the distribution function is spatially varying and describes the occupancy of eigenstates of the local Hamiltonian, which includes the exchange field and the gradient field. We refer to this approach as local, as the distribution function can vary spatially.

Due to the smoothness of the skyrmion structure and the large distance of skyrmions of the order of $\sim 200 \text{ \AA}$, violation of adiabaticity and such bandstructure effects are probably small suggesting that the most important corrections may arise from spin-flip scattering processes which scatter electrons, e.g., from a majority to a minority band. These spin-flip processes, which can be interaction- or disorder-induced, arise due to weak spin-orbit scattering and the modulation of the magnetisation \mathbf{M} . While

the non-spin-flip scattering length is estimated to be between 10 and 100 Å, the spin-flip scattering length is much larger and therefore probably also much larger than the distance between the skyrmions ≈ 200 Å [88].

Consequently we assume that the distribution function describes the occupancy of the eigenstates of the entire system and that the length of the magnetic moment is a constant $|\mathbf{M}(\mathbf{r}, t)| = M_0$. The off-diagonal terms in V^e and \mathbf{A}^e are suppressed and can be discarded rendering both V^e and \mathbf{A}^e proportional to σ_z . This means that an electron in the (upper) majority band collects the opposite Berry phase than an electron in the (lower) minority band. We can therefore regard V^e and the components of A_i^e as scalar potentials if we agree to define an “emergent charge” q_e which takes a value of $\frac{1}{2}$ for electrons in the upper band $-\frac{1}{2}$ in the lower band. The similarity to electrodynamics becomes now apparent. We therefore refer to the potential \mathbf{A}^e as the “emergent vector potential” and V^e as the “emergent scalar potential”.

The vector potential induces an emergent magnetic field which is felt by the conduction electron and for time dependent magnetic structures also an emergent electric field

$$\begin{aligned} B_i^e &= \epsilon_{ijk} \partial_j A_k^e = \frac{\hbar}{2} \epsilon_{ijk} \hat{M} \cdot (\partial_j \hat{M} \times \partial_k \hat{M}) \\ E_i^e &= -\partial_i V^e - \partial_t A_i^e = \hbar \hat{M} \cdot (\partial_t \hat{M} \times \partial_i \hat{M}) \end{aligned} \quad (4.12)$$

The emergent magnetic field can be understood as an emergent (fictitious) Aharonov-Bohm field, which accounts for the topology of the adiabatic changes of the spins orientation as the electron traverses the magnetic structure. Corrections due to non-adiabatic processes are discussed in Refs. [111, 88]. Furthermore dissipative drag forces acting on the electrons are not taken into account. A detailed discussion of these and the conditions under which their neglect is can be found in Ref. [24].

Emergent magnetic field

The reader might recognize the expression for the emergent magnetic field above, Eq. 4.12, as $4\pi\hbar$ times the winding number density of the magnetic configuration, Eq. 1.6. For a lattice of antiskyrmions one finds that the winding number density integrates to -1 for each magnetic unit cell as the magnetization wraps \mathbb{S}^2 once in spin space for each skyrmion in the lattice. The flux generated by the emergent magnetic field is therefore quantized to minus one emergent flux quantum $\phi_0 = h/q_e = 4\pi\hbar$ per magnetic unit cell. Hall measurements are sensitive to both the real and the emergent magnetic field and therefore allow a direct measurement of the winding number density. In chiral magnets no other but the A-phase displays a finite winding number density and therefore a non-vanishing emergent magnetic field. In the following we discuss the experimental detection of an additional contribution to the Hall signal due to the finite skyrmion density, i.e. the topological Hall effect (THE).

When a current flows through a conductor with a magnetic field applied perpendicular to the direction of electric charge carrier motion, they experience a Lorentz force perpendicular to both the direction of motion and the applied magnetic field. The paths of the charge carriers between collisions become curved so that moving

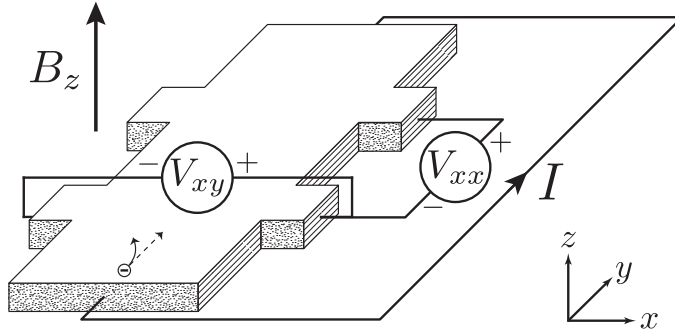


Figure 4.5: Hall Effect measurement setup for electrons. Initially, the electrons follow the curved arrow, due to the magnetic force. At some distance from the current-introducing contacts, electrons pile up on the left side and deplete from the right side, which creates an electric field. In steady-state, the electric field will be strong enough to exactly cancel out the magnetic force, so that the electrons follow the straight arrow (dashed).

charges accumulate on one face of the material. Fig. 4.5 shows a typical Hall measurement setup. Here a finite voltage drop across the sample along the y -direction creates a current. The external magnetic field is applied in the z -direction. For negatively charged carriers moving along the y -direction the Lorentz force causes a deflection along the negative x -direction, c.f. Fig. 4.5, and an accumulation of charge on one face of the material. A potential difference builds up across the x -direction of the sample which is recorded by the applied contacts as the Hall voltage V_{xy} . In steady-state, the electric field will be strong enough to exactly cancel out the magnetic force. The Hall resistivity ρ_{xy} is defined as the ratio of the Hall voltage V_{xy} and the applied current I , $\rho_{xy} = V_{xy}/I$ and the transverse resistivity as the ratio between the transverse voltage V_{xx} and the applied current I , ρ_{xx} as V_{xx}/I . In non-magnetic materials and for small fields the Hall resistivity increases linearly with the strength of the applied magnetic field B_z . The so called Hall conductivity is then given by $\sigma_{xy} = -\rho_{xy}/(\rho_{xy}^2 + \rho_{xx}^2)$.

In chiral magnets one finds several contributing mechanisms to the total Hall effect. The mechanism outlined above is referred to as the normal Hall effect $\rho_{xy}^n = R_0 B$ which is proportional to the strength of the applied magnetic field \mathbf{B} . The precise value of the coupling constant R_0 depends in multi band systems like MnSi on details of the band structure and the relative size of the scattering rates. A second contribution arises from the so called intrinsic anomalous Hall effect (IAHE), ρ_{xy}^{an} . Here spin-orbit coupling and local electric fields on the length scale of the atomic unit cell may lead to a dependence of the spin orientation on momentum. The resulting Berry phases may be described by an emergent magnetic field which acts in momentum space and leads to an additional contribution to the Hall signal. The IAHE typically scales with the total sample magnetisation M and the Hall conductivity σ_{xy} is independent of impurity scattering. The third contribution might arise from the topological Hall effect which can be seen as a complementary mechanism to the IAHE. Also Berry phases collected by the electrons lead to a deflection of the

charge carriers but here the phases are collected in real- instead of in momentum space. As already mentioned, spin textures where the orientation of the background magnetisation changes on length scales much larger than the Fermi wavelength of the electron give rise to Berry phases in real space which may be accounted for by an emergent magnetic field which acts in real space similar to a real magnetic field. As in the normal Hall effect ρ_{xy}^{top} is roughly independent of the total scattering rate, but depends in multi band systems on the relative strength of scattering rates from various bands.

An important motivation for the study of the THE was to prove the existence of the skyrmion lattice in the first place. Evidence of the skyrmion lattice phase in MnSi was given by an small angle neutron scattering study which found a sixfold Bragg peak pattern in a plane perpendicular to the applied magnetic field [72]. However whether this pattern is indeed due to a skyrmion lattice depends crucially on the phase relationship between the helices that are superimposed. This information is not available from the neutron scattering data. The THE as a direct probe of the winding number density would provide the most convincing evidence. Another motivation is due to the hope to find utility for skyrmions in spintronic applications. The current-driven dynamics of skyrmions are crucial for the fast manipulation of skyrmion configurations. Recent experiments have identified the effects of spin transfer torques in the skyrmion lattice of MnSi at tiny electric currents [49, 88, 46]. The size of the THE signal reflects the strength of the coupling between the electric currents and the spin structure [85] and may prove crucial to the understanding of the origin of spin-transfer torques.

A rough estimate for the size of the THE signal is given by $\rho_{xy}^{\text{top}} = PR_0 B_{\text{eff}}^z$ and can be inferred from the following reasoning [75]. As the relative strength of scattering rates in different bands enters into the coupling constant in the THE in a similar way to the normal Hall effect, one can simply try to approximate it by $R_0 \approx 1.7 \times 10^{-10} \Omega \text{ mT}^{-1}$ in MnSi. Majority- and minority electrons have opposite emergent charges and therefore collect Berry phases of opposite sign. The constant P is the charge carrier spin polarisation and depends on a complicated Fermi surface average. However it may be approximated as the ratio of the ordered magnetic moment μ_{spo} to the saturated moment $\mu_{\text{sat}} \approx 2.2 \pm 0.2 \mu_B$ in MnSi. In the skyrmion lattice phase the ordered magnetic moment $\mu_{\text{spo}} \approx 0.2 \pm 0.05 \mu_B$ which gives the estimate $P \approx 0.1 \pm 0.02$. To estimate the strength of the emergent magnetic field B_{eff}^z one has to take the geometry of the skyrmion lattice into account. With its hexagonal shape the real-space lattice vectors of the skyrmion lattice have length $\lambda_S / \sin(2\pi/3)$ where λ_S corresponds approximately to the wavelength of the helical state near T_c , $\lambda_S \approx \lambda_h \approx 165 \text{ \AA}$ in MnSi. Therefore the size of the unit cell is approximately $\lambda_h^2 / \sin(2\pi/3)$ and the strength of the effective magnetic field

$$B_{\text{eff}}^z = -\frac{h}{e} \left(\frac{\sqrt{3}}{2\lambda_S^2} \right) \approx -13.15 \text{ T} \quad (4.13)$$

where the minus sign reflects the fact the emergent magnetic field is antiparallel to the applied magnetic field. With these numbers one can estimate the absolute size of the THE contribution $\rho_{xy}^{\text{top}} \approx -20 \text{ n}\Omega \text{ cm}$.

An important information is the expected temperature dependence of the topological Hall effect. Since the THE depends on the difference in density of minority and majority electrons which decrease as the temperature rises, the THE signal is expected to decrease with increasing temperature. The temperature dependence may even be enhanced due to spin-flip scattering. Since spin-flip scattering typically increases with increasing temperature, the THE may therefore decrease even faster with temperature.

The topological Hall effect has been studied before in materials other than chiral magnets. For instance a topological Hall signal has been reported for three-dimensional pyrochlore lattices [98, 63]. However here the spin structure is due to frustration on short length scales. Therefore the spin structure can not be described as a continuous field for which topological properties are well defined. Moreover the topological Hall effect in these materials is related to a non-zero winding number.

The first experimental study which focused on the topological Hall effect in chiral magnets and consistently explained it in terms of real space Berry phases was performed in 2009 by Neubauer et al.[75]. Here however we present the results of a study of the same group with improved accuracy which also obtained information about the pressure dependence of the THE [85]. In this study single crystals of MnSi grown by optical float-zoning under ultrahigh vacuum compatible conditions with typical dimensions of 2.8 mm long, 1 mm wide and less than 0.2 mm thick were studied. They were oriented such that the magnetic field was applied perpendicular to the platelet and parallel to the crystal $\langle 110 \rangle$. This axis was chosen since $\langle 110 \rangle$ is neither a magnetically hard nor soft axis for the pressure range studied, i.e. the crystallographic direction is not distinct in any way. Electrical currents were applied either in the $\langle 100 \rangle$ or $\langle 110 \rangle$ direction. The resistivity and the Hall effect were measured simultaneously in a standard six terminal configuration, c.f. Fig. 4.5. An improved accuracy compared to an earlier study of the Hall effect in MnSi allowed to identify the THE contribution. For additional details see [75] and [85].

To observe the additional THE signal in the skyrmion lattice phase, magnetic field sweeps at different pressures and temperatures were performed. Fig. 4.6 shows the recorded magnetoresistance ρ_{xx} , Hall resistivity ρ_{xy} and Hall conductivity $\sigma_{xy} = -\rho_{xy}/(\rho_{xx}^2 + \rho_{xy}^2)$ as a function of the applied magnetic field up to 1 T for various temperature T at a pressure of 7 kbar. The temperatures in the legend are both stated as absolute and reduced values $T_{\text{ref}} = (T - T_c)/T_c$.

At high temperatures, the transverse magnetoresistance ρ_{xx} , shown in Fig. 4.6a, decreases with increasing magnetic field. The Hall resistivity ρ_{xy} , shown in Fig. 4.6b, displays a gradual field dependence with a pronounced top-hat-shaped enhancement in a small field and temperature range B_{A1} and B_{A2} , somewhat larger than the skyrmion lattice phase at ambient pressure. In other words, with increasing field the enhancement appears abruptly at a field B_{A1} , and vanishes again equally abruptly at a field B_{A2} . The magnitude of the top-hat-shaped signal contribution is substantially larger than a similar signal contribution in the skyrmion lattice phase at ambient pressure.

To distinguish if the signal contribution represents an anomalous or a topological Hall effect, we the temperature dependence of the magnetisation was measured. No change in the magnetisation was found which would allow to explain the additional

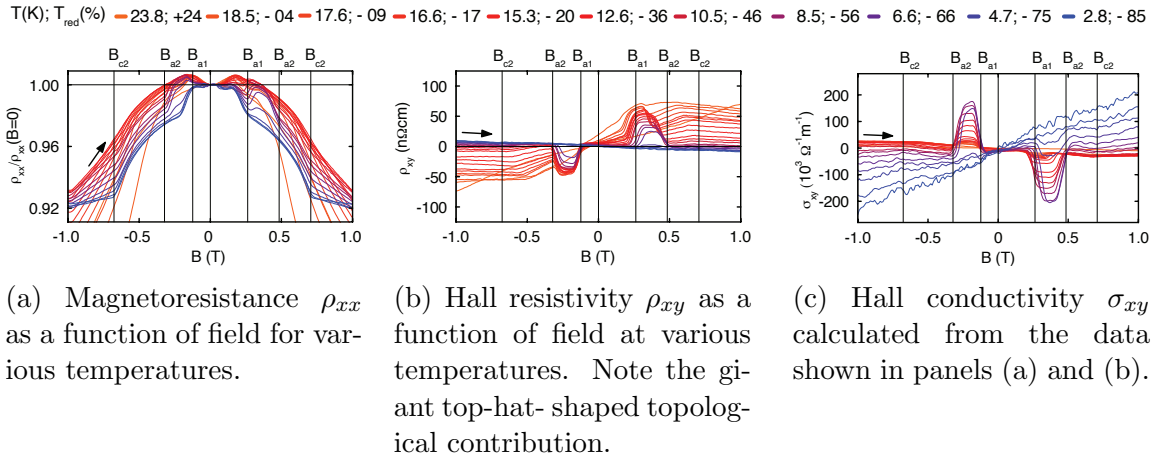


Figure 4.6: Typical magnetotransport data in single-crystal MnSi at a pressure of 7 kbar under applied magnetic fields up to 1 T for various temperatures. These figures were taken from Ref. [85].

top-hat contribution to the Hall signal due to the intrinsic anomalous Hall effect. To elucidate the origin of the large magnitude of the top-hat-shaped signal contribution further, in Fig. 4.6c the Hall conductivity $\sigma_{xy} = -\rho_{xy}/(\rho_{xx}^2 + \rho_{xy}^2) \approx -\rho_{xy}/\rho_{xx}^2$ is shown. The top-hat-shaped contribution in σ_{xy} grows much stronger for lower temperatures (and therefore lower ρ_{xx}) than the signal in ρ_{xy} . As discussed earlier, for the intrinsic anomalous Hall effect, one expects a universal Hall signal in σ_{xy} independent of the scattering time τ , while for the topological Hall effect ρ_{xy} is independent of τ (such that σ_{xy} increases proportional to $1/\rho_{xx}^2$). Therefore, these data suggest that the top-hat signal can be identified with the topological Hall signal which is switched on and switched off when the system enters and leaves the skyrmion phase, respectively.

Concerning the quantitative size of the THE as compared to the naive theoretical estimate made above a discrepancy between theory and experiment of an order of magnitude was found. In Ref. [85] several possible mechanisms which could lead to such a strong reduction of the topological Hall signal are listed. We refer the reader to the reference for a detailed discussion of the various effects.

In conclusion the study allowed to observe experimentally the emergent magnetic field due to the topologically non-trivial magnetisation configuration in the skyrmion lattice phase as felt by the conduction electrons

4.3.2 Unwinding of a Skyrmion Lattice

The detailed, microscopic study of B20 compounds has revealed a great variability in their electronic properties while small angle neutron scattering (SANS) and Lorentz transmission electron microscopy (Lorentz TEM) has shown that the magnetic phase diagram of those ordering helimagnetically is rather generic and always contains a Skyrmion lattice phase. These properties render chiral magnets ideal candidates for the study of topological phase transitions. In the following we study how the Skyrmion lattice unwinds by means of hedgehog point defects which can be interpreted as emergent magnetic monopoles in the language of emergent electrodynamics.

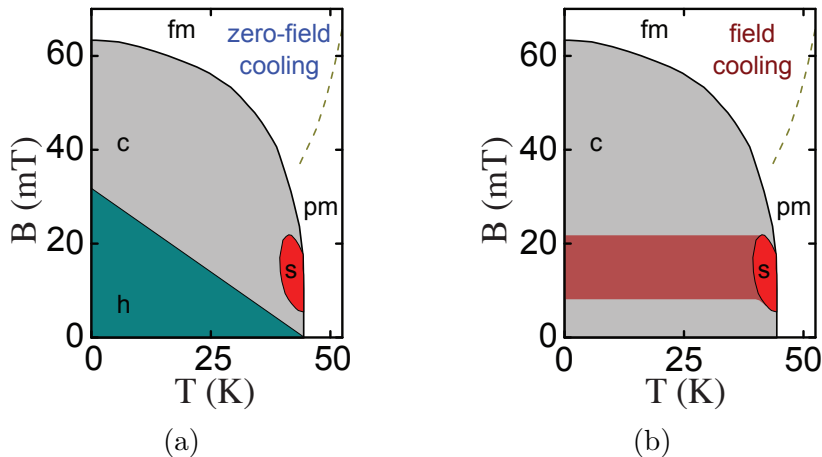


Figure 4.7: (a) Phase diagram observed under zero-field cooling (zfc). The Skyrmion lattice is confined to a small phase pocket (red) just below T_c . (b) Phase diagram observed under field cooling (fc). For field values in the range of the Skyrmion lattice as observed under zfc, the Skyrmion lattice phase persists under field cooling as a metastable state down to the lowest T (red shading).

Most of the results in this section have been published in Ref. [67]. Also note the extensive supplementary material which contains the real-time dynamics, results of SANS measurements and additional MFM data.

In section 4.3.1 we emphasised that Skyrmion lines have a one-to-one correspondence with a quantised (emergent) magnetic flux. Namely, if one integrates the emergent magnetic flux over a surface which intersects a single Skyrmion line once, one finds depending on the relative orientation of the surface normal and the core magnetisation of the Skyrmion plus or minus one emergent flux quantum. Consequently the removal of a Skyrmion from a system is associated with the change of the total magnetic flux through a surface intersecting the system by one emergent magnetic flux quantum. Changes in the Skyrmion number are therefore naturally tied to the appearance of sources and sinks of the emergent magnetic field. To observe the unwinding of the Skyrmion lattice in experiment both magnetic field microscopy (MFM) and SANS studies were performed on a bulk sample of the chiral magnet $\text{Fe}_{1-x}\text{Co}_x\text{Si}$. For more detailed description of SANS and MFM see appendix B. An extensive discussion of the magnetic phase diagram of $\text{Fe}_{1-x}\text{Co}_x\text{Si}$ can be found in appendix A, however here we briefly repeat the relevant points in order to give a coherent description of our study.

Iron-cobalt silicide ($\text{Fe}_{1-x}\text{Co}_x\text{Si}$) is a reasonable choice for MFM measurements as the length scale of the magnetic modulation is $\xi \approx 90$ nm which is large compared to the spatial resolution of the MFM of $\Delta x \approx 20$ nm. Under field cooling (fc), i.e. cooling while keeping the applied field constant, several important differences arise as compared to the zero field cooling (zfc) phase diagram (compare Fig. 4.7a and Fig. 4.7b). First for magnetic field values outside the range of the Skyrmion lattice one finds a paramagnetic to conical phase transition only. The helical phase is completely missing from the phase diagram. Secondly cooling the system at field

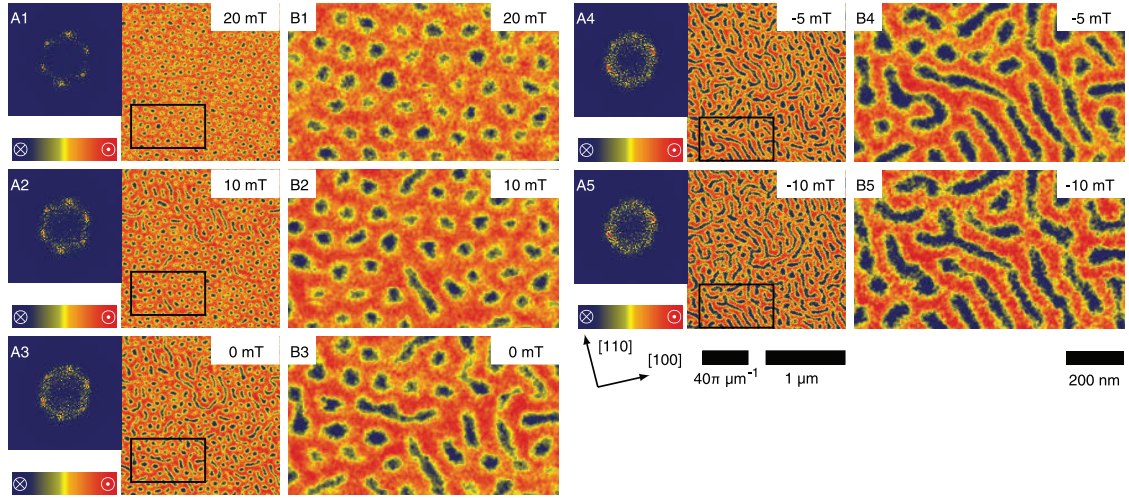


Figure 4.8: Typical magnetic force microscopy data for $\text{Fe}_{1-x}\text{Co}_x\text{Si}$ ($x = 0.5$) at various magnetic field strengths B . Red (blue) colours correspond to a magnetisation parallel (antiparallel) to the line of sight into (out of) the surface. Panels (A1) through (A5): Data recorded as a function of magnetic field after fc at 20 mT down to $T = 10$ K. Panel (A1) displays data immediately after fc. After the initial cool-down, the field was reduced at a fixed temperature of 10 K (A2 to A5). During this process, the Skyrmions, visible as blue spots, merge and form elongated, linelike structures. The left inset shows a Fourier transformation of the real-space signal. Panels (B1) to (B5) enlarge the region marked by the black rectangle in panels (A1) to (A5). Picture taken from Ref. [67].

value inside the Skyrmion lattice phase one finds an metastable extension of the Skyrmion lattice phase down to $T = 0$ with the same reversible phase boundaries near T_C as for zfc but irreversible phase boundaries below T_C . The irreversible phase boundaries of this extension reflect the metastability of the phase. As a result, the ability to study the destruction of the Skyrmion lattice at a temperature T well below T_c is helpful for two reasons. First, as the magnetic moment decreases considerably towards T_c it is important to choose a temperature low enough to achieve a sufficient contrast in the MFM measurement for unambiguous information about the state of the Skyrmion lattice. Apart from this technical reason, conceptually, the topological protection mechanism of the Skyrmion lattice relies on the fact that the magnetic moments are non-vanishing everywhere. Close to T_c strong thermal fluctuations may weaken the topological protection. A measurement at low T therefore exposes the generic unwinding mechanism respecting the topological constraints posed by the phase.

Fig. 4.8 summarises typical MFM data after sample preparation by field cooling at +20 mT to 10 K. For each B field value a real-space image is shown (middle), an enlarged section (right) and a fast Fourier transform (left). Subfigure A1 shows a hexagonal pattern with one of the reciprocal lattice vectors aligned along the $\langle 100 \rangle$ direction. The blue dots mark regions of the surface where the z -component of the magnetisation points in to the sample, the red surrounding an area where it

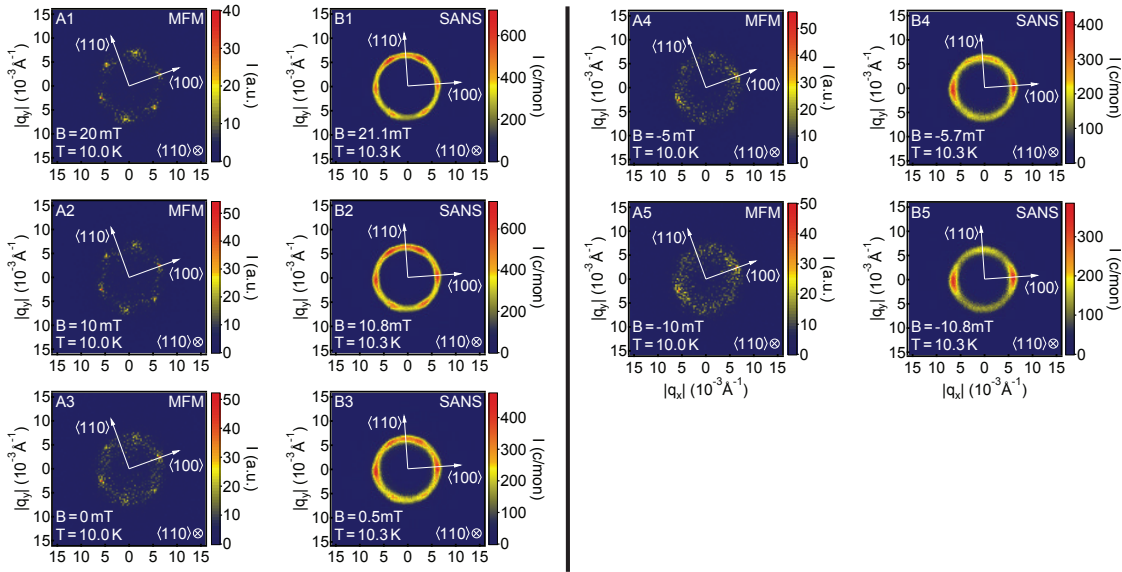


Figure 4.9: Comparison of the Fast Fourier Transforms (FFTs) (left column) of the MFM data of $\text{Fe}_{1-x}\text{Co}_x\text{Si}$ ($x = 0.5$) as shown in Fig. 4.8, with small angle neutron scattering (SANS) (right column) as recorded for the same sample. Data were recorded following the same temperature versus field protocol. Picture taken from Ref. [67].

points out of the sample. The hexagonal pattern of blue dots is clearly identified as Skyrmions arranged in a Skyrmion lattice forming its characteristic 6-fold symmetry pattern. Upon reducing the applied magnetic field to +10 mT, subfigure *A2* and *B2*, Skyrmions start to merge at the surface forming elongated structures. Upon further reducing the applied field and actually reversing it, the length of the elongated structures increases and the number of Skyrmions decreases until a strongly defected, stripy phase is reached (subfigure *A5*). The stripy phase is oriented with its q -vector in the $\langle 100 \rangle$ direction. The MFM requires a recording time of approximately 17 minutes per image. In comparison, the time scales of the metastable states depicted in the figures are large as compared to measurement time as we confirmed by waiting for 15 hours at an unchanged B field ($B = 0$ T) and recording an essentially unchanged image.

The MFM is a surface measurement and reveals no information about the bulk state of the system. Our collaborators performed SANS measurements to identify the bulk behaviour of the system during the B field reduction and to clarify whether the surface- reflects bulk behaviour. For comparison with the MFM data our collaborators recorded the SANS diffraction pattern following precisely the same temperature and field protocol. Data were recorded at the same decreasing field values for which MFM data were collected. The time between scans was approximately 50 minutes. Fig. 4.9 shows a comparison of the FFTs calculated from the MFM data (left column) with the SANS data recorded from the same sample (right column). Overall the qualitative agreement for the different field values is remarkable. In a closer comparison, however,

the SANS data show a ring of intensity absent in the FFTs of MFM data which we attribute to presence of disorder and the fact the SANS probes the entire sample while the MFM data show only a tiny region. The data suggests that indeed the surface- reflects bulk-behaviour and the same process that is visible on the surface reduces the total Skyrmion count: neighbouring Skyrmions start to merge forming more and more extended elongated structure modulated parallel to the $\langle 100 \rangle$ axis.

To investigate the conversion process in the bulk of the sample we turn to numerical simulations. Due to the topological winding number of the Skyrmion and its implications for the effective magnetic field, outlined in the last section, we are especially interested in the topological aspects of the Skyrmion merging. We performed both a Monte Carlo (MC) simulation and also calculated the real-time dynamics by numerically integrating the LLG equation. The discretised Hamiltonian used commonly for chiral magnets is

$$H = -J \sum_{\mathbf{r}} \hat{M}_{\mathbf{r}} \cdot \left(\hat{M}_{\mathbf{r}+\hat{x}} + \hat{M}_{\mathbf{r}+\hat{y}} + \hat{M}_{\mathbf{r}+\hat{z}} \right) - \mathbf{B} \cdot \sum_{\mathbf{r}} \hat{M}_{\mathbf{r}} - D \sum_{\mathbf{r}} \left(\hat{M}_{\mathbf{r}} \times \hat{M}_{\mathbf{r}+\hat{x}} \cdot \hat{x} + \hat{M}_{\mathbf{r}} \times \hat{M}_{\mathbf{r}+\hat{y}} \cdot \hat{y} + \hat{M}_{\mathbf{r}} \times \hat{M}_{\mathbf{r}+\hat{z}} \cdot \hat{z} \right) \quad (4.14)$$

where the $\hat{M}_{\mathbf{r}}$ is the normalised, local magnetisation vector arranged on a cubic lattice, J the ferromagnetic (FM) exchange, \mathbf{B} the magnetic field which we choose to lie along $\langle 100 \rangle$ direction and D the Dzyaloshinskii-Moriya (DM) interaction. As the ratio of the FM exchange and the DM interaction determine the pitch of the helix, we fix the wavelength of helical modulation to 10 lattice sites by choosing $D/J = \arctan(2\pi/10)$. We perform our simulation on a simple cubic lattice consisting of $2 \cdot 30^3$ spins with open boundary conditions in $[110]$ direction and periodic boundary condition in the other directions. The magnetic field is applied parallel to $[110]$ and thus perpendicular to the surfaces with the open boundary condition. Eq. 4.14 should be understood as the discretised version of a continuum model. The discretisation of the continuum model creates however lattice anisotropies for the otherwise rotationally-invariant continuum model [13, 67]. This can be seen as follows: On the lattice, the FM exchange term in Eq. 4.14 after Fourier transform reads

$$H_{\text{FM}} = J \sum_{\mathbf{k}} \alpha_{\mathbf{k}} \hat{M}(\mathbf{k}) \cdot \hat{M}(\mathbf{k}), \quad (4.15)$$

where we defined

$$\alpha_{\mathbf{k}} = -(\cos(k_x a) + \cos(k_y a) + \cos(k_z a)) \quad (4.16)$$

Expanding the cosines in the momentum generates all kinds of higher momentum terms; however if we contrast this with the Fourier transform of the FM exchange term in the continuum model, we see that there only the quadratic terms are present. This discrepancy is indeed worrisome as the ordering wave vector \mathbf{Q} for our choice of parameters D and J is not small, $|\mathbf{Q}|a \lesssim 1$, since we use relatively small lattice sizes. Consequently, the contribution of the higher order terms is not negligible and changes the physics of the model quantitatively. In order to compensate for these induced anisotropies next-nearest neighbour interactions are added to the Hamiltonian. For

a more detailed analysis of the finite size effects see Ref. [13]. With these additional terms one reproduces the phase diagram of chiral magnets.

In order track the motion of the emergent magnetic monopoles we periodically took snapshots of the magnetic texture during its temporal evolution and searched for hedgehog point defects by calculating the winding number of the 8 magnetic moments around each cube of size 1 in our lattice. A simple triangulation splits each of the 6 faces into 2 triangles. For every one of the 12 oriented triangles we compute the solid angle spanned by the three magnetic moments at its vertices, \hat{M}_i , $i = 1, 2, 3$ using the Oosterom and Strackee algorithm [106]

$$\tan\left(\frac{\Omega}{2}\right) = \frac{\hat{M}_1 \cdot (\hat{M}_2 \times \hat{M}_3)}{1 + \hat{M}_1 \cdot \hat{M}_2 + \hat{M}_2 \cdot \hat{M}_3 + \hat{M}_3 \cdot \hat{M}_1} \quad (4.17)$$

Summing the contributions from the 12 triangles and diving by 4π gives the winding number of the cube

$$n = \frac{1}{4\pi} \sum_{i=1}^{12} \Omega_i \quad (4.18)$$

which by construction can only take the value $+1$, 0 , -1 . Here $n = 1$ ($n = -1$) describes a singular spin configurations where the magnetisation winds one time (minus one times) around the sphere when surrounding the cube. This construction is the lattice analogue of calculating the total emergent flux in units of the flux quantum through a closed surface. Therefore configurations with $n = 1$ and $n = -1$ describe “emergent” quantised magnetic monopoles and antimonopoles, respectively. Using the same method, one can also calculate the winding number on the surface of the sample which gives the number of Skyrmions threading the surface. We start by outlining the general setup and results of the MC study and then turn to the real time dynamics.

Monte Carlo study

The MC calculation reproduces the equilibrium phase diagram [13] and captures the metastable behaviour, consistent with the micro magnetic simulations and our experiments. For the MC study we track the metastable state of the system by a Metropolis algorithm based on local updates (random reorientations of randomly chosen spins). For more detailed, including technical information about the MC study see Refs. [13, 67]. We have found that the maximal lattice size tractable in reasonable CPU time is given by $N = 2 \cdot 30^3$ spins, which already hosts up to nine skyrmion tubes in total. Therefore we model the system by $42 \times 42 \times 30$ spins coupled to their nearest neighbours by ferromagnetic exchange and Dzyaloshinsky-Moriya interactions.

The experiments explore the metastability of the skyrmion lattice using a protocol where the system is cooled at finite magnetic field to a specific temperature and in a second step the applied field is gradually reduced at fixed temperature. In the MC study we follow the same protocol and cool the system slowly at $|\mathbf{B}| = 0.16J$ down to various temperatures ranging from $0.4J$ to $0.7J$. The skyrmion lattice phase stays intact although the conical phase has a lower free energy here. The Monte-Carlo

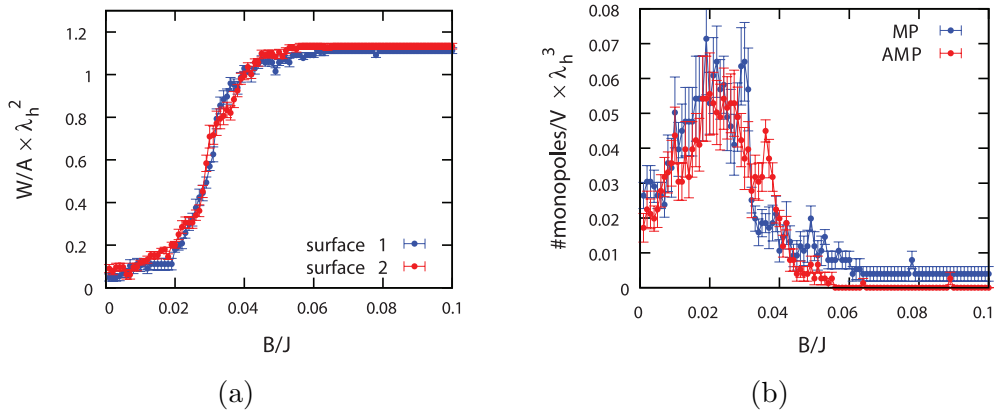


Figure 4.10: (a) Total winding number W (or equivalently number of Skyrmions) per area in units of the helical wavelength λ_h^2 for the front and back surface as determined by MC while reducing B averaged over 15 cooling cycles. (b) Number of monopoles (MP) and antimonopoles (AMP) per volume in units of λ_h^3 averaged over 15 cooling cycles. Picture taken from Ref. [67].

time dynamics of the phase conversion can be calculated by gradually reducing the strength of the applied field B in steps of ΔB . A fixed number local updates are performed for each step. Upon the gradual reduction of the applied field we observe a gradual conversion from the skyrmion phase into the helical phase. Fig. 4.10a shows the winding number W of the system as a function of the applied magnetic field \mathbf{B} for $T = 0.6J \approx 0.65T_C$. The red and blue curve correspond to the winding number of the front and back of the system respectively (with the understanding that $[001]$ is the axis pointing towards the viewer). Starting from an intact Skyrmion lattice ($W/A = 1$) the winding number reduces upon reduction of B until at $B = 0$ only a small density of Skyrmions survives. This small density is associated with a finite density of defects in the helical phase, c.f. Fig. 4.11c (although the data was recorded in the real-time study). A comparison of Fig. 4.10b shows the recorded a number of monopoles (MP) and antimonopoles (AMP) per volume in units of λ_h^3 averaged over 15 cooling cycles. A comparison of Fig. 4.10b and Fig. 4.10a reveals that the destruction of the Skyrmion lattice and the subsequent reduction in the total winding number of the system is indeed accompanied by a proliferation of emergent magnetic monopoles.

Real time dynamics

The phase conversion observed in the experiment is a non-equilibrium process and therefore the time scales on which the transition takes place is an interesting observable. Unfortunately the artificial Monte-Carlo dynamics is impossible to relate to real time scales. Several authors have questioned the rigour of the method and in certain cases has even been shown to give qualitatively incorrect results [29]. It is therefore important to ensure that a proper real-time dynamics method gives the same qualitative result. We calculated the real-time dynamics taking into account the precession dynamics of the spins, their damping and the thermal fluctuations which drive the

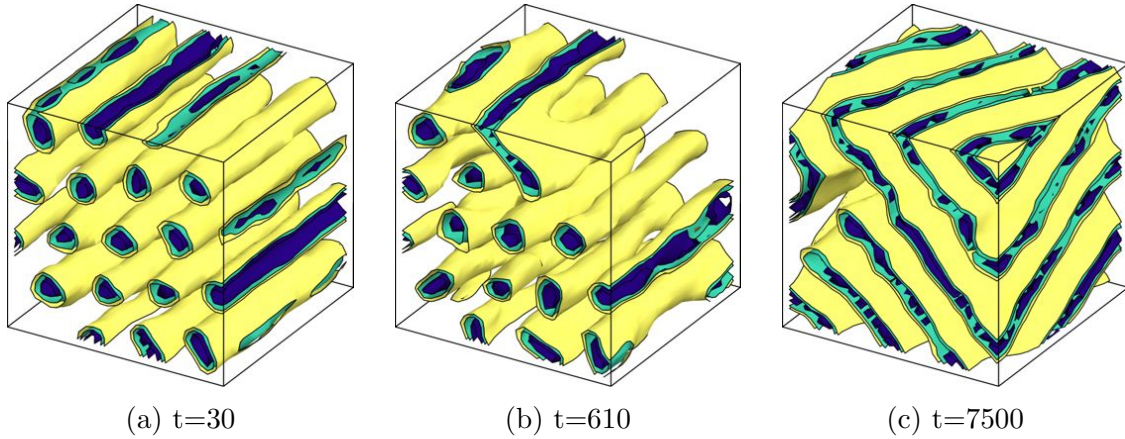


Figure 4.11: Typical magnetic configurations shown by contour surfaces for equal magnetisation component in the $[001]$ direction as computed from the sLLG at three different times with $B = 0$ and $T = 0.58$.

phase conversion (see below). This can be achieved by the numerical integration of the stochastic Landau-Lifshitz-Gilbert (sLLG) equation with the methods outlined in chapter 3.

For the sLLG study we applied the magnetic field along the $[001]$ direction with open boundary conditions on planes normal to $[001]$ using the same parameter set (system size $42 \times 42 \times 30$) as in the MC simulations described above. The Gilbert damping α that describes the magnetic relaxation we set to $\alpha = 0.04$. To prepare our initial state we first initialize the equations with a Skyrmion lattice with a lattice constant compatible with $K/J = \arctan(2\pi/10)$ and relax it for the time $1000/J$ at $T = 0.5J$ in a constant field $B = (0, 0, 0.16)J$ using our sLLG code. To investigate how the dynamics of monopoles and antimonopoles is driving the destruction of the skyrmion lattice, we suddenly switch off the external magnetic field after relaxation at $t = 0$ to observe the evolution of the skyrmions, monopoles and antimonopoles. To suppress spurious monopole-antimonopole pairs on neighboring sides arising from single spin-flip event, we average the magnetic configurations over a short time interval ($\Delta t = 10/J$). Then we determine the total number of skyrmions in each layer parallel to the surface and the position of all emergent magnetic monopoles and antimonopoles using Eq. 4.17.

Fig. 4.11 shows typical magnetic configurations at three different times after the quench as contour surfaces for equal magnetisation component in the $[001]$ direction computed from the sLLG with $B = 0$ and $T = 0.58$. For the earliest displayed time ($t = 30$) an intact Skyrmion lattice is visible with the Skyrmion lines pointing towards the observer. At $t = 610$ the first Skyrmion has started to merge. A point defect has entered the system through the front surface (open boundary condition) and is moving away from the observer along the negative z -axis merging two Skyrmions in the process. Fig. 4.11c shows the system at $t = 7500$. A defected helical phase with the wave vector pointing approximately in the $[111]$ direction can be seen.

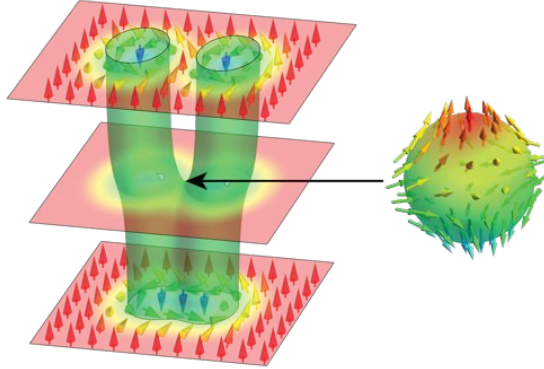


Figure 4.12: Schematic illustration of a magnetic configuration describing the merging of two Skyrmions. At the merging point the magnetisation vanishes in a singular point (black arrow). The magnetisation configuration around this point (right) can be interpreted as an emergent magnetic monopole, which acts like the slider of a zipper.

Topological considerations

To appreciate the physics of the merging of skyrmions observed both experimentally and numerically both in the MC study and in the real-time dynamics, we employ the language of emergent electrodynamics introduced in section 4.3.1. The topological nature of Skyrmions and their interaction with the electrons is best described in this language. The emergent electric and magnetic fields are given by Eq. 4.12. The integral of \mathbf{B}^e/\hbar over a surface measures the magnetic flux passing through it. For a surface intersected once by a Skyrmion line, the magnetic flux is exactly given by one (negative) flux quantum, $\int \mathbf{B}^e d\sigma = -2\pi/|q^e| = -\Phi_0$. Fig. 4.12 shows two Skyrmions in the process of merging. The color code is chosen such that red color indicates a z -component of the magnetisation pointing along the positive z -axis and blue color along the negative z -axis. The green surface is a contour plot for equal magnetisation component in the z -direction (here $\hat{M}_z = 0$). If we calculate the flux through the top surface (with the normal pointing along the positive z -axis) the value of the integral will be $-2\Phi_0$ while it is $-\Phi_0$ for the surface on the bottom. Sliding the top surface down the negative z -axis, the value of the integral jumps from $-2\Phi_0$ to $-\Phi_0$ as the merging point is traversed. Due to the topological nature of the Skyrmion a change in the winding number is always accompanied by a singular field configuration for which the local magnetisation vanishes at a point in space. To determine the properties of this point one can imagine calculating the magnetic flux through a closed surface $\partial\Omega$ containing the singular point and bordering the volume Ω

$$\oint \mathbf{B}^e d\sigma = \int_{\Omega} \nabla \mathbf{B}^e d\mathbf{r} = -\Phi_0(N_{\text{out}}^S - N_{\text{in}}^S) = -\Phi_0 \quad (4.19)$$

where N_{out}^S (N_{in}^S) is the number of outgoing (ingoing) Skyrmions lines (with the understanding that the observer is looking along the direction of the applied magnetic

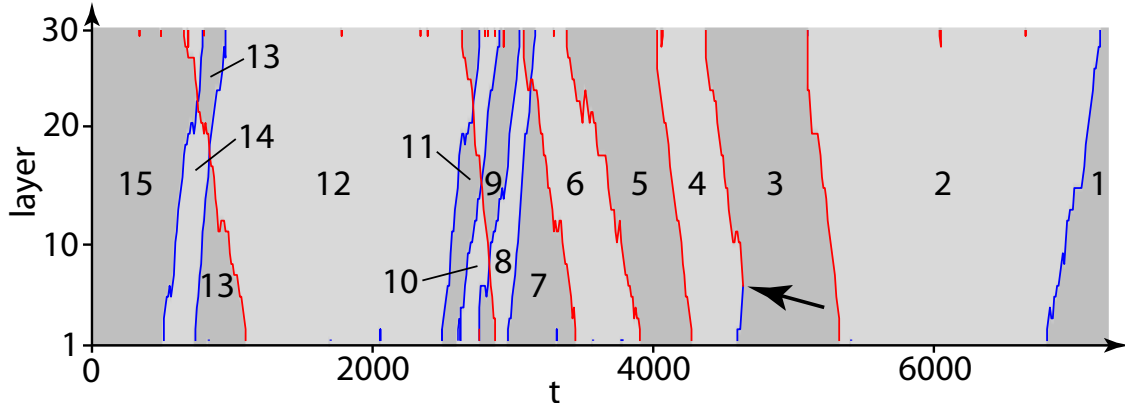


Figure 4.13: Dynamics of monopoles, antimonopoles and skyrmions after a sudden quench based on sLLG simulations. At $t = 0$ the external magnetic field ($\mathbf{B} = (0, 0, 0.16)^T J$) is suddenly set to 0, thus destabilizing an initially prepared skyrmion lattice. As a function of time (in units of $1/J$) the distance to the lower surface (z coordinate) of magnetic monopoles (red) and antimonopoles (blue) is shown as a function of time. The numbers in the figure denote the number of skyrmions, i.e., the winding number in each z -layer. The plot shows that the phase conversion is driven by the creation and motion of monopoles and antimonopoles. The black arrow marks an event where a monopole and an antimonopole annihilate.

field). Hence, when two ingoing Skyrmions merge there must be a singular configuration at the merging point with a winding number of $+1$, which creates one emergent magnetic flux quantum. In this sense the merging point carries a quantised emergent magnetic charge, i.e. it is an emergent magnetic monopole. Monopoles and antimonopoles are related to each other by the transformation $\mathbf{M} \rightarrow -\mathbf{M}$ followed by a rotation by π around an axis perpendicular to the magnetic field. Note these transformations applied to the situation depicted in Fig. 4.12 would exchange incoming and outgoing Skyrmions in consistency with Eq 4.19. The merging of two Skyrmions at the surface of the $\text{Fe}_{0.5}\text{Co}_{0.5}\text{Si}$ bulk sample as observed in the experimental data, Fig. 4.8, implies that one of two processes has taken place: Either a monopole has entered into the bulk from the surface of the sample or an anti-monopole from the bulk has excited the observed surface.

Figure 4.13 shows as a function of time the z coordinate (distance from the lower surface) of monopoles (red) and antimonopoles (blue). Monopoles are created at the top of the sample and move down while antimonopoles come from the bottom and move up. Their motion triggers a change of the number of skyrmions. The numbers in the figure 4.13 directly give the number of monopoles in the system. In the initial state there are 15 skyrmions in each layer. This number is reduced one-by-one by the creation and motion of monopoles and antimonopoles. This perfect correspondence of skyrmion destruction and monopole motion is enforced by topology and has been seen in all of our simulations. The black arrow marks an event where a monopole moving down meets an antimonopole moving up. In this case, the monopole and antimonopoles were zipping together the same pair of skyrmions. Therefore they

annihilate at their meeting point. Our simulations of the real-time dynamics show clearly that the magnetic monopoles are the driving mechanism of phase conversion.

Experiment, numerics and topological considerations suggest that the movement of emergent magnetic (anti-)monopoles underlies the phase conversion to the helical phase. The rate of phase should therefore be controlled by two important scales: the velocity with which these singular defects can move through the sample and the rate at which they are created, either as pairs in the bulk or single monopoles / anti-monopoles at the surface. An interesting question is therefore how these quantities depend on the system parameters. We turn to this question in section 4.3.3 below. A model of the creation process for the monopoles and for the forces acting on the them would allow to make predictions about the rate of phase conversion which could be compared to experiment. In Ref. [99] Takashima and Fujimoto investigate the effect the merging of two Skyrmions has on conduction electrons by calculating induced electric currents. They obtain an adiabatic current which is dissipationless, and dissipative currents driven by the effective electromagnetic fields including the effect of spin-orbit couplings. They find that a moving monopole at the merging point turns out to have both electric charge and magnetic charge, which is likely have observable consequences in experiment, too.

It is instructive to compare the emergent magnetic monopoles discussed here with the magnetic monopoles considered in spin ice mentioned above. Monopoles in spin ice are sources of the “real” magnetic H-field, but their magnetic charge is not quantised and depends on microscopic details. By contrast, the emergent monopoles that we identify here are sources of the emergent magnetic field that follows Dirac’s quantisation condition for monopoles; i.e., they carry one quantum of emergent flux. Furthermore, in spin-ice at zero magnetic field, the monopoles are “deconfined”; i.e., it requires only a finite amount of energy to separate monopole and antimonopole. In the skyrmion phase, the situation is different (similar arguments apply to the helical phase): Deep in the skyrmion phase, it requires a finite amount of energy per length to zip two skyrmions together. Consequently, there is a linear potential (i.e., a finite string tension) holding monopole and antimonopole together. Only during the conversion from one phase to the other, the string tension vanishes or becomes negative. In disordered materials, the string tension may be a random function that competes with potentials pinning the monopoles.

Author contributions

Milde, Kögler, Eng and Seidel performed the magnetic force microscopy study of $\text{Fe}_{0.5}\text{Co}_{0.5}\text{Si}$ while Bauer, Chacon, Kindervater, Mühlbauer and Pfeleiderer performed the small angle neutron scattering experiment. Rosch and Buhrandt carried out the Monte-Carlo study. Rosch and the author of this thesis developed, performed and analysed the simulation of the real-time dynamics.

4.3.3 Dynamics and energetics of emergent magnetic monopoles

In this section we study the energetics of and forces between emergent magnetic monopoles. An understanding of these properties is vital for any theory which aims

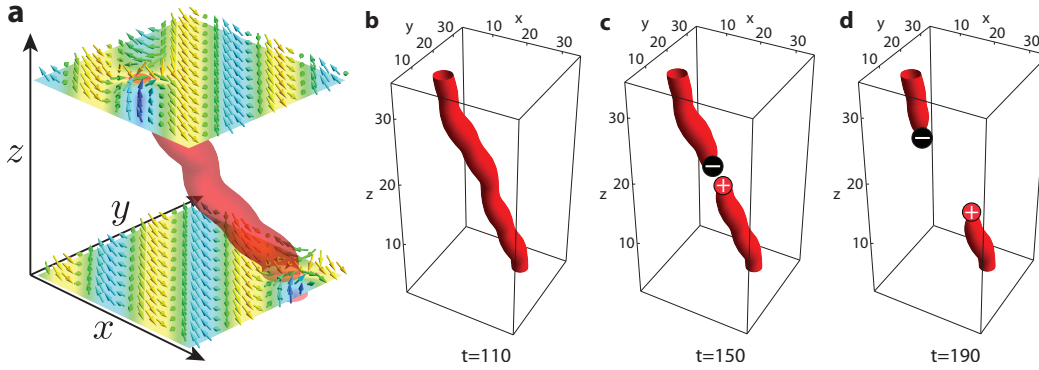


Figure 4.14: (a) Initial magnetic configuration in which a Skyrmion along a $[\bar{1}\bar{1}2]$ direction is embedded into a helical phase. (b)-(d) The Skyrmion unwinds by a monopole-antimonopole (MP-AMP) pair created in the bulk which is pulled apart.

to describe phase conversions from Skyrmion lattices to other phases. Motivated by our study in Ref. [67], outlined in the previous chapter, we investigate here how Skyrmions are destroyed and replaced by the helical phase. For a quantitative analysis of the process it is beneficial to simplify the setup and consider only how a single Skyrmion embedded into a helical phase unwinds instead of a dense Skyrmion lattice as in Ref. [67]. This helps to reduce finite-size effects in the numerics: The energy difference between N and $N - 1$ Skyrmions is due to boundary effects in conjunction with the Skyrmion-Skyrmion interaction a function of N . Such problems are absent when $N = 1$ as considered in the following. We use two numerical methods to address these questions. First, we perform micro magnetic simulations based on the stochastic Landau-Lifshitz-Gilbert equations (c.f. chapter 3). Second, based on the Ginzburg-Landau description for chiral magnets (c.f. chapter 2) we use a numerical minimisation algorithm to determine the mean-field configuration and free-energy of a monopole in a helical phase.

For the micro magnetic simulations we use the discretised Hamiltonian, Eq. 4.14, to calculate the effective magnetic field $\mathbf{B}_r^{\text{eff}} = -\delta H / \delta \mathbf{M}_r$. D is the coupling constant which parametrizes the strength of the Dzyaloshinskii-Moriya interaction and we choose $D/J = \arctan(2\pi/10)$ in our simulations. For the Gilbert damping in the LLG we set $\alpha = 0.04$. The creation of a monopole in the system requires an amount of energy roughly given by the core energy of the monopole, thus it is essential to include the effects of thermal fluctuations to allow the system to provide this energy. We therefore include random, normally distributed, fluctuating magnetic fields consistent with the fluctuation-dissipation theorem as outlined in chapter 3. The numerical integration of the system discretised on a lattice of $35 \times 35 \times 35$ spins is performed by Heun's method. The boundary conditions in the x and y direction are periodic, those in the z direction are open. The magnetic field \mathbf{B} is applied in the $[\bar{1}\bar{1}2]$ direction and this is also the direction the single Skyrmion line embedded into a surrounding helical phase is pointing in. The helical phase has its wave vector \mathbf{q} pointing in the $[111]$ direction, normal to the magnetic field. This setup was chosen since the anisotropies due to the discretisation (c.f. section 4.3.2) lead to a preferred wave vector orientation in the $[111]$ direction for the helical phase. If the helical

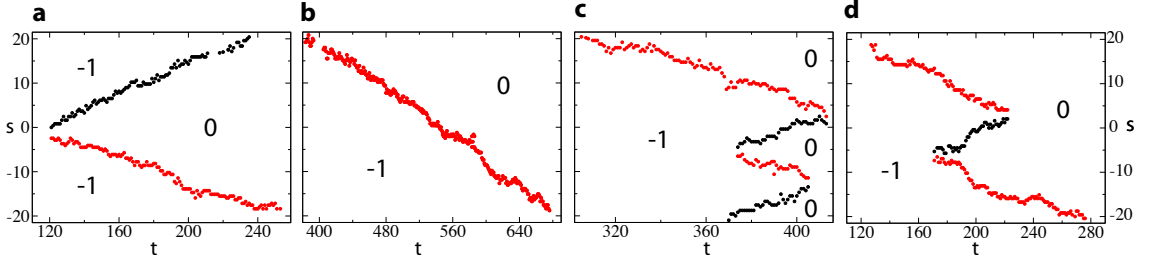


Figure 4.15: Typical trajectories of MPs (black) and AMPs (red) after a quench to $B = 0$ ($T = 0.7$) obtained from the sLLG simulations. The vertical axis shows the coordinate parallel to the Skyrmion orientation s , the horizontal axis the time in units of \hbar/J . The numbers inside the plots indicate winding numbers of the magnetic texture.

phase is oriented any other way, the thermal fluctuations will cause it to turn slowly throughout the simulation into its preferred direction. The initial configuration at $t = 0$ is depicted in Fig. 4.14a. For the definition of the Skyrmion centre coordinate we use the topological charge density defined as

$$\rho_{top}(\mathbf{r}) = \frac{1}{4\pi} \hat{\mathbf{n}}(\mathbf{r}) \cdot (\partial_x \hat{\mathbf{n}}(\mathbf{r}) \times \partial_y \hat{\mathbf{n}}(\mathbf{r})) \quad (4.20)$$

with $\hat{\mathbf{n}}(\mathbf{r}) = \mathbf{M}(\mathbf{r})/|\mathbf{M}|$ which integrates over a surface to the total number of Skyrmion intersecting the surface. For the system we are considering here $\rho_{top}(\mathbf{r})$ is normalised when integrated over the xy plane which allows us to define the centre of the Skyrmion as the centre of the topological charge

$$\mathbf{R}(z) \equiv \int dx \int dy \rho_{top}(\mathbf{r}) \mathbf{r} \quad (4.21)$$

The red line in Fig. 4.14a tracks this centre of topological charge. The three figures Fig. 4.14b-d shows an event recorded as temporal snapshots of the numerical data, where the Skyrmion string is cut into two by the creation of a monopole-antimonopole (MP-AMP) pair in the bulk of the system with the (anti-)monopole denoted by a + (-) sign in the figure. The movement of these monopoles towards the edges of the system is accompanied by a change in the winding number and a shortening of the two Skyrmion lines.

For $B = 0$ the generic magnetic phase of chiral magnets is given by the helical phase. The instability of the single Skyrmion state causes monopoles spontaneously created by thermal fluctuations to unwind the configuration to the helical state. We initialised our system with the configuration depicted in Fig. 4.14a and calculated the time evolution using numerical integration for an ensemble of thermal noise realisations. Snapshots of the magnetic configuration (averaged over short times to reduce noise) were analysed and the position of all monopoles were determined using Eq. 4.17. Especially for high system temperatures most of the MP-AMP pairs are created by a single, thermal spin flip event, do not separate and are short-lived. We developed a tracking algorithm which uses a proximity search to join the monopole

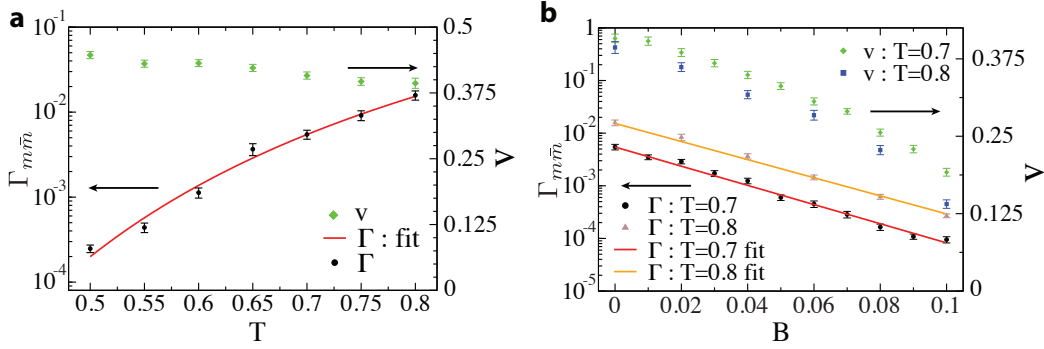


Figure 4.16: (a) Average pair creation rate $\Gamma_{m\bar{m}}$ and MP velocity V as a function of system temperature T for $B = 0$. The error bars indicate the standard deviation of the mean. (b) Average pair creation rate $\Gamma_{m\bar{m}}$ and MP velocity V as a function of B for two different temperatures $T = 0.7$ and $T = 0.8$.

positions found in subsequent snapshots into (A)MP trajectories. We filtered these trajectories removing short trails consisting of only a few events. Fig. 4.15 shows typical monopole trajectories extracted from time evolutions determined by numerical integration of the sLLG for a vanishing magnetic field. The monopoles move predominantly parallel to the Skyrmion orientation, so we show on the vertical axis of these plots the projection of the monopole position onto a $[\bar{1}\bar{1}2]$ -axis. Due to topological constraints monopole creation in the bulk is only allowed as MP-AMP pair creation, c.f. Fig 4.15a. AMPs move ‘up’, MPs move ‘down’ to reduce the winding number in the system. Single MPs or AMPs can only be create at the surfaces with open boundary conditions (top and bottom in Fig. 4.14), c.f. Fig 4.15b. The reverse process where a MP and an AMP come close together and annihilate can be seen in Fig 4.15c and d.

For the dynamics of the monopoles two quantities are of central importance: The rate $\Gamma_{m\bar{m}}$ at which MP-AMP pairs are created in the bulk and the typical velocity v with which they move through the system. The rate $\Gamma_{m/\bar{m}}^S$ at which single monopoles are created at the surface is of minor importance in the limit of large system sizes as the number of monopoles created in the bulk scales with the third power of the linear system dimension L , while the surface creation scales with L^2 . The monopole trajectories extracted from the ensemble of simulated systems allows to calculate averages for these quantities. Fig. 4.16a shows the average bulk creation rate $\Gamma_{m\bar{m}}$ (black symbols) and the average velocity of the MPs (green symbols) as a function of system temperature T for $B = 0$. The error bars indicate the standard deviation from the mean. Turning to the creation rate first, the data points can be consistently fitted within the error boundaries with a simple thermally activated behaviour of the form

$$\Gamma_{m\bar{m}} \sim \Gamma_0 e^{-\frac{E_0}{k_B T}} \quad (4.22)$$

with $E_0 \approx 5.8J$ for the chosen parameters. The average velocity of the MPs depends only weakly on temperature: With increasing thermal disorder there is a slight reduction in the velocities. Fig. 4.16b shows these two quantities as functions of the applied magnetic field B for two different temperatures $T = 0.7$ and $T = 0.8$. The creation

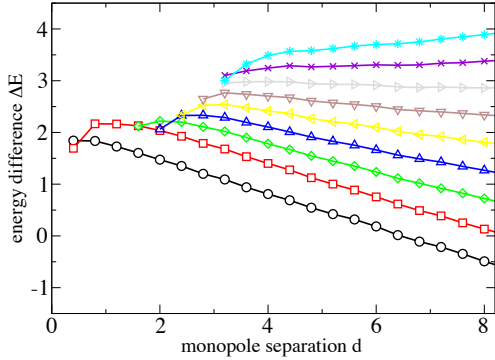
rate of MP-AMP pairs is strongly B dependent and can be consistently explained (within the error bars) by an exponential dependence of the form, $\Gamma_{m\bar{m}} \propto e^{-B/B_0}$. The exponential dependence could arise from a linear dependence of the monopole core energy E_0 on the applied field B , $E_0(B) = E_0^{(0)} + cB$. We determined the constant c and the prefactor $\Gamma_0 \exp(E_0^{(0)})$ from the $T = 0.7$ data and compared the prediction of this model with the observed data for $T = 0.8$. While a model based on this assumption gives an explanation of the observed data, more numerical data is needed to exclude the possibility of an additional, explicit B -dependence of the prefactor $\Gamma_0 = \Gamma_0(B)$. At this point we must therefore assume that the exponential dependence arises from a combination of the B dependence of the activation energy E_0 and that of the prefactor Γ_0 . The average MP velocity also has a strong dependence on the applied field and is suppressed by a factor of 3 in the considered B range. We expect that for larger values of the magnetic field the velocity reduces further. The monopole creation rate however decreases exponentially so that an exponentially increasing simulation time is necessary to gather the needed data. This limits the possible range of B -values.

A simple, physical picture emerges for the removal of the Skyrmion line defect from the helical phase. A free energy E_C is needed locally to create a MP. The thermal noise can cause a local energy fluctuation which is large enough for a MP-AMP pair to be created in the bulk of the system. Once the pair is created a constant force $F = T_S$, given by the so called line tension, pulls the pair apart. This line tension has its origin in the free energy per length of the Skyrmion line defect. The system gains the energy $T_S \Delta x$ when the pair separates a distance Δx , thus shortening the length of the Skyrmion string. Alternatively the line tension T_S can also be understood as a result of a linear interaction potential between MPs and AMPs. The E_0 we extracted from the sLLG data gives approximately twice the core energy of the MP. As we will see in the following $E_0/2$ is essentially given by E_C with a small correction included due to a short-ranged, attractive potential between MPs and AMPs.

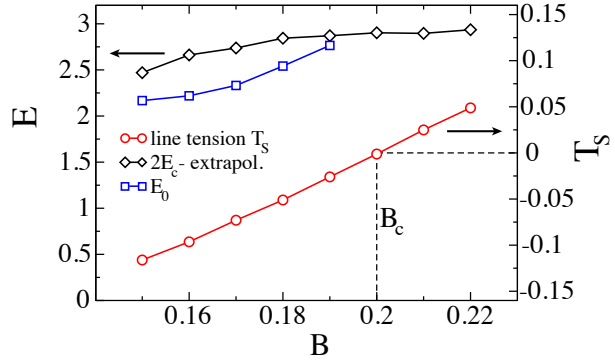
We explore the parameter dependence of the core energy E_C and the line tension T_S near the critical field strength B_c using an alternative theoretical approach. The energetics of Skyrmions and MP-AMP pairs can be determined using the Ginzburg-Landau (GL) description of the free energy. The standard GL functional for chiral magnet [2], Eq. 2.14,

$$F[\mathbf{M}] = \gamma \int d^3\mathbf{r} [(1 + t_0) \mathbf{M}^2 + (\nabla\mathbf{M})^2 + \mathbf{M} \cdot (\nabla \times \mathbf{M}) + \mathbf{M}^4 - \mathbf{B} \cdot \mathbf{M}] \quad (4.23)$$

with t_0 the distance to the $B = 0$ mean-field critical temperature, $t_0 = r_0 J/D^2 - 1 \propto T - T_C$. For our calculations we discretize the above continuum model as describe in chapter 2 on a cubic lattice of size $50 \times 50 \times 50$ and determine the mean-field configuration by numerical minimisation using a conjugate gradient method (for details see appendix C). Our main goal is to determine the free energy of a MP-AMP pair as a function of their distance d . For an initial configuration with a MP and an AMP a distance d apart, the minimal energy configuration depends on the sign of the line tension. For negative T_S the pair moves infinitely far apart, thus removing the Skyrmion line defect from the system altogether. For positive T_S the pair will move closer and closer together, eventually annihilating and leaving the system with



(a) Energy of a MP-AMP pair as a function of their distance. For large distances the force is linear and therefore described by a string tension (see subfigure (b)).



(b) Energy E_0 of a MP-AMP, sum of their core energies, $2E_C$ (both left axis), and the line tension T_S (right axis) as a function of the magnetic field B_z . At the dashed line the T_S changes sign.

Figure 4.17: Results obtained from minimisation of the GL free energy ($t_0 = -1.6$) for $B_z = 0.15$ to 0.22 (bottom to top).

a single Skyrmion line defect which extends through the whole system. In order to study the free energy dependence of the system as a function of the separation, one needs to fix the positions of the MP and the AMP. This can be achieved by noting that in the continuum the magnetisation at the core of each MP and AMP vanishes. We therefore fix their positions by demanding that the magnetisation vanishes at two lattice sites a distance d apart. This procedure works only as long as the forces on the MPs and AMPs are not stronger than the pinning energy due to the site with the vanishing magnetisation. This limits the range of the GL study to not too large values of t_0 , not too small distances d and magnetic field values close to B_C where the line tension T_S vanishes.

Fig. 4.17a shows the results of the numerical minimisation for $t_0 = -1.6$ and for $B_z = 0.15$ to $B_z = 0.22$ (bottom to top). For large distances the energy is linear in the separation d . The slope is - by definition - the string tension T_S , also shown in Fig. 4.17b as the red line (axis to the right). As expected T_S is exactly given by the energy per length of the Skyrmion line defect. The sign of T_S reflects the stability of the line defect and can be seen to change at a critical $B_c \approx 0.2$. For $B < B_C$ the Skyrmion is not stable, $T_S > 0$ and MP and AMP repel each other at large distances. For $B > B_C$ a helical phase with a single Skyrmion line defect embedded has a lower free energy than a purely helical phase, hence $T_S < 0$ and the MP and AMP attract each other. We checked that in the sLLG simulation this leads to spontaneous creation of Skyrmions in this regime. It should be noted that the bulk phase transition is not given by B_c . Due to Skyrmion-Skyrmion interactions in a dense Skyrmion lattice here the critical B is lower. In Fig. 4.18 the temperature dependence of T_S and E_C is plotted. With the increasing $|t_0|$, $t_0 < 0$, one goes deeper into the ordered phase and the core energy of the MP increases. The line tension T_S can be seen to vanish at a critical temperature t_c .

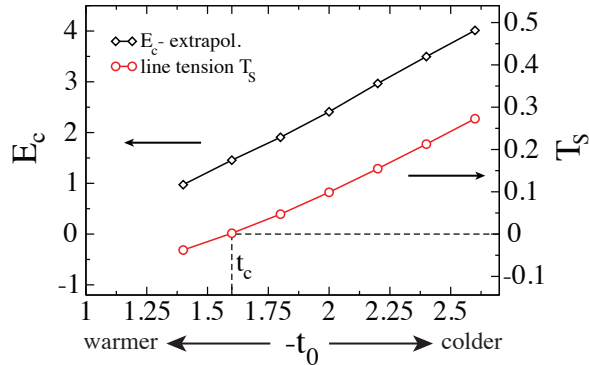


Figure 4.18: Core energy, E_C (left axis), and line tension T_S (right axis) as a function of the distance to T_C , t_0 , for $B_z = 0.2$. At the dashed line the T_S changes sign.

For $T_S > 0$ the system can always reduce its free energy by creating a MP-AMP pair and separating them by sufficiently large distance d . The creation rate is however strongly suppressed by the fact that for small d the large energy needed to create a MP-AMP pair not compensated by a sufficient gain in the MP-AMP interaction energy. The main contribution to this energy is the core energy, E_C , of a single MP or AMP which can be obtained by a linear extrapolation of ΔE in Fig. 4.17a to $d = 0$ and taking half of that value. The figure reveals however that once the MP and AMP come sufficiently close together, they feel a short-ranged attractive potential. We therefore expect that instead of $2E_C$, the maximum $E_0 = \max_D \Delta E$ controls the MP-AMP pair creation rate.

A surprising observation during the analysis of the sLLG data let us to the realisation that the energetics governing the creation of single MPs at the edges of the system is more subtle. We found that the creation rate of a single monopole at the surface of the simulated sample (we used open boundary condition in the z -direction) is of a similar order of magnitude as the creation rate for MP-AMP pairs in the bulk. Naively one would expect that the energy needed to create a MP-AMP pair in the bulk is twice as large as the energy needed to create a single (A)MP at a system edge. There is of course the argument that the first process scales with the size of the system surface while the latter scales with the volume. For systems of sufficiently large linear dimension L , bulk creation will always prevail. However for the small systems we were considering in our simulations this seemed an unlikely explanation. Indeed the above argument misses an important contribution to the energy: the surface energy of the Skyrmion. Creating a monopole at the edge means that the Skyrmion configuration is replaced by a helical configuration at the surface of the sample which is of higher energy. Fig. 4.19b shows the schematics of the two magnetisation configurations whose energy difference ΔE leads to the curves in Fig. 4.17a. The first diagram shows a MP-AMP pair (red dots) separated by a distance d and the Skyrmion line defect (blue line) that they cut into two pieces. The wiggly lines signify open boundary condition at the two edges of a system of length L . From this we subtract a system with a full-length Skyrmion line defect. Indeed extrapolation of the $\Delta E(d)$ to $d = 0$ gives $2E_C$. The creation of a single monopole on the other hand at an edge of the system is depicted in Fig. 4.19c. Here a MP at

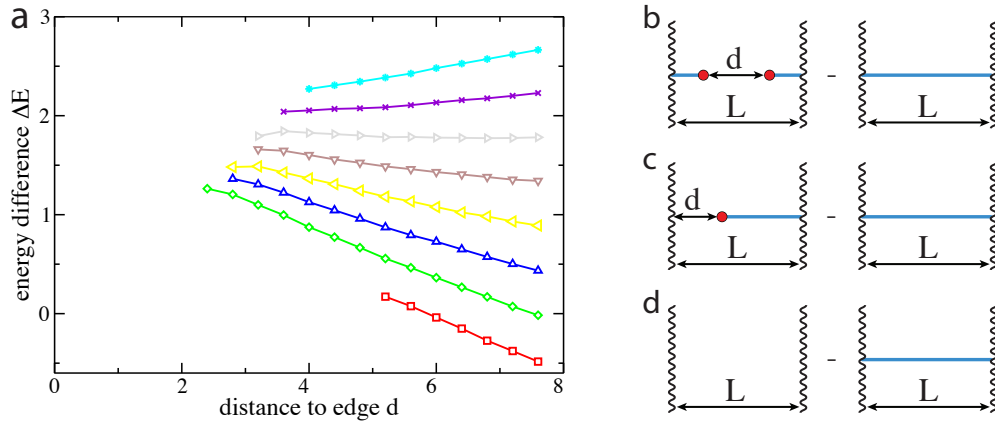


Figure 4.19: (a) Energy of a MP as a function of its distance to an edge of the system with an open boundary condition. For large distances the force is linear and therefore described by a string tension. (b),(c) and (d) Schematic representations of calculation we performed, see main text. The red dots signify (A)MPs, the blue line a Skyrmion line defect and the wiggly lines open boundary conditions.

a distance d from the edge of the sample is shown in the first diagram and again a full-length Skyrmion is subtracted. The $d \rightarrow 0$ -limit does not give E_C . Instead the asymptotic energy costs also include a contribution from the surface energy of the Skyrmion which turns out to be negative, thus increasing the total energy cost for MP creation at the surface. One way to determine this energy cost is to calculate for a cube of size L with open boundary conditions the energy difference between a single Skyrmion (Fig. 4.19c, first diagram) and the helical phase (Fig. 4.19c, second diagram), $\Delta E_S(L)$. $\Delta E_S(L)$ grows linearly with L and the extrapolated value for $L \rightarrow 0$ is twice (two surfaces) the surface energy of the Skyrmion, Δ_S . For $t_0 = -1.6$, for example, and $B_z = 0.16$, we find $\Delta_S \approx 0.5$. Indeed Fig. 4.19a shows the free energy of a single MP at a distance d from the edge of the sample (c.f. Fig. 4.19c, first diagram). For the same parameters (green curve) the extrapolated value for $d \rightarrow 0$ is ≈ 2.0 which the sum of $E_C \approx 1.5$ and $\Delta_S \approx 0.5$. The surface effect thus turns out to be of quantitatively equal importance as the reduction of the MP-AMP pair energy due to the short-ranged attractive potential, c.f. Fig. 4.17a. For the same parameter the difference between $2E_C$ and E_0 is also $2E_C - E_0 \approx 0.5$ (Fig. 4.17a). The cost for pair creation in the bulk ($E_0 \approx 2.2$) is of similar magnitude as the single MP creation on the edge of the sample ($\Delta_S + E_C \approx 2.0$), thus explaining the observation in the sLLG data.

A quantitative comparison between the sLLG simulation and the GL calculation was not possible as the former is restricted to a range of magnetic fields sufficiently small compared B_c to ensure tractable simulation times and the latter to small line tensions T_S and thus B fields close to B_c . A qualitative comparison is however possible. The velocity V of the monopoles is expected to be given by the product of the line tension T_S and a effective friction constant. We assume a friction constant which is approximately independent of temperature and applied field. Based on the temperature dependence of the line tension in Fig. 4.18 and the B_z dependence in Fig. 4.17b the expectation is that the velocity drops with increasing B_z for $B_z < B_c$

and increases upon lowering the temperature. The sLLG data reflect indeed both of these trends. More dramatically an approximately linear increase of the core energy E_C with the applied magnetic field B should result in an exponential decrease in the MP-AMP creation rate as is indeed observed in the sLLG data, c.f. Fig. 4.16.

To extent predictions about the parameter dependence of the line tension and the core energy of monopoles beyond the regimes available from the numerics, one can perform a scaling analysis of the discretised continuum model. We start with a discussion of the relevant length scales. Three length scales are of primary importance: (i) the lattice discretisation parameter a , (ii) the typical length scale on which the direction of the magnetisation changes due to spin-orbit coupling, which is given by the pitch of the helix, λ , and (iii) the length scale of which the modulus of the magnetisation vector changes, which determines the radius of the monopole, R_C . For a Skyrmion embedded in a ferromagnetic phase (see the following chapter) the size depends strongly on the strength of the applied magnetic field. In the present case where the surrounding phase is helical this is not the case and we always work in a regime where the Skyrmion radius is given by the helical pitch λ . Due to the weakness of the spin-orbit interaction, the Dzyaloshinskii-Moriya interaction D is weak compared to the exchange coupling J , and the resulting helical pitch λ is large when compared to the lattice spacing a , $a \ll \lambda$. Close the mean-field transition, $|t_0| \ll 1$ ($t_0 < 0$), the length of the magnetisation modulates on increasingly large length scales and $R_C \sim \lambda$. In real systems however a fluctuation-induced first order transition (Ref. [48]) preempts the mean-field transition and we therefore do not discuss this regime. Instead we focus on the cases where $R_C \ll \lambda$ and $|t_0| \gg 1$. One reexpress the rescaled free energy, Eq. 2.14, in its original, physical variables, c.f. Eq. 2.12, to translate the condition $|t_0| \gg 1$ into a more physical constraint. It assumes the form $a^2 D^2 / J \approx T_c a^2 D^2 / J^2 = T_c \lambda_{SO}^2 \ll T - T_c$ with λ_{SO} a dimensionless constant describing the strength of the spin-orbit coupling and T_c the mean-field transition temperature. In this regime, the length scales on which the direction of the magnetisation changes decouples from the scale on which the amplitude fluctuates. For the description of the magnetisation configuration up to a distance of the order of R_C from the monopole center, it is valid to make the ansatz $\mathbf{M}(\mathbf{r}) = M(r)\hat{\Omega}(\theta, \phi)$ where $\hat{\Omega}(\theta, \phi)$ describes a spin-configuration winding once around the unit sphere and $M(r)$ the variations of the magnetisation amplitude on the length scale R_C . In this limit, the energetics of the MP core is thus not affected by spin-orbit coupling but reflects the energy needed to suppress the amplitude of the magnetisation at the core. With two remaining length scales R_C and a in the problem, two regimes have to be distinguished

1. $\lambda_{SO}^2 T_c \ll T_c - T \ll T_c$: In this regime the radius of the monopole core is determined by balancing the term proportional to t_0 and quadratic in \mathbf{M} and the exchange coupling term. With $\mathbf{M}(\mathbf{r}) = M(r)\hat{\Omega}(\theta, \phi)$ this suggests $t_0 \mathbf{M}(\mathbf{r})^2 = t_0 M(r)^2 \sim (\nabla \mathbf{M}(\mathbf{r}))^2 \sim R_C^2 M(r)^2$ and therefore $R_c \sim 1/\sqrt{|t_0|} \sim a\sqrt{T_c/(T_c - T)}$. The core energy of the monopole therefore scales as $R_c^3 t_0 M^2 \sim T_c \sqrt{(T_c - T)/T_c}$ with $M \sim \sqrt{T_c - T}$. The string tension T_S is the energy per length of the Skyrmion, which is determined by the ferromagnetic exchange, the DM interaction and the strength of the applied field. For not so strong magnetic

fields the dominant terms are the ferromagnetic and DM interaction, which are both quadratic in M . The energy density within the Skyrmion is proportional to $1/\lambda_{SO}^2$ and the radius to λ_{SO} . The total energy per length, T_S , is therefore independent of the spin-orbit coupling and given by $T_S \sim c_B(T_C - T)/a$ with a prefactor c_B of the order 1, which depends strongly on the ratio B/M and is negative for small B as the Skyrmion costs energy when embedded into the helical phase at low B .

$$\frac{R_c}{a} \sim \left(\frac{T_c}{T_c - T} \right)^{1/2}, \quad \frac{E_c}{T_c} \sim \left(\frac{T_c - T}{T_c} \right)^{1/2}, \quad \frac{T_S}{T_c/a} \sim c_B \frac{T_c - T}{T_c} \quad (4.24)$$

2. $T \ll T_c$: For very low T the magnetisation amplitude M saturates and the core radius R_c locks in at the microscopic length scale a . For simple models without frustration the crossovers occur simultaneously at a temperature of the order $T_c/2$. For temperatures small compared to this, where $R_c \sim a$ and M is saturated, also the core energy saturates at a value determined by microscopic details. It is dominated to have the magnetisation on neighbouring sites in a hedgehog configuration instead of a parallel alignment. Generically this costs the energy scale $J \approx T_c$. Therefore we find in full consistency with the above equations

$$\frac{R_c}{a} \sim 1, \quad \frac{E_c}{T_c} \sim 1, \quad \frac{T_S}{T_c/a} \sim c_B \quad (4.25)$$

It is important to note that in the first regime, the creation rate of MPs and antimonopoles (AMPs) $\propto e^{-E_c/T}$ is *not* exponentially suppressed. As our analysis of creation rates and the motion of MPs relied on the existence of only a small number of MPs, it is therefore not surprising that the analysis of the stochastic LLG equations was restricted to regime 2. Indeed, for the highest temperature studied ($T = 0.8$) the time-averaged local magnetization far away from the MP core is of the order of 0.7, still close to the saturation value of 1 and in the distance of one lattice spacing from a MP core we find a magnetization of the order of 0.35.

4.4 Conclusion

In this section we have shown that both experiment and numerical calculations suggest that the merging of Skyrmions underlies the conversion from the Skyrmion lattice to the helical phase. We have found that the change of topology, i.e. the unwinding of Skyrmions, is governed by the creation and motion of topological point defects, which we identify as emergent magnetic monopoles and antimonopoles. The destruction of the Skyrmions is therefore directly associated with the proliferation of magnetic monopoles. Two factors dominate the creation rate and the dynamics of these defects: the core energy of monopoles and the string tension. We found that these quantities are key to understand the time scales for the creation and destruction of Skyrmions in three-dimensional bulk materials. An open question is how Skyrmions can be created and destroyed in quasi two-dimensional thin films. Here one could

expect that replacing the z axis with the time axis would result in an instant on picture for the monopoles. Another interesting question is whether phases of deconfined monopoles exist, where monopoles and antimonopoles proliferate as independent entities. A candidate might be the metallic state of MnSi under high pressure, where highly unconventional “partial” magnetic order on intermediate length scales has been observed [80].

Chapter 5

Effective Mass of the Skyrmion

Systems with solitonic solutions are often characterised by a degeneracy of classical vacua. The soliton solutions are then described by field configurations which interpolate between different vacua. They are classified by an associated topological charge, i.e. a winding number, which decomposes as a superselection rule the physical state space into disjointed topological sectors. Restricting the physical system to a specific (non-trivial) sector by an appropriate choice of boundary conditions for the fields, not only in time but also in space, often leads to a ground state, which breaks translational symmetry. The spontaneous breaking of this symmetry leads to the appearance of zero modes in the system associated with translations of the solitonic solution. These zero modes have to be distinguished from the massive excitations in the system. Mathematically they lead to divergencies in perturbative expansions around the classical soliton solution. However the introduction of a “collective coordinate” not only solves these mathematical troubles, but also makes sense from a physical point of view: these zero modes represent infinitesimal, translations which leads to a spread of the wave function and eventually a reemergence of translational symmetry [96].

In this chapter we restrict ourselves to the topological sector of a single chiral skyrmion in the ferromagnetic background. The introduction of a collective coordinate will provide the mathematical foundation for the particle interpretation of the skyrmion. In the first part of this chapter, section 5.1, we study how massive fluctuations lead to additional terms in the effective equations of motion for the particle coordinate. The fluctuation eigenstates will fall into two categories: (a) scattering states (“soliton + meson”) and (b) intrinsic, localised excitations (“excited soliton”). This generates an effective mass for the skyrmion even at $T = 0$, a quantum mass. This project is a joint effort in collaboration with Markus Garst.

In section 5.2 we study the temperature induced fluctuation statistics of the collective coordinate numerically. These fluctuations are responsible for the diffusion of the soliton’s position. The analysis of the velocity-velocity correlation function allows to reconstruct the full frequency dependence of the effective equations of motion for the skyrmion at finite temperature T and finite Gilbert damping α .

5.1 Quantum Mass of the Skyrmion

Before we outline the theory for the skyrmion it is instructive to remember how the collective coordinate approach and the emergence of an inertia term shows up in a simplified case. For this we will start with a ϕ^4 field theory in (1+1) dimensions possessing a soliton like solution. Subsequently we will turn to the case of a skyrmion in a chiral magnet.

5.1.1 Effective mass in the ϕ^4 field theory

Here we follow Ref. [96] and consider a ϕ^4 theory in (1+1) dimensions. The Lagrangian of the system is given by

$$\mathcal{L}[\phi] = \frac{1}{2} \partial_\mu \phi \partial^\mu \phi - \frac{1}{2} m^2 \phi^2 (g^2 \phi^2 - 1), \quad (5.1)$$

where $\phi(x, t)$ is a real scalar field, m is “mass” term for the field ϕ and g parametrizes the strength of the interaction. Although the ϕ^2 term is also referred to as a mass term it is not what we are after. This term determines (conjunction with ϕ^4 term) the modulus of ϕ . We are looking for the effective dynamical mass of solitonic solutions. After rescaling $\phi \rightarrow \phi/g$ it becomes apparent that g^2 plays the same role as \hbar and the latter can be absorbed therein,

$$\begin{aligned} \mathcal{Z} &= \int \mathcal{D}[\phi] \exp \left(\frac{i}{g^2} \int dx dt \mathcal{L}[\phi] \right) \\ \mathcal{L} &= \frac{1}{2} \partial_\mu \phi \partial^\mu \phi - \frac{1}{2} m^2 \phi^2 (\phi^2 - 1). \end{aligned} \quad (5.2)$$

Here the degenerate vacua are simply given by $\phi_0 = \pm 1$. Solitonic solutions therefore exists which interpolate between these two vacua at spatial infinity, i.e. $x = -\infty$ to $x = \infty$ and a winding number classifies them. The simplest topologically non-trivial, classical configuration ϕ_0 is given by a static solution of the Euler-Lagrange equations of Eq. (5.2),

$$-\partial_x^2 \phi_0(x) - m^2 \phi_0 (2\phi_0^2 - 1) = 0. \quad (5.3)$$

These solutions break the translational symmetry hence necessitating the introduction of a collective coordinate. As already mentioned a zero mode appears corresponding to infinitesimal, collective translations $\xi_0(x) \sim \partial_x \phi_0(x)$ of the classical field configuration $\phi_0(x)$.

A collective coordinate $R(t)$ for the fields ϕ is introduced through

$$\phi(x, t) = \chi(x - R(t), t) \quad (5.4)$$

In addition one considers the massive fluctuations $\xi(x, t)$ around this classical configuration which can be expanded in a basis of eigenfunctions $\xi_n(x)$,

$$\xi(x, t) = \sum_{n=1}^N a_n(t) \xi_n(x). \quad (5.5)$$

The eigenfunctions $\xi_n(x)$ and corresponding eigenvalues ϵ_n are defined by

$$-\partial_x^2 \xi_n(x) + m^2 \phi(2\phi^2 - 1) = \epsilon_n^2 \xi_n(x) . \quad (5.6)$$

which can be retrieved from an expansion of the action, Eq. (5.2), up to second order in the fluctuations. With this ansatz the Lagrangian of the system becomes

$$\mathcal{L}' = \frac{1}{2} \dot{\chi}^2 - \dot{R} \dot{\chi} \chi' - \frac{1}{2} (1 - \dot{R}^2) \chi'^2 - \frac{1}{2} m^2 \phi^2 (\phi^2 - 1) . \quad (5.7)$$

This equation only depends on R due to the arguments of the χ 's, namely, $x - R(t)$. This dependence can be removed by a suitable reparametrisation of the spatial integration. Eq. (5.7) is then independent of R but not of its first derivative \dot{R} . From the third term in Eq. (5.7) we can see that in case of this particular field theory an inertia term for the collective coordinate $R(t)$ is already generated in 0th order in the fluctuations, i.e. $\chi(x, t) = \phi_0(x - R(t))$,

$$\frac{1}{2} M_0 \dot{R}^2 \quad (5.8)$$

with the rest mass given by

$$M_0 = \int dy \phi_0'^2(y) . \quad (5.9)$$

The overall philosophy carries over to the case of chiral magnets and skyrmionic solitons therein. However an important difference should be mentioned from the outset: In what follows no inertia term will appear at 0th order in the fluctuations; instead we have to carry out the analysis up to second order. This stems from a structural difference in the dynamical terms of the action. While in the above case the dynamical term is second order in the time derivative, for spin systems, like chiral magnets, it is given by a Berry phase term with a single time derivative instead.

5.1.2 Model and skyrmion solution

To study the effective dynamics of a single skyrmion in a ferromagnetic background we consider a two-dimensional magnetic system described by the Euclidean action

$$S = \int_0^\beta d\tau \int d^2 \mathbf{r} (\mathcal{L}_{\text{dyn}} + \mathcal{L}_{\text{stat}}) \quad (5.10)$$

where $\beta^{-1} = k_B T$. The Lagrangian comprises two parts, a dynamical term \mathcal{L}_{dyn} and a static contribution

$$\mathcal{L}_{\text{stat}} = \frac{\varepsilon_0}{2} \left[(\partial_\alpha \hat{n}_i)^2 + 2Q \epsilon_{i\alpha j} \hat{n}_i \partial_\alpha \hat{n}_j - 2\kappa^2 (\hat{n}_i \hat{H}_i - 1) \right] . \quad (5.11)$$

Here and in the following we use greek indices for two dimensional vectors, $\alpha = 1, 2$, and latin indices for three dimensional vectors, $i, j = 1, 2, 3$. As chiral magnets are characterized by a hierarchy of energy scales we use the strongest one, the spin stiffness, to set the typical energy scale ε_0 . The strength of the spin-orbit induced

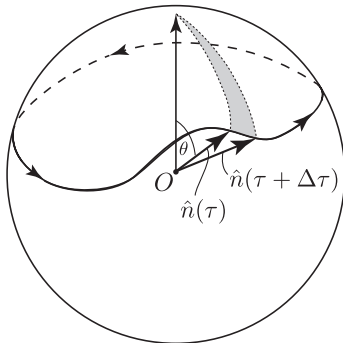


Figure 5.1: The geometric meaning of the Berry phase: $\int_0^\beta d\tau \left[1 - \cos \theta(\tau) \dot{\phi}(\tau) \right]$ simply measures the solid angle enclosed on \mathbb{S}^2 by the closed path $\hat{n}(\tau)$.

Dzyaloshinskii-Moriya interaction is parametrized by $Q > 0$ which we choose here to be positive. $\kappa > 0$ measures the strength of the magnetic field $\mathbf{H} = \frac{\mu_0 \epsilon_0 \kappa^2}{m} \hat{H}$ with m the length of the magnetization $\mathbf{m} = m\hat{n}$ and μ_0 the vacuum permeability. The energy of the Zeeman term is measured relative to a static, field polarized magnetization configuration $\hat{n}(\mathbf{r}) = \hat{H}$. In the following we will assume that the applied magnetic field is a static field, orthogonal to the two-dimensional system, $\hat{H} = \hat{z}$. The dynamical part of the Lagrangian is given by the Berry phase term,

$$\mathcal{L}_{\text{dyn}} = -\frac{i}{a^2} \vec{A}(\hat{n}) \frac{d}{d\tau} \hat{n} \quad (5.12)$$

where a is the typical distance between the magnetic moments. The geometric meaning of the Berry phase is depicted in Fig. 5.1. Here $\vec{A}(\hat{n})$ is a gauge potential of a magnetic monopole charge located at the center of \mathbb{S}^2 ,

$$\epsilon_{ijk} \partial \vec{A}_j / \partial \hat{n}_i = \hat{n}_k. \quad (5.13)$$

Since the bosonic fields $\hat{n}(\tau)$ fulfill the boundary conditions $\hat{n}(0) = \hat{n}(\beta)$ they describe closed paths on \mathbb{S}^2 . The Berry phase term is proportional to the solid angle subtended by the surface whose boundary is given by the loop $\hat{n}(\tau)$.

The dynamics of a classical magnet are described by the Landau-Lifschitz-Gilbert equation which may be derived from the action Eq. (5.10) by taking the Euler-Lagrange equations and subsequent analytic continuation

$$\partial_t \hat{n}(t) = \hat{n}(t) \times \frac{\delta H[\hat{n}]}{\delta \hat{n}} \quad (5.14)$$

where the Hamiltonian $H[\hat{n}]$ is given by the static part of the Lagrangian $\int d^2\mathbf{r} \mathcal{L}_{\text{stat}}[\hat{n}]$.

In the following we will consider the limit of small spin-orbit coupling, i.e. $Qa \ll 1$ is a small parameter. For large enough κ the Zeeman energy is the dominant term in the Hamiltonian and the fully polarized, static state $\hat{n} = \hat{z}$ minimizes the action, Eq. (5.10). As already noted in the introduction to this chapter, topological charges

can be used in the sense of superselection rules to divide the state space into disjointed subsets. The corresponding winding number is given by

$$W = \frac{1}{4\pi} \int d^2\mathbf{r} \hat{n} \cdot (\partial_x \hat{n} \times \partial_y \hat{n}) \quad (5.15)$$

The ground state lies in the topologically trivial sector, $W = 0$. We can consider the classical skyrmion solution \hat{n}_s as a large amplitude excitation in the ferromagnetic background. This solution will be uniquely determined upon supplementing the necessary condition of an extremized action with suitably chosen boundary conditions for the field configuration, which restrict the system to the correct topological sector, i.e. $W = -1$. With the parametrization

$$\hat{n}_s(\mathbf{r}) = \begin{pmatrix} \sin \theta(\mathbf{r}) \cos \varphi(\mathbf{r}) \\ \sin \theta(\mathbf{r}) \sin \varphi(\mathbf{r}) \\ \cos \theta(\mathbf{r}) \end{pmatrix} \quad (5.16)$$

and polar coordinates $\mathbf{r} = (\rho \cos \chi, \rho \sin \chi)^T$, a single skyrmion located at $\mathbf{r} = 0$ has

$$\varphi(\rho, \chi) = \varphi(\chi) = \chi + \frac{\pi}{2}. \quad (5.17)$$

Additionally the polar angle θ is a nodeless function of the radius ρ only, $\theta(\rho, \chi) = \theta(\rho)$, with the boundary conditions

$$\lim_{\rho \rightarrow 0} \theta(\rho) = \pi, \quad \lim_{\rho \rightarrow \infty} \theta(\rho) = 0. \quad (5.18)$$

Substituting this ansatz into the Euler-Lagrange equations of the static part of the action, Eq. (5.11), we find a second order ordinary differential equation [9], which determines the shape of the function $\theta(\rho)$

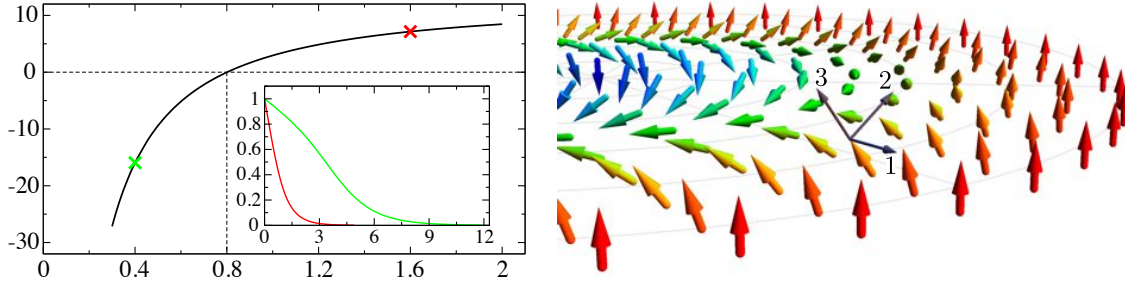
$$\theta'' + \frac{\theta'}{\rho} - \frac{\sin \theta \cos \theta}{\rho^2} + \frac{2Q \sin^2 \theta}{\rho} - \kappa^2 \sin \theta = 0 \quad (5.19)$$

For $\rho \gg 1$ the boundary condition forces $\theta \ll 1$ and one can expand the trigonometric functions to find the asymptotic form of the solution. With a similar argument for $\rho \ll 1$ one finds

$$\theta(\rho) \approx \begin{cases} \pi - c_1 \kappa \rho & \text{for } \rho \rightarrow 0 \\ \frac{c_2}{\sqrt{\kappa \rho}} e^{-\kappa \rho} & \text{for } \rho \rightarrow \infty \end{cases} \quad (5.20)$$

where c_1 and c_2 are positive constants. The exponential behaviour of $\theta(\rho)$ for large ρ identifies $\mathcal{R} \equiv 1/\kappa$ as the skyrmion radius.

The initial value problem posed by Eq. (5.19) and the small ρ asymptotics ($\theta(\rho_0) = \pi - c_1 \kappa \rho_0$ and $\theta'(\rho_0) = -c_1 \kappa$ with $\rho_0 \ll 1$) results for arbitrary c_1 in solutions with a superposition of an exponentially increasing and an exponentially decreasing function as their large ρ asymptotics. By a suitable choice of the constant c_1 one has to ensure that the coefficient in front of the exponentially increasing function vanishes in order to have a proper skyrmion solution ($\lim_{\rho \rightarrow \infty} \theta(\rho) = 0$). This numerical method for



(a) Energy dependence of the single skyrmion solution as a function of the dimensionless parameter κ^2/Q^2 . For $\kappa^2 \gtrsim 0.8Q^2$ the energy is positive hence the skyrmion a large amplitude excitation.

(b) Illustration of the static skyrmion solution and the local coordinate system. While $\hat{e}_3(\mathbf{r})$ locally points in the direction of the static skyrmion solution, $\hat{e}_1(\mathbf{r})$ points radially outward and $\hat{e}_2(\mathbf{r}) = \hat{e}_3(\mathbf{r}) \times \hat{e}_1(\mathbf{r})$.

Figure 5.2

solving boundary value problems is called the *shooting method* as one *shoots* the parameter c_1 such that the boundary conditions are satisfied¹. Later in this chapter we explain at length the details of this method. Substituting the solution into the static part of the Lagrangian density, Eq. (5.11), and integrating over space, one finds the saddle-point action $S_s^{(0)} = \beta E_s = \beta \varepsilon_0 \mathcal{E}(\kappa^2/Q^2)$ with E_s the energy of the skyrmion solution. The dimensionless function \mathcal{E} determines the energy dependence of the skyrmion solution on the dimensionless parameter combination $\kappa^2/Q^2 = 1/(\mathcal{R}^2 Q^2)$ and is shown in Fig. 5.2a. For $\kappa^2/Q^2 \gtrsim 0.8$ the energy is positive indicating that the skyrmion should be understood as an excitation in the ferromagnetic background. For smaller κ a negative energy indicates an instability of the system towards a proliferation of skyrmions. As $\kappa = 1/\mathcal{R}$ there is a maximum radius that the skyrmion can have without violating this excitation picture. In this chapter we restrict the discussion to the case $\kappa^2/Q^2 \gtrsim 0.8$.

For the parametrization of small amplitude fluctuations around the static skyrmion solution we introduce a local coordinate system

$$\begin{aligned}
 \hat{e}_1 &= -\sin \varphi \hat{e}_x + \cos \varphi \hat{e}_y \\
 \hat{e}_2 &= -\cos \theta \cos \varphi \hat{e}_x - \cos \theta \sin \varphi \hat{e}_y + \sin \theta \hat{e}_z \\
 \hat{e}_3 &= \sin \theta \cos \varphi \hat{e}_x + \sin \theta \sin \varphi \hat{e}_y + \cos \theta \hat{e}_z
 \end{aligned} \tag{5.21}$$

The vectors \hat{e}_n , $n = 1, 2, 3$, form a dreibein with $\hat{e}_1 \times \hat{e}_2 = \hat{e}_3$ and $\hat{e}_3(\mathbf{r})$ locally pointing in the direction of the static skyrmion solution $\hat{n}_s(\mathbf{r}) = \hat{e}_3(\mathbf{r})$, see Fig. 5.2b. Translational invariance is spontaneously broken by the skyrmion: the system is invariant with respect to the choice of its position and therefore the fluctuation spectrum contains two *zero modes* associated with translations of the skyrmion along the x - and y -axis. These modes will be accounted for by the introduction of a two-dimensional collective coordinate \mathbf{R} . The remaining *massive modes* are represented by the two-dimensional, real-valued vector field $\phi = (\phi_1, \phi_2)$. Explicitly the fluctuations are

¹In this metaphorical picture the solution of IVP would correspond to projectile's trajectory.

parametrised as (summations over repeated indices implied)

$$\hat{n}(\mathbf{r}, \tau) = \hat{e}_3(\mathbf{r} - \mathbf{R}(\tau)) \sqrt{1 - \vec{\phi}^2(\mathbf{r} - \mathbf{R}(\tau), \tau)} + \hat{e}_\alpha(\mathbf{r} - \mathbf{R}(\tau)) \phi_\alpha(\mathbf{r} - \mathbf{R}(\tau), \tau). \quad (5.22)$$

In the following we want to study the influence of massive fluctuations on the effective dynamics of the collective coordinate $\mathbf{R}(\tau)$, which defines the skyrmion position in a particle-interpretation. The program is to expand the Euclidian action, Eq. (5.10), up to second order in the massive fluctuation field $\vec{\phi}(\mathbf{r}, \tau)$. Expressing the fluctuation field in a suitable eigenbasis allows to perform the resulting Gaussian integral, which generates new terms for the effective action of the collective coordinate $\mathbf{R}(\tau)$.

5.1.3 Fluctuation spectrum and scattering phase shifts

We now expand the action, Eq. (5.10), up to second order in terms of the fluctuation fields ϕ_α . The resulting eigenvalue problem (EVP) yields the excitation spectrum.

Zerth order in massive fluctuations ϕ_α

Ignoring the presence of fluctuations and hence assuming a *rigid* skyrmion leads to equations of motion for the centre coordinate \mathbf{R} known as the Thiele equations [102]. The Lagrangian assumes the form $L^{(0)} = \int d^2\mathbf{r} \mathcal{L}^{(0)}$ with

$$L^{(0)} = \varepsilon_0 \mathcal{E}(\kappa^2/Q^2) - \frac{1}{a^2} \mathcal{A}(\mathbf{R}) i \frac{d}{d\tau} \mathbf{R}. \quad (5.23)$$

We already encountered the first term as the energy cost of the static skyrmion solution, Fig. 5.2a. This term is independent of \mathbf{R} and hence does not contribute to the equations of motion. The second contribution originates from the expansion of the Berry phase term, Eq. (5.12), and describes the coupling of the skyrmion located at \mathbf{R} to an emergent gauge field $\mathcal{A}_\alpha(\mathbf{R})$. The gauge field is given by

$$\mathcal{A}_\alpha(\mathbf{R}) = - \int d^2\mathbf{r} \vec{A}(\hat{e}_3(\mathbf{r} - \mathbf{R})) \partial_\alpha \hat{e}_3(\mathbf{r} - \mathbf{R}). \quad (5.24)$$

Since $\mathcal{A}_\alpha(\mathbf{R})$ is a static gauge field the associated electric field $\partial_\tau \mathcal{A}(\mathbf{R})$ vanishes. The emergent magnetic field however is finite and given by

$$\begin{aligned} \epsilon_{z\alpha\beta} \frac{\partial}{\partial \mathbf{R}_\alpha} \mathcal{A}_\beta(\mathbf{R}) &= \int d^2\mathbf{r} \hat{n}_s (\partial_x \hat{n}_s \times \partial_y \hat{n}_s) \\ &= 4\pi W \end{aligned} \quad (5.25)$$

where we recognized the expression for the winding number of the magnetization W . For the single skyrmion solution $W = -1$. Taking the Euler-Lagrange equations of the Lagrangian, Eq. (5.23), we arrive at the classical equations of motion

$$\mathbf{G} \times d_t \mathbf{R} = 0 \quad (5.26)$$

with the gyro-coupling vector $\mathbf{G} = -4\pi \hat{e}_z$ and thus reproduce the Thiele equations. Eq. (5.26) describes the motion of a massless, charged particle with a Lorentz force acting on it due to an effective, quantized magnetic field \mathbf{G} .

First order in the massive fluctuations ϕ_α

There are two kinds of terms first order in the fluctuation field ϕ_α : those linear in both the fluctuation fields ϕ_α and the collective coordinate $\dot{\mathbf{R}}$ and those that do not contain any $\dot{\mathbf{R}}$. The latter ones vanish by construction as the single skyrmion is the classical field configuration that extremizes the static action, i.e. $\dot{\mathbf{R}} = 0$. By calculation one can also confirm, that the coupling term between massive fluctuations and the collective coordinate \mathbf{R} linear in the fluctuations vanishes.

Second order in the massive fluctuations ϕ_α

Expanding the Lagrangian density in second order in the fluctuation field ϕ one finds after some algebra

$$\mathcal{L}^{(2)} = \frac{1}{2a^2} \phi_\alpha \tau_{\alpha\beta}^y \partial_\tau \phi_\beta + \frac{1}{2a^2} \phi_\alpha \tilde{H}_{\alpha\beta} \phi_\beta + \mathcal{L}_{\text{int}}^{(2)} \quad (5.27)$$

where τ^y is the second Pauli matrix and the expression for $\tilde{H}_{\alpha\beta}$ is given in the appendix D. The first term originates from the expansion of the Berry phase term Eq. (5.12). Due to translational invariance the Lagrangian $\mathcal{L}^{(2)}$ only depends on the collective coordinate \mathbf{R} through the combination $\mathbf{r} - \mathbf{R}$ and its velocity $\dot{\mathbf{R}}$. One can therefore eliminate the explicit \mathbf{R} dependence² by a change of integration variables $\mathbf{r} - \mathbf{R} \rightarrow \mathbf{r}$, effectively assuming a comoving frame of reference.

The Euler-Lagrange equations of Eq. (5.27) have the form of a two-component Schrödinger equation. The two components in this equation correspond to the two fluctuation directions: The upper component describes fluctuations along a direction towards or away from the skyrmion centre and the lower component along a direction orthogonal to both the aforementioned and the local magnetisation direction of the static skyrmion solution, c.f. Fig. 5.2b. The last term in Eq. (5.27), $\mathcal{L}_{\text{int}}^{(2)}$, describes the coupling between the massive fluctuations ϕ_α and the collective coordinate $\mathbf{R}(t)$. This term will generate additional contributions in the effective action of the collective coordinate once the Gaussian integral over the massive fluctuations is performed. One can simplify the interaction term $\mathcal{L}_{\text{int}}^{(2)}$ further with the help of the unitary transformation

$$\vec{\psi} = U^\dagger \vec{\phi}, \quad U = \frac{1}{\sqrt{2}} \begin{pmatrix} 1 & 1 \\ i & -i \end{pmatrix} \quad (5.28)$$

with $U^{-1} = U^\dagger$. Here we introduce a new complex, two-component field $\vec{\Psi}$. Since $\vec{\phi}$ is a real-valued field the new fields $\vec{\psi}$ possess the symmetry

$$\vec{\psi}^* = U^T \vec{\phi} = \tau^x U^\dagger \phi = \tau^x \vec{\psi} \quad (5.29)$$

²The velocity dependence $\dot{\mathbf{R}}$ remains! Note also that in the first term ∂_τ is only a partial derivative. There is an additional time dependence of ϕ_β through its argument $\mathbf{r} - \mathbf{R}(t)$ which generates a term proportional to $\dot{\mathbf{R}}$, however that term is contained in $\mathcal{L}_{\text{int}}^{(2)}$.

The Lagrangian now assumes the simplified form

$$\mathcal{L}^{(2)} = \frac{1}{2a^2} \vec{\psi}^\dagger \tau^z \partial_\tau \vec{\psi} + \frac{1}{2a^2} \vec{\psi}^\dagger H \vec{\psi} + \mathcal{L}_{\text{int}}^{(2)} \quad (5.30)$$

with the transformed Hamiltonian $H = U^\dagger \tilde{H} U$ given by

$$H_{\alpha\beta} = \varepsilon_0 a^2 \left[-\delta_{\alpha\beta} \nabla^2 + 2\tau_{\alpha\beta}^z \left(\frac{\cos \theta}{\rho^2} - Q \frac{\sin \theta}{\rho} \right) i\partial_\chi + \kappa^2 + \delta_{\alpha\beta} v_0 + \tau_{\alpha\beta}^x v_x \right]. \quad (5.31)$$

with $\nabla^2 = \partial_\rho^2 + (1/\rho)\partial_\rho + \partial_\chi^2/\rho^2$ and θ in the above equation is $\theta = \theta(\rho)$ the polar profile function of the static skyrmion solution.

The scattering potentials v_0 and v_x are exponentially localized at the skyrmion location (c.f. Fig. 5.3a) and given by

$$\begin{aligned} v_0 &= \frac{3(\cos(2\theta) - 1)}{4\rho^2} - \frac{3Q \sin(2\theta)}{2\rho} + \kappa^2(\cos \theta - 1) - Q\theta' - \frac{\theta'^2}{2} \\ v_x &= \frac{\sin^2(\theta)}{2\rho^2} + \frac{Q \sin(2\theta)}{2\rho} - Q\theta' - \frac{\theta'^2}{2}. \end{aligned} \quad (5.32)$$

They only depend on the radial component ρ . The potential v_x stems from the expansion of the DM interaction term and is the only one that couples the two components of the Schrödinger equation. The interaction between the collective coordinate \mathbf{R} and the massive modes ψ_α is given by

$$\mathcal{L}_{\text{int}}^{(2)} = -\frac{1}{2a^2} \vec{\psi}^\dagger \Gamma^\gamma \vec{\psi} i d_\tau \mathbf{R}_\gamma. \quad (5.33)$$

where interaction vertex assumes the simple form

$$\Gamma_{\alpha\beta}^\gamma = -\tau_{\alpha\beta}^z i\partial_\gamma - \delta_{\alpha\beta} \frac{\cos \theta}{\rho} \hat{\chi}_\gamma. \quad (5.34)$$

and we have defined the differential operator $\partial_\gamma = \hat{\rho}_\gamma \partial_\rho + \hat{\chi}_\gamma (1/\rho) \partial_\chi$ where $\hat{\rho}^T = (\cos \chi, \sin \chi)$ and $\hat{\chi}^T = (-\sin \chi, \cos \chi)$. In summary we the expansion we found has the following structure

$$L = \underbrace{\int d^2\mathbf{r} \mathcal{L}^{(0)}}_{\text{reproduces Thiele's equations}} + \underbrace{\int d^2\mathbf{r} \mathcal{L}_\alpha^{(1)} \psi_\alpha}_{\text{vanishes}} + \underbrace{\int d^2\mathbf{r} \psi_\alpha^\dagger G_{\alpha\beta}^{-1} \psi_\beta}_{\text{yields fluctuation spectrum}} - \underbrace{\frac{1}{2a^2} \int d^2\psi_\alpha^\dagger \Gamma_{\alpha\beta}^\gamma \psi_\beta \frac{d}{d\tau} \mathbf{R}_\gamma}_{\text{coupling between fluctuations and collective coordinate } \mathbf{R}} + \mathcal{O}(\Psi^3)$$

Normal modes of the fluctuation matrix

In the following we want to study the excitation spectrum of the massive fluctuations. This will provide us with a suitable eigenbasis to expand the fluctuating fields into. We therefore want to find the eigenfunction spectrum of the third term in the above expansion summary (ignoring the presence of the fourth term which is also quadratic

in the fluctuation fields however couples them to the collective coordinate). A Fourier-Laplace ansatz for the complex time dependence of the fields $\vec{\psi}(\tau) = \sum_{n\varepsilon} e^{-i\omega_n\tau} \vec{\psi}_\varepsilon a_{n,\varepsilon}$ allows us to obtain the fluctuation modes as the eigenstates of the equation

$$H\vec{\psi} = \varepsilon\tau^z\vec{\psi}. \quad (5.35)$$

The Hamiltonian possesses the following particle-hole symmetry which has important consequences for the eigenspectrum

$$\tau^x K H \tau^x K = H, \quad (5.36)$$

where K means complex conjugation. In particular if $\vec{\psi}$ is an eigenvector with eigenvalue ε then $\tau^x\vec{\psi}^*$ is an eigenvector with eigenvalue $-\varepsilon$. Eigenvalues therefore appear always in pairs $\pm\varepsilon$.

The Hamiltonian $H_{\alpha\beta}$ depends on the polar angle χ only through a partial derivate ∂_χ . Therefore the angular momentum is a good quantum number and we can use it to label the eigenstates. For this we set $\vec{\psi} = e^{im\chi}\vec{\eta}_m(\rho)$. With this ansatz we find $H(-i\partial_\chi) \rightarrow H(m)$ and the eigenvalue equation becomes

$$H(m)\vec{\eta}_m = \varepsilon\tau^z\vec{\eta}_m \quad (5.37)$$

In the following we limit ourselves to positive energies $\varepsilon > 0$ in the following. The eigenvectors with negative eigenenergies are simply given by $\tau^x K e^{im\chi}\vec{\eta}_m = e^{-im\chi}\vec{\zeta}_{-m}$ where $\vec{\zeta}_{-m} = \tau^x\vec{\eta}_m^*$ and

$$H(-m)\vec{\zeta}_{-m} = -\varepsilon\tau^z\vec{\zeta}_{-m}. \quad (5.38)$$

It is noteworthy that the fluctuation theory presented here bears structural resemblance to the Bardeen-Cooper-Schrieffer theory (BCS theory) of superconductivity. If one writes out the transformation Eq. (5.28) explicitly one finds

$$\vec{\psi} = \frac{1}{\sqrt{2}} \begin{pmatrix} \phi_1 - i\phi_2 \\ \phi_1 + i\phi_2 \end{pmatrix}. \quad (5.39)$$

We see that the two components are complex conjugates of each other. One can introduce now a Nambu spinor (for spinless particles) with a complex field Ψ to represent the ψ_α

$$\vec{\psi} = \begin{pmatrix} \Psi \\ \Psi^* \end{pmatrix} \quad (5.40)$$

The presence of the skyrmion creates the coupling potential $v_x\tau^x$, introduced above, between the two components of the Schrödinger equation leading to scattering terms of the form $\psi_1^*\psi_2$ and $\psi_2^*\psi_1$, which are in the Nambu language local, superconducting terms of the form $\Psi\Psi$ and $\Psi^*\Psi^*$. We will see later that it is only due to these induced superconducting correlations that we get a finite mass in the zero temperature limit.

For a localized object such as the skyrmion it is helpful to reformulate the above eigenvalue problem in terms of a scattering problem. For this we separate the Hamiltonian $H(m)$ into two contributions, $H(m) = H_{0m} + \mathcal{V}_m$. Here we choose the field polarized state ($W = 0$) as a reference state: H_{0m} describes magnon waves on top

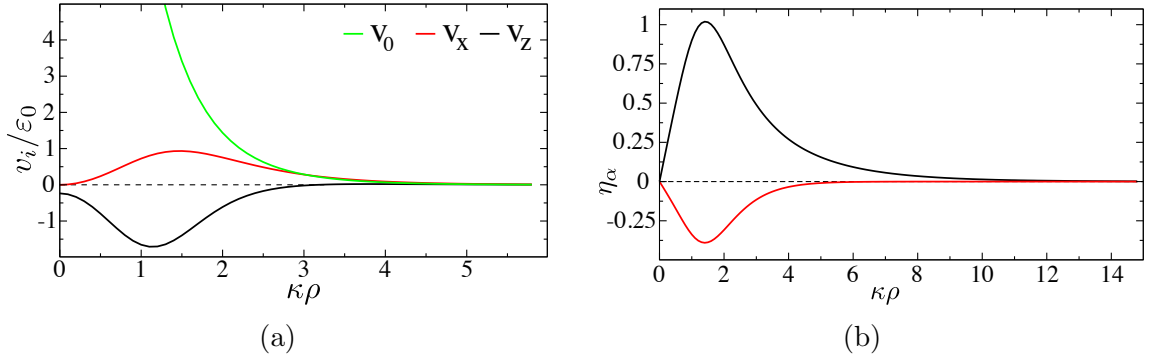


Figure 5.3: (a) The potentials v_0 , v_x and v_z in units of ε_0 plotted as functions of the dimensionless parameter $\kappa\rho$. All three potentials vanish exponentially for $\kappa\rho \gg 1$. (b) Exemplary solution of the eigenvalue problem, Eq. (5.35), for $\kappa = Q$ and $m = 0$ in the regime $0 < \varepsilon < \varepsilon_0 a^2 \kappa^2$ using the shooting method [71]. The numerical solution of the two-dimensional root-finding problem gives $\varepsilon = 0.839012$ and $c_1 = -0.331808$. For large $\kappa\rho$ both components of the eigenfunction vanish exponentially and therefore the wavefunction describes an internal excitation of the skyrmion.

of a collinear (field-polarised) state scattered by an exponentially localized scattering potential \mathcal{V}_m . Therefore H_{0m} describes the system in the absence of a skyrmion and is given by

$$H_{0m} = \varepsilon_0 a^2 \left[\mathbb{1} \left(-\partial_\rho^2 - \frac{\partial_\rho}{\rho} + \frac{m^2 + 1}{\rho^2} + \kappa^2 \right) - \tau^z \frac{2m}{\rho^2} \right] \quad (5.41)$$

This expression looks so unfamiliar due to the twist in the coordinate system, see Eq. 5.17. The skyrmion's scattering potential \mathcal{V}_m is given by

$$\mathcal{V}_m = \varepsilon_0 a^2 \left[v_0 \mathbb{1} + v_x \tau^x + v_z \tau^z \right] \quad (5.42)$$

with

$$v_z = -2m \left(\frac{\cos \theta - 1}{\rho^2} - \frac{Q \sin \theta}{\rho} \right) \quad (5.43)$$

and v_0 and v_x as given in Eq. (5.32). Fig. 5.3a shows the three components of the scattering potential \mathcal{V}_m . They vanish exponentially as $\kappa\rho \gg 1$. The potential v_x couples the two components of the wave function $\vec{\eta}$ and vanishes quadratically for $\kappa\rho \rightarrow 0$ and exponentially for $\kappa\rho \rightarrow \infty$.

Solutions of the free problem $H_{0m} \vec{\eta}_m^{(0)} = \varepsilon \tau^z \vec{\eta}_m^{(0)}$ only exist for energies $\varepsilon = \varepsilon_0 a^2 (\kappa^2 + K^2)$ with $K \geq 0$. They are given by

$$\vec{\eta}_{m,\varepsilon}^{(0)} = \begin{pmatrix} 1 \\ 0 \end{pmatrix} \frac{1}{\sqrt{2\varepsilon_0 a^2}} J_{m-1}(K\rho) \quad (5.44)$$

where J_ν are Bessel functions of the first kind. The solutions $\vec{\eta}_{m,\varepsilon}^{(0)}$ simply describe magnons with a gapped, quadratic dispersion relation in polar coordinates. They are normalized such that

$$\int_0^\infty d\rho \rho \vec{\eta}_{m,\varepsilon}^{(0)\dagger} \tau^z \vec{\eta}_{m,\varepsilon'}^{(0)} = \delta(\varepsilon - \varepsilon') \quad (5.45)$$

where we used the completeness relation of the Bessel functions

$$\delta(K - K') = K \int_0^\infty d\rho \rho J_\nu(K\rho) J_\nu(K'\rho). \quad (5.46)$$

We now turn to the solution of the full scattering problem. Depending on the eigenenergy of the excitation ε , the eigenmodes are either (1) spin-wave scattering states or (2) bound states which appear as internal excitations of the skyrmion. For energies $\varepsilon > \varepsilon_0 a^2 \kappa^2$ one finds scattering states with a continuum of eigenenergies and oscillating behaviour in the large $\kappa\rho$ -limit, for $\varepsilon < \varepsilon_0 a^2 \kappa^2$ internal excitation modes of the skyrmion are found which are exponentially localised.

The full scattering problem can only be solved numerically. We employ the *shooting method* [71] to find the solutions. We start by analysing the asymptotics of the eigenfunctions. For small distances $\rho\kappa \ll 1$, the Hamiltonian reduces to

$$H(m) \approx \varepsilon_0 a^2 \left[\mathbb{1} \left(-\partial_\rho^2 - \frac{\partial_\rho}{\rho} + \frac{m^2 + 1}{\rho^2} \right) + 2\tau^z \frac{m}{\rho^2} \right] \quad (5.47)$$

where we have omitted all terms with $O(\kappa^{-1}\rho^{-1})$ and above. Notice that the skyrmion essentially inverts the sign in the linear m term compared to the free Hamiltonian H_{0m} . From Eq. (5.47) follows the asymptotics of the eigenfunction for small distances

$$\vec{\eta}_m \approx \begin{pmatrix} \mathcal{N}(\kappa\rho)^{|m+1|} \\ \mathcal{N}_{c_1}(\kappa\rho)^{|m-1|} \end{pmatrix} \quad \text{for } \kappa\rho \ll 1, \quad (5.48)$$

with coefficients \mathcal{N} and c_1 . While the coefficient \mathcal{N} is fixed by the normalisation condition, Eq. (5.45), c_1 parametrizes the different initial value problems (IVPs). c_1 has to be chosen such that the solution of the IVP has the correct asymptotics for $\kappa\rho \gg 1$.

For $0 < \varepsilon < \varepsilon_0 a^2 \kappa^2$ the energy spectrum is discrete and all eigenmodes are localised near the skyrmion centre with exponentially decaying asymptotics for large distances. However for arbitrary c_1 one finds that solutions of the resulting IVP have asymptotics of the form

$$\vec{\eta}_m \approx \begin{pmatrix} A K_{m-1}(\sqrt{\varepsilon_0 a^2 \kappa^2 - \varepsilon\rho}) + B I_{m-1}(\sqrt{\varepsilon_0 a^2 \kappa^2 - \varepsilon\rho}) \\ C K_{m-1}(\sqrt{\varepsilon_0 a^2 \kappa^2 + \varepsilon\rho}) + D I_{m-1}(\sqrt{\varepsilon_0 a^2 \kappa^2 + \varepsilon\rho}) \end{pmatrix} \quad \text{for } \kappa\rho \gg 1 \quad (5.49)$$

where I_ν are modified Bessel functions of the first and K_ν of the second kind. For $\kappa\rho \gg 1$, I_ν shows exponentially increasing asymptotics. Therefore one has to choose the eigenenergy ε and the parameter c_1 such that the coefficients B and D vanish

$$\begin{aligned} B(\varepsilon, c_1) &\stackrel{!}{=} 0 \\ D(\varepsilon, c_1) &\stackrel{!}{=} 0 \end{aligned} \quad (5.50)$$

Effectively one needs to solve a two-dimensional root-finding problem which can be easily done on any computer.

In the energy range $\varepsilon \geq \varepsilon_0 a^2 \kappa^2$ the spectrum is a continuum of spin-wave scattering states with oscillating large $\kappa \rho$ asymptotics. Here the root-finding problem simplifies as the large distance asymptotics of the IVP is given by

$$\vec{\eta}_m \approx \begin{pmatrix} A J_{m-1}(\sqrt{\varepsilon - \varepsilon_0 a^2 \kappa^2} \rho) + B Y_{m-1}(\sqrt{\varepsilon - \varepsilon_0 a^2 \kappa^2} \rho) \\ C K_{m-1}(\sqrt{\varepsilon_0 a^2 \kappa^2 + \varepsilon} \rho) + D I_{m-1}(\sqrt{\varepsilon_0 a^2 \kappa^2 + \varepsilon} \rho) \end{pmatrix} \quad (5.51)$$

where J_ν is the Bessel functions of the first and Y_ν of the second kind. In order to have normalizable eigenfunctions we have to “kill” the exponentially increasing behaviour of I_{m-1} by choosing c_1 such that

$$D(\varepsilon, c_1) \stackrel{!}{=} 0 \quad (5.52)$$

For any $\varepsilon \geq \varepsilon_0 a^2 \kappa^2$ such a c_1 can be found numerically.

It is an important crosscheck that the translational modes of the skyrmion are indeed zero modes of the Hamiltonian H . The generator of translations along the γ -direction is given by $\nabla_\gamma \hat{e}_3$. With the help of Eq. (5.21) we find

$$\nabla_\gamma \hat{e}_3 = -\theta' \hat{\rho}_\gamma \hat{e}_2 + \frac{\sin \theta}{\rho} \hat{\chi}_\gamma \hat{e}_1. \quad (5.53)$$

which allows to identify the zero modes in terms of the ϕ 's by comparing coefficients

$$\begin{aligned} \phi_1^{\text{zm},\gamma} &= \frac{\sin \theta}{\rho} \hat{\chi}_\gamma \\ \phi_2^{\text{zm},\gamma} &= -\theta' \hat{\rho}_\gamma \end{aligned} \quad (5.54)$$

Using the unitary transformation Eq. (5.28) we find a zero mode with angular momentum $m = 1$,

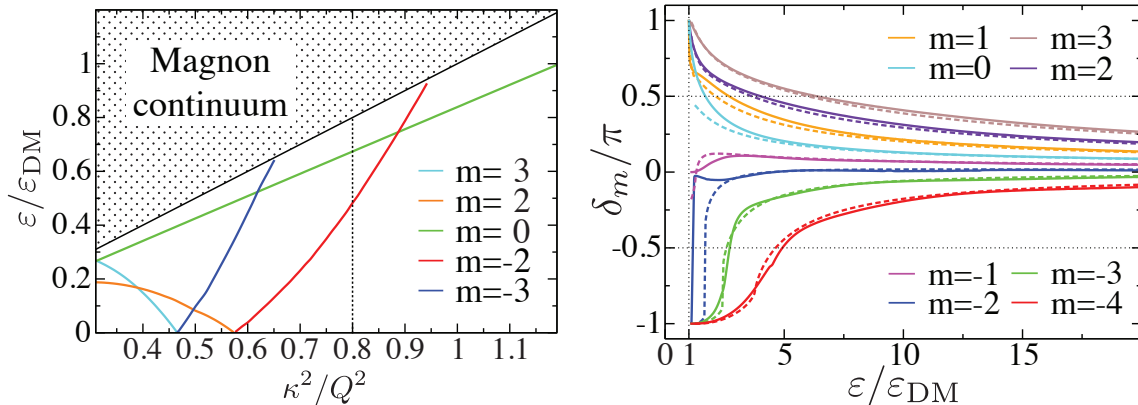
$$\vec{\eta}_1^{\text{zm}} \propto \begin{pmatrix} \frac{\sin \theta}{\rho} + \theta' \\ \frac{\sin \theta}{\rho} - \theta' \end{pmatrix}. \quad (5.55)$$

The second mode with $m = -1$ is then obtained via the relation $\vec{\zeta}_{-1}^{\text{zm}} = \tau^x (\vec{\eta}_1^{\text{zm}})^*$. One can then check explicitly, that $H(1)\vec{\eta}_1^{\text{zm}} = H(-1)\vec{\zeta}_{-1}^{\text{zm}} = 0$ using the differential equation obeyed by $\theta(\rho)$, Eq. (5.19).

Fluctuation spectrum

The energy spectrum for the regime $0 < \varepsilon < \varepsilon_0 a^2 \kappa^2$ (local modes) is shown in Fig. 5.4a. In the regime of a stable field-polarized state $\kappa^2 \gtrsim 0.8Q^2$, see Fig. 5.2a, we find two bound states in addition to the zero modes (which are not shown). There exists a bound state with $m = 0$ for all κ and an additional bound state with $m = 2$ below $\kappa^2 \lesssim 0.95Q^2$. Interestingly, the energy of the $m = 2$ mode decreases to zero at around $\kappa^2/Q^2 \approx 0.57$ below which it reappears as a $m = -2$ mode.

The point where the excitation energy of the $m = 2$ -mode vanishes is noteworthy. The presence of the skyrmion breaks translational symmetry which leads to the appearance of zero modes (translational modes in x and y direction) which we treat by introducing the collective coordinate \mathbf{R} . The spin-orbit interaction (in the



(a) Energy spectrum of spin-waves in the presence of a skyrmion on top of the field-polarized state. The latter becomes unstable for $\kappa^2 \lesssim 0.8Q^2$ (dotted vertical line). Bound states with larger m only appear well within the unstable regime $\kappa^2 < 0.5Q^2$.

(b) Phase shifts of the scattering states, numerically exact (solid lines) and in WKB approximation (dashed lines) for various angular momentum channels. For large angular momenta or high energies the WKB approximation renders satisfying results.

form of the DM interaction in our Hamiltonian) which allows for the skyrmion as a metastable solution breaks the separate rotational symmetries in spin and real space. However even in the presence of a finite magnetic field a symmetry operation is allowed which rotates spin and real space simultaneously around an axis parallel to the applied field through the skyrmion core. The vanishing of the eigenenergy of the quadrupolar mode, $m = -2$, at $\kappa^2 \approx 0.58Q^2$ probably indicates an instability of the single skyrmion for all $\kappa^2 \lesssim 0.58Q^2$ towards deformation into a bimeron as previously pointed out by Ezawa [27]. Fig. 5.5b illustrates the space-time dependence of the relevant bound magnon modes. The bimeron breaks rotational symmetry by picking out a certain direction, c.f. Fig. 5.5b. One would treat this point by introducing an additional collective variable (nematic director) which describes the chosen direction. Additional modes are seen to appear within the unstable regime, for example, a $|m| = 4$ bound state and also states with larger $|m|$ for even smaller values of κ which we don't show here. However the spectrum in this region is not reliable due to the rotationally invariant skyrmion being the wrong ground state. All bound state we found do not have any nodes, i.e., the corresponding $\vec{\eta}_m$ do not have zeros at a finite distance ρ . There is nothing in principle that forbids local modes with a node however their energies were simply so high that they lie in the magnon continuum in the investigated κ -regime.

In Ref. [60], Lin and coworkers use the Lanczos method for a finite system discretised on a two-dimensional, simple cubic lattice to determine the spectrum of the internal modes. The results from this numerical study agree with our results with the noteworthy exception of the zero-mode. In the Lanczos treatment the translational mode has a nonzero frequency because of the intrinsic pinning caused by the discrete lattice. The frequency depends on the ratio of the skyrmion size to the lattice constant and it becomes bigger for higher fields because the skyrmion becomes smaller [60].

Turning to the regime $\varepsilon \geq \varepsilon_0 a^2 \kappa^2$ now, we find that the scattering states obey the following asymptotics in the limit $\kappa \rho \gg 1$

$$\vec{\eta}_m \approx \begin{pmatrix} 1 \\ 0 \end{pmatrix} \frac{1}{\sqrt{2\varepsilon_0 a^2}} (\cos(\delta_m) J_{m-1}(K\rho) - \sin(\delta_m) Y_{m-1}(K\rho)). \quad (5.56)$$

where we introduced the phase shift δ_m . The second component is exponentially small (c.f. Eq. (5.51)) and has been set to zero. The above equation allows to extract the scattering phase shifts for the numerically determined wave functions as a function of the energy ε . The resulting phase shifts are shown in Fig. 5.4b. While the dependence of the phase shifts on the angular momentum quantum number m and energy ε is quite rich for small ε , the structure of the phase shifts at high ε significantly simplifies.

For high energies, approximate phase shifts can be obtained from the Wentzel-Kramers-Brillouin (WKB) approximation. The details of this procedure are outlined in appendix D. The resulting phase shifts are plotted in Fig. 5.4b as dashed lines with a matching color code to compare to the numerically exact phase shifts. For high energies the agreement is excellent.

5.1.4 Fluctuation-induced inertia terms

In the following we study the terms generated by the massive fluctuations for the effective action of the collective coordinate \mathbf{R} . We start by expanding the fields $\vec{\psi}$ in terms of normal modes of the fluctuation Hamiltonian $H_{\alpha\beta}$. We can regard the expansion coefficients as creation / annihilation fields for the corresponding excitations. Substituting this expression into the quadratic action $\mathcal{S}^{(2)}$ gives the interaction with the collective coordinate in terms of creation / annihilation fields for which Wick's theorem holds. Finally we perform perturbation theory in the interaction $\mathcal{S}_{\text{int}}^{(2)}$ to find the terms for the action of collective coordinate.

Expansion in terms of normal modes

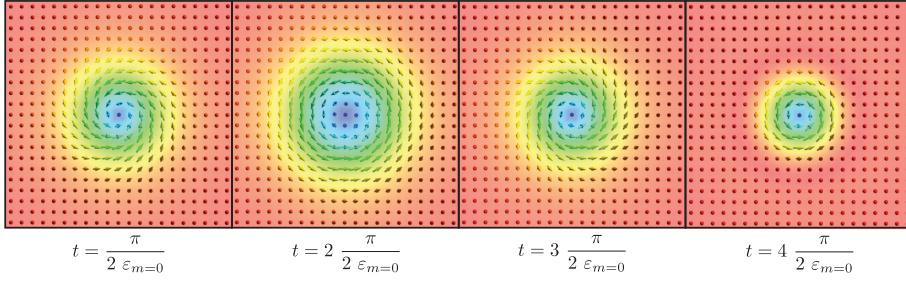
As already mentioned the original fluctuation fields ϕ are real-valued and therefore after transformation Eq. (5.28) the fields ψ obey the symmetry

$$\vec{\psi}^* = \tau^x \vec{\psi}. \quad (5.57)$$

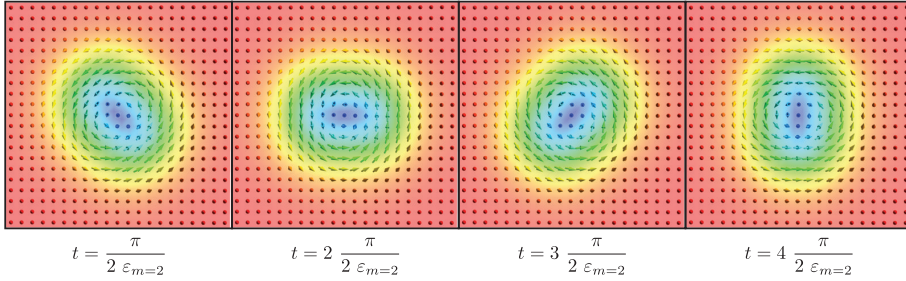
This is reflected in the expansion of the $\vec{\psi}$'s in terms of the normal modes, i.e. the eigenfunctions of the fluctuation matrix. The expansion takes the form

$$\begin{aligned} \vec{\psi}(\mathbf{r}, \tau) = \frac{1}{2\pi} \sum_m e^{im\chi} \left[\sum_n \left(a_{m,n}(\tau) \vec{\eta}_{m,n}(\rho) + a_{-m,n}^\dagger(\tau) \vec{\zeta}_{m,n}(\rho) \right) \right. \\ \left. + \int_{\Delta}^{\infty} d\varepsilon \left(a_{m,\varepsilon}(\tau) \vec{\eta}_{m,\varepsilon}(\rho) + a_{-m,\varepsilon}^\dagger(\tau) \vec{\zeta}_{m,\varepsilon}(\rho) \right) \right] \end{aligned} \quad (5.58)$$

where $\Delta = \varepsilon_0 a^2 \kappa^2$ is the lower bound for the energy of the magnon continuum and $K a_{m,n}^\dagger = a_{m,n}$ and $K a_{-m,\varepsilon}^\dagger = a_{m,\varepsilon}$ with K complex conjugation. The first contribution in the expansion expands in terms of the localised, internal excitation modes. Here



(a) Visualization of the $m = 0$ excitation mode as a sequence of 4 snapshots throughout one period of oscillation. The skyrmion shows a deformation where it grows and shrinks periodically which is why this mode is referred to as the “breathing mode”. This mode does not break the symmetry of simultaneous rotations of spin- and real-space.



(b) Visualization of the $m = 2$ excitation mode as a sequence of 4 snapshots throughout one period of oscillation. The skyrmion is deformed into an elongated shape which rotates slowly about its center.

Figure 5.5

m labels the angular momentum quantum number and n is an additional quantum number which labels the number of nodes in the solution. However we only found internal modes with $n = 0$ in the investigated κ regime. The second contribution expands in terms of the extended scattering states. Here the continuous variable ϵ with the lower bound Δ parametrizes the energy of the scattering solution. For $\epsilon < \Delta$ the large ρ asymptotics of the solutions change from oscillating to exponentially decaying.

As a short hand notation we omit the second term in the above expression and agree that the index of the sum \sum_n is either discrete or continuous for the bound and scattering states respectively. Indeed we find for the complex conjugate of the fields

ψ

$$\begin{aligned}
\vec{\psi}^*(\mathbf{r}, \tau) &= \frac{1}{2\pi} \sum_{m,n} e^{-im\chi} \left(a_{m,n}^\dagger(\tau) \vec{\eta}_{m,n}^*(\rho) + a_{-m,n}(\tau) \vec{\zeta}_{m,n}^*(\rho) \right) \\
&= \tau^x \frac{1}{2\pi} \sum_{m,n} e^{im\chi} \left(a_{-m,n}^\dagger(\tau) \tau^x \vec{\eta}_{-m,n}^*(\rho) + a_{m,n}(\tau) \tau^x \vec{\zeta}_{-m,n}^*(\rho) \right) \\
&= \tau^x \frac{1}{2\pi} \sum_{m,n} e^{im\chi} \left(a_{-m,n}^\dagger(\tau) \vec{\zeta}_{m,n}(\rho) + a_{m,n}(\tau) \vec{\eta}_{m,n}(\rho) \right) \\
&= \tau^x \vec{\psi}(\mathbf{r}, \tau)
\end{aligned} \tag{5.59}$$

where in the second equality we set $m \rightarrow -m$ and in the third we used $\vec{\zeta}_{-m} = \tau^x \vec{\eta}_m^*$ and $\vec{\eta}_{-m} = \tau^x \vec{\zeta}_m^*$. One can now substitute the above expansion into the quadratic part of the action $\mathcal{S}^{(2)} = \int d\mathbf{r} \mathcal{L}^{(2)}$ with $\mathcal{L}^{(2)}$ given by Eq. (5.30). For the calculation matrix elements between different wave functions are needed

$$\begin{aligned}
\int_0^\infty d\rho \rho \vec{\eta}_{m,j}^\dagger \tau^z \vec{\eta}_{m,j'} &= \delta_{j,j'} \\
\int_0^\infty d\rho \rho \vec{\zeta}_{m,j}^\dagger \tau^z \vec{\eta}_{m,j'} &= 0 \\
\int_0^\infty d\rho \rho \vec{\zeta}_{m,j}^\dagger \tau^z \vec{\zeta}_{m,j'} &= -\delta_{j,j'}
\end{aligned} \tag{5.60}$$

where in the last line we used $\tau^x \tau^z \tau^x = -\tau^z$. One finds for the quadratic part of the action

$$\mathcal{S}^{(2)} = \frac{1}{2\pi a^2} d\tau \sum_{m,n} a_{m,n}^\dagger (\partial_\tau + \varepsilon_{m,n}) a_{m,n} + \mathcal{S}_{\text{int}}^{(2)} \tag{5.61}$$

Since we expand in terms of normal modes the first part of the action assumes a simple form by construction, where $\varepsilon_{m,n}$ is the eigenenergy of the normal mode with quantum numbers (m, n) .

The expansion of the part interacting with collective coordinate $\mathcal{S}_{\text{int}}^{(2)}$ is a little more tricky. In the angular momentum representation the interaction vertex $\Gamma^\gamma(-i\partial_\gamma)$, Eq. (5.34), assumes the form

$$\Gamma^\gamma(m) = \tau^z \left(-\hat{\rho}_\gamma i\partial_\rho + \frac{m}{\rho} \hat{\chi}_\gamma \right) - \mathbb{1} \frac{\cos\theta}{\rho} \hat{\chi}_\gamma \tag{5.62}$$

Throughout the calculation one needs to calculate integrals of the following form which can be conveniently expressed using the vectors \hat{e}^\pm

$$\int_0^{2\pi} d\chi e^{i(m-m')\chi} \Gamma^\gamma(m) = 2\pi \sum_{\sigma=\pm 1} \Gamma^{\sigma,m} \delta_{m-m'+\sigma} \hat{e}_\gamma^{-\sigma}, \quad \text{with } \hat{e}^\pm = \frac{1}{\sqrt{2}} \begin{pmatrix} 1 \\ \pm i \end{pmatrix} \tag{5.63}$$

where we introduced the new vertex operator matrix on the right-hand-side

$$\Gamma^{\sigma,m} = \frac{i}{\sqrt{2}} \left[-\tau^z \partial_\rho - \sigma \left(-\tau^z \frac{m}{\rho} + \frac{\cos\theta}{\rho} \right) \right]. \tag{5.64}$$

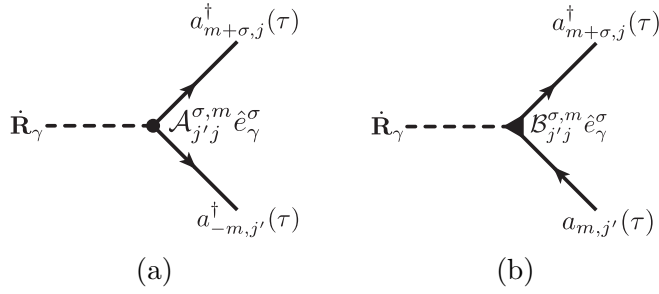


Figure 5.6: Diagrammatic representation of the contributions to \mathcal{S}_{int} . (a) Diagrams linear in $\mathcal{A}_{j'j}^{\sigma,m}$ couple the particle-particle (hole-hole) channel to the collective coordinate \mathbf{R} . (b) Diagrams linear in $\mathcal{B}_{j'j}^{\sigma,m}$ couple the particle-hole channel to the collective coordinate \mathbf{R} .

With this one finds the expansion of the interaction in the normal modes

$$\begin{aligned} \mathcal{S}_{\text{int}}^{(2)} = \frac{1}{2a^2} \frac{1}{2\pi} \int_0^\beta \sum_{m\sigma} \sum_{jj'} \left[\mathcal{A}_{j'j}^{\sigma,m} \frac{i}{2} \left(a_{-m,j'} a_{m+\sigma,j} \hat{e}_\gamma^\sigma - a_{-m,j'}^\dagger a_{m+\sigma,j}^\dagger \hat{e}_\gamma^{-\sigma} \right) \right. \\ \left. + \mathcal{B}_{j'j}^{\sigma,m} i a_{m,j'}^\dagger a_{m+\sigma,j} \hat{e}_\gamma^\sigma \right] i d_\tau \mathbf{R}_\gamma \end{aligned} \quad (5.65)$$

with the amplitudes

$$\begin{aligned} \mathcal{A}_{j'j}^{\sigma,m} &= \frac{\sigma}{\sqrt{2}} \langle \vec{\eta}_{m+\sigma,j}^T (\tau^z \frac{2m+\sigma}{\rho} - \mathbb{1} \frac{2 \cos \theta}{\rho}) \vec{\zeta}_{m,j'} \rangle \\ \mathcal{B}_{j'j}^{\sigma,m} &= \frac{\sigma}{\sqrt{2}} \langle \vec{\eta}_{m+\sigma,j}^T (\tau^z \frac{2m+\sigma}{\rho} - \mathbb{1} \frac{2 \cos \theta}{\rho}) \vec{\eta}_{m,j'} \rangle \end{aligned} \quad (5.66)$$

By now we have collected quite a number of indices. It is helpful to introduce a diagrammatic language at this point for a clearer presentation of the perturbation theory. The action due to the interaction term $\mathcal{S}_{\text{int}}^{(2)}$, Eq. (5.65) has three contributions: two linear in $\mathcal{A}_{j'j}^{\sigma,m}$, complex conjugates of each other, and one linear in $\mathcal{B}_{j'j}^{\sigma,m}$. We agree on the following code:

1. Time derivatives of the collective coordinate $\dot{\mathbf{R}}$ are represented by dashed lines.
2. Directed, solid lines mark creation / annihilation fields, where an arrow pointing away from the vertex signifies a creation field, $a_{m,j}^\dagger$, and towards the vertex a annihilation field, $a_{m,j}$.
3. The matrix element $\mathcal{A}_{j'j}^{\sigma,m}$ is represented by a circle and the matrix element $\mathcal{B}_{j'j}^{\sigma,m}$ by a triangle.

Fig. 5.6 shows two of three contributions where the remaining diagram is easily constructed from Fig. 5.6a by reversing the solid line directions.

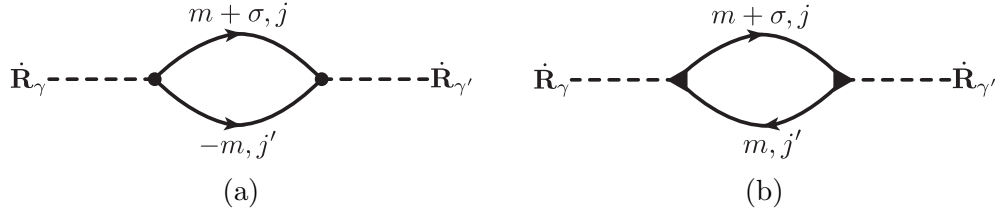


Figure 5.7: (a) The contribution quadratic in $\mathcal{A}_{j'j}^{\sigma,m}$ is also finite at $T = 0$. (b) The particle-hole bubble quadratic in $\mathcal{B}_{j'j}^{\sigma,m}$ vanishes at $T = 0$.

Second-order perturbation theory in \mathcal{S}_{int}

In order to study how the massive fluctuations $a_{m,n}$ modify the effective action of the collective coordinate \mathbf{R} we expand the action up to second order in the interaction \mathcal{S}_{int}

$$\begin{aligned}
e^{-S} &\approx e^{-(S^{(0)} + S_0^{(2)} + \mathcal{S}_{\text{int}}^{(2)})} \\
&\approx e^{-S^{(0)}} \left[\underbrace{1 - \langle \mathcal{S}_{\text{int}}^{(2)} \rangle_0}_{\text{vanishes}} + \frac{1}{2} \langle \mathcal{S}_{\text{int}}^{(2)} \mathcal{S}_{\text{int}}^{(2)} \rangle_0 \right] \\
&\approx e^{-S^{(0)}} e^{\frac{1}{2} \langle \mathcal{S}_{\text{int}}^{(2)} \mathcal{S}_{\text{int}}^{(2)} \rangle_0}
\end{aligned} \tag{5.67}$$

where $S^{(0)}$ is the quadratic part of the action without the interactions \mathcal{S}_{int} and

$$\langle \dots \rangle_0 = \frac{1}{\mathcal{Z}_0} \int \mathcal{D}(a, a^\dagger) \dots e^{-S^{(0)}} \tag{5.68}$$

with $\mathcal{Z}_0 = \int \mathcal{D}(a, a^\dagger) e^{-\int d\tau S^{(0)}}$. The trace over $\mathcal{S}_{\text{int}}^{(2)}$ vanishes as the terms proportional to $\mathcal{A}_{j'j}^{\sigma,m}$ are not particle number conserving and those proportional to $\mathcal{B}_{j'j}^{\sigma,m}$ only give a finite contribution if there is a difference of $\sigma = \pm 1$ in the angular momentum of the states right and left.

The expectation value of the square of the interaction \mathcal{S}_{int} takes the form of an inertia term for the collective coordinate $\mathbf{R}_\gamma(\tau)$

$$\frac{1}{2} \left\langle \left(\mathcal{S}_{\text{int}}^{(2)} \right)^2 \right\rangle_0 = \int d\tau \int d\tau' \frac{1}{2} id_\tau \mathbf{R}_\gamma(\tau) M_{\gamma,\gamma'}(\tau - \tau') id_\tau \mathbf{R}_{\gamma'}(\tau') \tag{5.69}$$

with the mass tensor $M_{\gamma,\gamma'}$. The expression for $M_{\gamma,\gamma'}$ is rather complicated however it simplifies in the zero temperature limit, $T \rightarrow 0$.

Quantum mass of the skyrmion

Considering the structure of Eq. (5.65) we expect to see three types of contributions to $M_{\gamma,\gamma'}$: (a) those quadratic in $\mathcal{A}_{j'j}^{\sigma,m}$, (b) those quadratic in $\mathcal{B}_{j'j}^{\sigma,m}$ and (c) those linear in both. Contributions of the last type vanish as they are not particle number conserving. They consist of either three annihilation fields $a_{m,n}$ and one creation field $a_{m,n}^\dagger$ or vice-versa. In the diagrammatic language this is expressed by the inability to

connect the diagram in Fig. 5.6a to the one in Fig. 5.6b. The diagrams of the first two contributions are given in Fig. 5.7. In the zero temperature limit contributions quadratic in $\mathcal{B}_{j'j}^{\sigma,m}$ also vanish as the corresponding diagram, Fig. 5.7b, is a particle-hole bubble and one takes the expectation value with respect to the ground state which is defined by the absence of all internal and magnon modes. However the hole-hole version of the diagram in Fig. 5.7a is finite even at $T = 0$. It is only due to the local, “superconducting” correlations that this diagram has a finite expectation value.

Subsequently the expression for $M_{\gamma,\gamma'}$ considerably simplifies and one finds

$$M_{\gamma\gamma'}^{T \rightarrow 0}(i\Omega) = \frac{1}{2\pi} \sum_{m,\sigma,j,j'} \frac{1}{8} |\mathcal{A}_{j,j'}^{\sigma,m}|^2 \frac{i\Omega \sigma \tau_{\gamma\gamma'}^y + (\varepsilon_{m+\sigma,j'} + \varepsilon_{-m,j}) \mathbb{1}_{\gamma\gamma'}}{(\varepsilon_{m+\sigma,j'} + \varepsilon_{-m,j})^2 - (i\Omega)^2}. \quad (5.70)$$

The evaluation of the above expression involves matrix elements $\mathcal{A}_{j,j'}^{\sigma,m}$ of scatter-scatter, bound-scatter and bound-bound wave function combinations with relative angular momentum difference of ± 1 . If one chooses $\kappa \gtrsim 0.95 Q$ (here $\kappa = Q$) only the $m = 0$ bound state exists below the magnon continuum, c.f. Fig. 5.4a. Therefore no bound-bound wave function combinations exist with $\Delta m = \pm 1$ and for the bound-scatter combinations only the scattering states with $m = \pm 1$ have to be considered. In Fig. 5.8 the frequency dependence of the analytical continuation of Eq. 5.70 is shown (blue line). We also separated the contributions from the overlaps for two scattering solutions (green line) from those of a scattering solution with the bound state $m = 0$ (red line). The scatter-scatter contributions peak at a characteristic frequency 2Δ with Δ the size of the magnon gap, which is the minimum energy required to emit two magnons. For $\kappa = Q$ the energy of the $m = 0$ bound state is given by $\approx 0.84 \Delta$. Therefore magnon-bound state contributions are seen to peak at a slightly smaller frequency than 2Δ approximately given by $\omega \approx 1.84 \Delta$ which is the minimum energy required to excite the $m = 0$ mode and emit a single magnon. It should be noted that the contributions from overlaps with the single bound state $m = 0$ are treated without any truncation. Scattering modes with $|m| \neq 1$, do not have any overlap with the $m = 0$ bound state. The contributions for the overlap of two scattering wave functions on the other have been truncated. Here only the lowest angular momentum states are considered with $m \in [-2, \dots, 2]$. It turns out that solving the boundary value problem and calculating the matrix elements $\mathcal{A}_{j,j'}^{\sigma,m}$ for higher angular momentum states is numerically more difficult. Unfortunately due to time constraints we were not able to sort the problems out before writing this thesis. We expect that the weight of higher angular momentum states is numerically quickly seen to diminish, however a more refined quantitative investigation is necessary to properly justify this truncation and left for the future.

A scaling analysis of Eq. 5.70 allows to determine how the quantum mass scales with the radius of the Skyrmion. The scattering wave functions scale due to the normalisation condition, Eq. 5.45, like $\vec{\eta}_{m\sigma} \sim \frac{1}{\rho\sqrt{\epsilon}}$. The matrix elements $|\mathcal{A}_{j,j'}^{\sigma,m}|$ therefore scale (with the two powers of ρ from the integration) according to $|\mathcal{A}_{j,j'}^{\sigma,m}| \sim \frac{1}{\rho^2\epsilon} \frac{1}{\rho} \rho^2 \sim \frac{1}{\epsilon\rho}$. In the $\Omega \rightarrow 0$ -limit the above expression for the mass is thus independent of the Skyrmion radius $M_{\gamma\gamma'}^{T \rightarrow 0}(i\Omega \rightarrow 0) \sim \frac{1}{\rho^2\epsilon} \sim \frac{Q^2}{\epsilon} \sim 1$. Thus, the expectation is to find a number for the mass of order 1. It is therefore surprising that the numerical

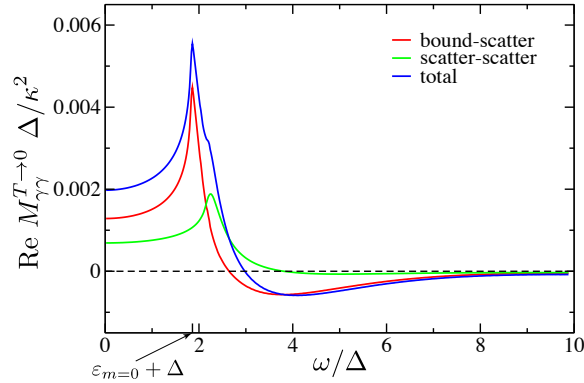


Figure 5.8: Real part of the diagonal entries of the mass tensor $M_{\gamma\gamma}^{T \rightarrow 0}(\omega)$ as a function of the real frequency ω in the $T \rightarrow 0$ limit evaluated from the lowest angular momentum eigenstates $m \in [-4, \dots, 3]$. The green line indicates the contribution from overlaps of two scattering solution, the red line from overlaps of a bound and a scattering solution and the blue line the sum of the two.

value is so small, especially as there does not appear to be a small parameter in the theory which could explain this. Several points should be mentioned here: First of all, it small numbers of order 1 do exist; there is nothing illegal about $\text{Re} M_{\gamma\gamma}^{T \rightarrow 0}(\omega)$ being small. Secondly, as already mentioned, the angular momentum number has been truncated (due to numerical problems) and only magnon states with m values, $m \in [-2, \dots, 2]$, have been considered. While it can be expected that higher angular momentum states give smaller contribution, there is strictly speaking currently no justification for this truncation. One possible scenario is that there is really a conservation law which enforces a vanishing of the mass for $T = 0$ and the small number seen here is really a 0. The clarification of these points is left for future work.

An interesting question now is: what are the observable physical consequences of the presence of the mass term? Massive particles in an applied magnetic field are known to give rise to gyro modes oscillating with the cyclotron frequency. Here the numerical value of the mass is extremely small. With the cyclotron frequency given by $\omega_c \sim \frac{\kappa^2}{\text{Re} M_{\gamma\gamma}(\omega_c)}$, one finds that due to the strong suppression of the mass term at higher frequencies no solution of the equation exists and therefore no observable cyclotron mode arises below the magnon gap.

5.2 Effective Equations of Motion from Micromagnetic Simulations

Compared to the previous section, here we approach the problem of finding the effective equations of motion for a single Skyrmion in the ferromagnetic background from a complementary perspective. The approach presented in the last section could be characterised as a bottom-up approach: Starting from a microscopic description of the system we determine the eigenfunctions of the system and by integrating these out we extract the effective system description for the macroscopic degree of freedom,

i.e. the Skyrmion position. This allows for instance to determine which microscopic modes are especially important for the characterisation of the macroscopics. Although the above approach yields a wealth of information, it is limited by the difficulty to solve the microscopic problem.

The approach presented in this section can be compared to the Langevin treatment of the Brownian motion. There the central degree of freedom is the position of the Brownian particle. One does not try to understand and model the microscopic degrees of freedom (the particles that make up the fluid that the Brownian particle is immersed in) but rather retreats to modelling the statistical properties of the surrounding particle ensemble to the extent that it leads to fluctuations of the Brownian particle's position. A statistical analysis of these fluctuations then allows to extract macroscopically observable properties, e.g. the mean-squared displacement. Our approach for the effective dynamics of a single Skyrmion in the ferromagnetic background will be very similar. Based on a symmetry analysis we propose a prototypical form for the equations of motion. Numerical simulations provide the necessary data for a statistical analysis of collective coordinate fluctuations and velocity-velocity correlations allow to fix the full frequency dependence of the parameters in the equations of motion. In a second step we consider the response of a Skyrmion to time-dependent driving forces and find interesting screening and anti-screening effects.

5.2.1 Effective equations of motion for a single skyrmion

Following Kubo [55] in his seminal work about the fluctuation-dissipation theorem we start with the deterministic part of the equations of motions for Skyrmion position \mathbf{R} and add the effects of temperature and fluctuations later. The Skyrmion position in the two dimensional-plane is determined by an x - and a y -coordinate and therefore the equations of motion in the presence of a weak, time-dependent force $\mathbf{F}(t)$ will be of the form

$$\int_{-\infty}^{\infty} \mathbf{G}^{-1}(t-t') \cdot \mathbf{V}(t') dt' = \mathbf{F}(t) \quad (5.71)$$

where $\partial_t \mathbf{R}(t) = \mathbf{V}(t)$ and $\mathbf{G}^{-1}(t)$ is the inverse of the real-valued 2×2 Green's function matrix. Any real-valued matrix can be expressed as superposition of the matrices $\mathbb{1}, \sigma_x, i\sigma_y$ and σ_z . We may therefore expand $\mathbf{G}^{-1}(t) = D_{\mathbb{1}}(t)\mathbb{1} + D_x(t)\sigma_x + D_y(t)\sigma_y + D_z(t)\sigma_z$. The dynamics are invariant under rotations about the z -axis and particularly for $\pi/2$ -rotations. Note that rigorously speaking this symmetry is not supported by the microscopic unit cell in the B20 compounds. However, since the magnetisation changes only on length scales much larger than the atomic unit cell, the magnetisation dynamics decouples very efficiently from the lattice and the $\pi/2$ -rotations emerge as an approximate symmetry. Under such a rotation σ_x and σ_z go to $-\sigma_x$ and $-\sigma_z$ and therefore $D_x(t) = D_z(t) = 0$. We choose to parametrize $D(t-t')$ with

$$\begin{aligned} D_{\mathbb{1}}(t-t') &= \alpha \mathcal{D}(t-t') + m(t-t') \partial_{t'} \\ D_y(t-t') &= \alpha \mathcal{G}(t-t') + \alpha \Gamma(t-t') \partial_{t'}. \end{aligned} \quad (5.72)$$

The ansatz for the symmetry adjusted equations of motion assumes the form

$$\int_{-\infty}^{\infty} dt' \mathcal{G}(t-t') \times \dot{\mathbf{R}}(t') + \alpha \mathcal{D}(t-t') \dot{\mathbf{R}}(t') + m(t-t') \ddot{\mathbf{R}}(t') + \alpha \mathbf{\Gamma}(t-t') \times \ddot{\mathbf{R}}(t') = \mathbf{F}(t) \quad (5.73)$$

where $\mathbf{\Gamma}(t) = \Gamma(t)\hat{e}_{\perp}$ and $\mathcal{G}(t) = \mathcal{G}(t)\hat{e}_{\perp}$. Here the ‘gyro-coupling’ \mathcal{G} acts as an effective magnetic field oriented perpendicular to the plane, α is the (dimensionless) Gilbert damping and has been pulled out of \mathcal{G} and $\mathbf{\Gamma}$ for later convenience. $\alpha \mathcal{D}$ describes the friction of the Skyrmion and m its mass. $\mathbf{\Gamma}$ parametrizes a peculiar type of damping proportional to the acceleration of the particle. We refer to this term as ‘gyro-damping’ since it describes the damping of a particle on a cyclotron orbit, which can be either stronger ($\mathbf{\Gamma}$ parallel to \mathbf{G}) or weaker ($\mathbf{\Gamma}$ parallel to \mathbf{G}) than for linear motion.

Thiele [102] found analytic expressions for \mathcal{G} and $\alpha \mathcal{D}$ under the assumption of a rigid spin texture $\mathbf{M}(\mathbf{r}, t) = \mathbf{M}_0(\mathbf{r} - \mathbf{R}(T))$ driven by a static force \mathbf{F} [26, 88, 25, 46]. One finds

$$\begin{aligned} \mathcal{G} &= \hbar \frac{1}{M_0^2} \int d\mathbf{r} \mathbf{M}_0 \cdot (\partial_x \mathbf{M}_0 \times \partial_y \mathbf{M}_0) \\ \mathcal{D} &= \hbar \frac{1}{M_0^2} \int d\mathbf{r} (\partial_x \mathbf{M}_0 \cdot \partial_x \mathbf{M}_0 + \partial_y \mathbf{M}_0 \cdot \partial_y \mathbf{M}_0) / 2 \end{aligned} \quad (5.74)$$

with M_0 the amplitude of the magnetisation. From the standpoint of applications in spintronics one is interested in the fast manipulation of Skyrmions. However for weak but rapidly changing forces the above approximations are too crude and one needs to include the retardation effects contained in the time dependence of the parameters in Eq. 5.73. We will regard 3 possible contributions to the time-dependent force $\mathbf{F}(t)$. For a system at finite temperature the Langevin approach models the impact of temperature fluctuations on the system by the appearance of random, delta-correlated forces $\mathbf{F}_{\text{th}}(t)$ acting on the collective coordinate $\mathbf{R}(t)$ resulting in a diffusive motion of the Skyrmion. A second contribution comes from the application of a time-dependent current which leads due to spin-transfer torques to an effective time-dependent, deterministic force $\mathbf{F}_c(t) = \int_{-\infty}^t \mathbf{S}_c(t-t') \cdot \mathbf{v}_s(t') dt'$ with $v_s(t)$ the time-dependent (spin-) drift velocity of the conduction electrons. The matrix $\mathbf{S}_c(t-t')$ describes possible screening-effects of the forces due to retardation effects. The last contribution we will investigate is due to the application of a time-dependent magnetic field gradient. The Skyrmion has a finite magnetisation and therefore a magnetic field gradient will exert a force $\mathbf{F}_g(t) = \int_{-\infty}^t \mathbf{S}_g(t-t') \cdot \nabla B_z(t') dt'$ on the Skyrmion parallel to the gradient direction. Here possible screening effects are also taken into account by the matrix $\mathbf{S}_g(t)$.

In the following it will be advantageous to describe the dynamics in frequency space. The Fourier transform of the equations of motion for the driven Skyrmion can be written as

$$\mathbf{G}^{-1}(\omega) \mathbf{V}(\omega) = \mathbf{S}_c(\omega) \mathbf{v}_s(\omega) + \mathbf{S}_g(\omega) \nabla B_z(\omega) + \mathbf{F}_{\text{th}}(\omega) \quad (5.75)$$

where the small ω expansion of the 2×2 matrix $\mathbf{G}^{-1}(\omega)$ defines the terms on the lhs of Eq. 5.73. For the resulting dynamics of the driven Skyrmion also the frequency

dependence of the rhs will be very important: the application of external forces excites internal modes of the Skymion which change the dynamics significantly.

In order to determine the matrix $\mathbf{G}^{-1}(\omega)$, we turn off the magnetic gradient ∇B_z and the conduction electron current and analyse the diffusive motion of the Skymion due to the stochastic, thermal forces $\mathbf{F}_{\text{th}}(\omega)$. Kubo's fluctuation-dissipation theorem [55] for generalised systems of Langevin equations links the strength of these fluctuations to the strength of the dissipative mechanisms in $\mathbf{G}^{-1}(\omega)$. Kubo defines the Green's function in the system by

$$\mathbf{G}_{\alpha\beta}(\omega) = \frac{1}{k_B T} \int_0^\infty \Theta(t-t') \langle v_\alpha(t) v_\beta(t') \rangle e^{i\omega(t-t')} dt \quad (5.76)$$

The Fourier transform of the velocity-velocity correlation function is then expressed in terms of the Green's function as

$$\begin{aligned} \langle v_\alpha(\omega) v_\beta(-\omega) \rangle &= \int_{-\infty}^\infty dt \langle v_\alpha(t) v_\beta(0) \rangle e^{i\omega t} \\ &= \int_0^\infty dt \langle v_\alpha(t) v_\beta(0) \rangle e^{i\omega t} + \int_{-\infty}^0 dt \langle v_\alpha(t) v_\beta(0) \rangle e^{i\omega t} \\ &= k_B T \left(\mathbf{G}_{\alpha\beta}(\omega) + \int_{-\infty}^0 (-dt') \langle v_\alpha(-t') v_\beta(0) \rangle e^{-i\omega t'} \right) \\ &= k_B T \left(\mathbf{G}_{\alpha\beta}(\omega) + \int_0^\infty dt' \langle v_\alpha(0) v_\beta(t') \rangle e^{-i\omega t'} \right) \\ &= k_B T (\mathbf{G}_{\alpha\beta}(\omega) + \mathbf{G}_{\beta\alpha}(-\omega)) \end{aligned} \quad (5.77)$$

The lhs can be linked to the force-force correlation function using the equations of motion, Eq. 5.73

$$\begin{aligned} \langle F_\alpha(\omega) F_\beta(-\omega) \rangle &= \mathbf{G}_{\alpha\alpha'}^{-1}(\omega) \mathbf{G}_{\beta\beta'}^{-1}(-\omega) \langle v_{\alpha'}(\omega) v_{\beta'}(-\omega) \rangle \\ &= k_B T \mathbf{G}_{\alpha\alpha'}^{-1}(\omega) \mathbf{G}_{\beta\beta'}^{-1}(-\omega) [\mathbf{G}_{\alpha'\beta'}(\omega) + \mathbf{G}_{\beta'\alpha'}(-\omega)] \\ &= k_B T [\mathbf{G}_{\beta\alpha}^{-1}(-\omega) + \mathbf{G}_{\alpha\beta}^{-1}(\omega)], \end{aligned} \quad (5.78)$$

In terms of the low- ω parametrisation of \mathbf{G}^{-1} , Eq. 5.72, one finds $\langle \mathbf{F}_{\text{th}}^x(\omega) \mathbf{F}_{\text{th}}^x(\omega') \rangle = k_B T \alpha \mathcal{D}(\omega) \delta(\omega + \omega')$ and $\langle \mathbf{F}_{\text{th}}^x(\omega) \mathbf{F}_{\text{th}}^y(\omega') \rangle = k_B T \alpha \Gamma(\omega) \delta(\omega + \omega')$. Indeed the strength of the mechanism for dissipation is parametrized by the dissipative tensor $\mathcal{D}(\omega)$ and the gyro-damping $\Gamma(\omega)$. This is why we pulled the Gilbert damping α out of these quantities.

By virtue of Eq. 5.76 it is now possible to reconstruct the full frequency dependence of the Green's function by tracking the Skymion motion $\mathbf{R}(t)$ and analysing the correlation function of the velocity [55]. The trajectories $\mathbf{R}(t)$ can be obtained from numerical simulations of the stochastic Landau-Lifshitz-Gilbert equation as outlined in chapter 3. We therefore perform micro-magnetic simulations for a single Skymion in the ferromagnetic background at finite temperature for an ensemble of thermal noise realisations. For all of our simulations we chose a Dzyaloshinskii-Moriya interaction of $\lambda = 0.18J$ and $B_z = 0.0278J$. Initially a single Skymion is embedded into the ferromagnetic background, then the time evolution in the presence of the thermal

fluctuations is calculated. For the chosen parameters the ground state is ferromagnetic, thus a single Skyrmion is a topologically protected, meta-stable excitation. For the extraction of the Skyrmion centre coordinate we tried two tracking algorithms: (i) tracking of the topological charge density and (ii) tracking the core of the Skyrmion. The topological charge density is defined as

$$\rho_{top}(\mathbf{r}) = \frac{1}{4\pi} \hat{\mathbf{n}}(\mathbf{r}) \cdot (\partial_x \hat{\mathbf{n}}(\mathbf{r}) \times \partial_y \hat{\mathbf{n}}(\mathbf{r})) \quad (5.79)$$

with $\hat{\mathbf{n}}(\mathbf{r}) = \mathbf{M}(\mathbf{r})/|\mathbf{M}|$ and integrates to the total number of Skyrmions in the system. For the system we are considering $\rho_{top}(\mathbf{r})$ is therefore normalised which allows us to define the centre of the Skyrmion as the centre of the topological charge

$$\mathbf{R} \equiv \int d^2\mathbf{r} \rho_{top}(\mathbf{r}) \mathbf{r} \quad (5.80)$$

For the case of finite temperature this method can, however, not be used directly. Thermal fluctuations in the ferromagnetic background far away from the skyrmion lead to a large noise to this quantity which diverges in the thermodynamic limit. A similar problem arises when tracking the center using the magnetization of the skyrmion.

One therefore needs a method which focuses only on the region close to the skyrmion center. To locate the skyrmion, we use the z-component of the magnetization but take into account only points where $M_z(\mathbf{r}) < -0.7$ (the magnetization of the ferromagnetic background at $T = 0$ is +1). We therefore use

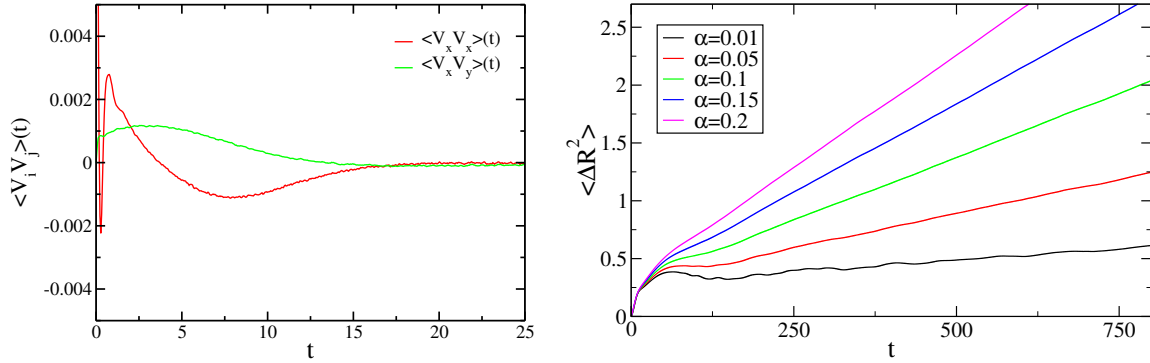
$$\rho(\mathbf{r}) = (1 - \mathbf{M}_z(\mathbf{r})) \Theta[-M_z(\mathbf{r}) - 0.7] \quad (5.81)$$

where $\Theta[x]$ is the theta function. A first estimate, $\mathbf{R}_{est} = \mathbf{R}_V$, for the radius is obtained from

$$\mathbf{R}_A = \frac{\int_A \mathbf{r} \rho(\mathbf{r}) d^2\mathbf{r}}{\int_A \rho(\mathbf{r}) d^2\mathbf{r}} \quad (5.82)$$

by integrating over the full sample volume V . \mathbf{R}_{est} is noisy due to the problems mentioned above but for the system sizes simulated one nevertheless obtains a good first estimate for the Skyrmion position. This estimate is refined by using in a second step for the integration area only $D = \{\mathbf{r} \in \mathbb{R}^2 \mid |\mathbf{r} - \mathbf{R}_{est}| < r\}$ where r is chosen to be larger than the radius of the Skyrmion core (we use $r = 1.3\sqrt{N_{<}}/\pi$, where $N_{<}$ is the number of spins with $M_z < -0.7$). Thus we obtain a reliable estimate, $\mathbf{R} = \mathbf{R}_D$, not affected by spin fluctuations far away from the Skyrmion.

From the resulting $\mathbf{R}(t)$, one can directly determine the diffusion constant of the Skyrmion. Fig. 5.9b plots the mean-squared displacement $\langle(\Delta\mathbf{R})^2\rangle_t = \langle(\mathbf{R}(t_0 + t) - \mathbf{R}(t_0))^2\rangle_t$ as a function of time t . As expected the motion of the Skyrmion is diffusive: for large times the mean-square displacement grows linearly in time $\langle(\Delta\mathbf{R})^2\rangle_t = 2Dt$ with D the diffusion constant. It is however surprising that the diffusion constant decreases with decreasing damping α . Usually one expects rate of diffusion to increase when the friction of the Skyrmion is reduced. This puzzling



(a) Time dependence of the correlation function $\langle \mathbf{V}_i(t_0+t)\mathbf{V}_j(t_0) \rangle$ for $T = 0.1$ and Gilbert damping $\alpha = 0.1$.

(b) Time dependence of the correlation function $\langle (\mathbf{R}_i(t_0+t) - \mathbf{R}_i(t_0))^2 \rangle$ for $T = 0.1$ and different values of the Gilbert damping α .

Figure 5.9

behaviour has its origin in the gyro-coupling \mathcal{G} which acts similar to a magnetic field. In the limit of system without friction the Skyrmion is completely localised on a cyclotron orbit. The diffusion constant D can be expressed as the low- ω limit of the Green's function. Upon noting that $2D = \partial_t \langle (\Delta R)^2 \rangle_t = \langle \mathbf{V} \cdot \mathbf{V} \rangle_t$. We find with Eq. 5.77 and the low- ω parametrisation of \mathbf{G} , Eq. 5.72

$$D = \lim_{\omega \rightarrow 0} k_B T \frac{\alpha \mathcal{D}(\omega)}{\mathcal{G}(\omega)^2 + \alpha^2 \mathcal{D}(\omega)^2} \quad (5.83)$$

The gyro-coupling \mathcal{G} suppresses the diffusive motion. For most materials the dissipative tensor \mathcal{D} is of the same order of magnitude as the gyro-coupling \mathcal{G} and the Skyrmion motion is characterised by both small friction and a small diffusion constant.

The trajectories $\mathbf{R}(t)$ extracted from the simulation data can be used to calculate the velocity-velocity correlation function $\langle \mathbf{V}_i(t_0+t)\mathbf{V}_j(t_0) \rangle$. An example is shown in Fig. 5.9a which is obtained after averaging over t_0 with $1000 < t_0 < 20000$ and 50 different noise realisations for $T = 0.1$ and $\alpha = 0.1$. This allows to analyse the dynamics on shorter time scales. Explicitly the low- ω parametrisation of the inverse Green's function in frequency space is given by

$$\mathbf{G}^{-1}(\omega) = \begin{pmatrix} \alpha \mathcal{D}(\omega) - i\omega m(\omega) & -\mathcal{G}(\omega) + i\alpha\omega\Gamma(\omega) \\ \mathcal{G}(\omega) - i\omega\alpha\Gamma(\omega) & \alpha \mathcal{D}(\omega) - i\omega m(\omega) \end{pmatrix}$$

By virtue of Eq. 5.77 the frequency dependent mass $m(\omega)$, gyro-coupling $\mathcal{G}(\omega)$, gyro-damping $\alpha\Gamma(\omega)$ and dissipation tensor $\alpha\mathcal{D}(\omega)$ can be determined from the velocity correlation function. Fig. 5.10a (black, solid line) shows these four quantities as functions of the frequency ω for $T = 0.05$ but the dependence on both temperature. \mathcal{G} and m are approximately independent of α , while the friction coefficients $\alpha\mathcal{D}$ and $\alpha\Gamma$ are linear in α . The gyro-coupling \mathcal{G} approaches in the limit $\mathcal{G}(\omega \rightarrow 0) = -4\pi$ for $T \rightarrow 0$ as it should due to the topology of the Skyrmion. The dynamics of the Skyrmion can be seen to have a strong frequency dependence. A characteristic frequency seems to

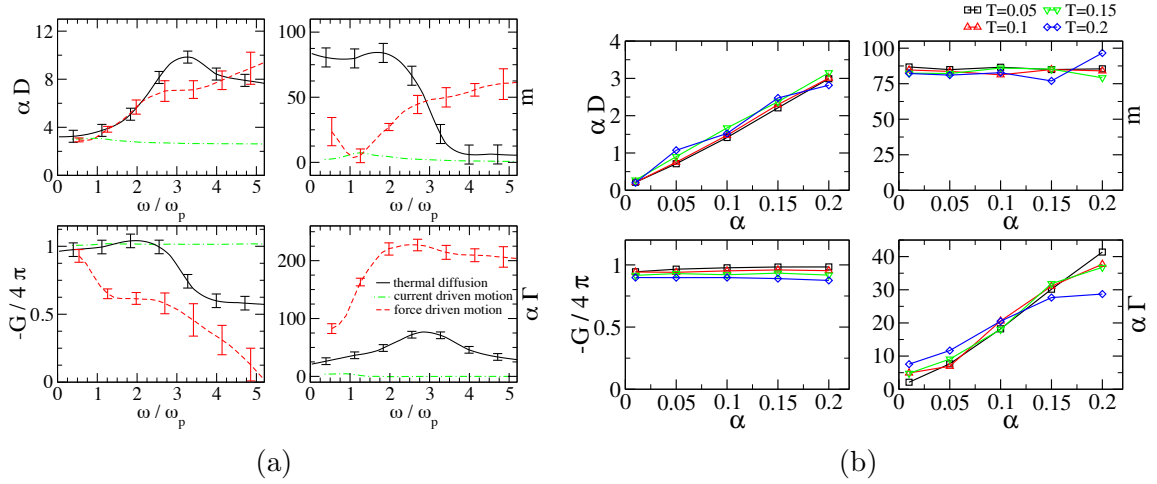


Figure 5.10: (a) Dissipative tensor $\alpha \mathcal{D}$, mass m , gyrocoupling \mathcal{G} and gyrodamping $\alpha \Gamma$ as functions of the frequency ω for the diffusive motion at $T = 0.05$ (solid black). The red and green curve show the ‘apparent’ coefficient for current- and force-driven motion. The error bars reflect estimates of systematic errors arising mainly from discretisation effects. (b) Dissipative strength $\alpha \mathcal{D}$, mass m , gyrocoupling \mathcal{G} and gyrodamping $\alpha \Gamma$ as functions of the Gilbert damping α for different temperatures T .

be $\omega_c \approx 0.1$ where the gyro-coupling \mathcal{G} abruptly drops by a factor of approximately a half and the mass m practically vanishes. A strong frequency dependence arises when internal modes of the Skyrmion are excited however this does not seem to be the case here. The upper edges of the spin wave gap lies at $\omega_p = B = 0.0278$ and therefore $\omega = 0.1$ lies about 3 times higher in energy than any possible internal mode. However we have seen in the last section that processes involving the emission of multiple magnons are of great importance for the mass generation. We therefore conjecture that such a process is responsible for the appearance of the characteristic frequency.

Both the gyro-damping Γ and the effective mass m have large numerical values. A simple scaling analysis of the Landau-Lifshitz-Gilbert equation reveals the origin. We investigate a scaling transformation, where the radius of the skyrmion is enlarged by a factor η , $\mathbf{M}(\mathbf{r}) \rightarrow \tilde{\mathbf{M}}(\mathbf{r}) = \mathbf{M}(\mathbf{r}/\eta)$. The Landau-Lifshitz-Gilbert equation is given by

$$H[\mathbf{M}] = \int d^2\mathbf{r} \left[\frac{J}{2} (\nabla \mathbf{M})^2 + \lambda \mathbf{M} \cdot \nabla \times \mathbf{M} - \mathbf{B} \cdot \mathbf{M} \right].$$

The three terms scale with η^0 , η and η^2 , respectively. To obtain a larger skyrmion, we therefore have to rescale $\lambda \rightarrow \lambda/\eta$ and $\mathbf{B} \rightarrow \mathbf{B}/\eta^2$. This implies that the \mathbf{B}_{eff} term in the sLLG equation scales with $1/\eta^2$ and therefore also the time axis has to be rescaled, $t \rightarrow \eta^2 t$, implying that all time scales are a factor of η^2 longer and all frequencies a factor $1/\eta^2$ smaller. The temperature remains unscaled. This implies that when $\mathbf{M}(\mathbf{r}, t)$ is a solution for a given value of λ , and \mathbf{B} and $\mathbf{G}(\omega)$ the corresponding velocity-correlation function of the skyrmion, then $\mathbf{M}(\mathbf{r}/\eta, t/\eta^2)$ is a solution for λ/η , \mathbf{B}/η^2 with correlation function $\mathbf{G}(\omega \eta^2)$. Accordingly, the $\omega \rightarrow 0$ limit and therefore the

gyrocoupling \mathcal{G} , the friction constant $\alpha\mathcal{D}$ and the diffusion constant of the skyrmion are independent of η , consistent with the analytical formulas, Eq. (5.74). In contrast, the mass of the skyrmion, m , and the gyrodamping $\alpha\Gamma$ scale with η^2 . They are therefore proportional to the number of spins constituting the skyrmion consistent with our numerical findings. For the chosen parameters we find $m \approx 0.3N_{\text{flip}}m_0$ and $\alpha\Gamma \approx \alpha 0.7N_{\text{flip}}m_0$, where $m_0 = \frac{\hbar^2}{Ja^2}$ is the mass of a single spin-flip in a ferromagnet which is 1 in our units. For realistic system parameters of $J = 1$ meV, $a = 5\text{\AA}$ and a Skyrmion radius of 200\AA , one finds a typical mass scale of 10^{-25} kg. The observation that the dissipative tensor $\alpha\mathcal{D}$ is independent of the size of the Skyrmion is counter-intuitive, but can be understood by recalling that a larger Skyrmion has a smoother magnetic configuration, which leads to less efficient damping.

In order to understand how lattice discretisation effects affect the numerical simulations, we have tested numerically the scaling properties for different skyrmion sizes and find that all features are quantitatively reproduced. Small variations on the level of a few percent do, however, occur reflecting the typical size of features arising from the discretisation of the continuum theory. A conservative estimate of such systematic discretisation effects for the diffusive motion is given by the error bars in Fig. 5.10a (all statistical errors are smaller than the thickness of the line).

Fig. 5.10a reveals that the sign of the gyro-damping constant $\alpha\Gamma$ is always opposite to that of the gyro-coupling \mathcal{G} . This shows that $\alpha\Gamma$ describes *anti*-damping: there is less friction for cyclotronic motion than for linear motion. If the frequency dependence in Eq. 5.84 is ignored, one finds that the poles of the Green's function are given by

$$\omega = \frac{1}{m^2 + \Gamma^2} \left[\pm (\mathcal{D}\Gamma - \mathcal{G}m) \mp i(\mathcal{D}m + \mathcal{G}\Gamma) \right] \quad (5.84)$$

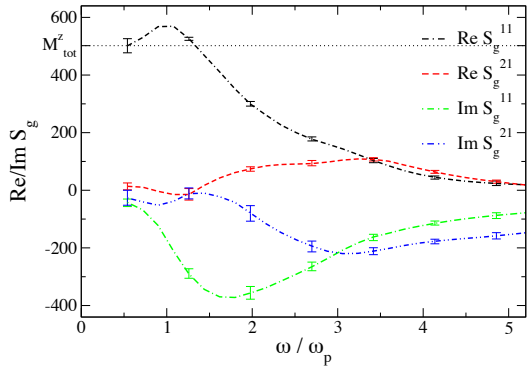
In the small- ω limit, the numerical value for Γ is so large that indeed $\mathcal{D}m + \Gamma\mathcal{G} < 0$. This signifies that it is invalid to ignore the ω -dependence as this would wrongly predict that some oscillations of the Skyrmion are not damped, but grow exponentially in time due to the strong antidamping. The correct way to test the stability of the system is to calculate the extractable power from the system for different driving frequencies. One finds that that no driving frequency exists at which power can be extracted from the system.

5.2.2 Dynamics of a driven Skyrmion

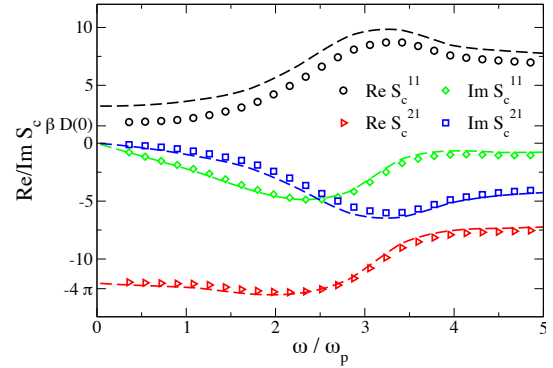
For possible applications of Skyrmions in spintronics fast manipulations of the magnetic texture are key to responsive devices. First we study the effects of an oscillating magnetic field gradient $\nabla B_z(t)$ in the absence of thermal fluctuations. The Skyrmion's large magnetic moment M_{tot}^z relative to the ferromagnetic background couples to the field gradient and leads to a force acting on the Skyrmion. In the static limit the force is exactly given by

$$\lim_{\omega \rightarrow 0} \mathbf{F}_g(\omega) = M_{\text{tot}}^z \nabla B_z \quad (5.85)$$

Using $\mathbf{G}^{-1}(\omega)$ from the analysis of the diffusive motion, the left hand side of Eq. 5.75 is known and we can determine the frequency dependence of the effective force $\mathbf{S}_g(\omega)\nabla B_z(\omega)$. For this we add to the constant magnetic field $B_z^{(0)} = 0.0278J$ a



(a) Dynamical coupling coefficients for the force driven motion ($\alpha = 0.2$, $\partial_x \mathbf{B}_z = 2.5 \times 10^{-4} J/a$). In the static limit everything but the real part of the diagonal vanishes. $\text{Re } S_g^{11}(\omega)$ however approaches the total magnetization M_{tot}^z as expected. The error bars reflect estimates of systematic errors.



(b) Dynamical coupling coefficients (symbols) for the current-driven motion ($\alpha = 0.2$, $\beta = 0.1$). These curves follow almost the corresponding matrix elements of $\mathbf{G}^{-1}(\omega)$ shown as dashed lines. A deviation of symbols and dashed line is only sizable for $\text{Re } S_c^{11}$.

time dependent component of the form $b_g(x - x_0) \sin(\omega t)$ with x_0 the x component of the initial Skyrmion position and determine the resulting Skyrmion trajectory by numerical integration of the LLG. For our simulations we choose a weak gradient with $b_g = 2.5 \times 10^{-4} J/a$. Fig. 5.11a shows the real and imaginary parts of the symmetric coupling matrix \mathbf{S}_g as a function of the driving frequency ω . For $\omega \rightarrow 0$ one obtains the expected result $\lim_{\omega \rightarrow 0} S_g^{ij}(\omega) = \delta_{ij} M_{\text{tot}}^z$. Above the magnon gap ($\omega > \omega_p \approx B_z^{(0)}$, the precession frequency of spins in the external field) a strong frequency dependence sets in. For the velocity response of the Skyrmion both the internal dynamics, $\mathbf{G}(\omega)$, and the screening of the force, $\mathbf{S}_g(\omega)$, are equally important, $\mathbf{V}(\omega) = \mathbf{G}(\omega) \mathbf{S}_g(\omega) \nabla B_z(\omega)$. This means that the determination of the coefficients describing the internal dynamics such as the mass of the Skyrmion cannot be extracted from a measurement of the response to a driving field alone. For a more intuitive understanding of the motion caused by the application of the field gradient it is instructive to calculate the ‘apparent’ dynamics. Here the frequency dependence of both the internal dynamics and the screening of the forces is described by a single matrix $\mathbf{G}_g^{-1}(\omega)$ by $\mathbf{G}_g(\omega) \mathbf{S}_g(\omega = 0) = \mathbf{G}(\omega) \mathbf{S}_g(\omega)$. The matrix elements of $\mathbf{G}_g^{-1}(\omega)$ are shown in Fig. 5.10a as red, dashed lines. The apparent mass of the Skyrmion in the small- ω limit, for example, turns out to be more than three times smaller than the value obtained from the diffusive motion. The importance of screening effects is even more impressive when Skyrmions are driven by electric currents.

For the field-driven motion spatial discretisation effects lead to a different source of errors. For very small field gradients and high frequencies the displacement of the skyrmion is much smaller than the lattice spacing and the response is affected by a tiny pinning of the skyrmion to the discrete lattice. For larger gradients, however, nonlinear effects set in and for small frequencies the skyrmion starts to approach the edge of the simulated area. In Fig. 5.11a, we therefore used for the force-driven

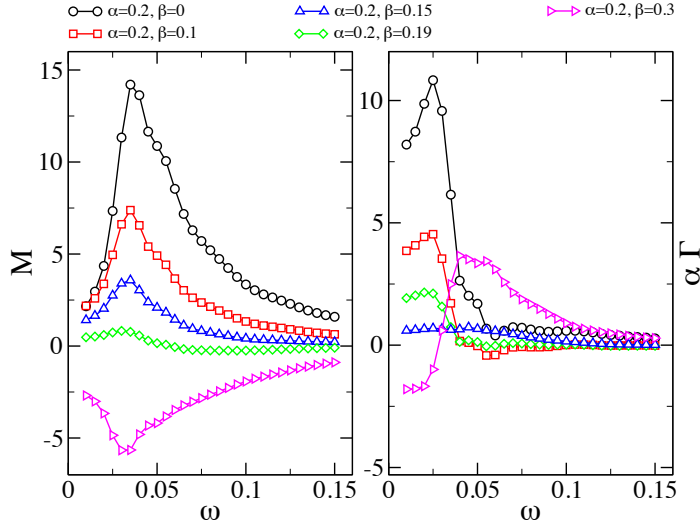


Figure 5.12: Mass $m(\omega)$ and gyrodamping $\alpha \Gamma(\omega)$ as functions of the driving frequency ω for the current-driven motion. Notice that both M and Γ vanish for $\alpha = \beta$.

motion $\nabla B = 0.0005$ for $\omega < 2\omega_P$ and $\nabla B = 0.0015$ for $\omega > 2\omega_P$. Error bars have been estimated from variations of the numerical values when ∇B was varied from 0.0001 to 0.0015.

Currents couple to the magnetic configuration both via adiabatic and non-adiabatic spin torques (c.f. Ref. [100]). Even in the static limit two types of forces on the spin texture are obtained. From the Thiele approach one finds

$$\mathbf{F}_c(\omega \rightarrow 0) = \mathcal{G} \times \mathbf{v}_s + \beta \mathcal{D} \mathbf{v}_s, \quad (5.86)$$

where the first terms due to adiabatic transfer torques and the dimensionless term β parametrises the dissipative spin-transfer torque. As shown in section 3.2.2 the case of a Galilei-invariant system is special and here one obtains $\alpha = \beta$. In this limit a solution of the LLG is obtained in the presence of a time-dependent current $\mathbf{v}_s(t)$ by $\mathbf{M}_0(\mathbf{r} - \int_{-\infty}^t \mathbf{v}_s(t') dt')$ where $\mathbf{M}_0(\mathbf{r})$ is a solution of the LLG for $\mathbf{v}_s = 0$. The Skrymion follows exactly the external current $\mathbf{V}(t) = \mathbf{v}_s(t)$. The coupling matrix $\mathbf{S}_c(\omega)$ in Eq. 5.75 is therefore simply given by the inverse of the Green's function, $\mathbf{S}_c(\omega) = \mathbf{G}^{-1}(\omega)$. The apparent dynamics, $\mathbf{G}_c(\omega) \mathbf{S}_c(\omega = 0) = \mathbf{G}(\omega) \mathbf{S}_c(\omega)$, therefore become frequency-independent $\mathbf{G}_c^{-1}(\omega) = \mathbf{S}_c(\omega = 0) = \beta \mathcal{D} \mathbf{1} - i \sigma_y \mathcal{G}$ with the mass and the gyro-damping exactly zero. For the current-driven motion errors determined by a scaling analysis are so tiny that they are not shown in Fig. 5.11b.

Even for $\alpha \neq \beta$ the above statements hold (approximately) true. The dot-dashed, green line in Fig. 5.10a shows both a very small apparent mass m_c and gyrodamping Γ_c . The gyro-coupling \mathcal{G} and dissipative tensor \mathcal{D} are to a good approximation given by their static values. Fig. 5.11b compares the inverse of the Green's function \mathbf{G}^{-1} to the coupling matrix $\mathbf{S}_c(\omega)$. The only sizeable deviation is observed for $\text{Re } S_c^{11}(\omega)$ for which the Thiele equation predicts $\text{Re } S_c^{11}(\omega \rightarrow 0) \rightarrow \beta \mathcal{D}$ and $\text{Re } \mathbf{G}_{11}^{-1}(\omega \rightarrow 0) \rightarrow \alpha \mathcal{D}$ in agreement with our numerical result. As the the apparent mass m_c and the gyrodamping Γ_c vanish in the case $\alpha = \beta$, one can expect that they are

proportional to $\alpha - \beta$, at least for small differences. Indeed this is the case as can be seen from Fig. 5.12. Here the frequency-dependence of m_c and Γ_c are shown for different combinations of α and β . For $\beta > \alpha$ even negative values of the mass can be obtained (without violation of causality³). Compared to the force-driven motion or the intrinsic dynamics the numerical values are comparatively small. This shows that retardation effects remain tiny when Skyrmions are controlled by electric currents.

5.3 Conclusion

Here we have shown that single Skyrmions embedded into ferromagnetic backgrounds in chiral magnets are characterised by a number of unique dynamical properties which are not easily found in other systems. Due to the smoothness of their texture their damping is small despite the fact that they are large composite objects. Despite the small damping their topological nature ensures an efficient suppression of the thermal diffusion by the cyclotron motion and their diffusion constant remains small. This indicates that the skyrmion position is stable, an important property for possible future applications in information storage devices. We also determined the response of Skyrmions to time-dependent external fields. We found that the frequency dependence of the effective dynamical parameters (gyro-coupling, diffusion tensor, gyro-damping and mass) is just as important as that of the screening mechanisms which determine the coupling to the driving field. Here we found that the Skyrmion's motion responds to the time-dependent current without delay or retardation even if the frequency is high. These findings demonstrate the advantages of skyrmions as information carriers.

It is interesting to compare the findings from the analytical treatment outlined in section 5.1 with those found using the numerical integration of the LLG as outlined in section 5.2. First of all it should be noted that both approaches predict a strong frequency dependence of the effective skyrmion mass with a pronounced threshold behaviour around a frequency about two times the magnon gap: for larger frequencies the mass strongly collapses. At the magnon gap neither quantities in the analytical nor the numerical treatment show any signature which highlights the fact that single magnon emission/absorption is not an important process in strong contrast to pair emission/absorption. A quantitative comparison of the two approaches however shows large differences. Not only is the numerical value completely different but also the predicted scaling behaviour with the skyrmion radius is different (the numerical treatment suggested a linear scaling with the area of the skyrmion, while section 5.1 suggests a mass that is independent of the skyrmion radius). First, the results of the analytical study are, at best, preliminary as the truncation of the m quantum number (due to numerical problems) is an approximation which cannot be justified. It should also be noted here that the parameter regimes of these two studies are very different from one another. While section 5.1 studied the quantum mass at $T = 0$, the temperature in section 5.2 is much larger than the magnon gap $T \gg \Delta$, which leads

³The important question when judging whether causality is violated or not is whether modes exists which allow to extract a positive amount of energy from the system. We have explicitly checked this and found that for no driving frequency the system becomes unstable in this sense.

to a situation where the skyrmion is surrounded by a bath of thermally activated magnons. The different suggested scaling behaviour of the mass with the skyrmion radius may therefore be attributed to a temperature effect, but further studies are necessary in order to clarify the situation.

Bibliography

- [1] Mario Norberto Baibich, JM Broto, Albert Fert, F Nguyen Van Dau, F Petroff, P Etienne, G Creuzet, A Friederich, and J Chazelas. Giant magnetoresistance of (001) fe/(001) cr magnetic superlattices. *Physical Review Letters*, 61(21):2472, 1988.
- [2] Per Bak and M Høgh Jensen. Theory of helical magnetic structures and phase transitions in mnsi and fege. *Journal of Physics C: Solid State Physics*, 13(31):L881, 1980.
- [3] SE Barrett, G Dabbagh, LN Pfeiffer, KW West, and R Tycko. Optically pumped nmr evidence for finite-size skyrmions in gaas quantum wells near landau level filling $\nu=1$. *Physical review letters*, 74(25):5112, 1995.
- [4] RA Battye, NS Manton, and PM Sutcliffe. Skyrmions and nuclei. *The Multifaceted Skyrmion*, page 1, 2010.
- [5] J Beille, J Voiron, and M Roth. Long period helimagnetism in the cubic b20 $\text{fe}_x\text{co}_{1-x}\text{si}$ and $\text{co}_x\text{mn}_{1-x}\text{si}$ alloys. *Solid state communications*, 47(5):399–402, 1983.
- [6] L Berger. Exchange interaction between ferromagnetic domain wall and electric current in very thin metallic films. *Journal of Applied Physics*, 55(6):1954–1956, 1984.
- [7] L Berger. Emission of spin waves by a magnetic multilayer traversed by a current. *Physical Review B*, 54(13):9353, 1996.
- [8] Grünberg Binasch, Peter Grünberg, F Saurenbach, and W Zinn. Enhanced magnetoresistance in layered magnetic structures with antiferromagnetic inter-layer exchange. *Physical review B*, 39:4828–4830, 1989.
- [9] A Bogdanov and A Hubert. Thermodynamically stable magnetic vortex states in magnetic crystals. *Journal of magnetism and magnetic materials*, 138(3):255–269, 1994.
- [10] AN Bogdanov and DA Yablonskii. Thermodynamically stable” vortices” in magnetically ordered crystals. the mixed state of magnets. *Zh. Eksp. Teor. Fiz*, 95:182, 1989.

- [11] L Brey, HA Fertig, R Côté, and AH MacDonald. Skyrme crystal in a two-dimensional electron gas. *Physical review letters*, 75(13):2562, 1995.
- [12] William Fuller Brown Jr. Thermal fluctuations of a single-domain particle. *Physical Review*, 130(5):1677, 1963.
- [13] Stefan Buhrandt and Lars Fritz. Skyrmion lattice phase in three-dimensional chiral magnets from monte carlo simulations. *Phys. Rev. B*, 88:195137, Nov 2013.
- [14] Claudio Castelnovo, Roderich Moessner, and Shivaji L Sondhi. Magnetic monopoles in spin ice. *Nature*, 451(7174):42–45, 2008.
- [15] Tapan Chatterji. *Neutron scattering from magnetic materials*. Access Online via Elsevier, 2005.
- [16] Sang-Wook Cheong and Maxim Mostovoy. Multiferroics: a magnetic twist for ferroelectricity. *Nature materials*, 6(1):13–20, 2007.
- [17] William T Coffey, Yu P Kalmykov, and John T Waldron. *The Langevin equation: with applications to stochastic problems in physics, chemistry, and electrical engineering*, volume 14. World Scientific, 2004.
- [18] Paul AM Dirac. Quantised singularities in the electromagnetic field. *Proceedings of the Royal Society of London. Series A, Containing Papers of a Mathematical and Physical Character*, 133(821):60–72, 1931.
- [19] Su Do Yi, Shigeki Onoda, Naoto Nagaosa, and Jung Hoon Han. Skyrmions and anomalous hall effect in a dzyaloshinskii-moriya spiral magnet. *Physical Review B*, 80(5):054416, 2009.
- [20] J.L. Doob. *Stochastic processes*. Wiley publications in statistics. Wiley, 1990.
- [21] RA Duine, AS Nunez, Jairo Sinova, and AH MacDonald. Functional keldysh theory of spin torques. *Physical Review B*, 75(21):214420, 2007.
- [22] I Dzyaloshinsky. A thermodynamic theory of “weak” ferromagnetism of antiferromagnetics. *Journal of Physics and Chemistry of Solids*, 4(4):241–255, 1958.
- [23] Albert Einstein. Über die von der molekularkinetischen theorie der wärme geforderte bewegung von in ruhenden flüssigkeiten suspendierten teilchen. *Annalen der physik*, 322(8):549–560, 1905.
- [24] Karin Everschor. *Current-Induced Dynamics of Chiral Magnetic Structures: Skyrmions, Emergent Electrodynamics and Spin-Transfer Torques*. PhD thesis, Universität zu Köln, 2012.

- [25] Karin Everschor, Markus Garst, Benedikt Binz, Florian Jonietz, Sebastian Mühlbauer, Christian Pfeiderer, and Achim Rosch. Rotating skyrmion lattices by spin torques and field or temperature gradients. *Physical Review B*, 86(5):054432, 2012.
- [26] Karin Everschor, Markus Garst, RA Duine, and Achim Rosch. Current-induced rotational torques in the skyrmion lattice phase of chiral magnets. *Physical Review B*, 84(6):064401, 2011.
- [27] Motohiko Ezawa. Compact merons and skyrmions in thin chiral magnetic films. *Phys. Rev. B*, 83:100408, Mar 2011.
- [28] H.A Fertig, L Brey, R Cote, and AH MacDonald. Charged spin-texture excitations and the hartree-fock approximation in the quantum hall effect. *Physical Review B*, 50(15):11018, 1994.
- [29] Kristen A Fichtorn and W Hh Weinberg. Theoretical foundations of dynamical monte carlo simulations. *The Journal of chemical physics*, 95:1090, 1991.
- [30] Martin Fink, Johannes Eiglsperger, Harald Friedrich, and Javier Madroñero. Smoothness properties of the quantum-mechanical and wkb phase shifts for two-dimensional scattering. *Physical Review A*, 80(2):24701, 2009.
- [31] Reeves Fletcher and Colin M Reeves. Function minimization by conjugate gradients. *The computer journal*, 7(2):149–154, 1964.
- [32] Reeves Fletcher and Colin M Reeves. Function minimization by conjugate gradients. *The computer journal*, 7(2):149–154, 1964.
- [33] PP Freitas and Luc Berger. Observation of s-d exchange force between domain walls and electric current in very thin permalloy films. *Journal of Applied Physics*, 57(4):1266–1269, 1985.
- [34] Jun-ichi Fukuda and Slobodan Žumer. Quasi-two-dimensional skyrmion lattices in a chiral nematic liquid crystal. *Nature communications*, 2:246, 2011.
- [35] DA Garanin. Fokker-planck and landau-lifshitz-bloch equations for classical ferromagnets. *Physical Review B*, 55(5):3050, 1997.
- [36] José Luis García-Palacios and Francisco J Lázaro. Langevin-dynamics study of the dynamical properties of small magnetic particles. *Physical Review B*, 58(22):14937, 1998.
- [37] Carl Friedrich Gauss. Nachlaß. *Blätter der DGVMF*, 8(2):263–277, 1967.
- [38] Michael Glazer, Gerald Burns, and Alexander N Glazer. *Space groups for solid state scientists*. Academic Press, 1990.
- [39] Luigi Grippo and Stefano Lucidi. A globally convergent version of the polak-ribiere conjugate gradient method. *Mathematical Programming*, 78(3):375–391, 1997.

- [40] PJ Grundy and RS Tebble. Lorentz electron microscopy. *Advances in Physics*, 17(66):153–242, 1968.
- [41] FDM Haldane. Geometrical interpretation of momentum and crystal momentum of classical and quantum ferromagnetic heisenberg chains. *Physical review letters*, 57(12):1488–1491, 1986.
- [42] U Hartmann. Magnetic force microscopy. *Annual review of materials science*, 29(1):53–87, 1999.
- [43] Mark C Hickey and Jagadeesh S Moodera. Origin of intrinsic gilbert damping. *Physical review letters*, 102(13):137601, 2009.
- [44] SX Huang and CL Chien. Extended skyrmion phase in epitaxial fege (111) thin films. *Physical Review Letters*, 108(26):267201, 2012.
- [45] Junichi Iwasaki, Masahito Mochizuki, and Naoto Nagaosa. Current-induced skyrmion dynamics in constricted geometries. *Nature nanotechnology*, 2013.
- [46] Junichi Iwasaki, Masahito Mochizuki, and Naoto Nagaosa. Universal current-velocity relation of skyrmion motion in chiral magnets. *Nature communications*, 4:1463, 2013.
- [47] Prashanth Jaikumar, Manjari Bagchi, and Rachid Ouyed. High-density skyrmion matter and neutron stars. *The Astrophysical Journal*, 678(1):360, 2008.
- [48] Marc Janoschek, Markus Garst, Andreas Bauer, Pascal Krautscheid, Robert Georgii, Peter Böni, and Christian Pfleiderer. Fluctuation-induced first-order phase transition in dzyaloshinskii-moriya helimagnets. *Physical Review B*, 87(13):134407, 2013.
- [49] F Jonietz, S Mühlbauer, C Pfleiderer, A Neubauer, W Münzer, A Bauer, T Adams, R Georgii, P Böni, RA Duine, et al. Spin transfer torques in mnsi at ultralow current densities. *Science*, 330(6011):1648–1651, 2010.
- [50] T Kimura, T Goto, H Shintani, K Ishizaka, T Arima, and Y Tokura. Magnetic control of ferroelectric polarization. *Nature*, 426(6962):55–58, 2003.
- [51] Gustav Kirchhoff. Ueber die auflösung der gleichungen, auf welche man bei der untersuchung der linearen vertheilung galvanischer ströme geführt wird. *Annalen der Physik*, 148(12):497–508, 1847.
- [52] Igor Klebanov. Nuclear matter in the skyrme model. *Nuclear Physics B*, 262(1):133–143, 1985.
- [53] Peter E Kloeden and RA Pearson. The numerical solution of stochastic differential equations. *The Journal of the Australian Mathematical Society. Series B. Applied Mathematics*, 20(01):8–12, 1977.

- [54] Michal Křížek. *Conjugate gradient algorithms and finite element methods*. Springer, 2004.
- [55] Rep Kubo. The fluctuation-dissipation theorem. *Reports on Progress in Physics*, 29(1):255, 1966.
- [56] Ryogo Kubo and Natsuki Hashitsume. Brownian motion of spins. *Progress of Theoretical Physics Supplement*, 46:210–220, 1970.
- [57] LD Landau and EM Lifshitz. Statistical physics, vol. 1. *Oxford: Pergamon*, 24:31–57, 1980.
- [58] B Lebech, J Bernhard, and T Freltoft. Magnetic structures of cubic fege studied by small-angle neutron scattering. *Journal of Physics: Condensed Matter*, 1(35):6105, 1989.
- [59] B Lebech, P Harris, J Skov Pedersen, K Mortensen, CI Gregory, NR Bernhoeft, M Jermy, and SA Brown. Magnetic phase diagram of mnsi. *Journal of magnetism and magnetic materials*, 140:119–120, 1995.
- [60] Shi-Zeng Lin, Cristian D Batista, and Avadh Saxena. Internal modes of a skyrmion in the ferromagnetic state of chiral magnets. *Physical Review B*, 89(2):024415, 2014.
- [61] Johann Benedikt Listing. *Vorstudien zur topologie*. Vandenhoeck und Ruprecht, 1848.
- [62] ME Lucassen, HJ van Driel, C Morais Smith, and RA Duine. Current-driven and field-driven domain walls at nonzero temperature. *Physical Review B*, 79(22):224411, 2009.
- [63] Y Machida, S Nakatsuji, Y Maeno, T Tayama, T Sakakibara, and S Onoda. Unconventional anomalous hall effect enhanced by a noncoplanar spin texture in the frustrated kondo lattice pr-₂ir-₂o-₇. *Physical review letters*, 98(5):057203, 2007.
- [64] AP Malozemoff and JC Slonczewski. *Magnetic domain walls in bubble materials*, volume 81. Academic Press New York, 1979.
- [65] Nicholas Manton and Paul M Sutcliffe. *Topological solitons*. Cambridge University Press, 2004.
- [66] Y Martin and H Kumar Wickramasinghe. Magnetic imaging by “force microscopy” with 1000 Å resolution. *Applied Physics Letters*, 50(20):1455–1457, 1987.
- [67] P Milde, D Köhler, J Seidel, LM Eng, A Bauer, A Chacon, J Kindervater, S Mühlbauer, C Pfeleiderer, S Buhbrandt, et al. Unwinding of a skyrmion lattice by magnetic monopoles. *Science*, 340(6136):1076–1080, 2013.

- [68] Hazime Mori. Transport, collective motion, and brownian motion. *Progress of Theoretical Physics*, 33(3):423–455, 1965.
- [69] Tôru Moriya. Anisotropic superexchange interaction and weak ferromagnetism. *Physical Review*, 120(1):91, 1960.
- [70] DJP Morris, DA Tennant, SA Grigera, B Klemke, C Castelnovo, R Moessner, C Czternasty, M Meissner, KC Rule, J-U Hoffmann, et al. Dirac strings and magnetic monopoles in the spin ice $\text{dy}_2\text{ti}_2\text{o}_7$. *Science*, 326(5951):411–414, 2009.
- [71] David D Morrison, James D Riley, and John F Zancanaro. Multiple shooting method for two-point boundary value problems. *Communications of the ACM*, 5(12):613–614, 1962.
- [72] S Mühlbauer, B Binz, F Jonietz, C Pfleiderer, A Rosch, A Neubauer, R Georgii, and P Böni. Skyrmion lattice in a chiral magnet. *Science*, 323(5916):915–919, 2009.
- [73] W Münzer, A Neubauer, S Mühlbauer, C Franz, T Adams, F Jonietz, R Georgii, P Böni, B Pedersen, M Schmidt, et al. Skyrmion lattice in a doped semiconductor. *arXiv preprint arXiv:0903.2587*, 2009.
- [74] O Nakanishi, A Yanase, A Hasegawa, and M Kataoka. The origin of the helical spin density wave in mnsi. *Solid State Communications*, 35(12):995–998, 1980.
- [75] A Neubauer, C Pfleiderer, B Binz, A Rosch, R Ritz, PG Niklowitz, and P Böni. Topological hall effect in the a phase of mnsi. *Physical review letters*, 102(18):186602, 2009.
- [76] Stuart SP Parkin, Masamitsu Hayashi, and Luc Thomas. Magnetic domain-wall racetrack memory. *Science*, 320(5873):190–194, 2008.
- [77] Linus Pauling. The structure and entropy of ice and of other crystals with some randomness of atomic arrangement. *Journal of the American Chemical Society*, 57(12):2680–2684, 1935.
- [78] Jean Perrin and Julius Donau. Die brown’sche bewegung und die wahre existenz der moleküle. *Kolloidchemische Beihefte*, 1(6-7):221–300, 1910.
- [79] C Pfleiderer, SR Julian, and GG Lonzarich. Non-fermi-liquid nature of the normal state of itinerant-electron ferromagnets. *Nature*, 414(6862):427–430, 2001.
- [80] C Pfleiderer, D Reznik, L Pintschovius, H v Löhneysen, M Garst, and A Rosch. Partial order in the non-fermi-liquid phase of mnsi. *Nature*, 427(6971):227–231, 2004.
- [81] Ch Pfleiderer, GJ McMullan, SR Julian, and GG Lonzarich. Magnetic quantum phase transition in mnsi under hydrostatic pressure. *Physical Review B*, 55(13):8330, 1997.

- [82] Christian Pfleiderer and Achim Rosch. Condensed-matter physics: Single skyrmions spotted. *Nature*, 465(7300):880–881, 2010.
- [83] ML Plumer and MB Walker. Wavevector and spin reorientation in mnsi. *Journal of Physics C: Solid State Physics*, 14(31):4689, 1981.
- [84] AP Ramirez, A Hayashi, RJ Cava, R Siddharthan, and BS Shastry. Zero-point entropy in ‘spin ice’. *Nature*, 399(6734):333–335, 1999.
- [85] R Ritz, M Halder, C Franz, A Bauer, M Wagner, R Bamler, A Rosch, and C Pfleiderer. Giant generic topological hall resistivity of mnsi under pressure. *Physical Review B*, 87(13):134424, 2013.
- [86] Niklas Romming, Christian Hanneken, Matthias Menzel, Jessica E Bickel, Boris Wolter, Kirsten von Bergmann, André Kubetzka, and Roland Wiesendanger. Writing and deleting single magnetic skyrmions. *Science*, 341(6146):636–639, 2013.
- [87] D Rugar, HJ Mamin, P Guethner, SE Lambert, JE Stern, I McFadyen, and T Yogi. Magnetic force microscopy: General principles and application to longitudinal recording media. *Journal of Applied Physics*, 68(3):1169–1183, 1990.
- [88] T Schulz, R Ritz, A Bauer, M Halder, M Wagner, C Franz, C Pfleiderer, K Everschor, M Garst, and A Rosch. Emergent electrodynamics of skyrmions in a chiral magnet. *Nature Physics*, 8(4):301–304, 2012.
- [89] S Seki, S Ishiwata, and Y Tokura. Magnetoelectric nature of skyrmions in a chiral magnetic insulator Cu_2OSeO_3 . *Physical Review B*, 86(6):060403, 2012.
- [90] Shinichiro Seki, XZ Yu, S Ishiwata, and Y Tokura. Observation of skyrmions in a multiferroic material. *Science*, 336(6078):198–201, 2012.
- [91] Jonathan Richard Shewchuk. An introduction to the conjugate gradient method without the agonizing pain, 1994.
- [92] Jairo Sinova, SM Girvin, T Jungwirth, and K Moon. Skyrmion dynamics and nmr line shapes in quantum hall ferromagnets. *Physical Review B*, 61(4):2749, 2000.
- [93] Tony Hilton Royle Skyrme. A non-linear field theory. *Proceedings of the Royal Society of London. Series A. Mathematical and Physical Sciences*, 260(1300):127–138, 1961.
- [94] John C Slonczewski. Current-driven excitation of magnetic multilayers. *Journal of Magnetism and Magnetic Materials*, 159(1):L1–L7, 1996.
- [95] M von Smoluchowski. Drei vortrage uber diffusion, brownsche bewegung und koagulation von kolloidteilchen. *Zeitschrift fur Physik*, 17:557–585, 1916.

- [96] R Sollacher. Collective coordinate quantization. Technical report, CM-P00070203, 1993.
- [97] SL Sondhi, A Karlhede, SA Kivelson, and EH Rezayi. Skyrmions and the crossover from the integer to fractional quantum hall effect at small zeeman energies. *Physical Review B*, 47(24):16419, 1993.
- [98] Y Taguchi, Y Oohara, H Yoshizawa, N Nagaosa, and Y Tokura. Spin chirality, berry phase, and anomalous hall effect in a frustrated ferromagnet. *Science*, 291(5513):2573–2576, 2001.
- [99] Rina Takashima and Satoshi Fujimoto. Electrodynamics in skyrmions merging. *arXiv preprint arXiv:1401.7140*, 2014.
- [100] Gen Tatara, Hiroshi Kohno, and Junya Shibata. Microscopic approach to current-driven domain wall dynamics. *Physics Reports*, 468(6):213–301, 2008.
- [101] C Thessieu, C Pfleiderer, AN Stepanov, and J Flouquet. Field dependence of the magnetic quantum phase transition in mnsi. *Journal of Physics: Condensed Matter*, 9(31):6677, 1997.
- [102] AA Thiele. Steady-state motion of magnetic domains. *Physical Review Letters*, 30(6):230, 1973.
- [103] M Uchida, N Nagaosa, JP He, Y Kaneko, S Iguchi, Y Matsui, and Y Tokura. Topological spin textures in the helimagnet fege. *Physical Review B*, 77(18):184402, 2008.
- [104] Masaya Uchida, Yoshinori Onose, Yoshio Matsui, and Yoshinori Tokura. Real-space observation of helical spin order. *Science*, 311(5759):359–361, 2006.
- [105] Nicolaas Godfried Van Kampen. *Stochastic processes in physics and chemistry*, volume 1. Access Online via Elsevier, 1992.
- [106] Allan Van Oosterom and J Strackee. The solid angle of a plane triangle. *Biomedical Engineering, IEEE Transactions on*, (2):125–126, 1983.
- [107] GE Volovik. Linear momentum in ferromagnets. *Journal of Physics C: Solid State Physics*, 20(7):L83, 1987.
- [108] TS Walhout. Dense matter in the skyrme model. *Nuclear Physics A*, 484(3):397–418, 1988.
- [109] Heribert Wilhelm, Michael Baenitz, Marcus Schmidt, UK Rößler, AA Leonov, and AN Bogdanov. Precursor phenomena at the magnetic ordering of the cubic helimagnet fege. *Physical review letters*, 107(12):127203, 2011.
- [110] David C Wright and N David Mermin. Crystalline liquids: the blue phases. *Reviews of Modern physics*, 61(2):385, 1989.

- [111] Jiang Xiao, Andrew Zangwill, and MD Stiles. Spin-transfer torque for continuously variable magnetization. *Physical Review B*, 73(5):054428, 2006.
- [112] Xiuzhen Yu, Maxim Mostovoy, Yusuke Tokunaga, Weizhu Zhang, Koji Kimoto, Yoshio Matsui, Yoshio Kaneko, Naoto Nagaosa, and Yoshinori Tokura. Magnetic stripes and skyrmions with helicity reversals. *Proceedings of the National Academy of Sciences*, 109(23):8856–8860, 2012.
- [113] XZ Yu, N Kanazawa, Y Onose, K Kimoto, WZ Zhang, S Ishiwata, Y Matsui, and Y Tokura. Near room-temperature formation of a skyrmion crystal in thin-films of the helimagnet fege. *Nature materials*, 10(2):106–109, 2010.
- [114] XZ Yu, Y Onose, N Kanazawa, JH Park, JH Han, Y Matsui, N Nagaosa, and Y Tokura. Real-space observation of a two-dimensional skyrmion crystal. *Nature*, 465(7300):901–904, 2010.
- [115] S Zhang and Z Li. Roles of nonequilibrium conduction electrons on the magnetization dynamics of ferromagnets. *Physical Review Letters*, 93(12):127204, 2004.
- [116] Robert Zwanzig. Nonlinear generalized langevin equations. *Journal of Statistical Physics*, 9(3):215–220, 1973.

Appendix A

Materials

The symmetry transformations for materials that crystallize in the B20 structure are described by the space group $P2_13$ with a cubic Bravais lattice [38]. With only 12 symmetry operations this space group is among the smallest compatible with the cubic lattice crystal system. The point symmetry at the component sites is C_3 , the cyclic group of 3-fold $2\pi/3$ rotations about an appropriate [111] axis. The nonsymmorphic group $P2_13$ contains in addition 3 screw rotations which involve 2-fold rotations about one of the three [100] axis followed by an appropriate non-primitive translation $(0, \frac{1}{2}, \frac{1}{2})$.

Among these MnSi became the first chiral magnet in 2009 where a lattice of chiral skyrmions was observed by neutron scattering [72]. The series of isostructural B20 transition metal silicides TSi shows great variability in their electronic properties and was therefore ideally suited to study whether skyrmion lattices appear generically in magnets without inversion symmetry. Indeed in 2010 the same group discovered a Skyrmion lattice phase in the doped semiconductor $Fe_{1-x}Co_xSi$ [73, 114]. The Skyrmion lattice phase in this material was also later confirmed by real-space images using Lorentz transmission electron microscopy (Lorentz TEM) [114]. Since then the Skyrmion lattice has been observed in a variety of different materials both as a bulk phase as well as in thin films. In this chapter we give an overview of the variability among the materials exhibiting the Skyrmion phase and give brief descriptions of four exemplary materials: MnSi (2009, Ref. [72]), $Fe_{1-x}Co_xSi$ (2010, Refs. [73, 114]), FeGe (2010, Ref. [113]) and Cu_2OSeO_3 (2012, Ref. [90]).

A.1 Iron-Cobalt-Silicide - $Fe_{1-x}Co_xSi$

In 2010 Müenzer et al. [73] investigated the magnetic phase diagram of the series $Fe_{1-x}Co_xSi$ using small angle neutron scattering. The question at hand was whether the appearance of a Skyrmion lattice in the metal MnSi was just a peculiarity of this particular material or whether one example of more general phenomenon was found as suggested by the theoretical treatment in Ref. [72]. The electronic properties of FeSi and CoSi are very different from those of MnSi. FeSi is a nonmagnetic insulator while CoSi is a diamagnetic metal. The $Fe_{1-x}Co_xSi$ series displays an insulator to metal transition upon the increase of the copper concentration above a critical $x = 0.02$.

Previously it had been confirmed [5] to display helimagnetic order in the interval $0.05 \leq x \leq 0.07$. The copper concentration also tunes the helical modulation length from about 200 \AA to 2000 \AA [5]. In contrast to MnSi where the crystal structure and the DM interaction have the same chirality, they are opposite in $\text{Fe}_{1-x}\text{Co}_x\text{Si}$.

Similar to MnSi the magnetic phase diagram exhibits three prominent phases: A state with helimagnetic modulation is found up to a critical B -field of B_{c_1} with propagation vector parallel to the [100] for all x . For magnetic fields in the range $B_{c_1} < B < B_{c_2}$ the helical modulation points parallel to the applied field and the system shows a uniform magnetization component in the direction of \mathbf{B} , i.e. conical order. Third, there is a small phase pocket close to T_C where the modulation direction points parallel to the applied field and the system orders in a hexagonal lattice of skyrmions. As opposed to MnSi, the magnetic phase diagram yields strong hysteric features. Depending on the cooling protocol used a (metastable) skyrmion lattice phase may be observed over a large temperature range.

Fig. A.1 shows the magnetic phase diagram for $x = 0.2$ as measured by small angle neutron scattering. Panels (A)-(C) show the magnetic phase diagram after zero field cooling (ZFC). Helimagnetic order appears below the critical temperature, $T_c \sim 30 \text{ K}$, with a modulation vector parallel to [100]. All three phases are found and the skyrmion lattice exists only in a small pocket below T_c . Well below T_c , the helimagnetic order undergoes a spin-flop transition to conical order. Panels (D)-(F) were recorded under field cooling (FC). For field values outside the range of the skyrmion lattice, there is only a paramagnetic to conical transition. The skyrmion lattice phase (in panels (E) and (F)) can be observed as a metastable state down to the smallest observed temperature. The reversible phase boundaries near T_c are found to be same as those under ZFC. For temperatures well below T_c they become irreversible. It is exactly this feature which makes it possible to observe the destruction of the skyrmion lattice using magnetic force microscopy (MFM) as we will see in chapter 4.

In Ref. [114] it was shown that in thin plates of $\text{Fe}_{1-x}\text{Co}_x\text{Si}$ (thickness less than the helical period) with the magnetic field applied perpendicular the competing conical phase is forbidden and hence the skyrmion lattice stabilizes over a wider range of the magnetic phase diagram.

A.2 Iron-Germanium - FeGe

Already in 1980 Bak and Jensen [2] noted that the helimagnetic order in non-inversion symmetric FeGe is the result of an instability in the ferromagnetic state due to the presence of DM interactions. As well as MnSi, FeGe is a helimagnet which crystallizes in the tetrahedral P2_13 structure. What sets it apart from MnSi is its extremely high helical transition temperature of 280K. Small angle neutron scattering revealed that the direction of helical q -vector depends on the temperature T : below 280 K it points along the [001] direction and changes to [111] as the temperature is lowered [58]. The flexibility of the q -vector was interpreted as a small magnetic anisotropy and therefore conjectured to be a possible candidate for magnetic phases with interesting topologies. Indeed first Lorentz electron transmission microscopy studies [103] on thin plates of

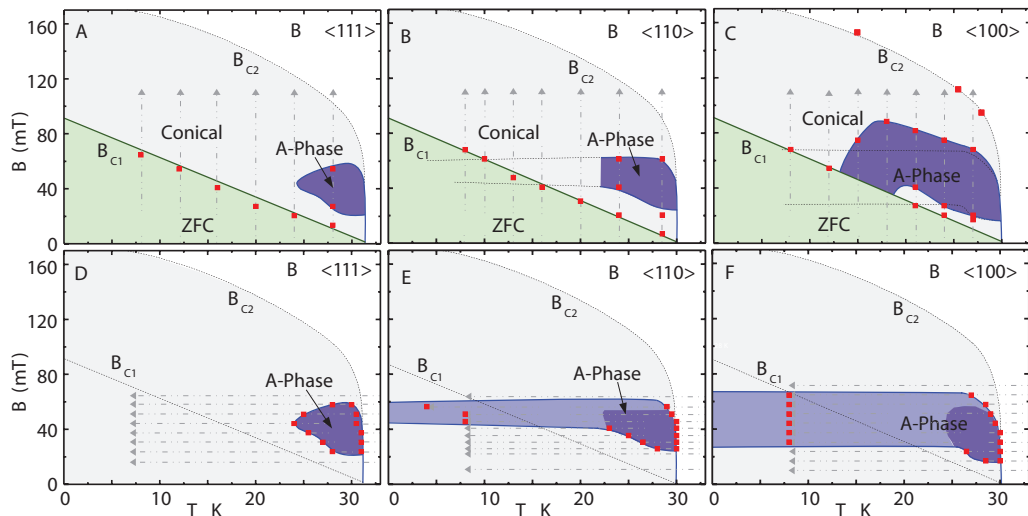
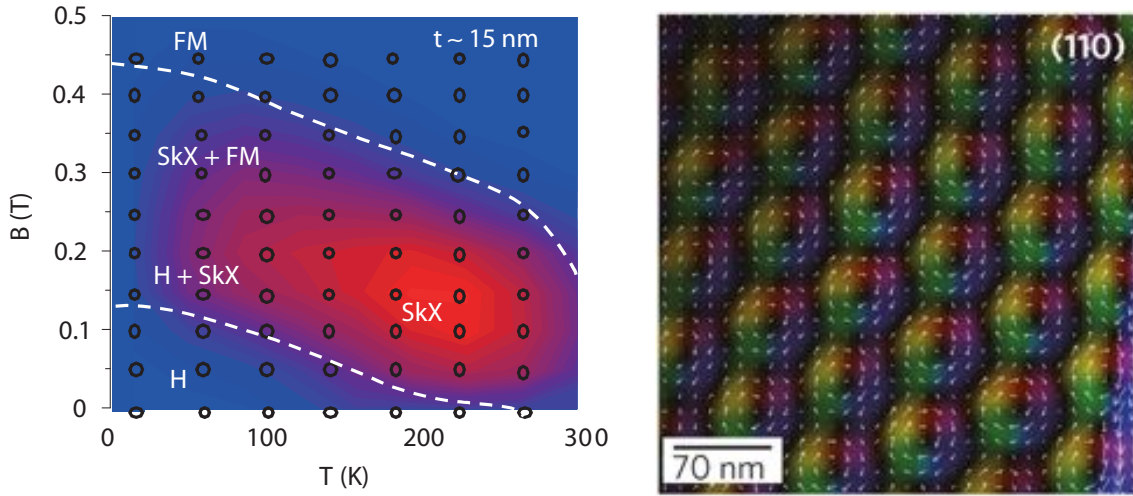


Figure A.1: Magnetic phase diagram for $\text{Fe}_{1-x}\text{Co}_x\text{Si}$ for $x = 0.2$. Panels (A)-(C) show the phase diagram under ZFC. Helimagnetic order appears below the critical temperature, $T_c \sim 30$ K. Panels (D)-(F) were recorded under field cooling (FC). For field values outside the range of the skyrmion lattice, there is only a paramagnetic to conical transition. The skyrmion lattice phase (in panels (E) and (F)) can be observed as a metastable state down to the smallest observed temperature. Image taken from Ref. [73].

FeGe revealed magnetic twin domains in a single crystallographic domain, curved spin stripe and a swiss-rod like stripe vertex stabilised by Berry phases. In 2010 Yu et al. [113] confirmed by Lorentz TEM of thin films of FeGe that also a skyrmion lattice phase with a lattice parameter of $a \sim 70$ nm exists at a temperature of around 250 – 270 K. For very low temperatures (~ 60 K) skyrmions start to emerge at the edges of the sample. As the temperature is increased to 180 K the magnetic structures become a mixture of skyrmions and stripy domains, c.f. Fig. A.2a. Around 260 K the structure changes to a hexagonal skyrmion lattice, c.f. Fig. A.2b. FeGe is therefore the first material which shows this magnetic vortex phase near room-temperature. For three dimensional samples the conical spin phase with the q -vector along the field direction is generally favoured in magnetic field and similar to MnSi and $\text{Fe}_{1-x}\text{Co}_x\text{Si}$ thermal fluctuations are necessary to stabilise skyrmions and the skyrmion lattice phase is confined to rather small region in the magnetic phase diagram [109]. However unlike MnSi and $\text{Fe}_{1-x}\text{Co}_x\text{Si}$ for which large single crystals exist, only mm-size FeGe crystals can be fabricated, which impedes the study of FeGe despite its favourable attributes. Recently the successful realisation of epitaxial thin films of FeGe has been reported [44].

A.3 Multiferroic Cu_2OSeO_3

Helical spin textures have been found to affect the symmetry of the charge distribution and magnetically induce electric polarization in compounds such as TbMnO_3 [50, 16].



(a) Magnetic phase diagram for a thin plate (15 nm) of FeGe observed by Lorentz TEM. H, SkX, and FM stand for the helical, Skyrmion lattice and ferromagnetic phase. Taken from Ref. [113].

(b) Lateral magnetisation distribution in the SkX phase induced by a magnetic field of 1 T. Taken from Ref. [113].

However Cu_2OSeO_3 is the first multiferroic material which has been demonstrated to possess a skyrmion lattice which induces electric polarization. Such coupling between ferroelectricity and magnetic structure enables versatile magnetoelectric responses, e.g. electric field control of spin chirality. From the perspective of applications in spintronic devices the electric field control of Skyrmions is particularly desirable as the energy dissipation due to the application of an electric field \mathbf{E} to an insulating material is negligible and promises more energy efficient manipulation without the side effects of Joule heating found in the current-driven dynamics.

The space group of Cu_2OSeO_3 is $P2_13$ - the same as the other $B20$ alloys - however the atom coordination differs significantly, c.f. Fig. A.3a. The copper sites (spin $S=\frac{1}{2}$) are surrounded by either a square pyramid of oxygen atoms (green) or a trigonal bipyramid (blue) with a ratio of 3:1 rendering the two sites inequivalent. The spins on the two inequivalent copper sites align antiparallel in the magnetic ground state below $T_c \sim 57$ K. Ref. [90] reports a Lorentz transmission electron microscopy study of thin films of about 100 nm thickness. Similar to the other materials, in the absence of a magnetic field the compound orders below 57 K helimagnetically in a stripy pattern with helical modulation period of ~ 50 nm. The bulk form of Cu_2OSeO_3 shows a Skyrmion lattice phase in a small phase pocket near T_c . In the thin-film form this phase is found in a large region of the phase diagram for finite magnetic fields down to $T = 0$.

The dielectric properties of bulk Cu_2OSeO_3 were investigated in Ref. [89] and it was found that it hosts magnetically induced polarisation in ferrimagnetic, helimagnetic and Skyrmion lattice phase. Fig. A.3 indicates the local electric polarisation (top row) and charge distribution (bottom row) for various magnetic field directions. For $\mathbf{H} \parallel [001]$ the Skyrmion can be seen to carry an electric quadrupole moment,

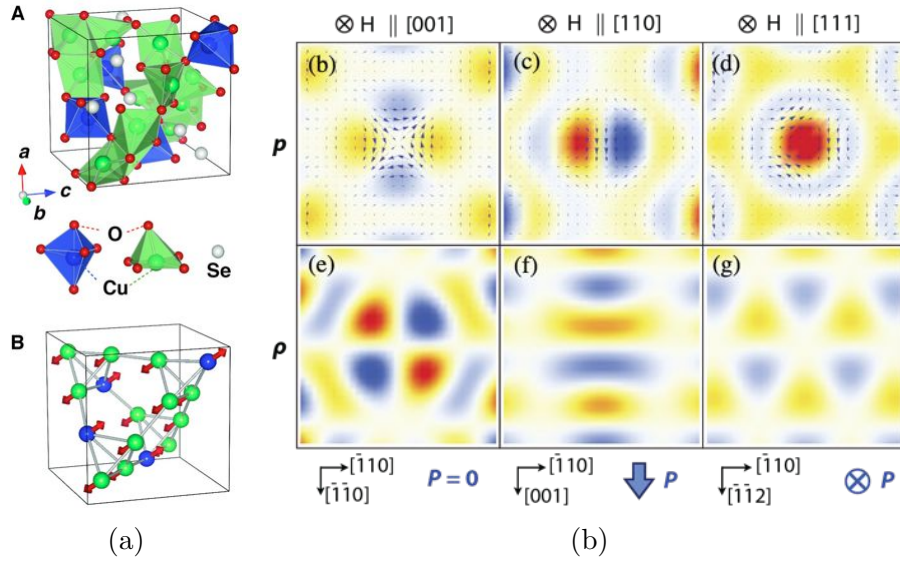


Figure A.3: (a) Crystal structure of Cu_2OSeO_3 . The two inequivalent Cu^{2+} are characterised by different oxygen configurations. Taken from Ref. [90]. (b) Local electric polarisation vector \mathbf{p} (top row) and local electric charge distribution ρ (bottom row) for the indicated directions of the applied magnetic field \mathbf{H} . Taken from Ref. [89].

while for $\mathbf{H}[110]$ one finds an in-plane and for $\mathbf{H}[111]$ an out of plane electric dipole moment.

Appendix B

Experimental Techniques

B.1 Small Angle Neutron Scattering

The first experimental technique used to prove the existence of a skyrmion lattice as a bulk phase in chiral magnet MnSi [72] was small angle neutron scattering (SANS) which uses elastic neutron scattering at small scattering angles to investigate magnetic order. Neutron scattering is an ideal tool for the study of magnetic order in bulk phases as neutrons predominantly scatter from the magnetic structure in a solid-state system due to their magnetic moment. The lack of an electric charge allows them to penetrate deep into the system under investigation. During a neutron scattering experiment a beam of neutrons of a specific wave-length is directed at the sample, typically a powder or a crystal. The neutrons scatter elastically due to the interaction of their spin with the nuclei and unpaired electrons of the magnetic atoms in the sample and the scattered neutrons are recorded by detectors placed behind the sample. The Fourier modes in the magnetic order are recorded as Bragg peaks in reciprocal space.

A typical neutron scattering set-up is depicted in Fig. B.1a. The incident beam is prepared by collimators, which define the direction of the beam and monochromators, which define the energy of the incident neutrons. Together these optical elements select an incident wave vector \mathbf{k}_i . These neutron optical elements are never perfect and a certain distribution of incident wave vectors around an average \mathbf{k}_i is selected. The sample immersed in a magnetic field \mathbf{B} scatters the incoming particles into a certain direction which is recorded by the detector as a scattered neutron beam. The scattering vector \mathbf{Q} is defined as the momentum transfer between the magnetic structure and the incoming and final momentum of the neutrons, $\mathbf{Q} = \mathbf{k}_f - \mathbf{k}_i$. SANS is employed whenever structures on length scales of about 10\AA to $10,000\text{\AA}$ are of interest. This range of real space lengths corresponds to a scattering vector \mathbf{Q} of magnitude 10^{-1}\AA^{-1} to 10^{-4}\AA^{-1} . For elastic neutron scattering the energy of the in- and outgoing neutrons is identical and the magnitude of scattering vector can be easily related to the wavelength of neutrons λ and the scattering angle Θ

$$Q = \frac{4\pi}{\lambda} \sin(\Theta) \quad (\text{B.1})$$

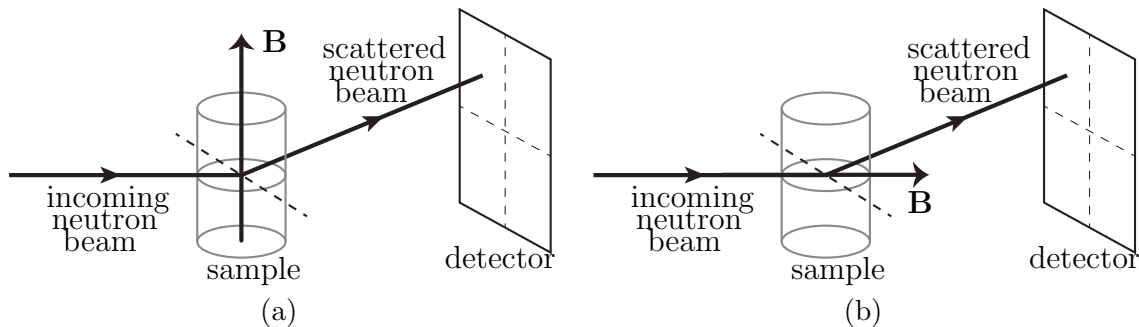


Figure B.1: Typical neutron scattering set-up where the cylindrically shaped sample is immersed in a magnetic field \mathbf{B} applied perpendicular / parallel to the direction of the incoming beam of neutrons.

For the observation of larger structures one chooses therefore a longer neutron wavelength in order to expand the diffractogram. Unfortunately there is little neutron flux at wavelength above 20\AA and typical neutrons of wavelength 10\AA to 15\AA are employed in SANS experiments.

For a given periodic structure $\mathbf{M}(\mathbf{r})$ we can decompose the magnetisation field into Fourier components $\mathbf{M}_{\mathbf{Q}}$

$$\mathbf{M}(\mathbf{r}) = \sum_{\mathbf{Q}} \mathbf{M}_{\mathbf{Q}} e^{i\mathbf{Q}\cdot\mathbf{r}} \quad (\text{B.2})$$

An incoming neutron scattering off of Fourier component $\mathbf{M}_{\mathbf{Q}}$ of the magnetic structure creates an event on the detector in the direction $\hat{\mathbf{Q}} = \mathbf{Q}/|\mathbf{Q}|$. In the following we briefly discuss the various magnetic phases found in chiral magnets and elaborate the neutron scattering setup and Bragg peak structure. The magnetic phase diagram of chiral magnets is rather generic and although we show neutron scattering data for MnSi as an example here other materials will show very similar scattering peak distributions. We start with a MnSi sample at vanishing magnetic field \mathbf{B} as discuss the evolution of the peak distribution as we turn on a magnetic field along the z direction.

Taking MnSi as a concrete example for a helimagnetic material, here the helical wavevector \mathbf{Q} pins weakly in the $[111]$ due to crystal field anisotropies and equivalent directions. There are four equivalent 3-fold axis piercing the unit cell and therefore eight equivalent ordering directions exist. Typically the magnetic order is not made up of a single domain but various parts of the probe order in another of the eight directions. The diffractogram shows an integrated scattering intensity and therefore eight Bragg peaks are in principle visible for a sample in the helical phase. Due to the limited size of the detector (a typical detector has an area of $\sim 200 \times 200 \text{ mm}^2$) not all of these peaks are visible. It depends on the relative orientation of the sample to the incoming beam of neutron how many of the eight reflection peaks are visible in the diffractogram. Fig. B.2D shows a result of a neutron scattering experiment on MnSi in the helical phase at $\mathbf{B} = 0$ and $T = 15 \text{ K}$. The reflection peaks are visibly aligned along the $[111]$ or equivalent directions.

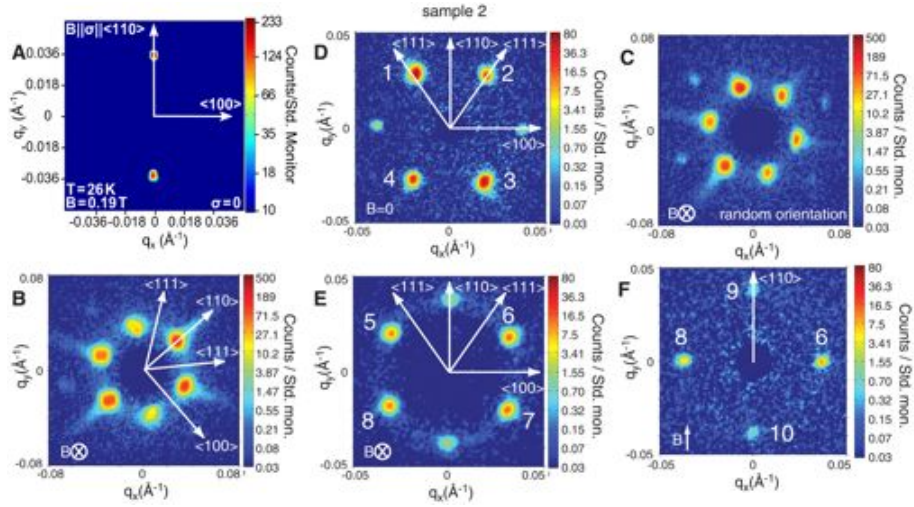


Figure B.2: Neutron scattering data for MnSi in the helical (D), conical (A) and SkX phase in the measurement setup Fig. B.1a (F) and Fig. B.1b (B,C,E). Adapted from Ref. [72].

Turning on a magnetic field along the z -direction with a magnitude in excess of a critical B_{c1} , the magnetic structure changes from the helical to a conical phase. Here the ordering wave vector \mathbf{Q} aligns with the applied magnetic field \mathbf{B} and for a neutron scattering setup with the incident beam perpendicular to the applied field \mathbf{B} Bragg reflection peaks are visible in the scattering plane at $\pm\mathbf{Q}$. Fig. B.2A shows the neutron scattering of bulk MnSi with an applied magnetic field of strength 0.19 T along the $[110]$ direction at $T = 26$ K. Indeed two reflection spots of high intensity are seen along the direction of the applied field. Since the \mathbf{q} -vector in the conical phase aligns with the applied magnetic field the field direction is usually chosen perpendicular to the incident neutron beam.

For the Skyrmion phase this proves highly disadvantageous. The SkX is a multi- \mathbf{Q} phase consisting of 3 helices at an angle of 120° with mutual phase relationships such that the magnetic moment at the center of the Skyrmion is antiparallel to the applied \mathbf{B} field. So the six \mathbf{Q} vectors lie in place perpendicular to the magnetic field. In the conventional measurement setup at most two of these can be brought to lie within the scattering plane, c.f. Fig. B.2F. If one applies the magnetic field however parallel to the beam direction as depicted in Fig. B.1b all six Bragg peaks are visible, c.f. Fig. B.2B,C & E. For more information about neutron scattering consult, for instance, Ref. [15].

B.2 Real-Space Imaging Techniques

In recent years powerful real-space imaging techniques have been modified and applied to chiral magnetic systems which allow for a direct visualization of the spatial magnetization configuration. The advantage of such methods is that not only a single spin texture, but also the crystallization and melting process during phase conversions can be observed. In chapter 4 we study the topological implications of a phase

conversion using such a real-space technique. Also magnetic-lattice defects such as edge dislocations were studied using real-space imaging techniques [104].

B.2.1 Magnetic Force Microscopy

In 1987 a new method for imaging magnetic surface configurations was pioneered [66] commonly referred to as magnetic force microscopy (MFM). Historically, the MFM has been derived from the Atomic Force Microscope (AFM) one year after its invention in 1986. MFM images forces between the surface of a sample and the magnetic stray field of a cantilever tip coated with a ferromagnetic film. The total force acting on the cantilever is inferred from small changes in its resonance frequency. For a reliable force determination the tip must be kept at constant distance from the sample while the surface is rastered. Therefore the MFM measurements typically proceed in two steps.

In a first step the topography of the sample is determined. Here the tip is scanned over the surface in close proximity and then retracted by a predefined amount. In a second scan, the tip follows the recorded surface topography at constant separation and the phase/frequency shift due to magnetic interaction forces is recorded. Since the atomic forces are short-ranged as compared to the magnetic forces, the collected force information is dominated by the magnetic interaction. The spatial resolution of the scanning probe can be increased by moving the top closer to the sample which in turn increases the effects of the atomic forces. In typical MFM measurements the tip is held at distance of $100 - 100\text{\AA}$ above the sample and spatial resolutions of 50 nm are regularly achieved. In dipole-point approximation the frequency shift Δf of the resonance frequency f_0 of the cantilever due to magnetic forces with the surface of a magnetic sample parallel to the x - y plane is given by (see supplementary information for Ref. [67])

$$\Delta f \approx -f_0 \frac{1}{2k} \mu_0 \mu_{tip,z} \frac{\partial^2 H_{S,z}}{\partial z^2} \quad (\text{B.3})$$

where k is the spring constant of the cantilever, μ_0 the vacuum permeability, $\mu_{tip,z}$ the magnetic dipole moment of the tip in the z direction and $H_{S,z}$ the magnetic field of the sample in the z direction. The MFM is therefore only sensitive to the out-of-plane component of the magnetisation. For more information about magnetic force microscopy consult, for instance, Refs. [66, 42, 87].

Fig. B.3 shows MFM imaging data from the surface of a bulk $\text{Fe}_{0.5}\text{Co}_{0.5}\text{Si}$ sample (top view) with a magnetic field of 20 mT applied perpendicular to the surface at $T = 10$ K. Blue (red) colors correspond to a magnetisation pointing parallel (antiparallel) to the line of sight. A skyrmion lattice phase can be seen with the Skyrmions, visible as blue spots, arranged in a regular hexagonal pattern.

B.2.2 Lorentz Transmission Electron Microscopy

Lorentz transmission electron microscopy (LTEM) is a modification of traditional electron microscopy in which the Lorentz forces between the electrons in a beam and the sample are utilised to generate images which allow for the real-space observation of the magnetic structure of materials.

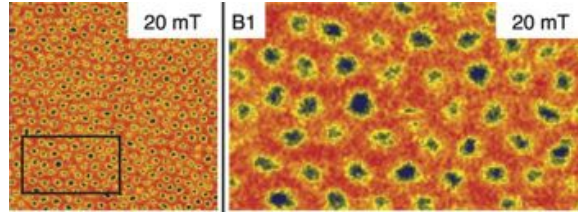


Figure B.3: MFM data collected from the surface of a bulk $\text{Fe}_{0.5}\text{Co}_{0.5}\text{Si}$ sample with a magnetic field of 20 mT applied perpendicular to the surface. The measurement was recorded after field-cooling to $T = 10$ K. A skyrmion lattice can be seen with the skyrmions (blue) arranged in the characteristic hexagonal pattern. Image taken from Ref. [67].

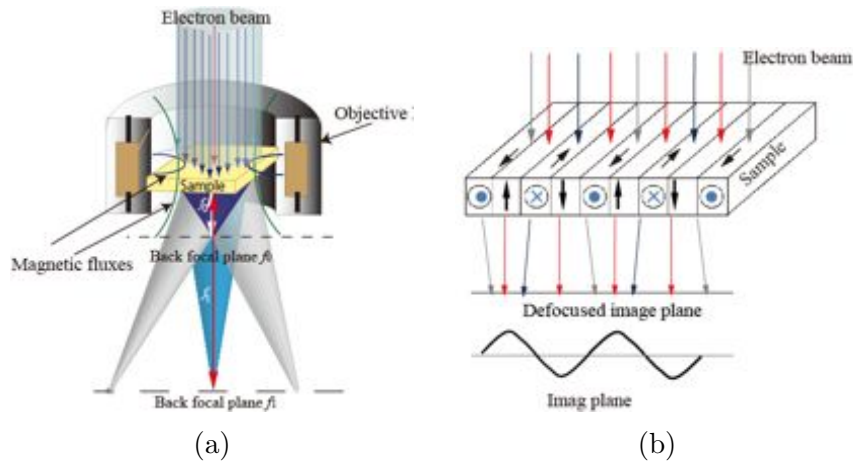


Figure B.4: Schematics of ray diagram for TEM (a) and Lorentz TEM (b). Image taken from Ref. [113].

An electron moving at a velocity \vec{v} through a magnetic field \mathbf{B} experiences a Lorentz force

$$\vec{F} = \frac{e}{c} \vec{v} \times \vec{B} \quad (\text{B.4})$$

where c is the speed of light and e the electronic charge. LTEM uses this interaction to study the spatial configuration of the magnetization. Electrons accelerated to an energy of around 100 keV by an electron gun mounted perpendicular to the sample are deflected by the in-place component of the magnetisation due to the Lorentz force they experience. The sample must be transparent for the electron beam and therefore in the form of a thin film not more than about 3000 Å thick. Magnetic lenses focus the scattered electron beam onto an image plane where the incident beam is analysed, c.f. Fig. B.4a. A quantitative evaluation is achieved by combining the observed intensities with a magnetic transport-of-intensity equation calculation. The method achieves high spatial resolution and large magnification. These features bring with them not only the ability to examine the magnetic configuration in greater detail but also have the advantage that the sample under examination does not have to be more than a few microns across [40]. A drawback of this method is apart from

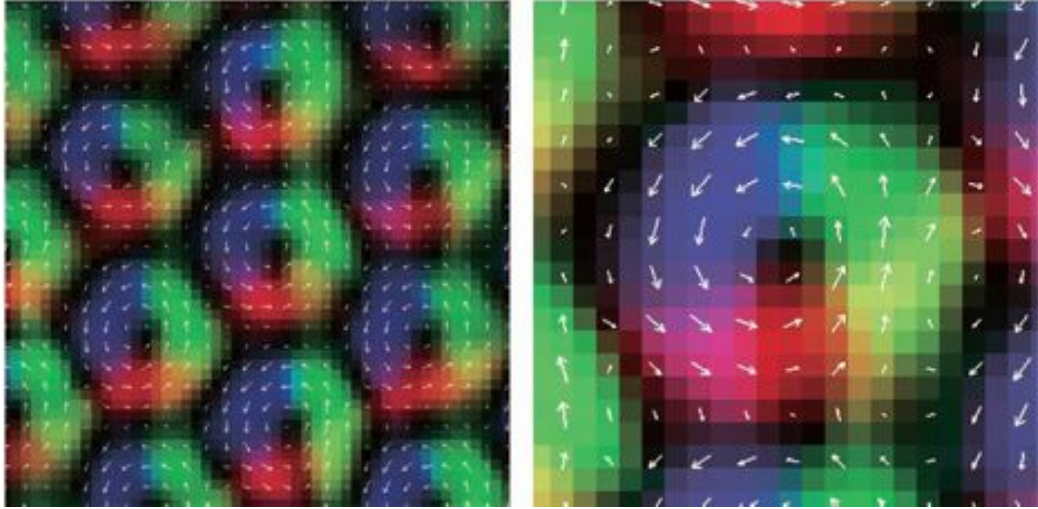


Figure B.5: Experimentally observed real-space images of the lateral magnetization configuration in $\text{Fe}_{0.5}\text{Co}_{0.5}\text{Si}$ at a weak magnetic field (50 mT) obtained by Lorentz TEM data. The right panel shows a magnified view a single Skyrmion. Image taken from Ref. [114].

the need for thin, electron-transparent materials the inability to specify the direction of the magnetisation normal to the plane (It is in this sense complementary to MFM).

In the conventional high-resolution TEM the deflection due to the magnetic field $B \sim 2$ T generated by the lens is large enough to shorten the focal length f_0 to a few millimetres. This achieves large magnification at the image plane. However under such a strong magnetic field, the specimen of the chiral magnet placed inside the objective lens typically field polarises along the z -direction and no in-plane magnetic field exists which could deflect the electrons. The interesting region of the magnetic phase diagram at small applied fields is unobservable. The observation of the Skyrmion phase therefore necessitates the reduction of the magnetic field strength in the lens which leads to a larger focal length (gray cones in Fig. B.4a). The deflection of the electrons due to the alteration of the in-plane component of the magnetisation leads to areas of enhanced and reduced intensity as depicted in Fig. B.4b. The out-of plane component of the magnetisation on the other hand cannot affect the electron trajectory and is therefore unobservable.

In the context of skyrmions thin films have the advantage that the competing conical phase is energetically suppressed and therefore not stabilised when the magnetic field is applied perpendicular to the plane and the film thickness is less than the helical wavelength. The skyrmion lattice phase is stabilised in a much larger portion of the phase diagram in these systems. In Ref. [113] the phase diagram of FeGe is studied using Lorentz TEM for different film thicknesses. For ever thicker samples the phase diagram smoothly approaches the bulk phase diagram indicating that the same skyrmion lattice phase is realized. Fig. B.5 shows a real space image of skyrmions in $\text{Fe}_{0.5}\text{Co}_{0.5}\text{Si}$ at a weak magnetic field (50 mT) obtained by Lorentz TEM data.

Appendix C

Conjugate Gradient Algorithm

The conjugate gradient method (CG) is probably the most popular iterative method for the solution of sparse linear equations of the form

$$\mathbf{A} \cdot \mathbf{x} = \mathbf{b} \tag{C.1}$$

where \mathbf{A} is a square, sparse, positive-definite matrix. In this appendix we briefly explain how this algorithm works and how it may be extended to find local minima of general functionals. In section C.1 we introduce the general method of conjugate directions (CD) and in section C.2 the specialisation that is known as the CG. In section C.3 we describe how the CG may be modified to calculate local minima of high dimensional functionals. There are a number of good reviews including Refs. [31, 91, 54]. This summary is mainly based on Ref. [91].

C.1 Conjugate directions

Let us assume that the solution to Eq. (C.1) is given by \mathbf{x}^* , i.e. $\mathbf{A} \cdot \mathbf{x}^* = \mathbf{b}$. An iterative algorithm \mathcal{A} attacks a problem such as Eq. (C.1) by starting from an initial guess \mathbf{x}_0 and updating it in subsequent iterations, $\mathbf{x}_{i+1} = \mathcal{A}(\mathbf{x}_i)$. The solution of the equation is a fixed point of the algorithm, $\mathbf{x}^* = \mathcal{A}(\mathbf{x}^*)$. We define the residual at step n as $\mathbf{r}_n = \mathbf{b} - \mathbf{A} \cdot \mathbf{x}_n$ and the error at step n as $\mathbf{e}_n = \mathbf{x}^* - \mathbf{x}_n$. The problem posed in Eq. C.1 can be rewritten as a minimisation problem for a bilinear functional. We define the quadratic form $f(\mathbf{x})$

$$f(\mathbf{x}) = \frac{1}{2} \mathbf{x}^T \cdot \mathbf{A} \cdot \mathbf{x} - \mathbf{b}^T \cdot \mathbf{x} . \tag{C.2}$$

If \mathbf{A} is positive-definite a minimum of the above functional corresponds to a solution of Eq. C.1

$$f(\mathbf{x}^*) \text{ minimal} \Leftrightarrow \mathbf{A} \cdot \mathbf{x}^* = \mathbf{b} \tag{C.3}$$

The idea of the conjugate directions method is that one finds a set of orthogonal directions $\mathbf{d}_0, \dots, \mathbf{d}_{n-1}$ and from the initial position \mathbf{x}_0 one takes exactly one step in each of these directions of exactly the right length to line up with \mathbf{x}^*

$$\mathbf{x}_{i+1} = \mathbf{x}_i + \alpha_i \mathbf{d}_i . \tag{C.4}$$

The step length α_i is defined by the fact that after the step the remaining error \mathbf{e}_{i+1} should be orthogonal to \mathbf{d}_i so that one never has to step in direction \mathbf{d}_i again

$$\begin{aligned}\mathbf{d}_i^T \cdot \mathbf{e}_{i+1} &= 0 \\ \mathbf{d}_i^T \cdot (\mathbf{e}_i + \alpha_i \mathbf{d}_i) &= 0 \\ \alpha_i &= -\frac{\mathbf{d}_i^T \cdot \mathbf{e}_i}{\mathbf{d}_i^T \cdot \mathbf{d}_i}\end{aligned}\tag{C.5}$$

The right hand side is unfortunately unknown. Knowledge of the error \mathbf{e}_i would immediately imply that one already knows the solution of the problem. However one can relax the above condition by demanding that the search direction should be \mathbf{A} -orthogonal instead of orthogonal

$$\mathbf{d}_i^T \cdot \mathbf{A} \cdot \mathbf{d}_j = 0, \quad \forall i \neq j\tag{C.6}$$

In turn one also demands that \mathbf{A} -orthogonality of \mathbf{d}_i and \mathbf{e}_{i+1} . Indeed this corresponds to finding the minimum along the line $\mathbf{x}_{i+1} = \mathbf{x}_i + \alpha_i \mathbf{d}_i$,

$$\begin{aligned}\frac{d}{d\alpha_i} f(\mathbf{x}_{i+1}(\alpha_i)) &\stackrel{!}{=} 0 \\ f'(\mathbf{x}_{i+1}) \cdot \frac{d}{d\alpha_i} \mathbf{x}_{i+1}(\alpha_i) &\stackrel{!}{=} 0 \\ -\mathbf{r}_{i+1}^T \cdot \mathbf{d}_i &\stackrel{!}{=} 0 \\ \mathbf{d}_i^T \cdot \mathbf{A} \cdot \mathbf{e}_{i+1} &\stackrel{!}{=} 0\end{aligned}\tag{C.7}$$

where we used that $f'(\mathbf{x}_{i+1}) = \mathbf{b} - \mathbf{A} \cdot \mathbf{x}_i = -\mathbf{r}_i$. For the step length α_i in step i one finds

$$\alpha_i = \frac{\mathbf{d}_i^T \cdot \mathbf{r}_i}{\mathbf{d}_i^T \cdot \mathbf{A} \cdot \mathbf{d}_i}\tag{C.8}$$

which is perfectly computable from the known quantities in step i . If one were to replace the search directions with the residuals in the above expression one would simply find that the equations describe the method of steepest descent.

For the construction of the n \mathbf{A} -orthogonal directions a possible route would be to start with the n linearly independent vectors $\mathbf{u}_0, \dots, \mathbf{u}_{n-1}$ (e.g. the coordinate axis) and then use a variation of the Gram-Schmidt algorithm to make them \mathbf{A} -orthogonal. We refer to this process as *conjugation*. Following this procedure would however defeat the purpose of the iterative procedure as the assumption is that the linear system is too large to invert directly. For the Gram-Schmidt algorithm one has to keep all the old search directions in memory and in contrast to the matrix \mathbf{A} these need not be sparse. Consequently considerable memory requirements arise. But also the computational cost is no less than that needed for a direct inversion as the complexity of Gram-Schmidt is $\mathcal{O}(n^3)$ with n the linear dimension of \mathbf{A} .

As a result the method of Conjugate Directions enjoyed little use until the discovery of the Conjugate Gradients [91]. The resolution to the mentioned troubles lies in a good choice of the search directions $\mathbf{d}_0, \dots, \mathbf{d}_{n-1}$.

C.2 Conjugate gradients

The method of Conjugate Gradients is simply the method of Conjugate Directions for the special case where the search directions are obtained by conjugation of the residuals ($\mathbf{u}_i = \mathbf{r}_i$). It turns out that this choice implies that the residual \mathbf{r}_{i+1} in step $i + 1$ is \mathbf{A} -orthogonal to all previous search directions \mathbf{d}_j , $j < i$, except for \mathbf{d}_i . It is therefore not necessary to store all the previous search directions in memory and the complexity of the Gram-Schmidt algorithm drops to $\mathcal{O}(m)$ where m is the number of non-zero entries in \mathbf{A} . In summary the conjugate gradients algorithm is given by

Algorithm 1.

1. $\mathbf{d}_0 = \mathbf{r}_0 = \mathbf{b} - \mathbf{A} \cdot \mathbf{x}_0$
2. $\alpha_i = \frac{\mathbf{r}_i^T \cdot \mathbf{r}_i}{\mathbf{d}_i^T \cdot \mathbf{A} \cdot \mathbf{d}_i}$
3. $\mathbf{x}_{i+1} = \mathbf{x}_i + \alpha_i \mathbf{d}_i$
4. $\mathbf{r}_{i+1} = \mathbf{r}_i - \alpha_i \mathbf{A} \cdot \mathbf{d}_i$
5. If the modulus of \mathbf{r}_{i+1} has dropped below a threshold value, $|\mathbf{r}_{i+1}| < \epsilon$, exit and return \mathbf{x}_{i+1} as an approximation for \mathbf{x}^* .
6. $\beta_{i+1} = \frac{\mathbf{r}_{i+1}^T \cdot \mathbf{r}_{i+1}}{\mathbf{r}_i^T \cdot \mathbf{r}_i}$
7. $\mathbf{d}_{i+1} = \mathbf{r}_{i+1} + \beta_{i+1} \mathbf{d}_i$ and goto 2.

C.3 Minimisation of general functions

The generalisation of the CG for the minimisation of a general functional $f(\mathbf{x})$ whose derivative $f'(\mathbf{x})$ is known involves three modifications of the above algorithm: (i) the recursive formula for the residuals (step 4 in the above algorithm) cannot be used, (ii) the computation of the step size α_i becomes more complicated and (iii) several choices for β_i exist.

In non-linear CG the residual is always given by the gradient, $\mathbf{r}_i = -f'(\mathbf{x}_i)$. The search directions are computed by conjugation with Gram-Schmidt algorithm as in the linear case. Then a line search is performed to find the minimum of $f(\mathbf{x}_{i+1})$ in along the given search direction, $\mathbf{x}_{i+1} = \mathbf{x}_i + \alpha_i \mathbf{d}_i$. One possibility is to determine α_i by an algorithm which determines zeros of $f'(\mathbf{x}_i + \alpha_i \mathbf{d}_i)^T \cdot \mathbf{d}_i$.

There are several choice for the β 's which are equivalent for linear CG. In the case of non-linear CG these are no longer equivalent and it is still debated in the literature which one is the best choice in what situation [91]. Usage of the same formulas as in the linear case (step 6 in the above algorithm) is known as the Fletcher-Reeves method [32]. The so-called Polak-Ribiere [39] is given by

$$\beta_{i+1} = \frac{\mathbf{r}_{i+1}^T \cdot (\mathbf{r}_{i+1} - \mathbf{r}_i)}{\mathbf{r}_i^T \cdot \mathbf{r}_i} \quad (\text{C.9})$$

In all of our calculation we used the Fletcher-Reeves method.

Appendix D

Appendix Quantum Mass

D.1 Expression for $\tilde{H}_{\alpha\beta}$

In the comoving, twisted reference frame the Hamilton operator assumes the form

$$\tilde{H}_{\alpha\beta} = \epsilon_0 a^2 \left[-\delta_{\alpha\beta} \nabla^2 + 2\tau_{\alpha\beta}^y \left(\frac{\cos \theta}{\rho^2} - Q \frac{\sin \theta}{\rho} \right) i\partial_\chi + \tilde{V}_{\alpha\beta} \right] \quad (\text{D.1})$$

with $\nabla^2 = \partial_\rho^2 + (1/\rho)\partial_\rho + \partial_\chi^2/\rho^2$. The potential depends only on the radial component ρ and is given by $\tilde{V}_{12} = \tilde{V}_{21} = 0$ and

$$\begin{aligned} \tilde{V}_{11} &= \frac{1 + \cos(2\theta)}{2\rho^2} - \frac{Q \sin(2\theta)}{\rho} + \kappa^2 \cos \theta - 2Q\theta' - \theta'^2 \\ \tilde{V}_{22} &= \frac{\cos(2\theta)}{\rho^2} - \frac{2Q \sin(2\theta)}{\rho} + \kappa^2 \cos \theta. \end{aligned} \quad (\text{D.2})$$

D.2 WKB

With the ansatz $\vec{\eta}_m(\rho) = \xi_m(\rho)/\sqrt{\rho}$ and after multiplying Eq. 5.37 with $\sqrt{\rho}\tau^z$ from the left, we find

$$[-\epsilon_0 a^2 \partial_\rho^2 + M_m(\rho)] \cdot \vec{\xi}_m(\rho) = \epsilon \vec{\xi}_m(\rho), \quad (\text{D.3})$$

$$\text{with } M_m(\rho) = \epsilon_0 a^2 \left[-\frac{1}{4\rho^2} + \frac{m^2 + 1}{\rho^2} + \kappa^2 \right] \tau^z + \tau^z \mathcal{V}_m - \epsilon_0 a^2 \frac{2m}{\rho^2} \mathbb{1}. \quad (\text{D.4})$$

To determine the ‘‘classical momenta’’, we make the usual WKB approach where the wavefunction $\vec{\xi}_m(\rho)$ is devided into a real-valued function $\vec{u}_m(\rho)$ and a real-valued phase factor $S_m(\rho)$,

$$\vec{\xi}_m(\rho) = \vec{u}_m(\rho) e^{iS_m(\rho)}. \quad (\text{D.5})$$

In the lowest order WKB approximation we neglect spatial derivatives of the amplitude $\vec{u}_m(\rho)$ and higher order spatial derivatives of the phase factor $S_m(\rho)$ and find within this approximation

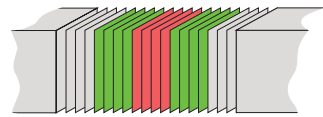
$$-\partial_\rho^2 \vec{\xi}_m(\rho) \approx - (S'_m(\rho))^2 \vec{\xi}_m(\rho) \quad (\text{D.6})$$

where we identify $S'_m(\rho) \equiv p_m(\rho)$ as the “classical momentum”. Within this approximation, the left-hand-side of Eq. D.3 can be written as a matrix $\mathcal{H}_m(p(\rho), \rho)$ which depends parametrically on the classical momentum and the radial coordinate ρ . From here on we suppress the suffix of the angular momentum quantum number m . For a given p and ρ one can determine the eigenvalues $\epsilon_{1/2}(p, \rho)$ and eigenvector $\vec{\xi}_{1/2}(p, \rho)$. For a given eigenenergy ϵ the above relation can be inverted to find the spatially dependent classical momenta $p_{1/2}(\rho; \epsilon)$ which are inserted into the eigenvector $\vec{\xi}_{1/2}(\rho; \epsilon)$ to find the WKB approximation for the wave functions

$$\vec{\eta}_{1/2}^{\text{WKB}}(\rho) = \frac{1}{\sqrt{\rho}} \vec{\xi}_{1/2}(\rho; \epsilon) e^{iS_{1/2}(\rho; \epsilon)} \quad (\text{D.7})$$

Only one of these has the correct asymptotic behaviour, Eq. 5.56, for $\rho \gg 1$, the other one can be discarded. For this wavefunction the usual formulas for the calculation of the WKB phase shift can be used [30].

Correlated Heterostructures



Introduction

The aim of solid state theory is the successful description and understanding of the intrinsic properties of rigid matter. The complicated interplay of a large number of simple, microscopic constituents gives rise to often intricate and surprising macroscopic properties. The complexity of these systems renders exact descriptions of such systems impossible. Even if they were available, physicists would still need to construct more abstract descriptions in order to categorise the natural phenomena in a unifying way. Along these lines of thought, free parameters in an approximate model may not necessarily be understood as a deficiency of the same, but rather they parametrise the unifying paradigms that allow us identify the mechanism behind a physical phenomenon. In the context of strongly correlated electron systems such descriptions are often provided by a model Hamiltonians.

Solids consist of positively charged atomic nuclei and negatively charged electrons. In crystals the much heavier nuclei are arranged in an orderly repeating pattern with a fraction of the electrons tightly bound to them due to strong Coulomb interactions. The resulting ions provide a periodic lattice potential for the remaining valence electrons. Often an effective description of this electronic subsystem already determines to leading order the properties of the solid.

Ignoring the interactions among the valence electrons, the lattice potential splits their dispersion relation into Bloch energy bands. The eigenfunctions in this periodically-repeating environment are the Bloch waves and their eigenenergies are commonly referred to as the kinetic energy of the valence electrons. Due to the Pauli exclusion principle each state, characterised by a complete set of quantum numbers, can only be occupied by a single electron. Thus already at the non-interaction level of the description the quantum system has some correlations. However it is the electron-electron interactions which introduces the true correlations between the valence electrons and makes the description of many-particle systems so involved. In the limit where the typical energy scale of the interactions is small compared to the kinetic energy of the electrons, Landau's phenomenological Fermi liquid theory successfully describes the normal state of most metals at sufficiently low temperatures. In this effective description interacting electrons are replaced by non-interacting quasiparticles with a finite lifetime and renormalised properties such as their mass, magnetic moment etc.

The transition metal oxides constitute probably one of the most interesting classes of solids. Due to partially occupied, well-localised $3d$ and $4f$ valence orbitals the electrons are subject to strong Coulomb interactions. These materials provide prototypical examples of strongly correlated electron system which cannot be described by effective single-particle theories. In these materials the interaction energy of the

similar magnitude as the kinetic energy and thus the important paradigm is the competition between itineracy and localisation. Often both regimes occur in the same material and a metal-insulator transition occurs as a function of temperature or pressure. The successful description of these systems calls for non-perturbative methods able to treat both limits reliably.

The Dynamical Mean-Field Theory (DMFT) is such a non-perturbative approximation for strongly correlated electron systems which becomes exact in the limit of infinite lattice connectivity. It neglects spatial correlations but takes full account of dynamical quantum fluctuations. In DMFT the lattice problem is simplified by mapping it onto a quantum impurity problem embedded in a self-consistently determined bath of non-interacting electrons. A variety of powerful numerical methods exist which allow for numerical exact solutions of such problems. Among these the Numerical Renormalisation Group(NRG) can be considered the state-of-the-art impurity solver for single-band DMFT at low temperatures.

A new and exciting direction in the material sciences has been the fabrication of artificial heterostructures and superlattices composed of different materials. With recent theoretical and experimental progress in the understanding and control of strongly correlated materials enormous interest has arisen in multilayered heterostructures involving materials where the electrons are strongly interacting. The sensitivity of intrinsic properties in strongly correlated materials to external fields promises interesting applications in electronic devices for information technology.

The main focus of this work is on interface effects occurring in strongly correlated heterostructures. Chapter 1 introduces the generalised electronic Hamiltonian and heuristic derivation of the Hubbard model is presented. In section 1.2 the single Anderson impurity model that the DMFT maps the Hubbard model onto is introduced. Chapter 2 briefly outlines the mean-field approach to magnetic ordering phenomena in the Hubbard model. Chapter 3 starts with a description of the simplifications in the limit of infinite spatial dimensions and goes on to derive the DMFT equations and the mapping to the impurity problem. The NRG is outlined in chapter 4 and it is explained how dynamical quantities needed for the DMFT cycle can be calculated. Chapter 5 gives an introduction to heterostructures and describe the generalisation of the DMFT algorithm to layered systems including long-range Coulomb interactions which lead to electronic charge reconstruction at interfaces. The last part of the thesis comprises two applications of the framework to strongly correlated heterostructures. In chapter 6 we investigate the layer-resolved conductivities of heterostructure made of Mott insulator sandwiched between two band-insulators. We study the temperature dependence of the layer-resolved optical conductivity. Chapter 7 addresses the transmission probability through a Mott insulating barrier. We find an interesting temperature dependence which has its roots in the strongly correlated character of the Mott insulator.

Contents

I	Models	151
1	Models of strongly interacting electrons	153
1.1	Hubbard model	153
1.1.1	Heuristic derivation	154
1.1.2	Symmetries of the Hubbard model	155
1.1.3	Limiting cases	157
1.1.4	The metal-insulator transition and magnetic order	159
1.2	Single impurity Anderson model	161
2	Itinerant electron magnetism in the Hubbard model	165
2.1	Spin susceptibility	165
2.2	Antiferromagnetic order on the mean-field level	168
2.2.1	Origin of the magnetisation gap	169
2.2.2	Gap equation and spectral functions	171
II	Methods	175
3	Dynamical Mean-Field Theory	177
3.1	Simplification from the $d \rightarrow \infty$ limit	178
3.1.1	Locality of the self-energy	179
3.2	Idea of the DMFT	183
3.3	Cavity derivation	184
3.4	Mapping to a quantum impurity problem	186
3.5	Self-energy functional approach	188
3.6	Application: Mott-Hubbard metal-insulator transition	191
3.7	Antiferromagnetic order	193
3.7.1	Application: Antiferromagnetic order in the Hubbard model	196
4	Solution of the impurity model	199
4.1	Introduction to the Kondo effect	199
4.2	Numerical Renormalization Group	201
4.2.1	Logarithmic discretization	202
4.2.2	Mapping onto a chain	204
4.2.3	Iterative diagonalisation	206
4.2.4	Renormalisation group transformations	208

4.3	Calculation of dynamical quantities	210
4.4	Broadening of discrete spectra	214
4.5	NRG as an impurity solver for the DMFT	215
4.5.1	Energy-dependent hybridisation functions	216
4.5.2	Calculation of the self-energy within NRG	217
4.6	Other impurity solvers	217
4.7	Spin-dependent hybridisation functions	218
5	DMFT for Heterostructures	221
5.1	Introduction to Heterostructures	221
5.2	Inhomogenous DMFT	222
5.3	The mathematics of the inversion problem	224
5.3.1	Inversion of finite dimensional tridiagonal symmetric matrices	224
5.3.2	Inversion of coupled tridiagonal symmetric matrices	225
5.4	The quantum zipper algorithm	226
5.4.1	Numerical implementation	229
5.5	Electronic charge reconstruction	230
5.5.1	Numerical implementation	232
5.5.2	Application: A strongly-correlated nanostructure	233
5.6	Antiferromagnetic order	235
III	Applications	239
6	Mott-Band-Insulator Heterostructures	241
6.1	Conductivity calculations in the DMFT	242
6.2	Layer-resolved conductivities	244
6.2.1	Longitudinal conductivity	249
6.2.2	Hall conductivity	251
6.3	Results	253
7	Transmission through a Mott Barrier	261
7.1	History of the problem	262
7.2	Landauer-Büttiker definition of the transmission	266
7.3	Transmission through a heterostructure	269
7.3.1	System layout	272
7.3.2	DMFT results	273
7.3.3	Conclusions	277
	Bibliography	278
IV	Appendix	289
A	Antiferromagnetic quantum zipper algorithm	291
B	Spectral functions for B-M-B heterostructure	293

C	Derivation of the Hall conductivity	295
D	Analytic continuation of $\Pi_{\mathbf{p}n\alpha\gamma}$	299
E	Analytic continuation of $\Pi_{\mathbf{p}n\delta}^H$	301
F	Approximate expressions for various densities of states	305

Part I
Models

Chapter 1

Models of strongly interacting electrons

Although Bloch band theory with its roots dating back to the 1920s is very successful in describing a number of so-called weakly correlated materials, many interesting electronic phenomena encountered in systems with strongly correlated signatures cannot be described within this framework. However the description of such systems on a similar level of detail as their weakly-correlated counterparts is a formidable problem. Physicists have retracted to the study of model hamiltonians to trade the overburdening complexity of realistic descriptions for simple models which still retain the dominant physics. They are aimed at simulating the key physics of notoriously complicated complete Hamiltonians of large-scale interacting systems.

1.1 Hubbard model

In 1963, Hubbard, Gutzwiller and Kanamori introduced the celebrated fermionic Hubbard model [43, 60, 53]. The Hubbard model (HM) can be considered as the minimal model for highly correlated electrons on a lattice as it describes the interplay between kinetic energy gain and cost of Coulomb interaction. We give an intuitive view on the main driving forces which govern the dynamics of electrons described by the HM before we present a heuristic derivation. Due to the Heisenberg uncertainty principle electrons seek to minimise the kinetic energy through dislocations, i.e. hopping processes between different atoms. However whenever two electrons come close together a Coulomb energy penalty has to be paid due to the mutual interaction. The overall movement is hence complicated and highly correlated, but there are two limits where the dynamics become simple.

In many electron systems screening may lead to an *effective* Coulomb interaction which is very short-ranged and the electrons are rather free to optimise their kinetic energy ignoring their mutual interaction. Strictly speaking such a view is only justified for the quasi particles in a Landau liquid theory as the screening itself is provided by the electronic system. On the other hand if screening is absent and the Coulomb energy dominates the energy balance in lattices with a commensurate filling a situation may arise where the mutual interaction drives the hopping tendency of the

electrons to zero thus localising them. The system enters an insulating state known as the *Mott insulator*. This state is in sharp contrast to a conventional band insulator where the interaction between electrons and atoms gives rise to a potential landscape in which effective single-particle Bloch bands are completely filled. A Mott insulator on the other hand is driven by the mutual electron interaction with a gap at the Fermi level which originates from the Coulomb interaction.

1.1.1 Heuristic derivation

The complete Hamiltonian \mathcal{H} of a condensed matter system can be split into a part which describes the nuclei \mathcal{H}_K , a purely electronic part \mathcal{H}_e and a coupling between the two subsystems \mathcal{V}_{Ke} . The Born-Oppenheimer approximation [7] decouples the problem of the nuclei from the electronic subsystem and derives an effective Hamiltonian for the electronic part of the form

$$H_e = \mathcal{H}_e + \mathcal{V}_{Ke}(\{\mathbf{R}_i\}) \quad (1.1)$$

where $\{\mathbf{R}_i\}$ denotes a set of lattice points for the positions of the nuclei and is a mere fixed parameter for the electronic problem. For a particular nuclei configuration $\{\mathbf{R}_i\}$ the electron-nuclei interaction in Eq. 1.1 gives rise to an external potential for the electrons $V_{\text{ext}} = \mathcal{V}_{Ke}(\{\mathbf{R}_i\})$. After decoupling the lattice degrees of freedom the remaining problem of interacting electrons in an external potential is still much to complicated.

Further progress can be made by removing details of the Hamiltonian which is not necessary for the basic modelling while still retaining the many-particle structure. This is best done in the language of second quantisation

$$H_e = - \sum_{\substack{i,j \\ \alpha,\beta,\sigma}} t_{\mathbf{R}_i\mathbf{R}_j}^{\alpha\beta} c_{\mathbf{R}_i\alpha\sigma}^\dagger c_{\mathbf{R}_j\beta\sigma} + \frac{1}{2} \sum_{\substack{i,j,k,l \\ \alpha,\beta,\gamma,\delta,\sigma,\sigma'}} V_{ee}^{\alpha\beta\gamma\delta\sigma\sigma'}(\{\mathbf{R}_i\}) c_{\mathbf{R}_i\alpha\sigma}^\dagger c_{\mathbf{R}_j\beta\sigma'}^\dagger c_{\mathbf{R}_k\gamma\sigma'} c_{\mathbf{R}_l\delta\sigma} \quad (1.2)$$

The electron creation (annihilation) operators $c_{\mathbf{R}_i\alpha\sigma}$ ($c_{\mathbf{R}_i\alpha\sigma}^\dagger$) for electrons with spin σ and orbital character α are written in a localised Wannier basis $\phi(\mathbf{r})$ at lattice site \mathbf{R}_i . The first term describes the kinetic energy as well as the interaction energy with the nuclei. The second part describes the electron-electron interaction. The matrix elements are given by

$$t_{\mathbf{R}_i\mathbf{R}_j}^{\alpha\beta} = \int d\mathbf{r} \phi_{\mathbf{R}_i\alpha}^*(\mathbf{r}) \left\{ \frac{\hbar^2}{2m} \Delta - V_{\text{ext}}(\mathbf{r}) \right\} \phi_{\mathbf{R}_j\beta}(\mathbf{r})$$

$$V_{ee}^{\alpha\beta\gamma\delta\sigma\sigma'}(\mathbf{R}_i, \mathbf{R}_j, \mathbf{R}_k, \mathbf{R}_l) = \int d\mathbf{r} d\mathbf{r}' \phi_{\mathbf{R}_i\alpha\sigma}^* \phi_{\mathbf{R}_j\beta\sigma'}^* \frac{e^2}{|\mathbf{r} - \mathbf{r}'|} \phi_{\mathbf{R}_k\gamma\sigma'} \phi_{\mathbf{R}_l\delta\sigma} \quad (1.3)$$

A reduction in the overburdening complexity of the model now arises from three simplifications. In order to model the competition between itineracy and localisation retaining the full orbital character of the model is not necessary. Also it is sufficient to keep only nearest neighbour terms (NN) for the hopping processes. Furthermore the Coulomb interaction is strongest if the two electron come closest to the same Wannier orbital.

We therefore simplify the model in the following radical way: We assume a model system with NN hopping between a single Wannier orbital for each lattice site and model the Coulomb interaction $V_{ee}(\mathbf{R}_i, \mathbf{R}_j, \mathbf{R}_k, \mathbf{R}_l)$ only by an appropriately chosen on-site interaction $V_{ee}(\mathbf{R}_i, \mathbf{R}_j, \mathbf{R}_k, \mathbf{R}_l) \approx U \delta_{\mathbf{R}_i \mathbf{R}_j} \delta_{\mathbf{R}_i \mathbf{R}_k} \delta_{\mathbf{R}_i \mathbf{R}_l}$. Note here that U is not simply given by the on-site matrix element of V_{ee} but rather a renormalised value which also includes the effects of screening by other bands. With these simplifications in place the Hamiltonian may be cast in the form of the famous Hubbard model

$$H_{\text{hub}} = -t \sum_{\langle ij \rangle \sigma} c_{i\sigma}^\dagger c_{j\sigma} + U \sum_i n_{i\uparrow} n_{i\downarrow} + \epsilon_0 \sum_{i\sigma} n_{i\sigma} \quad (1.4)$$

The only parameters left are the hopping amplitude t , the so called Hubbard U and the on-site energy ϵ_0 . The hopping term has a negative sign to reflect the gain in the kinetic energy of the system due to the hopping. The bandwidth W is connected to the size of the matrix element t , obviously a larger value of t results in a more itinerant behaviour of the electrons and an increase in the bandwidth W . An exact analytical solution only exists in the one-dimensional case which we will not discuss here since in 1D many peculiarities arise compared to higher dimensions (Fermi-liquid theory is replaced by Luttinger liquid theory, including spin-charge separation,...). For systems in the limit of infinite spatial dimensions a numerically exact solution exists which is given by the dynamical mean field theory (DMFT). The physically interesting cases, namely 2D and 3D, are however difficult to deal with. The difficulty arises from differences in the summation parts of Eq. 1.4. While the first sum can be diagonalised in momentum space, the second term is diagonal in real space, however diagonalising both parts simultaneously seems only possible for tiny systems.

1.1.2 Symmetries of the Hubbard model

SU(2) spin symmetry

Under a rotation of global spin quantisation axis parametrised by the SU(2) matrix U , the annihilation operators transform according to

$$c'_{i\sigma} = U_{\sigma\sigma'} c_{i\sigma'} \quad (1.5)$$

In turn the spin operator \vec{S} transform like

$$\begin{aligned} S_i^a &= R^{ab} S_i^b \\ &= \frac{\hbar}{2} c_{i\sigma}^\dagger \tau_{\sigma\sigma'}^a c_{i\sigma'} \\ &= \frac{\hbar}{2} c_{i\sigma}^\dagger (U^{-1} \tau^a U)_{\sigma\sigma'} c_{i\sigma'} \end{aligned} \quad (1.6)$$

with τ the vector of Pauli matrices and R^{ab} a rotation matrix induced by the SU(2) transformation $U^{-1} \tau^a U = R^{ab} \tau^b$. Although not immediately visible from the Eq. 1.4 the spin quantisation axis can be chosen arbitrarily and the Hubbard model is thus invariant under global rotations of the spin quantisation axis. Eq. 1.4 can be rewritten

in a way which makes the SU(2) symmetry obvious. Using the identity $\sum_i \vec{S}_i^2 = \sum_{i\sigma} \frac{1}{4} n_{i\sigma} - \sum_i \frac{3}{2} n_{i\uparrow} n_{i\downarrow}$ the interaction part can be rewritten as

$$U \sum_i n_{i\uparrow} n_{i\downarrow} = -\frac{2U}{3} \sum_i \vec{S}_i^2 + \frac{N_e U}{6} \quad (1.7)$$

with N_e the number of electrons. The last term in the above equation is for a particle number conserving model such as the Hubbard model a constant and can thus be dropped. The total Hamiltonian assumes a manifestly SU(2) invariant form. For the first term in the above equation the interaction energy is lowered in case of repulsive interaction, $U > 0$, if the total spin at each site is maximised. If each site has one particle one expects a magnetic ground state where the system breaks the global SU(2) symmetry by singling out a specific quantisation axis [31]. In chapter 2 we further investigate the magnetic properties of the Hubbard model.

U(1) charge symmetry

We are free to choose a global phase change for the one-particle wave functions

$$c'_{i\sigma} = e^{i\theta} c_{i\sigma} \quad (1.8)$$

Terms with an equal number of creation and annihilation operators are invariant under such a transformation, hence the U(1) symmetry is nothing but charge conservation. Terms inducing superconducting correlations however would break particle conservation and the U(1) symmetry.

If we couple the Hubbard system to an electromagnetic gauge field (A_0, \mathbf{A}) the global symmetry becomes a local symmetry, i.e. $\theta \rightarrow \theta(\mathbf{r})$. In the tight-binding Hamiltonian we must modify the kinetic energy term so that it assumes the form

$$-t \sum_{\langle i,j \rangle \sigma} c_{i\sigma}^\dagger e^{i\frac{e}{\hbar c} \int_{\mathbf{r}_i}^{\mathbf{r}_j} d\mathbf{r} \cdot \mathbf{A}(\mathbf{r})} c_{j\sigma} \quad (1.9)$$

The integral cancels phase difference picked up at different lattice sites. Under the local change of phase $\theta(\mathbf{r}) = -\frac{e}{\hbar c} \Lambda(\mathbf{r})$ the vector potential \mathbf{A} changes by $\mathbf{A}'(\mathbf{r}) = \mathbf{A}(\mathbf{r}) + \nabla \Lambda(\mathbf{r})$ and thus the integral by

$$\begin{aligned} A'(\mathbf{r}_i, \mathbf{r}_j) &= \int_{\mathbf{r}_i}^{\mathbf{r}_j} d\mathbf{r} \cdot \mathbf{A}'(\mathbf{r}) \\ &= A(\mathbf{r}_i, \mathbf{r}_j) + \Lambda(\mathbf{r}_i) - \Lambda(\mathbf{r}_j) \end{aligned} \quad (1.10)$$

The kinetic energy term is now invariant under local changes of the phase. In addition we expect an electrostatic coupling between the zero component of the gauge field and the particle density

$$H_{\text{e-static}} = \sum_{i\sigma} e A_0(\mathbf{r}_i) c_{i\sigma}^\dagger c_{i\sigma} \quad (1.11)$$

and a Zeeman coupling which couples the spin \vec{S}_i to the local magnetic field $\mathbf{B}(\mathbf{r}_i)$ so as to align it along the $\mathbf{B}(\mathbf{r})$ direction

$$H_{\text{Zeeman}} = g \sum_i \vec{S}_i \cdot \mathbf{B}(\mathbf{r}_i) \quad (1.12)$$

Particle-hole symmetry

In this thesis we will be solely concerned with simple cubic lattice which is bipartite (a union of two interpenetrating sublattices A and B). For bipartite lattices we find an additional symmetry for the Hubbard model. Consider the particle-hole transformation

$$\begin{aligned} c_{i\uparrow} &= d_{i\uparrow} \\ c_{i\downarrow} &= \begin{cases} +d_{i\downarrow}^\dagger & \mathbf{r}_i \in A \\ -d_{i\downarrow}^\dagger & \mathbf{r}_i \in B \end{cases} \end{aligned} \quad (1.13)$$

The Hamiltonian $H(t, U)$, Eq. 1.4, changes to $H(t, -U) + UN_\uparrow$ where N_\uparrow is the total number of up spins (which is conserved). The total charge Q and the component S_z of the total spin transform as

$$Q \rightarrow S_z + 1, \quad S_z \rightarrow Q - 1 \quad (1.14)$$

Thus the attractive and the repulsive Hubbard model map into each other and at the same time spin maps into charge and vice versa. This means that the SU(2) spin symmetry maps onto an SU(2) charge symmetry (for fixed U at half-filling).

1.1.3 Limiting cases

It is a good idea to first examine the limiting regimes when trying to understand the physics of the Hubbard model. In order to make the presentation as compact as possible we will limit ourselves to the presentation of the half-filled model.

Strong coupling limit ($U > 0$)

The simplest situation for the fermionic Hubbard model at half-filling arises when the on-site interaction U is the largest energy scale in the problem. We follow here the presentation of Emery[25]. Rewriting the interaction part of the Hamiltonian as in Eq. 1.7 it becomes apparent that for $\mu = U/2$ (half-filling) in the infinite U limit the spin \vec{S} is forced to be largest and hence doubly occupied and empty sites are forbidden. Only $|\uparrow\rangle$ and $|\downarrow\rangle$ states are kept in this large U limit at half-filling. Any spin configuration is therefore an eigenstate of the interaction part of the Hamiltonian. This massive degeneracy is lifted if one considers fluctuations induced by the kinetic part to leading order in an expansion in t/U .

We denote the kinetic part by H_0 and the interaction part by H_1 and perform a (degenerate) perturbation theory in H_0 around the eigenstates of H_1 . For an arbitrary eigenstate of the full system $H = H_0 + H_1$, $H|\Psi\rangle = E|\Psi\rangle$, we can rewrite this equation as

$$(E - H_1)|\Psi\rangle = H_0|\Psi\rangle \quad (1.15)$$

from which we formally get

$$\begin{aligned} |\Psi\rangle &= \frac{1}{E - H_1} H_0 |\Psi\rangle \\ &= \frac{\hat{P}}{E - H_1} H_0 |\Psi\rangle + \sum_{\alpha} |\alpha\rangle \frac{\langle \alpha | H_0 | \alpha \rangle}{E - E_1} \end{aligned} \quad (1.16)$$

where $|\alpha\rangle$ enumerates the eigenstates of the interaction part and \hat{P} is a projection operator onto the perturbing states

$$\begin{aligned} H_1 |\alpha\rangle &= E_1 |\alpha\rangle \\ \hat{P} &= 1 - \sum_{\alpha} |\alpha\rangle \langle \alpha| \end{aligned} \quad (1.17)$$

\hat{P} commutes with H_1 so that we can define a basis to expand the eigenstate $|\Psi\rangle = \sum_{\alpha} a_{\alpha} |\Psi_{\alpha}\rangle$ into by the equation

$$|\Psi_{\alpha}\rangle = |\alpha\rangle + \frac{\hat{P}}{E - H_1} H_0 |\Psi\rangle \quad (1.18)$$

where the expansion coefficients are given by

$$a_{\alpha} = \frac{\langle \alpha | H_0 | \alpha \rangle}{E - E_1} \quad (1.19)$$

Eq. 1.18 is an iterative equation for the states $|\Psi_{\alpha}\rangle$ and to first order in $\hat{P}/(E - H_1)H_0$ approximated by

$$|\Psi_{\alpha}\rangle \approx |\alpha\rangle + \frac{\hat{P}}{E - H_1} H_0 |\alpha\rangle \approx |\alpha\rangle - \frac{1}{U} H_0 |\alpha\rangle \quad (1.20)$$

The last approximate sign follows since for the half-filled lattice $H_0 |\alpha\rangle$ is orthogonal to any eigenstate of the interaction part. Inserting Eq. 1.20 into the expansion $|\Psi\rangle = \sum_{\alpha} a_{\alpha} |\Psi_{\alpha}\rangle$ and that in turn into Eq. 1.19 one finds

$$(E - E_1) a_{\alpha} = \frac{1}{U} \sum_{\beta} \langle \alpha | H_0^2 | \beta \rangle a_{\beta} \quad (1.21)$$

which is the same as the Schrödinger equation for the Hamiltonian $H^{U \gg 1} = H_0^2/U$ with the eigenenergy $\mathcal{E} = E - E_1$. For the case of half-filling the $H^{U \gg 1}$ can be rewritten as

$$H^{U \gg 1} = \frac{2t^2}{U} \sum_{\langle ij \rangle} \vec{S}_i \cdot \vec{S}_j \quad (1.22)$$

which is the spin- $\frac{1}{2}$ quantum Heisenberg Antiferromagnet with the exchange coupling $J = \frac{2t^2}{U}$. This result is valid for the half-filled system in any dimension and lattice [31].

Weak coupling limit

For the weak coupling limit, i.e. $U \ll t$, on the other hand one may think of the interaction H_1 as a weak perturbation of the Hamiltonian H_0 ¹. The expectation is that the states of a weakly interacting electron gas are similar to a free electron gas. This picture known as the Fermi liquid[77] relies on the main assumption that there exists a one-to-one correspondence between the states of a free fermion system and those of a weakly interacting one.

For a translationally invariant system it is convenient to transform the kinetic part of the Hamiltonian to Fourier space. For a lattice in d dimensions we find

$$H_0 = \sum_{\sigma} \int \frac{d^d k}{(2\pi)^d} \epsilon(k) c_{\sigma}^{\dagger}(k) c_{\sigma}(k) \quad (1.23)$$

with $\epsilon(k) = -2 \sum_{r_i - r_j} t(r_i - r_j) e^{-ik \cdot (r_i - r_j)}$. For the case of nearest neighbour hopping the dispersion relation is given by a cosine band

$$\epsilon(k) = -2t \sum_{j=1}^d \cos(k_j) \quad (1.24)$$

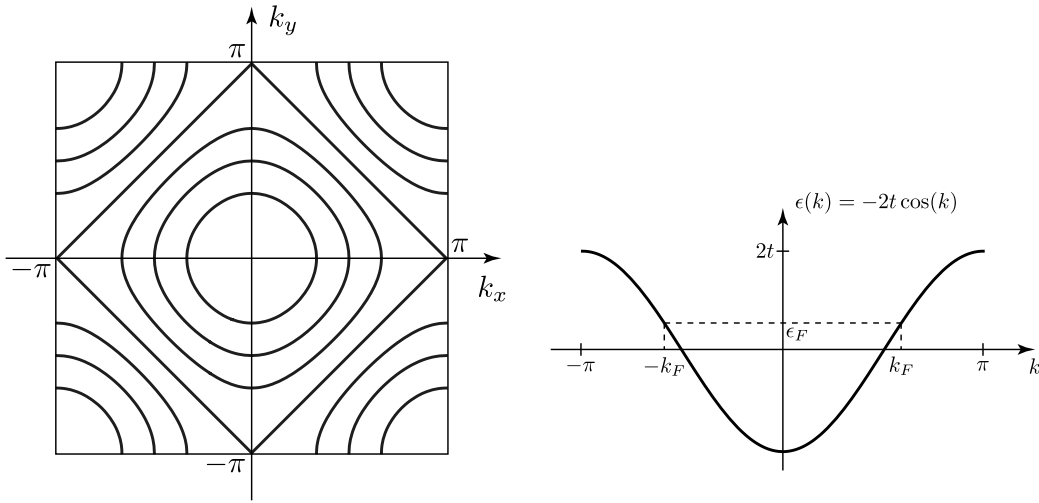
The ground is found by filling up the Fermi sea. Thus if N particles are in the system, the total number of momentum states with energy smaller than ϵ is determined by the constant energy curve $\epsilon(k) = \epsilon$, c.f. Figs 1.1a and 1.1b.

1.1.4 The metal-insulator transition and magnetic order

The existence of a metal-insulator transition in the paramagnetic phase of the half-filled Hubbard model has been known since the early work of Hubbard [53]. This transition is found in various transition metal oxides of which V_2O_3 and Cr are just two examples[9]. The mechanism driving the Mott-Hubbard metal-insulator transition (MHMIT) is the tendency towards localisation due to the local Coulomb interaction U between electrons on the same lattice site. The Hubbard model is the minimal model for the study this transition. Non-perturbative methods fail to describe the physics near the MHMIT correctly where the U and the bandwidth W are roughly of the same order of magnitude. The transition can however be studied within the framework of DMFT, a non-perturbative, controlled approximation, which maps the correlated lattice problem onto self-consistently determined single impurity Anderson model.

Many authors have studied the MHMIT by means of the DMFT[9, 45, 86, 102, 92, 98]. Fig. 1.2 summarises the results for a homogenous Hubbard model in infinite spatial dimensions at half filling. For $T < T_c$ one finds a first order transition with a discontinuous redistribution of weight in the spectral function and a pronounced

¹Actually for the single band Hubbard model on a simple cubic lattice, the model possesses a perfect nesting property which causes the system to order antiferromagnetically for arbitrary small interaction parameter U . Therefore it is only true that H_1 can be understood as a weak perturbation for the eigenstates of H_0 if the system is constrained to the paramagnetic phase by, say, frustration.



(a) Constant energy curves for H_0 on a square lattice ($d = 2$). (b) One particle spectrum of H_0 in one spatial dimension ($d = 1$).

Figure 1.1

hysteresis effect. From the side of the metal at weak interaction the transition sets in at $U > U_{c_2}$ while from the side of the Mott insulator one finds a transition to a metallic solution for $U < U_{c_1}$. The first order transition line ends at a critical point at $T = T_c$. For $T > T_c$ the transition turns into a crossover and dashed lines in Fig. 1.2 indicate the width of the crossover region. Filled and open circles and the solid line labeled IPT indicate results obtained from different impurity solvers. The numerical renormalisation group (NRG) results are denoted by open circles while the quantum Monte Carlo results[58] are shown by solid circles. The agreement of these two methods is rather good. The iterated perturbation theory (IPT) is in contrast to the aforementioned methods (as the name suggests) a perturbative method which is less accurate but computationally less expensive.

The large variety of physical phenomena that the transition metal oxides show also includes magnetic and orbital ordering phenomena and also superconductivity. V_2O_3 , $LaTiO_3$ and the cuprates are examples which all show metal-insulator transitions, ferro- and antiferromagnetic order and superconductivity depending on external control parameters.

In the discussion of the metal-insulator transition above the possibility of long-range magnetic order has been ignored by confining the Hubbard model to the paramagnetic regime. As we have seen above in the strong coupling limit the physics of the half-filled Hubbard model is described by a quantum Heisenberg model with antiferromagnetic exchange coupling $J = -t^2/U$. Combining this insight with a more refined weak-coupling analysis one can infer that the ground state of the Hubbard model with nearest neighbour hopping at half-filling is always antiferromagnetic. The important condition is the nearest neighbour hopping which ensures that the HM shows a perfect nesting property $\epsilon(\mathbf{k}) = \epsilon(\mathbf{k} + \mathbf{Q})$ with $\mathbf{Q} = (\pi, \dots, \pi)^T$ which strongly favours ordered insulating ground states. Indeed if one allows for antiferromagnetic order in the DMFT one finds that the Neel transition from a metal to an antiferromagnetic

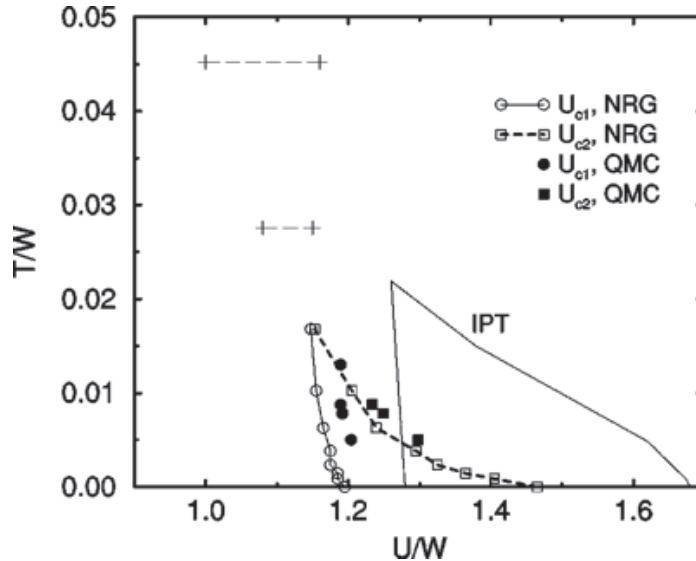


Figure 1.2: Results for the phase diagram of the Mott transition obtained from different methods: NRG (open symbols), quantum Monte Carlo (QMC, filled symbols), and iterated perturbation theory (IPT, solid lines). Taken from [9].

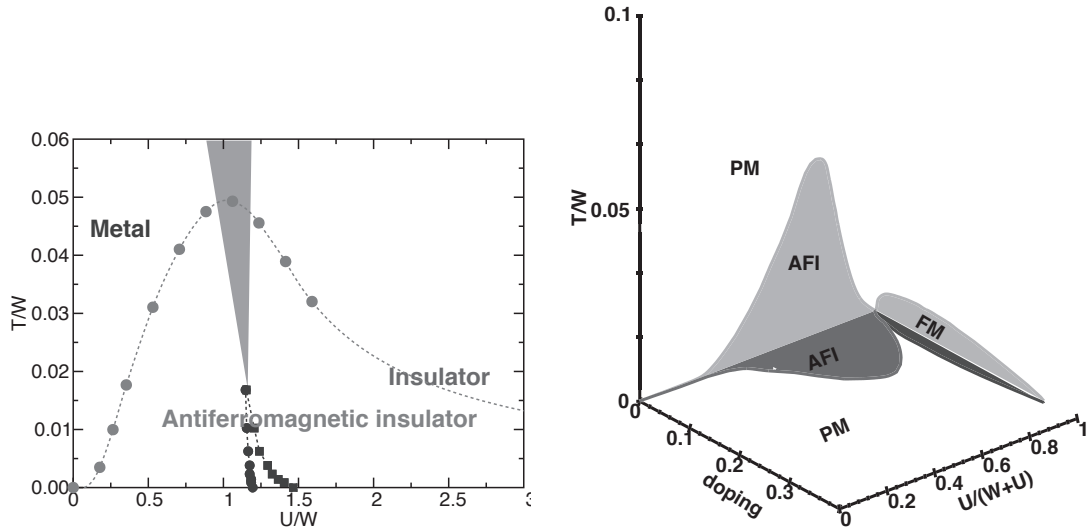
insulator always preempts the MHMIT transition. As can be seen from Fig. 1.3a, for any strength of the interaction parameter U the transition temperature T_c for the MHMIT lies below the Neel temperature T_N . This is however an artefact of the restriction to nearest-neighbour hopping. As shown by Zitzler et al.[118] the introduction of magnetic frustration by next-nearest neighbour hopping uncovers a region of a paramagnetic metal for small U . Fig. 1.3b shows a schematic of the magnetic phase diagram for the 3 control parameters temperature T , doping δ and interaction strength U . As already mentioned at half-filling the physics is dominated by an antiferromagnetic insulating phase. For finite doping $\delta > 0$ the antiferromagnetic phase persists up to a critical doping δ_c . Eventually for very large values of U , the antiferromagnetic phase is replaced by Nagaoka type ferromagnetism[75]².

1.2 Single impurity Anderson model

Instead of considering an ensemble of fully correlated lattice sites, in this section we concentrate on impurity models. Here only a few correlated sites exist within a given host lattice that consists of otherwise rather weakly correlated or free sites. Similarly to the case of the Hubbard model here we are again interested in the competition between itineracy and localisation.

When electrons localise they can form objects whose low energy excitations involve spin degrees of freedom. Such localised “magnetic moments” can be represented

²The conjecture due to Nagaoka is one of the few rigorous statements about itinerant ferromagnetism in the Hubbard model. Nagaoka considered a special case of the Hubbard model, in which the on-site interaction is infinite and there is exactly one hole, and showed that the unique ground state has the maximum total spin.



(a) DMFT phase diagram of the Hubbard model with nearest-neighbour hopping at half-filling on a hyper cubic lattice. Note that Neel transition preempts the MHI-MIT and completely covers it up. From Ref. [95].

(b) Schematic DMFT phase diagram of the Hubbard model on a hyper cubic lattice with nearest-neighbour hopping. PM denotes the paramagnetic phase, AFI antiferromagnetically ordered insulator and FM ferromagnetic order. From Ref. [95].

Figure 1.3

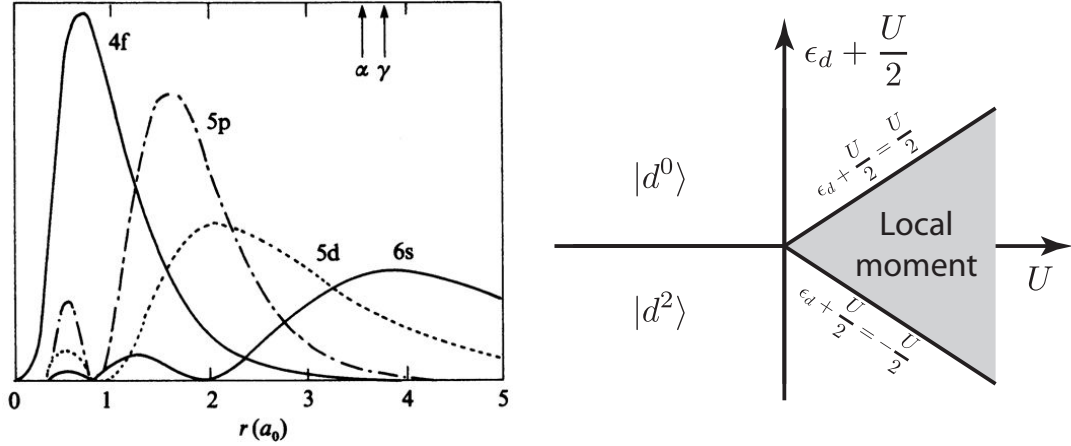
by a single spin operator \vec{S} . Localised moments usually develop in highly localised atomic orbitals such as the $4f$ shells of rare earth compounds[18], but also in the slightly more delocalised $3d$ levels of transition metal oxides. They are the origin of the so-called “Kondo effect” in metals which greatly alters the nature of the metallic state. A theoretical understanding of the quantum mechanical origin of local moment formation was not developed until experimentalists started to systematically study impurities in metals in the 60s. Detailed studies of magnetic iron impurities in copper showed that the magnetic susceptibility develops a Curie component indicating the formation of a local moment.

In 1961, motivated by these experiments P.W. Anderson identified interactions between localised electrons as the driving force behind local moment formation. The essential physics can be understood from a single spin- $\frac{1}{2}$ state which we refer to as the localised “d”-state. The Hamiltonian of the Anderson model comprises three parts. We will refer to the part describing the isolated “d” state including a Coulomb interaction term as H_d .

$$H_d = \epsilon_d \sum_{\sigma} n_{d\sigma} + U n_{d\uparrow} n_{d\downarrow} \quad (1.25)$$

Here the first part describes an isolated atomic d-state of energy ϵ_d and occupancy $n_{d\sigma}$. The second term accounts for the inter-atomic interaction due to the Coulomb repulsion between the up- and down-state. The host metal is modelled as a sea of free conduction electrons

$$H_c = \sum_{\mathbf{k}\sigma} \epsilon_{\mathbf{k}} c_{\mathbf{k}\sigma}^{\dagger} c_{\mathbf{k}\sigma} \quad (1.26)$$



(a) Wave functions of Ce in local density functional calculations. The $4f$ states are seen to be localised largely within the $5s$, $5p$ core and well within the Wigner-Seitz radius for α - and γ - Ce (indicated by arrows.). Taken from [49].

(b) Phase diagram for the Anderson impurity model in the atomic limit. Based on [18].

Figure 1.4

where the dispersion relation $\epsilon_{\mathbf{k}}$ of the conduction electrons surrounding the impurity site is determined by the lattice type and $c_{\mathbf{k}\sigma}^\dagger$ creates a conduction electron of momentum \mathbf{k} , spin σ and energy $\epsilon_{\mathbf{k}}$. When the impurity is embedded into the host metal the d -state starts to hybridise with conduction electrons which is modelled via the mixing term

$$H_{\text{mix}} = \sum_{\mathbf{k}\sigma} \left(V_{\mathbf{k}} c_{\mathbf{k}\sigma}^\dagger d_\sigma + V_{\mathbf{k}}^* d_\sigma^\dagger c_{\mathbf{k}\sigma} \right) \quad (1.27)$$

where d_σ^\dagger creates a electron on the impurity site with spin σ . The hybridisation matrix element $V_{\mathbf{k}}$ is determined by the overlap of the localised atomic wave function with the one of the conduction electrons and given by[49]

$$V_{\mathbf{k}} = \sum_i e^{i\mathbf{k}\cdot\mathbf{r}_i} \langle \phi_d | V_0 | \Psi_{\mathbf{r}_i} \rangle \quad (1.28)$$

where ϕ_d is the atomic d -state wave function, V_0 the ionic potential and $\Psi_{\mathbf{r}_i}$ the Wannier function of the conduction electron located at site \mathbf{r}_i . In summary the Hamiltonian of the Anderson impurity model (AIM) can be written in the mixed basis as

$$H_{\text{SIAM}} = \sum_{\mathbf{k}\sigma} \epsilon_{\mathbf{k}} c_{\mathbf{k}\sigma}^\dagger c_{\mathbf{k}\sigma} + \epsilon_d \sum_{\sigma} n_{d\sigma} + U n_{d\uparrow} n_{d\downarrow} + \sum_{\mathbf{k}\sigma} \left(V_{\mathbf{k}} c_{\mathbf{k}\sigma}^\dagger d_\sigma + V_{\mathbf{k}}^* d_\sigma^\dagger c_{\mathbf{k}\sigma} \right) \quad (1.29)$$

In comparison with the Hubbard model, although the Anderson impurity model describes a physical system which differs in many ways, the two are essentially representatives of the same paradigm: the competition between itineracy and localisation.

In the AIM the itineracy is represented by the delocalised conduction electrons H_c , while the localising tendencies are found in the isolated d-state H_d . The competition between the two is introduced into the model via the hybridisation H_{mix} through the coupling $V_{\mathbf{k}}$.

The physics described by the AIM is most easily understood by first concentrating on the atomic part of the Hamiltonian, H_d . The four states of the impurity and their respective energies are given by

state	energy
$ d^0\rangle$	0
$ d^2\rangle$	$2\epsilon_d + U$
$ d^1_\uparrow\rangle$ or $ d^1_\downarrow\rangle$	ϵ_d

where the superscript indicates the total occupancy of the impurity site. To obtain a magnetic doublet as the ground state the following inequalities have to be fulfilled

$$\begin{aligned} E(|d^2\rangle) - E(|d^1\rangle) &= \epsilon_d + U > 0 \Rightarrow \epsilon_d + U/2 > -U/2 \\ E(|d^0\rangle) - E(|d^1\rangle) &= -\epsilon_d > 0 \Rightarrow U/2 > \epsilon_d + U/2 \end{aligned} \quad (1.30)$$

so that $U/2 > |\epsilon_d + U/2|$. The phase diagram of the AIM in the atomic limit, Fig. 1.4b, summarises the inequality graphically. We see that for a sufficiently strong Coulomb interaction compared to the level spacing, the ground state indeed becomes magnetic. The excitation spectrum will involve two sharp resonances at ϵ_d and $\epsilon_d + U$.

If we now embed this atomic site into a host metal, i.e. turn on the coupling $V_{\mathbf{k}}$, the d-level will hybridise with the conduction electrons broadening the sharp δ -resonances into resonances with a finite width $\Delta(\epsilon)$, where $\Delta(\epsilon)$ is given Fermi's golden rule[18]

$$\Delta(\epsilon) = \pi \sum_{\mathbf{k}} |V_{\mathbf{k}}|^2 \delta(\epsilon_{\mathbf{k}} - \epsilon) \quad (1.31)$$

When the hybridisation is small one may regard it as a weak perturbation around the atomic limit as long as we ignore spin fluctuations which lead to the emergence of the Kondo effect as we will see in the following chapters. The ground state of the system will be essentially that of the atomic limit. For weak U the hybridisation with the conduction electron sea will produce a single d -resonance at ϵ_d of width $\Delta(\epsilon_d)$. In Anderson's model for moment formation the resonance peak splits up for interaction strengths U in excess of a critical $U_c \approx \pi\Delta$ into two d resonances centred around ϵ_d and $\epsilon_d + U$.

This is the essence of Anderson's mean-field theory for local moment formation. The physics by which the local moment is quenched at low temperatures however requires a more refined treatment of the model and is termed the "Kondo"-effect after the Japanese physicist Jun Kondo. To make this introductory section as short as possible we stop here and return to this interesting point in chapter 4.

Chapter 2

Itinerant electron magnetism in the Hubbard model

The Hubbard model was invented by John Hubbard (1931 - 1980) with the intention of explaining itinerant electron magnetism, primarily the ferromagnetism of *Fe*, *Co* and *Ni*. The initial success led to the hope that all major correlation phenomena ranging from (anti-)ferromagnetism, incommensurate magnetic structures, metal-insulator transitions and even high- T superconductivity may be understood from this simple model [29].

Although the Hubbard model is far from a realistic model for actual materials, the driving forces of the ordering transition may be understood from it nonetheless. Therefore the Hubbard model gives a good basis for understanding the anti-ferromagnetism, most prominently the anti-ferromagnetism of Mott insulators. The Hubbard model supports different phases of magnetic ordering. The normal metallic phase without magnetic ordering is referred to as *paramagnetic* (PM) and characterised by up- and down-spins on all sites and no ordering except for local correlations. The spin-spin correlator falls off exponentially with distance. Therefore only short-ranged order in the spin alignments is found. The *ferromagnetic* (F) phase is characterised by a net magnetic moment along a particular direction, while the *antiferromagnetic* (AF) ordering has an equal number of spin up and down conduction electrons, however the spin alignments show both short range and long range order.

2.1 Spin susceptibility

A convenient way to test whether the Hubbard model shows an instability towards a certain magnetic order is to calculate the \vec{q} -dependent spin susceptibility. Instabilities are signalled by a divergent response to an external magnetic field with a specific wave-vector \vec{q} . In the following we present a mean-field derivation of the magnetic susceptibility for the Hubbard model. For a more detailed presentation the interested reader is referred to Ref. [29].

We consider the following Hamiltonian

$$H = H_{\text{hub}} + H_{\text{field}} \tag{2.1}$$

where H_{hub} is the Hamiltonian of the Hubbard model, Eq. 1.4, and H_{field} describes the coupling of the spins to an external magnetic field. H_{field} is given by

$$H_{\text{field}} = -g\mu_B \int d\mathbf{r} \vec{S}(\mathbf{r}) \cdot \mathbf{H}_{\mathbf{q}} \cos(\mathbf{q} \cdot \mathbf{r}) \quad (2.2)$$

$$= -\frac{g\mu_B}{2} \left[\vec{S}(\mathbf{q}) + \vec{S}(-\mathbf{q}) \right] \cdot \mathbf{H}_{\mathbf{q}} \quad (2.3)$$

where g is the Landé factor, μ_B the Bohr magneton and $\mathbf{H}_{\mathbf{q}}$ the \mathbf{q} -component of the external magnetic field when expanded into Fourier components. The spin operator $\vec{S}(\mathbf{q})$ may be expressed by fermion operators as

$$\vec{S}(\mathbf{q}) = \frac{1}{2} \sum_{\mathbf{p}} \sum_{\alpha, \beta} c_{\mathbf{p}+\mathbf{q}, \alpha}^\dagger \vec{\sigma}_{\alpha\beta} c_{\mathbf{p}, \beta}. \quad (2.4)$$

where σ is the vector of Pauli matrices. The Hubbard model possesses a $SU(2)$ spin-rotational symmetry, therefore the spin susceptibility we are interested in must be isotropic. We may thus choose the magnetic field to point along the x -direction without loss of generality,

$$H_{\text{field}} = -\frac{g\mu_B}{2} (S^x(\mathbf{q}) + S^x(-\mathbf{q})) H_{\mathbf{q}}^x. \quad (2.5)$$

Now we turn to the interaction part of the Hubbard Hamiltonian $H_{\text{hub}} = H_0 + H_U$. Using the identities

$$\begin{aligned} \hat{n}_{j\uparrow} \hat{n}_{j\downarrow} &= \hat{n}_{j\uparrow} - S_j^+ S_j^- \\ \hat{n}_{j\downarrow} \hat{n}_{j\uparrow} &= \hat{n}_{j\downarrow} - S_j^- S_j^+ \end{aligned} \quad (2.6)$$

we may rewrite H_U as

$$H_U = \frac{U}{2} \hat{N} - U \sum_j ((S_j^x)^2 + (S_j^y)^2). \quad (2.7)$$

where we used $\hat{N} = \sum_j (\hat{n}_{j\uparrow} + \hat{n}_{j\downarrow})$ and $S^\pm = S^x \pm S^y$. Under the assumption that both the perturbing field $H_{\mathbf{q}}$ and the interaction strength U is small we may make a mean-field type decoupling of the form [29]

$$(S_j^x)^2 \approx 2 \langle S_j^x \rangle S_j^x - \langle S_j^x \rangle^2 \quad (2.8)$$

It is the external field which causes finite expectation values of these averages. The only non-vanishing average is due to the spin density wave induced by the external magnetic field and therefore only $\langle S_j^x \rangle$ is finite and of the form

$$\langle S_j^x \rangle = S \cos(\mathbf{q} \cdot \mathbf{j}). \quad (2.9)$$

We may use this approximation now to replace the interaction term H_U by a mean-field approximation quadratic in the fermion operators and linear in the spin expectation value S . Noticing that

$$\begin{aligned} 2 \sum_j \langle S_j^x \rangle S_j^x &= \sum_j S (e^{i\mathbf{q} \cdot \mathbf{j}} + e^{-i\mathbf{q} \cdot \mathbf{j}}) S_j^x \\ &= S (S^x(\mathbf{q}) + S^x(-\mathbf{q})) \end{aligned} \quad (2.10)$$

we may rewrite $H_U + H_{\text{field}}$ as

$$H_U + H_{\text{field}} = - \left(\frac{g\mu_B H^x}{2} + US \right) (S^x(\mathbf{q}) + S^x(-\mathbf{q})) \quad (2.11)$$

Assuming that the spin density S is small, $S \ll 1$, we may regard $H' = H_U + H_{\text{field}}$ as a weak perturbation to the free fermion system H_0 . We wish to calculate the expectation value of $\langle S^x(\mathbf{q}) \rangle$ to find a linear dependence on the external magnetic field H^x and thereby identify the magnetic susceptibility $\chi(\mathbf{q})$.

The ground state of H_0 is given by the filled Fermi sea, $|FS\rangle$. The energy correction to first order in H' vanishes, since the expectation value of spin-flip-type operators, i.e. $c_{\uparrow}^{\dagger}c_{\downarrow}$ etc., with the eigenstates of H_0 vanishes. We calculate therefore the first order correction to the ground state to find the magnetisation along the x -axis. The formula of first order perturbation theory gives for the perturbed ground state [29]

$$|\Psi'\rangle = |FS\rangle - \left(\frac{g\mu_B H^x}{2} + US \right) \sum_{\mathbf{p}\sigma} \left[\frac{c_{\mathbf{p}+\mathbf{q}\sigma}^{\dagger}c_{\mathbf{p}-\sigma}}{\epsilon_{\mathbf{p}} - \epsilon_{\mathbf{p}+\mathbf{q}}} + \frac{c_{\mathbf{p}-\mathbf{q}\sigma}^{\dagger}c_{\mathbf{p}-\sigma}}{\epsilon_{\mathbf{p}} - \epsilon_{\mathbf{p}-\mathbf{q}}} \right] |FS\rangle \quad (2.12)$$

Since this state is the Fermi sea with particle-hole pairs of momentum \mathbf{q} and $-\mathbf{q}$ superimposed the only contributions to expectation values of operators of the form $c_{\mathbf{p}+\mathbf{q}\sigma}^{\dagger}c_{\mathbf{p}-\sigma}$ comes from states with \mathbf{p} below the Fermi surface and $\mathbf{p} + \mathbf{q}$ above it, or vice versa. Using the orthogonality of the particle-hole superimposed state to the original ground state $|FS\rangle$ we find

$$\langle \Psi' | c_{\mathbf{p}+\mathbf{q}\sigma}^{\dagger}c_{\mathbf{p}-\sigma} | \Psi' \rangle = \left(\frac{g\mu_B H^x}{2} + US \right) \frac{f_{\mathbf{p}} - f_{\mathbf{p}+\mathbf{q}}}{\epsilon_{\mathbf{p}} - \epsilon_{\mathbf{p}+\mathbf{q}}} \quad (2.13)$$

where $f_{\mathbf{p}} = \Theta(\epsilon_F - \epsilon_{\mathbf{p}})$. The above results can be applied to the calculation of the spin expectation value. For the x -component we find

$$\langle \Psi' | S^x(\mathbf{q}) | \Psi' \rangle = \left(\frac{g\mu_B H^x}{2} + US \right) \chi^{(0)}(\mathbf{q}) \quad (2.14)$$

where we have defined the magnetic susceptibility function

$$\chi^{(0)}(\mathbf{q}) = \sum_{\mathbf{p}} \frac{f_{\mathbf{p}} - f_{\mathbf{p}+\mathbf{q}}}{\epsilon_{\mathbf{p}+\mathbf{q}} - \epsilon_{\mathbf{p}}}. \quad (2.15)$$

Although we have performed a $T = 0$ calculation the above result can be easily extended to the case of finite T . In this case $f_{\mathbf{p}}$ becomes the Fermi distribution. Self-consistency requires $\langle \Psi' | S^x(\mathbf{q}) | \Psi' \rangle = S$ which finally leads to

$$\chi(\mathbf{q}) = (g\mu_B)^2 \frac{\chi^{(0)}(\mathbf{q})}{1 - U\chi^{(0)}(\mathbf{q})} \quad (2.16)$$

This expression is the RPA susceptibility familiar from the calculation of the polarisation. $\chi(\mathbf{q})$ differs from the non-interacting susceptibility $\chi^{(0)}(\mathbf{q})$ by an enhancement factor.

In order to find wave-vectors which signal an instability of the system towards a specific magnetic ordering we are looking for divergencies of the generalised susceptibility $\chi(\mathbf{q})$. The denominator vanishes when

$$U \chi^{(0)}(\mathbf{q}) = 1 \quad (2.17)$$

which is the so-called generalised Stoner criterion. In the present case we are interested in the Hubbard model on the simple cubic lattice with nearest neighbour hopping in d spatial dimensions. The dispersion relation is given by

$$\epsilon(\mathbf{k}) = -2t \sum_{i=1}^d \cos(k_i) . \quad (2.18)$$

For this type of lattice a *perfect nesting condition* is satisfied by the spanning vector \mathbf{Q}

$$\epsilon(\mathbf{k} + \mathbf{Q}) = -\epsilon(\mathbf{k}), \quad \forall \mathbf{k} \quad (2.19)$$

where $\mathbf{Q} = (\pi, \pi, \dots, \pi)$. At half-filling $\epsilon_F = 0$ and $T = 0$ the susceptibility function, Eq. 2.15, can be written as

$$\begin{aligned} \chi^{(0)}(\mathbf{Q}) &= \sum_{\mathbf{p}} \frac{f_{\mathbf{p}} - f_{\mathbf{p}+\mathbf{Q}}}{\epsilon_{\mathbf{p}+\mathbf{Q}} - \epsilon_{\mathbf{p}}} \\ &= \sum_{\mathbf{p}} \frac{f_{\mathbf{p}}}{-2\epsilon_{\mathbf{p}}} \\ &\stackrel{T=0}{=} \int_0^{D/2} \frac{\rho(\epsilon)}{2\epsilon} \end{aligned} \quad (2.20)$$

$\chi^{(0)}(\mathbf{q})$ diverges logarithmically unless $\rho(\epsilon) \rightarrow 0$ as $\epsilon \rightarrow 0$. It follows that the critical interaction strength $U_c^{\mathbf{Q}}$ vanishes, $U_c^{\mathbf{Q}} = 0$. Thus for half-filled bands with a perfect nesting property the mean-field prediction is that arbitrary small interactions $U > 0$ cause a transition to a two-sublattice antiferromagnetic state.

The above statement assumes that the susceptibility for other $\mathbf{q} \neq \mathbf{Q}$ remains finite. If this is not the case we have a case of competing instabilities. Indeed for $d = 2$ the simple cubic lattice has a density of states which diverges logarithmically at $\epsilon = 0$ and causes in turn the generalised susceptibility $\chi(\mathbf{q} = 0)$ to diverge. We therefore have a competition between ferromagnetic and antiferromagnetic order. It turns out that the antiferromagnetic order prevails[29].

2.2 Antiferromagnetic order on the mean-field level

The antiferromagnetic order is the most robust kind of ordering for the Hubbard model. As the asymptotic model of strong coupling for the Hubbard model is the spin- $\frac{1}{2}$ quantum Heisenberg model, antiferromagnetic order is certainly expected for strong Hubbard U . On the d -dimensional simple cubic lattice the situation is special due to the perfect nesting property mentioned above. In the following we will see that the result is that for all $U > 0$ a magnetisation gap of finite size appears and antiferromagnetic order is present at the mean-field level.

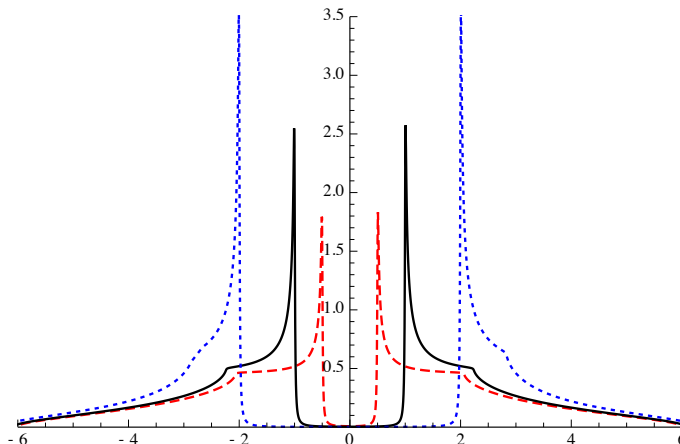


Figure 2.1: Imaginary part of the Green's function for different hybridisation strengths V : $V = 1$ (black, solid), $V = 0.5$ (red, dashed) and $V = 2$ (blue, dotted). Strong van Hove-singularities can be seen at the inner band edges. The dispersion relation is chosen to be $\epsilon_{\mathbf{k}}^{(c)} = -\epsilon_{\mathbf{k}}^{(d)} = -\cos(k)$ to give a hybridisation between particle- and hole-like degrees of freedom; see main text.

2.2.1 Origin of the magnetisation gap

Gaps in electronic spectra are common-place in condensed matter physics and many different mechanism exists which can give rise them. A trivial origin is the periodic arrangement of the ions in a solid, which causes a periodic potential which breaks translational invariance. However there are also intrinsic properties which may cause the appearance of a gap. In many of them the gap can be understood from the hybridisation of electrons with other degrees of freedom. As shown below the anti-ferromagnetic gap is one of these cases.

We start with a brief reminder on hybridisation gaps. Consider the following Hamiltonian

$$H = \sum_{\mathbf{k}} \epsilon_{\mathbf{k}}^{(c)} c_{\mathbf{k}}^{\dagger} c_{\mathbf{k}} + \epsilon_{\mathbf{k}}^{(d)} d_{\mathbf{k}}^{\dagger} d_{\mathbf{k}} + (V_{\mathbf{k}} c_{\mathbf{k}}^{\dagger} d_{\mathbf{k}} + h.c.) \quad (2.21)$$

where two different types of particles $c_{\mathbf{k}}^{\dagger}$ and $d_{\mathbf{k}}^{\dagger}$ hybridise with strength $V_{\mathbf{k}}$. The imaginary part of the Green's function for the c -electrons is easily found

$$\text{Im}[G(\mathbf{k}, \omega)] = \frac{-\omega + \epsilon_{\mathbf{k}}^{(c)}}{V_{\mathbf{k}}^2 - (\omega - \epsilon_{\mathbf{k}}^{(c)})(\omega - \epsilon_{\mathbf{k}}^{(d)})} \quad (2.22)$$

Two poles appear in the Green's function located at

$$w = \frac{\epsilon_{\mathbf{k}}^{(c)} + \epsilon_{\mathbf{k}}^{(d)}}{2} \pm \sqrt{V_{\mathbf{k}}^2 + \left(\frac{\epsilon_{\mathbf{k}}^{(c)} - \epsilon_{\mathbf{k}}^{(d)}}{2}\right)^2} \quad (2.23)$$

For simplicity let us assume that $\epsilon_{\mathbf{k}}^{(c)} = \sigma \epsilon_{\mathbf{k}}^{(d)}$ with $\sigma = \pm 1$ and $V_{\mathbf{k}} = V$. The positive sign corresponds to two particle-like degrees of freedom hybridising, the negative sign to hybridisation between electrons and holes.

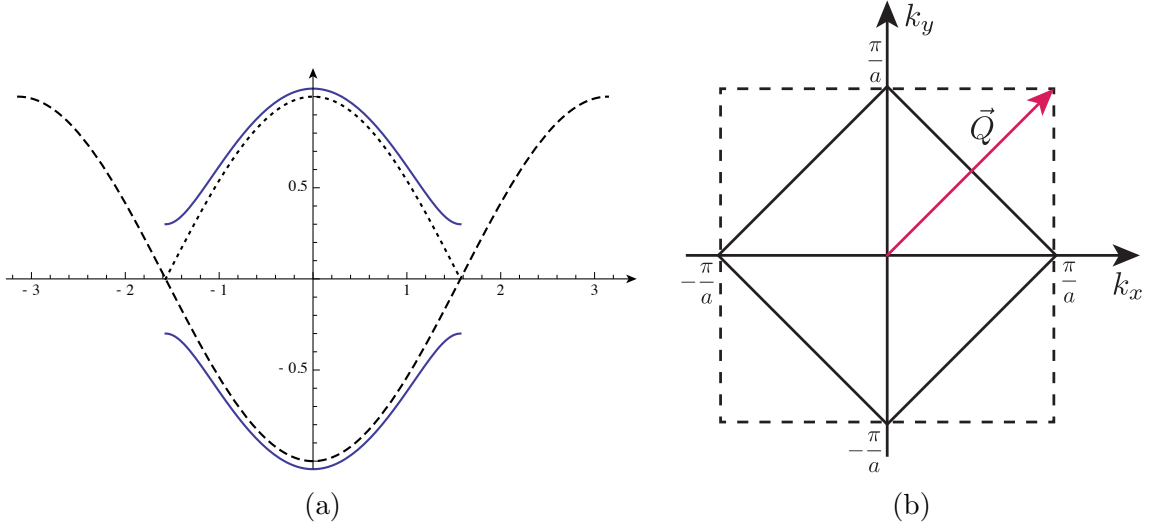


Figure 2.2

- $\sigma = 1$: From (2.23) it is immediately clear that the poles appear at $\omega = \epsilon_{\mathbf{k}} \pm V$. Therefore if the bandwidth of the dispersion D is greater than V a region of width $|D - V|$ exists around the Fermi surface that they do not enter. Consequently a gap of width $2(D - V)$ appears in the local Green's function $G(\omega) = \sum_{\mathbf{k}} G(\mathbf{k}, \omega)$ at the Fermi surface.
- $\sigma = -1$: Here the poles appear at $\omega = \pm \sqrt{V^2 + \epsilon_{\mathbf{k}}^2}$. As soon as $V > 0$ a region of width $2V$ appears that is free of poles. Therefore $\forall V > 0$ a gap opens in the local lattice Green's function, c.f. Fig. 2.1.

The logic of the above argument directly carries over to the case of antiferromagnetic order. We will work on the simple cubic lattice in three spatial dimensions which is a bipartite lattice so that we have simple AB-sublattice anti-ferromagnetism. Without loss of generality we assume that the magnetic order arises from spin- \uparrow electrons being the majority spin species on the A-sites and spin- \downarrow on the B-sites. Symmetry considerations tell us that

$$\langle \hat{n}_{A\sigma} \rangle = \langle \hat{n}_{B\bar{\sigma}} \rangle \quad (2.24)$$

which means the expectation value of the particle number operator can be written as

$$\langle \hat{n}_{i\sigma} \rangle = \frac{n}{2} + (-1)^\sigma m e^{i\mathbf{Q} \cdot \mathbf{r}_i} \quad (2.25)$$

with $n = \langle \hat{n}_{i\uparrow} \rangle + \langle \hat{n}_{i\downarrow} \rangle$ and m the sublattice spin polarisation $m = \frac{1}{2}(n_{i\uparrow} - n_{i\downarrow})e^{i\mathbf{Q} \cdot \mathbf{r}_i}$.

Performing the usual mean-field decoupling $\hat{n}_{j\uparrow}\hat{n}_{j\downarrow} \rightarrow \sum_{\sigma} \hat{n}_{j\sigma} \langle \hat{n}_{j\bar{\sigma}} \rangle - \langle \hat{n}_{j\uparrow} \rangle \langle \hat{n}_{j\downarrow} \rangle$ we see that i.e. spin- \uparrow electrons see a superposition of the lattice potential plus an average field $U \langle \hat{n}_{j\downarrow} \rangle$. The additional field enlarges the periodicity of the potential landscape from a to $2a$. Therefore the effective field has lower translational symmetry than the underlying lattice which halves the Brillouin zone. The states lying outside the new, magnetic Brillouin zone (MBZ) can be transported into the new Brillouin by application of a new reciprocal lattice vector $\pm \frac{\pi}{a}$, effectively splitting the formerly

single band into two (Fig. 2.2a). Defining new operators $d_{\mathbf{k}\sigma}^\dagger = c_{\mathbf{k}+\mathbf{Q}\sigma}^\dagger$ and $d_{\mathbf{k}\sigma} = c_{\mathbf{k}+\mathbf{Q}\sigma}$ the mean-field Hamiltonian may be written in the familiar form

$$H = \frac{2}{L} \sum_{\mathbf{k},\sigma}^{MBZ} \left(\frac{1}{2}Un + \epsilon_{\mathbf{k}} \right) c_{\mathbf{k}\sigma}^\dagger c_{\mathbf{k}\sigma} + \left(\frac{1}{2}Un - \epsilon_{\mathbf{k}} \right) d_{\mathbf{k}\sigma}^\dagger d_{\mathbf{k}\sigma} - (-1)^\sigma Um (c_{\mathbf{k}\sigma}^\dagger d_{\mathbf{k}\sigma} + h.c.) - U \sum_j \langle n_{j\uparrow} \rangle \langle n_{j\downarrow} \rangle \quad (2.26)$$

where we have used the perfect nesting property Eq. 2.19. We choose $\mu = \frac{1}{2}Un$ to push the model to the particle-hole symmetric point. Comparing with (2.21) we realise that this is just the case $\sigma = -1$ with $V = Um$. The term linear in the magnetisation m hybridises the particle-like $\epsilon_{\mathbf{k}}$ -band with the hole-like $\epsilon_{\mathbf{k}+\mathbf{Q}}$ -band. At half filling the enlarged magnetic unit cell contains two electrons completely filling the lower band while keeping the upper band unoccupied. From Fig. 2.2a we see that the appearance of a finite magnetisation pushed down the occupied band, while pushing up the unoccupied. This already hints at the energetical motivation for the symmetry breaking.

2.2.2 Gap equation and spectral functions

The Hamiltonian, Eq. (2.26), can be formally solved by diagonalisation. One finds for the eigenenergies of the state with momentum \mathbf{k}

$$\epsilon^\pm(\mathbf{k}) = \frac{Un}{2} \pm \sqrt{\epsilon_{\mathbf{k}}^2 + U^2m^2} - U \sum_j \langle n_{j\uparrow} \rangle \langle n_{j\downarrow} \rangle \quad (2.27)$$

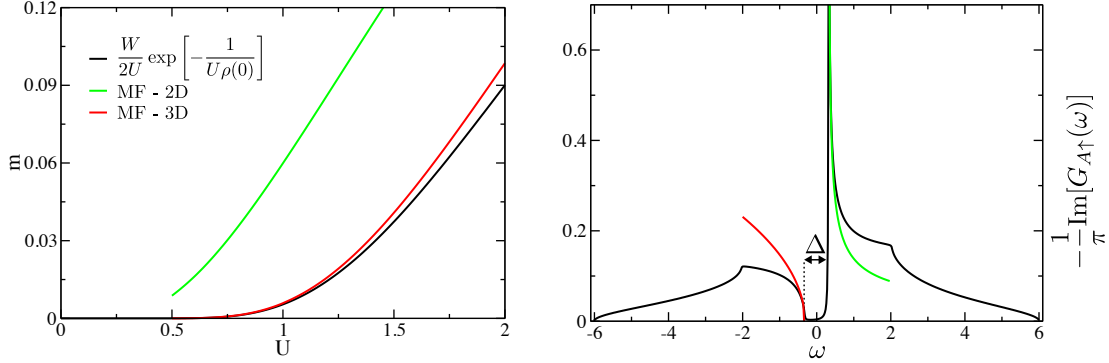
The ground state energy of the system can be obtained by summing over the occupied states. At $T = 0$ and half-filling the lower band in Fig. 2.2a is completely occupied, therefore

$$\begin{aligned} E &= \sum_{\mathbf{k}}^{MBZ} \left[\frac{Un}{2} - \sqrt{\epsilon_{\mathbf{k}}^2 + U^2m^2} \right] - U \sum_j \langle n_{j\uparrow} \rangle \langle n_{j\downarrow} \rangle \\ &= U \left(\frac{n^2}{4} + m^2 \right) - \frac{2}{L} \sum_{\mathbf{k}}^{MBZ} \sqrt{\epsilon_{\mathbf{k}}^2 + U^2m^2} \end{aligned} \quad (2.28)$$

The gap equation is found by considering the above ground state energy as a function of the unknown parameter m and requiring that $E(m)$ is minimum, $\partial E/\partial m = 0$, with the non-trivial solution

$$1 = \frac{1}{L} \sum_{\mathbf{k}}^{MBZ} \frac{U}{\sqrt{\epsilon_{\mathbf{k}}^2 + U^2m^2}} \quad (2.29)$$

The term in the sum depends only through the dispersion $\epsilon_{\mathbf{k}}$ on the momentum \mathbf{k} which allows us to trade the sum over momenta for an integral over the non-interacting



(a) Sublattice spin polarisation m as a function of the interaction strength U for two (green line) and three (red line) spatial dimensions as obtained for static mean-field theory. The black shows the weak coupling result, Eq. 2.31, which is in good agreement with the mean-field prediction.

(b) Spectral function for $U = W/4$ as obtained by static mean-field theory. At the Fermi surface a gap of width $\Delta = 2Um$ opens. The red in green line depict the asymptotic at the edge of the gap, Eq. (2.33).

Figure 2.3

density of states

$$\begin{aligned}
 1 &= U \int_0^{W/2} d\epsilon \frac{\rho(\epsilon)}{\sqrt{\epsilon^2 + U^2 m^2}} \\
 &\approx U \rho(0) \int_0^{Um} d\epsilon \frac{1}{Um} + \int_{Um}^{W/2} d\epsilon \frac{\rho(\epsilon)}{\epsilon} \\
 &\approx U \rho(0) + U \rho(0) \ln \frac{W}{2Um}
 \end{aligned} \tag{2.30}$$

where W is the bandwidth and we assumed in the first line that $\rho(\epsilon) = \rho(-\epsilon)$. Approximating the density of states by its value at the Fermi level is only valid if $\rho(0)$ is finite. This is not the case for $d = 2$. For $U \ll W$ we expect a small magnetisation m and the above approximation should hold. The small U dependence of the magnetisation is thus

$$m \approx \frac{W}{2U} \exp \left[-\frac{1}{U \rho(0)} \right] \tag{2.31}$$

Fig. 2.3b shows the magnetisation as a function of the local Coulomb interaction U as obtained from a self-consistent solution of the mean-field equations. The green line shows the result for two spatial dimensions. For three spatial dimensions (red line) the mean-field result is compared to the weak-coupling approximation, Eq. 2.31, and good agreement is found.

A quantity of great interest is the single-particle spectral function. The structure of the local Green's function in mean-field approximation is given by[95]

$$G_{\uparrow}(\omega) = \frac{\xi_{\downarrow}(\omega)}{\sqrt{\xi_{\uparrow}(\omega)\xi_{\downarrow}(\omega)}} \int_{-\infty}^{\infty} d\epsilon \frac{\rho(\epsilon)}{\sqrt{\xi_{\uparrow}(\epsilon)\xi_{\downarrow}(\epsilon)} - \epsilon} \tag{2.32}$$

where $\rho(\epsilon)$ denotes the non-interacting density of states and $\xi_\sigma(\omega) = \omega + i0^+ + \mu - \frac{U}{2}n + \sigma Um$. With $\omega_\pm = \frac{U}{2}n - \mu \pm Um$ both radiants are positive for $\omega < \omega_-$ and $\omega > \omega_+$. For particle-hole symmetric densities of states the imaginary part of Eq. (2.32) vanishes for $\omega_- < \omega < \omega_+$. Therefore a region of width $\Delta = 2Um$ exists which holds no spectral weight. For ω close to the gap edges one finds[95]

$$-\frac{1}{\pi}\text{Im}G_{A\uparrow}(\omega) = \begin{cases} \sqrt{\frac{Um}{|\omega-\omega_-|}}\rho(0) & \omega \nearrow \omega_- \\ \sqrt{\frac{|\omega-\omega_+|}{Um}}\rho(0) & \omega \searrow \omega_- \end{cases} \quad (2.33)$$

Fig. 2.3b shows a spectral function as obtained from mean-field theory. As expected a region of width $\Delta = 2Um$ exists which holds no spectral weight. The asymptotic, Eq. 2.33, are depicted as red and green lines in Fig. 2.3b and fit the mean-field solution very well.

Part II
Methods

Chapter 3

Dynamical Mean-Field Theory

Materials with strongly correlated electrons exhibit some of the most intriguing phenomena encountered in condensed matter physics. The theoretical description of such systems is among the most challenging of problems in the material sciences. The Dynamical Mean-Field theory (DMFT) provides an extensive and controlled framework for the study of such correlation phenomena. In this chapter we review the justification and construction of the DMFT. Detailed accounts can be found in Refs. [37, 62, 26, 52].

In materials with open d - and f -shells electrons occupy narrow orbitals and experience strong Coulomb repulsion due to their spatial confinement. The typical approach for the description of simple metals where the influence of the surrounding particles on a particular electron is modelled through self consistently determined, static mean-fields fails in these situations where the motion of each electron is strongly correlated with those of the others. A variety of numerical and analytical techniques have to been used to treat the physics of strongly correlated electron systems. The DMFT is one of these methods and, at the same time, stands out as a method which is both numerically tractable and flexible enough to allow theorists to incorporate material-specific details into the calculations[26].

The effects of correlations often makes materials extremely sensitive to small changes in external parameters, such as temperature, pressure and doping. The variety of phenomena ranges from strong changes in the electrical resistivity in metal-insulator transitions (vanadium oxide), through substantial volume changes (actinides and lanthanides) to remarkably high transition temperatures in the superconducting cuprates[62]. In materials termed “heavy fermion systems” mobile electrons behave at low temperatures as if their mass was a thousand times the mass of a free electron in a simple metal[52]. Other materials show great sensitivity in their electrical resistivity to changes in an applied magnet field resulting in “colossal magnetoresistance”[97]. Such properties spark the hope for exciting applications of strongly correlated electron physics. The theoretical description of these effects which often rely on microscopic details is however especially challenging.

The failure of band theory for strongly correlated materials was first noticed in the description of nickel- and manganese oxide. Both materials have a relatively low magnetic ordering temperature but large insulating gaps[62]. In parameter regimes where magnetic long-range order is absent band theory erroneously predicts these materials

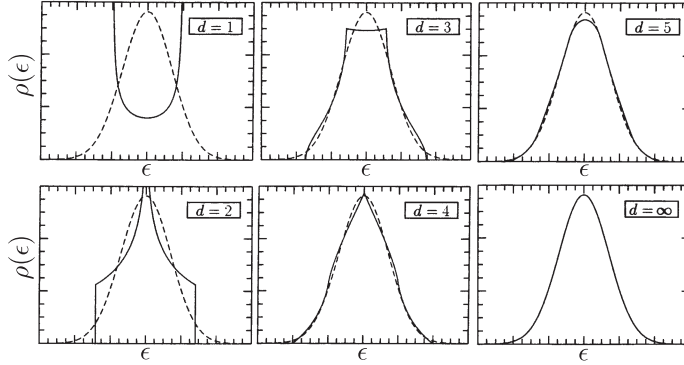


Figure 3.1: Tight-binding density of states in $d=1,2,3,4,5$ as compared with the result for $d = \infty$. Taken from Ref. [110].

to be metallic. Neville Mott showed that instead of understanding these materials from the perspective of delocalised electrons as in density functional theory the more natural perspective is a simple, real-space picture[73]: adding and removing electrons from the partially filled shells results in excited atomic configurations. Scattering by the internal degrees of freedoms of the other electrons causes these excitations to propagate incoherently through the crystal and broaden them to form bands. In the Hubbard model they appear as the upper and lower Hubbard band. Understanding and especially modelling the metal-insulator transition in such a set-up where the character of the electrons changes from itinerant to fully localised as a function of the Coulomb interaction is however very difficult.

In a well defined limit the DMFT allows for a numerically exact solution of this problem. In addition this framework paves the way to a systematic extension of the method to more intricate and realistic systems. In this chapter we start with a review of the simplifications which arise in the infinite spatial dimension (or more generally infinite lattice connectivity) limit in section 3.1. A derivation of the DMFT method by means of the cavity method is presented in section 3.3. An alternative derivation due to Potthoff and Nolting is detailed in section 3.5.

3.1 Simplification from the $d \rightarrow \infty$ limit

The birth of DMFT can be identified with the discovery of simplifications in perturbation theory in the limit of infinite spatial dimensions due to Metzner and Vollhardt[72]. We start with a derivation of the asymptotic density of states for the simple cubic lattice in the limit of infinite spatial dimensions.

Different lattices give rise to different dispersion relations $\epsilon(\mathbf{k})$. For non-interacting particles with a Hamiltonian $H - \mu N = \sum_{\mathbf{k},\sigma} (\epsilon_{\mathbf{k}} - \mu) c_{\mathbf{k}\sigma}^\dagger c_{\mathbf{k}\sigma}$ the free Green's function and the free density of states are given by

$$G_{\mathbf{k}\sigma}^{(0)}(\omega) = \frac{1}{\omega - \epsilon_{\mathbf{k}} + \mu}, \quad \rho(\omega) = \frac{1}{L} \sum_{\mathbf{k}} \delta(\omega - \epsilon_{\mathbf{k}}) \quad (3.1)$$

For a simple cubic lattice the dispersion relation is given by $\epsilon(\mathbf{k}) = \sum_{j=1}^d \cos(k_j)$. An elegant way to determine the asymptotic density of states for $d \rightarrow \infty$ is to invoke the central limit theorem (CLT). The argument goes as follows. We consider the random variables $X_j = \sqrt{2} \cos(k_j)$ where k_j is distributed uniformly in the interval $k_j \in [-\pi, \dots, \pi]$ for each $j \in \{1, \dots, d\}$. The X_j have zero mean and unit variance $\text{Var}(X_j) = \int_{-\pi}^{\pi} \frac{dk_j}{2\pi} X_j^2 = 1$. The central limit theorem applies to the random variables X_j and states that the random variable $\mathcal{X}_d = \frac{1}{\sqrt{d}} \sum_{j=1}^d X_j$ converges in law in the $d \rightarrow \infty$ -limit to a normally distributed random variable \mathcal{X} with zero mean and unit variance. The distribution function of \mathcal{X} is therefore given by $f(\mathcal{X}) = \exp(-\mathcal{X}^2/2)/\sqrt{2\pi}$. The density of states can be regarded as the distribution function of the random variable $\sqrt{2dt}\mathcal{X}_d$ [26]. Consequently a finite density of states is only obtained in the $d \rightarrow \infty$ -limit if the hopping scales as $d^{-1/2}$. The resulting density of states is given by

$$\rho(\epsilon) = \frac{1}{2\pi t_*} \exp\left(-\frac{\epsilon^2}{2t_*^2}\right), \quad \text{with } t = \frac{t_*}{\sqrt{2d}}. \quad (3.2)$$

Fig. 3.1 summarises the $d \rightarrow \infty$ limit graphically. The evolution towards the Gaussian density of states can be clearly observed. Generalising from the case of nearest neighbour hopping on a simple cubic lattice in d spatial dimensions, each hopping t_n must be scaled proportional to $1/\sqrt{Z_n}$ where Z_n is the number of sites reachable by t_n .

For the simple cubic lattice the bandwidth diverges in the $d \rightarrow \infty$ -limit (there are counterexamples such as the Bethe lattice which converges to a semi-elliptic density of states with a finite bandwidth in the $Z \rightarrow \infty$ -limit). One might object that the infinite band edges are problematic for the application of the infinite-dimensional limit as an approximation to finite-dimensional lattices (with finite bandwidths). As we will see in the following the dispersion relation enters only through the density of states into the simplified expression for the local lattice Green's function. The practical solution will be to use the non-interacting density of states for the lattice dimension of interest in all of these expressions. The $d \rightarrow \infty$ limit also has consequences for the many body theory in particular for the self-energy as pointed out by Metzner and Vollhard[72]. In the following we study the d dependence of the non-local Green's function $G_{ij\sigma}$ and the effects on the self-energy expansion.

3.1.1 Locality of the self-energy

In the previous section we showed how the hopping strength t has to be rescaled in order to obtain a finite kinetic energy in the $d \rightarrow \infty$ -limit for the special case of the simple cubic lattice with nearest neighbour hopping. This result can be generalised in the following way. For arbitrary, generalised hopping amplitudes t_{ij} connecting lattice sites i and j , t_{ij} has to be rescaled according to[72]

$$t_{ij} = t_{ij}^* d^{-\frac{1}{2} \|\mathbf{r}_i - \mathbf{r}_j\|} \quad (3.3)$$

for the kinetic energy to be finite in the $d \rightarrow \infty$ -limit. Here t_{ij}^* is d independent and $\|\mathbf{r}_i - \mathbf{r}_j\|$ is the shortest number of lattice steps from \mathbf{r}_i to \mathbf{r}_j and therefore proportional

to the number of lattice sites connected by t_{ij} . The kinetic energy can be expressed through the Green's function

$$E_{\text{kin}} = \sum_{i,j} t_{ij} \langle c_{i\sigma}^\dagger c_{j\sigma} \rangle = \sum_{i,j} t_{ij} \int_{-\infty}^{\infty} \frac{d\omega}{2\pi} G_{ij\sigma}(\omega) e^{i\omega 0^+} \stackrel{!}{=} \mathcal{O}(d^0) \quad (3.4)$$

Since the double sum yields a contribution of order $d^{\|\mathbf{r}_i - \mathbf{r}_j\|}$ consequently the Green's function has to scale like

$$G_{ij\sigma}(\omega) = \mathcal{O}(d^{-\frac{1}{2}\|\mathbf{r}_i - \mathbf{r}_j\|}), \quad G_{ii\sigma}(\omega) = \mathcal{O}(d^0). \quad (3.5)$$

The Green's function decays rapidly with distance. This has important implications for example for the perturbative, self-consistent skeleton expansion of the Green's function.

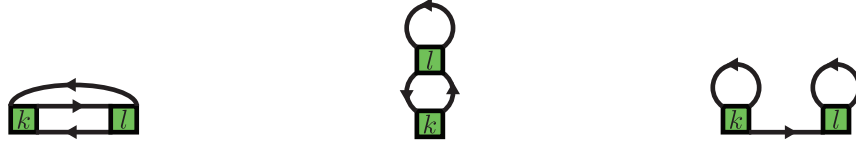
Here we concentrate on the essential argument which leads to a substantial reduction in the complexity of the self-energy for the Hubbard model in the limit of infinite spatial dimensions. For a more detailed account the interested reader is referred to the original paper by Metzner and Vollhardt[72] and to the review article about the dynamical mean field theory by Georges et al. [37]. Metzner and Vollhardt's result for the Hubbard model was later generalised by E. Müller-Hartmann who showed that the simplification is not restricted to Gaussian density of states. He found that also in more general models interactions between particles on different sites are shown to simplify to their Hartree substitute in the limit of large lattice coordination [74].

To make the description as transparent as possible we limit ourselves, for the most part, to the presentation of the perturbative series in its diagrammatic representation. A more rigorous account can be found in the two referenced sources. Separating the Hamiltonian for the Hubbard model $H = H_0 + H_U$ into a free (H_0) and an interacting part (H_U) one can write down a perturbative series in H_U for the Green's function of the system. We agree on the following diagrammatic code

$$\begin{aligned} G_{ij\sigma}^{(0)}(\omega) &= \overset{\sigma}{\overrightarrow{i} \text{---} j} \\ G_{ij\sigma}(\omega) &= \overset{\sigma}{\overleftrightarrow{i} \text{---} j} \\ U c_{i\sigma}^\dagger c_{i\sigma} c_{i\bar{\sigma}}^\dagger c_{i\bar{\sigma}} &= \begin{array}{c} \sigma \\ \swarrow \quad \searrow \\ \boxed{i} \\ \nwarrow \quad \nearrow \\ \bar{\sigma} \end{array} \end{aligned}$$

The perturbation expansion in H_U for the non-local Green's function $G_{ij\sigma}(\omega)$ from the lattice site i to j then yields a sequence of diagrams of which the lowest orders in H_U are given by

$$\overset{\sigma}{\overleftrightarrow{i} \text{---} j} = \overset{\sigma}{\overrightarrow{i} \text{---} j} + \overset{\sigma}{\overrightarrow{i} \text{---} \boxed{k} \text{---} j} + \overset{\sigma}{\overrightarrow{i} \text{---} \boxed{k} \text{---} \overrightarrow{j} \text{---} i} + \overset{\sigma}{\overrightarrow{i} \text{---} \boxed{k} \text{---} \overrightarrow{j} \text{---} i} + \overset{\sigma}{\overrightarrow{i} \text{---} \boxed{k} \text{---} \overrightarrow{j} \text{---} i} + \overset{\sigma}{\overrightarrow{i} \text{---} \boxed{k} \text{---} \overrightarrow{j} \text{---} i} + \dots \quad (3.6)$$



(a) one-particle irreducible (b) one-particle irreducible (c) one-particle reducible

Figure 3.2: Exemplary diagrams illustrating the concept of “one-particle irreducibility”.

Here summation over internal indices is assumed and we have suppressed the spin quantum number to avoid clutter in the notation. It is fairly obvious that many of the diagrams involve repeating structures. These can be efficiently resummed through the introduction of a “one-particle irreducible” self energy. For this we define the sum of those diagrams which cannot be cut into two pieces by cutting a single solid line as the self-energy Σ . Fig. 3.2 illustrates the concept. Three cuts are needed to separate Fig. 3.2a into two pieces, two for Fig. 3.2b and one for Fig. 3.2c. Therefore Fig. 3.2a and Fig. 3.2b are one-particle irreducible while Fig. 3.2c is not. The diagrams building the self energy are to lowest order in H_U given by

$$\textcircled{\Sigma}_{ij} = \text{diagram (a)} \delta_{ij} + \text{diagram (b)} \delta_{ij} + \text{diagram (c)} + \dots \quad (3.7)$$

The Dyson equation expressed in Feynman diagrams is given by

$$\overline{\overline{i \rightarrow j}} = \overline{i \rightarrow j} + \overline{i \rightarrow \textcircled{\Sigma} \rightarrow j} \quad (3.8)$$

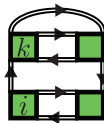
and indeed substituting Eq. 3.7 into Dyson’s equation Eq. 3.8 yields the expansion Eq. 3.6

The notation can be further compactified by going to the so-called skeleton expansion. So far we have considered an expansion of the form $\Sigma[G^{(0)}]$, where the brackets signify that the self-energy should be understood as a functional of $G^{(0)}$ since the whole matrix $G^{(0)}(\omega)$ including its frequency dependence enters into the Feynman diagrams due to the summation over the internal vertices (Section 3.5 takes this perspective more seriously and derives the DMFT equations in the self-energy functional approach). These diagrams still contain self-energy insertions. For instance the second diagram in Eq. 3.7 has the first diagram as a self-energy insertion. Going to the skeleton expansion means that we replace free Green’s functions (solid lines) by full Green’s functions (double lines). In doing this we have to take care not to overcount diagrams. In particular diagrams including self-energy insertions should not be included in the expansion. To lowest order in H_U the skeleton expansion of the self-energy is given by

$$\textcircled{\Sigma}_{ij} = \text{diagram (a)} \delta_{ij} + \text{diagram (b)} + \text{diagram (c)} + \dots \quad (3.9)$$

Note that the second diagram in Eq. 3.7 has been omitted. The skeleton expansion $\Sigma[G]$ is a useful expansion to analyse the self-energy in the limit $d \rightarrow \infty$.

The diagrams in the skeleton expansion series have the property that any two interaction vertices are joined by at least three independent paths. If there was only a single path the diagram would be one-particle reducible in contradiction with the rules of the expansion. If there were only two independent paths one part of the diagram could be understood as a self-energy insertion to the other again in violation of the expansion rules. The power counting in $1/d$ for these diagrams now allows to judge which of them survive the $d \rightarrow \infty$ -limit. Suppose we have a diagram with an interaction vertex at site i and one at site k . Let us suppose that i is the coordinate of one of the external legs and k is an internal index to be summed over.



(3.10)

As there are three independent paths joining the two vertices the three associated Green's functions scale according to Eq. 3.5 as $\mathcal{O}(d^{-\frac{3}{2}\|\mathbf{r}_i - \mathbf{r}_k\|})$. The sum over the internal vertex k scales proportional to $\mathcal{O}(d^{\|\mathbf{r}_i - \mathbf{r}_k\|})$ and therefore the whole diagram is suppressed at least by a factor of $\mathcal{O}(d^{-\frac{1}{2}\|\mathbf{r}_i - \mathbf{r}_k\|})$. If however $i = k$ the Green's functions are of order $\mathcal{O}(d^0)$ and there is no internal sum from k .

We therefore conclude: All diagrams in the skeleton expansion $\Sigma[G]$ have the same lattice site label at all their internal and external vertices. The self-energy is site-diagonal ("local")

$$\Sigma_{ij\sigma}(\omega) = \delta_{ij}\Sigma_{\sigma}(\omega) \quad (3.11)$$

In momentum space the self-energy is momentum \mathbf{k} independent

$$\Sigma_{\sigma}(\mathbf{k}, \omega) = \Sigma_{\sigma}(\omega) \quad (3.12)$$

Also the self-energy is a function only of the local component of the Green's function as all internal vertices have the same label. The immediate consequence for the Green's function is that it can be written as

$$G_{\sigma}(\mathbf{k}, \omega) = \frac{1}{\omega - \epsilon(\mathbf{k}) + \mu - \Sigma_{\sigma}(\omega)} = G_{\sigma}^{(0)}(\mathbf{k}, \omega - \Sigma_{\sigma}(\omega)) \quad (3.13)$$

The local Green's function depends only through the density of states on the dispersion relation and hence on the geometry of the lattice

$$\begin{aligned} G_{\sigma}(\omega) &= \int \frac{d^d \mathbf{k}}{(2\pi)^d} \frac{1}{\omega - \epsilon(\mathbf{k}) + \mu - \Sigma_{\sigma}(\omega)} \\ &= \int_{-\infty}^{\infty} d\epsilon \frac{\rho(\epsilon)}{\omega - \epsilon + \mu - \Sigma_{\sigma}(\omega)} \end{aligned} \quad (3.14)$$

where $\rho(\epsilon)$ is the non-interacting density of states.

In the following we present two derivations for the construction recipe of the functional $\Sigma[G]$, i.e. the DMFT equations. Before we present the derivations however we give the reader a feeling for the basic philosophy behind the DMFT.

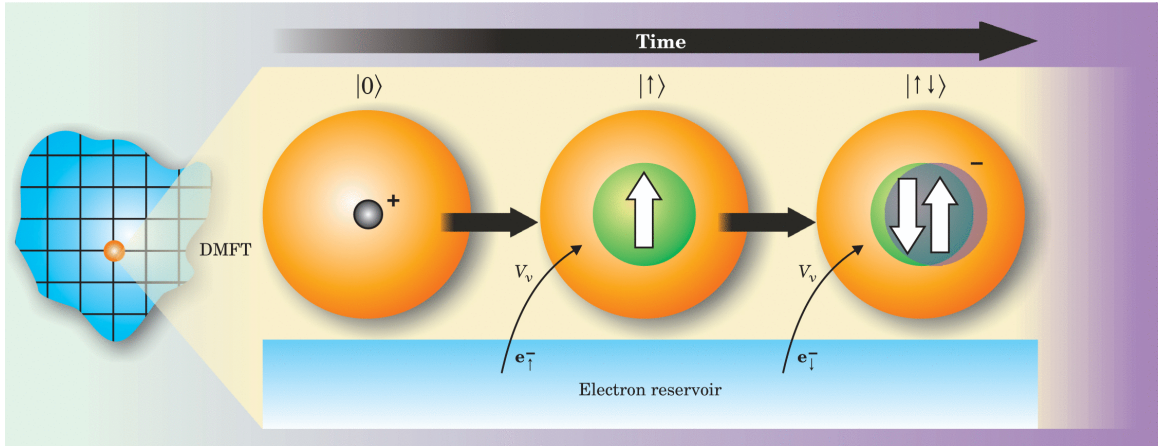


Figure 3.3: DMFT replaces the full lattice of correlated sites with a single site in a self-consistently determined, effective medium. The medium serves as a reservoir of non-interacting electrons. Taken from [62].

3.2 Idea of the DMFT

In 1992 Georges and Kotliar mapped the Hubbard model onto a self-consistent Anderson impurity model using the simplifications discussed in the previous section [36]. This idea is the basic construction recipe of the DMFT which allowed to solve different model Hamiltonians on the lattice using analytical and numerical techniques (Numerical Renormalization Group, Quantum Monte Carlo, etc.) originally developed for quantum impurity models. The DMFT provides a controlled approximation which becomes exact in the limit of infinite lattice connectivity.

Mean-field theories in general map many-body lattice problem onto single-site problems with effective parameters. Often DMFT is compared to the theory of classical magnetism. Here the spin at a specific site is the degree of freedom and the interaction with the surrounding spins on neighbouring lattice sites is accounted for (in an approximate fashion) by an effective medium modelled as an effective magnetic field. For the fermionic case the degrees of freedom are the atomic states of a single site and the rest of the crystal is described as reservoir of non-interacting electrons that can be emitted to or absorbed from the atom. Fig. 3.3 depicts the process of emission and absorption. The bath allows the atomic site to transition between different configurations. In contrast to the classical case where the effective medium (the effective magnetic field) is represented by a single number, the quantum case requires a hybridisation function $\Delta(\omega)$ to describe the ability of an electron to enter and leave the site on a time scale $1/\omega$ [62]. When the hybridisation is very small the electron is almost entirely localised at a single site, instead when it is large it can move through the whole crystal. The competition between localising and delocalising tendencies is thus captured in a local approximation which however takes full account of the quantum fluctuations.

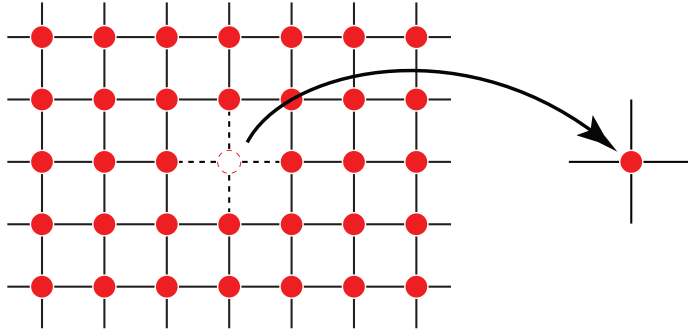


Figure 3.4: In the cavity derivation of the DMFT equations a cavity is created by removing a single site from the lattice including its adjacent bonds. An effective action is calculated by explicitly tracing out the all fermions except for removed site.

3.3 Cavity derivation

The cavity method is used in classical statistical mechanics to derive, for instance, the mean-field equations for a classical ferromagnet. Here one focuses on a specific site and explicitly integrates out the degrees of freedom of all other lattice sites in order to derive the effective dynamics of the singled out site. The general idea can be straight-forwardly extended to quantum many-body models. We briefly repeat here the derivation. A more detailed account can be found in the DMFT review article by Georges et al.[37].

One starts by writing the partition function of the Hubbard model as a functional integral over Grassman numbers $Z = \int \prod_i \mathcal{D}(c_{i\sigma}^\dagger, c_{i\sigma}) e^{-S[c_{i\sigma}^\dagger, c_{i\sigma}]}$ where

$$S = \int_0^\beta d\tau \left(c_{i\sigma}^\dagger \partial_\tau c_{i\sigma} - \sum_{\langle ij \rangle \sigma} t_{ij} c_{i\sigma}^\dagger c_{j\sigma} - \mu \sum_{i\sigma} c_{i\sigma}^\dagger c_{i\sigma} + U \sum_i n_{i\uparrow} n_{i\downarrow} \right). \quad (3.15)$$

Now the effective action for site 0 is calculated by explicitly integrating out all fermions except those on 0

$$\frac{1}{Z_{\text{eff}}} e^{-S_{\text{eff}}[c_{0\sigma}^\dagger, c_{0\sigma}]} = \frac{1}{Z} \int \prod_{i \neq 0\sigma} \mathcal{D}(c_{i\sigma}^\dagger, c_{i\sigma}) e^{-S[c_{i\sigma}^\dagger, c_{i\sigma}]} \quad (3.16)$$

To obtain an explicit expression for S_{eff} the action is split into three parts $S = S^{(0)} + S_0 + \Delta S$, where $S^{(0)}$ describes the lattice with site 0 removed, S_0 is the action of the isolated site 0 and ΔS the action due to hopping processes from the lattice with the cavity to the singled out site. Explicitly $S^{(0)}$ and ΔS are given by

$$\begin{aligned} S^{(0)} &= \int_0^\beta d\tau \left(\sum_\sigma c_{0\sigma}^\dagger (\partial_\tau - \mu) c_{0\sigma} + U n_{0\uparrow} n_{0\downarrow} \right) \\ \Delta S &= - \int_0^\beta d\tau \sum_{\langle i0 \rangle \sigma} t_{i0} \left(c_{i\sigma}^\dagger c_{0\sigma} + c_{0\sigma}^\dagger c_{i\sigma} \right) \end{aligned} \quad (3.17)$$

The terms in ΔS couple the lattice with the cavity to the isolated site. Setting $\eta_i = t_{i0}c_{0\sigma}$ one sees that the η_i play the role of source terms and the integration over the other fermions generates a connected Green's function $G^{(0)}$ of the cavity lattice. The effective action assumes the form

$$S_{\text{eff}} = \sum_{n=1}^{\infty} \sum_{i_1 \dots j_n} \int d\tau_{i_1} \dots d\tau_{j_n} \eta_{i_1}^\dagger(\tau_{i_1}) \dots \eta_{i_n}^\dagger(\tau_{i_n}) \eta_{j_1}(\tau_{j_1}) \dots \eta_{j_n}(\tau_{j_n}) G^{(0)}(\tau_{i_1}, \dots, \tau_{i_n}, \tau_{j_1}, \dots, \tau_{j_n}) + S_0 + \text{const.} \quad (3.18)$$

Due to the scaling properties Eq. 3.3 and Eq.3.5 the expression simplifies significantly in the $d \rightarrow \infty$ -limit. We analyse now the scaling properties order by order. For $n = 1$ the cavity Green's function is simply a two-point function, which scales like $1/\sqrt{d}^{||\mathbf{r}_i - \mathbf{r}_j||}$. $t_{0i}t_{0j}$ also scales like $1/\sqrt{d}^{||\mathbf{r}_i - \mathbf{r}_j||}$ while the double sum yields a contribution $d^{||\mathbf{r}_i - \mathbf{r}_j||}$ and therefore the $n = 1$ contribution is of order $\mathcal{O}(1)$ and survives the $d \rightarrow \infty$ -limit. For $n = 2$ the four-point function $G_{ijkl}^{(0)}$ scales like $1/\sqrt{d}^{||\mathbf{r}_i - \mathbf{r}_j||} 1/\sqrt{d}^{||\mathbf{r}_i - \mathbf{r}_k||} 1/\sqrt{d}^{||\mathbf{r}_j - \mathbf{r}_l||}$. On the simple cubic lattice $||\mathbf{r}_i - \mathbf{r}_j||$, $||\mathbf{r}_i - \mathbf{r}_k||$ and $||\mathbf{r}_j - \mathbf{r}_l||$ are at least 2 if they are not 0. So when i, j, k, l are all different, the four summations give d^2 and the four factors of t give $1/d^2$. The second order contribution scales in this case like $1/d$ and becomes unimportant for large spatial dimensions. Terms where $i = j$ contain three sums, which give d^3 , four factors of t giving $1/d^2$ and $1/d^2$ from $G^{(0)}$ and therefore also scale like $1/d$. The effective action therefore reduces to

$$S_{\text{eff}} = \sum_{ij} \int d\tau d\tau' t_{i0} t_{0j} c_{i\sigma}^\dagger c_{j\sigma} G_{ij\sigma}^{(0)}(\tau - \tau') + S_0 + \text{const.} \quad (3.19)$$

We now introduce the so-called Weiss effective field $\mathcal{G}_0(i\omega_n)$ as

$$\mathcal{G}_0^{-1}(i\omega_n) = i\omega_n + \mu - \sum_{ij} t_{0i} t_{0j} G_{ij\sigma}^{(0)}(i\omega_n). \quad (3.20)$$

One can identify $\mathcal{G}_0^{-1}(\tau - \tau')$ with the amplitude for a fermion to be created on the isolated site at time τ and being destroyed at τ' . Creation and annihilation processes on the isolated site can be understood as hopping processes moving particles from the isolated site into the bath which describes the surrounding lattice and vice versa. The main difference with a classical mean-field theory is that the effective field $\mathcal{G}_0^{-1}(\tau - \tau')$ is time dependent to take local quantum fluctuations into account. Indeed, the mean-field theory presented here freezes spatial fluctuations but takes full account of local temporal fluctuations. The effective action can be written as

$$S_{\text{eff}} = - \int_0^\beta d\tau \int_0^\beta d\tau' \sum_\sigma c_{0\sigma}^\dagger(\tau) \mathcal{G}_0^{-1}(\tau - \tau') c_{0\sigma}(\tau') + U \int_0^\beta d\tau n_{0\uparrow}(\tau) n_{0\downarrow}(\tau). \quad (3.21)$$

In order to obtain a closed set of equations by supplementing the above equation with an expression relating \mathcal{G}_0 to local quantities computable from S_{eff} itself. Eq. 3.20

relates \mathcal{G}_0 to the Green's function of cavity lattice $G^{(0)}$. It turns out[37] that indeed $G^{(0)}$ is related to the Green's function without site 0 removed by

$$G_{ij\sigma}^{(0)} = G_{ij\sigma} - G_{i0\sigma}G_{00\sigma}^{-1}G_{0j\sigma} . \quad (3.22)$$

The above equation states that the cavity Green's function accounts for all paths connecting i and j with those paths removed which pass through site 0. In the $d \rightarrow \infty$ limit only those path which go through 0 once have to be counted and hence $G_{00\sigma}$ is divided in the above equation. Inserting Eq. 3.22 into Eq. 3.20 one finds that the Weiss mean field is given by

$$\mathcal{G}_{0\sigma}^{-1}(i\omega_n) = \Sigma_{\sigma}(i\omega_n) + G_{\sigma}^{-1}(i\omega_n) \quad (3.23)$$

where $G_{\sigma}^{-1}(i\omega_n)$ is the local lattice Green's function $G_{ii\sigma}^{-1}(i\omega_n)$ with the site indices suppressed since we consider a homogenous problem and $\Sigma_{i\sigma}(i\omega_n)$ is the local self-energy which is related to the local lattice Green's function via

$$G_{\sigma}(i\omega_n) = \int d\epsilon \frac{\rho(\epsilon)}{i\omega_n - \epsilon + \mu - \Sigma_{\sigma}(i\omega_n)} \quad (3.24)$$

This provides us with a closed set of equations: Starting from an initial self energy Σ_{σ} the above equation allows to determine the Weiss effective field \mathcal{G}_0 . Inserting this into the effective action Eq. 3.21 we calculate the local Green's function G_{σ} and from that the self energy Σ_{σ} . The structure of the DMFT is thus that of a set of functional equations for the local lattice Green's function and the Weiss mean field. The problematic step is of course the calculation of the local Green's function given the Weiss effective field. In the next section we show that this problem is equivalent to the solution of a single impurity Anderson model and therefore the extensive techniques available for the solution of quantum impurity problems can be used.

3.4 Mapping to a quantum impurity problem

Integrating out the fermions on the other lattice sites $i \neq 0$ has introduced retardation effects into the effective action S_{eff} , Eq. 3.21, in the form of the Weiss mean field $\mathcal{G}_{0\sigma}(\tau - \tau')$. One can now return to a Hamiltonian formulation by introducing auxiliary (non-interacting) degrees of freedom. For this we consider the $c_{0\sigma}$ as an impurity and introduce the conduction electrons $a_{\mathbf{k}\sigma}$ as auxiliary degrees of freedom. The Hamiltonian of the single impurity Anderson model describes such a situation. Indeed starting from the Hamiltonian H_{SIAM} for the single impurity Anderson model, Eq. 1.29, we can rewrite it as an action. The impurity degrees of freedom are represented as the Grassmann numbers $d_{n\sigma}$ and the conduction electrons by the Grassmann numbers $c_{\mathbf{k}n\sigma}$ where σ is the spin of the impurity (electron), \mathbf{k} is the momentum of the conduction electron and n is a label for the Matsubara frequency ω_n . The action assumes the form

$$\begin{aligned} S_{\text{SIAM}}[c_{\mathbf{k}n\sigma}^{\dagger}, c_{\mathbf{k}n\sigma}, d_{n\sigma}^{\dagger}, d_{n\sigma}] = & \sum_{\mathbf{k}n\sigma} (-i\omega_n - \epsilon_{\mathbf{k}}) c_{\mathbf{k}n\sigma}^{\dagger} c_{\mathbf{k}n\sigma} + (-i\omega_n - \epsilon_d) d_{n\sigma}^{\dagger} d_{n\sigma} \\ & + \sum_{\mathbf{k}n\sigma} \left(V_{\mathbf{k}} c_{\mathbf{k}n\sigma}^{\dagger} d_{n\sigma} + \text{h.c.} \right) + U \sum_n n_{n\uparrow} n_{n\downarrow} \end{aligned} \quad (3.25)$$

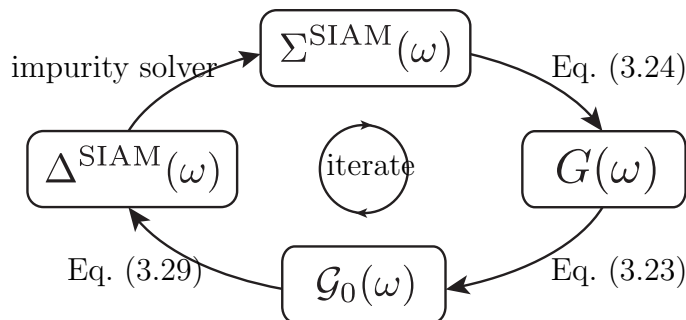


Figure 3.5: Illustration of the DMFT self-consistency loop: Starting from an initial $\Sigma_\sigma(z)$ use Eq. (3.24) to determine $G_\sigma(z)$, then use Eq. (3.23) to find $\mathcal{G}_{0\sigma}^{-1}(z)$ and determine $\Delta_{\text{SIAM}}(z)$ from that using Eq. (3.29). Solving the impurity problem gives a new self-energy $\Sigma_\sigma(z)$ and the loop is thus closed.

where $n_{n\sigma} = d_{n\sigma}^\dagger d_{n\sigma}$. The action is quadratic in the conduction electron degrees of freedom and therefore we can integrate them out find an effective action for the impurity degrees of freedom. One finds

$$S[d_{n\sigma}^\dagger, d_{n\sigma}] = \sum_n d_{n\sigma}^\dagger \mathcal{G}_{\text{SIAM}}^{-1}(i\omega_n) d_{n\sigma} + U \sum_n n_{n\uparrow} n_{n\downarrow} \quad (3.26)$$

where we have defined the bath function

$$\mathcal{G}_{\text{SIAM}}^{-1}(i\omega_n) = i\omega_n - \epsilon_d - \Delta_{\text{SIAM}}(i\omega_n) \quad (3.27)$$

with the hybridisation function $\Delta_{\text{SIAM}}(i\omega_n)$ defined as

$$\Delta_{\text{SIAM}}(i\omega_n) = - \sum_{\mathbf{k}} \int_{-\infty}^{\infty} d\omega \frac{|V_{\mathbf{k}}|^2}{i\omega_n - \omega} \delta(\omega + \epsilon_{\mathbf{k}}) \quad (3.28)$$

The influence of the bath is therefore completely determined by the hybridisation function Δ_{SIAM} . The effective action in the DMFT equations, Eq. 3.21, has the same structure the action of the impurity model, Eq. 3.26 if we identify the bath function of the impurity model with that of the lattice problem, $\mathcal{G}_{\text{SIAM}}^{-1}(i\omega_n) = \mathcal{G}_{0\sigma}^{-1}(i\omega_n)$. This relates the hybridisation function $\Delta_{\text{SIAM}}(i\omega_n)$ to the Weiss mean field in the DMFT equations,

$$\Delta_{\text{SIAM}}(z) = z - \epsilon_d - \Sigma_\sigma(z) - \mathcal{G}_0^{-1}(z) \quad (3.29)$$

It is now possible to solve the DMFT equations self-consistently using the solution of the SIAM.

The DMFT algorithm is thus:

Algorithm 1.

1. Start with an initial guess for the self-energy of the system. Often $\Sigma_\sigma(z) = 0$ is used.
2. Use Eq. 3.24 to calculate the local lattice Green's function $G_\sigma(z)$ from the current self-energy $\Sigma_\sigma(z)$.

Figure 3.6: The Luttinger-Ward functional.

3. Determine the local Weiss mean field $\mathcal{G}_{0\sigma}^{-1}(z)$ using Eq. 3.23.
4. Calculate the hybridisation function $\Delta_{\text{SIAM}}(z)$ for the impurity problem from the Weiss mean field $\mathcal{G}_{0\sigma}^{-1}(z)$ using Eq. 3.29.
5. Solve the impurity problem posed by hybridisation function $\Delta_{\text{SIAM}}(z)$ using an adequate impurity solver and determine the impurity self-energy $\Sigma_{\sigma}^{\text{SIAM}}$.
6. Identify the local lattice self-energy $\Sigma_{\sigma}(z)$ with the impurity self-energy $\Sigma_{\sigma}^{\text{SIAM}}(z)$ and goto step 2 if not already converged. Convergence can be tested using any function metric to measure the change in the self-energy from iteration n to $n + 1$, i.e. $\int d\omega |\Sigma_{\sigma}^{(n)}(\omega) - \Sigma_{\sigma}^{(n+1)}(\omega)| < \delta$?

3.5 Self-energy functional approach

Potthoff and Nolting provide an alternative derivation of the DMFT equations which offers an illuminating and slightly more abstract view on the approximative nature of the theory[87, 88]. Only a rudimentary derivation and description of the most important properties will be given here. Throughout this section we will consider Hamiltonians of the form

$$H(\mathbf{t}, \mathbf{U}) = H_0(\mathbf{t}) + H_1(\mathbf{U}) \quad (3.30)$$

where H_0 describes the ‘free’ dynamics of the system, parametrized by a hopping matrix \mathbf{t} and H_1 implements any kind of interaction for the interaction parameters \mathbf{U} .

The Luttinger-Ward functional (LW functional) $\hat{\Phi}[\mathbf{G}]$ [68], regards the system’s full Green’s function \mathbf{G} as a variational parameter, whose exact value is a stationary point of the functional $\hat{\Phi}[\mathbf{G}]$. It can be constructed by summing all connected skeleton diagrams where free propagators have been replaced by full propagators, c.f. Fig. 3.6. Generally it cannot be summed up to get a closed form expression [88]. It provides however a special relationship between static and dynamic system system quantities

- The grand canonical potential of the system Ω may be calculated by evaluating the LW functional at the exact Green’s function

$$\Omega = \Phi[\mathbf{G}] + \text{Tr} \ln \mathbf{G} - \text{Tr} \Sigma \mathbf{G} \quad (3.31)$$

- The functional derivative of the LW functional with respect to its variational parameter

$$\frac{1}{T} \frac{\delta \hat{\Phi}[\mathbf{G}]}{\delta \mathbf{G}} = \hat{\Sigma}[\mathbf{G}] \quad (3.32)$$

defines a self-energy functional $\hat{\Sigma}$ which gives the exact self-energy of the system if evaluated at the exact Green's function \mathbf{G} .

- The functional $\hat{\Phi}$ is 'universal' in the sense, that it only depends on the interaction part H_1 of the hamiltonian and is independent on the concrete choice of \mathbf{t} .

The LW functional provides a convenient starting point for the construction of approximative theories. Typically one has the self-energies in a theory as functionals of Green's function $\Sigma = \Sigma[G]$. The equations of motion for these Green functions have to be solved self-consistently and the true self-energy functionals have to be replaced by approximate ones. However these approximations cannot be made completely freely by choosing an arbitrary subset of diagrams as violations of conservation laws (continuity equation, momentum conservation. . .) might occur as shown by Kadanoff and Baym [6]. They showed that approximate self-energies derived from approximate Luttinger-Ward functionals $\hat{\Phi}$

$$\Sigma[G] = \frac{\delta \hat{\Phi}[G]}{\delta G} \quad (3.33)$$

automatically fulfill the required conservation laws, therefore $\hat{\Phi}$ -derivable approximations are called *conserving approximations*.

Similar to the case of the Luttinger-Ward functional, Potthoff's theory of the self-energy functional rests on variational approach which uses the self-energy Σ rather than the Green's function \mathbf{G} as the basic dynamical variable. Consequently the central building block is the Legendre transform of the Luttinger-Ward functional rather than the LW functional itself.

$$\hat{F}[\Sigma] = \Phi[\mathbf{G}[\Sigma]] - \text{Tr}(\Sigma \mathbf{G}[\Sigma]) \quad (3.34)$$

The functional \hat{F} may be constructed provided that the relation $\mathbf{G}[\Sigma]$ is (locally) invertible ([87] see appendix A). It can be shown that \hat{F} shares many of $\hat{\Phi}$'s valuable properties, most noteworthy: It is also *universal*. The functional derivative of \hat{F} evaluated at the exact self-energy gives the exact Green's function.

$$\frac{1}{T} \frac{\delta \hat{F}[\Sigma]}{\delta \Sigma} = \hat{\mathbf{G}}[\Sigma] \quad (3.35)$$

The first step is to express the system's grand canonical potential through \hat{F}

$$\hat{\Omega}_{\mathbf{t}}[\Sigma] = \text{Tr} \ln \left(-(\mathbf{G}_0^{-1} - \Sigma)^{-1} \right) + \hat{F}[\Sigma] \quad (3.36)$$

The functional $\hat{\Omega}_{\mathbf{t}}$ depends explicitly on the hopping matrix \mathbf{t} through the free Green's function \mathbf{G}_0 and it can be shown that $\hat{\Omega}_{\mathbf{t}}$ is stationary at the exact Green's function \mathbf{G} .

$$\frac{\partial \hat{\Omega}_{\mathbf{t}}}{\partial \Sigma} = 0 \Leftrightarrow \mathbf{G}[\Sigma] = (\mathbf{G}_0^{-1} - \Sigma)^{-1} \quad (3.37)$$

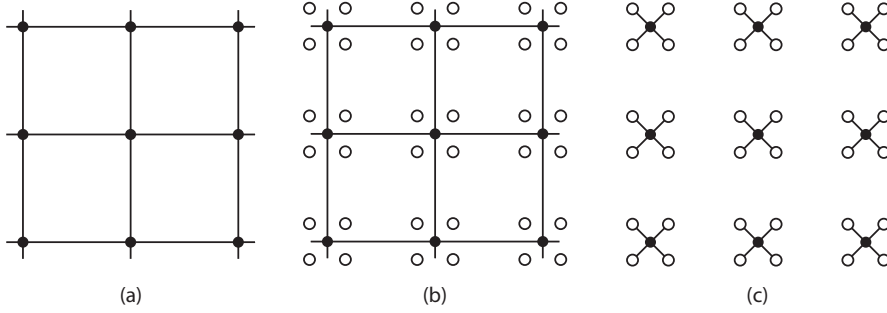


Figure 3.7: Schematic representation of the Hubbard model (a), an equivalent extension of the model (b) and a possible reference system (c). Adaption based on [87].

Knowledge of the grand potential would allow for the calculation of the exact self energy through the above relation, but the explicit form of the functional $\mathbf{F}[\Sigma]$ is in general unknown. The above scheme can however be used to construct an approximation for the self-energy by restricting the functional $\hat{\Omega}_t[\Sigma]$ onto a subspace of trial self-energies. $\hat{\Omega}_t[\Sigma]$ is then minimised on that subspace to find the best approximation to the exact self-energy.

To be more explicit we suppose that we have a reference system $H' = H'_0(\mathbf{t}') + H_1(\mathbf{U})$ with equal interaction part $H_1(\mathbf{U})$ but different free Hamiltonian $H'_0(\mathbf{t}')$ that we can solve exactly. The exact free energy of the reference system is given by $\Sigma(\mathbf{t}')$. The functional $F[\Sigma]$ for both systems coincide as $F[\Sigma]$ does not depend on the free but only on the interaction part. Thus the grand potential of the reference system has the form

$$\hat{\Omega}_t[\Sigma] = \text{Tr} \ln \left[- \left(\mathbf{G}'_0{}^{-1} - \Sigma \right)^{-1} \right] + F[\Sigma] \quad (3.38)$$

$F[\Sigma]$ can now be eliminated from the grand potential of our target system but solving the above expression of the reference system for $F[\Sigma]$ and substituting.

$$\hat{\Omega}_t[\Sigma] = \hat{\Omega}_{t'}[\Sigma] + \text{Tr} \ln \left[- \left(\mathbf{G}_0^{-1} - \Sigma \right)^{-1} \right] - \text{Tr} \ln \left[- \left(\mathbf{G}'_0{}^{-1} - \Sigma \right)^{-1} \right] \quad (3.39)$$

When restricted to the subspace spanned by the self-energies of the reference system, the above expression is equal to the exact grand potential of the target system. Noting that $\mathbf{G}'_0{}^{-1} - \Sigma$ is the Green's function of the reference system the above expression involves apart from the non-interacting Green's function of the target system $\mathbf{G}^{(0)}$ only quantities from the reference system. If the reference system is chosen such that it can be solved explicitly an approximation for the exact self-energy of the target system can be found by extremising the above expression. The condition $\partial \hat{\Omega}_t[\Sigma(\mathbf{t}')]/\partial \mathbf{t}' = 0$ gives

$$T \sum_{\omega_n} \sum_{\alpha, \beta} \left(\frac{1}{\mathbf{G}_0^{-1} - \Sigma(\mathbf{t}')} - \mathbf{G}' \right)_{\alpha\beta} \frac{\partial \Sigma_{\alpha\beta}(\mathbf{t}')}{\partial \mathbf{t}'} = 0 \quad (3.40)$$

The case of the Hubbard model is depicted graphically in Fig. 3.7. The original Hubbard model is shown in Fig. 3.7a, then a number $n_s = 4$ of non-interacting, decoupled reference sites are introduced to create an equivalent model, Fig. 3.7b. By changing the hopping a reference system is obtained, Fig. 3.7c. The n_s decoupled sites can be understood as discretised approximations for the Anderson impurity model. For $n_s \rightarrow \infty$ they coincide with an AIM with a local self-energy and hence $\partial \Sigma_{ij}(\mathbf{t}')/\partial \mathbf{t}' = \delta_{ij}$. Eq. 3.40 becomes for this particular case

$$\left(\frac{1}{\mathbf{G}_0^{-1}(i\omega_n) - \Sigma(i\omega_n)} \right)_{ii} = G'_{ii}(i\omega_n) \quad (3.41)$$

which is nothing but the DMFT self-consistency condition.

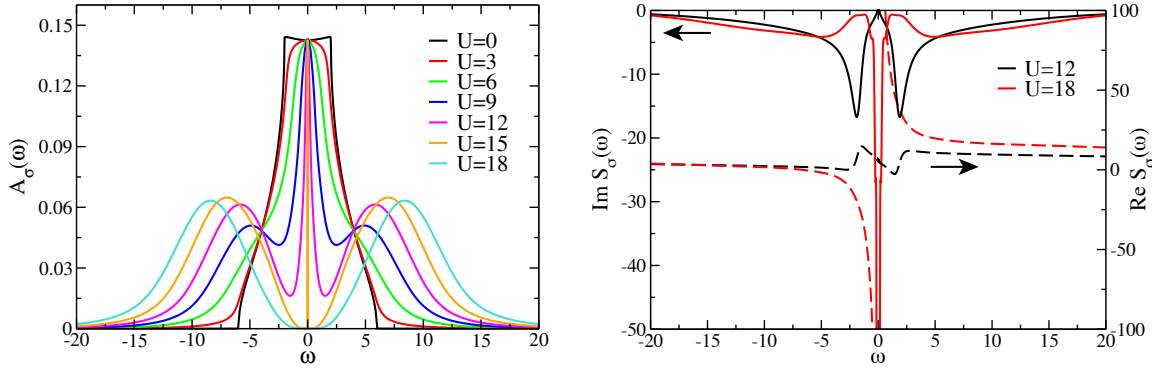
3.6 Application: Mott-Hubbard metal-insulator transition

The dynamical mean-field theory has been successfully employed to study the Mott-Hubbard metal-insulator transition for a Hubbard model at the particle-hole symmetric point on a simple cubic lattice in the limit of infinite spatial dimensions both at $T = 0$ and finite temperature T by Bulla[8], Bulla et al.[9] and other authors. Bulla used the non-perturbative numerical renormalisation group (NRG, [12]) to solve the impurity problem. For $T = 0$ a first-order phase transition at a finite value of the interaction strength $U = U_{c_2}$ was found where the metallic solution vanishes and the system becomes insulating. At zero temperature a suitable criterion to distinguish the metallic from the insulating phase is the quasi particle weight

$$Z = \frac{1}{1 - \left. \frac{\partial \text{Re } \Sigma(\omega)}{\partial \omega} \right|_{\omega=0}} \quad (3.42)$$

which is finite in the metallic phase but vanishes with increasing U when the insulating solution appears. Fig. 3.8a shows the spectral functions from a DMFT calculation (also using NRG as the impurity solver) for the Hubbard model on the simple cubic lattice in three spatial dimensions. The only information from the lattice that enters into the DMFT equations is the non-interacting density of states $\rho(\epsilon)$, which depends on the dimensionality of the lattice. However the modification is minor and we can still discuss the transition along the lines of Refs.[8, 9]. In the metallic phase for large values of U the spectral function shows a characteristic three-peak structure with a quasi-particle peak at the Fermi-level and (for the particle-hole symmetric model we are studying here) symmetric upper and lower Hubbard bands centred about $\pm U/2$. For interaction values close to the transition the quasi-particle peak stands isolated in a preformed gap ($U = 15$, orange curve). The width of the quasi particle peak is proportional to Z . When the interaction strength is increased further the width of the peak vanishes and the gap in the spectrum appears discontinuously ($U = 18$, cyan curve).

In the concrete calculations one observes that above the critical U_{c_2} the width of the peak vanishes exponentially with the DMFT iteration. Still a metallic input



(a) Spectral functions for different values of the interaction strength U . Above a critical U a gap opens at the Fermi level ($\omega = 0$). The upper and lower Hubbard band are centered about $\pm U/2$.

(b) Imaginary part of the self-energy for $U = 12$ (black, solid) and $U = 18$ (red, solid) - axis to the left and real part of the self-energy for $U = 12$ (black, dashed) and $U = 18$ (red, dashed) - axis to the right.

Figure 3.8

solution in the DMFT always produces a metallic solution in the following iteration independent of the applied U as long as U is finite. This is to be compared to the single impurity Anderson model the Hubbard model is mapped to in the self-consistency loop: here also the low-energy scale vanishes only exponentially with U and one has to go to $U \rightarrow \infty$ for it to disappear. It is only the condition of self-consistency in the solution which shifts the critical U value from ∞ to a finite value U_{c2} in the Hubbard model[8].

Fig. 3.8b shows the imaginary and real part of the self-energy for a value of $U = 12$ (black curves) in the metallic phase and $U = 18$ (red curves) in the insulating phase. For the metallic self-energy the imaginary part shows a two-peak structure where the weight in the peaks is approximately independent of U , but the position and width vanish as $U \rightarrow U_{c2}$. The low-energy behaviour for the self-energy is given by

$$\begin{aligned} \text{Re } \Sigma(\omega + i0^+) &= \frac{U}{2} + \left(1 - \frac{1}{Z}\right)\omega + \mathcal{O}(\omega^3) \\ \text{Im } \Sigma(\omega + i0^+) &= -b(Z)\omega^2 + \mathcal{O}(\omega^4) \end{aligned} \quad (3.43)$$

as predicted by Fermi liquid theory. The function $b(Z)$ is model specific. Upon approaching the transition the two peaks are seen to merge into a single pole located at the Fermi energy of weight α . Note that here in the numerical data the width of the single peak is not physical and only due to the numerical implementation. The width is controlled by the broadening parameter of the numerical renormalisation group used to solve the impurity problem. The structure of the self-energy can be understood from the shape of the spectral function. For the underlying single Anderson impurity model one has the relation (Eq. 3.23 into Eq. 3.27)

$$\Sigma(z) = z - \epsilon_d - \Delta(z) - \frac{1}{G(z)} \quad (3.44)$$

which shows that the self-energy develops peaks where the real and imaginary part of the Green's function are small. Therefore for any spectral function which shows a pronounced three-peak structure the self-energy develops two-peaks.

A coexistence region for metallic and insulating solutions is found in a particular interaction window $U_{c_1} < U < U_{c_2}$. Coming from the metallic side, the quasi-particle weight vanishes at the critical interaction strength U_{c_2} . From the insulating side the insulating solution shows the $1/z$ pole in the region of coexistence and at $U \rightarrow U_{c_1}$ the weight α of the pole vanishes. Such hysteresis effects are expected for first order phase transitions. The first order transition ends at finite temperature at a critical endpoint T_c as shown in Fig. 1.2. For $T > T_c$ we have a crossover and the two peak structure in the self-energy gradually evolves in to well-pronounced peak at $\omega = 0$. The critical values U for $T > T_c$ are defined via the value of U where the spectral function $A(\omega = 0)$ changes discontinuously.

We briefly discuss the situation for the Hubbard model away from the particle-hole symmetric point. In the following the chemical potential is measured relative to the particle-hole symmetric point, i.e. the on-site energy in the Hubbard model is always $\epsilon_d = -\frac{U}{2}$. We first concentrate on the $T = 0$ case. Starting at half-filling ($\mu = 0$) on the insulating side ($U > U_{c_2}$) due to the existence of the Mott gap around the Fermi energy no change in the occupation number is observed for a small increase in the chemical potential, the $n(\mu)$ -curve is flat around $\mu = 0$. Once the chemical potential has been increased enough that the Fermi level start to move into the upper Hubbard band, the local density of states at the Fermi level $A(\mu)$ becomes finite, which leads to an increase in the hybridisation function of the underlying impurity problem (c.f. Eq. 3.29) which leads to a finite Kondo temperature T_K and the appearance of a Kondo resonance and an increase in the occupation. The spectral weight in the Kondo peak increases continuously from zero as μ is raised and hence $n(\mu)$ is a continuous function for $T = 0$. At finite T the ‘‘gap’’ in the spectrum at $\mu = 0$ is thermally activated and the occupation immediately increases as the chemical potential is raised. $n(\mu)$ is not flat around $\mu = 0$. The Kondo temperature of the underlying impurity model is $T_K \propto \Delta(\mu)$ and therefore increases as the chemical potential is increased. When the chemical potential hits the upper Hubbard band the hybridisation strongly increases and so does the Kondo temperature. One can imagine having a chemical potential dependent Kondo temperature $T_K(\mu)$ and once the chemical potential is increased so much that the T_K lies above the system temperature T the Kondo effect sets in, a Kondo resonance appears and the occupation jumps. For $T > 0$ $n(\mu)$ is a discontinuous function which jumps at the μ_c where $T_K(\mu_{c_2}) = T$. The hysteresis in the disappearance of the metallic in favour of the insulating solution also affects $n(\mu)$. One finds a different critical chemical potential (μ_{c_1}) when starting from the metallic side at finite doping and moves towards half-filling[47].

3.7 Antiferromagnetic order

Although we have derived the mean-field equations in section 3.3 under the assumption that no long-range order is present, it is straightforward to generalise the DMFT to phases with broken symmetry. Here we consider the case of antiferromagnetic

order on a bipartite lattice. Bipartite lattices consist of two sublattices A and B such that the nearest neighbours for a site in the A (B) sublattice are only sites of sublattice B (A). Zitzler et al.[117] studied the phase separation for the doped Hubbard model using the method presented here. In a later study they determined the magnetic phase diagram of the magnetically frustrated Hubbard by including next-nearest neighbour hopping. Bauer and Hewson[5] analysed the properties of the quasiparticle excitations of metallic antiferromagnetic states. We start with a Hubbard model in a staggered magnetic field

$$H = \sum_{ij\sigma} (t_{ij} c_{Ai\sigma}^\dagger c_{Bj\sigma} + \text{h.c.}) + U \sum_{i\alpha} n_{\alpha i \uparrow} n_{\alpha i \downarrow} - \sum_{i\sigma} (\mu_\sigma n_{Ai\sigma} + \mu_{\bar{\sigma}} n_{Bi\sigma}) \quad (3.45)$$

where $\alpha \in \{A, B\}$ and the spin-dependent chemical potential $\mu_\sigma = \mu + \sigma h$ contains the effect of the staggered magnetic field h . The non-interacting part of the Hamiltonian can be diagonalised in terms of Bloch states when going to momentum space

$$H_0 = \sum_{\mathbf{k}\sigma}^{MBZ} C_{\mathbf{k}\sigma}^\dagger M_{\mathbf{k}\sigma} C_{\mathbf{k}\sigma} \quad (3.46)$$

with $C_{\mathbf{k}\sigma} = (c_{A\mathbf{k}\sigma}, c_{B\mathbf{k}\sigma})^T$ and M is given by

$$M_{\mathbf{k}\sigma} = \begin{pmatrix} -\mu_\sigma & \epsilon_{\mathbf{k}} \\ \epsilon_{\mathbf{k}} & -\mu_{\bar{\sigma}} \end{pmatrix} \quad (3.47)$$

The \mathbf{k} sum runs over the magnetic Brillouin zone and the energy of the Bloch state is given by $\epsilon_{\mathbf{k}}$. Here we have adopted a special real-space basis in terms of the sublattices A and B, $\{c_{A\mathbf{k}\sigma}, c_{B\mathbf{k}\sigma}\}$. The choice of basis in chapter 2 given by $\{c_{\mathbf{k}\sigma}, c_{\mathbf{k}+\mathbf{Q}\sigma}\}$, where $\mathbf{Q} = (\pi, \dots, \pi)^T$ is the reciprocal lattice vector for the commensurate spin density wave ordering, is related to our choice here by the linear transformation

$$\begin{pmatrix} c_{\mathbf{k}\sigma} \\ c_{\mathbf{k}+\mathbf{Q}\sigma} \end{pmatrix} = \frac{1}{\sqrt{2}} \begin{pmatrix} 1 & -1 \\ 1 & 1 \end{pmatrix} \begin{pmatrix} c_{A\mathbf{k}\sigma} \\ c_{B\mathbf{k}\sigma} \end{pmatrix} \quad (3.48)$$

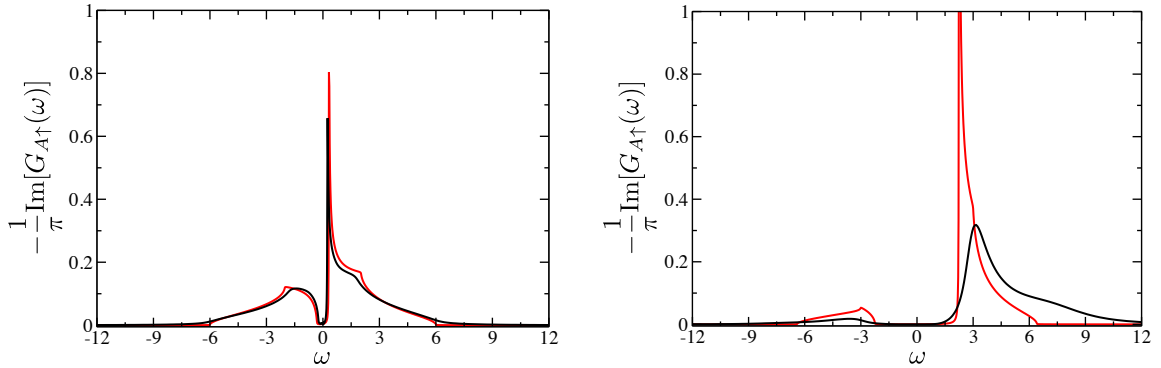
For the derivation of the DMFT equations the formulation in terms of the A – B sublattice is however more convenient. The non-interacting Green's function G_0 is given by

$$G_{\mathbf{k}\sigma}^{(0)} = \frac{1}{(\omega + \mu_\sigma)(\omega + \mu_{\bar{\sigma}}) - \epsilon_{\mathbf{k}}^2} \begin{pmatrix} \omega + \mu_{\bar{\sigma}} & \epsilon_{\mathbf{k}} \\ \epsilon_{\mathbf{k}} & \omega + \mu_\sigma \end{pmatrix} \quad (3.49)$$

The interacting Green's function is found by generalising the above expression with the inclusion of a sublattice dependent self-energy $\Sigma_{\alpha\sigma}(\omega)$ with $\alpha \in \{A, B\}$ and we assumed that the self-energy is local hence \mathbf{k} independent and sublattice space diagonal, so that the Green's function can be written as [5]

$$G_{\mathbf{k}\sigma} = \frac{1}{\xi_{A\sigma}(\omega)\xi_{B\sigma}(\omega) - \epsilon_{\mathbf{k}}^2} \begin{pmatrix} \xi_{B\sigma}(\omega) & \epsilon_{\mathbf{k}} \\ \epsilon_{\mathbf{k}} & \xi_{A\sigma}(\omega) \end{pmatrix} \quad (3.50)$$

where $\xi_{\alpha\sigma}(\omega) = \omega + \mu_\sigma - \Sigma_{\alpha\sigma}(\omega)$. Due to the symmetry of the bipartite lattice the self-energy fulfils $\Sigma_{A\sigma}(\omega) = \Sigma_{B\bar{\sigma}}(\omega) \equiv \Sigma_\sigma(\omega)$ and thus $\xi_{A\sigma}(\omega) = \xi_{B\bar{\sigma}}(\omega) \equiv \xi_\sigma(\omega)$. It is



(a) Single-particle spectral function for the A sublattice of a Hubbard model with $U = W/4$. The solid black line is the DMFT result, the solid red line indicates the SMT result. It can be seen that for small interactions the agreement is good.

(b) Same as (a) with $U = 5W/6$. The solid black line is the DMFT result, the solid red line indicates the SMT result. For large interaction strength it becomes obvious that the interaction induced increase in the effective bandwidth is greatly underestimated by the SMT.

Figure 3.9

therefore sufficient to focus on one sublattice alone, say A . The local lattice Green's function for sublattice A can be found by carrying out the \mathbf{k} -sum in Eq. (3.50) which can be written as an energy integral due to the \mathbf{k} independence of the self-energy $\Sigma_\sigma(\omega)$

$$G_{A\sigma}(\omega) = \xi_{\bar{\sigma}}(\omega) \int_{-\infty}^{\infty} d\epsilon \frac{\rho(\epsilon)}{\xi_\sigma(\omega)\xi_{\bar{\sigma}}(\omega) - \epsilon^2} \quad (3.51)$$

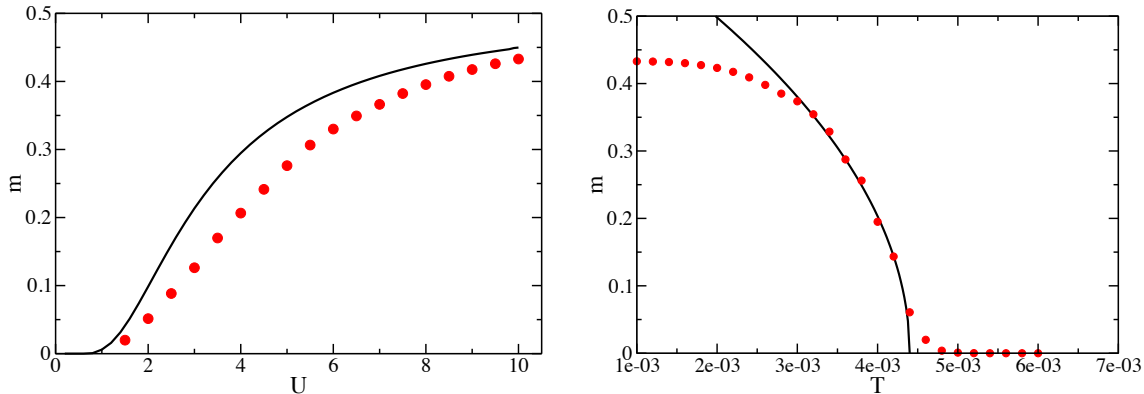
where $\rho(\epsilon)$ is the non-interacting density of states. Similarly to the paramagnetic case the Weiss mean field is determined from the equation

$$\mathcal{G}_{0\sigma}^{-1}(\omega) = \Sigma_\sigma(\omega) + G_\sigma^{-1}(\omega) \quad (3.52)$$

where however all quantities have acquired a non-trivial spin dependence. The single Anderson impurity model the problem is mapped to has a spin-dependent on-site energy for the impurity given by $\epsilon_{d\sigma} = \epsilon_d - \sigma h$. The hybridisation function $\Delta_{\text{SIAM}\sigma}(\omega)$ also acquires a spin-dependence and is determined in the usual way from the Weiss mean field $\mathcal{G}_{0\sigma}(\omega)$

$$\Delta_{\text{SIAM}\sigma}(\omega) = z - \epsilon_{d\sigma} - \Sigma_\sigma(\omega) - \mathcal{G}_{0\sigma}^{-1}(\omega) \quad (3.53)$$

For the solution of the actual impurity problem one needs to employ an impurity solver which can cope with the broken symmetry. In section 4.7 we describe how this can be achieved with the numerical renormalisation group (NRG). To find antiferromagnetic solutions one can calculate self-consistent solutions for a decreasing sequence of staggered magnetic field strengths to see if broken symmetry solutions exist as the staggered field is reduced to zero.



(a) Sublattice polarisation m as a function of the interaction strength U for $T = 10^{-8}$. The tendency towards magnetic order is overestimated by the SMT (solid black line) since it ignores quantum fluctuations on the correlated site which the DMFT (red dots) takes full account of.

(b) Sublattice polarisation m as a function of the temperature T for $U = 10$. The DMFT (red dots) shows that a finite m is only found for $T < T_N$ with $T_N \approx 0.0044$. The solid black line is a fit of $m(T) = \gamma\sqrt{T_N - T}$ with $\gamma \approx 10.16$.

Figure 3.10

3.7.1 Application: Antiferromagnetic order in the Hubbard model

In the following we present results for the half-filled Hubbard model on a simple cubic lattice with nearest-neighbour hopping in 3 spatial dimensions. As expected we find that for all $U > 0$ the symmetry broken, antiferromagnetic phase is energetically stable. Fig. 3.9 shows the single particle spectra for two different interaction strengths $U = W/4$ and $U = 5W/6$, both of which are below the MHMIT if the system is confined to the paramagnetic phase. The solid black line is the DMFT result, the solid, red line shows the result of static mean-field theory (SMT). For small interaction strengths (Fig. 3.9a) compared to the bandwidth of the non-interacting model, $U \ll W$, the agreement is rather well. The SMT reproduces the essential features of the DMFT which are slightly more smoothed out. For larger interaction strengths however (Fig. 3.9b) the insufficiencies of the SMT become apparent. Most notably the increase in the bandwidth is notoriously underestimated in comparison with the DMFT result. Fig. 3.10a shows the sublattice polarisation m as a function of the interaction strength U . The solid black line is the SMT result, the red dots indicate DMFT calculations. The tendency towards magnetic order is overestimated by the SMT. The reason is that it ignores quantum fluctuations on the correlated site which the DMFT takes full account of. These fluctuations have a tendency to disorder the state of the system and hence reduce the magnitude of the order parameter m . For finite temperatures close to the critical point $T = T_N$ where $m \approx 1$ one expects a square root behaviour from mean-field arguments, $m(T) \approx \gamma\sqrt{T_N - T}$. Fig. 3.10b shows DMFT results (red dots) for m as a function of the temperature T . Above the Neel temperature $T_N \approx 0.0044$ the sublattice polarisation m vanishes. The solid

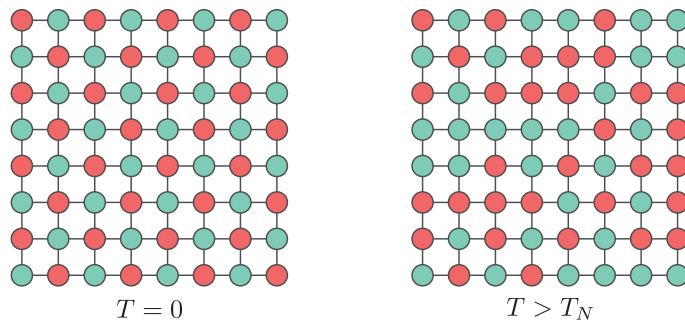


Figure 3.11: Pictorial depiction of the antiferromagnetic order for a bipartite lattice. Red sites are predominantly occupied by one spin species, green sites by the other.

black line is fit of a function prototype $\gamma\sqrt{T_N - T}$ to the DMFT data where we found $\gamma \approx 10.16$. Indeed the DMFT results fulfil the static mean-field prediction; the deviation for temperatures much smaller than T_N is expected.

Chapter 4

Solution of the impurity model

4.1 Introduction to the Kondo effect

In 1934 Wander Johannes de Haas [23] discovered a resistance minimum in a gold probe at low temperatures, c.f. Fig. 4.1a. This behaviour was utterly unexpected because at the time, the resistivity was thought to be determined by two effects: (a) the potential scattering by (non-magnetic) impurities and (b) scattering due to lattice excitations, e.g. phonons. The expected behaviour was therefore that the resistivity monotonically decreases as a function of T as $T \rightarrow 0$. At higher temperatures Curie-Weiss behaviour was observed in the magnetic susceptibility, c.f. Fig. 4.1b, and so it was conjectured that magnetic *Fe* impurities in the gold probe might be responsible for the unexpected behaviour. In 1961 Anderson introduced the single impurity Anderson model (SIAM) as a minimal model for the description of the effect. The Hamiltonian of the SIAM is given by

$$H_{\text{SIAM}} = \sum_{\mathbf{k}\sigma} \epsilon_{\mathbf{k}} a_{\mathbf{k}\sigma}^{\dagger} a_{\mathbf{k}\sigma} + \epsilon_d \sum_{\sigma} n_{d\sigma} + U n_{d\uparrow} n_{d\downarrow} + \sum_{\mathbf{k}\sigma} \left(V_{\mathbf{k}} a_{\mathbf{k}\sigma}^{\dagger} c_{d\sigma} + V_{\mathbf{k}}^* c_{d\sigma}^{\dagger} a_{\mathbf{k}\sigma} \right). \quad (4.1)$$

where $n_{d\sigma} = c_{d\sigma}^{\dagger} c_{d\sigma}$ is the number operator for spin $\sigma = \uparrow / \downarrow$ electrons on the impurity d -level. The SIAM can be understood as a paradigmatic model for local moment physics. The delocalised conduction electrons in the gold probe have extended wave functions which subject them to Coulomb screening rendering their interactions short-ranged. In the SIAM these electrons are modelled as non-interacting quasi-particles with a dispersion relation $\epsilon_{\mathbf{k}}$. The d -electrons of the impurity on the other hand are strongly localised and the inclusion of Coulomb interaction U is crucial for their faithful description. The hybridisation strength $V_{\mathbf{k}}$ tunnel-couples the impurity to the conduction electrons and allows for charge fluctuations on the impurity. If the impurity is empty or double occupied it has no net magnetic moment and thus only acts as a potential scatterer. It turns out that potential scattering alone cannot explain the appearance of the resistance minimum. The non-trivial behaviour is associated with the spin-sector. One can restrict the model to exact half filling by choosing $\epsilon_d \ll \epsilon_F \ll 2\epsilon_d + U$, where there is a particle-hole symmetry.

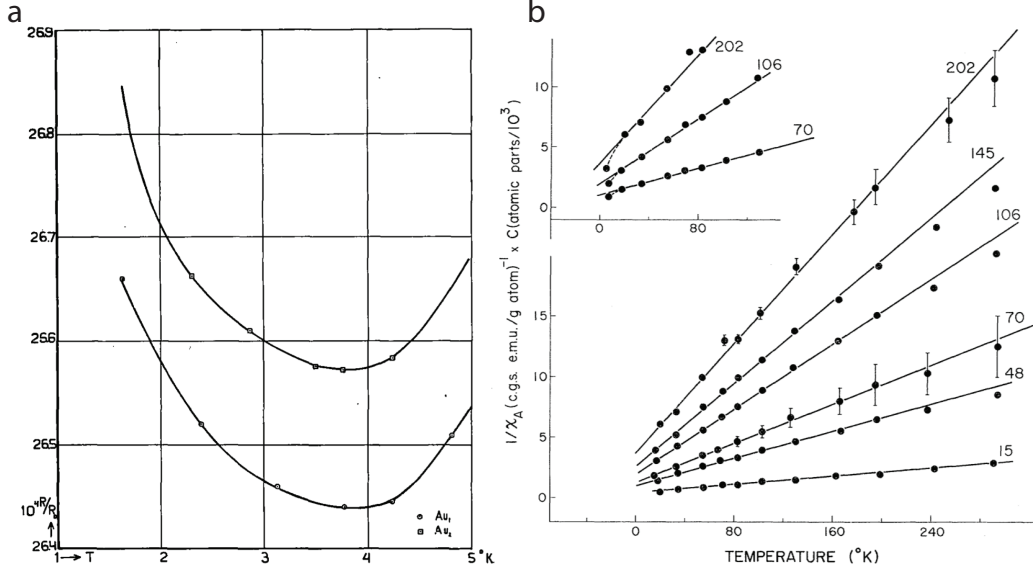


Figure 4.1: a) Resistivity for a gold probe with unexpected minimum as a function of temperature; measured by de Haas[23] b) Curie-Weiss behaviour for iron alloyed copper as measured by Hurd[54]. The number next to the curves measure the concentration in ppm.

In this parameter regime, changes of the charge state of the impurity only occur virtually. It is therefore permissible to project the Hamiltonian onto the singly occupied subspace by a perturbative, approximate canonical transformation known as the Schrieffer-Wolff transformation[106]. The effective low-energy Hamiltonian then assumes the form

$$H_{\text{Kondo}} = \sum_{\mathbf{k}\sigma} \epsilon_{\mathbf{k}} c_{\mathbf{k}\sigma}^{\dagger} c_{\mathbf{k}\sigma} + J \mathbf{S} \cdot \mathbf{s} \quad (4.2)$$

where $J = V^2/U$ is the antiferromagnetic coupling between the spin- $\frac{1}{2}$ local moment on the impurity, represented by the operator \mathbf{S} , and the spin density of the conduction electrons $\mathbf{s} = \frac{1}{2} \sum_{\mathbf{k}\mathbf{k}'\sigma\sigma'} \frac{V_{\mathbf{k}} V_{\mathbf{k}'}^*}{V^2} c_{\mathbf{k}\sigma}^{\dagger} \vec{\sigma}_{\sigma\sigma'} c_{\mathbf{k}'\sigma'}$, where $\vec{\sigma}$ is a vector of Pauli matrices and $V^2 = \sum_{\mathbf{k}} |V_{\mathbf{k}}|^2$. This is the Kondo model, valid for $T \ll U$.

Jun Kondo performed a third order perturbative calculation in the coupling constant J of the Kondo model, which describes scattering of conduction electrons by a local moment. By including second-order spin-flip processes to the elements of the T-matrix he found a $\ln(T/D)$ (D the bandwidth of the conduction electrons) correction term to the resistivity which gave rise to a minimum in the

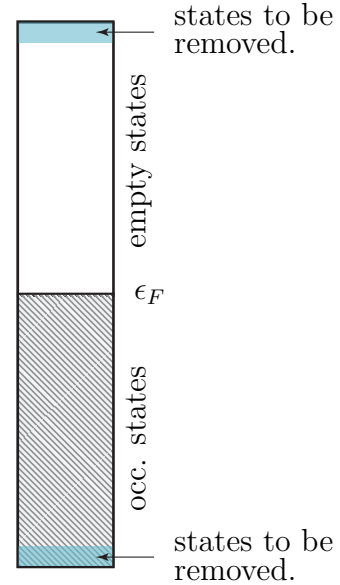


Figure 4.2: The particle and hole states which are removed from the conduction band when reducing the band width D by δD .

resistivity. Furthermore, the position of the predicted minimum,

$$T_{min} \propto c_{imp}^{1/5} \quad (4.3)$$

with c_{imp} the impurity concentration was in agreement with experimental data. The $\ln(T)$ term however has an unphysical divergence as $T \rightarrow 0$ which became known as the ‘‘Kondo problem’’.

In 1965 Abrikosov summed the perturbative series to infinite order in an attempt to remove the \ln -divergence and discovered that the perturbative treatment always breaks down leading to a divergence of the resistivity (for antiferromagnetic coupling J) at a finite temperature T_K , which would later become known as the Kondo temperature. The main obstacle turned out to be that the structure of the problem is such that information from all energy scales contribute to the solution. Hence it is not amendable to solution by perturbative approaches. Theoretically, the objective then was to find a non-perturbative technique, which allows for the calculation of transport properties as $T \rightarrow 0$ in the Kondo- and Anderson models. Experimentally the aim was to understand the behaviour of these quantities for $T < T_K$. The terms responsible for the break-down of perturbation theory were the log terms, $\ln(k_B T/D)$, implying that coupling to high energy excitations could not be ignored. The idea known as *poor man’s scaling*, put forward by Anderson in 1964, sought to incorporate the effect of high energy excitations into a renormalization of the coupling constants. The technique is similar to the derivation of the Kondo model from the Anderson impurity model, where one perturbatively accounts for the influence of the empty and doubly-occupied states on the singly occupied states. However, here virtual excitations occur to excited states located at the edges of the band (see fig. 4.2). As one repeatedly integrates out states within an energy window δD of the band edges, the coupling constants for the antiferromagnetic isotropic model ($J_{\pm} = J_z = J$) flow according to

$$\frac{dJ}{d \ln D} = -2\rho_0 J^2 \quad (4.4)$$

It was found that the scaling trajectories are characterized by a ‘scaling invariant’, the Kondo temperature $T_K \sim \Delta \exp(-1/\rho J)$. Nevertheless the divergence problem was still not solved because the coupling constants diverge as one reduces the effective band width below T_K . The Kondo temperature T_K thus marks the entry into a regime of ‘strong coupling’ between the impurity and the conduction band electrons, which is not accessible from any technique based on a perturbative series.

This is where the success story of the numerical perturbation group, a non-perturbative numerical method for the solution of the Kondo model put forward by Wilson in 1975, begins. The method was initially designed to compute thermodynamic properties of the Kondo model but later was extended to dynamic quantities and the single impurity Anderson model (SIAM).

4.2 Numerical Renormalization Group

In the early 1970s, Wilson developed a fully non-perturbative renormalisation group transformation for the Kondo problem. The application of this Numerical Renormalization Group (NRG) to the Kondo problem gave for the first time the full crossover

from the high-temperature regime of a free impurity spin, to the low-temperature regime where the impurity is completely screened. For a review, see Ref. [12]. It has become one of the standard tools to study correlation effects in quantum impurity models. One of its main advantages is that it is non-perturbative with respect to all system parameters (as opposed to many other renormalization group methods) and thus can treat interacting quantum many-body systems with a continuum of excitations spread over a broad range of energies. The fermionic NRG can be applied to systems of a quantum mechanical impurity with a small number of interacting degrees of freedom, coupled to a bath of non-interacting fermions, usually with a continuous spectrum. No restriction exists as to the structure of the impurity subsystem and arbitrary large Coulomb interactions are permissible. The bath however must consist of non-interacting fermions.

In the following we present a summary of the NRG derivation. We highlight the approximations and also describe the computational steps for the solution of the impurity problem on a computer. A more detailed presentation is given in the review by Bulla et al.[12], and Refs. [63, 64]. To make the derivation as transparent as possible we present, at first, a slightly more restrictive theory, which relies on the following assumptions: we ignore the energy dependence of the conduction electron density of states ρ and the \mathbf{k} -dependence of the hybridisation V and replace them with their Fermi level value. This is not a crucial approximation: Bulla et al.[12] show in their generalised derivation of the NRG how the full energy dependence of the density of states and the hybridisation function can be retained as required for application within DMFT. We return to this point in section 4.5.

Transforming the Hamiltonian Eq. 4.1 to an energy representation with the above assumptions one finds

$$H/D = \int_{-1}^1 d\epsilon \left[\epsilon a_{\epsilon\sigma}^\dagger a_{\epsilon\sigma} + \sqrt{\frac{\Gamma}{\pi D}} (a_{\epsilon\sigma}^\dagger c_{d\sigma} + c_{d\sigma}^\dagger a_{\epsilon\sigma}) \right] + \frac{1}{D} (\epsilon_d + \frac{1}{2}U) c_{d\sigma}^\dagger c_{d\sigma} + \frac{1}{2} \frac{U}{D} (c_{d\sigma}^\dagger c_{d\sigma} - 1)^2 \quad (4.5)$$

where $\Gamma = \pi\rho V^2$ and the Hamiltonian depends only on the dimensionless parameters ϵ_d/D , U/D and Γ/D . The temperature-dependent properties will be functions of $k_B T/D$ only.

4.2.1 Logarithmic discretization

Dealing with this simplified model numerically is a challenging task due to the infinite number of eigenstates of the system and the interactions. As already mentioned one of the key characteristics of the Kondo problem is the importance of high energy excitations for low energy properties. Therefore at the heart of the NRG lies a logarithmic discretisation of the conduction energy band, $\rho(\epsilon)$. By introducing a discretisation parameter Λ Wilson divided the normalised energy range $[-1, 1]$ into $2n$ intervals where the n th interval (for positive ϵ) extends from $\Lambda^{-(n+1)}$ to Λ^n , c.f. Fig. 4.3. One then approximates the continuum density of states $\rho(\epsilon)$ between $-D$ and D by a discrete set of poles. The logarithmic discretisation separates the electron energies into different orders of magnitude where energies close to the Fermi level $k_B T \ll D$, which determine the low temperature properties, are well sampled. One

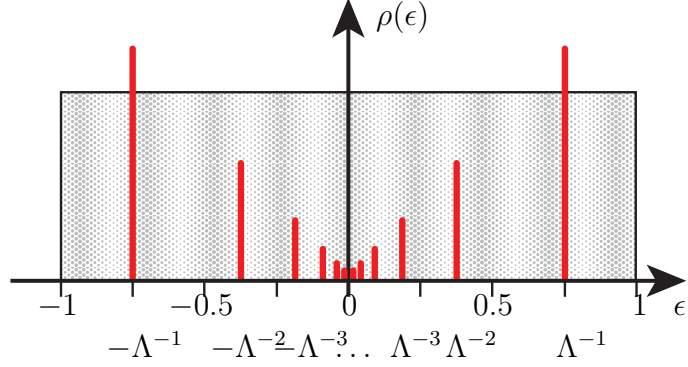


Figure 4.3: The continuous spectrum is approximated by a series of delta peaks (red) on the logarithmic grid, $\{-1, -\Lambda^{-1}, \dots, \Lambda^{-1}, 1\}$.

expects the low-energy eigenstates of the conduction band to be important for the description of the physics, which becomes non-perturbative at low energies [3].

To accomplish the logarithmic discretisation, Wilson introduced a Fourier series in each interval

$$\Psi_{np}^{\pm}(\epsilon) = \begin{cases} \frac{\Lambda^{n/2}}{\sqrt{1-\Lambda^{-1}}} \exp^{\pm i\omega_n p k} & \text{for } \Lambda^{-(n+1)} < \pm k < \Lambda^{-n} \\ 0 & \text{for } k \text{ outside interval} \end{cases} \quad (4.6)$$

where $\omega_n \equiv [2\pi\Lambda^n]/[1 - \Lambda^{-1}]$ and $n \in \mathbb{N}_{\geq 0}$, $p \in \mathbb{N}$ the Fourier harmonic index and $+$ ($-$) denotes the basis for positive (negative) ϵ . The conduction electron operators $a_{\epsilon\sigma}$ can be expanded in this basis

$$a_{\epsilon\sigma} = \sum_{np} [a_{np\sigma} \Psi_{np}^+(\epsilon) + b_{np\sigma} \Psi_{np}^-(\epsilon)] \quad (4.7)$$

where the new operators $a_{np\sigma}$ obey the standard anti-commutation relations and allow one to rewrite the hybridization term in (4.5) as

$$\int_{-1}^1 d\epsilon \left(c_{d\sigma}^{\dagger} a_{\epsilon\sigma} + \text{h.c.} \right) = \sqrt{1 - \Lambda^{-1}} \sum_n \Lambda^{-n/2} \left(c_{d\sigma}^{\dagger} (a_{n0\sigma} + b_{n0\sigma}) + \text{h.c.} \right) \quad (4.8)$$

Notice that only the operators $a_{n0\sigma}$ and $b_{n0\sigma}$ couple directly to the impurity operators $c_{d\sigma}$. States with finite p only couple indirectly: The term $\int_{-1}^1 \epsilon a_{\epsilon\sigma}^{\dagger} a_{\epsilon\sigma}$ couples operators of different p . This is a direct consequence of the impurity coupling locally in real-space, c.f. Ref. [12].

The wavefunctions created by the operators $a_{np\sigma}$ and $b_{np\sigma}$ are wave-packet states. They have energy Λ^{-n} , spread $\Lambda^{-n}(1 - \Lambda^{-1})$; they are peaked at a distance of $\Lambda^n p / (1 - \Lambda^{-1})$ from the impurity and have a radial extent of $\Lambda^{-n} / (1 - \Lambda^{-1})$, c.f. Fig. 4.4. The approximation (everything up until this point has been exact - ignoring the non-essential approximations introduced at the beginning for pedagogical reasons, c.f. Bulla[12]) of the NRG is to neglect terms containing $a_{np\sigma}$ and $b_{np\sigma}$ with $p \neq 0$. This approximation turns out to be good for two reasons:

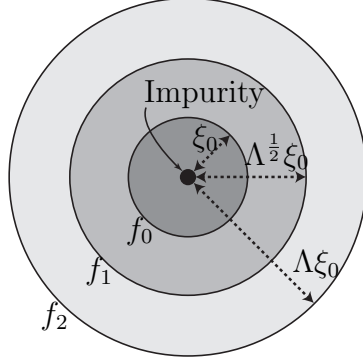


Figure 4.4: Spherical shells in r space depicting the extent of the wave functions of f_n .

1. the coupling of the impurity to operators with $p \neq 0$ is only indirect and
2. those term have a factor of $(1 - \Lambda^{-1})$ which becomes small as $|1 - \Lambda| \ll 1$.

As first shown by Wilson[113], it is safe to neglect all terms with $p \neq 0$ even for discretisation parameters as large as $\Lambda = 2.5$. Dropping the index p the Hamiltonian is given by

$$\begin{aligned}
H/D = \frac{1}{2}(1 + \Lambda^{-1}) \sum_{n=0}^{\infty} \Lambda^{-n} (a_{n\sigma}^\dagger a_{n\sigma} - b_{n\sigma}^\dagger b_{n\sigma}) + \sqrt{\frac{2\Gamma}{\pi D}} (f_{0\sigma}^\dagger c_{d\sigma} + c_{d\sigma}^\dagger f_{0\sigma}) \\
+ \frac{1}{D} (\epsilon_D + \frac{1}{2}U) c_{d\sigma}^\dagger c_{d\sigma} + \frac{1}{2} \frac{U}{D} (c_{d\sigma}^\dagger c_{d\sigma} - 1)^2 \quad (4.9)
\end{aligned}$$

where we have defined the new operator

$$f_{0\sigma} = \sqrt{\frac{1}{2}(1 - \Lambda^{-1})} \sum_{n=0}^{\infty} \Lambda^{-n/2} (a_{n0\sigma} + b_{n0\sigma}) \quad (4.10)$$

which describes the eigenstate maximally localized around the impurity. Observe that the eigenstates created by $f_{0\sigma}^\dagger$ are not orthogonal to the eigenstates defined by the conduction band operators $a_{n\sigma}^\dagger$ and $b_{n\sigma}^\dagger$.

4.2.2 Mapping onto a chain

In order to solve this Hamiltonian iteratively one introduces a set of operators $f_{n\sigma}$ with $n > 0$ in such a way that they exhibit only nearest neighbour coupling. The exact details of this procedure are explained in Ref. [12]. The resulting expression for the hamiltonian assumes the form

$$\begin{aligned}
H/D = \frac{1}{2}(1 + \Lambda^{-1}) \sum_{n=0}^{\infty} \Lambda^{-n/2} t_n [f_{n\sigma}^\dagger f_{n+1\sigma} + \text{h.c.}] + \sqrt{\frac{2\Gamma}{\pi D}} (f_{0\sigma}^\dagger c_{d\sigma} + \text{h.c.}) \\
+ \frac{1}{D} (\epsilon_D + \frac{1}{2}U) c_{d\sigma}^\dagger c_{d\sigma} + \frac{1}{2} \frac{U}{D} (c_{d\sigma}^\dagger c_{d\sigma} - 1)^2 \quad (4.11)
\end{aligned}$$

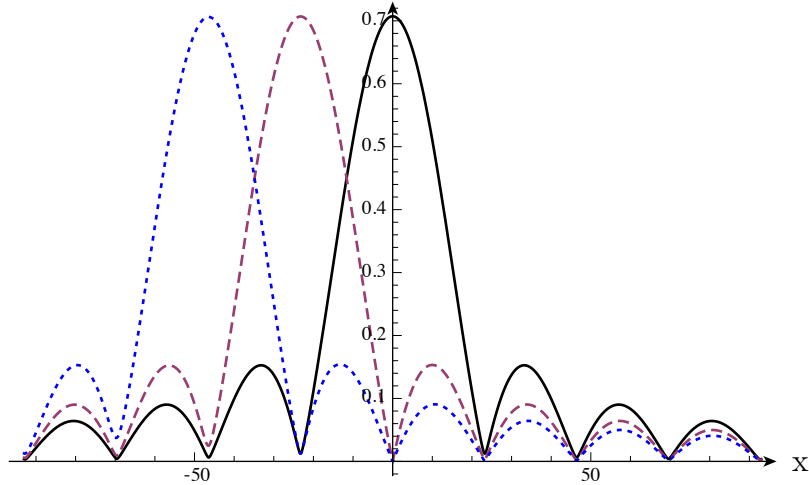


Figure 4.5: Position density of wilson operators $a_{np\sigma}$ with $n = 0$ and $p = 0$ (black, solid), $p = 1$ (red, dashed) and $p = 2$ (blue, dotted) for the special case of a tight binding chain with constant hopping strength t and an impurity which couples only to site 0 with strength V . Notice how the position density at near the impuriy vanishes for all $p \neq 0$

with $t_n = (1 - \Lambda^{-(n+1)})/\sqrt{(1 - \Lambda^{-2n-1})(1 - \Lambda^{-2n-3})}$ which quickly approaches 1 for large n and the new operators $f_{n\sigma}$ again obeying the standard anti-commutation relations. For a more complicated form of the hybridisation function, as for instance needed when the NRG is used as an impurity solver in the DMFT, the coefficients have to be calculated iteratively using a arbitrary precision routine. The Hamiltonian in Eq. (4.11) now has the desired structure of a hopping Hamiltonian on a semi-infinite chain, which is often referred to as the Wilson chain.

The structure of the above Hamiltonian becomes more apparent, when one thinks of the one-particle wavefunctions created by the various operators that we have defined throughout the sequence of transformations. The wavefunctions $|a_k\rangle$ that correspond to the operators in (4.5) describe delocalised, s-wave conduction band electron states which extend through out the metallic lead. In contrast the wave functions $|a_{np\sigma}\rangle$ and $|b_{np\sigma}\rangle$ form wave packet states with an extent limited to their respective phase-space shells. $|a_{np\sigma}\rangle$ has a mean energy Λ^{-n} , while $|b_{np\sigma}\rangle$ has a mean energy $-\Lambda^{-n}$, a spread in energy of $\Lambda^{-n} - \Lambda^{-(n+1)} = \Lambda^{-n}(1 - \Lambda^{-1})$ and is peaked at a distance of $\Lambda^n p/(1 - \Lambda^{-1})$ from the impurity and a radial extent of $\Lambda^n/(1 - \Lambda^{-1})$. We see that as n gets large these states become more and more delocalised and resemble more and more the original s-wave conduction electron states. All of this may be easily confirmed by transforming these operators back into real-space. Now the nature of the previous approximation becomes clear: throwing away states with $p \neq 0$ corresponds to throwing away those states which are peaked away from the impurity. Fig. 4.5 shows the position density of the Wilson operators for the special case, where the density of states of the conduction electrons is given by a one-dimensional, tight-binding change of constant hopping amplitude t , $\omega(k) = -2t \cos(k)$, and an impurity which couples only to the $x = 0$ site with hybridisation strength V . In general, the states $|f_{n\sigma}\rangle$ have a mean energy of 0. Their energy spread also decreases dramatically

with n . Therefore $f_{0\sigma}$ the only operator, which directly couples to the impurity has the biggest energy spread and is therefore the most localised of these operators.

4.2.3 Iterative diagonalisation

The transformations performed so far have rendered a form of the Hamiltonian which is amenable to an iterative diagonalisation procedure. It will be in this iterative diagonalisation procedure that the RG character of the method finally surfaces. In order to solve the problem iteratively, one defines a sequence of Hamiltonians as follows:

$$H_N = \Lambda^{(N-1)/2} \left[H_{\text{imp}} + \tilde{\Gamma}^{1/2} (f_{0\sigma}^\dagger c_{d\sigma} + \text{h.c.}) + \sum_{n=0}^{N-1} \Lambda^{-n/2} t_n (f_{n\sigma}^\dagger f_{n+1\sigma} + \text{h.c.}) \right] \quad (4.12)$$

where we have defined the impurity Hamiltonian H_{imp} containing the terms acting only at the impurity, and the renormalised couplings are given by,

$$\begin{aligned} \tilde{\delta}_d &= \left(\frac{2}{1 + \Lambda^{-1}} \right) \frac{1}{D} (\epsilon_d + \frac{1}{2}U) \\ \tilde{U} &= \left(\frac{2}{1 + \Lambda^{-1}} \right) \frac{U}{2D} \\ \tilde{\Gamma} &= \left(\frac{2}{1 + \Lambda^{-1}} \right)^2 \frac{2\rho|V_d|^2}{D} \\ H_{\text{imp}} &= \tilde{\delta}_d c_{d\sigma}^\dagger c_{d\sigma} + \tilde{U} (c_{d\sigma}^\dagger c_{d\sigma} - 1)^2 \end{aligned} \quad (4.13)$$

Note that the strength of the coupling between neighbouring chain elements decreases exponentially due to the factor $\Lambda^{-n/2}$ in front of t_n . This behaviour is due to the logarithmic discretisation of the energy band which leads to a separation of energy scales, between high- and low energy states. It is only due to this property that a truncation of the high energy states is justified. The full discrete Hamiltonian, Eq.4.11, is recovered in the limit $N \rightarrow \infty$ as

$$H = \lim_{N \rightarrow \infty} \frac{1}{2} (1 + \Lambda^{-1}) D \Lambda^{-(N-1)/2} H_N \quad (4.14)$$

The scale factor $\Lambda^{(N-1)/2}$ makes the lowest energy scale in H_N of order 1. Information about the many-electron energy-level structure of H at energies $\propto \Lambda^{-(N-1)/2} D$ is contained in the energy-level structure of H_N at energy $\propto 1$. Two successive Hamiltonians in the series are connected by the recursion relation

$$H_{N+1} = \Lambda^{1/2} H_N + t_N (f_{N\sigma}^\dagger f_{N+1\sigma} + f_{N+1\sigma}^\dagger f_{N\sigma}) \quad (4.15)$$

with the initial Hamiltonian in the series containing the impurity itself given by

$$H_0 = \Lambda^{-\frac{1}{2}} \left[\tilde{\delta}_d c_{d\sigma}^\dagger c_{d\sigma} + \tilde{\Gamma}^{1/2} (f_{0\sigma}^\dagger c_{d\sigma} + \text{h.c.}) + \tilde{U} (c_{d\sigma}^\dagger c_{d\sigma} - 1)^2 \right] \quad (4.16)$$

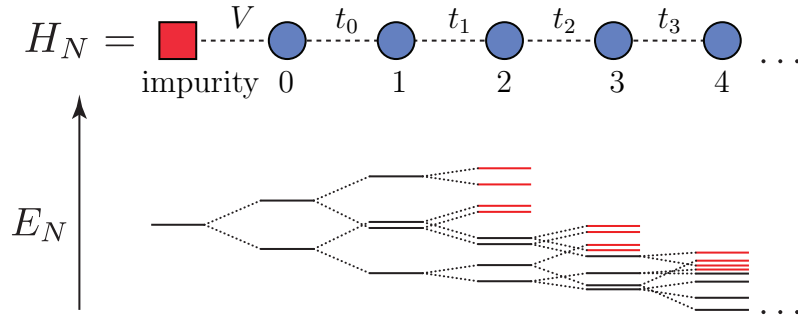


Figure 4.6: Illustration of the truncation procedure. The iterative diagonalisation splits each energy level into 4 levels upon the addition of another chain element. In this schematic picture however each energy level is split into only two levels in order not to make the illustration too cluttered. Due to the exponential decrease in the couplings it is safe to truncate the high energy states without altering the spectrum of the low energy states. The truncated states are marked red. Here $N_L = 4$.

In this form the single impurity Anderson model can be efficiently solved on a computer by taking advantage of the renormalisation group character of the above description. One starts with a diagonalisation of H_0 which can be easily accomplished numerically. From here on one continues iteratively using Eq. 4.15. Assuming that we have diagonalised a Wilson chain of length m and that the eigenstates are given by $|\mathbf{r}; m\rangle$ we construct a product basis for the Wilson chain of length $m + 1$ by

$$|(\mathbf{r}, \alpha_{m+1}); m + 1\rangle = |\mathbf{r}; m\rangle \otimes |\alpha_{m+1}\rangle \quad (4.17)$$

where $|\alpha_{m+1}\rangle$ are the eigenstates of the decoupled site $|\alpha_{m+1}\rangle = \{|\downarrow\rangle, |\uparrow\rangle, |\downarrow\downarrow\rangle, |\uparrow\uparrow\rangle\}$. The matrix elements of the Hamiltonian for the Wilson chain of length $m + 1$ for this product basis are given by

$$\begin{aligned} \langle(\mathbf{r}', \alpha'_{m+1}); m + 1| H_{m+1} |(\mathbf{r}, \alpha_{m+1}); m + 1\rangle &= \Lambda^{1/2} E_{\mathbf{r}, m} \delta_{\mathbf{r}\mathbf{r}'} \delta_{\alpha\alpha'} \\ &+ \left(\langle\mathbf{r}'; m| f_{m\sigma}^\dagger |\mathbf{r}; m\rangle \langle\alpha'| f_{m+1\alpha} |\alpha\rangle + \langle\mathbf{r}'; m| f_{m\sigma} |\mathbf{r}; m\rangle \langle\alpha'| f_{m+1\alpha}^\dagger |\alpha\rangle \right) \end{aligned} \quad (4.18)$$

The eigenvalue problem for the chain of length $m + 1$ can therefore be solved numerically using only a knowledge of the eigenspectrum of the chain of length m and the matrix elements of the operators $f_{m\sigma}^\dagger$. Diagonalising the Hamiltonian H_{m+1} , set up in the above product basis, can be described by a unitary transformation

$$|\mathbf{r}'; m + 1\rangle = \sum_{\alpha_{m+1}, \mathbf{r}} U_{\mathbf{r}', \mathbf{r}}^{\alpha_{m+1}} |\mathbf{r}; m\rangle \otimes |\alpha_{m+1}\rangle \quad (4.19)$$

where $|\mathbf{r}'; m + 1\rangle$ denotes the new eigenbasis of the Hamiltonian H_{m+1} . For the single impurity Anderson model the size of the Hilbert space grows exponentially with the length of the Wilson chain, $\propto 4^N$. Truncation becomes inevitable after a few iterations

as the computational complexity of the diagonalisation problem scales like the matrix dimension cubed. We thus only use the N_L lowest eigenstates in each iteration for the construction of the next Hamiltonian matrix. This truncation of high energy states marks the second approximation in the NRG and is well justified due to the separation of energy scales: High-lying states at one iteration cannot cross over and become low-lying states at a future iteration due to energy scale separation. Thus it is safe to discard them if we only wish to focus on the low-energy physics at each step. This is closely related to the renormalisation group structure of the problem - one studies the physics on progressively lower energy scales, discarding irrelevant high-energy degrees of freedom - as with Anderson's poor man's scaling. Fig. 4.6 illustrates the changes in the many-particle spectrum. In this schematic picture each energy level is split into only two levels in order not to make the illustration too cluttered.

4.2.4 Renormalisation group transformations

It is instructive to compare the NRG with a standard renormalisation group treatment such as the "poor man's scaling" introduced by Anderson. Here one defines a transformation \mathcal{R} which maps a Hamiltonian $H(\kappa)$ parametrized by a set of parameters κ to a new Hamiltonian with a renormalised parameter set κ' ,

$$\mathcal{R}_\Lambda [H(\kappa)] = H(\kappa') \quad (4.20)$$

where Λ parametrizes the step length. For the "poor man's scaling" the mapping is performed by perturbatively integrating out the high-energy degrees of freedom at the band edges $[-D, -D\Lambda^{-1}]$ and $[D\Lambda^{-1}, D]$ which leads to a renormalisation of the coupling between the impurity and the conduction electrons. Important physical limits are often marked by fixed points, i.e. points in the parameter space κ^* , such that

$$\mathcal{R}_\Lambda [H(\kappa^*)] = H(\kappa^*) \quad (4.21)$$

The fixed point κ^* can be categorised by examining the flow properties in its vicinity. Three different types of fixed points have to be distinguished:

1. **Stable** Fixed points, where any perturbation of the parameters κ^* leads to a flow back to κ^* , are referred to as stable fixed points.
2. **Unstable** For fixed points where all flows are directed away from κ^* , tiny perturbations in the parameters κ^* lead to flows away from the fixed point.
3. **Marginal** For marginal fixed points there exist some couplings which flow towards and some which flow away from the fixed point.

The fixed points of the SIAM can be obtained by choosing specific values for the renormalised interaction strength \tilde{U} and the hybridisation $\tilde{\Gamma}$ in Eq. (4.12). Fig. 4.7 shows a schematic of the renormalisation group flow in the SIAM. The three fixed points at the vertices of the coloured triangle are the free orbital fixed point (H_{FO}^*), the local moment fixed point (H_{LM}^*) and the strong coupling fixed point (H_{SC}^*). The free orbital fixed point H_{FO}^* is obtained when both couplings $\tilde{\Gamma}$ and \tilde{U} are set to zero. The

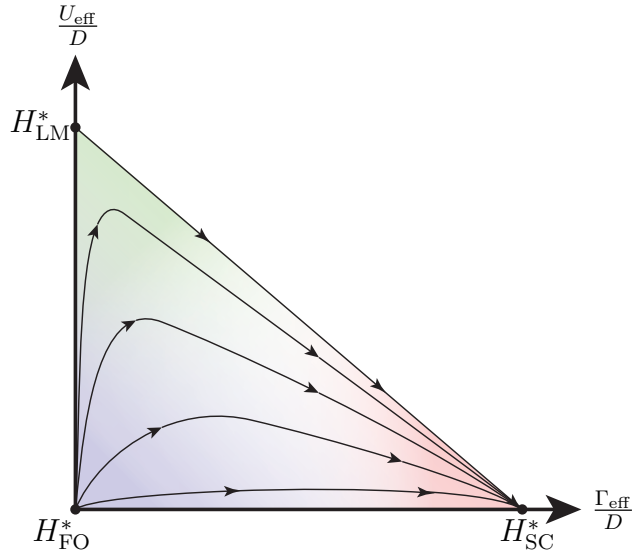


Figure 4.7: Schematic of the renormalisation group flow. Trajectories depict the flow of parameters U_{eff} and Γ_{eff} of the Hamiltonian H_N as function of the iteration N . Based on visualisation in [63].

resulting Hamiltonian is just the free-electron Hamiltonian of the conduction electrons plus a free-impurity orbital of zero energy. For each eigenstate of the conduction electron system one can construct four degenerate states by combining it with each of the four degenerate impurity states $|\rangle$, $|\uparrow\rangle$, $|\downarrow\rangle$ and $|\uparrow\downarrow\rangle$. Since the free Wilson chain is itself a fixed point of the RG transformation, H_{FO}^* must also be a fixed point. The impurity entropy is therefore $S = \ln(4)$. If for fixed hybridisation $\tilde{\Gamma}$ the interaction \tilde{U} becomes the largest energy scale in the problem, only impurity states with $|\uparrow\rangle$ and $|\downarrow\rangle$ have to be considered for $k_B T \ll \tilde{U}$. The impurity is therefore occupied by a single electron and can be understood as a local moment. This realises the situation described in the Kondo model. If in addition $\tilde{\Gamma} = 0$ the coupling between the conduction electrons and the impurity is switched off and the local moment becomes free. This is the local moment fixed point H_{LM}^* . The impurity has two degenerate states and thus the impurity entropy is given by $S = \ln(2)$. Finally we consider the case when $\tilde{\Gamma}/\tilde{U} \rightarrow \infty$. This is the strong coupling fixed point H_{SC}^* where the impurity is so strongly coupled to conduction electron state at the impurity site that both degrees of freedom are frozen out. A many-body Kondo singlet is formed such that the local moment of the impurity is dynamically screened by the surrounding conduction electrons. The impurity entropy is thus zero. As can be seen from Fig. 4.7 in the case of a flat conduction electron density of states all flows lead eventually to the strong coupling fixed point H_{SC}^* .

In the NRG the recursion expression, Eq. (4.15), can be viewed as a renormalisation group transformation $H_{m+1} = \mathcal{R}[H_m]$. For the SIAM one finds a flow of the eigenenergies of H_m as a function of the chain length. Fig. 4.8 shows the flow of the lowest eigenenergies for a SIAM calculation. For Fig. 4.8a the parameters are $V = 0.004$, $U = 0.001$ and $\Lambda = 2$. Three regimes can be distinguished: For iterations $N < 25$ the system is near the free orbital H_{FO}^* , then the energies cross over to the intermediate local moment fixed point H_{LM}^* in iterations $25 < N < 110$ before the

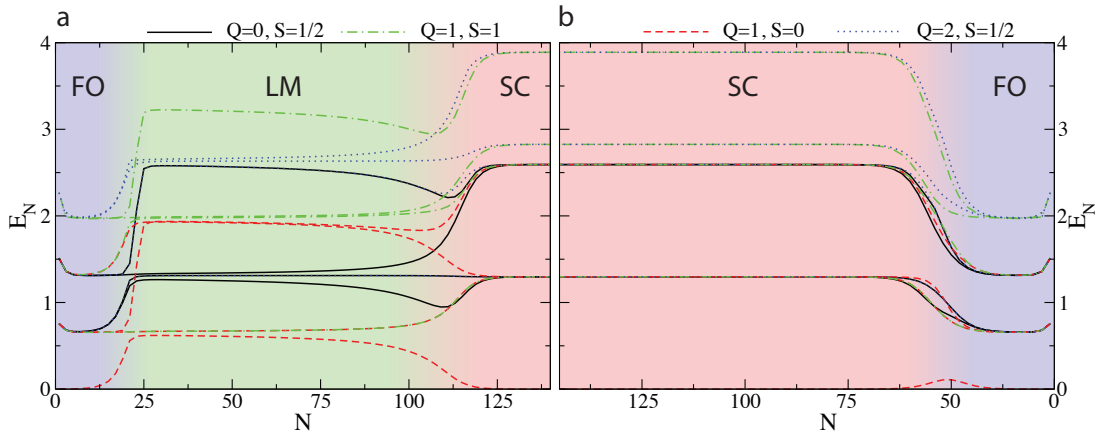


Figure 4.8: Flow of the lowest eigenenergies for an single Anderson impurity model with a) $V = 0.004$, $U = 0.001$ and $\Lambda = 2$; b) $V = 0.008$, $U = 0.0001$ and $\Lambda = 2$. Only odd iterations are shown here. We use $D = 1$.

system reaches the strong coupling fixed point for $N \geq 125$. For the second calculation depicted in Fig. 4.7b the hybridisation strength was increased to $V = 0.008$ and the interaction strength reduced to $U = 0.0001$. This moves the system away from the local moment H_{LM}^* towards the strong coupling fixed point H_{SC}^* as can be seen from Fig. 4.7. Indeed as the flow of the eigenenergies in Fig. 4.8b indicates the system stays near the free orbital fixed point H_{FO}^* for iterations $N < 50$ and then the system directly crosses over to the strong coupling fixed point H_{SC}^* without flowing close to the local moment fixed point H_{LM}^* . Importantly, the lowest energy physics (reached as $N \rightarrow \infty$) is always the characterised by the strong coupling fixed point in the metallic single impurity Anderson model.

4.3 Calculation of dynamical quantities

The first calculation of dynamical quantities using the NRG were realized by Frota and Oliveira[33], who calculated photoemission spectra for the single impurity Anderson model. Other calculations by Sakai et al. [100] and others followed. In the early 90s, the calculation of different transport coefficients also became possible[22, 49]. In the following we will describe techniques to calculate the single-particle spectra. One of the motivations to calculate this quantity was given by Meir and Wingreen[71] who showed that the knowledge of the single-particle spectra alone allows for the calculation of the zero-bias conductance through a quantum dot.

Lehmann resolving the impurity spectral function one obtains

$$A_\sigma(\omega) = \sum_{a,b} \langle b | c_{d\sigma} | a \rangle \frac{\exp[-\beta E_a]}{Z} \langle a | c_{d\sigma}^\dagger | b \rangle \delta(\omega + E_a - E_b) \quad (4.22)$$

where Z is the total partition function $Z = \sum_a \exp[-\beta E_a]$, $|a\rangle$ and $|b\rangle$ are a complete set of states and E_a is the eigenenergy of state $|a\rangle$. We see that the Lehmann representation gathers the necessary information to construct the spectrum from knowledge

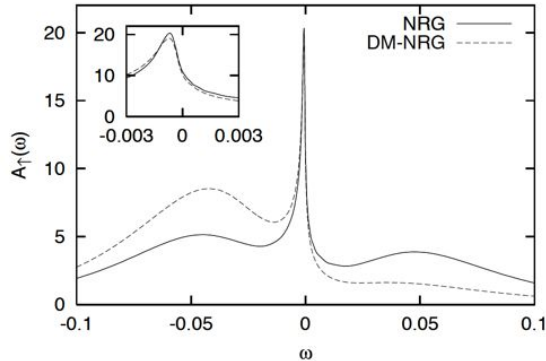


Figure 4.9: Comparison of single particle spectral functions for the symmetric SIAM ($\Delta = 0.01$, $U = 0.1$, $\epsilon_f = -0.05$) obtained by the traditional method (“NRG”) and the density matrix procedure (“DM-NRG”). From [51].

of certain matrix elements encoding hopping processes between the impurity and the conduction electron band. In the zero temperature limit these matrix elements only connect the ground state with excited states, while at finite temperature, excitations to and from all states must be considered. Certain matrix elements may be calculated in each step of the NRG using the states generated at a particular iteration. Approximate spectral reconstruction was performed using NRG in Refs. [22, 9] yielding useful results in certain ranges. It should be noted that also a full basis set of approximate eigenstates can be constructed from the iterative diagonalisation (see next pages).

However a number of complications arise from the logarithmic discretisation of the conduction band, which is at the heart of the NRG: the logarithmic energy discretisation ties the collection of spectral information for a certain energy ω to a specific iteration n . The characteristic energy scale of iteration n is given by $\Lambda^{-n/2}$. Therefore all spectral information for an energy window of width $\Lambda^{-(n+1)/2}$ would have to be reconstructed from states of iteration n . This is problematic in two ways: the states kept throughout the NRG iterations do not form a complete basis set, indeed they are not even orthonormal. Therefore double-counting ambiguities[21] arise when patching together the spectrum from peaks collected at different iterations[2]. Secondly spectral information concerning high energy features (such as the charge fluctuation “Hubbard satellites”) is collected at early iterations. However the correct ground state of the system is only found after many NRG iterations.¹ As pointed out by Hofstetter [51] this problem becomes particularly acute in the presence of a small, symmetry-breaking magnetic field h . The static magnetisation calculated directly from the appropriate expectation values during the NRG iterations does not agree with magnetisation obtained by integrating spectral functions for both spins up to the fermi level. The reason is simply that most of the spectral weight is tied to high

¹How many iterations are necessary exactly is actually an intriguing question. The most general answer to this question is a tautologic one: The NRG resolves energies of the order of $\Lambda^{-n/2}$ in the n th iteration. The recipe is that one should keep iterating until this resolution is smaller than the smallest physical energy scale in the problem. However how does one find the smallest physical energy scale? By solving the problem.

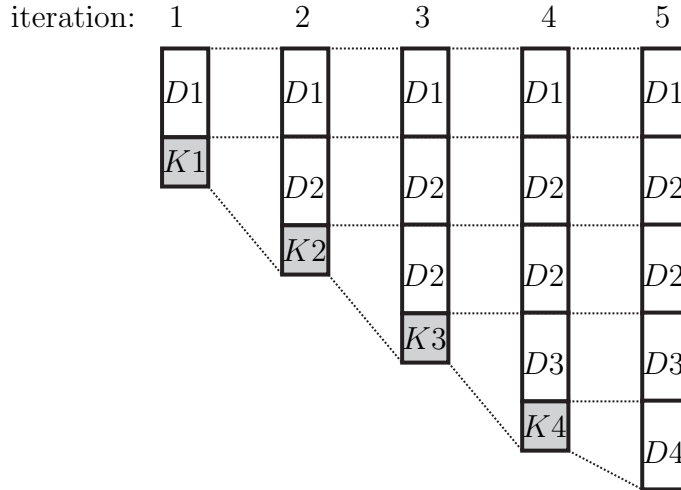


Figure 4.10: Labelling the states of each NRG iteration as either kept (K) or discarded (D), the discarded states of each iteration form a complete set of states (all the states from the last iteration are labeled discarded).

energy charge fluctuation peaks calculated from early NRG iterations that do not yet “know” of the small symmetry-breaking field. The problems arising from these circumstances may be easily understood by considering the following: As the iterative diagonalisation progresses down the Wilson chain, the quantum numbers for the ground state typically show an even-odd effect. For even iterations it might lie in the $S_z = 0$ -sector while for odd iterations it resides in $S_z = \frac{1}{2}$. As the small symmetry breaking field is not influential yet in these early iterations (here only high energy processes contribute) the $S_z = \frac{1}{2}$ states show erroneously a degeneracy which leads to an overestimation of the ground state manifold. For $T = 0$ the spectral function measures excitations from the ground state manifold and therefore high energy excitation peaks enter the spectrum which stem from the spurious ground state. This does not affect the paramagnetic case as these states are always degenerate here.

When using the NRG as an impurity solver for the DMFT to study symmetry broken phases it is especially important to fix these shortcomings. As all quantities in the DMFT have to be calculated self-consistently it is important get accurate single-particle spectra. Although here no *external* magnetic field is present an *intrinsic, molecular*, symmetry-breaking field may be generated due to different effective media for the \uparrow - and \downarrow -spins.

The first ingredient for the remedy was discovered by Anders and Schiller[2] who showed that a complete set of states can indeed be defined, based upon the states found throughout the NRG iterations. The key idea is to reconceptualise the Wilson chain from growing in each step of the iterative diagonalisation by one site to being of constant length N (where N is the total number of iteration that will be performed). Then, at each iteration, the hopping terms of the last (environment-) orbitals are iteratively switched on. Anders and Schiller (AS) therefore divided the system into two parts: a “system” block consisting of the first n coupled sites and an “environment” block of length $N - n$. The state of the environment is described by a product state of the individual uncoupled chain sites and provides a 4^{N-n} degeneracy, while the

system block is described by the NRG states of iteration n . Following Anders and Schiller we will denote the states of a Wilson chain of length N coming from iteration $n \leq N$, $|\mathbf{r}; \mathbf{e}\rangle_n^N$ where \mathbf{r} labels the diagonalized NRG states and \mathbf{e} denote the $N - n$ environmental degrees of freedom. Denoting the Hamiltonian for the chain of length n with H_n we find

$$H_n |\mathbf{r}; \mathbf{e}\rangle_n^N = E_n^r |\mathbf{r}; \mathbf{e}\rangle_n^N \quad (4.23)$$

As the states of the NRG iteration $n + 1$ are constructed from the kept states of iteration n they cannot be orthogonal to each other. However the discarded states of iteration n are necessarily orthogonal to the kept states of that same iteration and consequently to all states of iteration $n + 1$. Iterating this thought one quickly realises that the discarded states of all iterations are necessarily orthogonal to each other and form a complete albeit approximate set of states. The construction of the AS basis is illustrated in figure 4.10. The central approximation (always at the heart of the NRG calculations) is thus that E_n^r from Eq. 4.23 at iteration n closely approximates the true E_n^r as $N \rightarrow \infty$.

Having found a complete basis set one could now try to calculate the spectral functions using the Lehmann representation (4.22). However one is faced with another problem: matrix elements of local impurity operators $\langle b | c_{d\sigma} | a \rangle$ can be calculated in each iteration of the NRG, but this means that only matrix elements involving AS states of the *same* iteration are known, ignoring spectral contributions arising from excitations connecting states of different NRG iterations. The solution proposed by Weichselbaum and van Delft[112] reformulates the Lehmann sum in terms of the density matrix instead of the states. This exploits the relation for the thermal average $\langle \hat{\Omega} \rangle = \text{Tr}[\hat{\rho} \hat{\Omega}]$, where $\hat{\rho}$ is the full density matrix. The density matrix in the AS basis for iteration n is defined as,

$$[\hat{\rho}_n^{AS}]_{rr'} = \delta_{r,r'} \exp(-\beta E_n^r) / Z^n \quad (4.24)$$

where $Z^{tot} = \sum_n Z^n$ and $Z^n = \sum_r \exp(-\beta E_n^r)$. The total density matrix of the system can now be written as

$$\hat{\rho}^{tot} = \sum_n^N w_n \hat{\rho}_n^{AS} \quad (4.25)$$

$$w_n = d^{N-n} \frac{Z^n}{Z^{tot}} \quad (4.26)$$

The weighting factor w_n stems from the d^{N-n} -fold degeneracy of the AS states of iteration n due to the environmental degrees of freedom.² The utilisation of the matrix elements calculated from the NRG iterations is complicated by a basis issue: the

²The innocent looking factor w_n actually allows for a deep look into the information gathering strategy of the full density matrix approach: w_n contains two competing factors, the Boltzmann factors in the partition function of the n th iteration, Z^n , and the degeneracy factor d^{N-n} . For low system temperatures and early iterations (high energy) the Boltzmann factor will be strongly suppressed, however the degeneracy factor will be huge. In general for a given temperature the function w_n is seen to peak around the appropriate NRG iteration n ($T \approx \Lambda^{-n/2}$) collecting the bulk of the spectral information from a limited number of appropriately chosen NRG iterations.

matrix elements are given in the NRG basis which includes both kept and discarded states, while the density matrix however has been constructed using the AS basis (only discarded states). In order to evaluate (4.22) we wish to obtain the density matrix in the same basis. Referring the reader to Ref. [85] for technical details we introduce the “reduced density matrix” through

$$\hat{\rho}^{tot} = \sum_n^N \hat{\rho}^{red} \quad (4.27)$$

The part connecting discarded to discarded states of NRG iteration n in $\hat{\rho}^{red}$ is simply $w_n \hat{\rho}_n^{AS}$. Therefore for the last iteration $\hat{\rho}_N^{red} = \hat{\rho}_N^{AS}$. The kept part of $\hat{\rho}^{red}$ may be calculated by remembering that it is the kept states of iteration n which are used to construct the NRG states of iteration $n + 1$. Therefore performing the inverse of the unitary transformation used to diagonalize in iteration $n + 1$ on $\hat{\rho}_{n+1}^{red}$ yields the kept part of $\hat{\rho}_n^{red}$. Note that this is equivalent to tracing out the environmental degrees of freedom for orbital $(n + 1)$, hence the name *reduced*. This way all $\hat{\rho}_n^{red}$ can be constructed iteratively by starting from $\hat{\rho}_N^{red}$ and working backwards.

As a last step the Lehmann sum (4.22) needs to be expressed through the reduced density matrix. In [112] the appropriate expression is given

$$A_\sigma(\omega) = \sum_n^N \sum_{r,r'} [[c_{d\sigma}]^n \cdot [\hat{\rho}_n^{red}]]_{rr'} \cdot [c_{d\sigma}^\dagger]_{r'r}^n \cdot \delta(\omega - E_n^r + E_n^{r'}) \quad (4.28)$$

where $[c_{d\sigma}^\dagger]_{r'r}^n = {}_n \langle r' | c_{d\sigma}^\dagger | r \rangle_n$ are the local impurity elements which connect both kept and discarded states.

We have succeeded in determining the spectral function as a sum of discrete delta peaks. The discreteness of the data is due to the discretisation of the conduction band. In order to obtain a continuous spectrum one typically broadens these delta peaks by replacing them with logarithmic gaussians of the same weight. Details of this process are explained in the next section.

4.4 Broadening of discrete spectra

We have discussed already that the NRG yields spectral functions in the form of a Lehmann sum over discrete δ -functions. These will have to be broadened in a suitable manner to obtain a continuous function, which should ideally produce uniquely determined spectra independent of the discretisation of conduction electron band. In practice this is rather difficult due to the inescapable arbitrariness of the broadening scheme. However the procedure discussed here has been found to produce rather accurate results. Indeed, NRG has reliably reproduced exact results in the special cases where these are known [9, 112].

The smoothed spectral function $A_\sigma(\omega)$ is calculated by folding the discrete numerical data $A_{\sigma\text{disc}}(\omega) = \sum w_n \delta(\omega - \omega_n)$ against a certain broadening kernel $K(\omega, \omega')$.

$$A_\sigma(\omega) = \int d\omega' K(\omega, \omega') A_{\sigma\text{disc}}(\omega') \quad (4.29)$$

There are a number of desirable properties (due to physical implicitness) that $K(\omega, \omega')$ should respect[112]:

- *Frequency-dependent width:* Due to the logarithmic discretization of the conduction band, peaks are logarithmically distributed around $\omega = 0$, i.e. data is more coarse-grained at large frequencies. Choosing a Gaussian on a logarithmic scale is a natural choice, as a variable transformation of the data to a linear scale would simply mean replacing delta functions by Gaussians. Gaussians on a logarithmic scale show a frequency dependent width.
- *Conservation of peak weight:* The broadening kernel should be chosen in such a way, that the weight of individual peaks is faithfully represented. This amounts to the property, $\int d\omega' K(\omega, \omega') = 1 \forall \omega'$. Of course this also trivially ensures that $\int d\omega A_\sigma(\omega) = \sum_n w_n$.
- *Conservation of peak height:* It can be shown[112] that demanding that a constant function $w_n = w$ should be mapped onto a constant continuous function also restricts the integral $\int d\omega' K(\omega, \omega') = 1 \forall \omega$.

The first two properties may be fulfilled by the following broadening kernel

$$\begin{aligned}
K(\omega, \omega') &= L(\omega, \omega')h(\omega') + G(\omega, \omega')(1 - h(\omega')) \\
L(\omega, \omega') &= \frac{\Theta(\omega\omega')}{\sqrt{\pi}\alpha|\omega|} \exp\left[\frac{\log|\omega/\omega'|}{\alpha} - \gamma\right]^2 \\
G(\omega, \omega') &= \frac{1}{\sqrt{\pi}\omega_0} \exp[-(\omega - \omega')^2/\omega_0^2] \\
h(\omega') &= \begin{cases} 1 & |\omega'| \geq \omega_0 \\ \exp - \left[\frac{\log|\omega'/\omega_0|}{\alpha}\right]^2 & |\omega'| < \omega_0 \end{cases} \quad (4.30)
\end{aligned}$$

The choice $\gamma = \alpha/4$ also fulfills the third property.

4.5 NRG as an impurity solver for the DMFT

The NRG can only be applied to impurity systems, where the impurity couples to a non-interacting bath of electrons. Therefore a direct application to systems of coupled interacting lattice sites is not possible. Early attempts at an application have led to the development of the density-renormalisation group (DMRG) [104, 44]. As already mentioned in the last chapter, the DMFT is an approximation for correlated lattice models (which becomes exact in the limit large lattice connectivity) where the interacting lattice problem is mapped onto a quantum impurity which needs to be solved self-consistently. In the process the local self-energy is identified with the impurity self-energy. From the perspective of the NRG, the DMFT equations provide a closed set of equations which determine a new hybridisation function $\Delta(\omega)$ for a given impurity self-energy $\Sigma(\omega)$. The hybridisation function is manifestly energy-dependent and depends on model under consideration, its parameters, and even the

history of the previous DMFT iterations. It contains deeply non-trivial information on the structure of the lattice dynamics in the large coordination limit, and cannot be neglected. The approximation of a constant hybridisation function Δ and a constant density of states for the conduction electrons ρ is therefore not permissible. The full energy-dependence of the hybridisation function $\Delta(\omega)$ has to be taken into account in the logarithmic discretisation and the subsequent construction of the Wilson chain. Refs. [13] and [12] give a detailed account on how this may be achieved. In the following, we briefly summarise the key points.

4.5.1 Energy-dependent hybridisation functions

In order to incorporate the effects of an energy-dependent hybridisation function $\Delta(\omega)$ the Hamiltonian in its one-dimensional energy representation, Eq. (4.5), has to be generalised to

$$H/D = \int_{-1}^1 d\epsilon \left[g(\epsilon) a_{\epsilon\sigma}^\dagger a_{\epsilon\sigma} + h(\epsilon) (a_{\epsilon\sigma}^\dagger c_{d\sigma} + c_{d\sigma}^\dagger a_{\epsilon\sigma}) \right] + \frac{1}{D} (\epsilon_D + \frac{1}{2}U) c_{d\sigma}^\dagger c_{d\sigma} + \frac{1}{2} \frac{U}{D} (c_{d\sigma}^\dagger c_{d\sigma} - 1)^2 \quad (4.31)$$

where $g(\epsilon)$ is the dispersion of the conduction electron band and $h(\epsilon)$ parametrizes the hybridisation strength. Bulla et al.[11] showed that the two functions $g(\epsilon)$ and $h(\epsilon)$ are related to the hybridisation function by

$$\Delta(\epsilon) = \pi \frac{dg^{-1}(\epsilon)}{d\omega} h(g^{-1}(\epsilon)) \quad (4.32)$$

with $g(g^{-1}(\epsilon)) = \epsilon$. Ambiguity exists how the energy-dependence may be divided between $g(\epsilon)$ and $h(\epsilon)$ for a given $\Delta(\epsilon)$. Note that the constant hybridisation of strength Γ/D is recovered by the choice $h(\epsilon) = \sqrt{\Gamma/(\pi D)}$ and $g(\epsilon) = \epsilon$.

With $\xi_0 = \int_{-1}^1 d\epsilon \Delta(\epsilon)$ the hybridisation term between the impurity and the first site assumes the form

$$\sqrt{\frac{\xi_0}{\pi}} (f_{0\sigma}^\dagger c_{d\sigma} + c_{d\sigma}^\dagger f_{0\sigma}) . \quad (4.33)$$

The hopping elements of the chain have not the simple form as given below Eq. (4.11) anymore but acquire a complicated n dependence. In addition, on-site energies for the Wilson sites emerge when the bath is not particle-hole symmetric. Using a standard triangulation procedure (Lanczos method) the hopping elements t_n and onsite energies ϵ_n can be calculated from the hybridisation function $\Delta(\epsilon)$. The details of this procedure are given in Refs. [13, 12]. It should be noted that the recursion relations for the calculation of these coefficients are numerically very unstable. In order to find the true Wilson chain representation of the hybridisation function, high precision numbers must be used for the algorithm.

For the case of the flat band Campo and Olivera[16] showed that the spectral density of the coupling between the impurity and the conduction band is systematically underestimated. A discretisation parameter dependent renormalisation of the hybridisation function fixes this issue

$$\Delta_{\text{fixed}}(\epsilon) = \frac{1}{2} \frac{\Lambda + 1}{\Lambda - 1} \ln(\Lambda) \Delta(\epsilon) . \quad (4.34)$$

No exact expression is known for the general energy-dependent case - although it can be estimated - see Ref. [96].

4.5.2 Calculation of the self-energy within NRG

For the DMFT loop one of the quantities of interest is the impurity self-energy, $\Sigma(\omega)$. Bulla et al.[10] first showed that it is possible to write the self-energy as the ratio of two correlation functions, both of which can be calculated directly within the NRG. An equation of motion technique is used to show that the self-energy is given by,

$$\Sigma_\sigma(\omega) = U \frac{F_\sigma(\omega)}{G_\sigma(\omega)} \quad (4.35)$$

where $G_\sigma(\omega)$ is the impurity Green's function defined as

$$G_\sigma(\omega) = -i \int_{-\infty}^{\infty} dt e^{i\omega t} \Theta(t) \langle \{f_\sigma(t), f_\sigma^\dagger\} \rangle \quad (4.36)$$

and $F_\sigma(\omega)$ is an auxiliary correlation function given by

$$F_\sigma(\omega) = -i \int_{-\infty}^{\infty} dt e^{i\omega t} \Theta(t) \langle \left\{ \left(f_\sigma^\dagger f_{\bar{\sigma}} f_\sigma \right) (t), f_\sigma^\dagger \right\} \rangle \quad (4.37)$$

The imaginary parts of $F_\sigma(\omega)$ and $G_\sigma(\omega)$ are calculated from NRG data using the Lehman sum within the full density matrix approach, with the poles of the spectrum broadened as above. The real parts are then obtained by Kramers-Kronig transform. Discretisation artifacts cancel to some extent by dividing the two quantities. This produces a rather smooth self-energy, which in term can be used to calculate an improved spectrum for the impurity. Z-averaging [83] can also be used to further increase accuracy and resolution.

4.6 Other impurity solvers

It should be mentioned that a variety of different impurity solvers[37] exists each with its own merits and drawbacks. Quantum Monte Carlo (QMC) [50] has become a popular choice especially in the ab-initio community where realistic material-specific calculations are combined with the treatment of strong correlation physics by the DMFT. Naturally an impurity solver which can cope with a many orbital situation is desirable and QMC can do just that. The quantum Monte Carlo (QMC) method considers the single-impurity problem in discretized imaginary time. The effective bath only enters through \mathcal{G}_0 , and there is no need to discretize the conduction band. The first numerical solutions of the LISA equations using this QMC method were obtained independently by Jarrell[56], Rozenberg et al.[116], and Georges and Krauth[38]. QMC is however a rather expensive method [37] and thus not well suited for our purposes, since we need to solve the Anderson impurity problems many times per iteration, see above. Furthermore, one cannot access the low temperature regime and one is limited by the “sign problem” if one desires to study magnetic solutions.

Another solver which should be mentioned here is the exact diagonalisation (ED) [99, 15]. In this method, the single-impurity problem is approximated by a few orbitals only and solved exactly. The finite number of orbitals provide a parametrisation of the effective bath. With an appropriate choice of the geometry of their hopping interconnections the parameters are modelled by the site energies and hopping amplitudes. It is the physical insight on a particular problem that indicates the most appropriate choice, which allows one to determine an appropriate parametrization. The number of orbitals that one can effectively treat is severely limited by the size of an exponentially growing Hilbert space.

The third choice we want to mention here is the so-called iterated perturbation theory (IPT) [114, 120]. Here the self-energy of the Anderson impurity model is calculated to second order in the on-site interaction U . Only two diagrams contribute to this order and the self-energy assumes the form

$$\Sigma_{\sigma}(i\omega_n) = U \langle n_{\bar{\sigma}} \rangle + U^2 \int_0^{\beta} d\tau e^{i\omega_n \tau} \mathcal{G}_{0\sigma}(\tau)^3 + \mathcal{O}(U^3) \quad (4.38)$$

For the case of the half-filled Hubbard model at the particle-hole symmetric point the IPT has proven to be a good, computationally inexpensive method for the solution of the impurity problems. Not only the physics of the Kondo resonance but also incoherent features of the upper and lower Hubbard band are captured by this approach. Away from particle-hole the strong coupling limit is not correctly captured but there have been modifications to the method in an attempt to fix this [59, 93].

The continuous-time Monte Carlo method [41] is another powerful choice for an impurity solver and nowadays one of the most important and widely used methods. Here the basic idea is to split the Hamiltonian into two parts $H = H_a + H_b$ and write the partition function $\mathcal{Z} = e^{-\beta H}$ in the interaction representation with respect to H_a . Expanding in power of H_b one finds

$$\begin{aligned} Z &= \text{Tr} T_{\tau} e^{-\beta H_a} \exp \left[- \int_0^{\beta} H_b(\tau) \right] \\ &= \sum_k (-1)^k \int_0^{\beta} d\tau_1 \dots \int_0^{\beta} d\tau_k \text{Tr} \left[e^{-\beta H_a} H_b(\tau_k) H_b(\tau_{k-1}) \dots H_b(\tau_1) \right] \end{aligned} \quad (4.39)$$

The trace evaluates to a number and diagrammatic Monte Carlo methods enable a sampling over all orders k , all topologies of the paths and diagrams, and all times τ_1, \dots, τ_k in the same calculation. Because the method is formulated in continuous time from the beginning, time-discretisation errors do not have to be controlled.

4.7 Spin-dependent hybridisation functions

The NRG can be generalised to treat arbitrary spin-dependent hybridisation functions. A description of this generalisation can be found in Sindel et al. [107] where the interplay between the Kondo correlations on a quantum dot and itinerant ferromagnetism in the leads is studied. Ferromagnetic order in the conduction electron system leads to a suppression of the Kondo effect. This can be seen by considering the

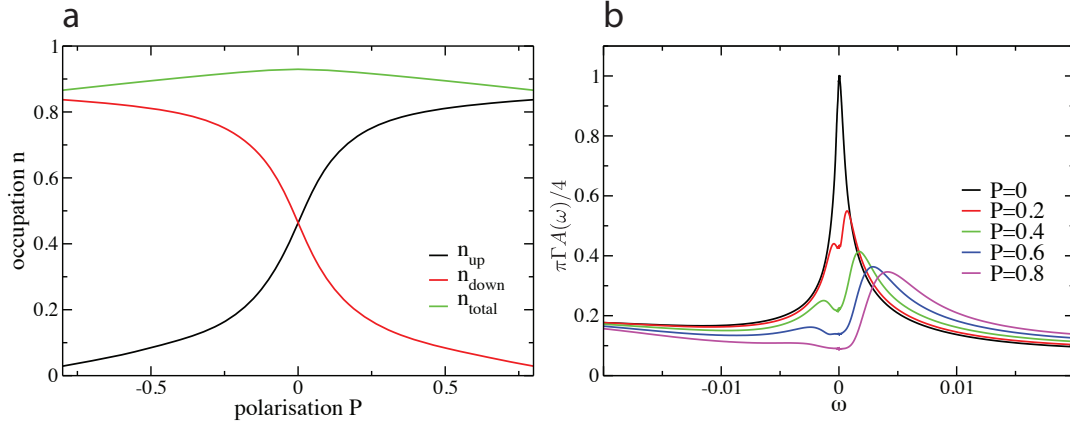


Figure 4.11: a) Total occupation $n(P)$ and spin species resolved occupations $n_\sigma(\omega)$ as functions of the spin polarisation P . b) Total spectral function $A(\omega) = \sum_\sigma A_\sigma(\omega)$ for different values of the spin polarisation P . An increase in P results in a splitting and suppression of the Kondo resonance. The parameters for this calculation were $U = 0.12$, $\Gamma = U/6$, $\epsilon_d = -U/3$ and $T = 10^{-20}$.

extreme limit, where the lead is fully polarised, i.e. only spin species exists: the effective screening of the impurity simply cannot develop because the spin-flip processes central to the Kondo effect are suppressed. The simplest way to model the competition between these two effects is to consider normalised flat bands with a finite spin polarisation. A consequence of the conduction electron ferromagnetism is that the spin-dependent bands are shifted relative to each other, which is the so-called Stoner splitting. On the simplest level of description this effect can be ignored. In this particular case the spin-dependent hybridisation can be parametrized as $\Gamma_\sigma = \frac{1}{2}\Gamma(1 \pm P)$. Since $\Gamma_\sigma = \pi\rho_\sigma V^2$ the spin dependence can be shifted from the conduction electron density of states to a spin-dependent hopping V_σ between the impurity and the first site of the Wilson chain. The advantage is that in this case the Wilson chain for the \uparrow - and \downarrow -electrons is identical and only the coupling V_σ between the impurity and the first site of the Wilson chain differs. The intermediate regime of the spin polarisation, $0 < P < 1$, can be investigated with the NRG now.

Fig. 4.11a shows the total occupation of the impurity n and the spin-resolved occupations n_σ as function of the spin polarisation P in the leads. For $\epsilon_d = -U/2$ the system is at the particle-hole symmetric point and therefore the system remains at half-filling even for a finite spin polarisation P (not shown). However, with an applied gate voltage of $\epsilon_d = -U/3$ between lead and dot the total occupation n decreases for finite spin polarisation P . For $P = 0$ the spin symmetry is unbroken and $n_\uparrow = n_\downarrow$. For finite $P > 0$ the occupation of the \uparrow -electrons is enhanced while n_\downarrow is suppressed, c.f. Fig. 4.11a. The total single particle spectral function is shown in Fig. 4.11b for different spins polarisations P . For $P \neq 0$ the charge fluctuations on the dot become spin-dependent as the different spin species see different leads. This causes the dot levels to split and the dot magnetisation $n_\uparrow - n_\downarrow$ becomes finite. As a result, the Kondo resonance is split and ultimately suppressed. This means that

Kondo correlations are reduced or even completely suppressed. Note that the data shown in Fig. 4.11 agree with the data of the original publication by Sindel et al.[107].

In order to treat arbitrary spin-dependent hybridisation functions the mapping to the Wilson chain outlined in section 4.2.2 needs to be generalised. Essentially the Lanczos tridiagonalisation procedure which brings the conduction electron Hamiltonian to the form of the Wilson chain is applied separately to the hybridisation function for the spin- \uparrow and spin- \downarrow electrons. This leads to a Wilson chain with spin-dependent on-site energies $\epsilon_{n\sigma}$ and hopping integrals $t_{n\sigma}$. The coupling between the impurity and the first site of the Wilson chain also becomes spin-dependent,

$$\xi_{0\sigma} = \int_{-1}^1 d\epsilon \Delta_{\sigma}(\epsilon) \quad (4.40)$$

and so the fully discretised Hamiltonian assumes the form

$$\begin{aligned} H/D = & \frac{1}{D}(\epsilon_D + \frac{1}{2}U)c_{d\sigma}^{\dagger}c_{d\sigma} + \frac{1}{2}\frac{U}{D}(c_{d\sigma}^{\dagger}c_{d\sigma} - 1)^2 + \sqrt{\frac{\xi_{0\sigma}}{\pi}} \sum_{\sigma} (c_{d\sigma}^{\dagger}f_{0\sigma} \\ & + f_{0\sigma}^{\dagger}c_{d\sigma}) + \sum_{\sigma, n=0}^{\infty} \left[\epsilon_{n\sigma} f_{n\sigma}^{\dagger} f_{n\sigma} + t_{n\sigma} (f_{n+1\sigma}^{\dagger} f_{n\sigma} + f_{n\sigma}^{\dagger} f_{n+1\sigma}) \right] \end{aligned} \quad (4.41)$$

The spin-dependent on-site energies $\epsilon_{n\sigma}$ and hopping integrals $t_{n\sigma}$ can be calculated from the spin-dependent hybridisation function $\Delta_{\sigma}(\epsilon)$ using the algorithm outlined in Ref. [107], Appendix B.

Chapter 5

DMFT for Heterostructures

5.1 Introduction to Heterostructures

The interface that occurs between two layers or regions of dissimilar solid-state materials is commonly referred to as a *heterojunction*. The combination of several such heterojunctions in a electronic device is called a *heterostructure*. Multilayered heterostructures in the nano sized realm (also known as multilayered nanostructures) are the most common electronic devices. Originally these devices were based on *pn*-junctions, interfaces between *p*- and *n*-type semiconducting materials, but also interfaces between superconducting materials were manufactured more recently.

The driving principle behind the functionality of these devices is often a non-linearity of one sort or the other. For instance in *pn*-junction devices it is the non-linearity of the current-voltage relation which ensures that current essentially flows only in one direction[76]. A classic multilayered nanostructure is a tunnel junction consisting of two metallic leads connected by a “weak link”, often a conventional band insulator. The connection between the two leads is thus governed by inherently quantum mechanical effects. Delocalised electrons in the metal can leak through the insulating region by tunnelling into the other lead. The characteristics of the connection can be understood by studying the overlap of the quantum mechanical wave functions. In the metallic region the wave function will oscillate while in the insulating region it will decay exponentially. This ultimately leads to the highly non-linear characteristics of the electronic device.

With recent theoretical and experimental progress in the understanding and control of strongly correlated materials enormous interest has arisen in multilayered nanostructures involving materials where the electrons are strongly interacting. One of the prospects which fuels this interest is the controllability of electronic devices. For example, many heterostructures made from semi-conducting materials have a voltage gate which can be used to tune the characteristics of the device. As already mentioned in the introduction of chapter 3 strongly correlated materials are often extremely sensitive to small changes in external parameters such as external \mathbf{B} - and \mathbf{E} fields, pressure and chemical doping and therefore are appealing alternative to conventional metals, semiconductors and insulators. Particularly interesting is the influence of magnetism in this respect. Inherently quantum mechanical in nature, the magnetic properties of strongly correlated electron systems might pave the way

towards devices which control the transport of the spin of the electron (spin-tronics). However due to the strong correlation effects such materials are less well understood and fewer devices have been made from them.

A range of multilayered nano structures involving strongly-correlated materials has been studied both experimentally and theoretically. Lee and MacDonald[67] argued that interesting strongly-correlated two-dimensional electron systems with weak disorder and controllable densities can be created at the interface between two different, modulation doped Mott insulators. They showed that the magnetic phase diagram can be altered by the dopant density. Kancharla and Dagotto[61] studied the interface between a Mott insulator and a conventional band insulator taking both the local and long-range Coulomb interaction into account and found by computing the layer-dependent local density of states also a quasi two-dimensional metallic state at the interface. They also took the antiferromagnetic correlations in the Mott insulator into account and found that it persists into the metallic region. Such a set-up had been previously studied by Okamoto and Millis[81, 82] who were the first to use the dynamical mean-field theory to investigate the electronic properties of such a heterostructure. They also demonstrated that there is a competition between the ferromagnetic metallic phase at the junction and the insulating anti-ferromagnetic phase in the bulk.

In this chapter we describe how the DMFT as outlined in the last chapter can be extended to treat systems with inhomogeneities. Special emphasis will be placed on the mathematical aspects of the Green's function matrix inversion problem and it will be shown how the mathematical structure can be exploited to arrive at an efficient algorithm ("Quantum zipper algorithm"[17]).

5.2 Inhomogenous DMFT

The foundations for the inhomogenous DMFT were laid by Potthoff and Nolting in 1999 [92]. Their focus was not so much on layered systems but they studied the Mott metal-insulator transition in the Hubbard model at a solid surface for a semi-infinite lattice by means of the dynamical mean-field theory. Their interest was the enhancement of correlation effects as the surface is approached [90, 91] and later on the metal-insulator transition in thin films [89].

The Potthoff and Nolting approach to multilayered nanostructures is designed to solve systems of translationally invariant $x - y$ planes stacked along the longitudinal z direction, see Fig. 5.1. All parameters that describe the system (hopping integrals, interaction strengths, chemical potentials. . .) must be constant within a given layer but may change between layers.

In introducing a mixed basis set by Fourier transforming the x - and y -direction into momentum vectors \mathbf{k}_x and \mathbf{k}_y but leaving the z -direction in real space Potthoff and Nolting exploited the special structure of the set-up. In order to map this problem onto effective impurity problems, one is interested in the local layer Green's functions. We will consider the equations for the non-interacting Green's function first. The

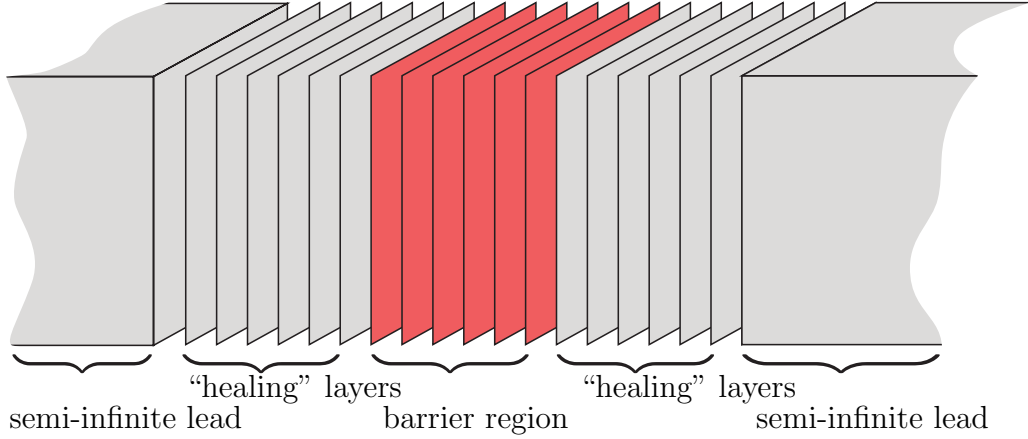


Figure 5.1: Layered system.

non-interacting real space Green's function $G_{ij}^{(0)}(z)$ satisfies

$$\sum_k [(z + \mu)\delta_{ik} + t_{ik}] G_{ij}^{(0)}(z) = \delta_{ij} \quad (5.1)$$

with $-t_{ik}$ the hopping integral between sites i and k . Following Potthoff and Nolting in Fourier transforming the x - and y -axis we find

$$\sum_{\gamma} [(z + \mu - \epsilon_{\alpha\mathbf{k}^{\parallel}})\delta_{\alpha\gamma} + t_{\alpha+1}\delta_{\alpha+1\gamma} + t_{\alpha}\delta_{\alpha-1\gamma}] G_{\alpha\beta}^{(0)}(\mathbf{k}^{\parallel}, z) \quad (5.2)$$

where $\mathbf{k}^{\parallel} = (k_x, k_y)^T$ is a 2-vector comprising the x - and y -component of the momentum, $\epsilon_{\alpha\mathbf{k}^{\parallel}} = -2t_{\alpha}^{\parallel}[\cos k_x + \cos k_y]$ is the two-dimensional, non-interacting tight-binding density of states for the simple cubic lattice and the greek letters α , β and γ are layer indices.

Writing Dyson's equation $G = G^{(0)} + G^{(0)}\Sigma G$ in real space and investing the DMFT assumption, that the self-energy Σ contains only local contributions we find

$$G_{\alpha\beta}(\mathbf{k}^{\parallel}, z) = G_{\alpha\beta}^{(0)}(\mathbf{k}^{\parallel}, z) + \sum_{\gamma} G_{\alpha\gamma}^{(0)}(\mathbf{k}^{\parallel}, z)\Sigma_{\gamma\gamma}(z)G_{\gamma\beta}(\mathbf{k}^{\parallel}, z) \quad (5.3)$$

The above expression can be used to write an equation similar to Eq. (5.2) for the full lattice Green's function, namely

$$[z + \mu - \Sigma_{\alpha\alpha}(z) - \epsilon_{\alpha\mathbf{k}^{\parallel}}] G_{\alpha\beta}(\mathbf{k}^{\parallel}, z) + t_{\alpha+1}G_{\alpha+1\beta}(\mathbf{k}^{\parallel}, z) + t_{\alpha}G_{\alpha-1\beta}(\mathbf{k}^{\parallel}, z) = \delta_{\alpha\beta} \quad (5.4)$$

We can see that for a fixed value of \mathbf{k}^{\parallel} the problem of computing the element $G_{\alpha\alpha}(\mathbf{k}^{\parallel}, z)$ reduces to the inversion of a tridiagonal matrix. This may seem computationally demanding at first sight. As we are interested in the local lattice Green's function it seems that the matrix has to be inverted for every value of ω and $\epsilon_{\mathbf{k}^{\parallel}}$.

5.3 The mathematics of the inversion problem

Helmes and Rosch[46] pointed out that the inversion problem may be simplified by diagonalising $G_{\alpha\alpha}(0, z)$ using an orthogonal matrix $O(\omega)$ which may be reused for all $\epsilon_{\mathbf{k}\parallel}$ in the calculation of $G_{\alpha\alpha}(\mathbf{k}\parallel, z)$. The drawback of this method is however that it can only cope with finite system sizes. However further simplifications arise when one exploits the special tridiagonal structure of the matrix and an efficient computational scheme free of finite-size effects can be constructed. The effect of the metallic leads in this approach is modelled by semi-infinite tridiagonal matrices attached to the finite dimensional matrix describing the barrier region by nearest neighbour hopping integrals. In the following we first discuss how the tridiagonal matrices can be inverted in linear time. Then we discuss how the attachment of the semi-infinite leads can be accounted for.

5.3.1 Inversion of finite dimensional tridiagonal symmetric matrices

In general a symmetric tridiagonal matrix T of order n has the following form

$$M = \begin{pmatrix} a_1 & -t_2 & & & \\ -t_2 & a_2 & -t_3 & & \\ & \ddots & \ddots & \ddots & \\ & & -t_{n-1} & a_{n-1} & -t_n \\ & & & -t_n & a_n \end{pmatrix} \quad (5.5)$$

A natural assumption is that all t_i are non-zero. If not, the problem may be decomposed into 2 smaller sub-problems, which may be solved seperately [4]. It can be shown [27] that for any tridiagonal matrix a sequence of v_i and u_i with $i = 1 \dots n$ exists so that

$$M^{-1} = \begin{pmatrix} u_1 v_1 & u_1 v_2 & u_1 v_3 & \dots & u_1 v_n \\ u_2 v_1 & u_2 v_2 & u_2 v_3 & \dots & u_2 v_n \\ u_3 v_1 & u_3 v_2 & u_3 v_3 & \dots & u_3 v_n \\ \vdots & \vdots & \vdots & \ddots & \vdots \\ u_n v_1 & u_n v_2 & u_n v_3 & \dots & u_n v_n \end{pmatrix} \quad (5.6)$$

Consequently the problem of finding the inverse of M has been reduced to finding the $2n$ quantities $\{u_i\}$, $\{v_i\}$ or equivalently: it is sufficient to compute its first and last columns. Actually it turns out that freedom exists in the choice of these coefficients and we will use the convention here that $u_1 = 1$. Other algorithms than the one presented here have been constructed[19], but the equations proved to be numerically unstable in certain situations [20].

We will first outline the calculation of $v = (v_1, v_2, \dots, v_n)^T$. Having chosen $u_1 = 1$ the first column of M^{-1} is given by v since $Mv = e_1$. Any invertible matrix permits a UL decomposition. As M is tridiagonal the UL decomposition assumes a special form

$$M = UD^{-1}U^T \quad (5.7)$$

where

$$U = \begin{pmatrix} r_1 & -t_2 & & & \\ & r_2 & -b_3 & & \\ & \ddots & \ddots & \ddots & \\ & & & r_{n-1} & -b_n \\ & & & & r_n \end{pmatrix}, \quad D = \begin{pmatrix} r_1 & & & & \\ & r_2 & & & \\ & & \ddots & & \\ & & & r_{n-1} & \\ & & & & r_n \end{pmatrix} \quad (5.8)$$

Since $\sum_i \delta_{ni} U_{ni} D_{ii}^{-1} U_{in}^T = r_n$ one can devise a recurrence relation for the d_i

$$r_n = a_n, r_i = a_i - \frac{b_{i+1}^2}{r_{i+1}}, i = n-1, \dots, 1 \quad (5.9)$$

Any upper-diagonal matrix U with only non-zero elements along its diagonal is invertible and $U^{-1}e_1 = \frac{1}{U_{11}}$. Therefore the solution of the linear equation $Mv = e_1$ is equivalent to solving

$$D^{-1}U^T v = \frac{1}{r_1} e_1. \quad (5.10)$$

Plugging in the concrete form of D and U we find

$$v_1 = \frac{1}{r_1}, v_i = \frac{t_2 \dots t_i}{r_1 \dots r_{i-1} r_i}, i = 2, \dots, n. \quad (5.11)$$

Repeating this procedure for the last column of M^{-1} and therefore solving $v_n T u = e_n$ where the UL decomposition is replaced by a LU decomposition we find

$$l_1 = a_1, l_i = a_i - \frac{t_i^2}{l_{i-1}}, i = 2, \dots, n \quad (5.12)$$

$$u_n = \frac{1}{l_n v_n}, u_{n-i} = \frac{t_{n-i+1} \dots t_n}{l_{n-i} \dots l_n v_n}, i = 1, \dots, n-1. \quad (5.13)$$

We insert this into (5.6) to find

$$(M^{-1})_{i,j} = t_{i+1} \dots t_j \frac{r_{j+1} \dots r_n}{l_i \dots l_n} \quad (5.14)$$

$$(M^{-1})_{i,i} = \frac{r_{i+1} \dots r_n}{l_i \dots l_n} \quad (5.15)$$

and the problem is solved. Using (5.14) and (5.15) we may prove two identities which will be handy later on

$$\frac{(M^{-1})_{i,i-1}}{(M^{-1})_{i,i}} = \frac{r_i}{t_i} \quad (5.16)$$

$$\frac{(M^{-1})_{i+1,i}}{(M^{-1})_{i,i}} = \frac{l_i}{t_{i+1}} \quad (5.17)$$

5.3.2 Inversion of coupled tridiagonal symmetric matrices

In order to solve the problem outlined in section 5.2 efficiently it will be beneficial to understand how the inversion problem may be divided into coupled subproblems. Consider the situation depicted in Fig. 5.2, $t_{AB} = t_{BA}$ and $t_{BC} = t_{CB}$. A , B and C are matrices of the general form 5.5 and dimension n_A , n_B and n_C . An interesting question is how the presence of the matrices A and C influence the inversion problem for the *diagonal* elements of matrix B . In order to avoid confusing among the various quantities defined in section 5.3.1 a matrix superscript (A), (B) or (C) will be added to these. When we refer to, i.e. ‘the inverse of B ’ what is meant is the part of the inverse of matrix Fig. 5.2 that lies within the part occupied by B .

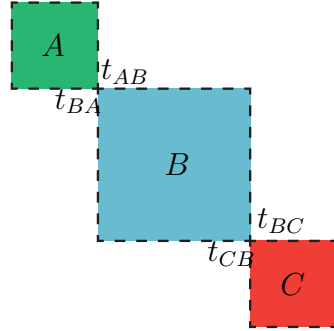


Figure 5.2: Layout of the coupled tridiagonal matrices.

Due to the nature of the recursion relations (5.9) and (5.12) it is immediately clear that the $\{l_i^B\}$ only depend through $l_{n_A}^A$ on A while the $\{r_i^B\}$ only depend through r_1^C on C . However (5.15) suggests, that one needs to know all the $\{l_i^C\}$ to compute the diagonal elements of the inverse of B . The question now is: Is that really so? The answer is that if A and C are semi-infinite matrices, then by virtue of the relations (5.16) and (5.17) one can express the i th diagonal entry in the section of the inverse occupied by B only through knowledge of r_i^B and l_i^B . This can be seen from considering

$$\begin{aligned} \sum_k M_{ik}(M^{-1})_{kj} &= (\delta_{ik}a_i^M - \delta_{i+1,k}t_{i+1}^M - t_i^M \delta_{i,k+1})(M^{-1})_{kj} \\ &= a_i^M(M^{-1})_{ij} - t_{i+1}^M(M^{-1})_{i+1j} - t_i^M(M^{-1})_{i-1j} \\ &= \delta_{ij} \end{aligned} \tag{5.18}$$

Solving for $(M^{-1})_{ii}$ yields

$$\begin{aligned} (M^{-1})_{ii} &= \frac{1}{a_i^M - t_{i+1}^M \frac{(M^{-1})_{i+1i}}{(M^{-1})_{ii}} - t_i^M \frac{(M^{-1})_{i-1i}}{(M^{-1})_{ii}}} \\ &= \frac{1}{a_i^M - r_i^M - l_i^M} \end{aligned} \tag{5.19}$$

where we used (5.16) and (5.17). Hence it has been proven, that to learn the diagonal elements of the inverse in the part occupied by B , it is sufficient to know $l_{n_A}^A$ of A and r_1^C of C .

5.4 The quantum zipper algorithm

Freericks[17] used this insight to construct an efficient algorithm for the solution of the inversion problem, Eq. 5.4, that he termed the ‘‘quantum zipper algorithm’’ (QZA). In the following we describe the algorithm as it is outlined in his book[32].

The equation of motion for the Green's function, Eq. (5.4), in case $\beta = \alpha - n$ with $n > 0$ can be brought to the form

$$-\frac{G_{\alpha, \alpha-n+1}(z, \mathbf{k}^{\parallel}) t_{\alpha-n+1, \alpha-n}}{G_{\alpha, \alpha-n}(z, \mathbf{k}^{\parallel})} = z + \mu - \Sigma_{\alpha-n}(z) - \epsilon_{\alpha-n, \mathbf{k}^{\parallel}}^{\parallel} + \frac{G_{\alpha, \alpha-n-1}(z, \mathbf{k}^{\parallel}) t_{\alpha-n-1, \alpha-n}}{G_{\alpha, \alpha-n}(z, \mathbf{k}^{\parallel})}. \quad (5.20)$$

In direct analogy to Eq. (5.17) we define a left function by

$$L_{\alpha-n}(\mathbf{k}^{\parallel}, z) = -\frac{G_{\alpha, \alpha-n+1}(\mathbf{k}^{\parallel}, z)}{G_{\alpha, \alpha-n}(\mathbf{k}^{\parallel}, z)} \quad (5.21)$$

which we will slide through the heterostructure left to right (similar to the slider of zipper) by the following recurrence relation (c.f. Eq. (5.12)) directly derived from Eq. (5.20)

$$L_{\alpha-n}(\mathbf{k}^{\parallel}, z) = z + \mu - \Sigma_{\alpha-n}(z) - \epsilon_{\alpha-n, \mathbf{k}^{\parallel}} - \frac{t_{\alpha-n, \alpha-n-1} t_{\alpha-n-1, \alpha-n}}{L_{\alpha-n-1}} \quad (5.22)$$

The starting point of this recurrence relation is the left lead in Fig. 5.1. Assuming that deep inside the lead the correction to the local layer self-energy due to the inhomogeneity of the far away barrier is negligible we substitute $L_{-\infty}$ into both sides of Eq. 5.22 and using for the self-energy the result of a bulk calculation for the material the lead is made out of. This gives a quadratic equation for $L_{-\infty}$ which is solved by

$$L_{-\infty}(\mathbf{k}^{\parallel}, z) = \frac{z + \mu - \Sigma_{-\infty}(z) - \epsilon_{-\infty, \mathbf{k}^{\parallel}}^{\parallel}}{2} \pm \frac{1}{2} \sqrt{\left(z + \mu - \Sigma_{-\infty}(z) - \epsilon_{-\infty, \mathbf{k}^{\parallel}}^{\parallel}\right)^2 - 4t_{-\infty}^2}. \quad (5.23)$$

Here $t_{-\infty}$ is the hopping integral inside the lead, $\epsilon_{-\infty, \mathbf{k}^{\parallel}}^{\parallel}$ the dispersion relation and $\Sigma_{-\infty}(z)$ the result of a bulk calculation. The sign in the above equation is chosen to yield an imaginary part less than zero for z lying in the upper half plane. The function $L_{-\infty}(\mathbf{k}^{\parallel}, z)$ is not subject to the self-consistency loop, Fig. 3.5, but it is fixed throughout the calculation. One has to take care that the approximation of using a bulk solution for $L_{-\infty}$ is justified. It can be ensured that this is the case by adding a sufficient amount of healing layers (with the material parameters of the lead) before attaching the lead itself. Usually 30 healing layers is sufficient. These 30 layers are self-consistently determined with L_{α} converging to $L_{-\infty}$ before attaching the left lead solution. For the right lead one should proceed accordingly. This approach is justified if the systems heals to its bulk value before entering the lead. If that is not the case one simply needs to include more healing layers.

Similarly one defines a right function

$$R_{\alpha-n}(\mathbf{k}^{\parallel}, z) = -\frac{G_{\alpha, \alpha+n-1}(\mathbf{k}^{\parallel}, z)}{G_{\alpha, \alpha+n}(\mathbf{k}^{\parallel}, z)} \quad (5.24)$$

and a recurrence relation to the right

$$R_{\alpha+n}(\mathbf{k}^{\parallel}, z) = z + \mu - \Sigma_{\alpha+n}(z) - \epsilon_{\alpha+n, \mathbf{k}^{\parallel}} - \frac{t_{\alpha+n, \alpha+n+1} t_{\alpha+n+1, \alpha-n}}{R_{\alpha+n+1}}. \quad (5.25)$$

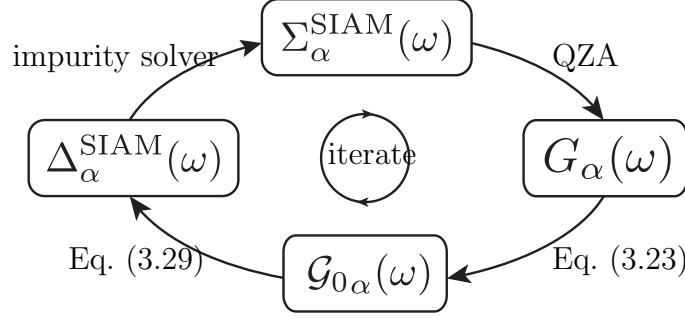


Figure 5.3: Illustration of the DMFT self-consistency loop for a heterostructure: Starting from an initial $\Sigma_\sigma(z)$ use the quantum zipper algorithm (QZA) to determine $G_\sigma(z)$, then use Eq. (3.23) to find $\mathcal{G}_{0\sigma}^{-1}(z)$ and determine $\Delta_{\text{SIAM}}(z)$ from that using Eq. (3.29). Solving the impurity problem gives a new self-energy $\Sigma_\sigma(z)$ and the loop is thus closed.

Similarly to the left function we solve the the recurrence relation for the right lead R_∞ and then iterate Eq. 5.25 up to $n = 0$. R_∞ is determined by substituting into both sides of Eq. 5.25 and solving the resulting quadratic equation. We find

$$R_\infty(\mathbf{k}^\parallel, z) = \frac{z + \mu - \Sigma_\infty(z) - \epsilon_{\infty\mathbf{k}^\parallel}^\parallel}{2} \pm \frac{1}{2} \sqrt{\left(z + \mu - \Sigma_\infty(z) - \epsilon_{\infty\mathbf{k}^\parallel}^\parallel\right)^2 - 4t_\infty^2} . \quad (5.26)$$

The sign is chose the same way as in Eq. 5.23. Using the right and left function we can obtain the Green's function by, c.f. (Eq. 5.19)

$$G_{\alpha\alpha}(\mathbf{k}^\parallel, z) = \left(L_\alpha(\mathbf{k}^\parallel, z) + R_\alpha(\mathbf{k}^\parallel, z) - \left[z + \mu - \Sigma_\alpha(z) - \epsilon_{\alpha\mathbf{k}^\parallel}^\parallel \right] \right)^{-1} \quad (5.27)$$

The local Green's function can be found by summing the above equation over the two-dimensional momenta \mathbf{k}^\parallel , which can be replaced by an integral over the two-dimensional tight-binding density of states

$$G_{\alpha\alpha}(z) = \int d\epsilon^\parallel \rho_\alpha^{2D}(\epsilon^\parallel) G_{\alpha\alpha}(\epsilon^\parallel, z) . \quad (5.28)$$

For the calculation of certain transport coefficients knowledge of the off-diagonal entries of the Green's function $G_{\alpha\beta}(z)$ is necessary. The recursion relations Eq. 5.22 and Eq. 5.25 can be used to shift the individual layer indices of the Green's functions. For instance, the off-diagonal Green's function $G_{\alpha\beta}(z)$ for $\alpha < \beta$ is is given by

$$G_{\alpha\beta}(z) = G_{\alpha\alpha}(z) \prod_{\gamma=\alpha}^{\beta-1} \left[-L_\gamma(z) \right] \quad (5.29)$$

This concludes our summary of the QZA. The algorithm for the solution of the inhomogenous DMFT equations is thus similar to that of the homogenous DMFT:

Algorithm 2.

1. We start with initial guesses for the self-energies $\Sigma_\alpha(z)$ of the layers $\alpha \in \{1, \dots, N_\alpha\}$ and determine $\Sigma_{-\infty}$ (Σ_∞) by a bulk DMFT calculation for the left (right) lead.
2. We use the the QZA to determine the local layer Green's functions $G_{\alpha\alpha}(z)$.
3. The local, layer-dependent Weiss mean field is extracted by virtue of Eq. (3.23) applied to each layer individually, $\mathcal{G}_\alpha^{-1}(z) = G_\alpha^{-1}(z) + \Sigma_\alpha(z)$.
4. We calculate the layer-dependent hybridisation functions $\Delta_\alpha^{\text{SIAM}}(z)$ for the impurity problem from the Weiss mean field $\mathcal{G}_\alpha^{-1}(z)$ using Eq. 3.29.
5. The N_α resulting impurity problems are solved using an adequate impurity solver giving the impurity self energies for each layer, $\Sigma_\alpha^{\text{SIAM}}$.
6. We identify the local lattice self-energy $\Sigma_\alpha(z)$ with the impurity self-energy $\Sigma_\alpha^{\text{SIAM}}(z)$ and goto step 2 if any of the layers is not converged.

5.4.1 Numerical implementation

At this point some remarks concerning the numerical implementation and computational complexity are in order. For a typical nanostructure calculation the number of layers in the barrier region is around 50. With an additional 20-30 healing layers on either side the typical number of self-consistently determined layers is of the order of 100. The DMFT algorithm has to be performed on each plane and thus 100 impurity problems have to be solved for each DMFT iteration and around ≈ 100 iterations have to be performed for the structure to converge (without long-range Coulomb interactions included that is; see below). This is a substantial computational complexity and one necessarily has to think about parallelisation. Fortunately certain steps in self-consistency loop allow for a natural division into subproblems.

Suppose we have N_C computational nodes at our disposal for the solution of the DMFT algorithm. Starting with an initial set of self-energies for the planes the QZA has to be performed to find the local Green's function on each layer for all frequencies. As the number of frequencies is typically much higher than the number of layers the more fine-grained division among processors is achieved if one divides in frequency rather than in layer space. The frequency space is divided into N_C ranges and each processor calculates the local Greens function on layers 1 to N_α for that frequency range. In a distribution step the function parts are exchanged among the nodes and complete local Green's functions are assembled. In order to find the local Green's functions for a specific frequency the energy integral in Eq. 5.28 has to be evaluated. There are two possible approaches for this. One can work on a fixed ϵ -grid which has to be sufficiently fine to resolve any sharp features on the energy axis. This approach has the advantage that the recursive relations for the left- and right functions allow a caching of the result for the calculations of quantities on other layers. Close to the MMIT transition however the features in the self-energy become increasingly sharper and more refined energy grid is needed. This slows down the computation and at some point it becomes advantageous to abandon the fixed grid and to use

a quadrature routine which automatically decides where to evaluate the integrand and does so in a refined way around the sharp features. However caching is now not possible anymore, because the routine usually does not evaluate the integrand for different layers at the same energies.

The other step which is amenable for parallelisation is the solution of the impurity problems. After the hybridisation functions have been calculated on each layer the impurity problems can be solved independent of each other. Parallelisation is therefore trivial and one simply assign the N_α impurity problem in a round robin fashion among the N_C computing nodes. When all impurity problems are solved the impurity self-energies are exchanged among the nodes in a distribution step.

5.5 Electronic charge reconstruction

Nanostructures fabricated from different materials often show interesting effects at the interfaces. A fundamental issue here has been atomic reconstruction which is driven by the difference in the surface lattice symmetry from that in the bulk. More recently Okamoto and Millis[81] showed that some of the observations obtained from an experiment by Ohtomo et al.[78], where an atomically precise digital heterostructure was fabricated by inserting a controllable number of Mott-insulating LaTiO_3 into a controllable number of planes of SrTiO_3 a conventional band-insulator, can be understood from what they refer to as “electronic charge reconstruction” (ECR). In the heterostructure a mismatch of the chemical potentials at the interface between the two materials causes charges to leak across the interface efficiently doping the Mott- and the band-insulator. This leads to a quasi two-dimensional metallic state at the interface of these otherwise insulating materials. The theoretical results obtained from DMFT calculations with a Hartree treatment of long-range Coulomb interactions are in qualitative agreement to the experimental study. Chen and Freericks[17] also used DMFT to calculate the electronic charge reconstruction of multilayered inhomogeneous devices composed of semi-infinite metallic lead layers sandwiching barrier planes of a strongly correlated material. They studied how electronic charge reconstruction can create well-defined Mott insulating barriers.

In the following we describe how the DMFT can be modified to include the electronic charge reconstruction that takes place at the interfaces of different materials. A more detailed account can be found in Freerick’s book[32]. A mismatch in the chemical potentials of two different materials causes charge to reorder in a such way at the interface that the electric potential created by the displaced charge compensates the difference in the chemical potentials. Long-range Coulomb interaction is necessary for this effect to take place and we treat it in a mean-field sense, consistent with the local approximation for the self-energy in the DMFT[32]. The basis for the iterative algorithm remains the quantum zipper algorithm, algorithm 3 above, however an additional contribution to the layer-dependent self-energy has to be calculated which accounts for electric field due to the charge displacement.

For a given set of excess charge densities $\rho_\alpha - \rho_\alpha^{\text{bulk}}$ on the layers where α is the layer index, ρ_α the electrical charge density and $\rho_\alpha^{\text{bulk}}$ the charge due to the ionic

background in layer α , the electric field \mathbf{E}_α due to layer α when treated as a plane of uniform charge is given by

$$\mathbf{E}_\alpha = -\frac{e(\rho_\alpha - \rho_\alpha^{\text{bulk}})}{2\epsilon_0\epsilon_{r\alpha}}\mathbf{e}_\perp \quad (5.30)$$

where $e > 0$ is the electric charge, ϵ_0 the permittivity in the vacuum, $\epsilon_{r\alpha}$ the relativity of plane α and \mathbf{e}_\perp is a unit vector perpendicular to plane pointing away from it. In the following we will assume that $\epsilon_{r\alpha} = \epsilon_r$. The electric potential of a system with translation invariance in the x - and y -direction is related to the electric field via $\mathbf{E}(\mathbf{r}) = -\frac{d}{dz}V(z)\mathbf{e}_z$. The contribution to the electric potential at plane α due to the excess charge at plane β is thus given by

$$V_\beta(\alpha) = -\frac{e(\rho_\alpha - \rho_\alpha^{\text{bulk}})}{2\epsilon_0\epsilon_r}|\alpha - \beta| \quad (5.31)$$

The additional potential energy for an electron on plane α due to the charge reordering in the system is thus given by $eV_\alpha \equiv e\sum_\beta V_\beta(\alpha)$ or alternatively we can pretend the chemical potential on layer α has been shifted by minus this number. The additional term in the Hamiltonian is therefore given by

$$H_{\text{Coulomb}} = e\sum_{\alpha\mathbf{k}\parallel\sigma} V_\alpha c_{\alpha\mathbf{k}\parallel\sigma}^\dagger c_{\alpha\mathbf{k}\parallel\sigma} \quad (5.32)$$

Since the leads are not treated self-consistently we have to require that the electric potential has become sufficiently small enough before entering the lead. For the system to have a finite energy the leads have to be charge neutral - an assumption which would be inconsistent with a finite electric potential extending into the leads. Hence the self-consistently calculated part of the system has to be overall charge conserving. No charge may thus leak out of this part of the device into the leads. Electronic charge reconstruction only occurs if the chemical potentials between two layers do not match. The mismatch is termed *contact potential* and we introduce layer dependent chemical potentials μ_α to model it.

The modified DMFT algorithm including charge reconstruction is thus given by

Algorithm 3.

1. We start with initial guesses for the self-energies $\Sigma_\alpha(z)$ and charge densities ρ_α on the layers $\alpha \in \{1, \dots, N_\alpha\}$ and determine $\Sigma_{-\infty}$ (Σ_∞) by a bulk DMFT calculation for the left (right) lead. The charge density in the lead has to match its bulk value at all times $\rho_{-\infty} = \rho_{-\infty}^{\text{bulk}}$ ($\rho_\infty = \rho_\infty^{\text{bulk}}$).
2. Determine the layer-dependent, electric potentials V_α using Eq. (5.31).
3. With the layer-dependent chemical potentials μ_α shifted by minus the electrical potential, $\mu_\alpha \rightarrow \mu_\alpha - V_\alpha$, we use the the QZA to determine the local layer Green's functions $G_{\alpha\alpha}(z)$.
4. The local, layer-dependent Weiss mean field is extracted by virtue of Eq. (3.23) applied to each layer individually, $\mathcal{G}_\alpha^{-1}(z) = G_\alpha^{-1}(z) + \Sigma_\alpha(z)$.

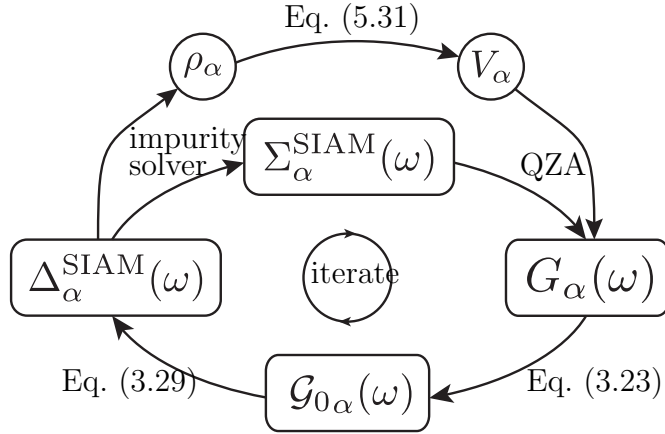


Figure 5.4: Illustration of the DMFT self-consistency loop for a heterostructure including electronic charge reconstruction (ECR): Starting from an initial set of $\Sigma_{\alpha\sigma}(z)$ and ρ_{α} use the QZA to determine $G_{\sigma}(z)$, then use Eq. (3.23) to find $\mathcal{G}_{0\sigma}^{-1}(z)$ and determine $\Delta_{\text{SIAM}}(z)$ from that using Eq. (3.29). Solving the impurity problem gives a new self-energy $\Sigma_{\sigma}(z)$ and new occupations ρ_{α} and the loop is thus closed.

5. We calculate the layer-dependent hybridisation functions $\Delta_{\alpha}^{\text{SIAM}}(z)$ for the impurity problem from the Weiss mean field $\mathcal{G}_{\alpha}^{-1}(z)$ using Eq. 3.29 (again with the chemical potentials shifted by minus the electric potential).
6. The N_{α} resulting, independent impurity problems are solved using an adequate impurity solver giving the impurity self energies for each layer, $\Sigma_{\alpha}^{\text{SIAM}}$.
7. For each impurity problem the impurity solver is used to determine the charge on the impurity which is then assigned to the layer charge $\rho_{\alpha} = \rho^{\text{impurity}}$.
8. We identify the local lattice self-energy $\Sigma_{\alpha}(z)$ with the impurity self-energy $\Sigma_{\alpha}^{\text{SIAM}}(z)$ and goto step 2 if any of the layers are not converged.

5.5.1 Numerical implementation

The addition of charge reconstruction makes it much more difficult to reach the correct physical fixed point in the iterative scheme described above. First the update of the electric potentials have to be strongly damped to slow the updating of the Green's function due to charge reordering. If that is not done the structure does not converge at all. We found the following strategy which is also used by Freericks[32] renders satisfactory results

$$V_{\alpha}^{(n+1)} = \alpha_V V_{\alpha}^{(n)} + (1 - \alpha_V) V_{\alpha}^{\text{update}} \quad (5.33)$$

where $V_{\alpha}^{\text{update}}$ is electric potential calculated from the current charge distribution in iteration $n + 1$. Good values for α_V are $0.99 \leq \alpha_V \leq 0.999$. The number of iterations needed to converge the structure is about 2000 – 5000. A way to reduce this number is to start from a charge distribution which is reasonably close to the converged result. This can be achieved by recording the site occupation as function of chemical potential, $n(\mu)$, in bulk calculations for all materials that the nanostructure is made

out of. Knowledge of these functions then allows to solve the non-interacting Poisson problem to find an adequate initial charge distribution.

As already mentioned the semi-infinite leads add a constraint of overall charge conservation to the self-consistently determined layers. An explicit implementation of this constraint also helps the calculation to converge. We define $\bar{\rho} = 1/N_\alpha \sum_\alpha (\rho_\alpha - \rho_\alpha^{\text{bulk}})$ which measures the average excess electron density per layer. The charge conservation constraint can be enforced when the excess charge $\bar{\rho}$ is uniformly distributed in the system. The expression for the calculation of the electric potential, Eq. 5.31, thus assumes the form

$$V_\beta(\alpha) = -\frac{e(\rho_\alpha - \rho_\alpha^{\text{bulk}} - \bar{\rho})}{2\epsilon_0\epsilon_r}|\alpha - \beta| \quad (5.34)$$

After convergence the parameter $\bar{\rho}$ will be close to zero. This has to be checked in every calculation.

5.5.2 Application: A strongly-correlated nanostructure

The effect of electronic charge reconstruction is illustrated in Fig. 5.5. Here we use the algorithm described above to find the layer-resolved spectral functions and occupations for a multilayered nanostructure. The structure consists out of 3 regions (I-III) where regions I and III are made from a weakly-correlated metal with $U = 1$ and the chemical potential tuned to the particle-hole symmetric point ($\mu_I = \mu_{III} = 0$) and semi-infinite leads made from the same metal are attached right and left. The barrier region II is made from a strongly-correlated metal with $U = 10$ and $\mu_{II} = -3$. The background charges for all 3 regions are set to half-filling, $\rho^{\text{bulk}} = 1$. The mismatch in the chemical potentials between regions I and II and II and III creates a contact potential which causes charge to leak from the barrier into the attached leads, thus hole-doping the barrier region while particle-doping the leads, c.f. Fig. 5.5a (black line). In response to the charge displacement an electric potentials builds up over the interfaces which seeks to compensate the change in the chemical potential, c.f. Fig. 5.5b (black line). The red line in Fig. 5.5 shows the layer-resolved occupation ρ_α and electric potential V_α for a structure with the same geometry and local chemical potentials μ_α but with all layers uncorrelated, $U_\alpha = 0$. For the chosen barrier thickness of 12 layers the uncorrelated system reorders the charge such that the generated electric potential (almost) compensates the drop in chemical potential from region I to region II, $\Delta\mu = \mu_{II} - \mu_I = -3$ as can be seen from the minimum at $V_{16} \approx -2.9$ in Fig. 5.5b. For strong correlations however the length scale on which the charge reorders becomes larger and consequently the system cannot compensate the drop in chemical potential by reordering the charge within 6 layers, i.e. the minimum of electric potential in Fig. 5.5b (black line) is $V_{16} \approx -1.5$. When the thickness of the barrier is increased the minimum of the electric potential for the correlated system also approaches $V \rightarrow -3$ (not shown).

Fig. 5.6a shows selected spectral functions for various layers of the correlated heterostructure. The spectral function for layer 1 (black line) resembles that of a non-interacting three-dimensional bulk system. The upper and lower band edges ($\omega = 6$ and $\omega = -6$) and the van-Hoove singularities ($\omega = 2$ and $\omega = -2$) are slightly smeared out due to the interactions. The wiggles at the top result from the broken

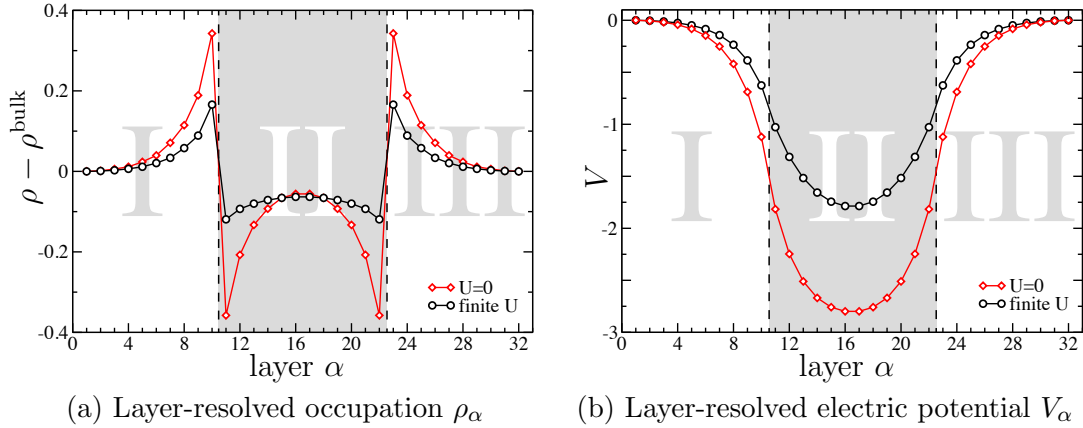
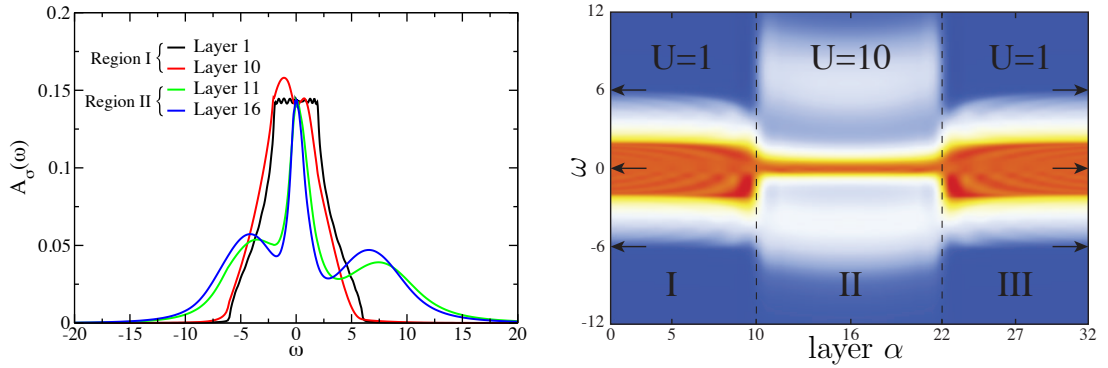


Figure 5.5: ECR for a multilayered nanostructure with 3 regions (I-III). Region I and III: 10 layers of $U = 1$ material, with $\mu_I = \mu_{II} = 0$ (PH symmetric point); left and right, semi-infinite lead same material. barrier region: 12 layers of $U = 10$ material, hole-doped due to $\mu_{II} = -3$. Black lines: with correlations as specified above, red lines: $U = 0$ for all layers.

translational symmetry due to the presence of the barrier. The spectral function for the last layer on the weakly-correlated side before the interface (layer 10, red line) shows a noticeable alteration from the bulk solution. Due to the strong particle-doping the function has been shifted to the left. Van-Hoove singularities have been almost completely washed out due to the hybridisation induced correlations. The first layer made of the strongly-correlated material after the interface (layer 11, green line) shows the characteristic three peak structure. The upper and lower Hubbard bands however show a pronounced asymmetry due to the hole-doping from the ECR, which decreases when going deeper into the barrier (layer 16, blue curve).

Fig. 5.6b shows a density plot of the spectral functions over the energy range $\omega \in [-12, 12]$ for layers $\alpha \in \{1, \dots, 32\}$. Weakly-correlated regions I and III show a broad range (red) of energies with large spectral weight around the fermi level $\omega = 0$ with a width of approximately $10t$. For the strongly correlated layers in region II this range is substantially narrower and shows only a width of approximately $3t$ to $4t$. This is expected as the quasi-particle weight decreases as a function of the interaction strength as more and more spectral weight is shifted into the incoherent background. Interestingly one can see bending in the bands on either side of the interface as one approaches it. Coming from the weakly correlated side, one starts with a particle-hole symmetric band. As the interface is approached the negative electric potential (Fig. 5.5b) shifts the band downwards. If the barrier were thick enough one would start with particle-hole symmetric spectral function coming from the middle of the barrier where $V = \Delta\mu$. Upon approaching the interface the strength of the electric potential weakens hence $V_\alpha - \mu_\alpha$ becomes positive and the spectral functions is shifted upwards.



(a) Spectral functions for different layers. Layer 10 (11) is located at the interface on the $U = 1$ ($U = 10$) side.

(b) Density plot of the spectral functions of the multilayered nanostructure.

Figure 5.6: ECR for a multilayered nanostructure with 3 regions (I-III). Region I and III: 10 layers of $U = 1$ material, with $\mu_I = \mu_{II} = 0$ (PH symmetric point); left and right, semi-infinite lead same material. barrier region: 12 layers of $U = 10$ material, hole-doped due to $\mu_{II} = -3$.

5.6 Antiferromagnetic order

The question how the presence of long-range order affects the transport properties of electronic devices based on multilayered nanostructures made from strongly-correlated materials is natural. Strongly correlated matter shows an abundance of interesting ordering phenomena and in many cases restricting the system to a paramagnetic phase only in a DMFT calculation is an approximation which is difficult to justify on general grounds. In this chapter we describe how the quantum zipper algorithm can be extended to allow for AB-sublattice antiferromagnetic order on bipartite lattices (AFQZA). The general outline of the derivation follows that of the paramagnetic case, section 5.4, however now the Green's functions and self-energies acquire a 2×2 -matrix structure similarly to the generalisation from the homogenous paramagnetic DMFT to the homogenous DMFT that allows for antiferromagnetic order, section 3.7.

The system should be thought as a stack of two dimensional subsystem connected to each other via spin-diagonal nearest-neighbour hopping terms similarly to the system considered in the original QZA. Here however the translational symmetry within the two dimensional system only holds for an enlarged unit cell which contains one site of type A and one of type B. In order to remove repetitive clutter from the matrices during the derivation we introduce the following functions

$$\begin{aligned} Z_\alpha(\omega) &= \omega + i0^+ + \mu - \bar{\epsilon}_\alpha - \bar{\Sigma}_\alpha(\omega) \\ \Delta_\alpha(\omega) &= -\Delta\Sigma_\alpha(\omega) \end{aligned} \quad (5.35)$$

where $\bar{\epsilon}_\alpha = \epsilon_{A\alpha} = \epsilon_{B\alpha}$, $\bar{\Sigma}_\alpha(\omega) = (\Sigma_{A\alpha}(\omega) + \Sigma_{B\alpha}(\omega))/2$ and $\Delta\Sigma_\alpha(\omega) = (\Sigma_{A\alpha}(\omega) - \Sigma_{B\alpha}(\omega))/2$. $\epsilon_{A\alpha}$ is the on-site energy of a site in layer α on sublattice A and $\epsilon_{B\alpha}$ on sublattice B. We will assume that these are equal. Similarly $\Sigma_{A\alpha}(\omega)$ is the local self-energy of a site in layer α on sublattice A and $\Sigma_{B\alpha}(\omega)$ on sublattice B.

In the derivation for the homogenous case we worked in the $(c_{A\mathbf{k}\sigma}, c_{B\mathbf{k}\sigma})^T$ basis, here however we start in the AB basis and then switch to the $(c_{\mathbf{k}\sigma}, c_{\mathbf{k}+\mathbf{Q}\sigma})^T$ basis, where $\mathbf{Q} = (\pi, \pi)^T$ is the ordering vector. This will be especially advantageous when we derive the left- and right functions for the leads. The basis are related by the unitary transformation

$$\begin{pmatrix} c_{A\mathbf{k}\sigma} \\ c_{B\mathbf{k}\sigma} \end{pmatrix} = \frac{1}{\sqrt{2}} \begin{pmatrix} 1 & -1 \\ 1 & 1 \end{pmatrix} \begin{pmatrix} c_{\mathbf{k}\sigma} \\ c_{\mathbf{k}+\mathbf{Q}\sigma} \end{pmatrix} \quad (5.36)$$

Starting from Eq. 5.4 one can easily write down the generalisation for the AB basis by replacing the self-energy $\Sigma_{\alpha\alpha}(z)$ and the Green's function $\mathbf{G}_{\alpha\beta}(z)$ with 2×2 -matrices. The self-energy $\Sigma_{\alpha\alpha}^{(AB)}(z)$ is diagonal in the AB basis and so are the hoppings, the chemical potential and the on-site energies. In exact analogy to the paramagnetic case one introduces the 2×2 -matrix valued function $\mathbf{L}_{\alpha}^{(AB)}(\mathbf{k}^{\parallel}, z)$ in the AB basis by

$$\mathbf{L}_{\alpha-n}^{(AB)}(\mathbf{k}^{\parallel}, z) = -t_{\alpha-n+1\alpha-n} \mathbf{G}_{\alpha\alpha-n+1}^{(AB)}(\mathbf{k}^{\parallel}, z) \left(\mathbf{G}_{\alpha\alpha-n+1}^{(AB)}(\mathbf{k}^{\parallel}, z) \right)^{-1} \quad (5.37)$$

and derives the recursion relation

$$\mathbf{L}_{\alpha-n}^{(AB)}(\mathbf{k}^{\parallel}, z) = (z - \bar{\epsilon} + \mu - \epsilon_{\alpha\mathbf{k}^{\parallel}}^{\parallel}) \mathbb{1} - \Sigma_{\alpha\alpha}^{(AB)}(z) - t_{\alpha-n\alpha-n-1} t_{\alpha-n-1\alpha-n} \left(\mathbf{L}_{\alpha-n}^{(AB)}(\mathbf{k}^{\parallel}, z) \right)^{-1} \quad (5.38)$$

We now switch to the (\mathbf{k}, \mathbf{Q}) basis by applying transformation Eq. 5.36 to the recursion relation above to find the relation in the (\mathbf{k}, \mathbf{Q}) basis

$$\mathbf{L}_{\alpha}(\omega, \epsilon_{\mathbf{k}^{\parallel}}) = \mathbf{M}_{\alpha}(\omega, \epsilon_{\mathbf{k}^{\parallel}}) - \frac{t_{\alpha\alpha-1} t_{\alpha-1\alpha}}{\det L_{\alpha-1}(\omega, \epsilon_{\mathbf{k}^{\parallel}})} \begin{pmatrix} L_{\alpha-1}^{(22)}(\omega, \epsilon_{\mathbf{k}^{\parallel}}) & L_{\alpha-1}^{(12)}(\omega, \epsilon_{\mathbf{k}^{\parallel}}) \\ L_{\alpha-1}^{(21)}(\omega, \epsilon_{\mathbf{k}^{\parallel}}) & L_{\alpha-1}^{(11)}(\omega, \epsilon_{\mathbf{k}^{\parallel}}) \end{pmatrix} \quad (5.39)$$

where we have defined the matrix

$$\mathbf{M}_{\alpha}(\omega, \epsilon_{\mathbf{k}^{\parallel}}) = \begin{pmatrix} Z_{\alpha}(\omega) - \epsilon_{\mathbf{k}^{\parallel}} & \Delta_{\alpha}(\omega) \\ \Delta_{\alpha}(\omega) & Z_{\alpha}(\omega) - \epsilon_{\mathbf{k}^{\parallel}} \end{pmatrix}. \quad (5.40)$$

Similarly for the right function $\mathbf{R}_{\alpha}(\omega, \epsilon_{\mathbf{k}^{\parallel}})$ one finds

$$\mathbf{R}_{\alpha}(\omega, \epsilon_{\mathbf{k}^{\parallel}}) = \mathbf{M}_{\alpha}(\omega, \epsilon_{\mathbf{k}^{\parallel}}) - \frac{t_{\alpha\alpha+1} t_{\alpha+1\alpha}}{\det \mathbf{R}_{\alpha+1}(\omega, \epsilon_{\mathbf{k}^{\parallel}})} \begin{pmatrix} R_{\alpha+1}^{(22)}(\omega, \epsilon_{\mathbf{k}^{\parallel}}) & R_{\alpha+1}^{(12)}(\omega, \epsilon_{\mathbf{k}^{\parallel}}) \\ R_{\alpha+1}^{(21)}(\omega, \epsilon_{\mathbf{k}^{\parallel}}) & R_{\alpha+1}^{(11)}(\omega, \epsilon_{\mathbf{k}^{\parallel}}) \end{pmatrix} \quad (5.41)$$

The relationship between the Green's function and the right and left function in the (\mathbf{k}, \mathbf{Q}) basis takes the same form as it does in the AB basis

$$\mathbf{G}_{\alpha}(\omega, \epsilon_{\mathbf{k}^{\parallel}}) = [\mathbf{R}_{\alpha}(\omega, \epsilon_{\mathbf{k}^{\parallel}}) + \mathbf{L}_{\alpha}(\omega, \epsilon_{\mathbf{k}^{\parallel}}) - \mathbf{M}_{\alpha}(\omega, \epsilon_{\mathbf{k}^{\parallel}})]^{-1} \quad (5.42)$$

The local Green's function on sublattice A and B can be found by transforming the above equation back to the AB basis and summing over the two-dimensional

momenta \mathbf{k}^{\parallel} , which can be replaced by an integral over the two-dimensional tight-binding density of states

$$\begin{aligned} G_{A\alpha\alpha}(z) &= \frac{1}{2} \int d\epsilon^{\parallel} \rho_{\alpha}^{2D}(\epsilon^{\parallel}) (G_{\alpha\alpha}^{(11)}(\epsilon^{\parallel}, z) + G_{\alpha\alpha}^{(22)}(\epsilon^{\parallel}, z) + G_{\alpha\alpha}^{(12)}(\epsilon^{\parallel}, z) + G_{\alpha\alpha}^{(21)}(\epsilon^{\parallel}, z)) \\ G_{B\alpha\alpha}(z) &= \frac{1}{2} \int d\epsilon^{\parallel} \rho_{\alpha}^{2D}(\epsilon^{\parallel}) (G_{\alpha\alpha}^{(11)}(\epsilon^{\parallel}, z) + G_{\alpha\alpha}^{(22)}(\epsilon^{\parallel}, z) - G_{\alpha\alpha}^{(12)}(\epsilon^{\parallel}, z) - G_{\alpha\alpha}^{(21)}(\epsilon^{\parallel}, z)) \end{aligned} \quad (5.43)$$

With these relations in place the only remaining difficulty is to find the right and left function of the semi-infinite leads by solving the quadratic equation that is obtained if the same 2×2 -matrix valued function $\mathbf{L}_{-\infty}(\omega, \epsilon_{\mathbf{k}^{\parallel}})$ is substituted in both sides of the recursion relation Eq. 5.39. This however is problematic. In general there are no closed form expressions for the solution of a quadratic equation of 2×2 -matrices. Worse still both existence and uniqueness can fail spectacularly. The special structure of the problem at hand however still allows for a solution and even an explicit expression.

Deep inside the semi-infinite lead the left and right functions coincide due to translational invariance, $\mathbf{L}_{-\infty}(\omega, \epsilon_{\mathbf{k}^{\parallel}}) = \mathbf{R}_{-\infty}(\omega, \epsilon_{\mathbf{k}^{\parallel}})$. By virtue of Eq. 5.42 the left function can be expressed as

$$\mathbf{L}_{-\infty}(\omega, \epsilon_{\mathbf{k}^{\parallel}}) = \frac{1}{2} [\mathbf{G}_{-\infty}^{-1}(\omega, \epsilon_{\mathbf{k}^{\parallel}}) + \mathbf{M}_{-\infty}(\omega, \epsilon_{\mathbf{k}^{\parallel}})] \quad (5.44)$$

The bulk Green's function $\mathbf{G}_{-\infty}(\omega, \epsilon_{\mathbf{k}^{\parallel}})$ of the left lead can be written as an integral over momenta in the direction perpendicular to the planes

$$\begin{aligned} \mathbf{G}_{-\infty}(\omega, \epsilon_{\mathbf{k}^{\parallel}}) &= \frac{1}{2\pi} \int_{-\pi}^{\pi} dk^{\perp} \quad (5.45) \\ &\left(\begin{array}{cc} Z_{-\infty}(\omega) - \epsilon_{\mathbf{k}^{\parallel}}^{\parallel} + 2t_{-\infty} \cos(k^{\perp}) & \Delta_{-\infty}(\omega) \\ \Delta_{-\infty}(\omega) & Z_{-\infty}(\omega) + \epsilon_{\mathbf{k}^{\parallel}}^{\parallel} - 2t_{-\infty} \cos(k^{\perp}) \end{array} \right)^{-1} \end{aligned}$$

This integral can be solved analytically with a computer algebra program. We used Wolfram's Mathematica[®] Version 8.0. The result is a complicated expression that we will not present here, but that the interested reader can find in appendix A. Substituting this expression into Eq. 5.44 gives an expression for the left function $\mathbf{L}_{-\infty}(\omega, \epsilon_{\mathbf{k}^{\parallel}})$ inside the left lead. The expression for the right function $\mathbf{R}_{\infty}(\omega, \epsilon_{\mathbf{k}^{\parallel}})$ can be found in the same fashion.

This concludes the necessary steps to generalise the quantum zipper algorithm to allow for antiferromagnetic order in the nanostructure. The individual steps in the overall iterative scheme are the same as those in the paramagnetic zipper, algorithm 3, above with all quantities replaced by their 2×2 -matrix counterparts and we will not repeat these steps here explicitly.

Part III
Applications

Chapter 6

Mott-Band-Insulator Heterostructures

A new and exciting direction in the material sciences has been the fabrication of artificial heterostructures and superlattices composed of different materials. The understanding of their electronic properties is not merely of scientific interest but also indispensable for the design and realisation of novel electronic devices based on the unique electronic effects found at interfaces but absent in the bulk. A variety of heterostructures have been fabricated and studied including high- T_c superconducting cuprates[105, 35, 1], Mott- and band-insulator heterostructures[78] and superlattices of transition metal oxides[55]. Surprisingly heterostructures comprising Mott- and band-insulators were reported to have metallic behaviour at the interface and even high mobility. In this chapter we are solely concerned with this type of heterostructures. A fundamental question is what effects contribute to the change in the electronic state at and near interfaces and surfaces.

In heterostructures made of Mott insulating LaTiO_3 and the more conventional band-insulating SrTiO_3 the transition metal Ti ions on the perovskite B sublattice are identical and only the charge-controlling A sublattice ions (La, Sr) change across the interface, c.f. Fig. 6.1. It was found that the electron density in the SrTiO_3 region does not depend significantly on the interaction strength or other strong correlation aspects of the problem, but is controlled mainly by the (self-consistently screened) potential arising from the La [81]. At the interface charge neutrality is violated which leads to a redistribution of charge to maintain an electrostatic stable solution.

In analogy to effects of lattice relaxation at interfaces which are referred to as “atomic reconstruction” the effect described above has been called “electronic reconstruction”¹. This observation has stimulated a considerable amount of theoretical investigations. Okamoto and Millis[81] used an unrestricted Hartree-Fock approximation to qualitatively explain the experimental findings of Ohtomo et al.[78] who first discovered the existence of metallic behaviour in atomically precise digital digital heterostructures by inserting a controllable number of LaTiO_3 into bulk SrTiO_3 . Later the same authors[82] improved their treatment of the electronic correlation effects

¹Originally this term was coined by Hesper et al.[48] to describe the compensation of polar charge at the surface of bulk K_3C_{60} but Okamoto and Millis have suggested to apply the term more generally to electronic surface and interface behaviour that is different from the bulk.

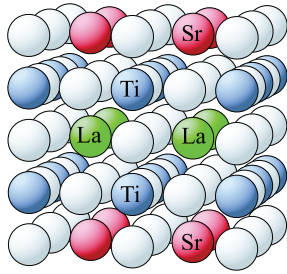


Figure 6.1: Illustration of the cubic perovskite structure (white spheres denote oxygen). An LaO layer lies in the center, bordered by two TiO_2 layers, with a SrO layer at top and bottom. Taken from Ref. [84].

when they employed DMFT calculations with the two-site approximation of Potthoff and Nolting for the solution of the impurity problem. In these studies the existence of strong charge reordering in an approximately three unit-cell-wide crossover region was found to give rise to metallic behaviour in otherwise bulk-insulating materials. Pentcheva and Pickett[84] performed density-functional theory calculations including a Hubbard-type on-site Coulomb repulsion (LDA/GGA + U). In contrast to earlier works that focussed on model Hamiltonians they tried to account for material specific aspects. They found that the charge mismatch at the interface is compensated by checkerboard charge order of Ti^{3+} and Ti^{4+} sites within the interface layer. For the ideal structure they found the interface state to be a narrow gap insulator, but atomic relaxation at the interface shifted the Ti^{3+} lower Hubbard upward leading to conducting behaviour.

Common to all these studies is the technical challenge to account for strong local, electronic correlation effects in a spatially non-uniform system. The DMFT generalised to inhomogenous systems with the addition of long-range Coulomb interactions on the Hartree level provides an excellent tool to study such systems. In addition it allows for the calculation of layer-resolved transport properties as we will see below. This is important as the study of the transport properties of the two-dimensional electron gas at the interface has been left unexplored for the most part. Although previous studies have taken such an approach[82] here the rather crude two-site approximation has been used for the solution of the impurity problem. The NRG is the state-of-the-art impurity for the single-band DMFT at low temperatures. In the following we derive expression for the layer-resolved in-plane conductivity and the Hall conductivity.

6.1 Conductivity calculations in the DMFT

Before we start with the actual derivation of the layer-resolved conductivities let us briefly review the role of vertex corrections in the calculation of conductivities and the special situation encountered in the DMFT approximation[37].

The measured current in a system in response to a perturbation of the Hamiltonian H by an electric field \mathbf{E} is given by the sum of two terms

$$\mathcal{J}^\lambda(\mathbf{r}, t) = \langle j_a(\mathbf{r}, t) \rangle + i \frac{e^2}{\omega} \left\langle \frac{\partial^2 \epsilon}{\partial \mathbf{k}^2} c_{\mathbf{k}}^\dagger c_{\mathbf{k}} \right\rangle E_\lambda(\mathbf{r}, t), \quad (6.1)$$

with $\epsilon(k)$ the dispersion relation. The first term is commonly referred to as the paramagnetic contribution while the second one is the diamagnetic term. The paramagnetic term has a contribution linear in the applied electric field \mathbf{E} . The proportionality constant which relates the linearised current response $\mathcal{J}^\lambda(\mathbf{r}, t)$ to the applied field $E_\lambda(\mathbf{r}, t)$ is given by the Kubo formula for the electrical conductivity

$$\begin{aligned} \mathcal{J}^\lambda(\mathbf{r}, t) &= \sum_\nu \int d^3 \mathbf{r}' \int_{-\infty}^t dt' \sigma^{\lambda\nu}(\mathbf{r} - \mathbf{r}', t - t') E_\nu(\mathbf{r}', t') \\ &= \sum_\nu \sigma^{\lambda\nu}(\mathbf{q}, \omega) E_\nu e^{i\mathbf{q}\cdot\mathbf{r} - i\omega t} \\ &= \sum_\nu \frac{i}{\omega} \left[\Pi_{\lambda\nu}(\mathbf{q}, \omega) + e^2 \left\langle \frac{\partial^2 \epsilon}{\partial \mathbf{k}^2} c_{\mathbf{k}}^\dagger c_{\mathbf{k}} \right\rangle \delta_{\lambda\nu} \right] E_\nu e^{i\mathbf{q}\cdot\mathbf{r} - i\omega t} \end{aligned} \quad (6.2)$$

where in the second line we assumed that the electric field $\mathbf{E}(\mathbf{r}, t)$ has only a single frequency and the system possesses a translational symmetry. $\Pi_{\lambda\nu}(\mathbf{q}, \omega)$ in the third line is the retarded current-current correlation function which is defined as

$$\Pi_{\lambda\nu}(\mathbf{q}, t - t') = -i\Theta(t - t') \left\langle \left[j_\lambda^\dagger(\mathbf{q}, t), j_\nu(\mathbf{q}, t') \right] \right\rangle. \quad (6.3)$$

For the actual calculation of the correlator Π it is usually most convenient to work in the Matsubara formalism where it assumes the form

$$\Pi_{\lambda\nu}(\mathbf{q}, i\Omega_n) = - \int_0^\beta d\tau e^{i\Omega_n \tau} \left\langle \mathcal{T}_\tau j_\lambda^\dagger(\mathbf{q}, \tau) j_\nu(\mathbf{q}, 0) \right\rangle \quad (6.4)$$

where the current operator is defined by $\mathbf{j}(\mathbf{q}) = \sum_{\mathbf{k}\sigma} v_{\mathbf{k}} c_{\mathbf{k}\sigma}^\dagger c_{\mathbf{k}+\mathbf{q}\sigma}$ with $v_{\mathbf{k}}$ the gradient of the dispersion $\epsilon_{\mathbf{k}}$. The correlator Π can be written in a series expansion in the usual way by expanding the S-matrix. The first terms in this expansion are given by

$$\begin{aligned} \Pi_{\lambda\nu}(\mathbf{q}, i\Omega_n) &= - \sum_{\mathbf{k}, i\omega_m, \sigma} v_{\mathbf{k}, \sigma}^\lambda G(\mathbf{k}, i\omega_m) G(\mathbf{k} + \mathbf{q}, i\omega_m + i\Omega_n) v_{\mathbf{k}+\mathbf{q}}^\nu \\ &+ \sum_{\mathbf{k}, i\omega_m, \sigma} \sum_{\mathbf{k}', i\omega'_m, \sigma'} v_{\mathbf{k}\sigma}^\lambda G(\mathbf{k}, i\omega_m) G(\mathbf{k} + \mathbf{q}, i\omega_m + i\Omega_n) \times \\ &\Gamma_{\mathbf{k}\mathbf{k}'\mathbf{q}}^{\sigma\sigma'}(i\omega_m, i\omega'_m, i\Omega_n) G(\mathbf{k}', i\omega'_m) G(\mathbf{k}' + \mathbf{q}, i\omega'_m + i\Omega_n) v_{\mathbf{k}'+\mathbf{q}\sigma'}^\nu + \dots \end{aligned} \quad (6.5)$$

Similar to the one-particle irreducible self-energy $\Sigma_{\mathbf{k}}(\omega) = \Sigma(\omega)$ also here simplifications arise in the $d \rightarrow \infty$ limit. The two-particle irreducible vertex function Γ becomes purely local hence momentum independent, $\Gamma_{\mathbf{k}\mathbf{k}'\mathbf{q}}^{\sigma\sigma'}(i\omega_m, i\omega'_m, i\Omega_n) = \Gamma^{\sigma\sigma'}(i\omega_m, i\omega'_m, i\Omega_n)$ [119]. This can be easily seen in real-space. In the derivation of

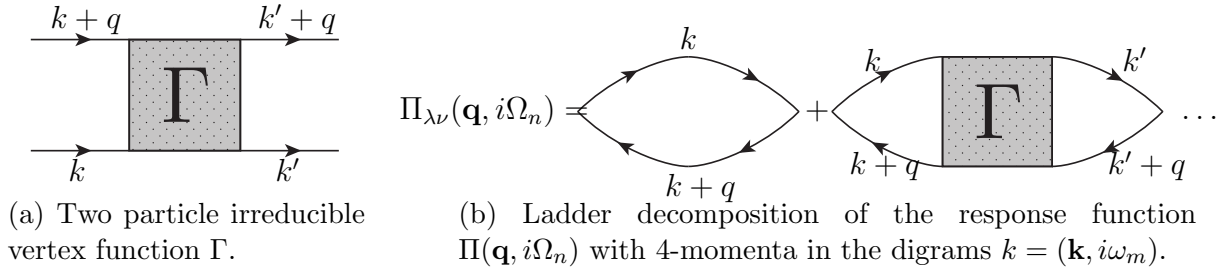


Figure 6.2

the DMFT we saw that the scaling rules are such that whenever two sites are connected by at least three independent paths, the corresponding diagram vanishes in the $d \rightarrow \infty$ -limit. For Γ in the real-space representation this is certainly the case. If it were not so, Γ could be cut into two pieces by cutting only two propagators in contradiction to the assumption that it is two-particle irreducible. The momentum sums in the second term Fig. 6.2b can therefore be performed independently in the left and right particle-hole bubble, ignoring momentum conservation at the vertex function. For a dispersion relation $\epsilon_{\mathbf{k}}$ that is even under $\mathbf{k} \rightarrow -\mathbf{k}$ the velocity $v_{\mathbf{k}}$ is odd. Since the Green's function $G(\mathbf{k}, i\omega_m)$ depends only through the dispersion relation on the momentum \mathbf{k} in the DMFT approximation it is an even function of \mathbf{k} . The terms under the momentum sums are therefore overall odd functions of the momentum and the sum vanishes. That means in the DMFT the current-current correlation function is given solely by the first particle-hole bubble and knowledge of the local self-energy and one-particle Green's function suffices to calculate it.

6.2 Layer-resolved conductivities

In this section we derive the layer-resolved in-plane component of the conductivity for a multi-layered heterostructure and Hall conductivity for a magnetic field \mathbf{B} applied perpendicular to the planes. In the following we orient the structure such that the magnetic field points along the z -direction with planes of the heterostructure parallel to the x - y plane. The system is assumed to possess a translational invariance along the x and y direction. Voruganti et al.[111] used a path integral formulation to study the linear response of a two-dimensional Hubbard model to electromagnetic perturbations at finite temperatures T . Here however the focus lay on non-trivial magnetic ordering phenomena and the local on-site Coulomb interaction U in the Hubbard model was either ignored completely or accounted for a crude way by the introduction of phenomenological damping rates in the Green's function through finite quasiparticle lifetimes τ . Here we extend their original derivation not only to multi-layered heterostructures but also consistently implement the description of interaction-induced correlation effects on the DMFT level.

We start from the non-interacting Hubbard model on a simple cubic lattice with nearest-neighbour hopping in three spatial dimensions

$$H_0 = \sum_{\langle i,j \rangle, \alpha} t_{ij, \alpha} c_{i\alpha}^\dagger c_{j\alpha} + \sum_{\langle \alpha, \beta \rangle, i} t_{\alpha\beta, i} c_{i\alpha}^\dagger c_{i\beta} \quad (6.6)$$

where we have separated inter- from intra-layer hopping processes. We choose to label the sites in the three-dimensional structure such that the indices i and j label sites within a given layer perpendicular to the z -direction while α and β are layer indices, i.e. the z -coordinate of the site. The hopping amplitude $t_{ij,\alpha}$ describes intra-layer hopping of electrons from site i to site j both located in layer α while $t_{\alpha\beta,i}$ describes inter-layer hopping. Due to the translational invariance along the x and y direction we can drop the index i in the latter hopping amplitude, $t_{\alpha\beta,i} \rightarrow t_{\alpha\beta}$. In the following we are not interested in magnetic symmetry-breaking and restrict the system to the paramagnetic regime. To remove clutter from the notation we omit the spin-index in the following. The spin degree of freedom can be accounted for by multiplying the transport coefficients by a factor of two. The effect of electromagnetic fields on the dynamics of the electrons can be implemented in a gauge-invariant way via Peierl's substitution. Here the hopping integral is modified by a phase-factor which is determined as the line integral of the vector potential $\mathbf{A}(\mathbf{r}, t)$ along the hopping path,

$$t_{i\alpha,j\beta}(A) = t_{i\alpha,j\beta} \exp\left(\frac{ie}{\hbar} \int_{\mathbf{r}_{i\alpha}}^{\mathbf{r}_{j\beta}} \mathbf{A}(\mathbf{r}, t) \cdot d\mathbf{r}\right). \quad (6.7)$$

where $\mathbf{A}(\mathbf{r}, t)$ is related to the applied fields $\mathbf{E}(\mathbf{r}, t) = -\partial\mathbf{A}/\partial t$ and $\mathbf{B}(\mathbf{r}, t) = \nabla \times \mathbf{A}(\mathbf{r}, t)$. We approximate the continuum phase factor above by the value of the vector potential at the midpoint between lattice site $i\alpha$ and $j\beta$

$$\int_{i\alpha}^{j\beta} \mathbf{A}(\mathbf{r}, t) \cdot d\mathbf{r} \sim \mathbf{A}(R_{i\alpha,j\beta}, t) \cdot \mathbf{r}_{i\alpha,j\beta} \equiv \mathbf{A}_{i\alpha,j\beta}(t) \cdot \mathbf{r}_{i\alpha,j\beta} \quad (6.8)$$

where $r_{i\alpha,j\beta} \equiv r_{j\beta} - r_{i\alpha}$ and $R_{i\alpha,j\beta} \equiv (r_{i\alpha} + r_{j\beta})/2$. In the following we are interested in situations where a weak, uniform, layer-independent electric field \mathbf{E} is applied perpendicular to the stacking axis (z), i.e. in x direction, and the applied magnetic field is a weak and both layer- and time-independent field which points along the z direction. The vector potential $\mathbf{A}_{q\alpha}$ therefore consists of a spatially uniform component $\mathbf{a}_{n\alpha}^E$ (subscript n indicates bosonic frequency Ω_n) modelling the electric field \mathbf{E} and a static contribution $\mathbf{a}_{q\alpha}^B$ modelling the constant magnetic field \mathbf{B} along the z -direction,

$$\mathbf{A}_{\mathbf{q},\Omega_n} = \mathbf{a}_n^E \delta_{\mathbf{q},0} + \mathbf{a}_{\mathbf{q}}^B \delta_{\Omega_n,0}. \quad (6.9)$$

We will mainly work in momentum space for the derivation and it will prove advantageous to introduce the relativistic notation for the momentum and frequency indices, e.g. $p \equiv (\mathbf{p}, \omega_m)$ for the fermions with $\omega_m = \pi(2m + 1)/\beta$ a fermionic Matsubara frequency and $q \equiv (\mathbf{q}, \Omega_n)$ for the bosonic gauge-field with $\Omega_n = 2\pi m/\beta$ a bosonic Matsubara frequency.

For the geometry we consider here it is always possible to choose a gauge where the corresponding vector potential \mathbf{A} has a vanishing z -component. We can already see that since $r_{i\alpha} - r_{i\beta}$ points along the z direction for inter-layer hopping events the phase factor $\mathbf{A}_{i\alpha,j\beta} \cdot \mathbf{r}_{i\alpha,j\beta}$ vanishes. Nontrivial phases are only picked up in intra-layer hopping events. For the derivation of the linear response to an electromagnetic perturbation \mathbf{A} at finite temperature T we start from the grand-canonical partition function of the system

$$Z[\mathbf{A}] = \text{Tr} [\exp [-\beta (H[\mathbf{A}] - \mu\mathcal{N})]] \quad (6.10)$$

where μ denotes the chemical potential, β the inverse temperature and $\mathcal{N} = \sum_{i\alpha} c_{i\alpha}^\dagger c_{i\alpha}$ is the total particle number operator. The partition function may be conveniently expressed as a path integral over Grassmannian fields $c_{i\alpha}(\tau)$ and $c_{i\alpha}^\dagger(\tau)$,

$$Z[\mathbf{A}] \equiv \exp^{-\beta\Omega[\mathbf{A}]} = \int D[c^\dagger, c] \exp \left[- \int_0^\beta d\tau (\mathcal{L}_0[c^*, c, \mathbf{A}] + \mathcal{L}_{\text{int}}[c^*, c, \mathbf{A}]) \right]. \quad (6.11)$$

Here $\Omega[\mathbf{A}]$ is the so-called grand-canonical potential which will be useful for the derivation of the conserved currents later. $\mathcal{L}_0[c^*, c, \mathbf{A}]$ is the non-interacting Lagrangian density and $\mathcal{L}_{\text{int}}[c^*, c, \mathbf{A}]$ describes the local Coulomb interactions U_α . $\mathcal{L}_0[c^*, c, \mathbf{A}]$ given by the following expression

$$\mathcal{L}_0[c^*, c, \mathbf{A}] = c_{i\alpha}^\dagger(\tau) [(\partial/\partial\tau - \mu) \delta_{\alpha\beta} \delta_{ij} + t_{ij,\alpha}(\mathbf{A}) \delta_{\alpha\beta} + t_{\alpha\beta} \delta_{ij}] c_{j\beta}(\tau). \quad (6.12)$$

The effects of local Coulomb interactions U_α can be included on the level of the DMFT description by adding layer-dependent, purely local self-energies $\Sigma_\alpha(i\omega_n)$ to the above Lagrangian density. This produces the correct DMFT single-particle Green's function. We will employ the DMFT for heterostructures as outlined in chapter 5 to determine the self-energies $\Sigma_\alpha(i\omega_n)$ for the concrete system. The Lagrangian density for an interacting system in this approximation thus assumes the form

$$\mathcal{L}[c^*, c, \mathbf{A}] = c_{i\alpha}^\dagger(\tau) [(\partial/\partial\tau - \mu + \Sigma_\alpha(i\omega_n)) \delta_{\alpha\beta} \delta_{ij} + t_{ij,\alpha}(\mathbf{A}) \delta_{\alpha\beta} + t_{\alpha\beta} \delta_{ij}] c_{j\beta}(\tau) \quad (6.13)$$

Note that this form of the Lagrangian can only be used to calculate the Green's function G_{ij} in the DMFT approximation and the conductivity σ only in the absence of vertex corrections. Since the current \mathcal{J} couples in the grand canonical potential to the vector potential \mathbf{A} , the component λ of a current response in layer α with Fourier component q in terms of a spatially uniform electric field component \mathbf{a}_n^E and a static magnetic component \mathbf{a}_q^B can be expressed as the functional derivative

$$\mathcal{J}_{q\alpha}^\lambda = -(1/V) \delta\Omega[\mathbf{A}] / \delta A_{-q\alpha}^\lambda \quad (6.14)$$

where V is the normalisation volume. Note that the exact current response is given when equation Eq. 3.36 is used. For the calculation of the conductivity we are interested in the current response linear in the applied field \mathbf{E} while for the Hall conductivity is must be linear in both \mathbf{E} and \mathbf{B} . Following Voruganti et al.[111] we thus expand the action $\mathcal{S} = \int_0^\beta \mathcal{L}$ in powers of the vector potential \mathbf{A} . Expanding the exponential function in Peierl's substitution we find that the term of order $n \geq 1$ in \mathbf{A} is given by

$$\begin{aligned} \mathcal{S}^{(n)} = \frac{(ie)^n}{n!} \int_0^\beta d\tau \sum_{\alpha, \langle ij \rangle} t_\alpha c_{i\alpha}^\dagger(\tau) (\mathbf{A}_{ij,\alpha} \cdot \mathbf{r}_{ij})^n c_{j\alpha}(\tau) \\ + \sum_{i \langle \alpha\beta \rangle} t_{\alpha\beta} c_{i\alpha}^\dagger(\tau) \underbrace{(\mathbf{A}_{\alpha\beta,i} \cdot \mathbf{r}_{\alpha\beta})^n}_{=0} c_{i\beta}(\tau) \end{aligned} \quad (6.15)$$

where the last term vanishes due to $\mathbf{r}_{\alpha\beta} \parallel \hat{\mathbf{e}}_z \perp \mathbf{A}_{\alpha\beta,i}$. We now Fourier transform in the x and y direction and leave the layer index in real space. The Grassmannian fields and the gauge potential can be written as

$$\begin{aligned} c_{i\alpha}(\tau) &= \frac{1}{\sqrt{\beta L}} \sum_p \exp(i\mathbf{p} \cdot \mathbf{r}_{i\alpha} - i\omega_m \tau) c_{\mathbf{p}\alpha} \\ A_{i\alpha,j\beta}(\tau) &= \sum_q \exp(i\mathbf{q} \cdot \mathbf{R}_{i\alpha,j\beta} - i\Omega_n \tau) A_{\mathbf{q},\alpha\beta} \end{aligned} \quad (6.16)$$

where $p = (\mathbf{p}, \omega_m)$, $q = (\mathbf{q}, \Omega_n)$, L is needed for proper normalisation and is given by the number of sites per layer and bosonic Matsubara frequencies Ω_n and fermionic frequencies ω_m . For each of the two-dimensional layers in the heterostructure the electronic dispersion relation is defined as

$$\epsilon_{\mathbf{p}\alpha} = \sum_{\langle ij \rangle} t_\alpha \exp(i\mathbf{p} \cdot \mathbf{r}_{ij}) = -2t_\alpha (\cos p_x + \cos p_y), \quad (6.17)$$

where t_α is the nearest-neighbour hopping strength in layer α . We now substitute the expansions Eq. 6.16 into the the action Eq. 6.15 and after a lengthy calculation[111] one finds for the $n \geq 1$ order term of the action

$$\mathcal{S}^{(n)} = \frac{e^n}{n!} \sum_\alpha \sum_{p,q} \sum_{q_1 \dots q_n} c_{p\alpha}^\dagger \left(\epsilon_{\mathbf{p}/2+\mathbf{q}/2}^{\delta_1 \dots \delta_n} A_{q_1\alpha}^{\delta_1} \dots A_{q_n\alpha}^{\delta_n} \right) c_{q\alpha}. \quad (6.18)$$

Here we introduced the short-hand notation $\epsilon_{\mathbf{p}}^\alpha$ where the subscripts signifies partial differentiation with respect to the indicated component, i.e. $\epsilon_{\mathbf{p}}^\alpha = \partial \epsilon_{\mathbf{p}} / \partial p_\alpha$. Due to momentum and energy conservation in the system the four-momenta are constrained by $\sum_{a=1, \dots, n} q_a = p - q$. Note that due to the vanishing z component of the vector potential \mathbf{A} only partial derivatives of the dispersion relation with respect to the x and y components appear. From Eq. 6.18 we find that to third order in the vector potential \mathbf{A} the action of the system is given by

$$\begin{aligned} \delta_3^{\mathbf{A}} S &= \sum_{p,q} \sum_\alpha c_{p\alpha}^\dagger (K_{pq,\alpha\beta} + T_{pq,\alpha\beta} + V_{pq,\alpha}[\mathbf{A}] \delta_{\alpha\beta}) c_{q\beta} \\ K_{pq,\alpha\beta} &= \delta_{pq} \delta_{\alpha\beta} (-i\omega_m + \epsilon_{\mathbf{p}} - \mu + \Sigma_\alpha(i\omega_m)) \\ T_{pq,\alpha\beta} &= \delta_{pq} t_{\alpha\beta} \\ V_{pq,\alpha}[\mathbf{A}] &= e \epsilon_{\mathbf{p}/2+\mathbf{q}/2}^\mu A_{pq,\alpha}^\mu + (e^2/2) \epsilon_{\mathbf{p}/2+\mathbf{q}/2}^{\mu\nu} \sum_{q_1} A_{p-q-q_1,\alpha}^\mu A_{q_1,\alpha}^\nu \\ &\quad + (e^3/6) \epsilon_{\mathbf{p}/2+\mathbf{q}/2}^{\mu\nu\eta} \sum_{q_1, q_2} A_{p-q-q_1-q_2,\alpha}^\mu A_{q_1,\alpha}^\nu A_{q_2,\alpha}^\eta \end{aligned} \quad (6.19)$$

The notation $\delta_i^{\mathbf{A}}$ signifies that we are expanding up to i th order in \mathbf{A} . In the diagrammatic analysis that follows we will refer to the contribution of order n in $\mathbf{A}_{q\alpha}$ as the “ V^n vertex”. Since the action is quadratic in the fermionic degrees of freedom we can integrate them out by virtue of the relation $\int D\Psi^\dagger D\psi \exp[\psi^\dagger (K + T + V)\psi] =$

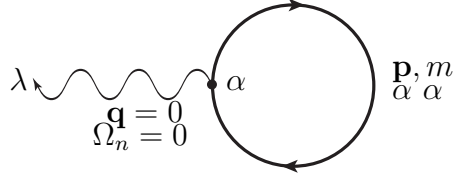


Figure 6.3: The diagram of order 0 in the vector potential \mathbf{A} . The contribution from this diagram vanishes for all even dispersion relations, $\epsilon_{\mathbf{p}\alpha} = \epsilon_{-\mathbf{p}\alpha}$.

$\det[K + T + V]$. The Green's function of the system in the absence of electromagnetic fields is with the help of the above expression easily found to be

$$G_{p\alpha\beta} = \delta_{pq} (T_{pp,\alpha\beta} + K_{pp,\alpha\beta})^{-1} \quad (6.20)$$

and the effective action can be written as

$$-\beta\Omega[A] = \text{Tr} \ln G^{-1} + \text{Tr} \ln [1 + G \cdot V[A]] . \quad (6.21)$$

Only the second term on the rhs of the above equation has a dependence on the vector potential and can be expanded using the following identity

$$\begin{aligned} \text{Tr} \ln(1 + G \cdot V[A]) &= - \sum_{n=1}^{\infty} \text{Tr}(G \cdot V[A])^n / n \\ &= - \sum_{n=1}^{\infty} \text{Tr}(G \cdot V[A])^n / n \end{aligned} \quad (6.22)$$

The component λ of the current density $\delta_0^{\mathbf{A}} \mathcal{J}_{q\alpha}^{\lambda}$ in layer α to zeroth order in the external fields is found by expanding the action up to first order in the vector potential \mathbf{A} using the above relations and application of the definition of the current density

$$\begin{aligned} \delta_0 \mathcal{J}_{q\alpha}^{\lambda} &= \frac{\delta}{\delta A_{-q\alpha}^{\lambda}} \frac{1}{\beta} \ln \left[\int D[c^{\dagger}, c] e^{-\sum_{p\alpha'} c_{p\alpha'}^{\dagger} (i\omega_n - \mu - \Sigma_{\alpha'}) c_{p\alpha'}} e^{-e \sum_{pq'\alpha'} c_{p\alpha'}^{\dagger} \epsilon_{\mathbf{p}-\mathbf{q}'\alpha}^{\nu} A_{q'\alpha'}^{\nu} c_{p-q'\alpha'}} \right] \\ &= \delta_{i\omega_n, 0} \delta_{\mathbf{q}, 0} \frac{e}{\beta} \sum_p G_{\mathbf{p}m, \alpha\alpha} \epsilon_{p\alpha}^{\lambda} \end{aligned} \quad (6.23)$$

where subscript on the Green's function indicates the fermionic frequency $m \equiv \omega_m$. The DMFT self-energy is momentum independent and hence the layer Green's function $G_{p\alpha\alpha}$ for layer α depends only through the dispersion relation $\epsilon_{\mathbf{p}\alpha}$ on \mathbf{p} . For dispersions with an inversion symmetry $\epsilon_{\mathbf{p}\alpha} = \epsilon_{-\mathbf{p}\alpha}$ the term under the sum above is an odd function of \mathbf{p} and therefore the right hand side vanishes as it should. Fig. 6.3 depicts a diagrammatic representation of the above expression. The small, black circles signify dispersion relation on the layer written next to it (here α) and with as many partial derivatives as wiggly lines are attached (here 1 only). The wiggly lines themselves are bosonic modes of the vector potential with the component written next to it (here λ) and the Fourier component bosonic frequency below (\mathbf{q}, Ω_n). Due to energy and momentum conservation $\mathbf{q} = 0$ and $\Omega_n = 0$. The solid black line with the arrow indicates a Green's function between the layers, Fourier component and fermionic frequency next to it.

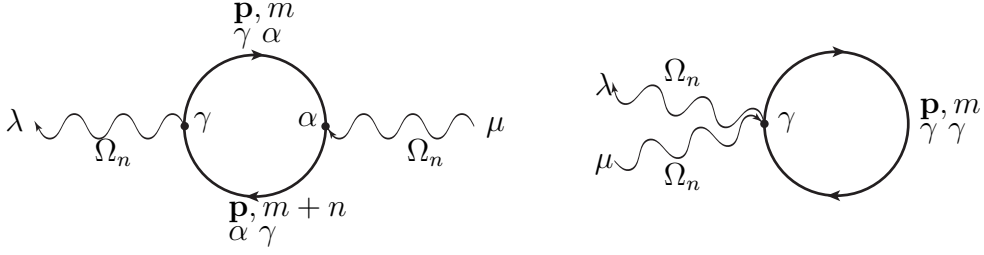


Figure 6.4: Diagrammatic representation of the first and second term in Eq. 6.24.

6.2.1 Longitudinal conductivity

For the calculation of the longitudinal, in-plane conductivity $\sigma_{\gamma\alpha}^{\lambda\nu}(\Omega_n)$ we are interested in the prefactor in front of the contribution to the response kernel linear in the electric part of vector potential $\delta_{\mathbf{q}\mathbf{0}}\mathbf{a}_n^E$ which describes a uniform electric field \mathbf{E} . The sub- and superscripts indicate that $\sigma_{\gamma\alpha}^{\lambda\nu}(\Omega_n)$ measures the λ -component of the current response in layer α due to the application of the ν -component of an electric field in layer γ . Contributions to $\mathcal{J}_{r\gamma}^\lambda$ linear in \mathbf{a}_n^E arise from loops with either one V^2 vertex or two V^1 vertices and they are given by

$$\delta_1^E \mathcal{J}_{q\gamma}^\lambda = -(e^2/V)\delta_{\mathbf{q}\mathbf{0}}\mathbf{A}_{n\gamma}^\nu \left[\sum_{\mathbf{p},\alpha} \epsilon_{\mathbf{p}}^\nu \epsilon_{\mathbf{p}}^{\lambda} \frac{1}{\beta} \sum_m G_{\mathbf{p}m,\gamma\alpha} G_{\mathbf{p}m+n,\alpha\gamma} - \sum_{\mathbf{p}} \epsilon_{\mathbf{p}}^{\lambda\nu} \frac{1}{\beta} \sum_m G_{\mathbf{p}m,\gamma\gamma} \right] \quad (6.24)$$

where subscript n indicates bosonic Matsubara frequency $n \equiv \Omega_n$. In real time we have $\mathbf{E}_\Omega = i\Omega\mathbf{a}_\Omega^E$. One finds that the $\Omega_n = 0$ contribution of the paramagnetic term (first one) cancels the diamagnetic contribution (second term). Fig. 6.4 shows a diagrammatic representation for the two contributions above (in that order). The imaginary-time response functions can be used to calculate the real-time response at any given temperature T by performing the analytic continuation, i.e. $i\Omega_n \rightarrow \Omega$. Writing the response to the electric field as $\delta_1^E \mathcal{J}_{\Omega\gamma}^\lambda = \sum_\alpha \sigma_{\gamma\alpha}^{\lambda\nu}(\Omega)\mathbf{E}_\alpha^\nu(\Omega)$ we find the conductivity by comparison with Eq. 6.24 to be given by

$$\sigma_{\gamma\alpha}^{\lambda\nu}(\Omega) = -(e^2/V) \sum_{\mathbf{p}} \epsilon_{\mathbf{p}}^\nu \epsilon_{\mathbf{p}}^{\lambda} (1/i\Omega) \Pi_{\alpha\gamma}(\mathbf{p}, \Omega) \quad (6.25)$$

where $\Pi_{\alpha\gamma}(\mathbf{p}, \Omega)$ is the analytic continuation of the bubble function

$$\Pi_{\alpha\gamma}(\mathbf{p}, i\Omega_n) = \frac{1}{\beta} \sum_m G_{\mathbf{p}m\gamma\alpha} G_{\mathbf{p}m+n\alpha\gamma} . \quad (6.26)$$

For the real part of the conductivity we need to find the imaginary part of the bubble function $\Pi_{\alpha\gamma}(\mathbf{p}, \Omega)$. We express the Matsubara Green's functions as the energy integral over the spectral function times a free Matsubara Green's function $G_0(\epsilon, i\omega_m)$

$$\begin{aligned} G_{p\alpha\beta} &= -i \int d\epsilon \frac{A_{\alpha\beta}(\mathbf{p}, \epsilon)}{i\omega_m - \epsilon} \\ &= -i \int d\epsilon G_0(\epsilon, i\omega_m) A_{\alpha\beta}(\mathbf{p}\epsilon) \end{aligned} \quad (6.27)$$

Using standard relations[69] for the analytic continuation one finds (Appendix D)

$$\text{Im } \Pi_{\alpha\gamma}(\mathbf{p}, \Omega)/\Omega = -\frac{1}{\pi} \int d\epsilon A_{\alpha\gamma}(\mathbf{p}, \epsilon) A_{\gamma\alpha}(\mathbf{p}, \epsilon + \Omega) \frac{n_F(\epsilon + \Omega) - n_F(\epsilon)}{\Omega} \quad (6.28)$$

In the limit $\Omega \rightarrow 0$ for static driving fields \mathbf{E} the expression simplifies and we find

$$\lim_{\Omega \rightarrow 0} \sigma_{\gamma\alpha}^{\lambda\nu}(\Omega) = (e^2/V) \int d\epsilon \frac{1}{\pi} \sum_{\mathbf{p}} \epsilon_{\mathbf{p}}^{\lambda} \epsilon_{\mathbf{p}}^{\nu} [A_{\alpha\gamma}(\mathbf{p}, \epsilon)]^2 \frac{\partial n_F(\epsilon)}{\partial \epsilon} \quad (6.29)$$

For an actual calculation performing the above momentum sum is computationally quite expensive. One usually prefers to trade momentum sums for one-dimensional energy integrals with a suitably chosen density of states like we did in the calculation of the local Green's function. This is also possible here although due to the factors $\epsilon_{\mathbf{p}}^{\lambda} \epsilon_{\mathbf{p}}^{\nu}$ in the sum it is not simply given by the non-interacting density of states. For a system on a simple cubic lattice with $\lambda = \nu$ such an expression is derived in Appendix F. The expression for the xx -component of the dc conductivity then assumes the form

$$\sigma_{\gamma\alpha}^{xx} = (e^2/V) \int d\epsilon \int d\epsilon_{\mathbf{p}} \rho^{xx}(\epsilon_{\mathbf{p}}) [A_{\alpha\gamma}(\mathbf{p}, \epsilon)]^2 \frac{\partial n_F(\epsilon)}{\partial \epsilon} \quad (6.30)$$

with $\rho^{xx}(\epsilon_{\mathbf{p}})$ the transport density of states. In the $T = 0$ limit the Fermi function $n_F(\epsilon)$ becomes a step function and the derivative a sharp peak located at the $\epsilon = \epsilon_F$. Then the conductivity depends only on the density of states at the Fermi level. Our dispersion relation is an even function of \mathbf{p} and thus $\epsilon_{\mathbf{p}}^{\alpha}$ is odd and the above expression is finite only if $\lambda = \nu$. $\sigma_{\gamma\alpha}^{\lambda\nu}(\Omega)$ describes the current response in layer γ due to an applied electric field in layer α . For a layer-independent electric field applied along the x -direction the total current in layer γ only has a non-vanishing x -component and is found by summing over all layers in the heterostructure

$$\delta_1^E \mathcal{J}_{\Omega\gamma}^x = E^x \sum_{\alpha} \sigma_{\gamma\alpha}^{xx}(\Omega) . \quad (6.31)$$

The total current through the system is obtained when the sum \sum_{γ} is performed. Note that for a homogenous system the expression Eq. (6.29) after Fourier transforming in the z direction reduces to the known expression[94]

$$\lim_{\Omega \rightarrow 0} \sigma^{xx}(\Omega) = \frac{\pi e^2}{2V} \int d\epsilon \sum_{\mathbf{p}} (\epsilon_{\mathbf{p}}^x)^2 [A(\mathbf{p}, \epsilon)]^2 \frac{\partial n_F(\epsilon)}{\partial \epsilon} \quad (6.32)$$

where $\mathbf{p} = (p_x, p_y, p_z)$. Before we turn to the Hall conductivity in the next section we briefly discuss the role of vertex corrections for the conductivity. Indeed in layered systems one has to be careful because not all vertex corrections drop out in all cases. For instance if we had calculated the longitudinal conductivity in the stacking direction of the planes we would be in trouble. Here vertex corrections cannot be argued to drop out and their neglect is indeed a crude approximation. For the in-plane component of the conductivity however the same arguments as in the homogenous system can be invoked (one might think about the system as being made up of unit cells of infinite length in the z direction) and indeed it suffices to calculate simply the particle-hole bubble as we did.

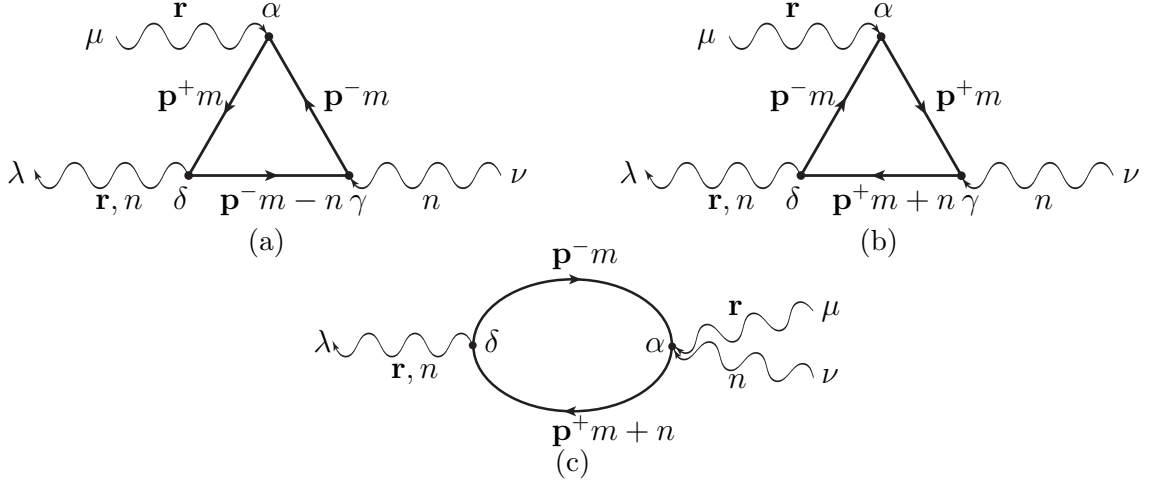


Figure 6.5: Triangle graphs, (a) & (b), with three V^1 vertices and the other diagram (c) for the calculation of the Hall conductivity.

6.2.2 Hall conductivity

For the calculation of the Hall conductivity we are interested in the current response $\delta_2^{EB} \mathcal{J}_{q\delta}^\alpha$ linear in both the electric field \mathbf{E} and the magnetic field \mathbf{B} . Contributions may arise from diagrams with three V^1 vertices, or one V^1 and one V^2 vertex or diagrams with one V^3 vertex. Recalling that $\mathbf{A}_{q\alpha} = \mathbf{a}_{n\alpha}^E \delta_{\mathbf{q},\mathbf{0}} + \mathbf{a}_{\mathbf{q}\alpha}^B \delta_{\Omega_n,0}$ each such diagram gives terms quadratic in either $\mathbf{a}_{n\alpha}^E$ and $\mathbf{a}_{\mathbf{q}\alpha}^B$ or linear in both. For the Hall conductivity only the latter kind contributes. In real time we have $\mathbf{E}_\Omega = i\Omega \mathbf{a}_\Omega^E$ and $\mathbf{B}_\mathbf{q}^\alpha = i\epsilon^{\alpha\beta\gamma} q^\beta a_{\mathbf{q}}^{B\gamma}$ and thus the real part of the Hall conductivity $\sigma_H^{\alpha\beta\epsilon}{}_{\delta\gamma\alpha}(\Omega)$ requires us to evaluate the real part of each Matsubara sum to linear order in \mathbf{q} and Ω . As it turns out only three of the six diagrams linear in $\mathbf{a}_{n\alpha}^E$ and $\mathbf{a}_{\mathbf{q}\alpha}^B$ contain contributions linear in both \mathbf{q} and Ω_n . Two are given by the triangle graphs depicted in Fig. 6.5 (a) and (b) and one is the diagram with one V^1 and one V^2 vertex in Fig 6.5 (c). We split the response current $\delta_2 \mathcal{J}_{r\delta}^\lambda$ into a contribution from the triangle graphs (1) and a contribution from the other diagram (2)

$$\delta_2^{EB} \mathcal{J}_{q\delta}^\lambda = \delta_2^{(1)} \mathcal{J}_{q\delta}^\lambda + \delta_2^{(2)} \mathcal{J}_{q\delta}^\lambda \quad (6.33)$$

Under the assumption that the dispersion relation $\epsilon_{\mathbf{q}}$ is layer-independent, any layer-dependence in the response current is entirely due to interaction effects. After a lengthy calculation (Appendix C) one finds that the contribution due to the triangle graphs is given by

$$\delta_2^{(1)} \mathcal{J}_{q\delta}^\lambda = \frac{e^3}{2} \mathbf{a}_n^{E\nu} \mathbf{a}_{\mathbf{q}}^{B\mu} \sum_{\alpha,\gamma} \mathbf{q}^\chi \sum_{\mathbf{p}} \epsilon_{\mathbf{p}}^\lambda \epsilon_{\mathbf{p}}^\mu \epsilon_{\mathbf{p}}^{\nu\chi} \Pi_{\mathbf{p}n\delta} \quad (6.34)$$

where we have defined the vertex function

$$\Pi_{\mathbf{p}n\delta\gamma\alpha}^H = \sum_m G_{\mathbf{p}m,\alpha\delta} G_{\mathbf{p}m,\alpha\gamma} [G_{\mathbf{p}m+n,\gamma\delta} - G_{\mathbf{p}m-n,\gamma\delta}] \cdot \quad (6.35)$$

The contribution due to the diagram depicted in Fig. 6.5 (c) takes the form

$$\delta_2^{(2)} \mathcal{J}_{q\delta}^\lambda = -\frac{e^3}{2} \mathbf{a}_{\mathbf{q}}^{B\mu} \mathbf{a}_n^{E\nu} \sum_{\alpha,\gamma} \mathbf{q}^\chi \sum_{\mathbf{p}} \epsilon_{\mathbf{p}}^\lambda \epsilon_{\mathbf{p}}^{\mu\nu} \epsilon_{\mathbf{p}}^\chi \Pi_{\mathbf{p}n\delta\gamma\alpha}^H \quad (6.36)$$

Upon summation of the two contributions and comparison with the definition of the Hall conductivity

$$\delta_2^{EB} \mathcal{J}_{(\mathbf{q},\Omega)\delta}^\lambda = E_\Omega^\mu B_{\mathbf{q}}^\nu \sum_{\alpha,\gamma} \sigma_H^{\lambda\mu\nu}{}_{\delta\gamma\alpha}(\Omega) \quad (6.37)$$

one finds for \mathbf{E} -field in y -direction, the \mathbf{B} -field along the z -axis and the current response in x -direction

$$\sigma_H^{xyz}{}_{\delta\gamma\alpha}(\Omega) = \frac{e^3}{2} \sum_{\mathbf{p}} (\epsilon_{\mathbf{p}}^x)^2 \epsilon_{\mathbf{p}}^{yy} \Pi_{\mathbf{p}\delta}^H(\Omega)/\Omega \quad (6.38)$$

with $\Pi_{\mathbf{p}\delta}^H(\Omega) = \sum_{\alpha\gamma} \Pi_{\mathbf{p}\delta\gamma\alpha}^H(\Omega)$ the analytic continuation of the vertex function. Similar to the case of the conductivity one can use the standard tricks for the analytical calculation. However here the calculation is slightly more involved and can be found in Appendix E. After a lengthy calculation one finds

$$\begin{aligned} \lim_{\Omega \rightarrow 0} \Pi_{\mathbf{p}\delta}^H(\mathbf{p}, \Omega)/\Omega &= +\frac{1}{\pi} \sum_{\alpha\gamma} \int d\epsilon \frac{\partial}{\partial \epsilon} G'_{\alpha\gamma}(\mathbf{p}, \epsilon) G''_{\alpha\delta}(\mathbf{p}, \epsilon) G'_{\gamma\delta}(\mathbf{p}, \epsilon) n_F(\epsilon) \\ &\quad -\frac{1}{\pi} \sum_{\alpha\gamma} \int d\epsilon G''_{\alpha\gamma}(\mathbf{p}, \epsilon) G'_{\alpha\delta}(\mathbf{p}, \epsilon) \frac{\partial}{\partial \epsilon} G'_{\gamma\delta}(\mathbf{p}, \epsilon) n_F(\epsilon) \\ &\quad +\frac{1}{\pi} \sum_{\alpha\gamma} \int d\epsilon G''_{\alpha\gamma}(\mathbf{p}, \epsilon) G''_{\alpha\delta}(\mathbf{p}, \epsilon) G''_{\gamma\delta}(\mathbf{p}, \epsilon) \frac{\partial}{\partial \epsilon} n_F(\epsilon) \\ &\quad +\frac{1}{\pi} \sum_{\alpha\gamma} \int d\epsilon G''_{\alpha\gamma}(\mathbf{p}, \epsilon) G''_{\alpha\delta}(\mathbf{p}, \epsilon) \frac{\partial}{\partial \epsilon} G''_{\gamma\delta}(\mathbf{p}, \epsilon) n_F(\epsilon) \end{aligned} \quad (6.39)$$

Note here that this expression does not only probe the properties of the system at the Fermi level in the dc limit $\Omega \rightarrow 0$ for $T = 0$. To find the total Hall current one performs the remaining sum over all layers, $\mathcal{J}^\lambda = \sum_{\delta} \mathcal{J}_{\delta}^\lambda$. Under the three sums the terms in Eq. 6.39 can be reordered and one sees that the first terms cancels the second one. Partial integration of the last term allows one to combine it with the second to last one to find

$$\lim_{\Omega \rightarrow 0} \Pi_{\mathbf{p}}^H(\mathbf{p}, \Omega)/\Omega = \frac{2}{3\pi} \sum_{\alpha\gamma\delta} \int d\epsilon G''_{\alpha\gamma}(\mathbf{p}, \epsilon) G''_{\alpha\delta}(\mathbf{p}, \epsilon) G''_{\gamma\delta}(\mathbf{p}, \epsilon) \frac{\partial}{\partial \epsilon} n_F(\epsilon) \quad (6.40)$$

which only probes low energy properties for $T \rightarrow 0$. After Fourier transformation in the z direction the above expression agrees with the one found by Pruschke et al.[94] for a homogenous system. We believe that vertex corrections drop out of this expression in the $d \rightarrow \infty$ limit for similar arguments as in the case of the conductivity, but we haven't proven this formerly.

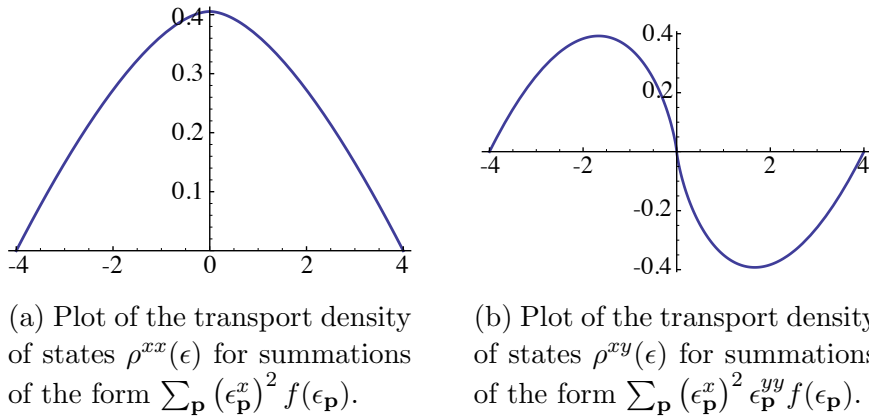


Figure 6.6

6.3 Results

The DMFT generalised for long-range Coulomb interactions as outlined in section 5.5 allows to study a variety of strongly-correlated heterostructures including charge re-ordering phenomena at the interfaces. Electronic charge reconstruction has profound influence - especially when strong interactions are involved - on the electronic state of the system near the interface. Transport measurements provide an efficient probe for the low-energy degrees of freedom in complex system. Therefore the study how charge leakage across the interface affects transport coefficients such as the conductivity and the Hall coefficient is key to the successful understanding of any strongly-correlated inhomogeneous device. The temperature in these systems is an important parameter in this regard. We know from DMFT bulk studies that the first order Mott-Hubbard metal insulator transition has a critical endpoint at a finite temperature T_c . The phase transition line is shaped such that in certain parameter regimes of the interaction strength U an increase in the system temperature leads to the disappearance of the metallic solution and the system becomes insulating. This is surprising as one usually expects thermal activation of band gaps and therefore an increase in the conductivity when the temperature is raised. From these considerations one can already expect interesting behaviour from the interplay between interface doping and quenching of the Kondo effect by temperature fluctuations.

We concentrate here on Mott-Band insulator heterostructures modelled as single band Hubbard models on a simple cubic lattice with nearest-neighbour hopping. The restriction to such a simplified model neglects important orbital degrees of freedom and also any possible atomic reconstruction which might appear at the interface[84]. This is justified as our motivation is not the quantitative explanation of experiments but rather to work out the fundamental effects which are key to the understanding of charge transport for these types of systems. We are also currently not interested in magnetic ordering phenomena, so we restrict the DMFT equations to the paramagnetic regime and do not allow for symmetry breaking by the introduction of the AB-unit cell².

²Note that the combination of the DMFT generalisations for electronic charge reconstruction and AB-sublattice anti-ferromagnetic order can be readily combined in a straightforward manner.

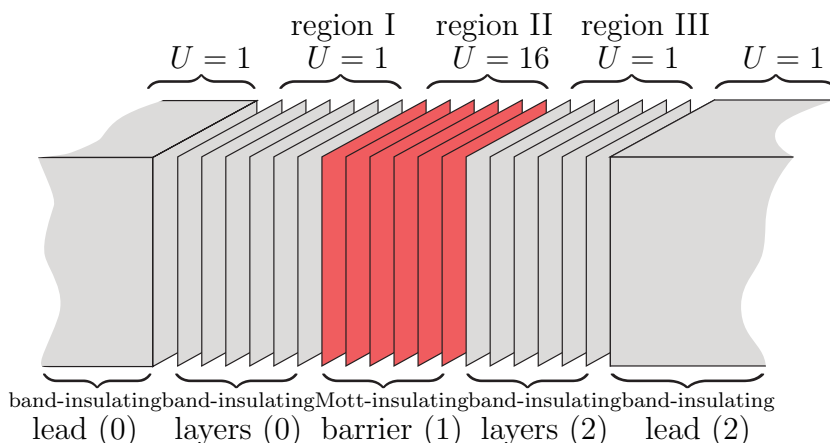
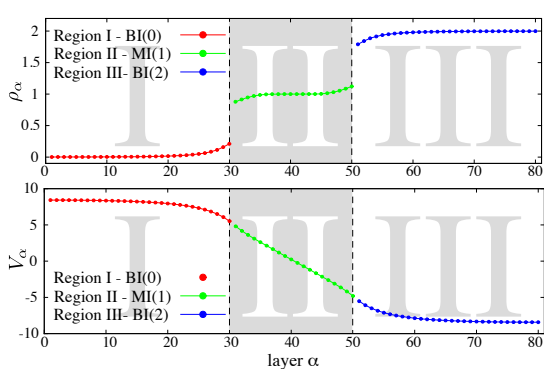
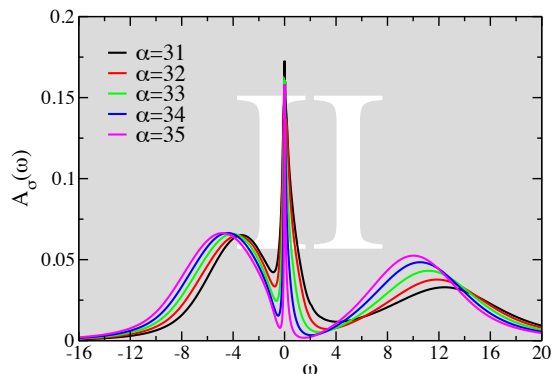


Figure 6.7: The system is composed of 30 band-insulating layers with $U = 1$ attached to semi-infinite, band-insulating lead with the same parameters to the left. The barrier region comprises 20 Mott-insulating layers with $U = 16 > U_c$ followed by 20 band-insulating layers with $U = 1$ and capped off with a semi-infinite, band-insulating lead to the right. The numbers in the round brackets are bulk occupation numbers.

Fig. 6.7 shows the layout of the system we are considering. The first 30 layers have very weak on-site interaction, $U = 1$, and their background charge $\rho^{(0)}$ is set to 0 so as to model a band-insulator with its single band completely emptied (region I). The central region consists of 20 layers with a Hubbard interaction of $U = 16$ which is in excess of the critical U for Mott-insulating behaviour in bulk calculations at half-filling (region II). The background charge $\rho^{(0)}$ for these layers is indeed set to $\rho^{(0)} = 1$. The system ends on the right side with another 30 weakly-correlated layers, $U = 1$, with their background filling set to $\rho^{(0)} = 2$ to model a band-insulator with its conduction band completely filled (region III). To remove finite size effects we attach semi-infinite leads right and left to the system with the same parameters as the adjacent layers. To complete the system description we have to specify the local chemical potential in each of the three regions and the two leads. The potential mismatch at the interface will be the energetic motivation for charges to accumulate on one side of the interface while avoiding the other. Of course this process does not continue indefinitely. As more and more charges pile up on one side and more and more holes on the other the background charges will no longer be compensated and an electric field builds up in response. Charge will continue to cross the interface and the electric potential will grow in size until it compensates the jump in the chemical potential. The exact shape of the electric interface potential will however depend on microscopic details such as the band-structure. In our calculation we choose a $\mu_I = 2$ for region I, $\mu_{II} = 0$ for region II and $\mu_{III} = -2$ for region III. The leads are infinite in size and therefore have to be electrostatically neutral as any deviation from this state would cost an infinite amount of energy. Since the background charge in the left (right) lead has been set to 0 (2), the chemical potential therefore has to be smaller $\mu_L \lesssim -6$ ($\mu_R \gtrsim +6$) so as to push all of the spectral weight above (below) the Fermi level. For our calculation we chose $\mu_L = -6$ and $\mu_R = +6$. The potential mismatch at the interface between region I and II is therefore $\Delta\mu_{I-II} = \mu_I - \mu_I^{\text{bulk}} - \mu_{II} + \mu_{II}^{\text{bulk}} = (-6 - 2 - 0 + 0) = -8$. Charge will therefore rearrange at the interface until an electric potential has built



(a) Layer-resolved occupation ρ_α (top panel) and electric potential V_α (bottom panel). The electronic charge reconstruction can be seen to create linear potential across part of the system with $U > U_c$ (region II).



(b) Spectral functions for layers 31-35 in the Mott-insulating region II close to the I-II interface. The width of the quasiparticle peak rapidly diminishes when the center of the region is approached.

up which takes a value of $+8$ inside region I. For the right interface we find likewise $\Delta\mu_{II-III} = (6 - (-2) - 0 + 0) = 8$.

The setup we have chosen here possesses a special symmetry which helps the convergence of the calculation. The system is invariant under the transformation $\alpha \rightarrow N_\alpha - \alpha$ plus a particle-hole transformation, where N_α is the total number of layers not including the leads. Note that above all chemical potentials change sign under $\alpha \rightarrow N_\alpha - \alpha$. This symmetry ensures that the overall system is always charge neutral and one does not have to take special precautions in the calculation to make ensure convergence to the charge neutral point.

Fig. 6.8a shows the layer-resolved occupation ρ_α and the electric potential V_α after convergence for a system temperature of $T = 10^{-8}$. Far away from the I-II interface inside region I the occupation assumes the background value $\rho_\alpha = \rho_I^{(0)} = 0$ and the electronic configuration for layers 1 to ≈ 20 is that of a band-insulator with an empty band. Closer to the interface charge accumulates thus particle-doping the band-insulator. The last layer before the interface ($\alpha = 30$) has an occupation of $\rho_{30} \approx 0.2$. The adjacent Mott-insulating layer on the other side of the interface is hole-doped with $\rho_{31} \approx 0.89$. The Mott-insulating layers however quickly return to their bulk charge of $\rho_{II}^{(0)} = 1$ within 3 – 4 layers and so Layers 34 – 47 are locally charge neutral. Due to the symmetry discussed above we have $\rho_\alpha = 2 - \rho_{N_\alpha - \alpha}$ and $V_\alpha = -V_{N_\alpha - \alpha}$: the electric potential vanishes at the center of the system. Region II sees an approximately linear electric potential from about $V_{31} \approx 5.6$ to $V_{50} \approx -5.6$ and connects with a potential which starts deep in region I at a bulk value of $V_1 \approx 8$ and drops within about 10 layers to the interface slightly. The asymptotic values of the electric potential are expected from our considerations above. It is however noteworthy that the Mott insulator deviates only slightly from its bulk charge although the electric potential causes substantial deviations of the local Fermi level compared to their bulk value. For example for layer 31 in region II the shift of the local Fermi level from the bulk

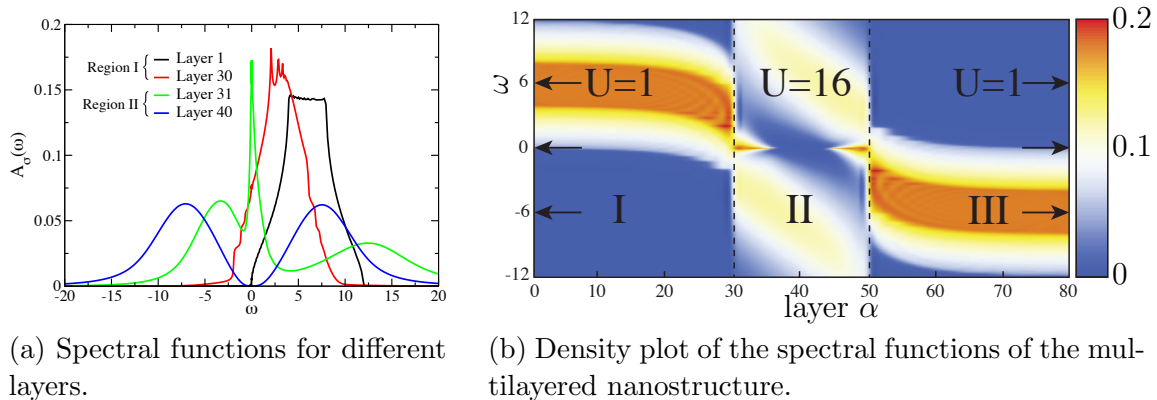


Figure 6.9

value is ≈ 5.6 while for layer 30 in region I it is only ≈ -1.8 , but the deviation in the background charge is only $\Delta\rho_{31} \approx -0.12$ while for layer 30 it is larger, $\Delta\rho_{30} \approx 0.2$.

The explanation for this behaviour is linked to the strong correlations within region II. Initially the Fermi level lies in a wide Mott gap and substantial potential strength is needed to push it into either the upper or lower Hubbard band. These bands are centered around $\pm U/2 = 8$. Once the Fermi level starts to move into, say, the upper band, the local density of states becomes finite which leads to an increase in the hybridisation function of the underlying impurity model and the appearance of a finite Kondo temperature T_K . If $T < T_K$ a Kondo resonance appears and the occupation deviates from half-filling. The width of the resonance is controlled by the Kondo temperature. Fig. 6.8b shows the spectral functions for layers 31 – 35. A narrow Kondo resonance can indeed be seen at the Fermi level with a width which decreases rapidly as one goes towards the region center. For $E_F \approx 5.6 < 8$ this resonance will be narrow and therefore the change in occupation in the Mott insulator is much smaller than the one in the band-insulators on the other side of the interface. As one walks goes deeper into region the lower Hubbard band moves away from the Fermi level resulting in ever narrower resonance peaks and in turn ever lower Kondo temperature T_K . Once the local Kondo temperature falls below the system temperature $T = 10^{-8}$ the resonance is cut off by temperature and the corresponding layer falls out of its Fermi liquid states. In principle not only doping due to the electric potential can create a Kondo resonance. Helmes et al. [46] showed that a metallic layer imposes due to the tunnel-coupling an effective lower bound on the hybridisation function of an adjacent Mott-insulating layer. This induces, even at half-filling, a finite T_K in the Mott insulator and a resonance may appear if $T < T_K$. This effect is however much weaker than the effect of the electric potential in our set-up.

Fig. 6.9 summarises the electronic state of the system. In subfigure (a) spectral functions of four different layers are shown. As already deduced from the charge distribution weakly-correlated layer 1 (black) indeed resembles a non-interacting three-dimensional density of states which has been shifted due to the electric potential such that no spectral weight resides below the Fermi level. The last weakly correlated layer 31 (red) before the I-II interface is indeed heavily particle doped as some of the spectral weight has been transferred below the Fermi level due to band bending. For

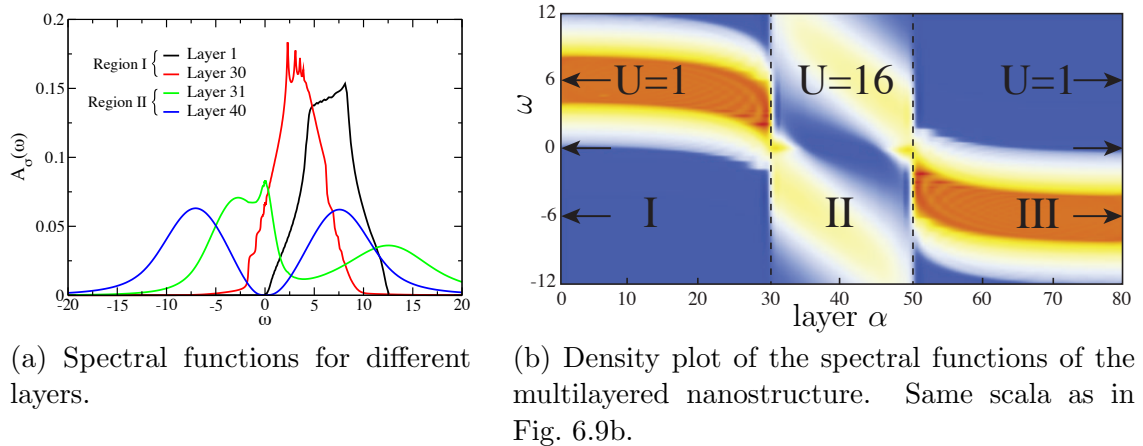
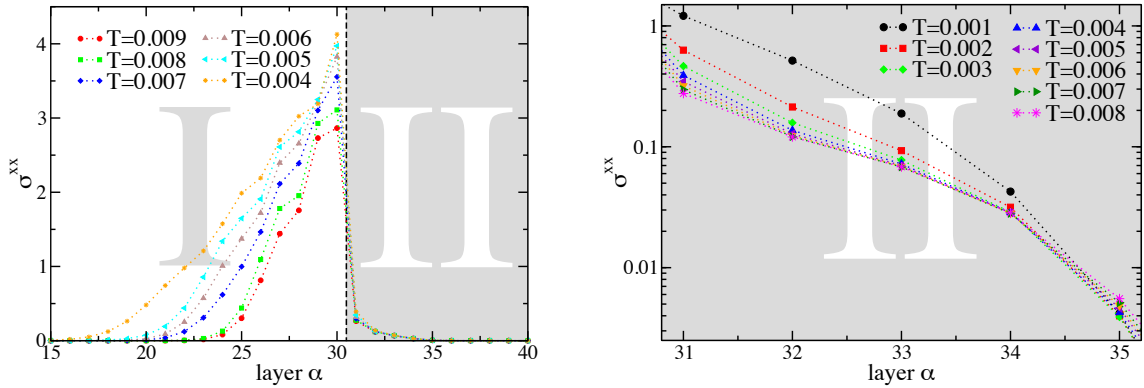


Figure 6.10

the strongly correlated region II, layer 40 (blue) at the center of region II bears clear signatures of a Mott-insulating state. The particle-hole symmetric spectrum shows well pronounced Hubbard bands and a large gap about the Fermi level. Right before the interface the spectrum of layer 31 (green) has been shifted due to the electric potential by $\Delta\omega \approx 5.6$ relative to layer 40 partly moving the Fermi level into the lower Hubbard band. This has indeed created a narrow Kondo resonance peak at the Fermi level resulting in metallic behaviour. The peak reaches up to the non-interacting value due to the Friedel sum rule. Fig. 6.9b shows a density plot of the spectral weight distribution in the system. The black arrows mark the upper and lower edge of a non-interacting, particle-hole symmetric density of states (upper and lower arrow) and the Fermi level (middle arrow). Regions of high spectral weight are colored red and those with low weight blue. Starting from the right one can see the conduction band (red) of the band-insulator completely above the Fermi level. Approaching the interface the electric potential bends the band downward pushing it partly into the Fermi level, resulting in metallic behaviour at the interface. Strongly-correlated region II shows the linearly deformed upper and lower Hubbard bands (yellow). Close to the interface metallic states can be seen as sharp red lines which end 3-4 layers into the region from either side.

Closer inspection of the weakly-interacting band in region I, reveals an interesting pattern of interference fringes superimposed onto the area colored red as yellowish lines. Appendix B lists spectral functions for all layers in the heterostructure. One can indeed see the change in the number of peaks appearing in the flat part of the density of states as one moves away from the interface. Due to the mismatch in the band structure delocalised particle states in the weakly-correlated region are reflected at the interface and interfere. The number of interference peaks at a distance L from the interface is therefore determined by the number of standing wave states in a box of length L . Closer inspection of the spectra indeed reveals that the number of peaks grows linearly with the distance.

Fig. 6.10 shows the spectral weight distribution for a higher system temperature of $T = 0.004$. The band-insulating region of the heterostructure is only mildly affected. The sharper features - especially the interference peaks at the top of the density of



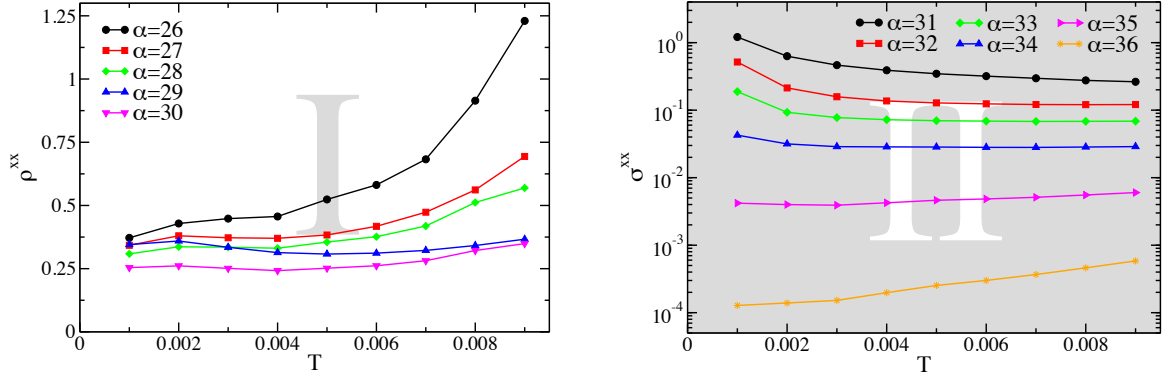
(a) Layer-resolved conductivity near the interface I-II for various temperatures. For higher temperatures the number of charge transporting layers reduces.

(b) Layer-resolved conductivity in the strongly-correlated region. The enhancement in the conductivity upon lowering the temperature sets in at layer-dependent threshold temperatures.

Figure 6.11

states - are slightly washed out from the thermal fluctuations. However the temperature has had a really dramatic effect on strongly-correlated region II. The metallic states at the interface have almost completely disappeared. We understand this from the perspective of the layer-dependent Kondo temperatures. With Kondo temperatures decreasing for layers further away from the interface the system temperature is currently so high that even the layer closest to the interface has its Kondo effect quenched by temperature. Indeed the corresponding spectral function in Fig. 6.10a (green) shows the on-set of a tiny peak at the Fermi level which shows that the system temperature is on the brink of the particular T_K . In the following we analyse the layer-resolved conductivity σ_{α}^{xx} in this interesting temperature regime.

Fig. 6.11 and Fig. 6.12 present spatially resolved conductivity data calculated from the one-particle Green's functions according to Eq. 6.30. As expected for temperatures $T = 0.004$ and above Fig. 6.11a shows that the strongly-correlated part of the system is essentially non-conducting and all charge transport is performed by the doped band-insulator close to the interface. In general electrical resistivity $\rho^{xx} = 1/\sigma^{xx}$ in metals increases with temperature and this behaviour is found here as well. With higher temperatures the number of layers near the interface which contribute to the transport reduces. For $T = 0.009$ only the 5 layers closest to the interface take an appreciable part in the charge transport. One finds that the imaginary parts of the self-energies $\Sigma_{\alpha}(\omega)$ show an increase - especially around the Fermi level - upon raising the temperature. This leads to a reduction in the quasiparticle lifetime and explains the increase in resistivity. Fig. 6.11b shows the conductivity for the 5 strongly-correlated layers closest to the I-II interface for a variety of different temperatures. For a given temperature the conductivity shows an approximately exponential drop with the distance to the interface. The temperature dependence is very rich. For layers 31-34 the conductivity increases with the reduction of the system temperature. However the enhancement starts at different threshold temperatures.



(a) Conductivity as a function of temperature T for different layers in weakly-correlated region I close to the interface I-II.

(b) Conductivity as a function of the temperature T for different layer in the strongly-correlated region II close to the interface I-II. Note the inversion of the $T - \sigma^{xx}$ relationship for layer 35 and 36.

Figure 6.12

One clearly sees that layers further away from the interface have a lower threshold temperature which is explained by the suppression of the Kondo temperature away from the interface. Once the threshold temperature T_K for a particular layer has been exceeded the layer turns into a strongly correlated metal and the conductivity increases strongly, i.e. Fig. 6.11b shows an increase in σ^{xx} by a factor of more than 3 for layer 31. For layer 35 one can see a reversal of the temperature-conductivity relationship. Here, 5 layers from the interface the conductivity has dropped to such low values that an increase in the conductivity can actually be seen due to thermal activation of the Mott gap. This is however a tiny effect due to the strong Coulomb interaction U and the large gap. Fig. 6.13 shows layer-resolved conductivities for the very low temperature regime where the Kondo effect on the strongly-correlated layers close to the interface has almost fully developed. Unfortunately the temperature regime below $T = 10^{-5}$ is numerically difficult to access. One has to add a tiny imaginary part to the real-frequency ($\omega + i\delta$) to broaden the delta peaks to a finite width. For low temperatures the Fermi distribution becomes a step function which means that the conductivity formula, Eq. 6.30, essentially probes only the spectral function at the Fermi energy. Below $T = 10^{-5}$ the imaginary parts of the self-energies at the Fermi level reach the order of magnitude of δ . Reducing δ is however difficult since this leads to problems with the adaptive integration routine in the Hilbert transforms due to ever sharper and sharper peaks encountered in the integration interval.

We regret that due to time restrictions we were not able to finish our calculations with regard to the Hall coefficient which is why no data of the same are presented in this thesis. We believe however that the presented layer-resolved formula is correct and the implementation should be straight forward (with the appropriate transport density of states given in Appendix F).

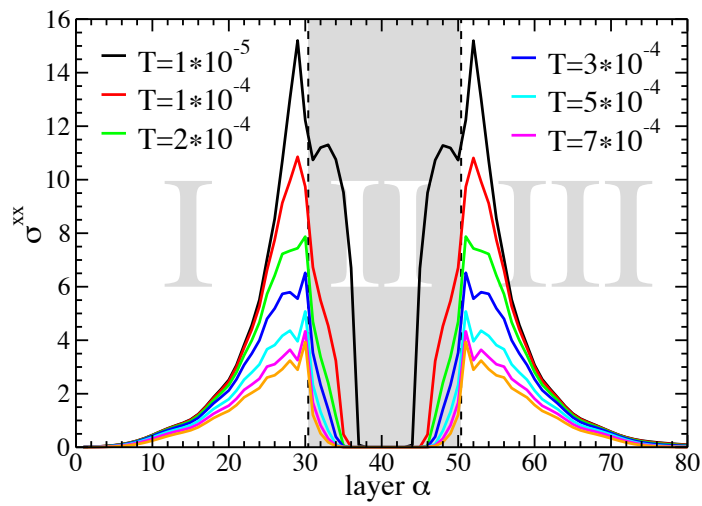


Figure 6.13: Layer-resolved in-plane conductivity for various temperatures T . Note the strong suppression of the conductivity in the strongly correlated region when the temperature is increased.

Chapter 7

Transmission through a Mott Barrier

The response of a system to external fields provides an efficient probe of its correlation effects. An extreme form of such a probe is the study of the dielectric breakdown. Here a strong electrical field is applied to a material in an insulating state and the parameter dependence of the breakdown of the insulating to a metallic state is studied. Experimental studies of both conventional band- and strongly correlated Mott-insulators supply the theorist with sufficient information to check hypothesis extracted from approximate theories for this extremely difficult non-equilibrium problem against actual data.

The breakdown of semiconductors with weak correlations can be well understood from Zener's theory of electrical breakdown [115] where so called Zener-tunnelling across the valence and conduction bands, triggers an electron avalanche which causes the dielectric breakdown. However for strongly interacting materials the situation is much more involved as one is faced with a many-body non-equilibrium problem. A simple argument already hints at the difference between the two types of systems: electron-hole excitations produced by the presence of the field may move freely in the band-insulator while they interact and eventually become dissipated in the Mott insulator. The study of such problems has proven very difficult as instead of a single energy gap between the valence and conduction band, many different energy gaps among the many-body levels become important.

Motivations to study this problem especially for strongly-correlated (Mott-) insulators are numerous. As non-equilibrium phase transitions and non-linear transport have become central issues in the study of strongly correlated systems, the dielectric breakdown as one of the most basic of such phenomena acquires a special role. As the motion of electrons in Mott insulators at half-filling is frozen due to strong repulsive interactions and doping of such materials leads to interesting quantum states such as high- T_c superconductivity a question that is not far to seek is how non-equilibrium carriers behave in response to a strong electric field. Systematic study of electron systems in the Mott insulating phase is believed to provide important information to understand such unconventional states of matter. Observing the breakdown of the Mott insulator may therefore provide a paradigm for strongly correlated electron systems in non-equilibrium.

Also recent progress in the cold-atom community, where realisations of both bosonic[40, 57, 28] and fermionic[103] Mott insulators have been constructed, have sparked renewed interest into the dielectric breakdown. Different experiments on oxides as well as organic materials have given valuable insight into non-equilibrium transport.

In this chapter we will use the inhomogenous DMFT to answer the following equilibrium question: How does temperature T and barrier length L affect the transmission probability through a Mott insulating region under a linear electric potential connected to non-interacting leads? The motivation is two-fold. We have seen in the last chapter that such a situation indeed arises when a Mott insulator is sandwiched between two band-insulators with a chemical potential mismatch and electronic charge reconstruction is taken into account: the charge redistribution creates on the one hand a linear electric potential in the Mott insulating region and on the other shifts the spectral function of the band insulators close to the interface into the Fermi level such that they can be seen as almost non-interacting leads. The other motivation stems from the hope that such a calculation might provide important insights into the dielectric breakdown of a Mott insulator. One might wonder how an equilibrium calculation can ever reveal information about the dielectric breakdown, after all, the non-equilibrium problem par excellence. Here one should remember Zener's theory for band insulators where an electron avalanche effect causes the destruction of the insulating state. For the earliest moments of the breakdown it can be argued that one is in a situation where the typical time between tunneling events is large as compared to the equilibration time in the system. In such a situation an equilibrium theory is justified and one might be able to understand how different system parameters affect the earliest moments of the dielectric breakdown.

This chapter starts with a short introduction to past works on the topic. Section 7.2 reviews the Landauer-Büttiker theory of conductance. In 7.3 we show how the transmission probability T may be calculated from quantities readily available in the DMFT for heterostructures. We conclude with a summary of our numerical findings.

7.1 History of the problem

We begin our retrospective of works concerned with the problem of the dielectric breakdown with a review of Zener's seminal paper about the breakdown of band-insulators before we sketch the more recent approaches for Mott insulators.

Zener's theory of dielectric breakdown for band-insulators

In 1934 Zener[115] studied the problem of the dielectric breakdown in one-dimensional band insulators. Starting from conventional band theory he sought to find an explanation for the strong non-linearities found in the I-V characteristic of the dielectric breakdown phenomenon. Realising that carriers thermally activated across the band gap are not able to account for the 'sudden rise' in current, he deemed a mechanism analogous to the auto-ionisation of free atoms by large electric fields. Applied to

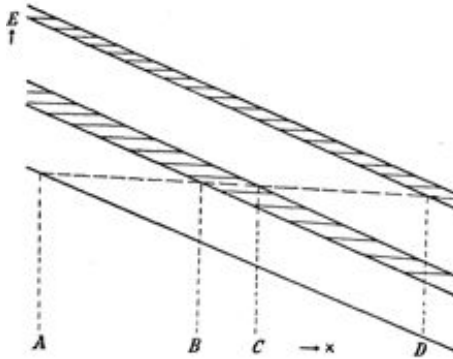


Figure 7.1: Band-structure diagram. The shaded regions represent zones of forbidden energies in the presence of an electric field. Spatial tunnelling allows for transitions to energetically higher lying bands. Taken from Ref. [115].

solids the basic realisation is that in a constant electric field, energy bands have significance only with respect to particular spatial positions as the presence of a linear potential makes each energy band degenerate with each other, c.f. Fig 7.1. Therefore in the presence of an electric field an electron may spatially tunnel from one band into another band that would otherwise lie energetically higher if it were not for the presence of the electric field.

Starting from Bloch's theorem Zener argued that the crystal momentum of the electrons linearly increases in time with the field E , $k \rightarrow k - \frac{2\pi eE}{h}t$ which causes the electrons to move in the direction of the field until they are reflected by the lattice and move back and forth (Bloch oscillations). Each time the electron is reflected by the lattice a small fraction of the wave packet will pass through the energetically forbidden zone into another band. The total tunnelling probability per unit time γ is given by the tunnelling probability per lattice reflection p times the period of the oscillatory motion $\nu = \frac{h}{eEa}$.

$$\gamma = \nu p \tag{7.1}$$

The calculation of p where performed using a semi-classical WKB approximation with the assumption that the linear electrical potential can be locally approximated on the scale of a single lattice constant. Using this ansatz he found the tunnelling probability to depend exponentially on the strength of the electrical field

$$\gamma = \frac{eEa}{h} \exp \left[-\frac{\pi^2}{h^2} \frac{ma\epsilon^2}{|eE|} \right] \tag{7.2}$$

here a denotes the lattice constant and ϵ the size of the energy gap between conduction and valence band. The result received from such a simple treatment of the problem is actually quite remarkable in a number of ways: For typical values of $\epsilon = 2\text{eV}$ and $a = 3 \cdot 10^{-8}\text{cm}$ equation (7.2) becomes $\gamma = 10^7 E 10^{-2 \cdot 10^7/E}$. One can see here that both the magnitude of the critical field strength ($\approx 10^6\text{V/cm}$) and the suddenness of the transition are reflected by the formula.

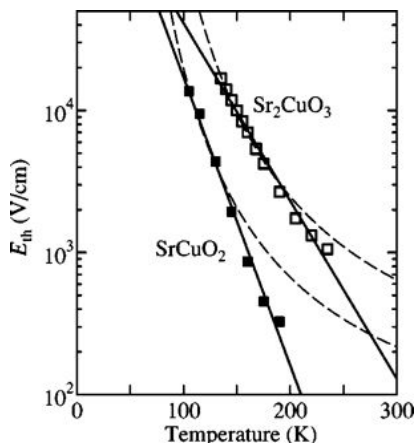


Figure 7.2: Temperature dependence of the threshold electric-field E_{th} measured with the use of 200-msec voltage pulses for Sr_2CuO_3 and SrCuO_2 . The solid line is a fit of the form of equation (7.3). From [108].

Modern approaches for Mott insulators

A number of authors have employed a variety of different methods to attack the problem of dielectric break-down in Mott insulators. The earliest work on the dielectric breakdown of a Mott insulator is by Fukui and Kawakami[34]. To be precise they studied a variation of the original problem: they considered a one-dimensional Hubbard ring at finite U and investigated the effect the introduction of an asymmetric hopping term on a single site had on the Mottness of the system. The asymmetric hopping term was supposed to model dissipative tunnelling into the environment, however rendering the Hamiltonian non-hermitian: the appearance of a asymmetric hopping term can be understood as the presence of an imaginary gauge potential. These kinds of problem had been previously studied using the *Bethe ansatz* and exact solutions were available. Calculating the phase diagram as a function of interaction strength U and hopping asymmetry, they were able to confirm that the Mott gap closes monotonically with the strength of asymmetry in the system due to the effect of dissipative tunnelling driving the system metallic. However as pointed out by Taguchi et al.[108] who experimentally studied the breakdown of the one-dimensional Mott insulating crystals Sr_2CuO_3 and SrCuO_2 a quantitative comparison with the mentioned work cannot be made due to the lack of direct correspondence between the asymmetric hopping strength in the theory and the applied electric field. Nevertheless their work gave important stimuli to the further development of the theory.

Taguchi et al.[108] found in their measurements an exponential dependence of the critical field strength E_{th} on the temperature of the form

$$E_{th}(T)/E_{th}(0) = \exp[-T/T_0] \quad (7.3)$$

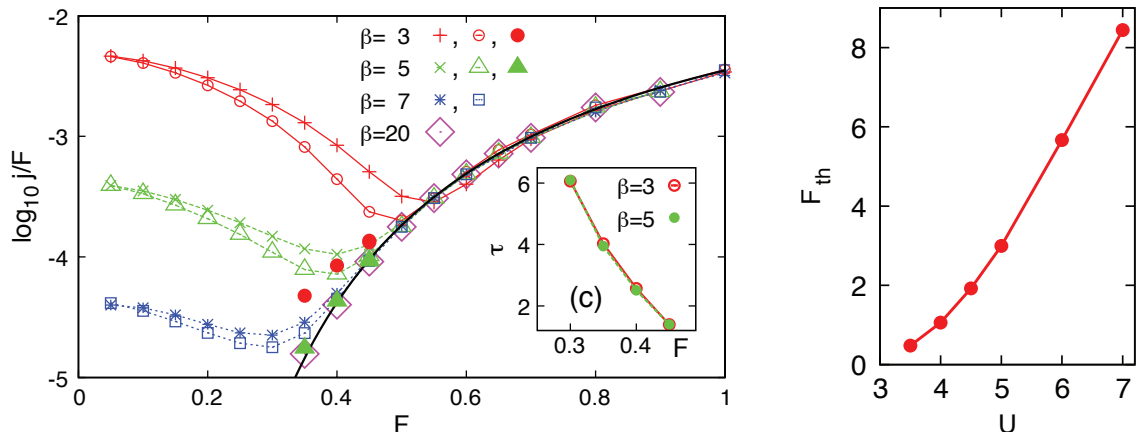
This kind of T dependence has often been found in the depinning physics of charge density wave systems. Here the depinning potential V is weakened due to thermal fluctuations of the CDW phase ϕ in such a manner as $V(T)/V(0) = \exp[-\langle\phi^2\rangle/2]$, where $\langle\phi^2\rangle/2 = T/T_0$ [70]. Here the conclusion may be drawn that the exponential

dependence of E_{th} suggests that the collective motion of carriers is responsible for the strong non-linearities. The critical field strengths were found to be larger than the depinning field for conventional CDW states pinned by impurities, however weaker than the typical critical field strength found in band insulators. Also the current switching was accompanied by a characteristic delay time.

In 2003 Oka, Arita and Aoki[80] sought to explain the phenomenon by properly taking the presence of the electric field into account. They considered a small ($N \approx 10$) periodic Hubbard model, where the effect of the electrical field E was accounted for by a time-dependent flux $\Phi(t) = eLEt$ with L the system size piercing the Hubbard ring and inducing a current due to Faraday's law. Using a Lanczos method they determined the ground state of the system and calculated the zero temperature time-evolution using a numerical integration of the time-dependent Schrödinger equation. They explained their numerical findings by non-adiabatic Landau-Zener tunnelling: If a parameter of the Hamiltonian is slowly (adiabatically) varied the energy levels plotted against this parameter contain anti-crossings as they repel each other and a system initially prepared in the ground state of the system will stick to this state. However when the parameter is varied with a finite velocity the state will make a transition across the anti-crossing with a finite probability $p \neq 0$. The transition probability depends exponentially on the LZS parameter which is proportional to the velocity that the anti-crossing is approached with. They suspected that these kind of tunnelling events between the ground state and the first excited many-body state are the relevant process for the break-down and indeed found that the expectation value of the current operator collapses onto a single universal curve when plotted against the LZS parameter. However this picture is not free of problems. While the theory as described above works fine for finite systems the derived expression for the critical field strength E_{th} contains a factor which depends on the system size and diverges in the thermodynamic limit. Therefore for an infinite system the theory predicts that no breakdown will take place. Ignoring this issues for the moment, at least for finite systems a finite threshold field was found and upon increasing E beyond E_{th} a linear dependence of the current upon E . The conclusion here was that the non-adiabatic tunnelling was a quantum version of dissipation mixing different states and driving the system after many level crossings into steady state.

Oka and Aoki[79] revisited the topic and resolved some of the open questions and puzzle their last paper had left behind. Most importantly using Dykhne-Davis-Pechukas (DDP) formalism they were able to consider tunnelling events beyond the Landau-Zener picture, resolving the asymptotic issues found in the thermodynamic limit. Another virtue of their paper was that it finally reconciled the the Landau-Zener-Schwinger theories for the breakdown with the model which incorporated the effect of the electric field via non-hermitian Hamiltonians: they showed how within their approach the Hubbard model in an electric field is mapped onto a non-hermitian hamiltonian.

The first DMFT study of the dielectric breakdown phenomenon was performed by Eckstein, Oka and Werner [24]. Here a single-band Hubbard with nearest-neighbour hopping was studied and the time-dependent electric field F was incorporated into the Hamiltonian in a pure vector potential gauge via Peierl's substitution. They



(a) Time-averaged current j/F for $U = 5$. Crosses and open symbols denote a time-average of $8 < t < 10$ and $10 < t < 12$.

(b) Threshold electric field F_{th} as a function of U .

Figure 7.3: Taken from [24].

solved the problem in $d \rightarrow \infty$ -limit using nonequilibrium DMFT and solved the impurity problem using the self-consistent hybridisation expansion. For weak fields F they found that a time-independent current sets in after the decay of the transient behaviour. Although the system was not coupled to a heat bath and the effective temperature T_{eff} rose by a factor 1.5 during the simulation time $j(t)$ remained constant. Fig. 7.3a shows the time-averaged current as a function of the driving field F . The current due to the linear response conductivity at small F which vanishes in the $T \rightarrow 0$ limit can be clearly distinguished from a temperature-independent contribution at large F . They refer to the latter contribution as the tunneling current which has a non-zero temperature limit. The data could be fitted with the same law (black line) that determines the ground state decay rate[79, 80]

$$j_{\text{tun}}(F) = F\sigma_{\text{tun}}^{\infty} \exp(-F_{\text{th}}/F), \quad (7.4)$$

with a threshold field F_{th} . The values for the threshold field as extracted from their numerical data is displayed in Fig. 7.3b.

7.2 Landauer-Büttiker definition of the transmission

Landauer[66] considered a general barrier problem in a 1D conductor realised for instance by a quantum wire in the extreme quantum limit where only one conduction channel exists. Ideal conduction leads free of scattering connect right and left to the barrier region. Due to an applied bias voltage these two leads have different carrier densities parametrised by different chemical potentials μ_L and μ_R for the left and right lead respectively. We assume that the difference is such that current flows from the left to the right lead. Landauer thought of these contacts to have a phase randomising

effect¹ for the injected and absorbed electrons through inelastic processes such that no phase relationship exists between different particles. The total current through such an idealised one-dimensional system may be written as the difference between the flux of the right- and left-moving particles

$$I = \frac{e}{\pi} \left[\int_0^\infty dk v(k) f_L(k) T(k) - \int_0^\infty dk' v(k') f_R(k') T(k') \right] \quad (7.5)$$

where $T(k)$ is the probability that a particle of momentum k is transmitted through the barrier. The overall prefactor stems from the one-dimensional density of states $\partial n / \partial k = 1/\pi$ and integrations are over positive k relative to the direction of injection. For low temperatures the Fermi distributions f_L and f_R can be approximated by step functions. Then particles up to an energy μ_L (μ_R) are injected into the left (right) lead. Converting to integrals over energy one finds

$$I = \frac{e}{\pi} \left[\int_0^{\mu_L} dE \left(\frac{dk}{dE} \right) v(k) T(E) - \int_0^{\mu_R} dE \left(\frac{dk'}{dE} \right) v(k') T(E) \right] = \frac{e}{\pi \hbar} \int_{\mu_R}^{\mu_L} dE T(E) \quad (7.6)$$

For small applied voltages the difference in the chemical potentials is small, we can neglect the energy dependence of the transmission probability $T(E)$ and the integral is approximated by $T(\mu_L - \mu_R)$. It has been debated in the literature[101, 39, 30] how the difference in the chemical potentials should be related to the potential drop across the device. The answer depends on the geometry of the experiment and more specifically on how the drop in the potential is actually measured. A result of the transmission and reflection about the barrier and the flow of current is a reduction in the carrier density on the right side while charge piles up on the left side. This charge rearrangement leads to screening effects and can be accounted for by shifted chemical potentials for the left (μ'_L) and right lead (μ'_R). The actual voltage drop across the device is therefore given by $e(\mu'_L - \mu'_R)$ which is less than $e(\mu_L - \mu_R)$. From self-consistency considerations one can relate the two by $\mu'_L - \mu'_R = (1-T)(\mu_L - \mu_R)$ [14]. If the current is applied through a pair of contacts and the voltage drop across the barrier measured non-invasively by a separate pair of contacts (4-terminal measurement) one measures the reduced drop. For standard 2-terminal measurement where the same leads are used for the current supply and the voltage measurement one finds $V = e(\mu_L - \mu_R)$ and so

$$G = \frac{I}{V} = \left(\frac{2e^2}{h} \right) T . \quad (7.7)$$

This is the celebrated Landauer formula for the single-channel case[65, 66] with the fundamental unit of conductance given by $2e^2/h = 7.748 \times 10^{-5}$ S. This quantum-mechanical result expresses a transport coefficient in terms of static scattering properties, rather than in the usual temporal correlation functions of linear response theory.

¹In his own words he referred to these contacts as “independent black-body reservoirs”[66]

Multi-channel case

The generalisation to the multi-channel case is now straight-forward. Such a multi-channel device can be realised when one departs from the one-dimensional idealisation of the wire and enlarges for instance one of the two transverse dimensions such that the system is not only restricted to the lowest mode in the transverse box potential but other low-energy modes are accessible for transport. A lateral quantum structure develops where the wave functions in the leads might be given by (in a simple case)

$$\langle x, y, z | n, k_z \rangle = \frac{1}{\sqrt{L}} \phi_n(x, y) e^{ik_z z} . \quad (7.8)$$

Here x and y are the coordinates in the transversal direction and particles move along the z direction through the device. n is a quantum number that labels the different conduction channels and $\phi_n(x, y)$ is the confinement wavefunction in the transversal direction. The eigenenergies in this example would be given by $\epsilon_n(k_z) = E_n + \frac{\hbar k_z^2}{2m}$ with E_n the confinement energy for channel $n \in \{1, \dots, N\}$. For simplicity we consider the case where the number of channels in the right and left lead are equal. Then an incoming wave in channel i with total energy E has a finite probability, $T_{ij}(E) = |t_{ij}|^2$, to be transmitted to channel j in the right lead and probability $R_{ij} = |r_{ij}|^2$ to be reflected into channel j in the left lead. The transmission and reflection coefficient can be organised in the $2N \times 2N$ scattering matrix

$$\mathbf{S} = \begin{pmatrix} r & t \\ t & r \end{pmatrix} \quad (7.9)$$

Carriers are fed equally into all channels up to chemical potential μ_L (μ_R) in the left (right) lead. The current injected into channel i on the left side and transmitted to channel j on the right side is with the same reasoning as in the single-channel case given by

$$I_{ij} = \frac{2e}{h} \int_{\mu_L}^{\mu_R} T_{ij}(E) dE \approx \frac{2e}{h} T_{ij}(\mu_L - \mu_R) \quad (7.10)$$

where we have again assumed that the energy dependence of the transmission probability T_{ij} is small in the energy window $E \in [\mu_L, \mu_R]$. The total current transmitted through the N independent sending and receiving channels is thus given by

$$I = \frac{2e}{h} \sum_{ij} \int_{\mu_L}^{\mu_R} T_{ij}(E) dE \approx \frac{2e}{h} \left[\sum_{ij} T_{ij} \right] (\mu_L - \mu_R) \quad (7.11)$$

$$= \frac{2e}{h} (\mu_L - \mu_R) \text{Tr}(t^\dagger t) \quad (7.12)$$

with t the transmission submatrices. For a two terminal measurement the conductance is thus given by

$$G = \frac{2e^2}{h} \text{Tr}(t^\dagger t) \quad (7.13)$$

which is the Landauer-Büttiker formula for the multi-channel case[14].

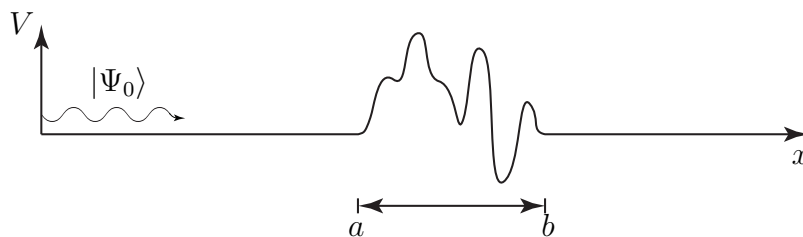


Figure 7.4: Schematic illustration of the transmission problem set-up. The scattering potential has a finite support, $x \in [a, b]$.

7.3 Transmission through a heterostructure

In order to apply the Landauer-Büttiker theory of conductance to heterostructures, we need to relate the transmission probability T through the barrier region to a quantity readily available in the inhomogeneous DMFT. A natural candidate is the off-diagonal Green's function connecting layers on different sides of the barrier, which answers a closely related question: What is the amplitude for creating a particle on a layer left of the barrier with energy E and transversal momentum \mathbf{k}^\parallel and destroying it on a layer right of the barrier? Due to the translational invariance in the transversal directions, x and y , the corresponding momenta \mathbf{k}^\parallel are conserved and take no active part in the transmission problem but merely parametrise a family of one-dimensional scattering problems. We therefore restrict the derivation of the relation between the off-diagonal Green's function and the transmission amplitude to one-dimensional problems. The application of the derived formulas to each member of the family gives the transmission amplitude of the three-dimensional system.

The Landauer-Büttiker theory thinks about transport as essentially a scattering problem. This paradigm already imposes certain approximations that need to be mentioned here. Usually in scattering problems one has non-interacting particles incident on a spatially confined potential. In such a situation the one-particle description is adequate. The strongly-correlated heterostructure however does not fall into this category. Here the disturbing effect on the incident particle is not due to a simple scattering potential but rather to the particle entering a region in space where strong two-body interactions exist. This makes the transmission problem through a correlated heterostructure inherently a many-body problem. For instance one might think about a situation where a particle impinges on the barrier region and gets reflected, but leaves the barrier subsystem in an excited state, which does not thermalise before the arrival of the next particle. Also one could envision a situation where two incident particles enter into the strongly-correlated region at the same time. Their mutual interaction will certainly alter their probability to be transmitted or reflected compared to a situation where they enter one after the other. All of these effects are not accounted for in the Landauer-Büttiker description of transport. In our set-up we assume that the time between scattering events is much larger than the typical time scale in the barrier region. An excited barrier a particle might have left behind is (on average) long thermalised before another particle arrives. In such a situation the Landauer-Büttiker approach is a meaningful approximation.

Typically, the scattering formalism is described in the following way: an incident particle in state $|\Psi_0\rangle$ is scattered by a localised perturbation V resulting in a scattered state $|\Psi_S\rangle$. The incident state $|\Psi_0\rangle$ is assumed to be an eigenstate of the non-interacting hamiltonian H_0 with Eigenvalue E

$$(E - H_0) |\Psi_0\rangle = 0 \quad (7.14)$$

For the sake of the argument we will assume H_0 to be the Hamiltonian of free particles

$$H_0 = \frac{\hat{p}^2}{2m} . \quad (7.15)$$

The incident state in this case will be a plane wave with wavevector k

$$\langle \mathbf{r} | \Psi_0 \rangle = \Psi_0(\mathbf{r}) = \frac{1}{\mathcal{N}} e^{i\mathbf{k}\cdot\mathbf{r}} \quad (7.16)$$

We will use a momentum normalisation, therefore $\mathcal{N} = \sqrt{2\pi}$. The goal of scattering theory is then to solve the full energy-eigenstate problem

$$(E - H_0 - V) |\Psi\rangle = 0 \quad (7.17)$$

The scattered state $|\Psi_S\rangle$ is defined as

$$|\Psi_S\rangle = |\Psi\rangle - |\Psi_0\rangle \quad (7.18)$$

We will assume that the perturbation V has a compact support, i.e. is non-vanishing only within some interval $[a \dots b]$.

We can now choose from two possible routes to find a connection between the Green's function and physical observables of the scattering problem, i.e. transmission- and reflection amplitudes. We could try to relate the T-matrix of the scattering problem to the transmission amplitude by noting that the scattered wavefunction $|\Psi_S\rangle = G_0 T |\Psi_0\rangle$ and making the typical assumption that on the far side at a great distance from the scattering region the full wavefunction $|\Psi\rangle$ of the problem is given by the unperturbed wavefunction $|\Psi_0\rangle$ times the transmission amplitude.

$$\langle x_\infty | \Psi \rangle = \tau(E) \langle x_\infty | \Psi_0 \rangle \quad (7.19)$$

The remaining task of relating the Green's function to the T-matrix is easily accomplished by a series expansion of the full propagator in the potential V . However for the situation at hand the exact Green's function may be derived in terms of the scattered wave functions and this direct route turns out to be more feasible here. The scattering solutions $\Psi^\pm(x)$ of an incoming plane wave from the left (+) and the right (-) are given by

$$\Psi^\pm(x) = \frac{1}{\mathcal{N}} \begin{cases} e^{\pm ikx} + \rho^{(\pm)} e^{\mp ikx} & \begin{cases} x < a & \text{for } (+) \\ x > b & \text{for } (-) \end{cases} \\ \mathcal{A}^{(\pm)}(k) u_k^\pm(x) + \mathcal{B}^\pm(k) s_k^\pm(x) & a < x < b \\ \tau(k) e^{\pm ikx} & \begin{cases} x > b & \text{for } (+) \\ x < a & \text{for } (-) \end{cases} \end{cases} \quad (7.20)$$

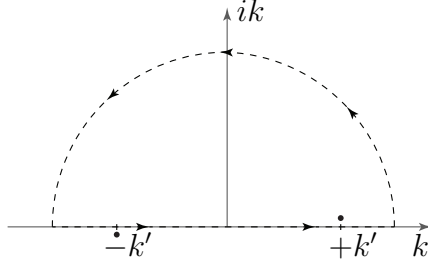


Figure 7.5: Contour integration.

where we have used $\tau^{(\pm)}(k) = \tau(k)$ which follows from reciprocity. $u_k^\pm(x)$ and $s_k^\pm(x)$ are possibly complicated wave functions which describe the particle as it passes through the barrier region. Explicit expression for the coefficients $\mathcal{A}^\pm(k)$ and $\mathcal{B}^\pm(k)$ as well as for the transmission- $\tau(k)$ and reflection amplitude $\rho(k)$ may be derived. Naturally these expression only depend on the values of the independent solutions of the Schrödinger equation at the borders of the domains.

Assuming that there are no bound states in the energy window we are interested in, we may express the exact Green's function of the system as

$$G(x_f, x_i; E) = \sum_{\sigma=\pm} \int_0^\infty \frac{dk}{2\pi} \frac{\Psi_k^\sigma(x_f) \Psi_k^{\sigma*}(x_i)}{E + i\epsilon - \frac{\hbar^2 k^2}{2m}} \quad (7.21)$$

Substituting (7.20) into (7.21) we find for $x_i < a$ left of the barrier and $x_f > b$ right of the barrier

$$\begin{aligned} G_{LR}(x_f, x_i; k') &= \frac{2m}{\hbar^2} \int_0^\infty dk \frac{1}{k'^2 + i\epsilon - k^2} [\tau(k) e^{ik(x_f - x_i)} \\ &\quad + \tau^*(k) e^{-ik(x_f - x_i)} \\ &\quad + (\rho^{(+)*}(k) \tau(k) + \rho^{(-)}(k) \tau^*(k)) e^{ik|x_f - x_i|}] \\ &= \frac{2m}{\hbar^2} \frac{1}{2\pi} \int_{-\infty}^\infty dk \frac{1}{k'^2 + i\epsilon - k^2} \tau(k) e^{ik|x_f - x_i|} \end{aligned} \quad (7.22)$$

where $E = \frac{\hbar^2 k'^2}{2m}$ and we used $\tau^*(k) = \tau(-k)$ and $\rho^{(\pm)*}(k) \tau(k) + \rho^{(\mp)}(k) \tau^*(k) = 0$. The integral may be easily solved using contour integration. In order to prepare the denominator we notice that

$$\begin{aligned} k'^2 + i\epsilon - k^2 &= (k' + \sqrt{k^2 - i\epsilon})(k' - \sqrt{k^2 - i\epsilon}) \\ &= (k' + k - i\epsilon)(k' - k + i\epsilon) \end{aligned} \quad (7.23)$$

We consider a contour in the upper half of the complex plane, therefore encircling only one of the poles of first order. We thus find

$$G_{LR}(x_f, x_i; k) = \frac{m}{i\hbar^2 k} \tau(k') e^{ik|x_f - x_i|} \quad (7.24)$$

The transmission probability is defined as $T(k) = |\tau(k)|^2$. With the velocity $v_k = \partial E / \partial k = \hbar^2 k / m$ we can solve for the transmission probability to find

$$T(E) = v_k^2 |G_{LR}(x_f, x_i; E)|^2 \quad (7.25)$$

The off-diagonal Green's functions $G_{\alpha\beta}(\mathbf{k}^\parallel, \omega)$ are readily available from the inhomogenous DMFT algorithm by virtue of Eq. 5.29.

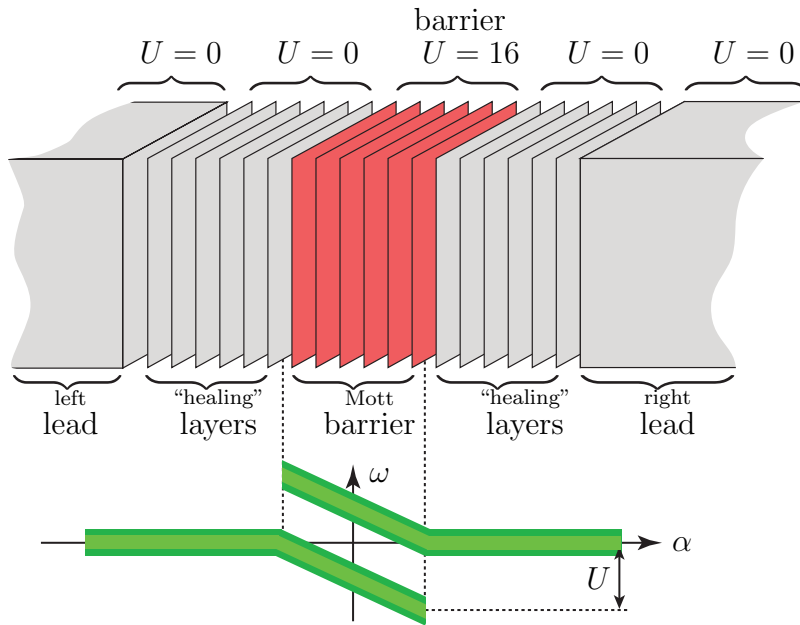


Figure 7.6

7.3.1 System layout

In order to study the transmission probability through a Mott barrier in in-homogenous mean-field theory we will consider the setup depicted in Fig. 7.6. The arrangement reflects typical experimental setups: two leads are connected to a barrier of a Mott insulating material with a finite width. The leads are modelled as a non-interacting region². The barrier region consists of a varying number of N Mott-insulating layers which with $U > U_C$. In order to account for the effects of a strong electric field \mathbf{E} across the Mott region, we choose a gauge where a linear gradient potential ϕ gives rise to \mathbf{E} . The effect is analogous to a local chemical potential. We have already seen that doping the Mott insulator away from half-filling drives the Mott insulator metallic. Therefore we can expect the effective barrier thickness to be considerably lowered, as the outermost Mott layers will feel a chemical potential in excess of their charge gap and therefore fall out of their Mott insulating state due to doping.

The barrier region is sandwiched between two segments which are marked as “healing” layers in fig. 7.6. These layers are actually part of the lead and therefore non-interacting. The necessity for these self-consistently calculated lead layers arises from inhomogeneities in the system. The presence of the barrier region causes deviations of the adjacent non-interacting layers from their bulk state, which only die off slowly as one walks away from the interface. These deviations must sufficiently fall off before the semi-infinite leads begin. As these leads are not self-consistently determined, they should rather be thought of as boundary conditions for the heterostructure. A mismatch between the physics enforced by the boundary conditions and the physics happening in the first and last layer would cause finite size effects in

²This is especially important when one considers the case of magnetic ordering in the system as the Hubbard model on a simple cubic lattice at half-filling shows a perfect nesting property and so our leads would become antiferromagnetic insulators for arbitrary interaction strength.

the system. For our calculation we choose 30 healing layers which ensures that the system has approached the bulk behaviour closely enough so that no visible finite size effects are apparent in any calculated quantity. In this chapter we are predominantly interested in the behaviour of the barrier region. We therefore choose to count the layers starting from the first Mott-insulating layer to the left ($\alpha = 1$).

The lower part of Fig. 7.6 depicts a schematic view of the expected band structure. Particle-hole symmetric bands in the non-interacting leads connect to the linearly deformed upper- and lower Hubbard bands of the Mott-insulating barrier region. The strength of the linear potential is chosen such that it reaches a value of $\pm U/2$ at the left / right edge of the Mott insulating barrier connecting the deformed Hubbard bands to the non-interacting bands of the leads. This is not an artificial setup as we have seen in the last chapter: a mismatch in the bands causes charge reordering which shifts the bands such that they match up. In the spirit of Zener's breakdown theory electrons may tunnel spatially from the energetically lower lying Hubbard band into the upper Hubbard band. We study here the amplitude of these processes.

The system possesses a translational invariance along the x and y direction. It is therefore useful to Fourier transform in these directions and introduce the conserved in-plane momentum \mathbf{k}^{\parallel} . In section 7.2 we derived the Landauer-Büttiker formula for the conductance in the multi-channel case. The channel label n is given here by the in-plane momentum \mathbf{k}^{\parallel} . We saw that the eigenenergies of the states in the non-interacting leads comprise two parts, $\epsilon_n(k_z) = E_n + \frac{\hbar k_z^2}{2m}$. The confinement potential³ E_n is given in our case by the two-dimensional in-plane dispersion relation $\epsilon_{\mathbf{k}^{\parallel}}^{\parallel} = -2t [\cos(k_x) + \cos(k_y)]$ while the plane wave part $\frac{\hbar k_z^2}{2m}$ is replaced by the eigenenergy of a Bloch wave travelling in z direction, $-2t \cos(k_z)$. Due to the conservation of the in-plane momentum there is no inter-channel mixing, i.e. the transmission matrix is diagonal $\tau(\omega)_{\mathbf{k}^{\parallel}\mathbf{k}'^{\parallel}} = \tau(\omega)_{\mathbf{k}^{\parallel}} \delta_{\mathbf{k}^{\parallel}\mathbf{k}'^{\parallel}}$. The square of the velocity in Eq. 7.25 is for homogenous, isotropic hopping integrals t given by $v_{k_z}^2 = 4t^2 - \epsilon_{k_z}^2$. In a non-interacting system, the total conductance for particles with energy ω from the right to the left lead is therefore

$$\begin{aligned} G(\omega) &= \frac{2e^2}{h} \sum_{\mathbf{k}^{\parallel}} \left[4t^2 - \left(\omega - \epsilon_{\mathbf{k}^{\parallel}}^{\parallel} \right)^2 \right] |G_{LR}(\omega, \mathbf{k}^{\parallel})|^2 \\ &= \frac{2e^2}{h} \int_{-4t}^{4t} d\epsilon_{\mathbf{k}^{\parallel}} \rho^{2D}(\epsilon_{\mathbf{k}^{\parallel}}) \left[4t^2 - \left(\omega - \epsilon_{\mathbf{k}^{\parallel}}^{\parallel} \right)^2 \right] |G_{LR}(\omega, \mathbf{k}^{\parallel})|^2 \end{aligned} \quad (7.26)$$

For an interacting system the above formula is not exact, however it can be used in the tunneling limit when the time between particle transmissions is the largest time scale in the problem.

7.3.2 DMFT results

To study the transmission through a Mott barrier in a linear electric potential we calculate the Landauer-Büttiker conductance G from the left to the right lead of

³We are aware that this term is very misleading for the present case, where the confinement wave functions are completely delocalised Bloch waves.

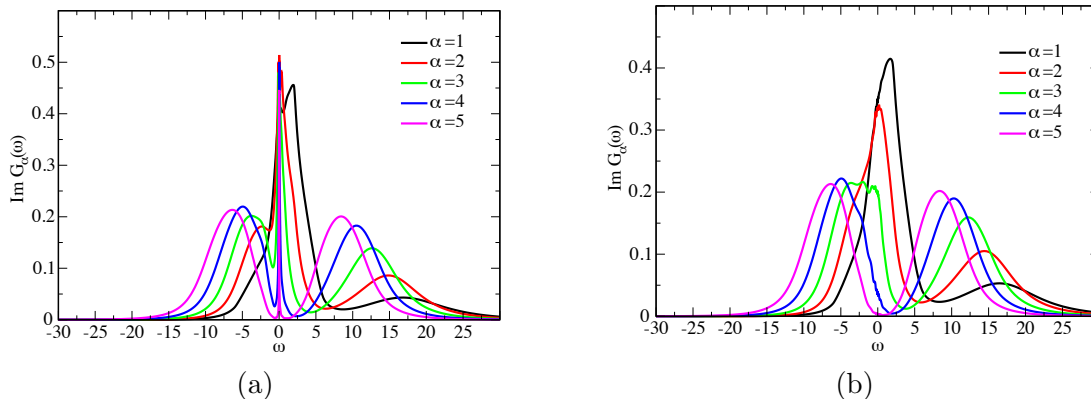
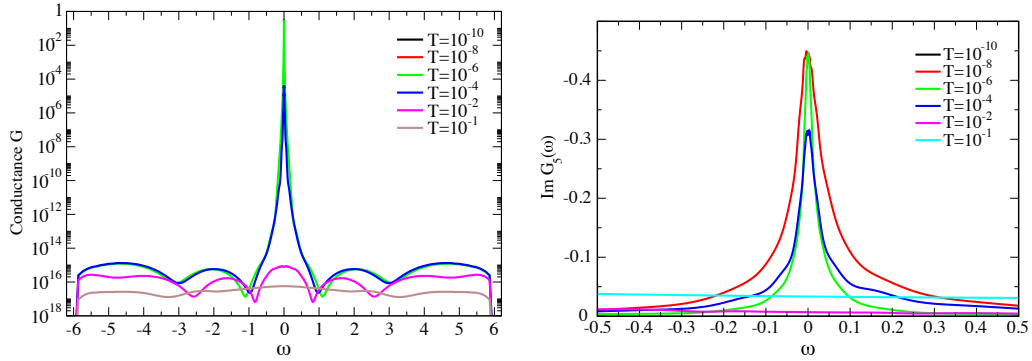


Figure 7.7: Local layer spectral functions for (a) $T = 10^{-10}$ and (b) $T = 10^{-2}$.

heterostructures with the layout Fig. 7.6 of varying barrier thicknesses N at different temperatures T . Here the influence of temperature on the breakdown physics is especially intricate. One can already guess at the non-trivial role temperature will play when one recalls that for a strongly-correlated metal an increase in temperature can actually trigger a transition to an insulating state. On the other hand this reinforcing role the temperature plays for Mott insulators will not go on indefinitely: Once the temperature increases so dramatically that thermal excitations across the Hubbard gap become possible, we will witness a “melting” of the Mott insulator and the system becomes a ‘bad’ metal.

Fig. 7.7 shows spectral functions for the first 5 layers at the very left of the Mott insulating region of width $N = 10$ for (a) $T = 10^{-10}$ and (b) $T = 10^{-2}$. For the low temperature narrow resonance peaks appear for all layers α . For the first two layers the strong electric potential has shifted the Fermi level into the lower Hubbard band giving rise to a Kondo effect. Closer towards the centre of the region as due to the weaker potential less and less spectral density from the lower Hubbard band lies in the Fermi level the width of the resonance peaks quickly decreases and so does the respective Kondo temperature T_K . For the central layer in the region ($\alpha = 5$) the Fermi level lies within the Mott gap but due to the Kondo proximity (which provides a lower bound for the hybridisation function of the underlying impurity model) a narrow resonance peak is induced. Upon increasing the temperature to $T = 1e-2$ the Kondo effect in the system is completely switched off. Even the spectral functions for the first two layers do not reach the non-interacting value anymore. The resonances in the inner layers are gone and the spectral function for the layer in the centre $\alpha = 5$ shows a Fermi level centred about an charge gap.

Fig. 7.8a shows the temperature dependence of the conductance for the same system. Starting with the lowest temperature, $T = 10^{-10}$, one of the most prominent features is a large conductance peak at $\omega = 0$ reaching up to unity. The origin of this peak lies in the Kondo effect which causes the spectral function to take the non-interacting value at the Fermi level and therefore perfect conductance. The outermost layers of the system are heavily doped due to the presence of the linear potential. As the total potential difference between the first and last layers of the barrier is given by U comparing this to the half-bandwidth shows that the outermost 3 – 4 layers will



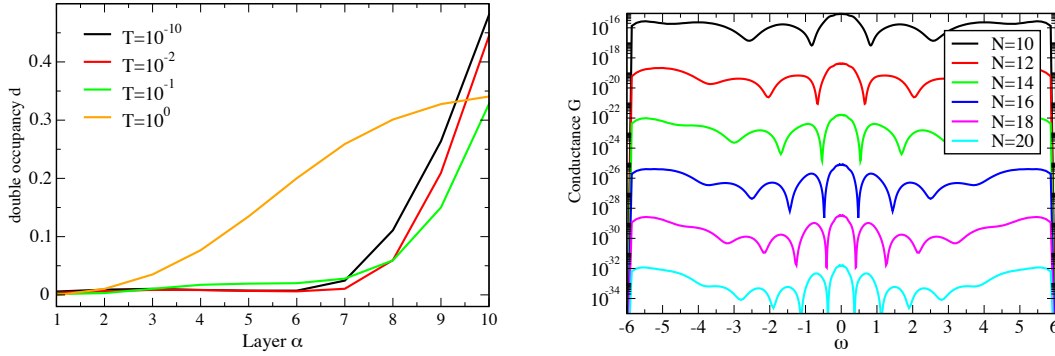
(a) Landauer conductance G from left to the right lead as a function of the particle energy ω for different temperatures.

(b) Spectral function of the innermost layer in the barrier region for different temperatures T . For high T layers start to fall out of their Fermi liquid state.

Figure 7.8

be doped so heavily by the linear potential that their upper/lower Hubbard bands have been pushed into the Fermi energy, hence have become metallic. The Mott-insulating core, where the effect of the potential has left the Fermi energy within the Hubbard gap is however affected by the presence of the adjacent metal: The “Kondo proximity” effect allows for tunnelling from these layers into the Mott core, effectively bounding the density of states at the Fermi energy from below. The availability of a finite density of states at the Fermi level allows for a Kondo effect and therefore a resonance peak. The induced Kondo temperature T_K of the underlying impurity model, that the DMFT maps the problem onto, becomes quickly diminished as one walks deeper into the Mott core of the barrier region. However at $T = 0$ even the innermost layer will be in a Fermi liquid state, which effectively pins the value of the spectral functions to the non-interacting value due to the quadratic dependence of the self-energy on frequency and thereof leads to perfect transmission through the structure for particles at the Fermi energy. The induced Kondo temperature controls the width of the conductance peak. For particle energies $\omega > 0.5$ large imaginary parts in the self-energies give short lifetimes to the quasi-particles and the conductance is strongly suppressed and drops dramatically by 14 orders of magnitude.

Increasing the temperature from $T = 10^{-10}$ to 10^{-8} and even 10^{-6} leaves the conductance completely unaffected. The reason is simply that as long as the temperature stays below the Kondo temperature of the innermost layer, no change will occur. As the temperature however approaches $T = 10^{-4}$ thermal fluctuations suppress the Kondo effect and the innermost layer starts to fall out of his Fermi liquid state. This can be seen from deviation of the conductance from its value of unity at the Fermi level. Temperature drives the innermost layer towards a Mott insulating state despite the presence of the adjacent metal. At $T = 10^{-2}$ the Kondo resonance has completely collapsed. Increasing the temperature further thermally activates particles of all energies. The conductance for $T = 10^{-1}$ is a constant of particle energy ω . The Mott insulators have melted as thermal fluctuations have become of the order of the Hubbard gap.



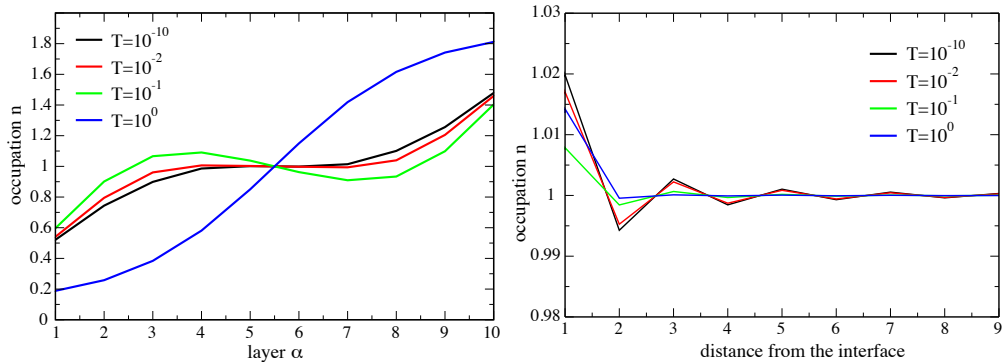
(a) Layer resolved expectation values for the double occupancy for different system temperatures. Barrier thickness is 10 layers.

(b) Conductance G for systems of different barrier thicknesses as a function of the particle energy ω for a temperature of $T = 10^{-2}$.

Figure 7.9

To confirm this hypothesis we have calculated the layer-resolved expectation values of the double occupancy. Fig. 7.9a shows this quantity for various system temperatures. Indeed as one increases the system temperature from $T = 10^{-10}$ to $T = 10^{-2}$ the double occupancy drops. A further increase in the system temperature starts to thermally activate particles across the Hubbard gap, doublon-holon pairs are created as one sees from the increase in double occupancy by several order of magnitudes. These excitations are indeed mobile and lead to a dramatic increase in the kinetic energy. The Mott insulator has melted. As the value of the linear potential at the first and last layer of the barrier is fixed to $\pm U/2$ increasing the thickness of the barrier can be understood as reduction in the slope of the linear potential and hence as a decrease in the strength of the applied electric field. Again comparing the size of the Hubbard gap to the half-bandwidth shows that the number of layers with their Fermi energy in the Hubbard gap increases linearly. Therefore we expect an exponential dependence of the differential conductance on the strength of the electric field. Indeed such a relationship is suggested by Fig. 7.9b for a temperature of $T = 10^{-2}$.

As expected the leads are really only weakly affected by the presence of the barrier region. The most prominent effect is due to the strong doping of the outermost barrier layers. As can be seen from Fig. 7.10a first and last layer of the barrier have been doped by $\approx 40\%$. As the leads are at half-filling, there is a tremendous charge mismatch between lead and barrier. Usually such a great mismatch would lead to strong charge reconstructions at the interface. Effectively doping the lead away from half-filling. However as we have turned off the effect of long-range Coulomb interactions the only effect is the induction of Friedel charge oscillations in the lead with a characteristic period of $2k_F = \pi$. The temperature dependence of these oscillations can be seen in Fig. 7.10b. Friedel oscillations are due to the existence of a sharp Fermi surface, therefore at non-zero temperatures Friedel oscillations will be strongly suppressed due to the smeared Fermi surface.



(a) Layer-resolved expectation value of the occupation for different system temperatures. (b) Effect of the doped Mott barrier on the occupation for different system temperatures. Friedel oscillation appear with the characteristic period $2k_F = \pi$.

Figure 7.10

7.3.3 Conclusions

In this chapter we have studied how the thickness of an Mott insulating barrier and the system temperature T influence the transmission probability and thus the Landauer Bütticker conductance G through the barrier. Indeed we found that the interplay of the strong correlations in the barrier region and the system temperature produce due to the intricate Kondo physics and interesting temperature dependence. The important physical mechanism for the possibility to transmit a particle through an otherwise insulating region is the Kondo proximity effect, which induces (at $T=0$) narrow resonance peaks even in the innermost layers of the barrier. The width of these peaks is given by the Kondo temperature T_k . We found that this is the important reference temperature to look when one tries to understand the temperature dependence of the conductance: When the system temperature T starts to exceed the Kondo temperature of the innermost layers, the conductance starts to drop dramatically. Only for very large temperature one has a thermal activation of the Mott gap and conductance starts to increase again. We have seen that at $T = 0$ the $\omega = 0$ value of the spectral function is pinned to its non-interacting value which creates perfect zero-bias transmission independent of the barrier thickness. For finite system temperatures we found that once the threshold temperature set by the Kondo temperature of the innermost layer has been exceeded by the system temperature, the conductance drops exponentially with the thickness of the barrier.

In conclusion we can summarize that the dielectric break-down of a Mott insulator is an intricate problem. The above equilibrium treatment allows to understand some effects early in the breakdown process (when the tunneling time of electrons is still small) but is far from sufficient description of this non-equilibrium process. Maybe future works involving non-equilibrium DMFT will be able to treat this problem appropriately.

Bibliography

- [1] CH Ahn, KM Rabe, and J-M Triscone. Ferroelectricity at the nanoscale: local polarization in oxide thin films and heterostructures. *Science*, 303(5657):488–491, 2004.
- [2] Frithjof B Anders and Avraham Schiller. Real-time dynamics in quantum-impurity systems: A time-dependent numerical renormalization-group approach. *Physical review letters*, 95(19):196801, 2005.
- [3] PW Anderson. A poor man’s derivation of scaling laws for the kondo problem. *Journal of Physics C: Solid State Physics*, 3(12):2436, 1970.
- [4] W.W. Barrett. A theorem on inverse of tridiagonal matrices. *Linear Algebra and Its Applications*, 27:211–217, 1979.
- [5] J Bauer and AC Hewson. Renormalized quasiparticles in antiferromagnetic states of the hubbard model. *The European Physical Journal B*, 57(3):235–249, 2007.
- [6] G. Baym and L.P. Kadanoff. Conservation laws and correlation functions. *Physical Review*, 124(2):287, 1961.
- [7] Max Born and Robert Oppenheimer. Zur quantentheorie der molekeln. *Annalen der Physik*, 389(20):457–484, 1927.
- [8] R Bulla. Zero temperature metal-insulator transition in the infinite-dimensional hubbard model. *Physical review letters*, 83(1):136, 1999.
- [9] R Bulla, TA Costi, and D Vollhardt. Finite-temperature numerical renormalization group study of the mott transition. *Physical Review B*, 64(4):045103, 2001.
- [10] R Bulla, AC Hewson, and Th Pruschke. Numerical renormalization group calculations for the self-energy of the impurity anderson model. *Journal of Physics: Condensed Matter*, 10(37):8365, 1998.
- [11] R Bulla, Th Pruschke, and AC Hewson. Anderson impurity in pseudo-gap fermi systems. *Journal of Physics: Condensed Matter*, 9(47):10463, 1997.

- [12] Ralf Bulla, Theo A Costi, and Thomas Pruschke. Numerical renormalization group method for quantum impurity systems. *Reviews of Modern Physics*, 80(2):395, 2008.
- [13] Ralf Bulla, Hyun-Jung Lee, Ning-Hua Tong, and Matthias Vojta. Numerical renormalization group for quantum impurities in a bosonic bath. *Physical Review B*, 71(4):045122, 2005.
- [14] M Büttiker, Y Imry, R Landauer, and S Pinhas. Generalized many-channel conductance formula with application to small rings. *Physical Review B*, 31(10):6207, 1985.
- [15] Michel Caffarel and Werner Krauth. Exact diagonalization approach to correlated fermions in infinite dimensions: Mott transition and superconductivity. *Physical review letters*, 72(10):1545, 1994.
- [16] Vivaldo L Campo Jr and Luiz N Oliveira. Alternative discretization in the numerical renormalization-group method. *Physical Review B*, 72(10):104432, 2005.
- [17] Ling Chen and JK Freericks. Electronic charge reconstruction of doped mott insulators in multilayered nanostructures. *Physical Review B*, 75(12):125114, 2007.
- [18] P Coleman. Local moment physics in heavy electron systems. *arXiv preprint cond-mat/0206003*, 2002.
- [19] P. Concus, GH Golub, and G. Meurant. Block preconditioning for the conjugate gradient method. *SIAM J. Sci. Statist. Comput*, 6(1), 1985.
- [20] P. Concus and G. Meurant. On computing inv block preconditionings for the conjugate gradient method. *BIT Numerical Mathematics*, 26(4):493–504, 1986.
- [21] T. A. Costi. Renormalization-group approach to nonequilibrium green functions in correlated impurity systems. *Phys. Rev. B*, 55:3003–3009, Feb 1997.
- [22] TA Costi, AC Hewson, and V. Zlatic. Transport coefficients of the anderson model via the numerical renormalization group. *Journal of Physics: Condensed Matter*, 6:2519, 1994.
- [23] WJ De Haas, J De Boer, and GJ Van den Berg. The electrical resistance of gold, copper and lead at low temperatures. *Physica*, 1(7):1115–1124, 1934.
- [24] M. Eckstein, T. Oka, and P. Werner. Dielectric breakdown of mott insulators in dynamical mean-field theory. *Physical review letters*, 105(14):146404, 2010.
- [25] VJ Emery, JT Devreese, and RP Evrard. Highly conducting one-dimensional solids, 1979.

- [26] Dieter Vollhardt Eva Pavarini, Erik Koch, editor. *The LDA+DMFT approach to strongly correlated materials*. Forschungszentrum Jülich GmbH, Institute for Advanced Simulations, 2011.
- [27] DK Faddeev. Properties of a matrix, inverse to a hessenberg matrix. *Journal of Mathematical Sciences*, 24(1):118–120, 1984.
- [28] L. Fallani, L. De Sarlo, JE Lye, M. Modugno, R. Saers, C. Fort, and M. Inguscio. Observation of dynamical instability for a bose-einstein condensate in a moving 1d optical lattice. *Physical review letters*, 93(14):140406, 2004.
- [29] Patrik Fazekas. *Lecture notes on electron correlation and magnetism*, volume 24. World scientific Singapore, 1999.
- [30] R. M. Feenstra, D. A. Collins, D. Z. Y. Ting, M. W. Wang, and T. C. McGill. Interface roughness and asymmetry in inas/gasb superlattices studied by scanning tunneling microscopy. *Phys. Rev. Lett.*, 72:2749–2752, Apr 1994.
- [31] E. Fradkin. *Field Theories of Condensed Matter Systems*. Levant Books, 2006.
- [32] J.K. Freericks. *Transport in multilayered nanostructures*. World Scientific, 2006.
- [33] H. O. Frota and L. N. Oliveira. Photoemission spectroscopy for the spin-degenerate anderson model. *Phys. Rev. B*, 33:7871–7874, Jun 1986.
- [34] T. Fukui and N. Kawakami. Breakdown of the mott insulator: Exact solution of an asymmetric hubbard model. *Physical Review B*, 58(24):16051, 1998.
- [35] S Gariglio, CH Ahn, D Matthey, and J-M Triscone. Electrostatic tuning of the hole density in CuO_2 films and its effect on the hall response. *Physical review letters*, 88(6):067002, 2002.
- [36] Antoine Georges and Gabriel Kotliar. Hubbard model in infinite dimensions. *Physical Review B*, 45(12):6479, 1992.
- [37] Antoine Georges, Gabriel Kotliar, Werner Krauth, and Marcelo J Rozenberg. Dynamical mean-field theory of strongly correlated fermion systems and the limit of infinite dimensions. *Reviews of Modern Physics*, 68(1):13, 1996.
- [38] Antoine Georges and Werner Krauth. Numerical solution of the d= hubbard model: Evidence for a mott transition. *Physical review letters*, 69(8):1240, 1992.
- [39] SM Goodnick, DK Ferry, CW Wilmsen, Z Liliental, D Fathy, and OL Krivanek. Surface roughness at the si (100)- SiO_2 interface. *Physical Review B*, 32(12):8171, 1985.
- [40] M. Greiner, O. Mandel, T. Esslinger, T.W. Hänsch, I. Bloch, et al. Quantum phase transition from a superfluid to a mott insulator in a gas of ultracold atoms. *Nature*, 415(6867):39–44, 2002.

- [41] Emanuel Gull, Andrew J. Millis, Alexander I. Lichtenstein, Alexey N. Rubtsov, Matthias Troyer, and Philipp Werner. Continuous-time monte carlo methods for quantum impurity models. *Rev. Mod. Phys.*, 83:349–404, May 2011.
- [42] J.L. Gustafson. *Asymptotic formulas for elliptic integrals*. PhD thesis, Iowa State University, 2002.
- [43] Martin C Gutzwiller. Effect of correlation on the ferromagnetism of transition metals. *Physical Review Letters*, 10(5):159, 1963.
- [44] Karen A Hallberg. New trends in density matrix renormalization. *Advances in Physics*, 55(5-6):477–526, 2006.
- [45] Karsten Held, Georg Keller, Volker Eyert, Dieter Vollhardt, and Vladimir I Anisimov. Mott-hubbard metal-insulator transition in paramagnetic v_{-2} o_{-3} : An lda+ dmft (qmc) study. *Physical review letters*, 86(23):5345, 2001.
- [46] RW Helmes, TA Costi, and A. Rosch. Kondo proximity effect: How does a metal penetrate into a mott insulator? *Physical review letters*, 101(6):66802, 2008.
- [47] RW Helmes, TA Costi, and A Rosch. Mott transition of fermionic atoms in a three-dimensional optical trap. *Physical review letters*, 100(5):056403, 2008.
- [48] R Hesper, LH Tjeng, A Heeres, and GA Sawatzky. Photoemission evidence of electronic stabilization of polar surfaces in $k_3 c 60$. *Physical Review B*, 62(23):16046, 2000.
- [49] Alexander Cyril Hewson. *The Kondo problem to heavy fermions*. Number 2. Cambridge university press, 1997.
- [50] JEi Hirsch and RM Fye. Monte carlo method for magnetic impurities in metals. *Physical review letters*, 56:2521–2524, 1986.
- [51] W. Hofstetter. Generalized numerical renormalization group for dynamical quantities. *Physical review letters*, 85(7):1508–1511, 2000.
- [52] Lucas Hollender. *From Periodic to Dilute Anderson Models*. PhD thesis, Universität zu Köln, 2012.
- [53] John Hubbard. Electron correlations in narrow energy bands. *Proceedings of the Royal Society of London. Series A. Mathematical and Physical Sciences*, 276(1365):238–257, 1963.
- [54] CM Hurd. Some magnetic properties of mn dissolved in cu, ag and au. *Journal of Physics and Chemistry of Solids*, 30(3):539–550, 1969.
- [55] M Izumi, Y Ogimoto, Y Konishi, T Manako, M Kawasaki, and Y Tokura. Perovskite superlattices as tailored materials of correlated electrons. *Materials Science and Engineering: B*, 84(1):53–57, 2001.

- [56] M Jarrell. Hubbard model in infinite dimensions: A quantum monte carlo study. *Physical review letters*, 69(1):168–171, 1992.
- [57] M. Jona-Lasinio, O. Morsch, M. Cristiani, N. Malossi, JH Müller, E. Courtade, M. Anderlini, and E. Arimondo. Asymmetric landau-zener tunneling in a periodic potential. *Physical review letters*, 91(23):230406, 2003.
- [58] Jaewook Joo and Viktor Oudovenko. Quantum monte carlo calculation of the finite temperature mott-hubbard transition. *Phys. Rev. B*, 64:193102, Oct 2001.
- [59] Henrik Kajueter and Gabriel Kotliar. Band degeneracy and the mott transition: Dynamical mean field study. *International Journal of Modern Physics B*, 11(06):729–751, 1997.
- [60] Junjiro Kanamori. Electron correlation and ferromagnetism of transition metals. *Progress of Theoretical Physics*, 30(3):275–289, 1963.
- [61] Srivenkateswara S Kancharla and E Dagotto. Metallic interface at the boundary between band and mott insulators. *Physical Review B*, 74(19):195427, 2006.
- [62] Gabriel Kotliar and Dieter Vollhardt. Strongly correlated materials: Insights from dynamical mean-field theory. *Physics Today*, 57(3):53–60, 2004.
- [63] HR Krishna-Murthy, JW Wilkins, and KG Wilson. Renormalization-group approach to the anderson model of dilute magnetic alloys. i. static properties for the symmetric case. *Physical Review B*, 21(3):1003, 1980.
- [64] HR Krishna-Murthy, JW Wilkins, and KG Wilson. Renormalization-group approach to the anderson model of dilute magnetic alloys. ii. static properties for the asymmetric case. *Physical Review B*, 21(3):1044, 1980.
- [65] Rolf Landauer. Spatial variation of currents and fields due to localized scatterers in metallic conduction. *IBM Journal of Research and Development*, 1(3):223–231, 1957.
- [66] Rolf Landauer. Electrical resistance of disordered one-dimensional lattices. *Philosophical Magazine*, 21(172):863–867, 1970.
- [67] Wei-Cheng Lee and AH MacDonald. Modulation doping near mott-insulator heterojunctions. *Physical Review B*, 74(7):075106, 2006.
- [68] JM Luttinger. Fermi surface and some simple equilibrium properties of a system of interacting fermions. *Physical Review*, 119(4):1153–1163, 1960.
- [69] G.D. Mahan. *Many-particle physics*. Springer, 2000.
- [70] K. Maki. Thermal fluctuations of the order parameter in charge-density waves. *Physical Review B*, 33(4):2852, 1986.
- [71] Y. Meir and N.S. Wingreen. Landauer formula for the current through an interacting electron region. *Physical review letters*, 68(16):2512–2515, 1992.

- [72] Walter Metzner and Dieter Vollhardt. Correlated lattice fermions in $d=$ dimensions. *Physical review letters*, 62(9):1066–1066, 1989.
- [73] Nevill Francis Mott and L Friedman. Metal-insulator transitions in VO_2 , Ti_2O_3 and $\text{Ti}_2\text{-x V x O}_3$. *Philosophical Magazine*, 30(2):389–402, 1974.
- [74] E Müller-Hartmann. Correlated fermions on a lattice in high dimensions. *Zeitschrift für Physik B Condensed Matter*, 74(4):507–512, 1989.
- [75] Yosuke Nagaoka. Ferromagnetism in a narrow, almost half-filled s band. *Physical Review*, 147(1):392, 1966.
- [76] Donald A Neamen and Boris Pevzner. *Semiconductor physics and devices: basic principles*, volume 3. McGraw-Hill New York, 2003.
- [77] Philippe Nozières and David Pines. *The theory of quantum liquids*, volume 6. Perseus books Cambridge, Massachusetts, 1999.
- [78] Akira Ohtomo, DA Muller, JL Grazul, and H Yu Hwang. Artificial charge-modulation in atomic-scale perovskite titanate superlattices. *Nature*, 419(6905):378–380, 2002.
- [79] T. Oka and H. Aoki. Dielectric breakdown in a mott insulator: Many-body schwinger-landau-zener mechanism studied with a generalized bethe ansatz. *Physical Review B*, 81(3):033103, 2010.
- [80] T. Oka, R. Arita, and H. Aoki. Breakdown of a mott insulator: A nonadiabatic tunneling mechanism. *Physical review letters*, 91(6):66406, 2003.
- [81] Satoshi Okamoto and Andrew J Millis. Electronic reconstruction at an interface between a mott insulator and a band insulator. *Nature*, 428(6983):630–633, 2004.
- [82] Satoshi Okamoto and Andrew J Millis. Spatial inhomogeneity and strong correlation physics: A dynamical mean-field study of a model mott-insulator–band-insulator heterostructure. *Physical Review B*, 70(24):241104, 2004.
- [83] Wanda C Oliveira and Luiz N Oliveira. Generalized numerical renormalization-group method to calculate the thermodynamical properties of impurities in metals. *Physical Review B*, 49:72070–11994, 1994.
- [84] Rossitza Pentcheva and Warren E Pickett. Correlation-driven charge order at the interface between a mott and a band insulator. *Physical review letters*, 99(1):016802, 2007.
- [85] R. Peters, T. Pruschke, and F.B. Anders. *Physical Review B*, 74(24):245114, 2006.
- [86] AI Poteryaev, AI Lichtenstein, and G Kotliar. Nonlocal coulomb interactions and metal-insulator transition in TiO_2 : A cluster lda+ dmft approach. *Physical review letters*, 93(8):086401, 2004.

- [87] M. Potthoff. Self-energy-functional approach to systems of correlated electrons. *The European Physical Journal B-Condensed Matter and Complex Systems*, 32(4):429–436, 2003.
- [88] M. Potthoff. Non-perturbative construction of the luttinger-ward functional. *Arxiv preprint cond-mat/0406671*, 2004.
- [89] M. Potthoff and W. Nolting. Dynamical mean-field study of the mott transition in thin films. *The European Physical Journal B-Condensed Matter and Complex Systems*, 8(4):555–568, 1999.
- [90] M. Potthoff and W. Nolting. Effective mass at the surface of a fermi liquid. *Physica B: Condensed Matter*, 259:760–761, 1999.
- [91] M. Potthoff and W. Nolting. Metallic surface of a mott insulator–mott insulating surface of a metal. *Physical Review B*, 60(11):7834, 1999.
- [92] M. Potthoff and W. Nolting. Surface metal-insulator transition in the hubbard model. *Physical Review B*, 59(4):2549, 1999.
- [93] M Potthoff, T Wegner, and W Nolting. Interpolating self-energy of the infinite-dimensional hubbard model: Modifying the iterative perturbation theory. *Physical Review B*, 55(24):16132, 1997.
- [94] Th Pruschke, M Jarrell, and JK Freericks. Anomalous normal-state properties of high- T_c superconductors: intrinsic properties of strongly correlated electron systems? *Advances in Physics*, 44(2):187–210, 1995.
- [95] Thomas Pruschke. Antiferromagnetism and metal insulator transition in the frustrated hubbard model. *Progress of Theoretical Physics Supplement*, 160:274–295, 2005.
- [96] Thomas Pruschke et al. Energy resolution and discretization artifacts in the numerical renormalization group. *Physical Review B*, 79(8):085106, 2009.
- [97] AP Ramirez. Colossal magnetoresistance. *Journal of Physics: Condensed Matter*, 9(39):8171, 1997.
- [98] Marcelo J Rozenberg, R Chitra, and Gabriel Kotliar. Finite temperature mott transition in the hubbard model in infinite dimensions. *Physical review letters*, 83(17):3498, 1999.
- [99] Marcelo J Rozenberg, Goetz Moeller, and Gabriel Kotliar. The metal–insulator transition in the hubbard model at zero temperature ii. *Modern Physics Letters B*, 8(08n09):535–543, 1994.
- [100] O. Sakai, Y. Shimizu, and T. Kasuya. Single-particle and magnetic excitation spectra of degenerate anderson model with finite coulomb interaction. *J. Phys. Soc. Jpn*, 58:3666, 1989.

- [101] H Sakaki, T Noda, K Hirakawa, M Tanaka, and T Matsusue. Interface roughness scattering in GaAs/AlAs quantum wells. *Applied physics letters*, 51(23):1934–1936, 1987.
- [102] J Schlipf, M Jarrell, PGJ Van Dongen, N Blümer, S Kehrein, Th Pruschke, and D Vollhardt. Absence of hysteresis at the Mott-Hubbard metal-insulator transition in infinite dimensions. *Physical review letters*, 82(24):4890, 1999.
- [103] U. Schneider, L. Hackermüller, S. Will, T. Best, I. Bloch, TA Costi, RW Helmes, D. Rasch, and A. Rosch. Metallic and insulating phases of repulsively interacting fermions in a 3d optical lattice. *Science*, 322(5907):1520–1525, 2008.
- [104] Ulrich Schollwöck. The density-matrix renormalization group. *Reviews of Modern Physics*, 77(1):259, 2005.
- [105] JH Schön, Ch Kloc, and B Batlogg. High-temperature superconductivity in lattice-expanded C₆₀. *Science*, 293(5539):2432–2434, 2001.
- [106] JR Schrieffer and PA Wolff. Relation between the Anderson and Kondo Hamiltonians. *Physical Review*, 149:491–492, 1966.
- [107] M Sindel, L Borda, J Martinek, R Bulla, J König, G Schön, S Maekawa, and J Von Delft. Kondo quantum dot coupled to ferromagnetic leads: Numerical renormalization group study. *Physical Review B*, 76(4):045321, 2007.
- [108] Y. Taguchi, T. Matsumoto, and Y. Tokura. Dielectric breakdown of one-dimensional Mott insulators Sr₂VO₃ and SrVO₂. *Physical Review B*, 62(11):7015, 2000.
- [109] G.S. Uhrig. Conductivity in a symmetry-broken phase: Spinless fermions with 1/d corrections. *Physical Review B*, 54(15):10436, 1996.
- [110] Dieter Vollhardt. Investigation of correlated electron systems using the limit of high dimensions. *Correlated Electron Systems*, 57, 1993.
- [111] Puru Voruganti, Andrey Golubentsev, and Sajeev John. Conductivity and Hall effect in the two-dimensional Hubbard model. *Physical Review B*, 45(24):13945, 1992.
- [112] A. Weichselbaum and J. Von Delft. Sum-rule conserving spectral functions from the numerical renormalization group. *Physical review letters*, 99(7):76402, 2007.
- [113] Kenneth G Wilson. The renormalization group: Critical phenomena and the Kondo problem. *Reviews of Modern Physics*, 47(4):773, 1975.
- [114] Kei Yosida and Kosaku Yamada. Perturbation expansion for the Anderson Hamiltonian. *Progress of Theoretical Physics Supplement*, 46:244–255, 1970.
- [115] C. Zener. A theory of the electrical breakdown of solid dielectrics. *Proceedings of the Royal Society of London. Series A*, 145(855):523–529, 1934.

- [116] XY Zhang, MJ Rozenberg, and G Kotliar. Mott transition in the $d=$ hubbard model at zero temperature. *Physical review letters*, 70(11):1666, 1993.
- [117] R Zitzler, Th Pruschke, and R Bulla. Magnetism and phase separation in the ground state of the hubbard model. *The European Physical Journal B-Condensed Matter and Complex Systems*, 27(4):473–481, 2002.
- [118] R Zitzler, N-H Tong, Th Pruschke, and R Bulla. Phase diagram of the frustrated hubbard model. *Physical review letters*, 93(1):016406, 2004.
- [119] V Zlatic and B Horvatic. The local approximation for correlated systems on high dimensional lattices. *Solid State Communications*, 75(3):263–267, 1990.
- [120] V Zlatić, B Horvatić, and D Šokčević. Density of states for intermediate valence and kondo systems. *Zeitschrift für Physik B Condensed Matter*, 59(2):151–157, 1985.

Part IV
Appendix

Appendix A

Antiferromagnetic quantum zipper algorithm

The determination of the asymptotic left-/right-functions for the leads turns out to be more difficult for the antiferromagnetic than for the paramagnetic zipper algorithm, because closed form expressions for matrix-valued quadratic equations exist only for special cases. The asymptotic form of the L-/R-functions in the lead is determined by the assumption that deep inside the lead the system is homogenous. We have $\mathbf{R}_\alpha(\omega, \epsilon_{\mathbf{k}\parallel}) = \mathbf{L}_\alpha(\omega, \epsilon_{\mathbf{k}\parallel})$. So we can define the left function $\mathbf{L}_\alpha(\omega, \epsilon_{\mathbf{k}\parallel})$ by solving

$$\mathbf{G}_\alpha(\omega, \epsilon_{\mathbf{k}\parallel}) = [2\mathbf{L}_\alpha(\omega, \epsilon_{\mathbf{k}\parallel}) - \mathbf{M}_\alpha(\omega, \epsilon_{\mathbf{k}\parallel})]^{-1} \quad (\text{A.1})$$

for $\mathbf{L}_\alpha(\omega, \epsilon_{\mathbf{k}\parallel})$

$$\mathbf{L}_\alpha(\omega, \epsilon_{\mathbf{k}\parallel}) = \frac{1}{2} [\mathbf{G}_\alpha^{-1}(\omega, \epsilon_{\mathbf{k}\parallel}) + \mathbf{M}_\alpha(\omega, \epsilon_{\mathbf{k}\parallel})] \quad (\text{A.2})$$

For homogenous systems ($t_{\alpha\alpha+1} = t$) the local Greens function can be expressed as

$$\mathbf{G}_\alpha(\omega, \epsilon_{\mathbf{k}\parallel}) = \frac{1}{2\pi} \int_{-\pi}^{\pi} dk_z \begin{pmatrix} Z_\alpha(\omega) - \epsilon_{\mathbf{k}\parallel} + 2t \cos(k_z) & \Delta_\alpha(\omega) \\ \Delta_\alpha(\omega) & Z_\alpha(\omega) + \epsilon_{\mathbf{k}\parallel} - 2t \cos(k_z) \end{pmatrix}^{-1} \quad (\text{A.3})$$

$$\begin{aligned} Z_\alpha(\omega) &= \omega + i0^+ + \mu - \bar{\epsilon}_\alpha - \bar{\Sigma}_\alpha(\omega) \\ \Delta_\alpha(\omega) &= -\Delta\epsilon_\alpha - \Delta\Sigma_\alpha(\omega) \end{aligned} \quad (\text{A.4})$$

This integral can indeed be solved by computer-algebra software. We used Mathematica[®] Version 8.0. The resulting expression is long and complicated with some repeating structures. Substitution into Eq. A.2 yields the 2×2 -valued left and right functions which we call jointly $S^{(ij)}$ here,

$$\mathbf{L}_{-\infty}(\omega, \epsilon_{\mathbf{k}\parallel}) = \begin{pmatrix} S^{(11)}(\omega, \epsilon_{\mathbf{k}\parallel}) & S^{(12)}(\omega, \epsilon_{\mathbf{k}\parallel}) \\ S^{(12)}(\omega, \epsilon_{\mathbf{k}\parallel}) & S^{(22)}(\omega, \epsilon_{\mathbf{k}\parallel}) \end{pmatrix} \quad (\text{A.5})$$

$$\mathbf{R}_\infty(\omega, \epsilon_{\mathbf{k}\parallel}) = \begin{pmatrix} S^{(11)}(\omega, \epsilon_{\mathbf{k}\parallel}) & S^{(12)}(\omega, \epsilon_{\mathbf{k}\parallel}) \\ S^{(12)}(\omega, \epsilon_{\mathbf{k}\parallel}) & S^{(22)}(\omega, \epsilon_{\mathbf{k}\parallel}) \end{pmatrix} \quad (\text{A.6})$$

where

$$S^{(11)}(\omega, \epsilon_{\mathbf{k}\parallel}) = \frac{1}{4W_1W_2W_3} \left[W_1(-W_3(2\epsilon_{\mathbf{k}\parallel}W_2 + \epsilon_{\mathbf{k}\parallel} + 2) - (\epsilon_{\mathbf{k}\parallel} + 2)W_2 + Z_\alpha(\omega)(2W_2W_3 + W_2 + W_3)) \right. \\ \left. + (W_2 - W_3) (-(\epsilon_{\mathbf{k}\parallel} + 2)Z_\alpha + Z_\alpha^2 - \Delta_\alpha^2) \right] \quad (\text{A.7})$$

$$S^{(12)}(\omega, \epsilon_{\mathbf{k}\parallel}) = \frac{1}{4W_1W_2W_3} \left[\Delta_\alpha(W_2(-\epsilon_{\mathbf{k}\parallel} + 2W_1W_3 + W_1 - 2) + W_3(\epsilon_{\mathbf{k}\parallel} + W_1 + 2)) \right] \quad (\text{A.8})$$

$$S^{(22)}(\omega, \epsilon_{\mathbf{k}\parallel}) = \frac{1}{4W_1W_2W_3} \left[W_1(W_2(2\epsilon_{\mathbf{k}\parallel}W_3 + \epsilon_{\mathbf{k}\parallel} + 2W_3Z_\alpha + Z_\alpha + 2) \right. \\ \left. + W_3(\epsilon_{\mathbf{k}\parallel} + Z_\alpha + 2)) - (W_2 - W_3) (Z_\alpha(\epsilon_{\mathbf{k}\parallel} + Z_\alpha + 2) - \Delta_\alpha^2) \right] \quad (\text{A.9})$$

$$W_1(\omega) = \sqrt{Z_\alpha^2 - \Delta_\alpha^2} \quad (\text{A.10})$$

$$W_2(\omega, \epsilon_{\mathbf{k}\parallel}) = \sqrt{\frac{\epsilon_{\mathbf{k}\parallel}^2 - 4W_1(\omega) - Z_\alpha^2(\omega) + \Delta_\alpha^2(\omega) - 4}{(\epsilon_{\mathbf{k}\parallel} - 4)\epsilon_{\mathbf{k}\parallel} - Z_\alpha^2(\omega) + \Delta_\alpha^2(\omega) + 4}} \quad (\text{A.11})$$

$$W_3(\omega, \epsilon_{\mathbf{k}\parallel}) = \sqrt{\frac{\epsilon_{\mathbf{k}\parallel}^2 + 4W_1(\omega) - Z_\alpha^2(\omega) + \Delta_\alpha^2(\omega) - 4}{(\epsilon_{\mathbf{k}\parallel} - 4)\epsilon_{\mathbf{k}\parallel} - Z_\alpha^2(\omega) + \Delta_\alpha^2(\omega) + 4}} \quad (\text{A.12})$$

where we have defined W_1 , W_2 and W_3 for repeating structures to make the final expression more compact. The

The recursion relation for right function takes the form

$$\mathbf{R}_\alpha(\omega, \epsilon_{\mathbf{k}\parallel}) = \mathbf{M}_\alpha(\omega, \epsilon_{\mathbf{k}\parallel}) - \frac{t_{\alpha\alpha+1}t_{\alpha+1\alpha}}{\det R_{\alpha+1}(\omega, \epsilon_{\mathbf{k}\parallel})} \begin{pmatrix} R_{\alpha+1}^{(22)}(\omega, \epsilon_{\mathbf{k}\parallel}) & R_{\alpha+1}^{(12)}(\omega, \epsilon_{\mathbf{k}\parallel}) \\ R_{\alpha+1}^{(21)}(\omega, \epsilon_{\mathbf{k}\parallel}) & R_{\alpha+1}^{(11)}(\omega, \epsilon_{\mathbf{k}\parallel}) \end{pmatrix} \quad (\text{A.13})$$

and for the left function

$$\mathbf{L}_\alpha(\omega, \epsilon_{\mathbf{k}\parallel}) = \mathbf{M}_\alpha(\omega, \epsilon_{\mathbf{k}\parallel}) - \frac{t_{\alpha\alpha-1}t_{\alpha-1\alpha}}{\det L_{\alpha-1}(\omega, \epsilon_{\mathbf{k}\parallel})} \begin{pmatrix} L_{\alpha-1}^{(22)}(\omega, \epsilon_{\mathbf{k}\parallel}) & L_{\alpha-1}^{(12)}(\omega, \epsilon_{\mathbf{k}\parallel}) \\ L_{\alpha-1}^{(21)}(\omega, \epsilon_{\mathbf{k}\parallel}) & L_{\alpha-1}^{(11)}(\omega, \epsilon_{\mathbf{k}\parallel}) \end{pmatrix} \quad (\text{A.14})$$

where

$$\mathbf{M}_\alpha(\omega, \epsilon_{\mathbf{k}\parallel}) = \begin{pmatrix} Z_\alpha(\omega) - \epsilon_{\mathbf{k}\parallel} & \Delta_\alpha(\omega) \\ \Delta_\alpha(\omega) & Z_\alpha(\omega) - \epsilon_{\mathbf{k}\parallel} \end{pmatrix} \quad (\text{A.15})$$

The expression for the Green's function has the same structure as in the paramagnetic case, however now all quantities are 2×2 matrices.

$$\mathbf{G}_\alpha(\omega, \epsilon_{\mathbf{k}\parallel}) = [R_\alpha(\omega, \epsilon_{\mathbf{k}\parallel}) + L_\alpha(\omega, \epsilon_{\mathbf{k}\parallel}) - \mathbf{M}_\alpha(\omega, \epsilon_{\mathbf{k}\parallel})]^{-1} \quad (\text{A.16})$$

The Green's functions for the sub lattices A and B are now easily derived by transformation Eq. 5.36,

$$G^{(A)}(\omega, \epsilon_{\mathbf{k}\parallel}) = \frac{1}{2} [G_\alpha^{(11)}(\omega, \epsilon_{\mathbf{k}\parallel}) + G_\alpha^{(12)}(\omega, \epsilon_{\mathbf{k}\parallel}) + G_\alpha^{(21)}(\omega, \epsilon_{\mathbf{k}\parallel}) + G_\alpha^{(22)}(\omega, \epsilon_{\mathbf{k}\parallel})] \\ G^{(B)}(\omega, \epsilon_{\mathbf{k}\parallel}) = \frac{1}{2} [G_\alpha^{(11)}(\omega, \epsilon_{\mathbf{k}\parallel}) - G_\alpha^{(12)}(\omega, \epsilon_{\mathbf{k}\parallel}) - G_\alpha^{(21)}(\omega, \epsilon_{\mathbf{k}\parallel}) + G_\alpha^{(22)}(\omega, \epsilon_{\mathbf{k}\parallel})] \quad (\text{A.17})$$

Appendix B

Spectral functions for B-M-B heterostructure

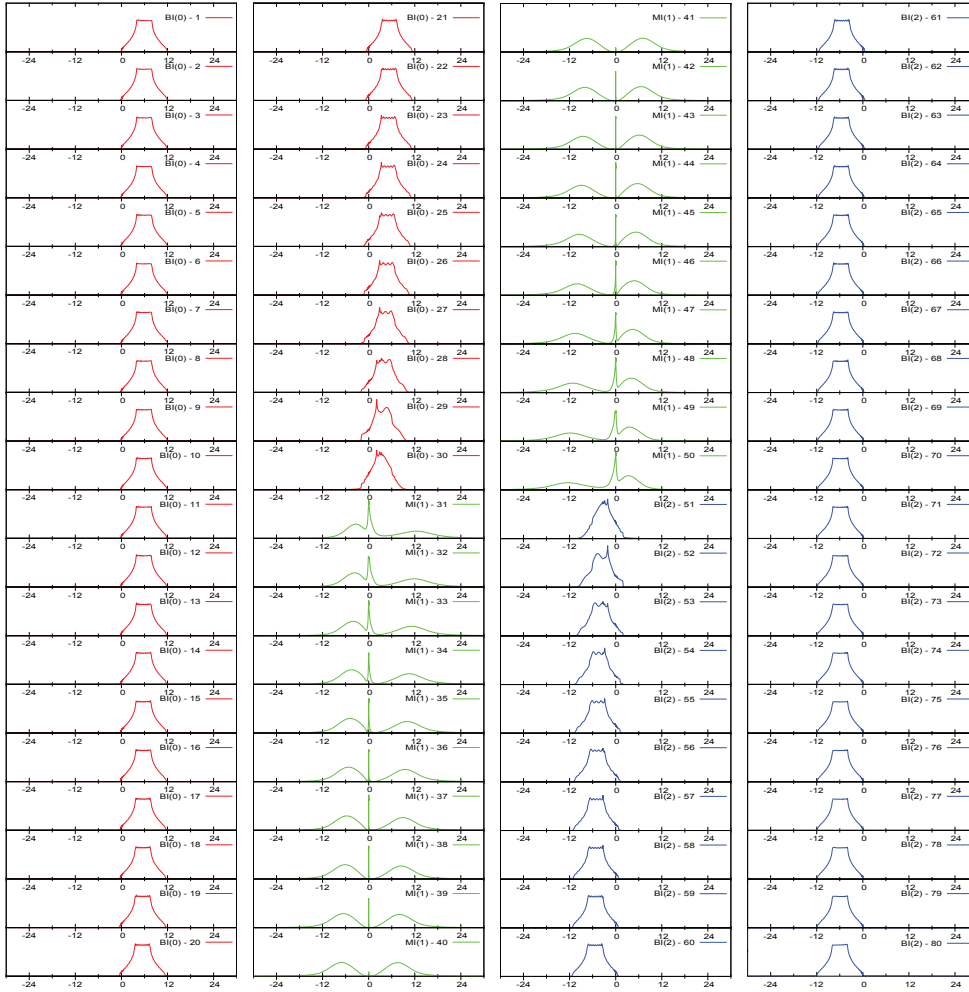


Figure B.1: Spectral functions for the Band-Mott-Band insulator heterostructure for a system temperature of $T = 10^{-8}$. Layers 1-30 depict the spectral function for the band insulator (red lines), layers 31-50 the Mott-insulating layers (green lines), and layers 51-80 band-insulating layers.

Appendix C

Derivation of the Hall conductivity

Triangle graphs

Adding the two diagrams with three V^1 vertices and keeping only terms linear in \mathbf{A}^E and \mathbf{A}^B we find

$$\begin{aligned} \delta_2^{(1)} \mathcal{J}_{r\delta}^\lambda &= e^3 \sum_{p,\alpha,\gamma} G_{\mathbf{p}m,\alpha\delta} \epsilon_{\mathbf{p}+\frac{\mathbf{r}}{2}}^\lambda G_{\mathbf{p}+\mathbf{r}m+n,\delta\gamma} \epsilon_{\mathbf{p}+\frac{\mathbf{r}}{2}}^\nu \mathbf{a}_{\mathbf{r}\gamma}^{B\nu} G_{\mathbf{p}m+n,\gamma\alpha} \epsilon_{\mathbf{p}}^\mu \mathbf{a}_{n\alpha}^{E\mu} \\ &\quad - e^3 \sum_{p,\alpha,\gamma} G_{\mathbf{p}m,\alpha\delta} \epsilon_{\mathbf{p}+\frac{\mathbf{r}}{2}}^\lambda G_{\mathbf{p}+\mathbf{r}m+n,\delta\gamma} \epsilon_{\mathbf{p}+\mathbf{r}}^\nu \mathbf{a}_{n\gamma}^{E\nu} G_{\mathbf{p}+\mathbf{r}m,\gamma\alpha} \epsilon_{\mathbf{p}+\frac{\mathbf{r}}{2}}^\mu \mathbf{a}_{\mathbf{r}\alpha}^{B\mu} \end{aligned} \quad (\text{C.1})$$

Exchanging α and γ labels in the second term and shifting the momentum sum by $-\frac{\mathbf{r}}{2}$ and the second frequency sum by $-\Omega_n$ we arrive at

$$\begin{aligned} \delta_2^{(1)} \mathcal{J}_{r\delta}^\lambda &= e^3 \sum_{\alpha,\gamma} \mathbf{a}_{n\gamma}^{E\nu} \mathbf{a}_{\mathbf{r}\alpha}^{B\mu} \sum_{\mathbf{p}} \epsilon_{\mathbf{p}}^\lambda \epsilon_{\mathbf{p}}^\mu \left[\epsilon_{\mathbf{p}-\frac{\mathbf{r}}{2}}^\nu \sum_m G_{\mathbf{p}^{-m},\alpha\gamma} G_{\mathbf{p}^{-m-n},\gamma\delta} G_{\mathbf{p}^+m,\delta\alpha} \right. \\ &\quad \left. + \epsilon_{\mathbf{p}+\frac{\mathbf{r}}{2}}^\nu \sum_m G_{\mathbf{p}^{-m},\alpha\delta} G_{\mathbf{p}^+m+n,\delta\gamma} G_{\mathbf{p}^+m,\gamma\alpha} \right] \end{aligned} \quad (\text{C.2})$$

where $\mathbf{p}^\pm = \mathbf{p} \pm \frac{\mathbf{r}}{2}$, c.f. Fig C.1a and Fig. C.1b. We are interested in contributions linear in \mathbf{r} therefore using

$$\frac{\partial}{\partial \epsilon_{\mathbf{p}}} G_{\mathbf{p}m,\alpha\beta} = - \sum_{\gamma} G_{\mathbf{p}m,\alpha\gamma} G_{\mathbf{p}m,\gamma\beta} \quad (\text{C.3})$$

we may expand

$$\epsilon_{\mathbf{p}^\pm \frac{\mathbf{r}}{2}}^{\delta_1 \dots \delta_n} = \epsilon_{\mathbf{p}}^{\delta_1 \dots \delta_n} \pm \frac{\mathbf{r}^\delta}{2} \epsilon_{\mathbf{p}}^{\delta_1 \dots \delta_n \delta} \quad (\text{C.4})$$

$$G_{\mathbf{p}^\pm m,\alpha\beta} = G_{\mathbf{p}m,\alpha\beta} \mp \left(\frac{\mathbf{r}^\delta}{2} \right) \epsilon_{\mathbf{p}}^\delta \sum_{\gamma} G_{\mathbf{p}m,\alpha\gamma} G_{\mathbf{p}m,\gamma\beta} \quad (\text{C.5})$$

Now a number of simplifications arises: Expanding the first Green function in the first term we see that its contribution is exactly cancelled by the contribution of

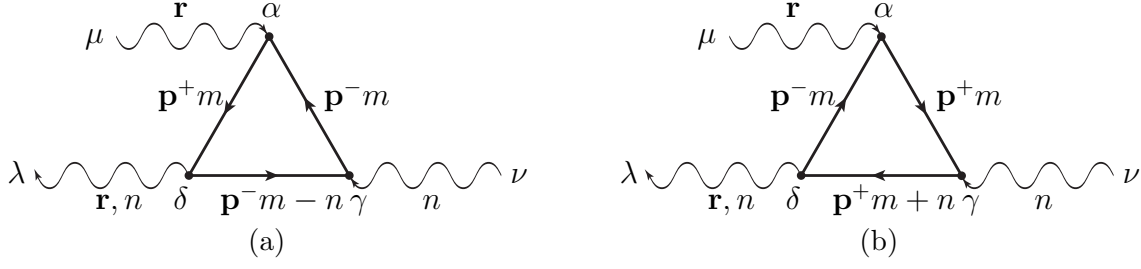


Figure C.1: Triangle graphs with three V^1 vertices for the calculation of the Hall conductivity, c.f. Eq. C.2.

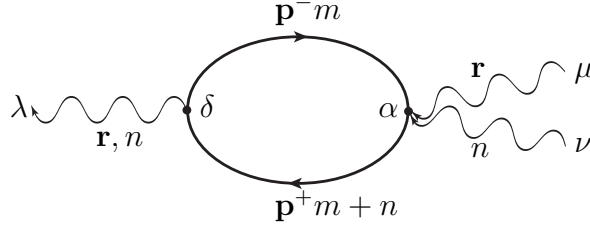


Figure C.2

the third Green function in the second term and vice versa. Contributions from the Green functions in the middle cancel in the limit $\Omega \rightarrow 0$, which is the limit we are interested in. Therefore the only contributions stem from the expansion of the dispersion relations. Adding these contributions we get

$$\delta_2^{(1)} \mathcal{J}_{r\delta}^\lambda = \frac{e^3}{2} \mathbf{a}_n^{E\nu} \mathbf{a}_r^{B\mu} \sum_{\alpha, \gamma} \mathbf{r}^\chi \sum_{\mathbf{p}} \epsilon_{\mathbf{p}}^\lambda \epsilon_{\mathbf{p}}^{\mu} \epsilon_{\mathbf{p}}^{\nu\chi} \Pi_{\mathbf{p}n\delta} \quad (\text{C.6})$$

where we have defined the frequency sum

$$\Pi_{\mathbf{p}n\delta\gamma\alpha} = \sum_m G_{\mathbf{p}m, \alpha\delta} G_{\mathbf{p}m, \alpha\gamma} [G_{\mathbf{p}m+n, \gamma\delta} - G_{\mathbf{p}m-n, \gamma\delta}] \quad (\text{C.7})$$

V^2 graph

The other contribution stems from a one V^1 and one V^2 vertex diagram and reads

$$\delta_2^{(2)} \mathcal{J}_{r\delta}^\lambda = -e^3 \sum_{p, \alpha} G_{\mathbf{p}m, \alpha\delta} \epsilon_{\mathbf{p}+\frac{\mathbf{r}}{2}}^\lambda G_{\mathbf{p}+\mathbf{r}m+n, \delta\alpha} \epsilon_{\mathbf{p}+\frac{\mathbf{r}}{2}}^{\mu\nu} \mathbf{A}_{\mathbf{r}\alpha}^{B\mu} \mathbf{A}_{n\alpha}^{E\nu} \quad (\text{C.8})$$

Shifting the momentum sum by $-\frac{\mathbf{r}}{2}$ we arrive at

$$\delta_2^{(2)} \mathcal{J}_{r\delta}^\lambda = -e^3 \sum_{\alpha} \mathbf{A}_{\mathbf{r}\alpha}^{B\mu} \mathbf{A}_{n\alpha}^{E\nu} \sum_{\mathbf{p}} \epsilon_{\mathbf{p}}^\lambda \epsilon_{\mathbf{p}}^{\mu\nu} \sum_m G_{\mathbf{p}-m, \alpha\delta} G_{\mathbf{p}+m+n, \alpha\delta} \quad (\text{C.9})$$

To linear order in \mathbf{r} we have

$$\begin{aligned} \sum_m G_{\mathbf{p}-m, \alpha\delta} G_{\mathbf{p}+m+n, \alpha\delta} &\approx \sum_{m, \gamma} \frac{\mathbf{r}^\chi}{2} \epsilon_{\mathbf{p}}^\chi [G_{\mathbf{p}m, \alpha\gamma} G_{\mathbf{p}m, \gamma\delta} G_{\mathbf{p}m+n, \alpha\delta} - G_{\mathbf{p}m, \alpha\delta} G_{\mathbf{p}m+n, \alpha\gamma} G_{\mathbf{p}m+n, \gamma\delta}] \\ &= \sum_{m, \gamma} \frac{\mathbf{r}^\chi}{2} \epsilon_{\mathbf{p}}^\chi G_{\mathbf{p}m, \alpha\gamma} G_{\mathbf{p}m, \gamma\delta} [G_{\mathbf{p}m+n, \alpha\delta} - G_{\mathbf{p}m-n, \alpha\delta}] \end{aligned} \quad (\text{C.10})$$

therefore renaming α and γ and again assuming that the fields are layer-independent

$$\delta_2^{(2)} \mathcal{J}_{r\delta}^\lambda = -\frac{e^3}{2} \sum_{\alpha,\gamma} \mathbf{A}_r^{B\mu} \mathbf{A}_n^{E\nu} \mathbf{r}^\chi \sum_{\mathbf{p}} \epsilon_{\mathbf{p}}^\lambda \epsilon_{\mathbf{p}}^{\mu\nu} \epsilon_{\mathbf{p}}^\chi \sum_m G_{\mathbf{p}m,\alpha\gamma} G_{\mathbf{p}m,\alpha\delta} [G_{\mathbf{p}m+n,\gamma\delta} - G_{\mathbf{p}m-n,\gamma\delta}] \quad (\text{C.11})$$

$$= -\frac{e^3}{2} \sum_{\alpha,\gamma} \mathbf{A}_r^{B\mu} \mathbf{A}_n^{E\nu} \mathbf{r}^\chi \sum_{\mathbf{p}} \epsilon_{\mathbf{p}}^\lambda \epsilon_{\mathbf{p}}^{\mu\nu} \epsilon_{\mathbf{p}}^\chi \Pi_{\mathbf{p}n\delta\gamma\alpha} \quad (\text{C.12})$$

Appendix D

Analytic continuation of $\Pi_{\mathbf{p}n\alpha\gamma}$

In order to calculate the analytic continuation of $\Pi_{\alpha\gamma}(\mathbf{p}, \Omega_n)$ it is easiest to express the Matsubara Green functions as energy integrals over the spectral function times a free Matsubara Greens function, i.e.

$$G_{\mathbf{p}m,\alpha\beta} = -i \int d\epsilon \frac{A_{\mathbf{p},\alpha\beta}(\epsilon)}{i\omega_m - \epsilon} \quad (\text{D.1})$$

$$= -i \int d\epsilon \mathcal{G}_0(\epsilon, i\omega_m) A_{\mathbf{p},\alpha\beta}(\epsilon) \quad (\text{D.2})$$

Using standard relations for Matsubara sums [69]

$$\frac{1}{\beta} \sum_m \mathcal{G}_0(\epsilon, i\omega_m) \mathcal{G}_0(\epsilon', i\omega_m + i\Omega_n) = \frac{n_F(\epsilon) - n_F(\epsilon')}{i\Omega_n + \epsilon - \epsilon'} \quad (\text{D.3})$$

we arrive at

$$I_{\alpha\gamma}(\mathbf{p}, \Omega) = - \int d\epsilon \int d\epsilon' A_{\alpha\gamma}(\mathbf{p}, \epsilon) A_{\gamma\alpha}(\mathbf{p}, \epsilon')$$

$$\text{Im} \left[\frac{1}{\beta} \sum_m \mathcal{G}_0(\epsilon, i\omega_m) \mathcal{G}_0(\epsilon', i\omega_m + i\Omega_n) \right]_{i\Omega_n=\Omega} / \Omega \quad (\text{D.4})$$

$$= - \int d\epsilon \int d\epsilon' A_{\alpha\gamma}(\mathbf{p}, \epsilon) A_{\gamma\alpha}(\mathbf{p}, \epsilon') \text{Im} \left[\frac{n_F(\epsilon) - n_F(\epsilon')}{i\Omega_n + \epsilon - \epsilon'} \right]_{i\Omega_n=\Omega} / \Omega \quad (\text{D.5})$$

$$= \frac{1}{\pi} \int d\epsilon \int d\epsilon' A_{\alpha\gamma}(\mathbf{p}, \epsilon) A_{\gamma\alpha}(\mathbf{p}, \epsilon') \frac{n_F(\epsilon) - n_F(\epsilon')}{\Omega} \delta(\Omega + \epsilon - \epsilon') \quad (\text{D.6})$$

$$= -\frac{1}{\pi} \int d\epsilon A_{\alpha\gamma}(\mathbf{p}, \epsilon) A_{\gamma\alpha}(\mathbf{p}, \epsilon + \Omega) \frac{n_F(\epsilon + \Omega) - n_F(\epsilon)}{\Omega} \quad (\text{D.7})$$

where $I_{\alpha\gamma}(\mathbf{p}, \Omega) = \text{Im} \Pi_{\alpha\gamma}(\mathbf{p}, \Omega) / \Omega$. Performing $\lim_{\Omega \rightarrow 0} I_{\alpha\gamma}(\mathbf{p}, \Omega)$ and noting that $A_{\alpha\gamma}(\mathbf{p}, \epsilon) = A_{\gamma\alpha}(\mathbf{p}, \epsilon)$, we finally get

$$I_{\alpha\gamma}(\mathbf{p}, 0) = -\frac{1}{\pi} \int d\epsilon A_{\alpha\gamma}(\mathbf{p}, \epsilon)^2 \frac{\partial n_F(\epsilon)}{\partial \epsilon} \quad (\text{D.8})$$

$$\lim_{\Omega \rightarrow 0} \sigma_{\gamma\alpha}^{\lambda\nu}(\Omega) = (e^2/V) \int d\epsilon \frac{1}{\pi} \sum_{\mathbf{p}} (\epsilon_{\mathbf{p}}^x)^2 A_{\alpha\gamma}(\mathbf{p}, \epsilon)^2 \frac{\partial n_F(\epsilon)}{\partial \epsilon} \quad (\text{D.9})$$

Appendix E

Analytic continuation of $\Pi_{\mathbf{p}n\delta}^H$

We wish to find the analytic continuation of

$$\Pi_{\mathbf{p}m\delta}^H = \frac{1}{\beta} \sum_{m\alpha\gamma} G_{\mathbf{p}m\alpha\gamma} G_{\mathbf{p}m\alpha\delta} (G_{\mathbf{p}m+n\gamma\delta} - G_{\mathbf{p}m-n\gamma\delta}) \quad (\text{E.1})$$

Using the spectral representation $\Pi_{\mathbf{p},m}$ assumes the form

$$\Pi_{\mathbf{p}m\delta}^H = \sum_{\alpha\gamma} \int d\epsilon_1 \int d\epsilon_2 \int d\epsilon_3 A_{\alpha\gamma}(\mathbf{p}, \epsilon_1) A_{\alpha\delta}(\mathbf{p}, \epsilon_2) A_{\gamma\delta}(\mathbf{p}, \epsilon_3) (S^+ - S^-) \quad (\text{E.2})$$

$$= \Pi_{\mathbf{p}m\delta}^+ - \Pi_{\mathbf{p}m\delta}^- \quad (\text{E.3})$$

where

$$S^\pm = \frac{1}{\beta} \sum_m \frac{1}{ip_m - \epsilon_1} \frac{1}{ip_m - \epsilon_2} \frac{1}{ip_m \pm i\omega_n - \epsilon_3} \quad (\text{E.4})$$

Here

$$A_{\alpha\gamma}(\mathbf{p}, \epsilon) = -\frac{1}{\pi} \text{Im} G_{\alpha\gamma}(\mathbf{p}, \epsilon) = -\frac{1}{\pi} G''_{\alpha\gamma}(\mathbf{p}, \epsilon) \quad (\text{E.5})$$

We will use contour integration to perform the frequency sum

$$S^\pm = -\frac{1}{\beta} \sum_m f^\pm(ip_m) \quad (\text{E.6})$$

$$f^\pm(z) = -\frac{1}{z - \epsilon_1} \frac{1}{z - \epsilon_2} \frac{1}{z - (\epsilon_3 \mp i\omega_n)} \quad (\text{E.7})$$

Consider

$$I = \lim_{R \rightarrow \infty} \int \frac{dz}{2\pi i} f^\pm(z) n_F(z) \quad (\text{E.8})$$

$$= -\frac{1}{\beta} \sum_m f^\pm(ip_m) + \sum_i R_i^\pm \quad (\text{E.9})$$

where R_i^\pm enumerates all the residues of $f^\pm(z_i)$ times $n_F(z_i)$. As $I = 0$ we find

$$S^\pm = -\sum_i R_i^\pm \quad (\text{E.10})$$

$$\begin{array}{l}
z_m = i(2m + 1)\pi/\beta \\
z_1 = \epsilon_1 \\
z_2 = \epsilon_2 \\
z_3 = \epsilon_3 \mp i\omega_n
\end{array}
\left\| \begin{array}{l}
-\frac{1}{\beta} f^\pm(ip_m) \\
-\frac{1}{\epsilon_1 \mp \epsilon_2} \frac{1}{\epsilon_1 \pm i\omega_n - \epsilon_3} n_F(\epsilon_1) \\
-\frac{1}{\epsilon_2 - \epsilon_1} \frac{1}{\epsilon_2 \pm i\omega_n - \epsilon_3} n_F(\epsilon_2) \\
-\frac{1}{\epsilon_3 \mp i\omega_n - \epsilon_1} \frac{1}{\epsilon_3 \mp i\omega_n - \epsilon_2} n_F(\epsilon_3)
\end{array} \right.$$

Table E.1: Residues

The table E.1 summarizes the residues. For the last residue we used that $n_F(\epsilon_3 \mp i\omega_n) = n_F(\epsilon_3)$ with ω_n a bosonic excitation frequency. Consequently S^\pm is given by

$$S^\pm = \frac{1}{\epsilon_1 - \epsilon_2} \frac{n_F(\epsilon_1)}{\epsilon_1 \pm i\omega_n - \epsilon_3} + \frac{1}{\epsilon_2 - \epsilon_1} \frac{n_F(\epsilon_2)}{\epsilon_2 \pm i\omega_n - \epsilon_3} + \frac{1}{\epsilon_3 \mp i\omega_n - \epsilon_1} \frac{n_F(\epsilon_3)}{\epsilon_3 \mp i\omega_n - \epsilon_2} \quad (\text{E.11})$$

Performing the analytic continuation for S^\pm and taking the real part we find

$$\begin{aligned}
\text{Re } S^\pm &= \frac{n_F(\epsilon_2)}{\epsilon_2 - \epsilon_1} \mathcal{P} \left(\frac{1}{(\epsilon_2 \pm \omega) - \epsilon_3} \right) + \frac{n_F(\epsilon_1)}{\epsilon_1 - \epsilon_2} \mathcal{P} \left(\frac{1}{(\epsilon_1 \pm \omega) - \epsilon_3} \right) \\
&\quad + \mathcal{P} \left(\frac{1}{(\epsilon_1 \pm \omega) - \epsilon_3} \right) \mathcal{P} \left(\frac{1}{(\epsilon_2 \pm \omega) - \epsilon_3} \right) n_F(\epsilon_3) - \pi^2 \delta(\epsilon_1 \pm \omega - \epsilon_3) \delta(\epsilon_2 \pm \omega - \epsilon_3) n_F(\epsilon_3) \\
&= \frac{n_F(\epsilon_2)}{\epsilon_2 - \epsilon_1} \mathcal{P} \left(\frac{1}{(\epsilon_2 \pm \omega) - \epsilon_3} \right) + \frac{n_F(\epsilon_1)}{\epsilon_1 - \epsilon_2} \mathcal{P} \left(\frac{1}{(\epsilon_1 \pm \omega) - \epsilon_3} \right) \\
&\quad + \mathcal{P} \left(\frac{1}{\epsilon_1 - (\epsilon_3 \mp \omega)} \right) \mathcal{P} \left(\frac{1}{\epsilon_2 - (\epsilon_3 \mp \omega)} \right) n_F(\epsilon_3) - \pi^2 \delta(\epsilon_1 - (\epsilon_3 \mp \omega)) \delta(\epsilon_2 - (\epsilon_3 \mp \omega)) n_F(\epsilon_3)
\end{aligned} \quad (\text{E.12})$$

We can now plug this into eq. (E.2) to find

$$\begin{aligned}
\Pi^\pm(\mathbf{p}\omega\delta) &= -\frac{1}{\pi^3} \sum_{\alpha\gamma} \int d\epsilon_1 \int d\epsilon_2 \int d\epsilon_3 G''_{\alpha\gamma}(\mathbf{p}, \epsilon_1) \frac{G''_{\alpha\delta}(\mathbf{p}, \epsilon_2)}{\epsilon_2 - \epsilon_1} \mathcal{P} \left(\frac{G''_{\gamma\delta}(\mathbf{p}, \epsilon_3)}{\epsilon_3 - (\epsilon_1 \pm \omega)} \right) n_F(\epsilon_1) \\
&\quad - \frac{1}{\pi^3} \sum_{\alpha\gamma} \int d\epsilon_1 \int d\epsilon_2 \int d\epsilon_3 \frac{G''_{\alpha\gamma}(\mathbf{p}, \epsilon_1)}{\epsilon_1 - \epsilon_2} G''_{\alpha\delta}(\mathbf{p}, \epsilon_2) \mathcal{P} \left(\frac{G''_{\gamma\delta}(\mathbf{p}, \epsilon_3)}{\epsilon_3 - (\epsilon_2 \pm \omega)} \right) n_F(\epsilon_2) \\
&\quad - \frac{1}{\pi^3} \sum_{\alpha\gamma} \int d\epsilon_1 \int d\epsilon_2 \int d\epsilon_3 \mathcal{P} \left(\frac{G''_{\alpha\gamma}(\mathbf{p}, \epsilon_1)}{\epsilon_1 - (\epsilon_3 \mp \omega)} \right) \mathcal{P} \left(\frac{G''_{\alpha\delta}(\mathbf{p}, \epsilon_2)}{\epsilon_2 - (\epsilon_3 \mp \omega)} \right) G''_{\gamma\delta}(\mathbf{p}, \epsilon_3) n_F(\epsilon_3) \\
&\quad + \frac{1}{\pi} \sum_{\alpha\gamma} \int d\epsilon_1 \int d\epsilon_2 \int d\epsilon_3 G''_{\alpha\gamma}(\mathbf{p}, \epsilon_1) G''_{\alpha\delta}(\mathbf{p}, \epsilon_2) G''_{\gamma\delta}(\mathbf{p}, \epsilon_3) \delta(\epsilon_1 - (\epsilon_3 \mp \omega)) \delta(\epsilon_2 - (\epsilon_3 \mp \omega)) n_F(\epsilon_3)
\end{aligned} \quad (\text{E.13})$$

Remembering the Kramers-Kronig relation

$$G'_{\alpha\gamma}(\mathbf{p}, \epsilon) = \frac{1}{\pi} \mathcal{P} \int_{-\infty}^{\infty} \frac{G''_{\alpha\gamma}(\mathbf{p}, \epsilon')}{\epsilon' - \epsilon} d\epsilon' \quad (\text{E.14})$$

we find

$$\begin{aligned}
\Pi^\pm(\mathbf{p}, \omega) = & -\frac{1}{\pi} \sum_{\alpha\gamma} \int d\epsilon_1 G''_{\alpha\gamma}(\mathbf{p}, \epsilon_1) G'_{\alpha\delta}(\mathbf{p}, \epsilon_1) G'_{\gamma\delta}(\mathbf{p}, \epsilon_1 \pm \omega) n_F(\epsilon_1) \\
& -\frac{1}{\pi} \sum_{\alpha\gamma} \int d\epsilon_2 G'_{\alpha\gamma}(\mathbf{p}, \epsilon_2) G''_{\alpha\delta}(\mathbf{p}, \epsilon_2) G'_{\gamma\delta}(\mathbf{p}, \epsilon_2 \pm \omega) n_F(\epsilon_2) \\
& -\frac{1}{\pi} \sum_{\alpha\gamma} \int d\epsilon_3 G'_{\alpha\gamma}(\mathbf{p}, \epsilon_3 \mp \omega) G'_{\alpha\delta}(\mathbf{p}, \epsilon_3 \mp \omega) G''_{\gamma\delta}(\mathbf{p}, \epsilon_3) n_F(\epsilon_3) \\
& +\frac{1}{\pi} \sum_{\alpha\gamma} \int d\epsilon_3 G''_{\alpha\gamma}(\mathbf{p}, \epsilon_3 \mp \omega) G''_{\alpha\delta}(\mathbf{p}, \epsilon_3 \mp \omega) G''_{\gamma\delta}(\mathbf{p}, \epsilon_3) n_F(\epsilon_3) \quad (\text{E.15})
\end{aligned}$$

Shifting the ϵ_3 integration in the third and fourth term we arrive at

$$\begin{aligned}
\Pi_{\mathbf{p}m\delta}^\pm(\mathbf{p}, \omega) = & -\frac{1}{\pi} \sum_{\alpha\gamma} \int d\epsilon G'_{\alpha\gamma}(\mathbf{p}, \epsilon) G''_{\alpha\delta}(\mathbf{p}, \epsilon) G'_{\gamma\delta}(\mathbf{p}, \epsilon \pm \omega) n_F(\epsilon) \\
& -\frac{1}{\pi} \sum_{\alpha\gamma} \int d\epsilon G''_{\alpha\gamma}(\mathbf{p}, \epsilon) G'_{\alpha\delta}(\mathbf{p}, \epsilon) G'_{\gamma\delta}(\mathbf{p}, \epsilon \pm \omega) n_F(\epsilon) \\
& -\frac{1}{\pi} \sum_{\alpha\gamma} \int d\epsilon G'_{\alpha\gamma}(\mathbf{p}, \epsilon) G'_{\alpha\delta}(\mathbf{p}, \epsilon) G''_{\gamma\delta}(\mathbf{p}, \epsilon \pm \omega) n_F(\epsilon \pm \omega) \\
& +\frac{1}{\pi} \sum_{\alpha\gamma} \int d\epsilon G''_{\alpha\gamma}(\mathbf{p}, \epsilon) G''_{\alpha\delta}(\mathbf{p}, \epsilon) G''_{\gamma\delta}(\mathbf{p}, \epsilon \pm \omega) n_F(\epsilon \pm \omega) \quad (\text{E.16})
\end{aligned}$$

In the static limit we find

$$\begin{aligned}
\lim_{\omega \rightarrow 0} \Pi_{\mathbf{p}m\delta}^H(\mathbf{p}, \omega) = & -\frac{1}{\pi} \sum_{\alpha\gamma} \int d\epsilon G'_{\alpha\gamma}(\mathbf{p}, \epsilon) G''_{\alpha\delta}(\mathbf{p}, \epsilon) \frac{d}{d\epsilon} G'_{\gamma\delta}(\mathbf{p}, \epsilon) n_F(\epsilon) \\
& -\frac{1}{\pi} \sum_{\alpha\gamma} \int d\epsilon G''_{\alpha\gamma}(\mathbf{p}, \epsilon) G'_{\alpha\delta}(\mathbf{p}, \epsilon) \frac{d}{d\epsilon} G'_{\gamma\delta}(\mathbf{p}, \epsilon) n_F(\epsilon) \\
& -\frac{1}{\pi} \sum_{\alpha\gamma} \int d\epsilon G'_{\alpha\gamma}(\mathbf{p}, \epsilon) G'_{\alpha\delta}(\mathbf{p}, \epsilon) G''_{\gamma\delta}(\mathbf{p}, \epsilon) \frac{d}{d\epsilon} n_F(\epsilon) \\
& +\frac{1}{\pi} \sum_{\alpha\gamma} \int d\epsilon G''_{\alpha\gamma}(\mathbf{p}, \epsilon) G''_{\alpha\delta}(\mathbf{p}, \epsilon) G''_{\gamma\delta}(\mathbf{p}, \epsilon) \frac{d}{d\epsilon} n_F(\epsilon) \\
& -\frac{1}{\pi} \sum_{\alpha\gamma} \int d\epsilon G'_{\alpha\gamma}(\mathbf{p}, \epsilon) G'_{\alpha\delta}(\mathbf{p}, \epsilon) \frac{d}{d\epsilon} G''_{\gamma\delta}(\mathbf{p}, \epsilon) n_F(\epsilon) \\
& +\frac{1}{\pi} \sum_{\alpha\gamma} \int d\epsilon G''_{\alpha\gamma}(\mathbf{p}, \epsilon) G''_{\alpha\delta}(\mathbf{p}, \epsilon) \frac{d}{d\epsilon} G''_{\gamma\delta}(\mathbf{p}, \epsilon) n_F(\epsilon) \quad (\text{E.17})
\end{aligned}$$

Partial integration in the first term

$$\begin{aligned}
\Pi_{\mathbf{p}m\delta}^H(\mathbf{p}, \omega) = & + \frac{1}{\pi} \sum_{\alpha\gamma} \int d\epsilon \frac{d}{d\epsilon} G'_{\alpha\gamma}(\mathbf{p}, \epsilon) G''_{\alpha\delta}(\mathbf{p}, \epsilon) G'_{\gamma\delta}(\mathbf{p}, \epsilon) n_F(\epsilon) \\
& + \frac{1}{\pi} \sum_{\alpha\gamma} \int d\epsilon G'_{\alpha\gamma}(\mathbf{p}, \epsilon) \frac{d}{d\epsilon} G''_{\alpha\delta}(\mathbf{p}, \epsilon) G'_{\gamma\delta}(\mathbf{p}, \epsilon) n_F(\epsilon) \\
& + \frac{1}{\pi} \sum_{\alpha\gamma} \int d\epsilon G'_{\alpha\gamma}(\mathbf{p}, \epsilon) G''_{\alpha\delta}(\mathbf{p}, \epsilon) G'_{\gamma\delta}(\mathbf{p}, \epsilon) \frac{d}{d\epsilon} n_F(\epsilon) \\
& - \frac{1}{\pi} \sum_{\alpha\gamma} \int d\epsilon G''_{\alpha\gamma}(\mathbf{p}, \epsilon) G'_{\alpha\delta}(\mathbf{p}, \epsilon) \frac{d}{d\epsilon} G'_{\gamma\delta}(\mathbf{p}, \epsilon) n_F(\epsilon) \\
& - \frac{1}{\pi} \sum_{\alpha\gamma} \int d\epsilon G'_{\alpha\gamma}(\mathbf{p}, \epsilon) G'_{\alpha\delta}(\mathbf{p}, \epsilon) G''_{\gamma\delta}(\mathbf{p}, \epsilon) \frac{d}{d\epsilon} n_F(\epsilon) \\
& + \frac{1}{\pi} \sum_{\alpha\gamma} \int d\epsilon G''_{\alpha\gamma}(\mathbf{p}, \epsilon) G''_{\alpha\delta}(\mathbf{p}, \epsilon) G''_{\gamma\delta}(\mathbf{p}, \epsilon) \frac{d}{d\epsilon} n_F(\epsilon) \\
& - \frac{1}{\pi} \sum_{\alpha\gamma} \int d\epsilon G'_{\alpha\gamma}(\mathbf{p}, \epsilon) G'_{\alpha\delta}(\mathbf{p}, \epsilon) \frac{d}{d\epsilon} G''_{\gamma\delta}(\mathbf{p}, \epsilon) n_F(\epsilon) \\
& + \frac{1}{\pi} \sum_{\alpha\gamma} \int d\epsilon G''_{\alpha\gamma}(\mathbf{p}, \epsilon) G''_{\alpha\delta}(\mathbf{p}, \epsilon) \frac{d}{d\epsilon} G''_{\gamma\delta}(\mathbf{p}, \epsilon) n_F(\epsilon) \tag{E.18}
\end{aligned}$$

Under sum $\sum_{\alpha\gamma}$ one may relabel α and γ which leads to a “transposition of the second and third column”. We see that the second and seventh term and the third and fifth term cancel and finally arrive at

$$\begin{aligned}
\Pi_{\mathbf{p}m\delta}^H(\mathbf{p}, \omega) = & + \frac{1}{\pi} \sum_{\alpha\gamma} \int d\epsilon \frac{d}{d\epsilon} G'_{\alpha\gamma}(\mathbf{p}, \epsilon) G''_{\alpha\delta}(\mathbf{p}, \epsilon) G'_{\gamma\delta}(\mathbf{p}, \epsilon) n_F(\epsilon) \\
& - \frac{1}{\pi} \sum_{\alpha\gamma} \int d\epsilon G''_{\alpha\gamma}(\mathbf{p}, \epsilon) G'_{\alpha\delta}(\mathbf{p}, \epsilon) \frac{d}{d\epsilon} G'_{\gamma\delta}(\mathbf{p}, \epsilon) n_F(\epsilon) \\
& + \frac{1}{\pi} \sum_{\alpha\gamma} \int d\epsilon G''_{\alpha\gamma}(\mathbf{p}, \epsilon) G''_{\alpha\delta}(\mathbf{p}, \epsilon) G''_{\gamma\delta}(\mathbf{p}, \epsilon) \frac{d}{d\epsilon} n_F(\epsilon) \\
& + \frac{1}{\pi} \sum_{\alpha\gamma} \int d\epsilon G''_{\alpha\gamma}(\mathbf{p}, \epsilon) G''_{\alpha\delta}(\mathbf{p}, \epsilon) \frac{d}{d\epsilon} G''_{\gamma\delta}(\mathbf{p}, \epsilon) n_F(\epsilon) \tag{E.19}
\end{aligned}$$

Appendix F

Approximate expressions for various densities of states

Rather than using the exact expressions for the densities of states, we will derive here approximate expressions. The reason is simple: the exact expressions are expensive to evaluate and as DMFT is a theory which is concerned with local quantities, we have to perform \mathbf{k} -sums quite regularly. Here we will use an approach similar to the one Uhrig [109] used for the three dimensional density of states: Based on our knowledge about the asymptotics of the exact expression, we will make an appropriate ansatz and fix the parameters by demanding that the first non-trivial moments of the distributions coincide.

The two-dimensional density of states of a tight-binding hamiltonian on a hyper-cubic lattice is given by

$$\rho^{2D}(\epsilon) = \frac{1}{2\pi^2 t a^2} \mathbb{K} \left(\sqrt{1 - \frac{\epsilon^2}{(4t)^2}} \right) \quad (\text{F.1})$$

where a is the lattice constant, t the hopping amplitude and \mathbb{K} is related to the complete elliptic integral of the first kind. Closer examination of the function reveals a peak at $\epsilon = 0$. Our aim will be to find the nature of this peak. Elliptic integrals are classically defined as integrals of the form

$$\int r(x, y(x)) dx \quad (\text{F.2})$$

where r is a rational function of x and y , and y^2 is a cubic or quartic polynomial in x . If y^2 is linear or quadratic in x , then the integral can be evaluated using logarithms and rational functions of x and y , but if y^2 is cubic or quartic then the integral is said to be elliptic and is not in general expressible in terms of elementary functions [42].

Legendre showed that only three non-elementary functions are needed to express all elliptic integrals. The one we are concerned with in the case above is

$$R_F(x, y, z) = \frac{1}{2} \int_0^\infty \frac{1}{\sqrt{(x+t)(y+t)(z+t)}} dt \quad (\text{F.3})$$

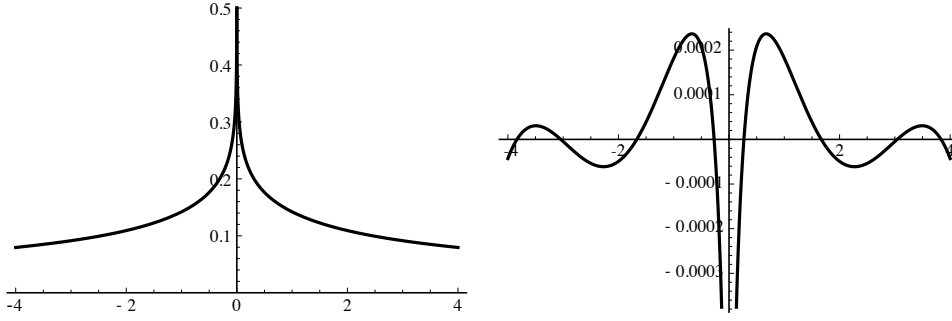


Figure F.1: (a) $D(\epsilon)$, (b) $\rho^{2D}(\epsilon) - D(\epsilon)$

The function $R_F(x, y, z)$ which is symmetric in x, y and z is called the elliptic integral of the first kind. The definition of the complete elliptic integral of the first kind is

$$R_K(x, y) = \frac{1}{\pi} \int_0^\infty \frac{1}{\sqrt{t(x+t)(y+t)}} dt \quad (\text{F.4})$$

which are related via

$$R_K(x, y) = \frac{2}{\pi} R_F(x, y, 0) \quad (\text{F.5})$$

The function $\mathbb{K}(k)$ in formula F.1 is related to $R_K(x, y)$

$$\mathbb{K}(k) = \frac{\pi}{2} R_K(1, 1 - k^2) \quad (\text{F.6})$$

Gustafson[42] derived asymptotic expressions for the elliptic integrals and we can make use of his result

$$\lim_{y \rightarrow 0^+} R_K(x, y) = \frac{1}{\pi} x^{-\frac{1}{2}} \log \left(\frac{16x}{y} \right) \quad (\text{F.7})$$

We find that

$$\rho^{2D}(\epsilon) = \frac{1}{4\pi^2 t a^2} R_K \left(1, \frac{\epsilon^2}{(4y)^2} \right) \quad (\text{F.8})$$

$$\stackrel{\epsilon \ll 1}{\approx} \frac{1}{4\pi^2 t a^2} \log \left(\frac{(16t)^2}{\epsilon^2} \right) \quad (\text{F.9})$$

This insight might motivate the following ansatz for the density of states

$$D(\epsilon) = -\frac{1}{4\pi^2 t a^2} \log(\epsilon^2) + m_0 + m_2 \epsilon^2 + m_4 \epsilon^4 \quad (\text{F.10})$$

Demanding that the first zeroth, second and fourth moment coincide we arrive at Table F.1. In order to calculate the various response functions to electromagnetic fields evaluations of momentum sums are needed. Typically one evaluates such a sum by noting that the summand depends only through the dispersion relation on momentum and rewriting the sum as an energy integration weight by a density of

m_0	0.141458
m_2	0.000646212
m_4	-0.0000115157

Table F.1: Fit parameters

states (DOS). This is the numerically most feasible way to evaluate such sums and multi-dimensional integration is always costly.

In the calculation of optical conductivities the situation is a little more involved as one usually finds the summand to be dependent on the dispersion relation as well as partial derivatives of the dispersion with respect to different components of the momenta. Here we will deduce different “transport DOS” to ease the calculation of such sums.

Transport density of states for the ordinary conductivity

Let us start with the following type of sum

$$\sum_{\mathbf{p}} \left(\frac{\partial \epsilon_{\mathbf{p}}}{\partial \mathbf{p}_x} \right)^2 f(\epsilon_{\mathbf{p}}) \quad (\text{F.11})$$

In order to evaluate this sum let define the following DOS

$$\rho^{xx}(\epsilon) = \frac{1}{(2\pi)^2} \int dk_x \int dk_y \left(\frac{\partial \epsilon_{\mathbf{p}}}{\partial \mathbf{p}_x} \right)^2 \delta(\epsilon - \epsilon_{\mathbf{p}}) \quad (\text{F.12})$$

where $i \in \{1 \dots N\}$. Noting that

$$\frac{d}{d\epsilon} \delta(\epsilon - \epsilon_{\mathbf{p}}) = - \left(\frac{\partial \epsilon_{\mathbf{p}}}{\partial \mathbf{p}_i} \right)^{-1} \frac{\partial}{\partial \mathbf{p}_i} \delta(\epsilon - \epsilon_{\mathbf{p}}) \quad (\text{F.13})$$

In the last line we have assumed symmetry of the density of states with respect to the different components of the momentum vector. We find

$$\frac{d\rho^{xx}(\epsilon)}{d\epsilon} = \frac{1}{(2\pi)^2} \int dk_x \int dk_y \left(\frac{\partial \epsilon_{\mathbf{p}}}{\partial \mathbf{p}_x} \right)^2 \frac{d}{d\epsilon} \delta(\epsilon - \epsilon_{\mathbf{p}}) \quad (\text{F.14})$$

$$= -\frac{1}{2} \int dk_x \int dk_y \sum_{i=1}^2 \frac{\partial \epsilon_{\mathbf{p}}}{\partial \mathbf{p}_i} \frac{\partial}{\partial \mathbf{p}_i} \delta(\epsilon - \epsilon_{\mathbf{p}}) \quad (\text{F.15})$$

$$= \frac{1}{2} \frac{1}{(2\pi)^2} \int dk_x \int dk_y \sum_{i=1}^2 \frac{\partial^2 \epsilon_{\mathbf{p}}}{\partial \mathbf{p}_i^2} \delta(\epsilon - \epsilon_{\mathbf{p}}) \quad (\text{F.16})$$

Assuming a hypercubic lattice $\sum_{i=1}^N \frac{\partial^2 \epsilon_{\mathbf{p}}}{\partial \mathbf{p}_i^2} = -\epsilon_{\mathbf{p}}$ and therefore

$$\frac{d\rho^{xx}(\epsilon)}{d\epsilon} = -\frac{\epsilon}{2} \rho(\epsilon) \quad (\text{F.17})$$

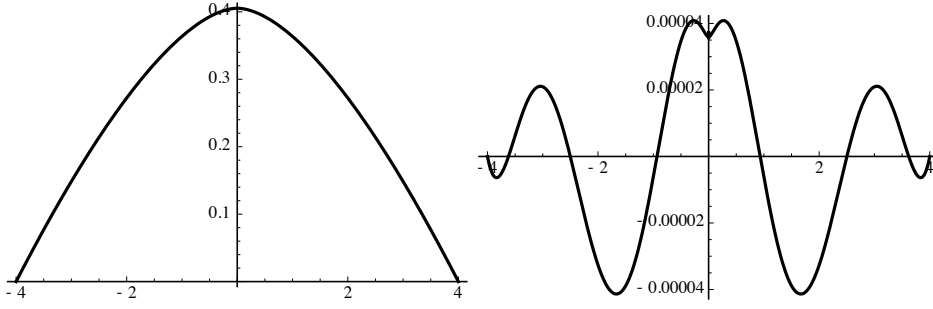


Figure F.2: (a) $D^{xx}(\epsilon)$, (b) $\rho^{xx}(\epsilon) - D^{xx}(\epsilon)$

We can make use of the approximate DOS $D(\epsilon)$ we found above to derive an approximate expression for $\rho^{xx}(\epsilon)$

$$D^{xx}(\epsilon) = -\frac{\epsilon^2 (3 + 2a^2\pi^2t(6m_0 + 3m_2\epsilon^2 + 2m_4\epsilon^4)) - 3\log(\epsilon^2)}{48a^2\pi^2t} \quad (\text{F.18})$$

Transport density of states for the Hall conductivity

For the calculation of the Hall conductivity we need to evaluate sums of the form

$$\sum_{\mathbf{p}} \left(\frac{\partial \epsilon_{\mathbf{p}}}{\partial \mathbf{p}_x} \right)^2 \left(\frac{\partial^2 \epsilon_{\mathbf{p}}}{\partial \mathbf{p}_y^2} \right) f(\epsilon_{\mathbf{p}}) \quad (\text{F.19})$$

with f some arbitrary function. Therefore we will define the following density of states

$$\rho^{xy}(\epsilon) = \frac{1}{(2\pi)^N} \int dk_1 \dots \int dk_N \left(\frac{\partial \epsilon_{\mathbf{p}}}{\partial \mathbf{p}_x} \right)^2 \left(\frac{\partial^2 \epsilon_{\mathbf{p}}}{\partial \mathbf{p}_y^2} \right) \delta(\epsilon - \epsilon_{\mathbf{p}}) \quad (\text{F.20})$$

Using eq. F.13 we find

$$\frac{d}{d\epsilon} \rho^{xy}(\epsilon) = \frac{1}{(2\pi)^2} \int dk_x \int dk_y \left(\frac{\partial^2 \epsilon_{\mathbf{p}}}{\partial \mathbf{p}_x^2} \right) \left(\frac{\partial^2 \epsilon_{\mathbf{p}}}{\partial \mathbf{p}_y^2} \right) \delta(\epsilon - \epsilon_{\mathbf{p}}) \quad (\text{F.21})$$

Again assuming a hypercubic dispersion relation we have

$$\epsilon_k^2 = 4t^2 (\cos(k_x)^2 + \cos(k_y)^2 + 2\cos(k_x)\cos(k_y)) \quad (\text{F.22})$$

therefore

$$\left(\frac{\partial^2 \epsilon_{\mathbf{p}}}{\partial \mathbf{p}_x^2} \right) \left(\frac{\partial^2 \epsilon_{\mathbf{p}}}{\partial \mathbf{p}_y^2} \right) = \frac{1}{2} \epsilon_k^2 - 4t^2 + \frac{1}{2} \left(\frac{\partial \epsilon_{\mathbf{p}}}{\partial \mathbf{p}_x} \right)^2 + \frac{1}{2} \left(\frac{\partial \epsilon_{\mathbf{p}}}{\partial \mathbf{p}_y} \right)^2 \quad (\text{F.23})$$

We can now plug this into our expression for $\rho^{xy}(\epsilon)$ and find

$$\frac{d}{d\epsilon} \rho^{xy}(\epsilon) = \left(\frac{1}{2} \epsilon^2 - 4t^2 \right) \rho(\epsilon) + \rho^{xx}(\epsilon) \quad (\text{F.24})$$

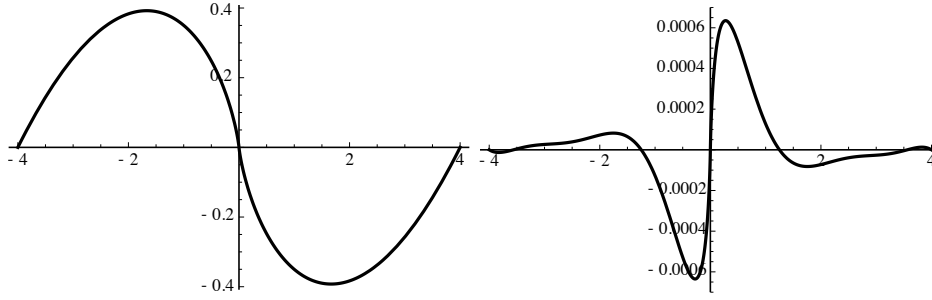


Figure F.3: (a) $D^{xy}(\epsilon)$, (b) $\rho^{xy}(\epsilon) - D^{xy}(\epsilon)$

Using our approximate expression for $\rho(\epsilon)$ and $\rho^{xx}(\epsilon)$ we find

$$\begin{aligned}
 D^{xy}(\epsilon) = & -2t \left(\frac{1}{\pi^2} + 2m_0 t \right) \epsilon + \frac{1}{144} \left(12m_0 - \frac{1}{\pi^2 t} - 192m_2 t^2 \right) \epsilon^3 \\
 & + \frac{1}{40} (3m_2 - 32m_4 t^2) \epsilon^5 + \frac{5}{84} m_4 \epsilon^7 - \frac{\epsilon^2 - 48t^2}{48\pi^2 t} \epsilon \log(\epsilon^2) \quad (\text{F.25})
 \end{aligned}$$

Acknowledgments

First of all, I would like to thank my thesis supervisor Prof. Dr. Achim Rosch for many invaluable discussions and elucidations, for his guidance and support. Working with him has been a pleasure, both on a scientific but also on a personal level. His genuine enthusiasm for physics is highly contagious and leaves one infected with a deeply-rooted admiration for physics. I am also very grateful to PD Dr. Ralf Bulla for his supervision of the numerical renormalisation group implementation and many questions regarding the DMFT. Only his patience and insightful advice have made the implementation of the algorithms such a pleasure. I thank PD Dr. Markus Garst for many insightful explanations and interesting discussions. It has been a pleasure to work with him on the Skyrmion mass project.

Similarly, I am indebted to Prof. Dr. Naoto Nagaosa, with whom I had the honor to work with and who welcomed me during three months at the University of Tokyo. I would also like to acknowledge the great hospitality and very inspiring atmosphere both at the Department of Applied Physics, University of Tokyo, and the Correlated Electron Research Group (CERG) at the RIKEN Advanced Science Institute. I would also like to thank Masahito Mochizuki, Takashi Oka and Junichi Iwasaki for many insightful discussions and Tae Tokuyoshi for organizing my accomodation and the uncounted translations of very important documents. My time in Tokyo was definitely one of the highlights of my PhD, and I believe also an important opportunity for personal development. Related to that, I am also grateful for the financial support of the Bonn-Cologne graduate school of Physics and Astronomy (BCGS) for the financial support. Similarly, I would like to acknowledge the support of the Quantum Matter and Materials (QM2) cluster.

Throughout my PhD I had the pleasure to share my time with many great colleagues. I am grateful to Akos, Adel, Alex, Andrew, Benjamin, Carolin, David, Dmitry, Eran, Etienne, Fanny, Johanna, Johannes, Jonathan, Karen, Karin, Kevin, Koos, Lars, Lucas, Maria, Mario, Mascha, Matthias, Max, Maximilian, Michael, Pascal, Peter, Robert, Stefan, Stefan ans Stephan. A big thank you also to Andreas Sindermann and Dr. Stefan Borowski for

competent advice on computing related questions and keeping the HPC infrastructure running that I relied on so heavily. Thanks to Yasemin Tieben, Claudia Herrmann and D. Hochscheid from the administrative staff. Last but not least, my thanks go to all of my friends, to my family and especially to Ramona, who always supported me.

Erklärung

Ich versichere, dass ich die von mir vorgelegte Dissertation selbständig angefertigt, die benutzten Quellen und Hilfsmittel vollständig angegeben und die Stellen der Arbeit - einschließlich Tabellen, Karten und Abbildungen -, die anderen Werken im Wortlaut oder dem Sinn nach entnommen sind, in jedem Einzelfall als Entlehnung kenntlich gemacht habe; dass diese Dissertation noch keiner anderen Fakultät oder Universität zur Prüfung vorgelegen hat; dass sie - abgesehen von unten angegebenen Teilpublikationen - noch nicht veröffentlicht worden ist sowie, dass ich eine solche Veröffentlichung vor Abschluss des Promotionsverfahrens nicht vornehmen werde. Die Bestimmungen der Promotionsordnung sind mir bekannt. Die von mir vorgelegte Dissertation ist von Prof. Dr. Achim Rosch betreut worden.

Teilpublikationen

- P. Milde, D. Köhler, J. Seidel, L. M. Eng, A. Bauer, A. Chacon, J. Kindervater, S. Mhlbauer, C. Pfeiderer, S. Buhrandt, C. Schütte, A. Rosch; *Unwinding of a Skyrmion Lattice by Magnetic Monopoles*, Science 340(6136):1076-1080, 2013.



Christoph Schütte

Lebenslauf

Persönliche Daten

Name Christoph Schütte
Geburtsdatum 1.11.1982
Geburtsort Köln
Familienstand ledig
Nationalität deutsch

Schulbildung

1988-1992 Katholische Grundschule am Kronenpützchen, Dormagen
1992-2002 Norbert Gymnasium Knechtede, Dormagen
Juni 2002 Abitur

Anderer Dienst im Ausland

2002-2003 First Contact Place, Ashaiman, Ghana

Hochschulstudium

2003-2006 Studium der Mathematik an der Universität zu Köln
2003-2009 Studium der Physik an der Universität zu Köln
03/2006 Vordiplom in Physik und Vordiplom in Mathematik
2004-2012 Stipendiat der Studienstiftung des deutschen Volkes
2007-2012 Mitglied der Bonn-Cologne-Graduate School
09/2009 Diplom in Physik
2010-2014 Promotionsstudium am Institut für theoretische Physik der Universität zu Köln
02-05/2013 Forschungsaufenthalt in der Arbeitsgruppe von Herrn Prof. Nagaosa an der Universität von Tokio

Arbeitsverhältnisse

2005-2007 Studentische Hilfskraft am Institut für theoretische Physik der Universität zu Köln
2007-2008 Software Entwickler am Max-Planck Institut für neurologische Forschung
2008-2009 Studentische Hilfskraft am Max-Planck Institut für neurologische Forschung
2009-2014 Wissenschaftliche Hilfskraft am Institut für theoretische Physik der Universität zu Köln